



HAL
open science

Magnetocaloric materials for magnetic refrigeration at room temperature

Xueying Hai

► **To cite this version:**

Xueying Hai. Magnetocaloric materials for magnetic refrigeration at room temperature. Thermics [physics.class-ph]. Université Grenoble Alpes, 2016. English. NNT : 2016GREAY073 . tel-01597585

HAL Id: tel-01597585

<https://theses.hal.science/tel-01597585>

Submitted on 28 Sep 2017

HAL is a multi-disciplinary open access archive for the deposit and dissemination of scientific research documents, whether they are published or not. The documents may come from teaching and research institutions in France or abroad, or from public or private research centers.

L'archive ouverte pluridisciplinaire **HAL**, est destinée au dépôt et à la diffusion de documents scientifiques de niveau recherche, publiés ou non, émanant des établissements d'enseignement et de recherche français ou étrangers, des laboratoires publics ou privés.

THÈSE

Pour obtenir le grade de

DOCTEUR DE LA COMMUNAUTÉ UNIVERSITÉ GRENOBLE ALPES

Spécialité : **Physique des Matériaux**

Arrêté ministériel : 7 août 2006

Présentée par

Xueying HAI 海雪莹

Thèse dirigée par **Salvatore MIRAGLIA** et co-encadrée par
Charlotte MAYER

préparée au sein de l'**Institut Néel, CNRS, Grenoble** dans
l'École Doctorale de Physique

Financée par l'ANRT et Erasteel SAS sous projet CIFRE
N°2013/0827

Matériaux magnéto-caloriques pour la réfrigération à température ambiante

Thèse soutenue publiquement le **24 novembre, 2016**,
devant le jury composé de :

M. Olivier ISNARD

Professeur, Université Grenoble Alpes, Grenoble, Président

Mme. Valérie PAUL-BONCOUR

Directrice de Recherche, CNRS-ICMPE, Thiais, Rapportrice

Mme. Florence PORCHER

Chercheuse, CEA-LLB, Gif-sur-Yvette, Rapportrice

Mme. Sophie TENCE

Chargée de Recherche, CNRS-ICMCB, Bordeaux, Examinatrice

M. Salvatore Miraglia

Directeur de Recherche, CNRS-Institut Néel, Grenoble, Membre

Mme. Charlotte MAYER

Ingénieure de Recherche, Erasteel SAS, Paris, Membre



THÈSE

Pour obtenir le grade de

DOCTEUR DE LA COMMUNAUTÉ UNIVERSITÉ GRENOBLE ALPES

Spécialité : **Physique des Matériaux**

Arrêté ministériel : 7 août 2006

Présentée par

Xueying HAI 海雪莹

Thèse dirigée par **Salvatore MIRAGLIA** et co-encadrée par
Charlotte MAYER

préparée au sein de l'**Institut Néel, CNRS, Grenoble** dans
l'École Doctorale de Physique

Financée par l'ANRT et Erasteel SAS sous projet CIFRE
N°2013/0827

Matériaux magnétocaloriques pour la réfrigération à température ambiante

Thèse soutenue publiquement le **24 novembre, 2016**,
devant le jury composé de :

M. Olivier ISNARD

Professeur, Université Grenoble Alpes, Grenoble, Président

Mme. Valérie PAUL-BONCOUR

Directrice de Recherche, CNRS-ICMPE, Thiais, Rapportrice

Mme. Florence PORCHER

Chercheuse, CEA-LLB, Gif-sur-Yvette, Rapportrice

Mme. Sophie TENCE

Chargée de Recherche, CNRS-ICMCB, Bordeaux, Examinatrice

M. Salvatore Miraglia

Directeur de Recherche, CNRS-Institut Néel, Grenoble, Membre

Mme. Charlotte MAYER

Ingénieure de Recherche, Erasteel SAS, Paris, Membre



Preface page

This thesis is submitted in partial fulfillment of the requirements for obtaining the degree of Ph.D. at the Grenoble Alpes University (UGA). The thesis work was carried out from December 2013 to November 2016 at the Néel Institute, which is part of the French National Centre for Scientific Research (CNRS). Financial support is provided by a grant (CIFRE N°2013/0827) from the National Association of Research and Technology (ANRT). The thesis work is an Industrial Training through Research (CIFRE) project in partnership with Erasteel S.A.S., an ERAMET branch.

Grenoble November 2016

Xueying Hai

Copyright © Xueying Hai, 2016. All rights reserved.

To my parents

给我的父亲母亲

Acknowledgements

This thesis work could not have been possible without the help of so many colleagues and friends! I am extremely grateful for working on this innovative project.

First and foremost, I would like to thank the director the Néel Institute to welcome me in this laboratory. In fact, with the changes in organization during my thesis, I would like to thank the three directors in these years, Alain Schuhl, Hervé Courtois, and Etienne Bustarret. I have been very well integrated in the laboratory and have been able to do my work with all the help I can get.

The constitution of the CIFRE project has made the financial support of this thesis possible, I would like to thank the director of the R&D department of Erasteel, an ERAMET branch, Serge Sella, for recruiting me and giving me useful suggestions from time to time. I appreciate the exchanges with Peter Vikner and Michel Pierronnet. I would like to thank all the administrative staff at Erasteel who have accompanied me through these years. I appreciate their understanding and support.

I would like to express my sincere gratitude and appreciation for my supervisors, Salvatore Miraglia and Charlotte Mayer. They have not only guided me in my everyday work but also shared with me anecdotes, jokes, and life lessons. Salvatore has been extremely helpful in terms of not only physics but also facilitating administrative procedures in every way he can. I appreciate Charlotte for making her monthly travel to meet with us to discuss the project and for teaching me so much insight on working in the private sector without reservation. I appreciate their patience and diligence in reading and correction of my manuscript. For all this, I could not have been more grateful to have very understanding and humane supervisors, who have made working with them extremely easy and delightful.

I have been able to exercise in diverse experiments thanks to all the researchers, technicians, and engineers in the laboratory.

I would like to acknowledge Cécile Berne, who has initiated me with different experimental techniques and has taught me so many things since the beginning! It was always a pleasure to discuss with her about life, wine, having an organic life, etc., always something new to learn!

I thank Claire Colin for her dedication as local contact at the ILL, for her help in resolving the magnetic structure in neutron data, and for making herself available in general. I thank Vivian Nassif and Sofian Djellit for helping me with the neutron diffraction experiment. I would like to express my appreciation for Florence Porcher for her expertise and help in the neutron experiments at LLB and in the data interpretation. I am grateful for the French CRG project for making it possible to have access to neutron facilities during my thesis.

For the preparation of samples, I would like to express my sincere appreciation for Paul Chômeton, Arnaud Quillery, Jérôme Debray, and Sébastien Pairis. I thank Muriel Legendre for her help and time in the annealing process. Special thanks to Philippe Plaindoux, for his expertise in metallurgy, who has helped me in so many ways in different thermal experiments (DSC/DTA) and melt-spinning techniques. Special thanks to Richard Raettel, who is always in good mood and speaks with an open mind, has trained me in the melting

and related techniques. His workshop is always well organized and I can always find help whenever needed.

I would like to thank the help and guidance of Pierre Bordet, Daniel Bourgault, Patricia Derango, Marine Liotaud, Sophie Rivoirard, Remy Bruyère, Didier Dufeu, Yves Deschanel, Christophe Bouchard, Frédéric Gay, and Emmanuel Verloop. I thank Lilian De-Coster and Florence Fernandez for helping me with organizing the reception after my defense.

How can I forget all my fellow doctorate students, post-docs, and interns for the moral support, the encouragement at the most difficult times, and the days and nights we spent together? Special thanks to Pauline, Elodie, Céline, Mériam, Khalil and Justin, who have also defended their thesis or about to this year. It seems like we have grown up together during these three years. A big thank you to Cyril, Shridevi, Peng, Feng, Josephine, Arnaud, Nathaniel, (and Christophe, though not a student) and so many others who just started their projects at Néel. Thank you so much for making the wonderful graduation hat, I love it! I came into the laboratory thinking that I would only meet colleagues in a professional setting, but I am leaving now with friends! Who would have thought of that? Whether it is grabbing a drink, playing board games, going to restaurants, even to a wedding (!), or spending the day in the nature hiking, skiing, you have made my job fun.

At the same time, I would like to thank those who animate my life outside the laboratory: old and new friends from Grenoble, the US, and China.

I want to thank my parents for believing in me and supporting my decisions, no matter where it takes me. What a great effort they have made in flying all the way here to attend my defense and preparing the perfect reception. I would like to thank my lovely French family, the Scheids and the Maffres. I could not be happier that I was able to celebrate with all of them. Thank you Tristan for always making me smile and for venturing out on the future without hesitation. Thank you so much, Kate, for always being my kindred spirit across the ocean.

I would like to express my appreciation for my jury members. I have been so fortunate and proud to have a jury with a great female representation of the scientific committee. I would like to thank Mme. Valérie Paul-Boncour from ICMPE at Thiais and Mme. Florence Porcher from LLB at Gif sur Yvette to have accepted the task of being the reporters of my thesis. They have given me valuable suggestions and support in their reports and during my defense. I would like to thank Mme. Sophie Tencé from ICMCB at Bordeaux and M. Olivier Isnard, professor at Université Grenoble Alpes as the examiners of my work. Their expertise in magnetism and intermetallics was of great value in writing the final version of my manuscript.

So many thanks to my jury members who have put in effort to judge my work in order to give me the honor of a degree in Doctor of Materials Physics at Université Grenoble Alpes.

It is such a privilege to embark on this journey and to those who are about to begin this wonderful adventure of a thesis, I say “break the wind, ride the waves, and sail forward”.

Abstract:

The magnetocaloric effect (MCE) is characterized by a magnetic entropy change and an adiabatic temperature change. The NaZn₁₃-type La(Fe,Si)₁₃ system has attracted wide interest because of its first-order ferromagnetic phase transition with a large magnetocaloric effect. The transition temperature can be flexibly adjusted through substitution or interstitial insertion. Particularly, hydrogen interstitials can adapt the temperature range to room-temperature applications. Precise adjustment can be achieved by full hydrogen absorption then partial desorption. However, fully hydrogenated alloys are unstable upon heating. It is important to have a better understanding of its hydrogen stability to optimize its application potential.

In the first part, the structural, magnetic, and magnetocaloric properties of La(Fe,Si)₁₃ phases are studied. In particular, we have investigated the effect of substitution of Ce on the La site and Mn on the Fe sites. The partial substitution of Ce results in the decrease of T_C with decreasing lattice constant. At the same time, Ce substitution for La results in a reduced volume of the octahedral interstitial site due to steric effect. The interstitial insertion is impeded by Ce partial substitution.

Secondly, the effects of interstitial atoms such as hydrogen and carbon are examined. These elements are able to enter the interstitial voids in the La(Fe,Si)₁₃ phase, expanding the lattice. Through the extension of Fe-Fe distances, the Curie temperature of the magnetocaloric phase can be raised up to room temperature range. The influence of small concentration of carbon on the magnetic properties of samples is examined prior to hydrogenation and carbon content is optimized. In order to investigate the interstitial dynamics, the hydrogen sorption kinetics is studied by the means of Sieverts' volumetric method and neutron diffraction. Particular attention has been given to the adjustment of the structure in the course of hydrogen/deuterium interstitial absorption and desorption.

Steady-state and *in-situ* neutron diffractions provide precise information of the interstitial atom location of the sequential filling of the accommodating sites. The structural investigation allows specifying the deformations undergone in the complex metallic alloys La-Fe-Si when subjected to light interstitial insertion or rare earth substitution at the cation site. We show that the depression or enhancement of the hydrogenation kinetics may be related to the particular inhomogeneous cell variation of bonding in the structure. A mechanism for the diffusion path is suggested.

The mechanism is light atom insertion into the interstitial sites is not only strongly related to the available space for accommodation, but also associated with the facility of the diffusion path in the lattice. We demonstrate with experimental results that a modest addition of carbon in the La-Fe-Si phase prior to hydrogenation can effectively slow down the hydrogen insertion kinetics. In Ce-substituted La-Ce-Fe-Si phases, carbon insertion can help retain hydrogen atoms during desorption, therefore, offering a prospect to have improved stability of hydrogenated materials for long-term applications. The hydrogen stability of the material is examined by means of thermal desorption in DSC and an enhancement of the thermal stability of the material is achieved with carbon-doping.

Lastly, in the search of new rare-earth-free materials for magnetocaloric applications, we have explored the capacity of alloys of types Fe-Cr-Ni and Fe-Cr-Mn. The magnetic and structural transitions of these alloys of different compositions are studied and their potential for magnetocaloric application is examined in this thesis.

Keywords: magnetocaloric effect, intermetallic, light interstitial insertion, neutron diffraction, hydrogenation kinetics

Résumé :

La réfrigération magnétique, basée sur l'effet magnétocalorique (EMC), est une alternative intéressante aux méthodes de réfrigération traditionnelles, basées sur des cycles de compression/détente, car elle présente des rendements énergétiques nettement plus élevés et permet d'éviter l'utilisation de gaz nocifs contribuant à l'effet de serre et problématiques pour l'environnement. Cette technologie s'appuie sur l'EMC géant de certains matériaux magnétiques autour de la température ambiante. Cet effet permet d'augmenter ou de diminuer la température du matériau lors de son aimantation ou désaimantation adiabatique autour de sa température de transition magnétique.

La majeure partie des travaux de thèse se focalise sur la famille des matériaux de type $\text{La}(\text{Fe},\text{Si})_{13}$ dans lesquels un effet magnétocalorique géant a été mis en évidence et pour lesquels la faisabilité industrielle semble la plus favorable. Dans un premier temps, les propriétés structurales et magnétiques de ces alliages sont explorées et optimisées, en remplaçant aussi bien la terre rare que le métal de transition par d'autres éléments. Les méthodes d'élaboration, des traitements thermiques, ainsi que le contrôle de la stœchiométrie sont guidées par les caractérisations structurales, microstructurales, physiques (thermiques et magnétiques).

D'autre part, l'effet de l'insertion d'éléments interstitiels légers est également étudié et une grande partie du travail porte sur la détermination des conditions de stabilité de ces interstitiels dans les matériaux. Grâce à l'extension des distances Fe-Fe, la température de Curie de la phase magnétocalorique peut être augmentée jusqu'à des plages proches de la température ambiante. L'influence d'une faible concentration en carbone sur les propriétés magnétiques des échantillons est examinée avant hydrogénation et la teneur en carbone est optimisée.

Afin d'étudier la diffusion des éléments interstitiels, la cinétique de sorption d'hydrogène est étudiée par la méthode de Sieverts ainsi que par diffraction neutronique. La diffraction neutronique in situ et à haute résolution permet une localisation des atomes interstitiels et donne accès au schéma d'insertion. Cette étude permet de préciser l'effet de l'insertion d'interstitiels légers et des substitutions d'éléments de terre rare sur la structure des alliages métalliques complexes de type La-Fe-Si. Nous montrons que la dépression ou l'accélération de la cinétique d'hydrogénation peut être liée à la variation hétérogène particulière de la maille et des liaisons dans la structure de type NaZn_{13} . Un mécanisme pour le chemin de diffusion est suggéré.

Le mécanisme d'insertion d'atomes légers est non seulement fortement lié à l'espace disponible, mais aussi associés à la facilité du chemin de diffusion dans le réseau. Nous démontrons avec des résultats expérimentaux qu'une addition modérée de carbone dans la phase $\text{La}(\text{Fe},\text{Si})_{13}$ avant l'hydrogénation peut effectivement ralentir la cinétique d'insertion de l'hydrogène. Dans les phases La-Ce-Fe-Si, une insertion de carbone peut aider à retenir les atomes d'hydrogène lors de la désorption, par conséquent, offre une possibilité d'avoir une meilleure stabilité des matériaux hydrogénés pour des applications à long terme. La stabilité des matériaux hydrogénés est mesurée par DSC et une amélioration de la stabilité thermique du matériau est réalisée par un dopage au carbone.

Un volet exploratoire est consacré aux alliages Fe-Cr-Ni et Fe-Cr-Mn qui pourraient potentiellement avoir un effet magnétocalorique exploitable. Les transitions magnétiques et structurales de ces alliages de compositions différentes sont étudiées et leur potentiel d'application magnétocalorique est discuté.

Mots-clés : Effet magnétocalorique, intermétalliques, insertion des éléments interstitiels, diffraction des neutrons, cinétique d'hydrogénation

Table of Contents

General introduction	5
Chapter I. Magnetocaloric refrigeration and material: state of the Art	11
1. Context	11
1.1. Age of the energy trilemma.....	11
1.2. Alternative solution	12
2. General notions.....	13
2.1. From history to demonstration unit.....	14
2.2. Thermodynamic principles.....	17
2.3. Measurement of MCE	21
2.4. Magnetic transition order	22
2.5. Employment of Maxwell relation	25
3. Magnetic refrigerant selection	26
4. Introduction of the $\text{La}(\text{Fe},\text{Si})_{13}$ intermetallics	30
4.1. Structure characteristics	30
4.2. Magnetic properties.....	32
4.3. Magnetocaloric properties.....	34
4.4. Composition tuning	35
References	41
Chapter II. Experimental techniques	49
1. Synthesis.....	49
1.1. Materials.....	49
1.2. Arc melting.....	49
1.3. Electromagnetic induction melting	50
1.4. Annealing	51
1.5. Gas atomization.....	52
2. Characterization Tools.....	54
2.1. Structure determination	54
2.2. Magnetic measurements	60
2.3. Thermal measurements	63
2.4. Hydrogen dynamics.....	64
References	68

Chapter III. Studies on the composition optimization.....	71
1. Structural and metallographic study.....	71
1.1. Phase identification	71
1.2. Magnetic properties	74
1.3. Evaluation of the magnetocaloric effect	76
2. Effect of substitution	76
2.1. Substitution on the La site by Ce	76
2.2. Substitution on the Fe site.....	87
3. Process optimization	90
3.1. Microstructure.....	91
3.2. Structural properties.....	95
3.3. Magnetic and magnetocaloric properties	96
4. Conclusion.....	98
References	99
Chapter IV. Influence of interstitial elements	103
1. Overview of interstitial element insertion.....	103
2. Influence of hydrogen/deuterium	105
2.1. Neutron diffraction.....	106
2.2. Magnetic properties	112
2.3. Hydrogen instability.....	114
3. Influence of carbon interstitial	118
3.1. Synthesis conditions.....	118
3.2. Influence of carbon concentration	124
3.3. Effect of carbon interstitials in La-Fe-Si and La-Ce-Fe-Si.....	128
4. Conclusion.....	136
References	136
Chapter V. Hydrogen dynamics	143
1. Hydrogen sorption kinetics	143
1.1. Pressure-composition isotherms	143
1.2. Hydrogen kinetics	146
1.3. Effect of Si concentration	152
1.4. <i>In-situ</i> neutron diffraction	153
1.5. Evaluation of the stability	158
1.6. Discussion.....	159
2. Hydrogenation behavior with Ce substitution.....	160

2.1. <i>In-situ</i> Neutron diffraction	160
3. Hydrogenation behavior with C insertion	163
3.1. Effect of carbon insertion on La-Fe-Si.....	163
3.2. Effect of C insertion in Ce-substituted samples	174
4. Conclusion.....	181
References	184
Chapter VI. Phase transformation in Fe-based alloys for magnetocaloric applications....	187
1. Motivation	187
2. General notions.....	190
2.1. Alloying elements and microstructure	190
2.2. Experimental details.....	192
3. Fe-Cr-Ni system	193
3.1. Series Fe-Cr-Ni with 15 wt%Cr.....	195
3.2. Effect of Ni with 5% Cr	205
3.3. Effect of Cr with 10% Ni	211
4. Fe-Cr-Mn system.....	215
4.1. Series Fe-Cr-Mn with 15% Cr	216
4.2. Addition of carbon in Fe-Cr-Mn alloy 15/25	223
4.3. Series Fe-Cr-Mn with 5% Cr	228
5. Conclusion.....	231
References	232
Conclusion and outlook.....	235
Appendix	239
Journal articles.....	251
Paper in preparation.....	265
Conferences	267
Curriculum vitae.....	268

General introduction

The project developed by Erasteel aims to provide technological and industrial response to current deficiencies in the field of refrigeration and air conditioning in terms of energy saving and limiting the environmental impact. Magnetic refrigeration is an interesting alternative to traditional cooling methods, based on gas compression cycles because it has higher energy yields and avoids the use of harmful greenhouse gases. This technology is based on the giant magnetocaloric effect (MCE) of certain magnetic materials around room temperature. This effect can increase or decrease the temperature of the material during its magnetization or adiabatic demagnetization cycles around its magnetic transition temperature. A sequence “magnetization / heat exchange to warm / demagnetization / heat exchange to cold” allows a new cycle of cooling applications from the current machines.

Since 2011, Erasteel has developed magnetocaloric components by powder metallurgy processes. This development includes the development of magnetocaloric alloy powder by gas atomization, the functionalization of the powder and the shaping processes to meet the requirements of magnetic refrigeration systems.

It is in this context that this CIFRE thesis project is developed in partnership between the Néel Institute and Erasteel. The major part of this thesis work focuses on the $\text{La}(\text{Fe},\text{Si})_{13}$ -based family of materials, in which a promising magnetocaloric effect has been demonstrated and where the industrial feasibility seems most favorable.

The structure of this thesis is organized as the following:

Chapter I gives a brief review for the development of the domain of magnetic cooling, especially the efforts in near room temperature refrigeration applications. An introduction of the magnetocaloric effect and its thermodynamics is given in order to lay solid grounds for the other Chapters in this thesis. We focus on magnetocaloric materials that exhibit a first-order phase transition. Issues on the transition order and the employment of the Maxwell relation to determine the magnetocaloric characteristics are discussed. The applicability of the giant MCE materials for room temperature magnetic refrigeration is evaluated and the main subject of this thesis, La-Fe-Si material family is introduced.

The steps of the elaboration process for the samples in this work are described in Chapter II. After each stage, the structural and magnetic properties of the samples can be characterized. The principles of primary characterization techniques are explained.

In Chapter III, the structural, magnetic and magnetocaloric properties of La-Fe-Si phase are studied. In particular, samples with substitution of Ce and Mn are investigated to study the effect of substitution on the structural and magnetic properties of the original phase. The laboratory elaboration process is optimized in terms of excess rare earth elements.

Small elements are able to enter the interstitial voids in the $\text{La}(\text{Fe}_{1-x}\text{Si}_x)_{13}$ phase, which can expand the lattice parameter. Through the extension of Fe-Fe distances, the Curie temperature of the magnetocaloric phase can be raised up to room temperature range. Chapter IV explores the effect of hydrogen and carbon interstitial atoms on the structural and magnetic properties of the La-Fe-Si material.

In order to investigate the interstitials dynamics, hydrogen sorption kinetics is studied by the means of Sieverts' method and *in-situ* neutron diffraction. In Chapter V, the influence of diverse composition changes is compared in the course of hydrogen uptake and release. Neutron diffraction provides useful information at the scale of interatomic distances, which allows a better understanding of the gas sorption mechanism. The hydrogen stability in the material is associated with the sorption kinetics and the desorption temperature can be evaluated with DSC.

In the search of new rare-earth-free materials for magnetocaloric applications, we have explored the capacity of Fe-based alloys with compositions close to common stainless steel alloys in the systems of Fe-Cr-Ni and Fe-Cr-Mn. In Chapter VI, the magnetic and structural phase transitions for alloys of different compositions are studied with Faraday's Balance and DSC techniques.

Introduction générale

Le projet développé par Erasteel vise à apporter une réponse technologique et industrielle aux manques actuels dans le domaine de la réfrigération et de la climatisation en termes d'économie énergétique et de limitation de l'impact écologique. La réfrigération magnétique est une alternative intéressante aux méthodes de réfrigération traditionnelles, basées sur des cycles de compression/détente, car elle présente des rendements énergétiques nettement plus élevés et permet d'éviter l'utilisation de gaz nocifs contribuant à l'effet de serre et problématiques pour l'environnement. Cette technologie s'appuie sur l'effet magnétocalorique (EMC) géant de certains matériaux magnétiques autour de la température ambiante. Cet effet permet d'augmenter ou de diminuer la température du matériau lors de son aimantation ou désaimantation adiabatique autour de sa température de transition magnétique. Une séquence « aimantation / échanges thermiques vers chaud / désaimantation / échanges thermiques vers froid » permet ainsi un nouveau cycle de machine frigorifique, très différent d'une machine actuelle.

Depuis 2011, Erasteel développe des composants magnétocaloriques par métallurgie des poudres. Ce développement inclut l'élaboration de poudres d'alliages magnétocaloriques par atomisation au gaz, la fonctionnalisation des poudres et leur mise en forme afin de répondre aux exigences des systèmes de réfrigération magnétique.

C'est dans ce contexte que ce projet de thèse CIFRE est développé autour d'un partenariat entre l'Institut Néel et Erasteel. La majeure partie des travaux de thèse va se focaliser sur la famille des matériaux de type $\text{La}(\text{Fe},\text{Si})_{13}$ dans lesquels un effet magnétocalorique géant a été mis en évidence et pour lesquels la faisabilité industrielle semble la plus favorable.

La structure de cette thèse est organisée comme suit :

Le Chapitre I donne un bref aperçu du développement du domaine du refroidissement magnétique, en particulier les efforts déployés pour les applications de réfrigération proches de la température ambiante. Une introduction de l'effet magnétocalorique et des aspects thermodynamiques est donnée afin de constituer des bases solides pour les autres chapitres de cette thèse. Nous nous concentrons sur les matériaux magnétocaloriques qui présentent une transition de phase du premier ordre. Les questions de l'ordre de transition et de l'emploi de la relation de Maxwell pour déterminer les caractéristiques magnétocaloriques sont discutées. Enfin, l'applicabilité des matériaux à MCE géants pour la réfrigération magnétique à température ambiante est évaluée et le sujet principal de cette thèse, la famille de matériaux La-Fe-Si est introduit.

Dans Chapitre II, les étapes du processus d'élaboration des échantillons mis en œuvre dans ces travaux de thèse sont décrites. Après chaque étape, les propriétés structurales et magnétiques des échantillons peuvent être caractérisées. Les principes de base des techniques de caractérisation sont expliqués.

Les propriétés structurales, magnétiques et magnétocaloriques de la phase La-Fe-Si sont étudiées dans Chapitre III. En particulier, les échantillons avec une substitution de Ce et Mn sont étudiés pour voir l'effet de la substitution sur les propriétés structurales et magnétiques de la phase initiale. Le processus d'élaboration de laboratoire est optimisé en termes d'excès d'éléments de terres rares.

Les éléments légers sont capables d'entrer dans les sites interstitiels dans la phase $\text{La}(\text{Fe}_{1-x}\text{Si}_x)_{13}$, qui peut agrandir le paramètre de maille. Grâce à l'extension des distances Fe-Fe, la température de Curie de la phase magnétocalorique peut être ajustée jusqu'à la gamme de température ambiante. Le Chapitre IV explore l'effet de l'hydrogène et du carbone interstitiels sur les propriétés structurales et magnétiques du matériau La-Fe-Si.

Afin d'étudier la dynamique des éléments interstitiels, la cinétique de sorption de l'hydrogène est étudiée à l'aide de la méthode de Sievert et de la diffraction des neutrons « in-situ ». Dans Chapitre V, l'influence des diverses modifications de composition est étudiée et comparée au cours de l'absorption et de la désorption de l'hydrogène. La diffraction de neutrons fournit des informations utiles à l'échelle des distances interatomiques, ce qui permet une meilleure compréhension du mécanisme de sorption de gaz. La stabilité de l'hydrogène dans le matériau est associée à la cinétique d'adsorption et la température de désorption peut être évaluée par DSC.

Dans la recherche de nouveaux matériaux sans éléments de terres rares pour les applications magnétocaloriques, nous avons exploré la capacité d'alliages base Fe dans les systèmes Fe-Cr-Ni et Fe-Cr-Mn. Dans Chapitre VI, les transitions de phase magnétiques et structurales pour différentes compositions sont étudiées avec les techniques de la balance de Faraday et la DSC.

Chapter I. Magnetocaloric refrigeration and material: State of the Art

Table of Contents

Chapter I. Magnetocaloric refrigeration and material: state of the Art	11
1. Context	11
1.1. Age of the energy trilemma	11
1.2. Alternative solution.....	12
2. General notions	13
2.1. From history to demonstration unit.....	14
2.2. Thermodynamic principles	17
2.3. Measurement of MCE.....	21
2.4. Magnetic transition order	22
2.5. Employment of Maxwell relation	25
3. Magnetic refrigerant selection.....	26
4. Introduction of the $\text{La}(\text{Fe},\text{Si})_{13}$ intermetallics	30
4.1. Structure characteristics	30
4.2. Magnetic properties	32
4.3. Magnetocaloric properties	34
4.4. Composition tuning.....	35
4.4.1. Rare earth element tuning.....	35
4.4.2. Transition metal tuning.....	37
4.4.3. Interstitial tuning.....	38
4.4.4. State of the art of performance	39
References	41

Chapter I. Magnetocaloric refrigeration and material: state of the Art

1. Context

1.1. Age of the energy trilemma

We are entering the age of *the Energy Trilemma* [1]: not only do we need effective management of primary energy supply from domestic and external sources to ensure energy security and energy equity, but also we face the challenge of achieving energy supply from renewable and other low-carbon sources.

Energy consumption in residential and commercial buildings accounts for about 40% of total primary energy use in the European Union [2]. Cooling in its various forms (air conditioning, refrigeration, freezing, and chilling) takes up at least 15% of this figure [3]. Therefore, improving energy efficiency with respect to refrigeration plays an important role in reducing the overall energy consumption. Even marginal efforts in reducing power consumption in household and industrial refrigeration will have a large economic and ecological impact due to the size of this area.

Today, nearly all commercial refrigeration and air-conditioning devices work with the gas compressor system (Figure I-1), which benefits from the energetic difference between gas and liquid to provide cooling via the expansion and contraction of a volatile refrigerant. Since their commercialization in the 1850s, hardly few other technologies have been able to compete on efficiency, price, or manufacturability.

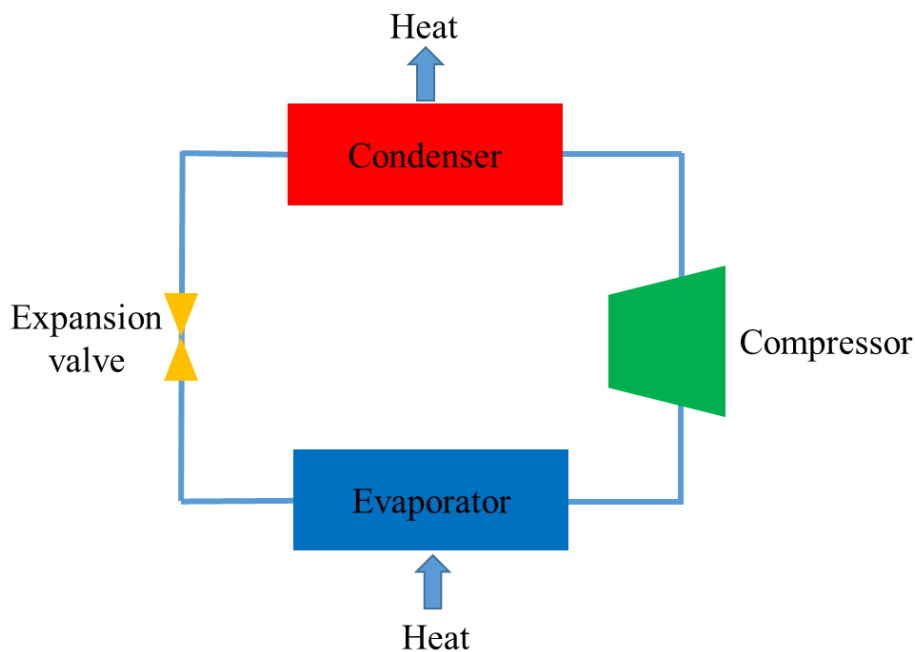


Figure I-1. Simplified representation of the vapor compression cycle.

However, the vapor compression refrigeration poses serious threats to the environment. The refrigerant gases such as fluorocarbons have been phased out due to its ozone depletion potential. Most other volatile refrigerants in use today are also classified as greenhouse gases. A 2009 study predicted that hydrofluorocarbons (HFCs) could account for between 28 and 45 percent (CO₂-equivalent basis) of projected global CO₂ emissions by 2050 [4]. Even though they are contained in refrigeration and air conditioning equipment during short-term application, there are long-term issues as to what to do with the buildup of HFC reservoir. Scientists today advocate earlier phase-outs of HFCs, which can provide as much as 40 percent more benefits for climate change because of reduction of the reservoir [5]. Vapor-compression has been the leading technology for the last century after outcompeting natural ice as the primary source of refrigeration. Today vapor-compression is a reliable and low-cost technology; however, possible improvements are limited. What are alternative solutions that contribute to an overall reduction in the carbon footprint of cooling systems?

1.2. Alternative solution

Among others, a number of alternative refrigeration technologies exist today, including thermoacoustic [6], thermoelectric [7], and magnetic refrigeration. The concept of room temperature magnetic refrigeration can be understood as an analogue of the conventional gas compression and decompression system. Based on the magnetocaloric effect of suitable magnetic materials, this gas-free alternative solution harnesses the energy difference between different magnetic states in suitable solid refrigerant through magnetization and demagnetization cycles. When applied in household refrigerators, we expect a 25-30 percent efficiency improvement over vapor compression for this technology [8], which is equivalent to about 60% of Carnot efficiency [9]. This advantage in energy efficiency and environmental benefits make this technology particularly interesting for air-conditioning or domestic refrigeration applications.

Besides the efficiency improvement, a few other improvements can be expected from the magnetic refrigeration technology. A noise-reduction can be achieved due to few numbers of movable parts. Magnetic refrigeration can be used under ambient pressure with the heat transfer fluid. Since the high-pressure environment is no longer an issue, it is possible to use plastic casting that is less sophisticated and lightweight.

In practice, the magnetic refrigerant changes states when moved in and out of the magnetic field of a permanent magnet. The principle of a magnetic refrigeration cycle is illustrated in Figure I-2. With the application and removal of the field, the magnetocaloric material responds with a temperature change. A heat exchange fluid can then transfer the heat from or to the refrigerant at appropriate parts of a magnetic cooling cycle. Magnetocaloric technology can be used in both cooling application such as refrigeration and air conditioning and in heating applications like water heaters and clothes dryers.

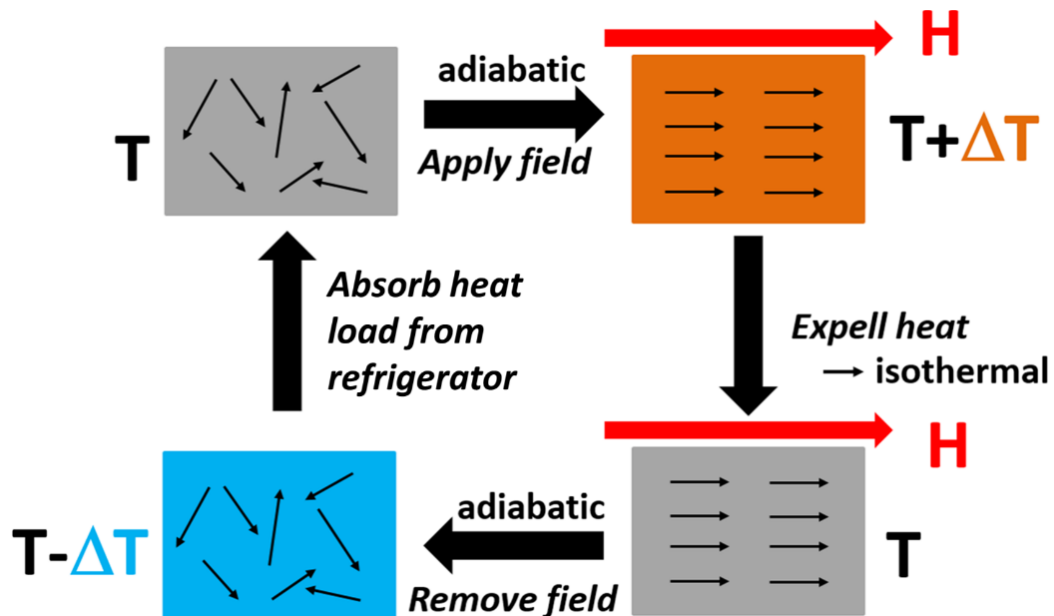


Figure I-2. The principle of a magnetic refrigeration cycle.

In addition, the reversal use of magnetocaloric effect can result in power generation. By taking advantage of the low value waste heat from various sources, magnetocaloric materials can be heated and cooled. Thermomagnetic generators can then convert the corresponding changing magnetization to electricity with a coil [10]. This application is a prospective recycling method for the waste heat generated in both urban setting and industrial environment.

2. General notions

Generally speaking, any thermal response of a material to an external applied field can be defined as a *Caloric Effect*. The different caloric effects can be classified based on the nature of the external stimulus, such as magnetic field (magnetocaloric effect), mechanical stress (elastocaloric effect), hydrostatic pressure (barocaloric effect), electric field (electrocaloric effect), and so on.

The core of magnetic refrigeration is the emission or absorption of heat in any suitable material in response to a changing magnetic field, i.e. the magnetocaloric effect (MCE). It is an intrinsic property of some magnetic materials. In a simplified definition, MCE is described as a reversible temperature change of a material as it undergoes a change in external magnetic field (magnetization and demagnetization) under adiabatic conditions. The conventional MCE occurs when the temperature increases upon application of a magnetic field, and the inverse MCE results in a decrease of temperature upon the application of a magnetic field.

2.1. From history to demonstration unit

In 1917 and 1918, French and Swiss physicists P. Weiss and A. Piccard first discovered a reversible heating of a Nickel sample near its Curie temperature (627 K) when a magnetic field was applied [11, 12]. A “novel magnetocaloric phenomenon”, they called it. Historically, the discovery of the MCE was attributed to German physicist E. Warburg. This mis-citation has percolated through the literature for two decades. Recently, A. Smith re-examined the original works and found that the work of E. Warburg in 1881 [13] was the first to explain magnetic hysteresis but it was the work of Weiss and Piccard that should be acknowledged for the observation of the MCE [14].

Debye [15] and Giauque [16] independently suggested in the 1920s that this effect can be used to reach ultra-low temperature (<1 K). In 1933, Giauque and MacDougall first experimentally demonstrated how adiabatic demagnetization of paramagnetic salts like $\text{Gd}_2(\text{SO}_4)_3 \cdot 8\text{H}_2\text{O}$ can be used to reach 0.25 K [17]. Adiabatic demagnetization was soon developed into a standard laboratory technique to reach milliKelvin temperature, prior to the advent of dilution refrigerator, that is.

In the late 1970s, it has been recognized that a much larger MCE can be obtained in a ferromagnet in the vicinity of its Curie temperature and the effect can be used for heat pumping near room temperature [6]. G.V. Brown achieved a first breakthrough on magnetic refrigeration close to room temperature in 1976 with Gadolinium as the working material [18]. In his report, Brown showed that with an external applied magnetic field of 7 T, Gd produced an isothermal entropy change of $4 \text{ J/kg}\cdot\text{K}$ or an adiabatic temperature change of 14 K at its Curie point. Brown showed that a continuously operating device working near room temperature could achieve much larger temperature spans than the maximum observed MCE. After 50 cycles, a maximum temperature span of 47 K was attained. The cyclic operation to maintain a large temperature span between the hot and cold sources is where magnetic refrigeration differs from adiabatic demagnetization. This prompted the development of various devices and led to the establishment of the Active Magnetic Regenerator (AMR) cycle, described by J. A. Barclay in 1983 [19]. By virtue of accumulating temperature span with fluid cycles, AMR allows improved exploitation of the magnetocaloric effect, giving rise to the consideration of magnetic refrigeration as a potentially viable technology.

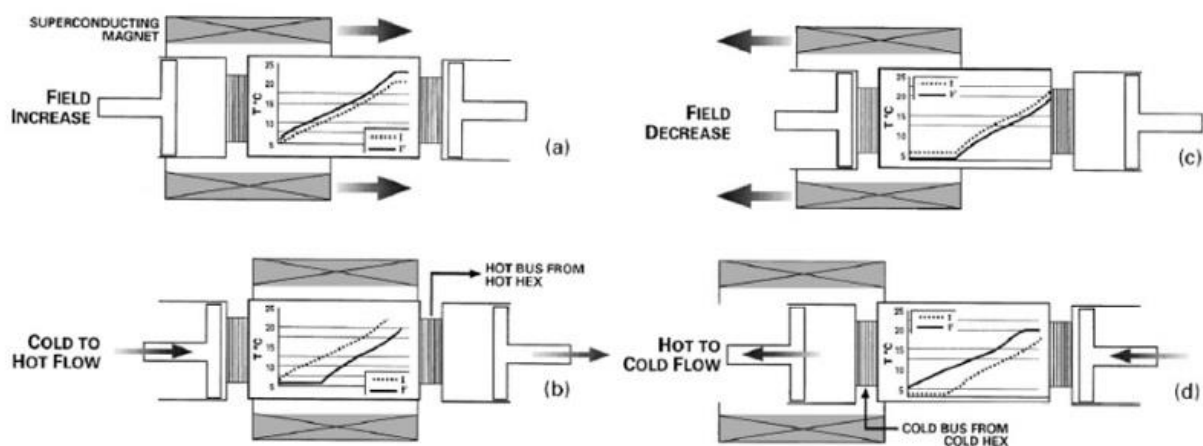


Figure I-3. The principles steps in a refrigeration cycle using active magnetic regenerator (AMR), taken from reference [20].

The principle steps are shown in Figure I-3. In this system, the magnetocaloric material is used as both a thermal regenerator, which stores temporarily the positive or negative temperature variation and then exchange with the heat transfer fluid, and the active magnetic component that induces the temperature change. Regeneration allows the heat rejected by the system at a step of the cycle, to be restored and given back to the system at another step of the cycle. It is considered that the refrigerant material has a flat initial temperature profile between cold and hot sources. The four steps of this cycle are the following:

- (a) Adiabatic magnetization: the whole regenerator temperature increases.
- (b) Isofield cooling: the calorific fluid flows from the cold source toward the hot source thus evacuating heat and creating a thermal gradient in the regenerator.
- (c) Adiabatic demagnetization: the whole regenerator temperature decreases.
- (d) Isofield heating: at zero field, the fluid flows from the hot source towards the cold source, thus gives its heat to the hot side of the refrigerant and increases the thermal gradient.

In such an AMR cycle, the geometry of the regenerator will determine the efficiency of the heat transfer. This is the reason why we normally find the magnetocaloric material used in the shape of a porous bed or a superimposition of plates spaced to facilitate fluid exchange.

As the refrigerant material also acts as a regenerator, the temperature span of an AMR cycle can widely exceed the temperature variation of the material. Moreover, the regenerator can have several layers of magnetocaloric material or composite materials in order to extend the working temperature range and bring about higher performance of the system. In an example of a domestic refrigerator, the cold source is typically less than 269 K and the hot source around the ambient temperature is expected to be around 293 K in average.

In 1997, Pecharsky and Gschneider showed a “giant” MCE in $\text{Gd}_5\text{Si}_2\text{Ge}_2$, setting a milestone in magnetocaloric effect for potential room-temperature cooling application [21]. The MCE of $\text{Gd}_5\text{Si}_2\text{Ge}_2$ was about 50% larger than that of Gd metal, and the authors attributed this to a coupled first-order magneto-structural transformation.

Based on this result, Zimm and colleagues designed the first proof-of-principle near room-temperature magnetic refrigerator unit (Figure I-4) in 1998 [22]. Using commercial grade Gadolinium metal, this demonstration unit was capable of delivering a maximum cooling power of 600 watt and ran for over 5000 hours during an 18-month period with no significant problems and only minor maintenance.

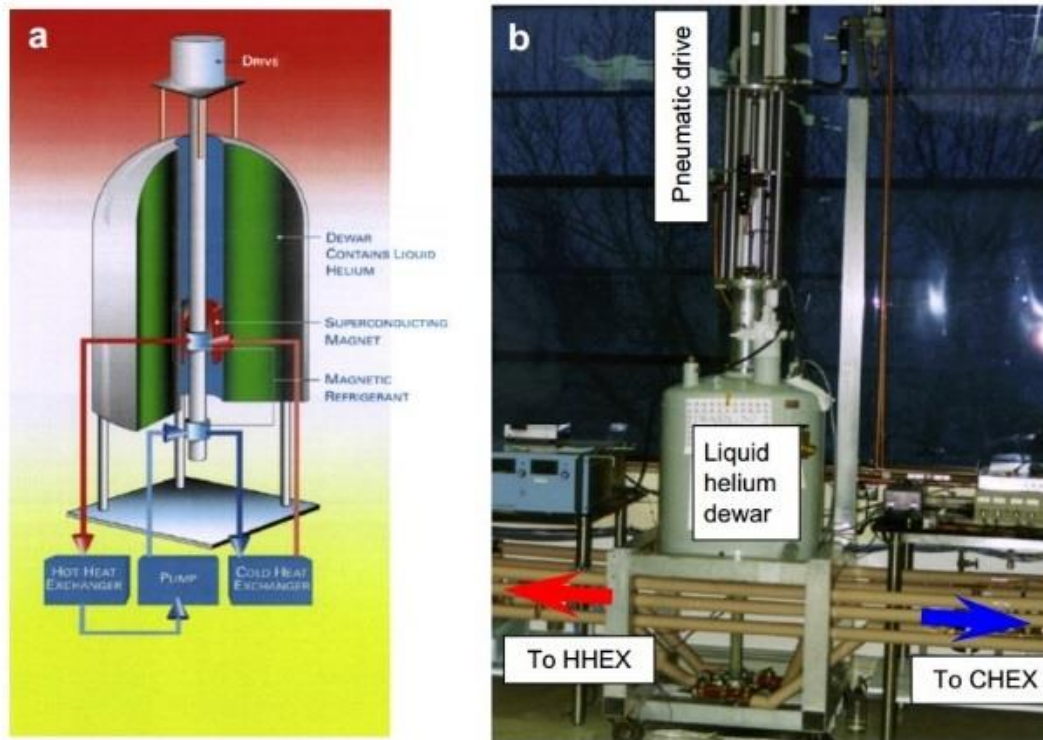


Figure I-4. (a) Schematic and (b) photograph of the Ames Laboratory/Astronautics Corporation of America's reciprocating proof-of-principle magnetic refrigerator, taken from [22].

These events stimulated a new wave of research on both the materials front and the device design department. In 2015, Haier, Astronautics Corporation of America, and BASF presented the first industrial proof-of-concept wine cooler based on a magnetocaloric heat pump at the International Consumer Electronics Show (CES, Kan.6-9, 2015) in Las Vegas, USA [23]. The basic working principle of the prototype wine cooler using magnetocaloric material is shown in Figure I-5.

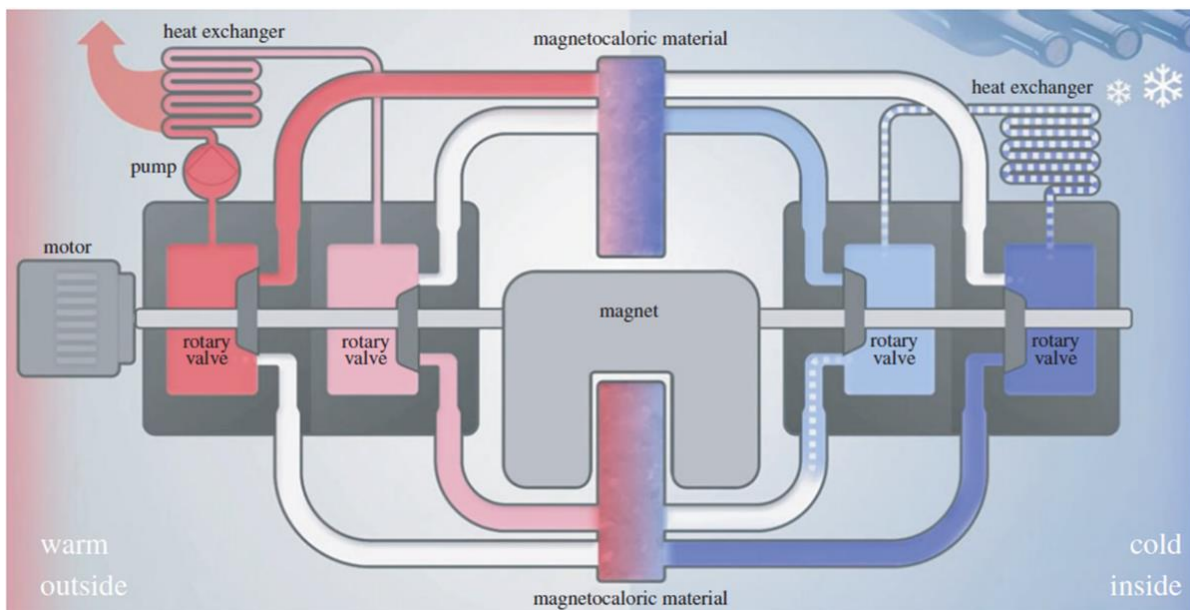


Figure I-5. Schematic picture of a magnetocaloric wine cooler using MnFePSi type of materials, taken from reference [24].

Although the magnetic cooling technology has not been yet commercialized at the time of writing, currently a few companies are involved in the manufacturing of magnetic refrigeration technology, including (in alphabetical order) Astronautics Corporation of America (U.S.), BASF SE (Germany), Camfridge Ltd (U.K.), Cooltech Applications (France), ERAMET SA (France), General Electric CO. (U.S.), Hitachi metals (Japan), Qingdao Haier Co., Ltd (China), Vacuumschmelze GmbH & Co. KG (Germany), Samsung Electronics Co., Ltd (South Korea), Sigma-Aldrich Corporation (U.S.), Toshiba Corporation (Japan) and Whirlpool Corporation (U.S.).

Many challenges still lie ahead to achieve a commercial magnetic refrigeration system at room temperature, among which a great deal of the physics is still yet to be understood completely. In the next section, some basic notions and theories related to magnetocaloric phenomenon will be presented.

2.2. Thermodynamic principles

Theoretical description of the MCE will help us build fundamental frames in which the common notions in magnetocaloric materials shall be introduced. This reversible (heating or cooling) effect can be generally represented by the **adiabatic temperature change** (ΔT_{ad}) or the **isothermal entropy change** (ΔS_M). The principal subject in the following section is what is classified as conventional MCE, which means that the material heats up upon magnetization (negative ΔS_M) and cools down upon demagnetization (positive ΔS_M). Within the conventional MCE systems, paramagnetic materials are out of the scope of this work, as they exhibit very small relative entropy change except at very low temperatures. Room temperature magnetic refrigeration generally involves ferromagnets, which are the most frequently studied systems to illustrate magnetocaloric effect.

In order to describe the thermodynamic potential of a magnetic material under a magnetic field, we use the description of the Gibbs free energy, G , as a function of the internal energy, U , intrinsic variables such as volume, V , entropy, S , and magnetization, M (the magnetic dipole moment per unit volume), and extrinsic parameters such as temperature, T , pressure, P , and applied magnetic field, H (μ_0 denotes the vacuum permeability).

$$G = U - TS + PV - M\mu_0H \quad (\text{I-1})$$

The differential free energy of the system as a function of the state functions T, P, H is given by

$$dG(T, P, H) = \left(\frac{dG}{dT}\right)_{H,P} dT + \left(\frac{dG}{dP}\right)_{H,T} dP + \left(\frac{dG}{dH}\right)_{P,T} dH \quad (\text{I-2})$$

The total differential can be written as

$$dG(T, P, H) = dU + PdV - \mu_0 HdM - TdS + VdP - \mu_0 MdH - SdT \quad (\text{I-3})$$

Recall the first law of thermodynamics: $dU(T, P, H) = TdS + \mu_0 HdM - PdV$, we can simplify Eq.(I-2) to the following equation:

$$dG(T, P, H) = -SdT + VdP - \mu_0 M dH \quad (\text{I-4})$$

From Eq.(I-4) and analogy to Eq.(I-2), we can derive the expression for both the entropy and the magnetization of the system:

$$S(T, P, H) = - \left(\frac{\partial G}{\partial T} \right)_{H,P} \quad (\text{I-5})$$

$$\mu_0 M(T, P, H) = - \left(\frac{\partial G}{\partial H} \right)_{T,P} \quad (\text{I-6})$$

With Eq. (I-5) and (I-6), the well-known Maxwell relation can be obtained,

$$\left(\frac{\partial S}{\partial H} \right)_{T,P} = \mu_0 \left(\frac{\partial M}{\partial T} \right)_{H,P} \quad (\text{I-7})$$

Under constant temperature and pressure, we can derive the entropy differential as

$$dS = \mu_0 \left(\frac{\partial M}{\partial T} \right)_{H,P} dH \quad (\text{I-8})$$

The **isothermal entropy change** from the change in external magnetic field can then be obtained through integrating Eq. (I-8),

$$\Delta S_M(T, P, \Delta H) = S(T, P, H_f) - S(T, P, H_i) = \mu_0 \int_{H_i}^{H_f} \left(\frac{\partial M}{\partial T} \right)_{H,P} dH \quad (\text{I-9})$$

The entropy change induced by external field is generally calculated from magnetization data. On the other hand, the entropy change can be expressed in terms of specific heat under constant pressure, $C_p(T, H) = T \left(\frac{\partial S}{\partial T} \right)_H$, according to the second law of thermodynamics [25]:

$$\left(\frac{\partial S}{\partial T} \right)_H = \frac{C_p(T, H)}{T} \quad (\text{I-10})$$

which allows us to calculate the isothermal entropy change from the heat capacity:

$$\Delta S_M(T, \Delta H) = \int_0^T \frac{C_p(T, H_f) - C_p(T, H_i)}{T} dT \quad (\text{I-11})$$

Another important parameter used for the characterization of magnetocaloric materials is the **adiabatic temperature change**. The temperature change in a material during adiabatic magnetization under isobaric conditions is

$$\Delta T_{ad} = T_{f,H_f} - T_{i,H_i} \quad (\text{I-12})$$

where H_f and H_i represent the final and initial applied magnetic field ($H_i < H_f$). In order to associate temperature with entropy, let us consider the total differential of the entropy S in a closed system:

$$dS(P, T, H) = \left(\frac{\partial S}{\partial P}\right)_{T, H} dP + \left(\frac{\partial S}{\partial T}\right)_{P, H} dT + \mu_0 \left(\frac{\partial S}{\partial H}\right)_{P, T} dH \quad (\text{I-13})$$

Under adiabatic and isobaric conditions, the following assumptions can be written:

$$\left(\frac{\partial S}{\partial P}\right)_{T, H} dP = 0 \quad (\text{I-14})$$

$$dS = \frac{\partial Q}{T} = 0 \quad (\text{I-15})$$

Eq. (I-13) can now be rewritten as

$$dT = -\mu_0 \left(\frac{\partial S}{\partial H}\right)_T \left(\frac{\partial T}{\partial S}\right)_H dH \quad (\text{I-16})$$

By taking into account the Maxwell relation and the definition of the specific heat under constant pressure previously mentioned, the right hand side of Eq. (I-16) can be replaced by a specific heat term and a magnetization term and we obtain

$$dT = -\mu_0 \frac{T}{C_p(T, H)} \left(\frac{\partial M}{\partial T}\right)_H dH \quad (\text{I-17})$$

Although the right hand side of Eq. (I-17) is not an exact differential, we can “integrate” to get the expression of the adiabatic temperature change ΔT_{ad} .

$$\Delta T_{ad}(T, \Delta H) = -\mu_0 \int_{H_i}^{H_f} \left(\frac{T}{C_p(T, H)}\right)_H \left(\frac{\partial M(T, H)}{\partial T}\right)_H dH \quad (\text{I-18})$$

It is important to note that the integral is not independent of the integration path so this relation has to be evaluated explicitly along the relevant isentrope (constant entropy line). Both magnetization and heat capacity are required to determine ΔT_{ad} , a so-called indirect technique.

Figure I-6 illustrates the effect of an external field changing from H_i to H_f on the entropy and spin system of a ferromagnetic material. The material undergoes a ferromagnetic to paramagnetic transition upon cooling. Different path lines are used to show the relation between ΔS_M and ΔT_{ad} in such transitions.

Path A→B corresponds to the process of increasing magnetic field while keeping temperature constant, i.e. the isothermal magnetization process. The ordering of the system results in a decrease in the magnetic part of the entropy, ΔS_M . In an adiabatic environment, no heat exchange takes place between magnetic solid and its surroundings.

Along path B→C, adiabatic demagnetization takes place. The field change occurs while the entropy stays constant, $\Delta S_M = 0$. The resulting temperature difference, ΔT_{ad} , is then the “cooling” effect associated with the removal of the external field in conventional MCE. The described temperature change is the manifestation of the MCE.

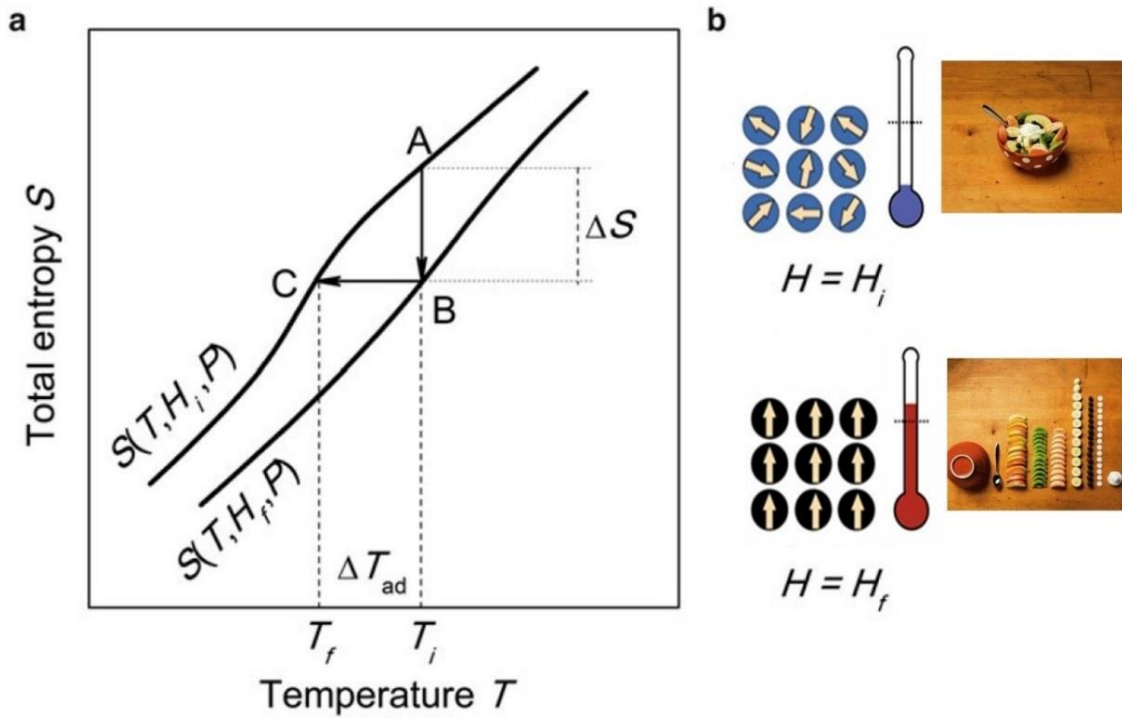


Figure I-6. Schematic representation¹ of the effect of an external field changing from H_i to H_f ($H_i < H_f$) on the entropy of a magnetic material (a) and on the spin system (b), illustrating the relation between ΔS_M and ΔT_{ad} , adapted from reference [26].

While the term ΔS_M is often used to characterize MCE in this domain, it is not always a clear definition of the entropy we measure from magnetization and demagnetization experiments. In the solid system exhibiting localized electron magnetism, the total entropy of the solid can be considered as a sum of the magnetic entropy (S_M), the lattice entropy (S_L), and electronic entropy (S_E). Under constant pressure, the system entropy depends on both the external field H and the temperature T . The magnetic entropy is associated with the magnetic degree of freedom and can be determined by the free energy of the magnetic sublattice within the mean-field approximation:

$$S_M(T, H) = Nk_B \left[\ln \frac{\sinh(\frac{2J+1}{2J}x)}{\sinh(\frac{1}{2J}x)} - xB_J(x) \right] \quad (\text{I-19})$$

where $x = gJ\mu_B H/k_B T$, with J being the quantum number of angular momentum, k_B the Boltzmann constant, g the Landé factor, and B_J the Brillouin function. In the high temperature and low-field limit ($x \ll 1$), we have

$$S_M = Nk_B \left[\ln(2J+1) - \frac{1}{2} \frac{C_J H^2}{(T - T_C)^2} \right] \quad (\text{I-20})$$

¹ Images taken online from art-opology.blogspot.hk

For a complete order to disorder transition, the magnetic entropy will get its maximal value of $S_M = Nk_B \ln(2J + 1)$.

The electronic entropy can be written as

$$S_E = \gamma T \quad (\text{I-21})$$

where γ is the coefficient of electronic heat capacity. At high temperatures, the contribution from electronic entropy is often ignored.

From the Debye approximation, entropy associated with lattice vibration can be expressed as

$$S_L = R \left[-3 \ln \left(1 - e^{-\frac{\theta_D}{T}} \right) + 12 \left(\frac{T}{\theta_D} \right)^3 \int_0^{\frac{\theta_D}{T}} \frac{x^3 dx}{e^x - 1} \right] \quad (\text{I-22})$$

where R is the gas constant, and θ_D the Debye temperature.

In contrast to insulating materials whose magnetism is often expressed in terms of localized electrons in each atom, metals (especially many well-known 3d magnets such as Ni, Fe, or Co) have a picture of nearly free electrons, which are shared among the entire solid in an electron gas. In such itinerant systems, it is common to speak of the entropy of the system consisting of the phonon (S_L) and magnetic terms (S_M). The contribution from electronic and lattice entropy is negligible for a second-order transition, whereas it cannot be ignored for a first-order transition due to the discontinuous change of order parameter at T_C .

2.3. Measurement of MCE

The two characteristics of magnetocaloric material, ΔT_{ad} and ΔS_M , can be determined either directly or indirectly. Direct isothermal measurement of the heat transfer and, therefore, direct measurement of ΔS_M is inconvenient and it is rarely performed in practice. For the measurement of ΔT_{ad} , both direct and indirect methods are straightforwardly employed. A number of parameters affect the accuracy of such measurements of ΔT_{ad} , among which are the thermal contact between the sample and the temperature sensor, and the influence of external field on the temperature sensor. Therefore, the measured ΔT_{ad} is generally smaller than the real value.

The majority of the characterization of the MCE is based on Eq. (I-9), which can be used to calculate ΔS_M indirectly from experimentally measured magnetization as a function of temperature and field. Isofield measurement determines the critical temperature, thermal hysteresis, and the width of the transition. Isothermal measurement is used to calculate the isothermal magnetic entropy change using the Maxwell relations. Both measurements probe the same phenomenon, and therefore should be equivalent.

In an isofield measurement, the sample is brought down to a temperature where the phase is completely magnetic (ferromagnetic in our case) without any external field. Then a small field (typically 0.05 T) is applied and the magnetic transition is probed continuously at

constant field while ramping up the temperature until the phase is completely paramagnetic. A cooling curve under the same field is often applied to determine any thermal hysteresis.

As for an isothermal measurement, the usual procedure is to start in zero field at a given temperature (typically $T_C - 30$ K), ramp the field from 0 to H_f (1 T or 2 T) in discrete steps while recording the magnetization. At each step the magnetization is measured with fixed temperature and field. Once H_f is reached the field is brought back to zero and the temperature is increased by a discrete step and the process of increasing field is repeated. This is repeated for every temperature until the maximum temperature ($T_C + 30$ K) is reached.

From these isothermal measurements, the isothermal magnetic entropy change can be calculated by integration of the Maxwell relation Eq.(I-9). Because the measurements are made at discrete temperature intervals, ΔS_M can be numerically calculated using

$$\Delta S_M(T, \Delta H) = \mu_0 \sum_j \frac{M\left(T + \frac{\Delta T}{2}, H_j\right) - M\left(T - \frac{\Delta T}{2}, H_j\right)}{\Delta T} \Delta H_j \quad (\text{I-23})$$

where ΔH is the sum of ΔH_j , $M\left(T + \frac{\Delta T}{2}, H_j\right)$ and $M\left(T - \frac{\Delta T}{2}, H_j\right)$ represent the value of the magnetization in a magnetic field H_j at the temperatures $T + \frac{\Delta T}{2}$ and $T - \frac{\Delta T}{2}$, respectively.

It might also be useful to note that the measured entropy change is smaller than the total entropy change associated with a transition from full disorder to total order. The difference comes from the dynamics of ordering processes in condensed matter. Just above T_C , the ferromagnetic state still has long range order, but the magnetization is reduced due to thermal excitation. As the transition passes just above T_C , there still remains short range order. Therefore, the entropy change is not really changing from an “on” state to an “off” state.

2.4. Magnetic transition order

A distinction is usually made between first-order magnetic transition (FOMT) and second-order magnetic transition (SOMT) in solids. Based on the Ehrenfest classification, in a FOMT, the first derivative of the Gibbs energy is discontinuous across the phase boundary. According to the relation from Eq. (I-4), the volume and entropy are discontinuous as well. A FOMT is characterized by a latent heat associated with the phase transition and can be found in the case of magnetocaloric material $\text{Gd}_5\text{Si}_2\text{Ge}_2$ [21], which exhibits a magneto-structural transformation. SOMT involves the intrinsic spontaneous magnetization that goes continuously to zero when the temperature approaches T_C from below (as shown in Figure I-7). A phase transition is of second order when the first derivative of the Gibbs potential is continuous while the second derivative is discontinuous. Such type of transition is observed in Gadolinium [27] during the transition from ferromagnetic to paramagnetic state. Gadolinium remains as the prototype testing material for magnetic refrigerator at time of writing.

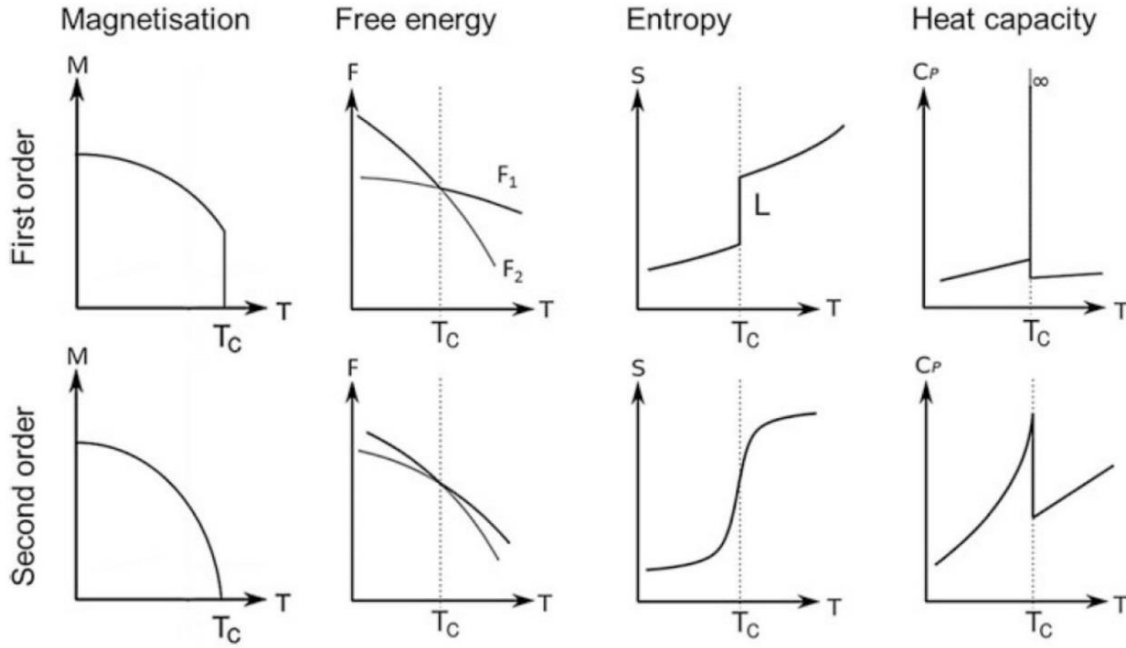


Figure I-7. Schematic temperature dependence of the magnetization, free energy, entropy, and heat capacity according to the classification of magnetic phase transitions, taken from reference [26].

It is important to identify several generic features between the magnetic transitions of first and second order. For second-order transitions, the specific heat is expected to be a discontinuous parameter as it is proportional to the first derivative of entropy with temperature. As seen from Figure I-8, as the applied field increases, we observe a broadened peak in the specific heat curve as a function of temperature, and the peak shifts to higher temperature. As for FOMT, increasing the applied field stabilizes the low temperature state, *i.e.* the ferromagnetic state. This implies that the peak shifts in temperature while the width of the peak maintains its sharp shape as it is still a first-order transition.

Since the specific heat is less field-dependent for FOMT, the ΔS peak height is often observed not very sensitive with field strength while the peak shape broadens with increasing field, as seen in Figure I-8. For SOMT, the maximum magnitude of ΔS increases with increasing field. A $H^{2/3}$ dependence was predicted from the mean field theory [28] and reported for many magnetocaloric systems [29, 30]. The maximum ΔT_{ad} also increases with increasing field for SOMT, although the field-dependence is not linear. Therefore, the optimization of ΔT_{ad} is associated with both the initial and final fields, and not just their difference. In order to maximize the MCE, it is important to ensure a very small initial field (generally, zero-field). It is useful to report adiabatic temperature change with both the initial and final fields.

In SOMT systems, the largest MCE is expected when the heat capacity of a material is strongly influenced by the magnetic field. When the system undergoes a first order phase transition, the total entropy as a function of temperature exhibits a discontinuous (however, in reality it is almost always continuous) change of entropy at a critical temperature. The maximum ΔS_M is expected when the entropy difference between the low- and high-field phases is the largest. The largest ΔT_{ad} in first-order materials is expected when T_C is strongly affected by the magnetic field.

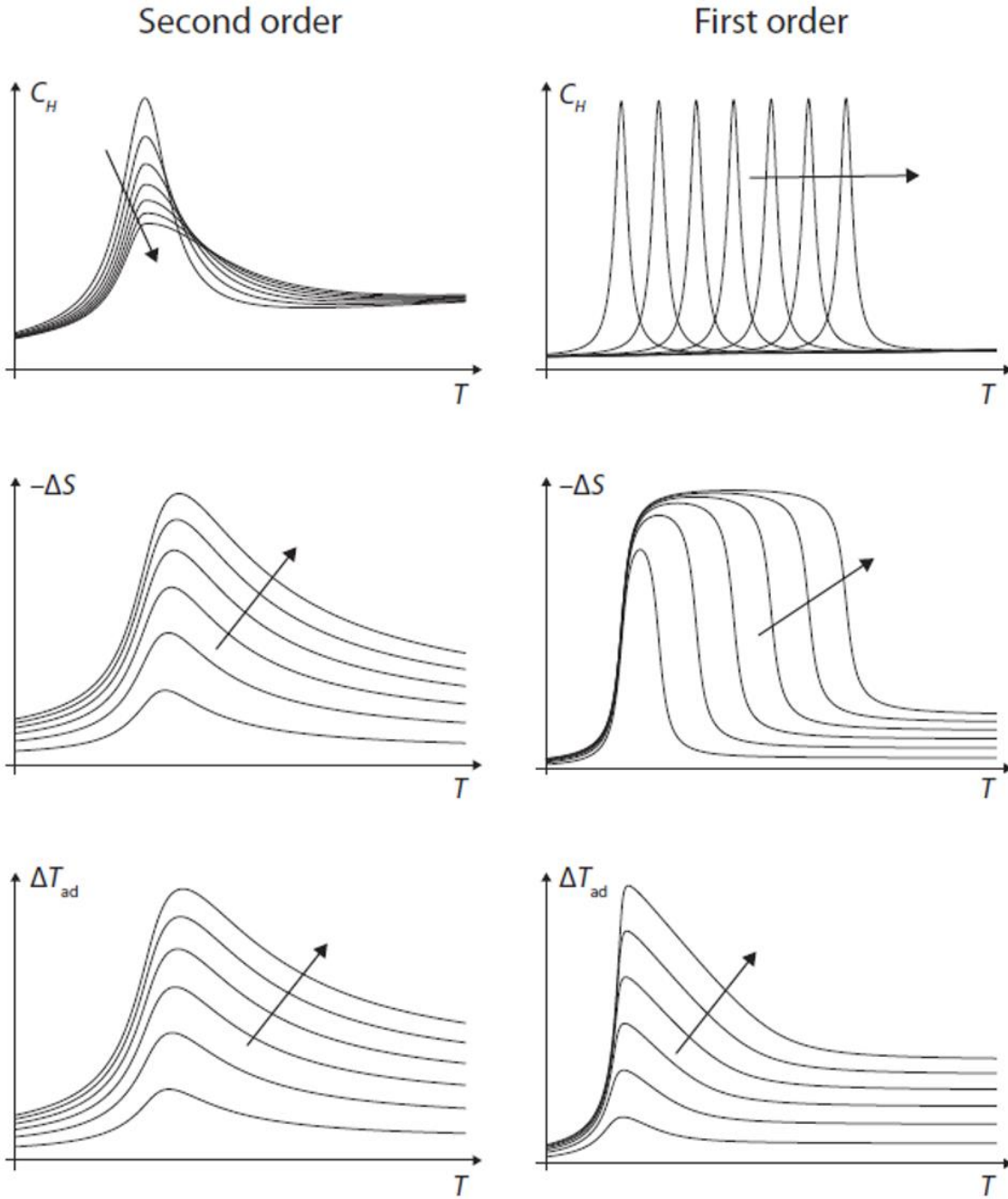


Figure I-8. The difference on the field-dependence of heat capacity (top), isothermal entropy change (middle), and adiabatic temperature change (bottom) between FOMT and SOMT, the arrow points at increasing field direction, taken from reference [14].

Another common feature for magnetocaloric materials exhibiting FOMT is the thermal or magnetic hysteresis accompanying the transition. The hysteresis loss is an issue for magnetic refrigerator. FOMTs fall into two sub-categories: magneto-structural transitions such as in the case of $Gd_5Si_xGe_{4-x}$, $MnAs_{1-x}Sb_x$, and $Ni_{0.5}Mn_{0.5-x}Sn_x$, and magneto-elastic transition such as in the case of $MnFeP_{1-x}As_x$ and $La(Fe_{1-x}Si_x)_{13}$ family compound. Usually, the compounds exhibiting a magneto-elastic transition reveal small or tunable hysteresis [31] [32]. In real systems, we often observe a blurred line between idealized FOMT and SOMT as some FOMT systems can have continuous transition in the presence of impurities and variations in the stoichiometry.

2.5. Employment of Maxwell relation

For a FOMT, the derivative of magnetization becomes discontinuous near the transition temperature by definition, resulting in an abrupt transformation. Equation (I-9) raises questions when describing the MCE in the vicinity of a truly discontinuous first-order phase transition when $(\frac{\partial M(T,H)}{\partial T})_H$ does not exist. The critical behavior of the physical quantities in the phase transition region sparks frequent debates that there seems to have no unified theory. The interpretations of some reported colossal MCE for MnAs [33] and the partially Fe- [34] and Cu- [35] substituted systems, as well as for the systems $\text{La}_{0.8}\text{Ce}_{0.2}\text{Fe}_{11.4}\text{Si}_{1.6}$ [36] have spiked discussion within the community. The observation of unphysical magnetic entropy change brings problem of how to correctly determine the isothermal magnetic entropy change from magnetic measurements.

What is the origin of the spurious peak in ΔS_M calculated by indirect means? The Maxwell relation is valid under the condition that the material is assumed to be in equilibrium. Hysteresis corresponds to a region of metastability of mixed phases, where the high-temperature and low-temperature phases may co-exist. In this case, the results depend on the details of the experimental procedure.

By applying the Maxwell relation, we assume also that the magnetization is differentiable as a function of temperature. However, this is problematic for pure first-order materials as the transition becomes discontinuous. For a first-order phase transition near the transition temperature, Giguere *et al.* [37] proposed to employ an approximation based on the Clausius-Clapeyron (C-C) equation, rather than the Maxwell relation:

$$-\left(\frac{dH}{dT}\right)_{eq} = \mu_0 \left(\frac{\Delta S}{\Delta M}\right)_T \quad (\text{I-24})$$

In response to this proposition, Amaral and colleagues [38] have argued that all the magnetic entropy change and the “non-magnetic contribution” (entropy change due to the lattice volume change, for example) are accounted for in calculations using the Maxwell relation. Thus, there is no real gain nor deeper understanding of the systems by applying the C-C relation to estimate magnetic entropy change. Sun *et al.* [39] have also shown that the C-C relation is just a special case of the integrated Maxwell relations and thus the latter should be applicable.

In the work of L. Caron *et al.*, the authors argue that by properly probing the first-order phase transition, the application of Maxwell relation should not incur any spurious effect [40]. They show that a loop process in magnetization measurements can take into account the history dependence of the magnetization. After each temperature step, the sample is cooled from its paramagnetic state before starting a new isothermal measurement. This process seems to be particularly effective when the hysteresis far exceeds the temperature step size.

For a magneto-structural transition, the measured entropy change can be partitioned into a structural part and a magnetic part. The structural entropy change accounts for the difference between magnetocaloric properties of materials that exhibit a first order magneto-structural transition and those that exhibit a second order magnetic transition. It is possible to calculate the contribution of the itinerant electrons S_M and of the crystalline lattice S_L to the total entropy, based on theoretical work by de Oliveira and colleagues [41, 42].

V. Basso has presented a theoretical study to treat first-order magneto-elastic phase transitions [43]. He proposes a dimensionless parameter ξ that determines the sign and the amplitude of the structural contribution to the entropy change ΔS . ξ depends on the steepness of the change of exchange forces with volume and the thermal expansion coefficient of the structural lattice.

Therefore, the use of Maxwell relation requires necessary considerations of non-equilibrium states of the sample and the history-dependence of the transition. In this work, the compounds elaborated both in laboratory-scale and by industrial process do not exhibit magnetic transitions that are purely of first-order. The existences of impurity phases and local shifts in stoichiometry can both result in a spreading of the transition. The majority of samples elaborated, especially post-hydrogenated ones, exhibits very small hysteresis and tends to behave slightly second-order-like. For some Ce-substituted samples that display strong first-order characteristics, the loop measurement procedure proposed by L. Caron *et al.* [40] is employed. An example is provided in Appendix A. We have seen that for such systems temperature step size of 3 K to 5 K is compatible with the transition nature.

3. Magnetic refrigerant selection

In order to bring magnetic refrigerants to the commercial market, it is not only necessary to consider the material property specific to each material, it is also of critical importance to look into the application requirements. The benchmark material in magnetic refrigeration is considered to be the rare-earth element Gadolinium. With its Curie temperature at room temperature (294 K), Gd shows an entropy change $-\Delta S_M = -10.4 \text{ J/kg}\cdot\text{K}$ and adiabatic temperature change of 5.8 K for a field change from 0 T to 2 T [44]. The material itself is not used directly for refrigeration, but instead it is integrated into a regenerative cycle to make the device temperature span exceed the adiabatic temperature change. Usually the device contains a porous matrix of magnetocaloric material acting as a thermal regenerator, and a heat transfer fluid can pass back and forth through the porous matrix. For most applications, the working field has to be generated by permanent magnets, which limits the available maximum field change to 1-2 T.

In practice, there are several important criteria to take into account in order to select materials that are technologically relevant [26]. First and foremost, maximum cooling capacity needs to be harnessed under moderate field ($< 2\text{T}$) with materials containing non-critical elements. This is a primary assessment of the suitability of any particular material for magnetic refrigeration and heat pump applications. The intensity of the MCE is highly dependent on the properties of each material. In the research community, ΔS_M is used to measure the cooling power while ΔT_{ad} is crucial to transfer heat from the refrigerant to the heat transfer fluid. By the time of writing, there are still a number of debates around what is the suitable figure of merit to take when comparing performances of different materials. There are significant efforts going on today in standardizing measuring protocol and analysis procedure in order to construct a comparable material database in the magnetic refrigeration community.

The Curie temperature of the suitable refrigerant should be tunable in order to have a layered bed of materials with different T_C to cover a large temperature span. By either substitution or interstitial insertion, ideally the material varies its ordering temperature while maintaining its entropy change.

In order to eliminate efficiency loss in the refrigeration cycle, magnetic and thermal hysteresis need to be minimized. This is a question of both intrinsic latent heat during the first-order transition and extrinsic history-dependence caused by microstructure and the kinetics of the transformation.

Thermal transport characteristics of the material should favor good heat transfer, which involve engineering the thermal conductivity and specific heat property of the material. Cyclic performance is highly important for the magnetic refrigerant. Therefore, it is necessary to have good mechanical stability. This is important as many material candidates today are brittle intermetallic compounds. Crack formation and pulverization risks should be carefully eliminated.

To ensure stable performance over a long period of time, the material manufacturer needs to also consider corrosion-resistance and aging effects, including the hydrogen instability within the $\text{La}(\text{Fe}_{1-x}\text{Si}_x)_{13}\text{H}_n$ compounds, which will be described in details in Chapter V.

The life cycle of the magnetic refrigerant is also to be evaluated. From the various steps of material fabrication to production, one should take into account the raw material cost, production cost, toxicity, recycling capability, and other environmental impacts.

Figure I-9 illustrates a perspective of the magnetocaloric materials today. First of all, the reference material Gd and its compounds $\text{Gd}_5\text{Si}_2\text{Ge}_2$ [45] are among the best candidate materials for ambient magnetocaloric devices. These two systems, however, are unlikely to be considered for large-scale commercialization since they require raw material Gd and Ge that are considered “critical” in reserve and production quantities.

Several intermetallic families among MnAs-based [46] and Fe_2P -based alloys [47] have shown interesting magnetocaloric performances. MnAs presents a first-order magnetic transition from ferromagnetic (hexagonal) to paramagnetic (orthorhombic) state at 317 K, accompanied with a volume change of about 2.2% [48]. This transition is accompanied by a large thermal hysteresis, which can be tuned by substituting As by Sb. However, the presence of highly-toxic As limits application potential. Having a Fe_2P -type hexagonal structure, solid solution $\text{MnFeP}_x\text{As}_{1-x}$ displays a first-order ferromagnetic transition with T_C between 168 and 330 K by varying the P/As ratio. Replacing As with Si, $\text{MnFeP}_{0.5}\text{Si}_{0.5}$ shows magneto-elastic transitions with a small volume change and a thermal hysteresis of 35 K [49].

For industrial upscaling, price, abundance, easy production and shaping, and non-toxicity become highly relevant.

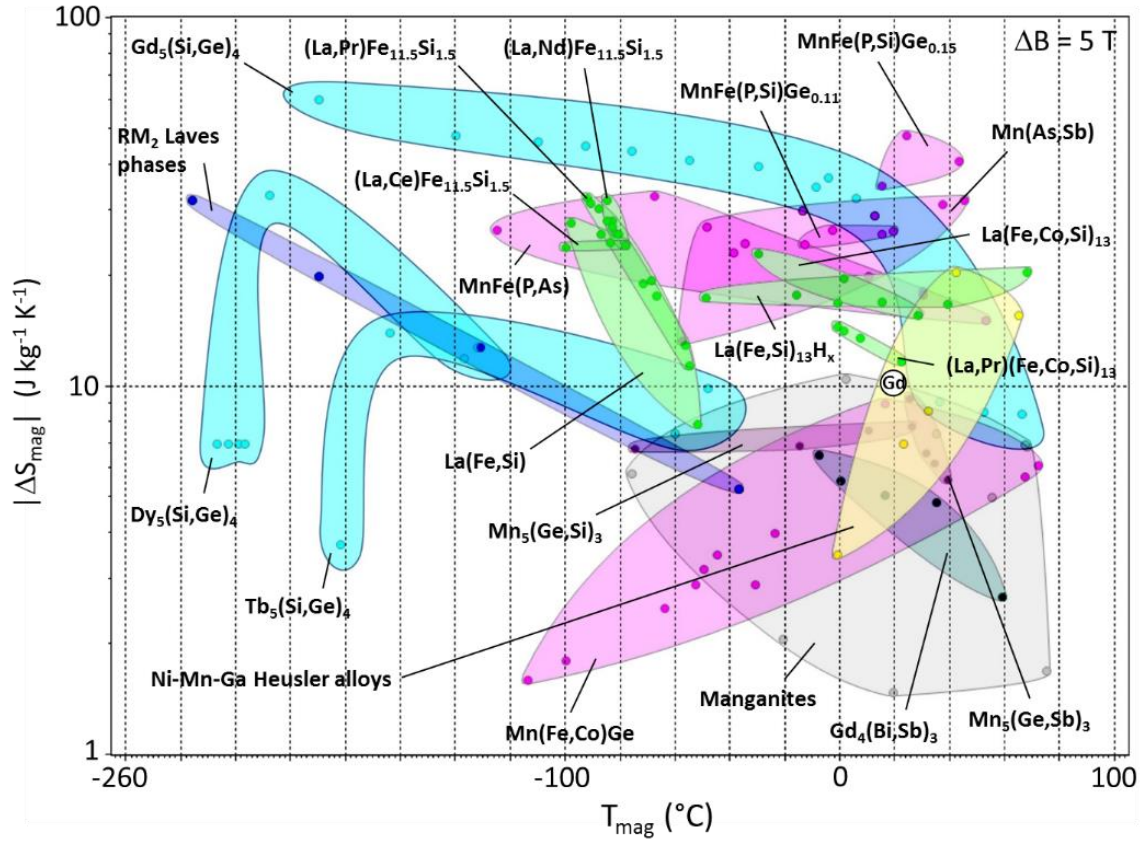


Figure I-9. Magnetocaloric materials property diagram containing 21 families and 143 different compositions in a space of “magnetic entropy variation ($|\Delta S_{\text{mag}}|$) – magnetic transition temperature (T_{mag})” for a field variation from 0 to 5 T. Taken from reference [50], submitted to *Techniques de l’Ingénieur*, 2016.

The cubic NaZn_{13} -type $\text{La}(\text{Fe}_{1-x}\text{Si}_x)_{13}$ compounds have drawn great attention because they show large MCE at relatively low field. Besides the significant MCE, the most remarkable feature of $\text{La}(\text{Fe}_{1-x}\text{Si}_x)_{13}$ is the strong dependence of its T_C on element doping or external perturbations such as magnetic field and pressure. The transition temperature can be tailored to span a substantial range and approach room temperature.

In first-order transitions, hysteresis (thermal or magnetic) can arise due to the extrinsic specifics of the microstructural state of the material. The $\text{La}(\text{Fe}_{1-x}\text{Si}_x)_{13}$ compounds have a very low intrinsic hysteresis. More importantly, the hysteresis can be tuned by composition modification and microstructure manipulation. For instance, the hysteresis is nearly absent in melt-spun and porous $\text{La}(\text{Fe}_{1-x}\text{Si}_x)_{13}$ alloys even though the transition is rather first-order [51, 52]. This behavior has been ascribed to the removal of internal constraints, which hinders the volume expansion [52]. The absence of hysteresis is an essential practical advantage of $\text{La}(\text{Fe}_{1-x}\text{Si}_x)_{13}$ since hysteresis results in heat loss during cycling.

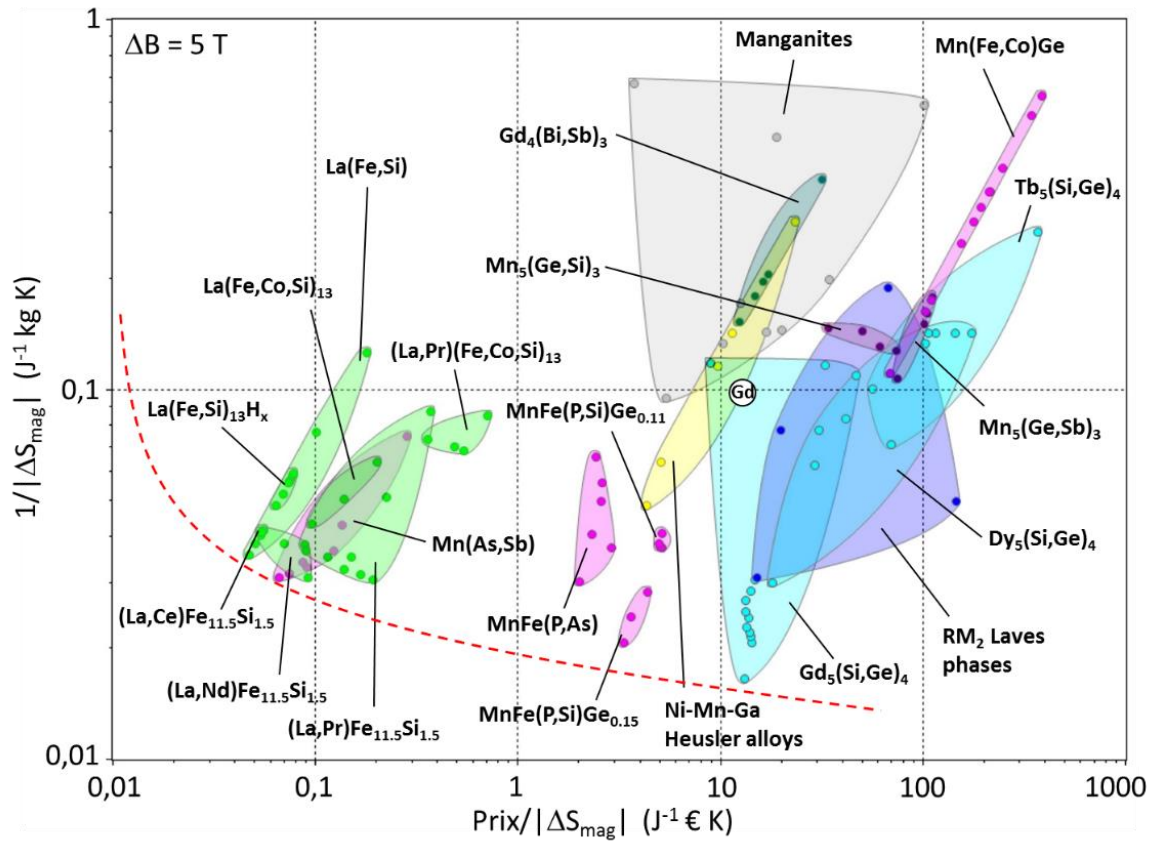


Figure I-10. Magnetocaloric materials property diagram containing 21 families and 143 different compositions showing a compromise between maximizing the magnetic entropy variation (high $|\Delta S_{\text{mag}}|$) and minimizing the cost (represented by a ratio of bulk price and magnetic entropy variation) for a field variation from 0 to 5 T. Taken from reference [50], submitted to *Techniques de l'Ingénieur*, 2016.

From a practical point of view, it is very important to evaluate the price of the magnetic refrigerant candidate for upscaling. Figure I-10 illustrates the compromise between maximizing the magnetic entropy variation and minimizing cost. The axis are set with the objective of minimizing the compromise. The discontinuous curve defines the dominant solutions, for which there is no other offers that are more performant ($|\Delta S_{\text{mag}}|$) and less expensive at the same time. This figure demonstrates clearly the viability of the $\text{La}(\text{Fe}_{1-x}\text{Si}_x)_{13}$ -based materials and the $\text{Mn}(\text{As}, \text{Sb})$ pnictides in the magnetic refrigeration for room-temperature application.

The concern of the rising cost of rare-earth materials lies mostly with the use of Nd-Fe-B permanent magnets as the magnetic field source. $\text{La}(\text{Fe}_{1-x}\text{Si}_x)_{13}$ phase contains a majority of Fe and La is one of the by-products from the processing for the permanent magnet market. Thus, it is expected that the price for this magnetic refrigerant family to remain fairly constant. With 80 % in weight composed of iron, the $\text{La}(\text{Fe}_{1-x}\text{Si}_x)_{13}$ family of intermetallics is highly attractive for large-scale production. It is, therefore, chosen as the subject of this thesis and it has been previously developed on an industrial scale by Erasteel.

4. Introduction of the $\text{La}(\text{Fe},\text{Si})_{13}$ intermetallics

Previously, we have discussed the selection of magnetocaloric materials for commercial applications. This section will be devoted to the introduction of the structural characteristics and physical properties of intermetallic family $\text{La}(\text{Fe}_{1-x}\text{Si}_x)_{13}$. This section is organized as follows: after a brief introduction, we survey the different aspect of this material family in terms of its structural and magnetic characteristics. The particular phenomena associated with this material are introduced. Different approaches to modify the material property with compositional change are discussed.

4.1. Structure characteristics

No intermetallic compounds form in the La-Fe binary system due to a positive enthalpy of formation [53]. Palstra [54] has shown that minor additions of Si or Al will be required to stabilize a pseudo-binary compound. The $\text{La}(\text{Fe}_{1-x}\text{M}_x)_{13}$ ($\text{M}=\text{Si}, \text{Al}$) intermetallics were first successfully synthesized by Kripyakevich *et al.* in 1968 [55]. The phase $\text{La}(\text{Fe}_{1-x}\text{Si}_x)_{13}$ ($0.08 < x < 0.2$) is an intermetallic phase that crystallizes in a NaZn_{13} -type cubic structure (space group $Fm\bar{3}c$, No. 226).

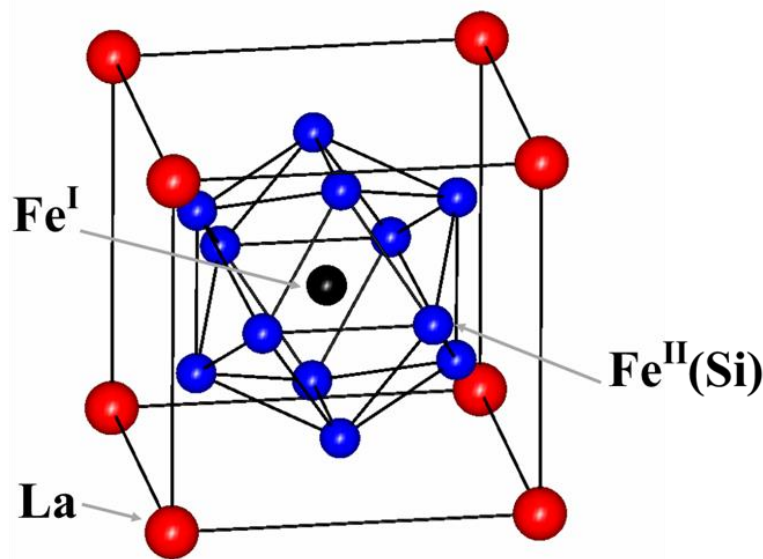


Figure I-11. 1/8 of the unit cell of the NaZn_{13} -type cubic structure.

The unit cell (the 1/8 representation shown in Figure I-11) contains 112 atoms in three crystallographic sites. Lanthanum atoms occupy the $8a$ ($\frac{1}{4}, \frac{1}{4}, \frac{1}{4}$) position. The cubic structure has two different sites for Fe atoms in a ratio 1:12. The Fe^{I} atoms occupy the $8b$ ($0, 0, 0$) position and the Fe^{II} atoms are on the $96i$ ($0, y, z$) position.

Back in 1986, Palstra *et al.* [56] probed the site occupancy and structure of $\text{La}(\text{Fe}_{1-x}\text{Al}_x)_{13}$ with neutron source. They found that the structure favored the fcc-like coordination of the Fe atoms, with Al statistically distributed only over the Fe^{II} sites. Previous findings on both single crystal [57] and powder neutron diffraction data from 2008 to 2011 [58, 59, 60] all demonstrated the same preference of Si atoms for the crystallographic $96i$ position. In this

work, our neutron diffraction results are consistent with these reports and we take the same conclusion for our refinements.

Lanthanum and Fe^I atoms form a CsCl-type packing. Lanthanum and the surrounding 24 Fe^{II}/Si atoms form an almost spherical “snub cube” arrangement with all equal La- Fe^{II}/Si distances. The Fe^I atoms are located at the center of an icosahedron of 12 Fe^{II}/Si atoms with local site symmetry of $T_h(m\bar{3})$. The two Fe^I-centered icosahedra are interconnected by tetrahedral stars [61] such that they are arranged in an alternate pattern with adjacent icosahedra rotated 90° with respect to each other (Appendix B). Within the unit cell, there are 8 icosahedra and therefore 104 spins. Each Fe^{II}/Si site is surrounded by 9 nearest Fe^{II}/Si atoms, one Fe^I atom and two La atoms.

The substitution of Si for Fe induces a linear reduction of the lattice volume and an increase of the magnetic ordering temperature, as shown in Figure I-12. The lattice contraction is expected from the difference between the metallic radii of Fe (1.25 Å) and Si (1.18 Å) [62].

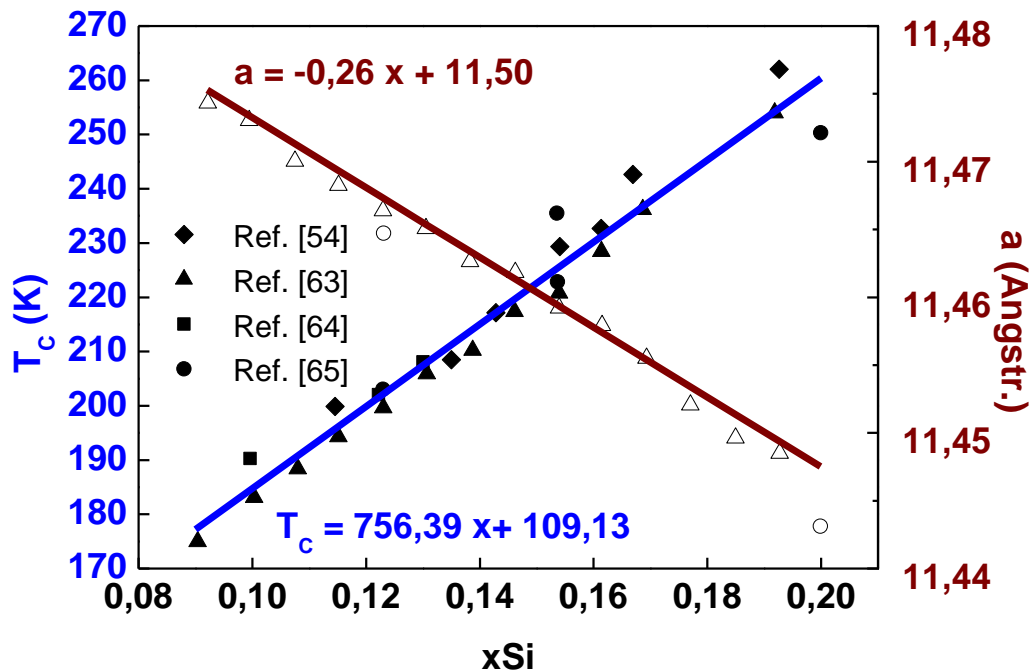


Figure I-12. Variation of the unit cell parameter and the Curie temperature of the phase $\text{La}(\text{Fe}_{1-x}\text{Si}_x)_{13}$ with Si concentration. Data extracted from reference [54, 63, 64, 65].

At higher Si content, the $\text{La}(\text{Fe}_{1-x}\text{Si}_x)_{13}$ system exhibits a structural transformation from cubic to a tetragonal derivative of the NaZn_{13} -type structure. The composition-dependent phase transformation has been demonstrated by Han and Miller [57]. A transition range from cubic to the tetragonal structure is observed in composition range around $0.2 < x < 0.25$, with mixed phases and sign of splitting. For higher concentration of Si, a reduction of symmetry is observed and the structure shifts into the body-centered tetragonal structure (space group $I4/mcm$, No. 140).

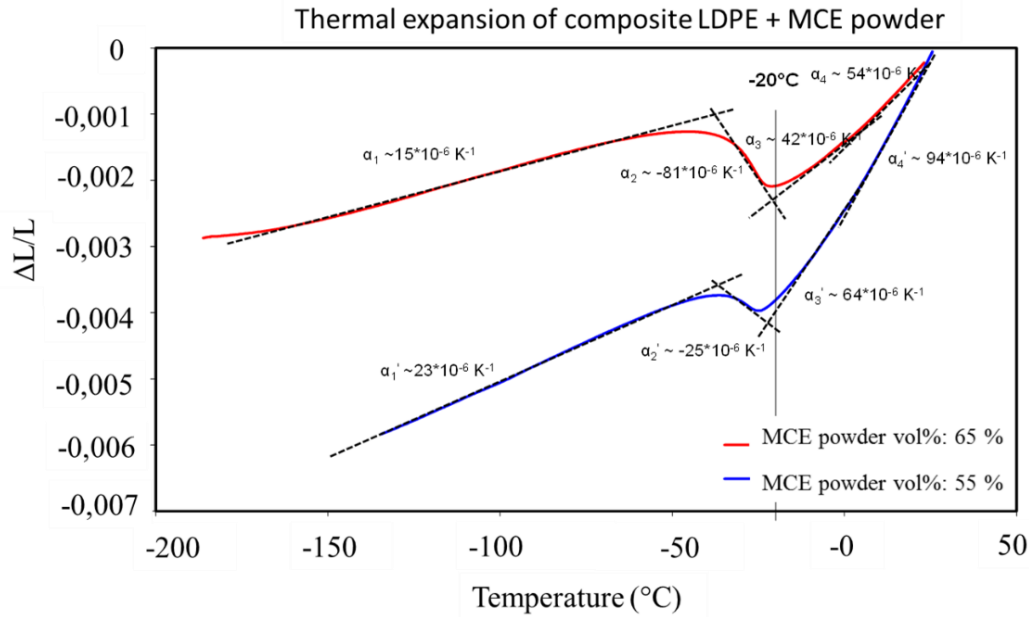


Figure I-13. Invar behavior of the magnetocaloric powder $\text{La}(\text{Fe}_{1-x}\text{Si}_x)_{13}$ close to T_C , measured in polymer-mixed composites.

Palstra *et al.* noted a lattice softening near the T_C of these compounds and associated this with the Invar effect [54]. Indeed, we found typical negative thermal expansion behavior with magnetocaloric powder around its T_C , as shown in Figure I-13. Far from its ordering temperature, lattice expands with rising temperature. Close to T_C , a contraction peak is observed due to the magneto-volume contraction of the $\text{La}(\text{Fe}_{1-x}\text{Si}_x)_{13}$ phase, which is expressed in negative thermal expansion coefficients.

4.2. Magnetic properties

The magnetic properties of $\text{La}(\text{Fe}_{1-x}\text{Si}_x)_{13}$ were investigated by Palstra *et al.* [54, 66, 67], later on Tang *et al.* [68] and Fujita *et al.* [69]. These studies have shown that the compound has a paramagnetic state near room temperature and undergoes a transition towards a ferromagnetic state upon cooling. The ordering temperature varies linearly with increasing Si content from 180 K ($x=0.09$) to 260 K ($x=0.2$), as illustrated in Figure I-12.

In the $\text{La}(\text{Fe}_{1-x}\text{Si}_x)_{13}$ phases, the magnetization is entirely carried by the Fe atoms. Although Si atoms is non-magnetic, they play an important role in the value of the magnetic ordering temperature of the phase. Palstra *et al.* [67] and Rosca [64] have observed a monotonic decrease of the saturation magnetization with increasing Si content, as shown in Figure I-14. The substitution of Si for Fe produces two effects, the lattice contraction and the hybridization between the electronic orbitals of Si and Fe atoms. The hybridization between the Fe-3d and Si-2p orbitals modifies the density of states below Fermi level, which Wang *et al.* [70] have proposed as the reason for the change in Fe magnetic moment. Previous results have shown that the magnetic moment of Fe atoms at the 8b site is smaller than at the 96i site for the NaZn_{13} -type structure [56].

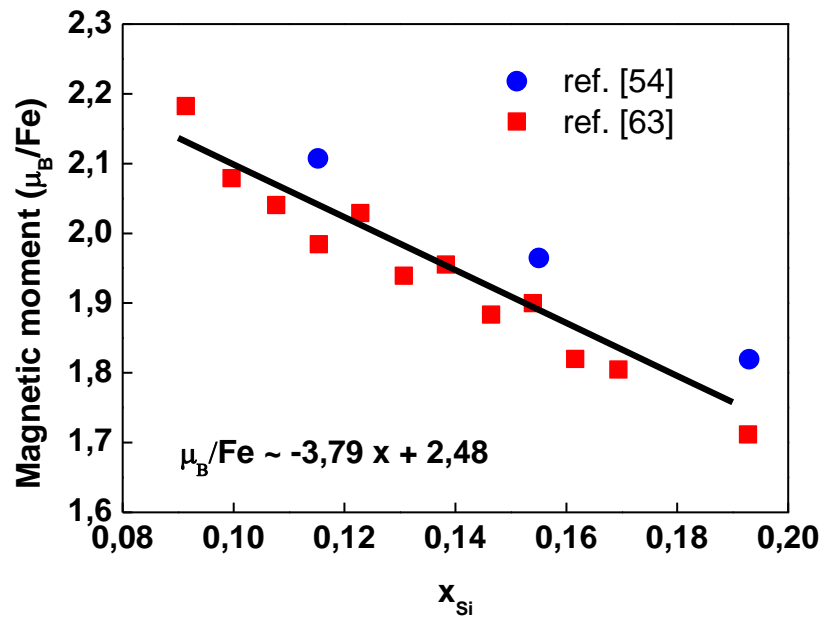


Figure I-14. Magnetic moment of Fe atoms in $La(Fe_{1-x}Si_x)_{13}$ as a function of Si content. Data were obtained from reference [54, 63].

One key aspect of the magnetic responses of $La(Fe_{1-x}Si_x)_{13}$ is that magnetic field can drive the Curie temperature of the first-order transition to high temperatures at a rate of 4 K/T, regardless of the composition. This shift of T_C under applied field implies a field-induced meta-magnetic transition from a paramagnetic to a ferromagnetic state just above the zero-field T_C . Fujita *et al.* [69] have explained this phenomenon by the stabilization of the FM state under applied field, which is due to a field-induced change in the band structure of $3d$ electrons. The so-called itinerant-electron metamagnetic (IEM) transition usually presents a characteristic S-shape in the M^2 - H/M isotherms (Arrott-Belov [71] plot).

In the Rhodes-Wohlfarth model [72], an itinerant ferromagnet has an effective moment above T_C much larger than the saturation moment in the ferromagnetic phase, as calculated from a Curie-Weiss fit to the susceptibility. The IEM transition is said to contribute to the large volume increase (1%) accompanying the transition to the ferromagnetic state [69] and the asymmetric broadening of the ΔS_M curve with increasing field [73].

There is no structural change accompanying the phase transition and the material maintains the cubic structure in both the PM and FM state. However, there is a significant volume difference (1%) between the two magnetic states. No crystal structure change allows the material to be cycled without having detrimental effect to the MCE values, which is consistent with observations by Fujita *et al.* after repeated thermal cycles [74].

The simultaneous sharp change of lattice parameter and magnetization at a transition temperature strongly influences the magnetic entropy change. Zhang *et al.* [75] have argued that the associated strain contributes to the surface energy term in the nucleation and growth model of a FOMT. A quantitative relation is then proposed by Shen *et al.* [63] that for $\partial V/V$ bigger than 0.5%, the transition becomes first order. Consequently, the magnetic transition is highly sensitive to pressure [76, 77].

Therefore, not only can we expect the magnetic transition to be sensitive to composition and the elaboration methods, but also we need to anticipate a strain-sensitive effect. Large polycrystalline samples can show a variation of chemical composition and broad transition, and thus, it is necessary to control the sample grain size to ensure homogeneity.

4.3. Magnetocaloric properties

The magnetocaloric property of $\text{La}(\text{Fe}_{1-x}\text{Si}_x)_{13}$ did not come into focus until the observations done by Hu *et al.* in 2000 [78]. They reported a large MCE for compound $\text{LaFe}_{11.4}\text{Si}_{1.6}$, exhibiting a $-\Delta S_M$ of about $19.4 \text{ J/kg}\cdot\text{K}$ (equivalent of $16 \text{ J/mol}\cdot\text{K} = 140 \text{ mJ/cm}^3\cdot\text{K}$) at 208 K for a magnetic field change of 5 T. The magneto-elastic coupling results in a 1% volume reduction from the ferromagnetic to the paramagnetic phase. For comparison, under similar conditions of a magnetic field change of 5 T, $\text{Gd}_5\text{Ge}_2\text{Si}_2$ [21] shows a $-\Delta S_M$ of $18.5 \text{ J/kg}\cdot\text{K}$ at 276 K and $\text{MnFeP}_{1-x}\text{As}_x$ has an entropy change reported around $18 \text{ J/kg}\cdot\text{K}$ at 300 K [46].

For small concentration of Si, the magnetic transition of $\text{La}(\text{Fe}_{1-x}\text{Si}_x)_{13}$ is first-order-like, which exhibits an abrupt drop in magnetization around the Curie temperature. The transition is characterized by large thermal and magnetic hysteresis. Wen *et al.* [79] and Fujieda *et al.* [80] observed typical second-order behavior with the disappearance of hysteresis for $x > 0.18$, as the structure shifts towards the tetragonal symmetry mentioned above. The transition from a strongly FOMT to a strongly SOMT also leads to a decrease of MCE, represented in Figure I-15.

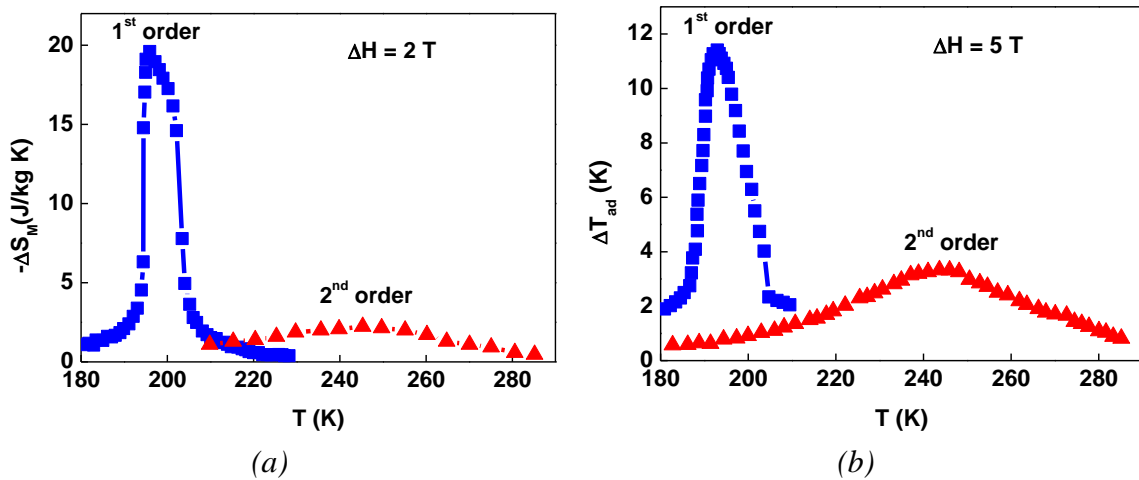


Figure I-15. (a) Isothermal entropy change for a field variation from 0 to 2 T for compositions $\text{La}(\text{Fe}_{0.88}\text{Si}_{0.12})_{13}$ and $\text{La}(\text{Fe}_{0.8}\text{Si}_{0.2})_{13}$ showing first and second order transition, data extracted from reference [81]. (b) Adiabatic temperature change for a field change from 0 to 5 T for composition $\text{La}(\text{Fe}_{0.89}\text{Si}_{0.11})_{13}$ and $\text{La}(\text{Fe}_{0.83}\text{Si}_{0.17})_{13}$, data extracted from [63].

Figure I-16 shows the influence of Si content and Curie temperature on the peak value of ΔS_M for $\text{La}(\text{Fe}_{1-x}\text{Si}_x)_{13}$ compounds for a field change from 0 to 2 T. The MCE performance shows a degradation with increasing Si content, which leads to more second-order characteristics of the transition. The adiabatic temperature change data are rather scarce in the literature and more difficult to obtain. However, given the large thermal hysteresis for the materials exhibiting first-order transition, the respective ΔT_{ad} performance should be less advantageous for the compounds with low content of Si.

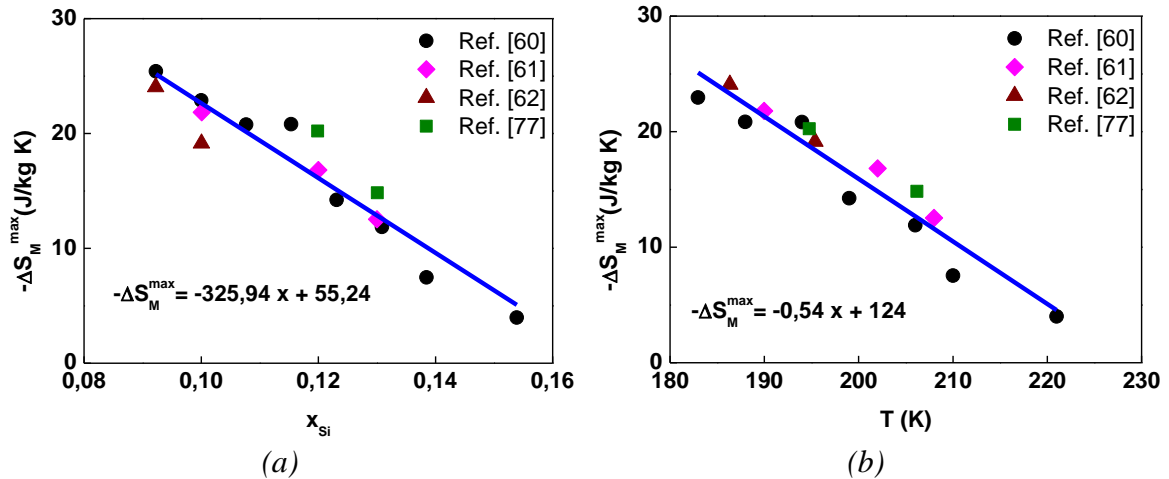


Figure I-16. Variation of the peak value of $-\Delta S_M$ for $\text{La}(\text{Fe}_{1-x}\text{Si}_x)_{13}$ samples as a function of (a) Si content and (b) T_c under a field change from 0 to 2 T, data extracted from [63, 64, 65, 81].

4.4. Composition tuning

Generally, we look at the neighboring elements of La, Fe, and Si for substitutional candidates. After partial substitution, the lattice is either expanded or contracted, depending on the relative size of the substituent. This leads to not only a modification of the interatomic distances within the structure, but also a change in the electronic structure [82].

Substitutional composition changes can take place on the three elemental contents of the $\text{La}(\text{Fe}_{1-x}\text{Si}_x)_{13}$ phase. Al, instead of Si, can also stabilize the pseudo-binary compound formation. Hu *et al.* [83] have mentioned $\text{LaFe}_{11.47}\text{Co}_{0.23}\text{Al}_{1.3}$ exhibiting a second-order phase transition at 200 K with ΔS_M in the order of Gd. K. Morrison *et al.* [84] have shown that partial substitution of Al on the $\text{Fe}^{\text{II}}/\text{Si}$ site leads to a broadening of the magnetic transition, which is less interesting due to the decrease of ΔS_M . Increasing Al concentration on the Si site leads to a lattice expansion due to the larger atomic radius of Al than that of Si [85]. The magnetic transition also shifts towards an AFM-PM transition. Substitutions on the Fe and La sites are discussed below.

4.4.1. Rare earth element tuning

A. Fujita and colleagues at the Tohoku University have performed systematic studies on the effect of rare earth doping on the La site [86]. In order to avoid occurrence of impurity phases, the content of rare earth substitution is generally quite small. The ionic radius of lanthanide elements decreases with increasing the atomic number, therefore, the decrease in unit cell parameter of the Ce-substituted compound is attributed to the lanthanide contraction. The subsequent decrease in the Curie temperature is proportional to the rare earth substituent concentration, as illustrated in Figure I-17.

The T_C reduction caused by Ce is much stronger than that by Pr, which is due to the perturbation of the molecular field from the magnetic moments from Pr atoms [86]. For similar reasons, the impact of Pr on the magnetocaloric performance is also less dramatic as compared with Ce. Another remark from Figure I-17 is the slight enhancement of MCE with

Ce and Pr substitution. The first-order nature of the phase transition is strengthened with substitution on the rare earth site. Therefore, it should be noted that thermal hysteresis also increases with Ce partial substitution, which can have a negative effect on the reversibility of the adiabatic temperature change.

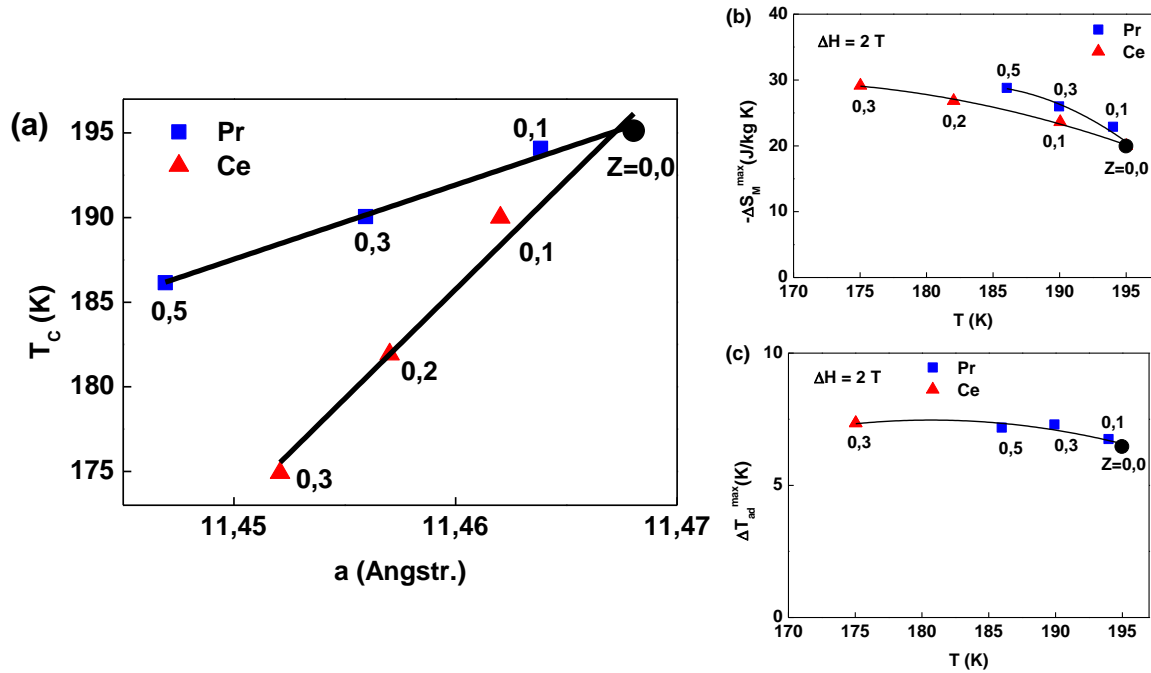


Figure I-17 (a) Variation of T_c in function of the lattice parameter a ; and the MCE performance represented by the peak height of (b) $-\Delta S_m^{max}$ and (c) ΔT_{ad}^{max} for $La_{1-z}R_z(Fe_{0.88}Si_{0.12})_{13}$ samples ($R=Pr$ and Ce), taken from reference [86].

Curie temperature of the 1:13 phase decreases with Ce substitution, which is mainly attributed to magnetovolume effect in the $(LaFe_{1-x}Si_x)_{13}$ phase as Ce carries no magnetic moment. The isothermal magnetic entropy change is found to increase after Ce partial substitution [87].

The first-order character is found to increase with Ce partial substitution. For instance, $LaFe_{11.18}Si_{1.82}$ exhibits a second order magnetic transition. By partially substituting La with Ce, the transition can be tuned towards lower temperature range with first-order characteristics and enhanced MCE.

Fujieda *et al.* [81] have found that substitution of La by Ce atoms has similar effect as reducing the Si content. For instance, $LaFe_{11.18}Si_{1.82}$ exhibits a second-order magnetic transition. By either partially substituting La with Ce or increasing slightly the Fe content, the transition can be tuned towards lower temperature range with first-order characteristics and enhanced MCE. Moreover, partial Ce substitution does not significantly decrease the magnetization in the ground state. By considering the effect of pressure on the Landau coefficient, Fujita *et al.* [82] have concluded that Ce substitution to La results in a change in the electronic structure, and not just a magnetovolume effect.

4.4.2. Transition metal tuning

The transition temperature can also be tuned by replacing Fe by other transition metals. The effects of Cr, Ni, and Mn substitutions for Fe on the Curie temperature of the 1:13 phase have been previously studied. Chromium and Ni have only weak impact on T_C , whereas Mn strongly decreases the magnetic ordering temperature from 195 K in $\text{LaFe}_{11.44}\text{Si}_{1.56}$ to 136 K in $\text{LaFe}_{11.05}\text{Mn}_{0.39}\text{Si}_{1.56}$ [88]. The introduction of Mn is found to decrease the transition temperature in a linear fashion [89]. The thermal hysteresis is reduced with Mn substitution, indicating the transition characteristics is transforming from first to second order. Krautz *et al.* [90] suggested that Mn might inhibit the formation of the $\text{La}(\text{Fe},\text{Si})_{13}$ phase during homogenization, as observed particularly in Si-poor samples. Specific heat measurements at zero magnetic field show that Mn decreases the height of the peak of the specific heat capacity and the difference between heating and cooling curves disappears [91]. The gradual change of the phase transition drives a decrease of ΔS_M values with increasing Mn substitution.

Cobalt substitution on the Fe site is attractive because not only it raises T_C close to room temperature, but also it helps to control T_C change precisely. The variations of isothermal entropy change under a field change of 2 T are shown in Figure I-18 for two series of samples.

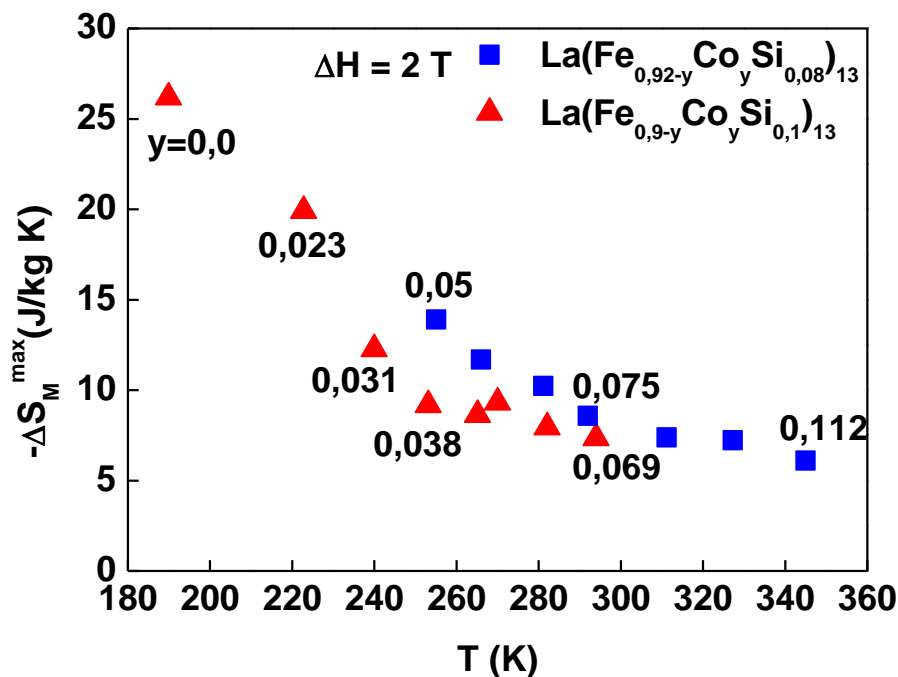


Figure I-18. Variation of the peak value of the isothermal entropy change for two series of samples: $\text{La}(\text{Fe}_{0.92-y}\text{Co}_y\text{Si}_{0.08})_{13}$ (reference [92]) and $\text{La}(\text{Fe}_{0.9-y}\text{Co}_y\text{Si}_{0.1})_{13}$ (reference [93]) under a field change of 2 T.

The Curie temperature of the LaCo_{13} alloy is around 1297 K, which is much higher than that of $\text{La}(\text{Fe},\text{Si})_{13}$ alloys. This is an indication that the Co-Co interactions are much stronger than those of between Fe atoms in LaFe_{13} alloys. The unit cell parameter barely changes with Co partial substitution. The increase of T_C in the Co-substituted La-Fe-Si alloys can be attributed to (1) the strong Co-Fe exchange interaction and (2) the Fe-Co and Co-Co interactions. Hu *et al.* investigated $\text{LaFe}_{11.2}\text{Co}_{0.7}\text{Si}_{1.1}$ with T_C at 274 K and reported a peak

value of ΔS_M at 20.3 J/kg·K under a field change of 5 T [94]. The temperature hysteresis reduces with the augmentation of Co content. This implies that the incorporation of Co weakens the first-order characteristic of magnetic transition at T_C . The field-induced IEM transition is driven from first to second-order as well [95, 96]. Consequently, this leads to a reduction of the MCE. Therefore, Co substitution can be accompanied by a small concentration in Si in order to counterbalance the effect of driving the transition towards second-order, as can be seen from Figure I-18.

4.4.3. Interstitial tuning

As we add light elements such as hydrogen, carbon, boron, and nitrogen to the interstitial voids, the $\text{La}(\text{Fe}_{1-x}\text{Si}_x)_{13}$ lattice is expanded. Interstitial atoms take up space in the lattice, leading to a reduction of the Fe 3d wave function overlap and thus, an increase in T_C [80]. The size of the interstitial element is directly associated with the extent of T_C increase per interstitial element. This is another method to approach the working temperature of this phase towards room temperature range.

Boron insertion in $\text{LaFe}_{11.5}\text{Al}_{1.5}$ leads to a ferromagnetic to paramagnetic transition, compared to the antiferromagnetic to paramagnetic transition normally observed in $\text{La}(\text{Fe}_{1-x}\text{Al}_x)_{13}$ compounds [97]. With increasing B content, T_C increases and thermal hysteresis is depressed. The magnetic transition shifts towards second-order and the maximum magnetic entropy change is reduced [98].

Liu *et al.* [99] have shown that nitrogen interstitial in $\text{La}(\text{Fe}_{1-x}\text{Al}_x)_{13}$ can increase the T_C to almost 900 K with about 9% lattice expansion. Brück [100] attributed the increase of ordering temperature by interstitial N to changes in the electronic structure, rather than in the interatomic distances. Nitrogenation also leads to increased amount of impurity phase, $\alpha\text{-Fe}(\text{Si})$, as observed by Balli *et al.* [101].

Liu *et al.* [102] investigated the effect of carbon insertion in the $\text{La}(\text{Fe}_{0.88}\text{Al}_{0.12})_{13}$ structure due to the improved chemical stability compared with the N and H in $\text{La}(\text{Fe}_{0.88}\text{Al}_{0.12})_{13}$ compounds. Carbon interstitials are also able to increase T_C , but at the expense of lowering ΔS_M because the first-order IEM transition shifts progressively towards a second-order one with increasing C addition [103, 104]. Moreover, C content can be easily controlled by direct melting using Fe-C alloys, whereas for H and N, solid-gas reaction becomes necessary, which limits the potential of industrial upscaling if one wants to control precisely the interstitial content.

Hydrogen insertion leads to a symmetric expansion of the lattice volume, which, as a results, increases significantly T_C . Hydrogen is by far the most effective choice in interstitial insertion while maintaining high MCE performance.

As shown in Figure I-19, the ordering temperature increases linearly with the concentration of hydrogen. The first-order nature of the transition is maintained after hydrogenation and the isothermal magnetic entropy peak height shows only minor reduction. Contrary to the substitution of Co or Si, hydrogenation is an effective method to approach the working temperature of the alloy to room temperature without driving the transition towards second-order.

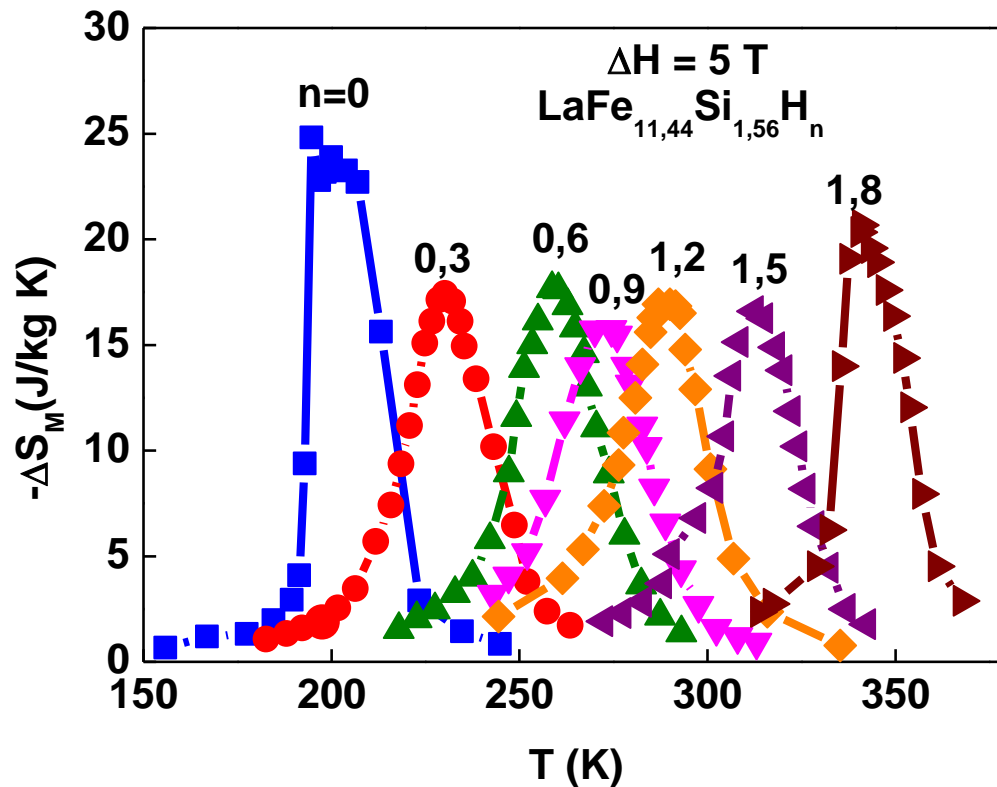


Figure I-19. Isothermal entropy change as a function of hydrogen atoms per unit formula in sample series $\text{LaFe}_{11.44}\text{Si}_{1.56}\text{H}_n$ under a field variation of 5 T, data extracted from reference [105].

Hydrogenation can be easily achieved through a heat treatment of the material under hydrogen atmosphere or hydrogen pressure between 473 to 673 K. The maximum capacity of accommodation for hydrogen interstitials is about 1.8 atom per unit formula, which is 60% of the theoretical limit. The hydrogen content can be controlled through the mass difference, although it is possible to determine the concentration by gas chromatography and gas fusion analyses. Hydrogen insertion was introduced from as early as 2003 [74], yet low stability of hydrides at elevated temperature is still an issue. Chapter IV and V will focus on addressing the issue of hydrogen instability.

4.4.4. State of the art of performance

In terms of composition development, it seems like we are approaching the limit of this family of materials today. Figure I-20 summarizes the isothermal entropy change as a function of T_C for various types of $\text{La}(\text{Fe}_{1-x}\text{Si}_x)_{13}$ materials for a magnetic field change from 0 to 2 T. This is the most commonly reported magnetocaloric data in the literature and allows us to understand the notion of limit we are approaching for these materials. The two principle strategies to control T_C (substitution and interstitial insertion) are complementary in terms of the resulting working temperature for room temperature refrigeration application. The $\text{La}(\text{Fe}_{1-x-y}\text{Co}_y\text{Si}_x)_{13}$ compositions with a low concentration of Si ($x_{\text{Si}} = 0,08$) are more performant in the temperature below 0 °C, whereas the $\text{La}(\text{Fe}_{1-x-y}\text{Mn}_y\text{Si}_x)_{13}\text{H}_z$ materials with a typical Si content of $x_{\text{Si}} = 0,10$ is more adapted for above 0 °C range.

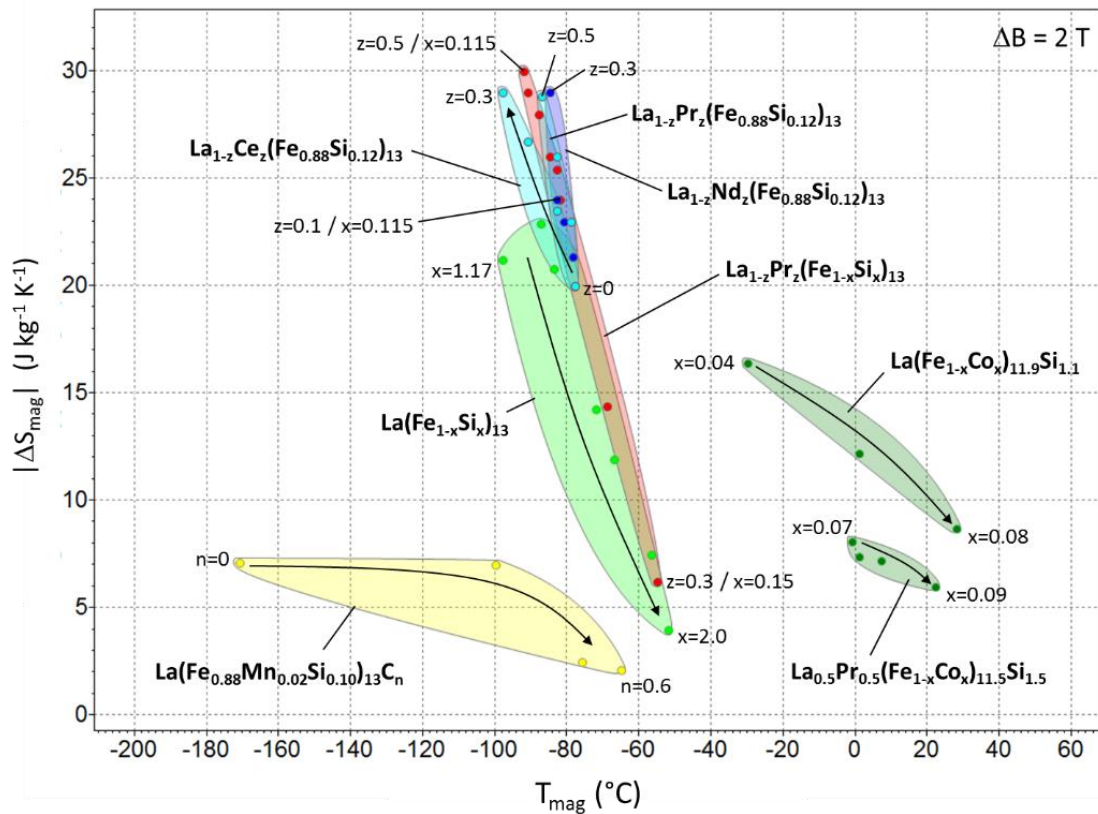


Figure I-20. Properties of $\text{LaFe}_{13-x}\text{Si}_x$ -based materials in a space of “magnetic entropy variation ($|\Delta S_{\text{mag}}|$) – magnetic transition temperature (T_{mag})” for a field variation from 0 to 2 T. Taken from reference [50], submitted to *Techniques de l’Ingénieur*, 2016.

The main challenge today for these materials lies, on one hand, in the solution of developing an industrial process that is technically feasible and economically exploitable, so that one that can obtain T_C precision of 1 to 2 K. On the other hand, it lies in the long-term stability insurance for these materials, particularly for the hydrogenated ones.

References

- [1] World Energy Council, "2015 World Energy Trilemma report," May 2015. [Online]. Available: <https://www.worldenergy.org/publications/2015/world-energy-trilemma-2015-priority-actions-on-climate-change-and-how-to-balance-the-trilemma/>. [Accessed 1 March 2016].
- [2] "European Commission, Energy Efficiency, Building," 2015. [Online]. Available: <http://ec.europa.eu/energy/en/topics/energy-efficiency/buildings>. [Accessed 11 March 2016].
- [3] W. Goetzler, S. Goffri, S. Jasinski, R. Legett, H. Lisle, A. Marantan, M. Millard, D. Pinault, D. Westphalen and R. Zogg, "Energy Savings Potential and R&D Opportunities for Commercial Refrigeration," 2009.
- [4] G. Velders, D. Fahey, J. Daniel, M. McFarland and S. Andersen, *Proc. Natl. Acad. Sci.*, vol. 106, p. 10949, 2009.
- [5] G. Velders, S. Solomon and J. Daniel, *Atmos. Chem. Phys.*, vol. 14, p. 4563, 2014.
- [6] S. Dufourd, Réfrigérateur thermoacoustique : études analytiques et expérimentales en vue d'une miniaturisation, Ecole centrale de Lyon, 2001.
- [7] D. Zhao and G. Tan, *Appl. Therm. Eng.*, vol. 66, p. 15, 2014.
- [8] L. Kuhn, N. Pryds, C. Bahl and A. Smith, *J. Phys.: Conf. Ser.*, vol. 303, p. 1, 2011.
- [9] D. Brown, J. Dirks, N. Fernandez and T. Stout, "The prospects of Alternatives to Vapor Compression Technology for Space Cooling and Food refrigeration Applications," Pacific Northwest National Laboratory (U.S.), Washington D.C., 2010.
- [10] T. Christiaanse and E. Brück, *Metall. Mater. Trans. E*, vol. 1, p. 36, 2014.
- [11] P. Weiss and A. Piccard, *J. Phys. (Paris)*, vol. 7, p. 103, 1917.
- [12] P. Weiss and A. Piccard, *Comptes Rendus*, vol. 166, p. 352, 1918.
- [13] E. Warburg, *Ann. Phys.*, vol. 249, p. 141, 1881.
- [14] A. Smith, C. Bahl, R. Bjork, K. Engelbrecht, K. Nielsen and N. Pryds, *Adv. Energy Mater.*, vol. 2, p. 1288, 2012.
- [15] P. Debye, *Ann. Physik.*, vol. 81, p. 1154, 1926.
- [16] W. Giauque, *J. Amer. Chem. Soc.*, vol. 49, p. 1864, 1927.
- [17] W. Giauque and D. MacDougall, *Phy. Rev.*, vol. 43, p. 768, 1933.
- [18] G.V. Brown, *J. Appl. Phys.*, vol. 47, p. 3673, 1976.
- [19] J. Barclay, in *Proceeding of the Second Biennial on Refrigeration for Cryocooler Sensors and Electronic Systems*, 1983.

- [20] V. Pecharsky and K. Gschneidner, *J. Magn. Magn. Mater.*, vol. 200, p. 44, 1999.
- [21] V. K. Pecharsky and K. A. Gschneider Jr., *Phys. Rev. Lett.*, vol. 78, p. 4494, 1997.
- [22] C. Zimm, A. Jastrab, A. Sternberg, V. Pecharsky, K. Gschneider Jr., M. Osborne and I. Anderson, *Adv. Cryog. Eng.*, vol. 43, p. 1759, 1998.
- [23] Cooling post, "Debut for magnetic refrigeration wine cooler," 2015. [Online]. Available: <http://www.coolingpost.com/world-news/debut-for-magnetic-refrigeration-wine-cooler/>. [Accessed 11 March 2016].
- [24] E. Brück, H. Yibole and L. Zhang, *Phil. Trans. R. Soc. A*, vol. 374, 2016.
- [25] A. Morrish, in *The Physical Principles of Magnetism*, New York, Wiley, 1965.
- [26] J. Lyubina, "Magnetocaloric materials," in *Novel functional magnetic materials*, Springer, 2016, pp. 115-186.
- [27] G. Urbain, P. Weiss and F. Trombe, *Comptes Rendus*, vol. 200, p. 2132, 1935.
- [28] H. Oesterreicher and F. Parker, *J. Appl. Phys.*, vol. 55, p. 4334, 1984.
- [29] M. Kuz'min, K. Skokov, D. Karpenkov, J. Moore, M. Richter and O. Gutfleisch, *Appl. Phys. Lett.*, vol. 99, 2011.
- [30] J. Lyubina, M. Kuz'min, K. Nenkov, O. Gutfleisch, M. Richter, D. Schlagel, T. Lograsso and K. Gschneider, *Phys. Rev. B*, vol. 83, 2011.
- [31] S. Fujieda, A. Fujita and K. Fukamichi, *Mat. Trans.*, vol. 49, p. 1994, 2008.
- [32] N. Trung, Z. Ou, T. Gortenmulder, O. Tegus, K. Buschow and E. Brück, *Appl. Phys. Lett.*, vol. 94, p. 102513, 2009.
- [33] S. Gama, A. Coelho, A. de Campos, A. Carvalho, F. Gandra, P. von Ranke and N. de Oliveira, *Phys. Rev. Lett.*, vol. 93, p. 237202, 2004.
- [34] A. de Campos, D. Rocco, A. Carvalho, L. Caron, A. Coelho, S. Gama, L. Da Silva, F. Gandra, A. dos Santos, L. Cardoso, P. von Ranke and N. de Oliveira, *Nat. Mat.*, vol. 5, p. 802, 2006.
- [35] D. Rocco, A. de Campos, A. Carvalho, L. Caron, A. Coelho, S. Gama, F. Gandra, A. dos Santos, L. Cardoso, P. von Ranke and N. de Oliveira, *Appl. Phys. Lett.*, vol. 90, p. 242507, 2007.
- [36] C. Xu, G. Li and L. Wang, *J. Appl. Phys.*, vol. 99, p. 123913, 2006.
- [37] A. Giguere, M. Foldeaki, B. Gopal, R. Chahine, T. Bose, A. Frydman and J. Barclay, *Phys. Rev. Lett.*, vol. 83, p. 2262, 1999.
- [38] J. Amaral and V. Amaral, *J. Magn. Magn. Mater.*, vol. 322, p. 1552, 2010.
- [39] J. Sun, F. Hu and B. Shen, *Phys. Rev. Lett.*, vol. 85, p. 4191, 2000.
- [40] L. Caron, Z. Ou, T. Nguyen, D. Cam Thanh, O. Tegus and E. Brück, *J. Magn. Magn. Mat.*, vol. 321, p. 3559, 2009.

- [41] N. de Oliveira, *Eur. Phys. J. B*, vol. 40, p. 259, 2004.
- [42] N. de Oliveira and P. von Ranke, *J. Phys. Condens. Matter*, vol. 17, p. 3325, 2005.
- [43] V. Basso, *J. Phys.: Condens. Matter*, vol. 23, p. 226004, 2011.
- [44] S. Dan'kov, A. Tishin, V. Pecharsky and K. Gschneider, *Phys. Rev. B*, vol. 57, p. 3478, 1998.
- [45] K. Gschneider Jr., V. Pecharsky and A. Tsokol, *Rep. Prog. Phys.*, vol. 68, p. 1479, 2005.
- [46] O. Tegus, E. Brück, K. Buschow and F. de Boer, *Nature*, vol. 415, p. 150, 2002.
- [47] L. Caron, M. Hudl, V. Hoglin, N. Dung, C. Gomez, M. Sahlberg, E. Brück, Y. Andersson and P. Nordblad, *Phys. Rev. B*, vol. 88, p. 094440, 2013.
- [48] H. Fjellvag and A. Kjekshus, *Acta Chem. Scand.*, vol. A38, p. 1, 1984.
- [49] D. T. Cam Thanh, E. Brück, N. T. Trung, J. C. P. Klaasse, K. H. J. Buschow, Z. Q. Ou, O. Tegus and L. Caron, *J. Appl. Phys.*, vol. 103, p. 07B318, 2008.
- [50] C. Mayer, S. Miraglia and S. Gorsse, "Matériaux magnéto-caloriques," submitted to *Techniques de l'Ingénieur*, vol. K733, 2016.
- [51] J. Lyubina, O. Gutfleisch, M. Kuz'min and M. Richter, *J. Magn. Magn. Mater.*, vol. 320, p. 2252, 2008.
- [52] J. Lyubina, R. Schäfer, N. Martin, L. Schultz and O. Gutfleisch, *Adv. Mater.*, vol. 22, p. 3735, 2010.
- [53] G. Gao, S. Wu, X. Yan, Y. Zhang, W. Tang and J. Liang, *J. Alloys. compds.*, vol. 202, p. 101, 1993.
- [54] T. Palstra, J. Mydosh, G. Nieuwenhuys, A. van der Kraan and K. Buschow, *J. Magn. Magn. Mater.*, vol. 36, p. 290, 1983.
- [55] P. Kripyakevich, O. Zarechnyuk, E. Gladushevsky and O. Bodak, *Z. Anorg. Chem.*, vol. 358, p. 90, 1968.
- [56] T. Palstra, G. Nieuwenhuys, J. Mydosh, R. Helmholtz and K. Buschow, *J. Magn. Magn. Mater.*, vol. 54, p. 995, 1986.
- [57] M. Han and G. Miller, *Inorg. Chem.*, vol. 47, p. 515, 2008.
- [58] S. Fujieda, A. Fujita, K. Fukamichi, Y. Yamaguchi and K. Ohoyama, *J. Phys. Soc. Jpn.*, vol. 77, pp. 1-8, 2008.
- [59] M. Rosca, M. Balli, D. Fruchart, D. Gignoux, E. Hlil, S. Miraglia, B. Ouladdiaf and P. Wolfers, *J. Alloy Compd.*, no. 490, p. 50, 2010.
- [60] J. Lyubina, *J. Appl. Phys.*, vol. 109, p. 07A902, 2011.
- [61] H. Nyman and S. Andersson, *Acta Cryst.*, vol. A35, p. 937, 1979.

- [62] J. Huheey, E. Keiter and R. Keiter, *Inorganic Chemistry: Principles of Structure and Reactivity*, 4th ed., Harper Collins College Publishers, 1993, p. 292.
- [63] B. Shen, J. Sun, F. Hu, H. Zhang and Z. Cheng, *Adv. Mater.*, vol. 21, p. 4545, 2009.
- [64] M. Rosca, Ph.D. thesis manuscript "*Matériaux de type LaFe_{13-x}Si_x à fort pouvoir magnétocalorique - Synthèse et optimisation de composés massifs et hypertexturés – Caractérisations fondamentales*", Grenoble: l'Université Joseph Fourier, 2012. French. <tel-00663184>
- [65] J. Liu, M. Krautz, K. Skokov, T. G. Woodcock and O. Gutfleisch, *Acta. Mater.*, vol. 59, p. 3602, 2011.
- [66] T. Palstra, H. Werij, G. Nieuwenhuys, J. Mydosh, F. de Boer and K. Buschow, *J. Phys. F: Met. Phys.*, vol. 14, p. 1961, 1984.
- [67] T. Palstra, G. Nieuwenhuys, J. Mydosh and K. Buschow, *Phys. Rev. B*, vol. 31, p. 4622, 1985.
- [68] W. Tang, J. Liang, G. Rao and X. Yan, *Phys. Stat. Sol.*, vol. 141, p. 217, 1994.
- [69] A. Fujita, Y. Akamatsu and K. Fukamichi, *J. Appl. Phys.*, vol. 85, p. 4756, 1999.
- [70] F. Wang, J. Zhang, Y. Chen, G. Wang, J. Sun, S. Zhang and B. Shen, *Phys. Rev. B*, vol. 69, p. 094424, 2004.
- [71] K. Belov and A. Goriga, *Fiz. Metal. Metalloved. Aked. Nank SSSR*, Vols. 2-3, 1956.
- [72] P. Rhodes and E. Wohlfarth, *Proc. R. Soc. Lond. A*, vol. 273, p. 247, 1963.
- [73] F. Hu, B. Shen, J. Sun, Z. Cheng, R. Rao and X. Zhang, *Appl. Phys. Lett.*, vol. 78, p. 3675, 2001.
- [74] A. Fujita, S. Fujieda, Y. Hasegawa and K. Fukamichi, *Phys. Rev. B*, vol. 67, p. 104416, 2003.
- [75] H. Zhang, F. Wang, T. Zhao, S. Zhang, J. Sun and B. Shen, *Phys. Rev. B*, vol. 70, p. 212402, 2004.
- [76] A. Fujita, K. Fukamichi, K. Koyama and K. Watanabe, *J. Appl. Phys.*, vol. 95, no. 11, p. 6687, 2004.
- [77] L. Jia, J. Sun, Q. Dong, F. Hu, T. Zhao and B. Shen, *Appl. Phys. Lett.*, vol. 92, p. 182503, 2008.
- [78] F. Hu, B. Shen, J. Sun and X. Zhang, *Chin. Phys.*, vol. 9, p. 550, 2000.
- [79] G. Wen, R. Zheng, X. Zhang, W. Wang, J. Chen and G. Wu, *J. Appl. Phys.*, vol. 91, p. 8537, 2002.
- [80] S. Fujieda, A. Fujita and K. Fukamichi, *Appl. Phys. Lett.*, vol. 81, p. 1276, 2002.
- [81] S. Fujieda, A. Fujita and K. Fukamichi, *IEEE Trans. on Mag.*, vol. 41, p. 2787, 2005.
- [82] A. Fujita, S. Fujieda and K. Fukamichi, *J. Phys. D: Appl. Phys.*, vol. 44, p. 064013, 2011.

- [83] F. Hu, B. Shen, J. Sun, Z. Cheng and X. Zhang, *J. Phys.: Condens. Matter*, vol. 12, p. L691, 2000.
- [84] K. Morrison, S. Podgornykh, Y. Shcherbakova, A. Caplin and L. Cohen, *Phys. Rev. B*, vol. 83, p. 144415, 2011.
- [85] Q. Dong, H. Zhang, J. Sun and B. Shen, *J. Phys.: Condens. Matter*, vol. 20, p. 135205, 2008.
- [86] A. Fujita, S. Fujieda and K. Fukamichi, *J. Magn. Magn. Mater.*, vol. 321, pp. 3553-3558, 2009.
- [87] S. Fujieda, A. Fujita and K. Fukamichi, *Mat. Trans.*, vol. 45, p. 3228, 2004.
- [88] S. Fujieda, N. Kawamoto, A. Fujita and K. Fukamichi, *Mater. T. JIM*, vol. 47, p. 482, 2006.
- [89] F. Wang, Y. Chen, G. Wang and B. Shen, *J. Phys. D.: Appl. Phys.*, vol. 36, p. 1, 2003.
- [90] M. Krautz, K. Skokov, T. Gottschall, C. Teixeira, A. Waske, J. Liu, L. Schultz and O. Gutfleisch, *J. Alloys Compd.*, vol. 598, p. 27, 2014.
- [91] V. Basso, M. Küpferling, C. Curcio, C. Bennati, A. Barzca, M. Katter, M. Bratko, E. Lovell, J. Turcaud and L. Cohen, *J. Appl. Phys.*, vol. 118, p. 053907, 2015.
- [92] B. Hansen, L. Kuhn, C. Bahl, M. Lundberg, C. Ancona-Torres and M. Katter, *J. Magn. Magn. Mater.*, vol. 322, p. 3447, 2010.
- [93] M. Balli, D. Fruchart and D. Gignoux, *J. Phys.: Cond. Matter*, vol. 19, p. 236230, 2007.
- [94] F. Hu, B. Shen, J. Sun, G. Wang and Z. Cheng, *Appl. Phys. Lett.*, vol. 80, p. 826, 2002.
- [95] X. Liu, D. Ryan and Z. Altounian, *J. Magn. Magn. Mater.*, vol. 270, p. 305, 2004.
- [96] C. Xiang, Y. Chen and Y. Tang, *J. Magn. Magn. Mater.*, vol. 323, p. 3177, 2011.
- [97] D. Zhang, J. Zhao, J. Shen, H. Zhang and M. Yue, *J. Appl. Phys.*, vol. 115, p. 183908, 2014.
- [98] S. Xie, J. Li and Y. Zhang, *J. Magn. Magn. Mater.*, vol. 311, p. 589, 2007.
- [99] J. Liu, N. Tang, F. de Boer, P. de Chatel and K. Buschow, *J. Magn. Magn. Mater.*, vol. 140, p. 1035, 1995.
- [100] E. Brück, *J. Appl. D: Appl. Phys.*, vol. 38, p. 381, 2005.
- [101] M. Balli, M. Rosca, D. Fruchart and D. Gignoux, *J. Magn. Magn. Mater.*, vol. 321, p. 123, 2009.
- [102] X. Liu, Z. Altounian and A. Beath, *Journal of Applied Physics*, vol. 95, p. 7067, 2004.
- [103] Y. Chen, F. Wang, B. Shen, G. Wang and J. Sun, *J. Appl. Phys.*, vol. 93, p. 1323, 2003.
- [104] Y. Chen, F. Wang, B. Shen, J. Sun, G. Wang, F. Hu, Z. Cheng and T. Zhu, *J. Appl. Phys.*, vol. 93, p. 6981, 2003.

Chapter I. State of the Art

- [105] Y. Chen, F. Wang, B. Shen, F. Hu, J. Sun, G. Wang and Z. Cheng, *J. Phys.: Condens. Matter*, vol. 15, p. L161, 2003.
- [106] A. Fujita, S. Fujieda, K. Fukamichi, H. Mitamura and T. Goto, *Phy. Rev. B*, vol. 65, p. 14410, 2002.

Chapter II. Experimental techniques

Chapter II. Experimental techniques	49
1. Synthesis.....	49
1.1. Materials	49
1.2. Arc melting	49
1.3. Electromagnetic induction melting	50
1.4. Annealing	51
1.5. Gas atomization	52
2. Characterization Tools	54
2.1. Structure determination.....	54
2.1.1. Scanning electron microscopy (SEM)	54
2.1.2. X-Ray powder diffraction (XRD).....	55
2.1.3. Powder neutron diffraction	56
2.1.4. Rietveld analysis.....	59
2.2. Magnetic measurements.....	60
2.2.1. Extraction vector magnetometer.....	60
2.2.2. Thermomagnetic analysis	62
2.3. Thermal measurements	63
2.4. Hydrogen dynamics	64
2.4.1. Kinetics	64
2.4.2. Pressure-Composition-Isotherm	66
References	68

Chapter II. Experimental techniques

1. Synthesis

1.1. Materials

All starting elements were obtained from commercial sources and their sources and forms are listed in Table II-1. Most of them were used as received. Mn pieces were cleaned with acid baths to remove oxides. The rare earth metals were filed down to remove the oxide layer on the surface right before melting. The raw elements were carefully weighed to desired stoichiometric proportion with precision in the order of milligrams.

Table II-1. Source and form of all starting elements.

Element	Supplier	Purity	State
La	Alfa Aesar	99.9 %	Rod packed in mineral oil
Ce	Sigma Aldrich	99.9 %	Chips
Fe	Sigma Aldrich	99.99 %	Pieces, irregularly shaped
Mn	Sigma Aldrich	99.9 %	Broken plate
Si	Sigma Aldrich	99.95 %	Pieces
C	Alfa Aesar	99.9995 %	Graphite rod

1.2. Arc melting

The arc melting apparatus used in this work was constructed at the Néel Institute. Its working principle is shown in Figure II-1. The tungsten electrode creates an electric arc at proximity of the sample, providing sufficient temperature to melt the elements. Sample was placed in a water-cooled copper crucible. The chamber was generally purged with Ar several times before melting. The ingot was turned over and remelted several times to ensure homogeneity.

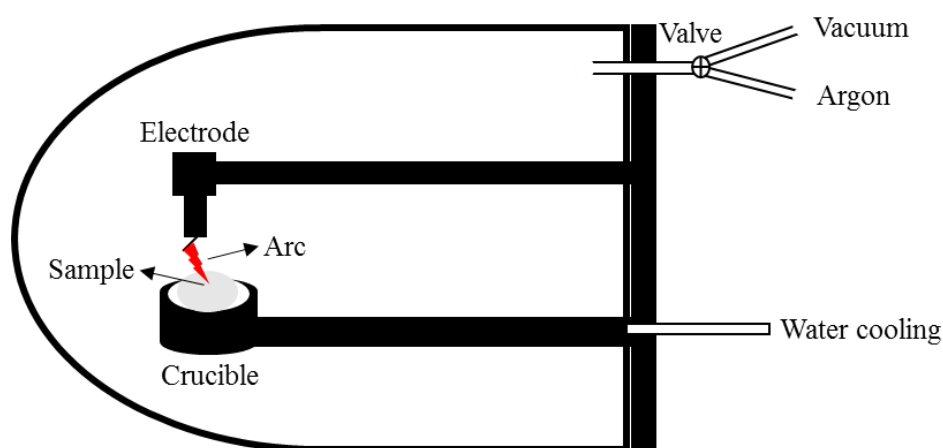


Figure II-1. Schematic representation of the laboratory-developed arc-melting furnace at the Néel Institute.

As the furnace was connected to only a primary pumping device and the rare-earth metals were very sensitive to oxidation, the resulting melted buttons were often oxidized. M. Rosca has reported in her Ph.D. work [1] that the samples elaborated with the laboratory arc melting technique showed an external layer rich in α -(Fe,Si) and LaFeSi phases. Even after long term

annealing (15 days at 1323 K), this layer did not recombine with the rest of the sample to form the $\text{LaFe}_{13-x}\text{Si}_x$ phase. The external layer was formed from the thermal gradient during solidification as the edge of the sample was in direct contact with the cold copper crucible. Meanwhile the vacuum level inside the chamber was not specifically controlled. The purging was done with primary pump and inert gas atmosphere. It is for the same reason that we have abandoned two other induction-melting setups that were not equipped with the secondary condenser of a vacuum pump. In the next section, we present the working principle and setup of a high-frequency induction-melting furnace that was successfully employed.

1.3. Electromagnetic induction melting

Electromagnetic processing of material (EPM) is a unique technology that utilizes various kinds of interactions between material and electromagnetic field for materials processing. The high frequency induction heating and melting is one of the first applications of electromagnetic fields [2]. The alloys are prepared by co-melting according to the technique of high frequency induction melting, also called levitation in cold crucible. The setup used is shown schematically in Figure II-2. An induction coil is connected to the power supply so that a magnetic field is generated from the current flow.

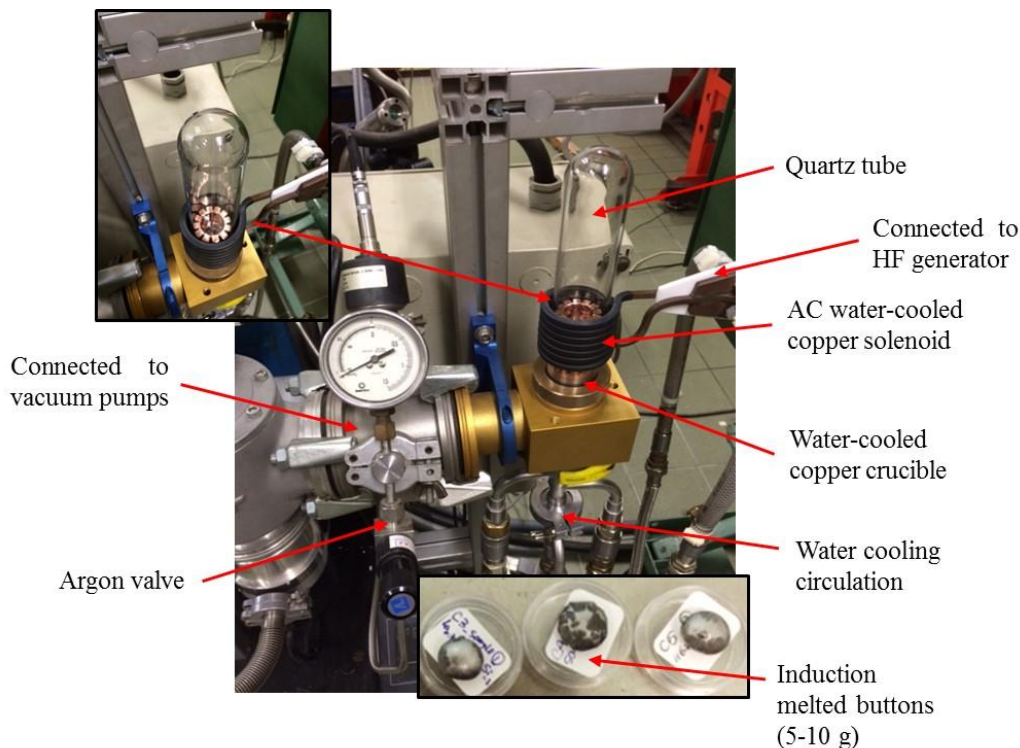


Figure II-2. HF induction melting equipment and sample.

The starting materials with stoichiometric quantities are placed in the copper crucible with water cooling circulation. The crucible is surrounded by water-cooled alternating current solenoid coil of copper wire. An aperiodic generator provides maximum power of 50 kW and delivers a high-frequency alternating current (up to 120 kHz).

The principle is based on heating electrically conductive materials by the application of a varying magnetic field. In this process, the varying magnetic field induces an electric potential, which can then create an electric current depending on the shape and the electrical characteristics of the workpiece. The so-called eddy current dissipates energy and produces heat by flowing against the resistance of the imperfect conductor. The electromagnetic induction follows Faraday's law [3]:

$$e = -N_c \frac{d\Phi}{dt} \quad (\text{II-1})$$

which relates an induced voltage (e) to the time rate of change of the magnetic flux (Φ) and the number of turns (N_c) in the coil.

The induced current circulates through the metallic constituents and heats the sample until melting by Joule effect. The sectional shape of the cold copper crucible is constructed so that the electromagnetic force from the interaction between the exciting field and the induced current counterbalance a part of the gravitational force. Sample is therefore, levitated, which eliminates contact contamination with the crucible. Once melted, the eddy currents cause vigorous stirring of the melt, assuring homogenization of the liquid melt. Moreover, the levitation of the sample can effectively reduce the temperature gradient in the sample during cooling. Once the current is cut, the sample falls abruptly on the cold crucible, which helps to solidify the entire sample rapidly.

The induction melting was performed in collaboration with Richard Haettel (TEMA-Néel-CNRS). Polycrystalline samples of a few grams were synthesized from highly pure elemental components. Elaboration was performed under ultra-pure argon gas (99.995 %) and before each experiment, sample environment was kept under vacuum of at least 10^{-7} Pa. Once all elements have melted, the ingot was turned over and remelted several times to ensure homogeneity.

1.4. Annealing

The as-cast samples display very little trace of the 1-13 phase with the majority being α -Fe(Si) phase and LaFeSi phase, which is discussed in detail in Chapter III. Therefore, it is necessary to proceed with a high-temperature solid-state annealing to allow atomic diffusion in order to favor a single-phase crystallization. Preparation of homogeneous $\text{La}(\text{Fe}_{1-x}\text{Si}_x)_{13}$ compounds is difficult and requires a lengthy homogenization treatment due to the large proportion of α -Fe(Si) dendrites.



Figure II-3. Example of sample preparation for high temperature annealing.

The annealing was performed in collaboration with Muriel Legendre (X'Press-Néel-CNRS) and Rémy Bruyere (X'Press-Néel-CNRS). We used classic high temperature resistance

furnaces, which were controlled by a programmable temperature controller. The buttons were enveloped in a sheet of Molybdenum foil and then placed in a sealed quartz ampoule with partial argon pressure, shown in Figure II-3. The quartz tube was first evacuated and a small amount of Ar gas was introduced before sealing.

Typical annealing temperature varied from 1323 K to 1523 K and the heat treatment was maintained for two weeks before furnace cooling. Even after the long term annealing, the alloys can still contain a small amount of secondary phases, typically α -Fe(Si) and LaFeSi. Industrial processes of these compounds take advantage of rapid solidification methods such as gas atomization or melt-spinning in order to shorten the annealing time needed to homogenize the sample.

1.5. Gas atomization

Since 2011, Erasteel has developed a large-scale process based on powder metallurgy techniques to elaborate $\text{La}_{1-z}\text{Ce}_z(\text{Fe}_{1-x-y}\text{Mn}_y\text{Si}_x)_{13}$ compounds [4]. In this process, raw elements of La, Ce, Fe, Mn, and Si, weighed according to the targeted stoichiometric composition, are first melted in argon atmosphere (1). The liquid metal is then poured through a nozzle (2) to form a metal jet that is subsequently atomized by several argon jets, leading to the formation of liquid metal droplets (3). A schematic representation is shown in Figure II-4. As the droplets fall down the cold atomization tower, they cool down very rapidly and solidify into spherical powder (90-100 μm in mean size diameter) with fine distribution of phases.

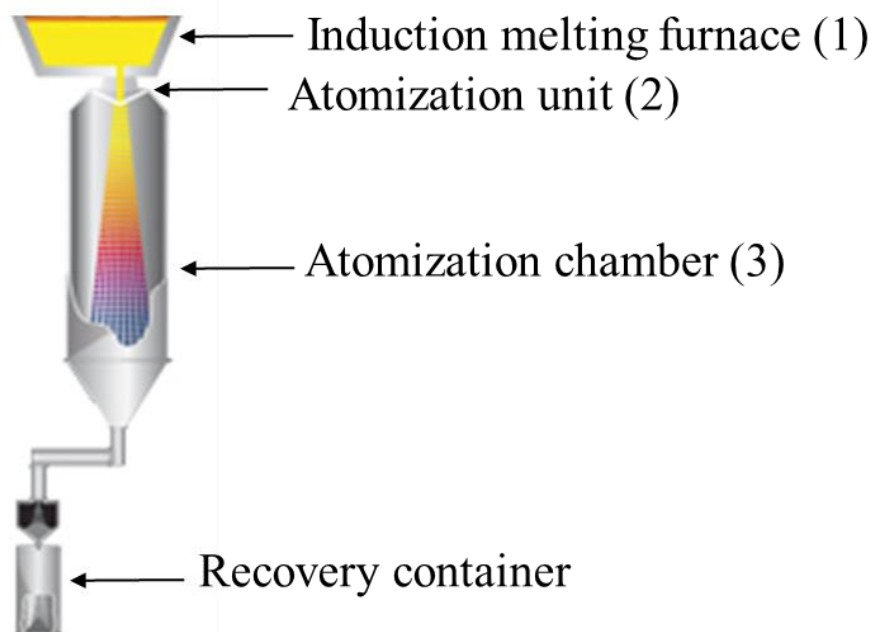


Figure II-4. Schematic representation of the gas atomization tower.

Comparing to conventional casting, gas atomization results in finely segregated microstructures as the iron dendrites did not have enough time to grow due to rapid solidification. The obtained green powder (Figure II-5) is then annealed under Ar for a few hours at temperatures between 1353 K and 1393 K.

The small size of particles and phase domains in the gas atomized powder is advantageous in reducing the necessary time for heat treatment. About 1 hour of annealing at 1373 K is enough to reach about 95 wt% of the cubic magnetocaloric phase. Subsequent hydrogenation is usually necessary to raise the Curie temperature close to room temperature. Hydrogen insertion is achieved by heating between 473 and 673 K under H₂ flow for a few hours and the hydrogen content is estimated by mass gain.

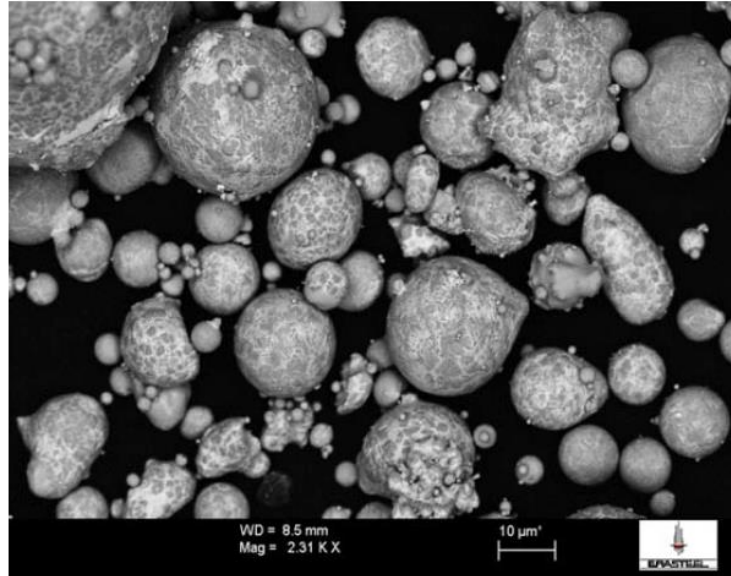


Figure II-5. SEM observation of unpolished gas atomized La-Ce-Fe-Mn-Si- powder.

As potential magnetic refrigerants, $\text{La}_{1-z}\text{Ce}_z(\text{Fe}_{1-x-y}\text{Mn}_y\text{Si}_x)_{13}\text{H}_{\text{max}}$ compounds need to be able to interact efficiently with heat exchange fluid. Thin solid plates seem to be a viable geometry for the material to be cycled in and out of a magnetic field at a certain frequency while exchanging heat. Material processing and shaping is the important next step in the magnetic refrigerant development chain. The intermetallic $\text{La}(\text{Fe}_{1-x}\text{Si}_x)_{13}$ phase gets even more brittle after hydrogenation, making it very difficult to machine. One way to overcome this issue is by extrusion with polymer.

The hydrogenated magnetocaloric powder is first mixed with a thermoplastic polymer to obtain a “ready to shape” feedstock. Then the feedstock is extruded at low temperature to maintain the hydrogen concentration. The polymer composite has the form of bulk plates with the thickness down to 0.5 mm, shown in Figure II-6.



Figure II-6. Extruded profiled plates made of 91.5 wt% of magnetocaloric powder and 8.5 wt% of polymer.

The thin shapes are achieved at relatively low cost. It should be noted that there is a 15% decrease in the magnetocaloric performance (ΔT_{ad}) for the composite. Certainly further development can optimize the balance between magnetocaloric effect and the other properties such as mechanical strength and corrosion resistance.

Today, the process developed by Erasteel, based on gas atomization of the material and subsequent annealing, hydrogenation, and shaping is well controlled apart from minor improvements, but there are still room for further development regarding the compositions, material stability, and overall performance.

2. Characterization Tools

Once the samples were elaborated, it is necessary to identify their phases and microstructures. The magnetocaloric property was evaluated by magnetic characterizations. Lastly, the hydrogen dynamics measurements helped exploring the long-term stability of hydrogenated phases.

2.1. Structure determination

2.1.1. Scanning electron microscopy (SEM)

By bombarding the sample with a monochromatic electron beam, scanning electron microscopy (SEM) takes advantage of the diverse interactions between the electrons and the sample to obtain phase and morphological information on the material.

The images in secondary electrons give information on the surface morphology of the sample. The angular emission of backscattered electrons (BSE) is characteristic of the atomic number on the probe path. Heavy atoms (big atomic number Z) induce stronger elastic scattering between the incident electron and the nucleus. Therefore, BSE images can provide chemical contrast of the specimen.

Qualitative analysis is a routine test on interesting samples to verify chemical compositions. Energy dispersive spectroscopy (EDS) quantitative analysis is performed using a Zeiss Ultra field emission scanning electron microscope equipped with a Bruker SDD EDS analyzer.

Accurate quantitative analysis requires a flat, microscopically smooth surface to maintain the validity of the path length calculation and to ensure that the surface to be analyzed is homogeneous. The sample surface was polished by silicon nitride abrasive paper of different mesh sizes. The finishing step was achieved with substrates containing diamond particles of 3 and 1 μm .

The sample preparation and microstructure observation were performed in collaboration with Sébastien Pairis (Optics and Microscopy-Néel-CNRS), Jérôme Debray (Bulk Crystals-Néel-CNRS), and Paul Chomêton (TEMA-Néel-CNRS). Samples were inspected with back scattered and secondary electron modes to determine the sites for elemental analysis. Typical data collections utilized a beam of the 20 kV accelerating voltage.

2.1.2. X-Ray powder diffraction (XRD)

XRD is the primary method for determining the crystalline structure. It is a non-destructive characterization technique, which can probe length scales from Å to several μm. In order to obtain information at the scale of atomic ordering, the probing wavelength should be within the order of magnitude of the lattice spacing (0.5 to 2 Å for X-rays and 0.5 to 10 Å for neutrons). X-rays interact with the electron cloud in the material and they can be elastically or inelastically scattered. The elastic or coherent scattering gives rise to the interference phenomenon, whereas inelastic or incoherent scattering contributes to the background noise. The Bragg condition dictates constructive interference when the path difference is at integral number of wavelengths:

$$n\lambda = 2d_{hkl}\sin\theta \quad (\text{II-2})$$

with λ being the wavelength, d the inter-planar spacing of a specific family of planes (h , k , l) and θ the angle of incidence.

The intensity of the XRD patterns I_{hkl} is associated with the structure factor F_{hkl} :

$$I_{hkl} = sJ_{hkl}L_{hkl}A|F_{hkl}|^2 \quad (\text{II-3})$$

where s is the scale factor independent of the Miller index of plane hkl , J_{hkl} is the multiplicity of sites, L_{hkl} represents the Lorentz factor and polarization, A is the absorption factor, and F_{hkl} is given by the expression (II-4)

$$F_{hkl} = \sum_j f_j e^{2\pi i(hx_j + ky_j + lz_j)} e^{-\frac{B_j \sin^2\theta}{\lambda^2}} \quad (\text{II-4})$$

In this expression, j describes the sum of all atoms in the unit cell, f_j is the scattering length of atom j at position (x_j, y_j, z_j) , B_j is the isotropic thermal agitation factor of atom j , and the term $e^{-\frac{B_j \sin^2\theta}{\lambda^2}}$ is the Debye-Waller factor that describes the attenuation of X-ray scattering caused by thermal motion.

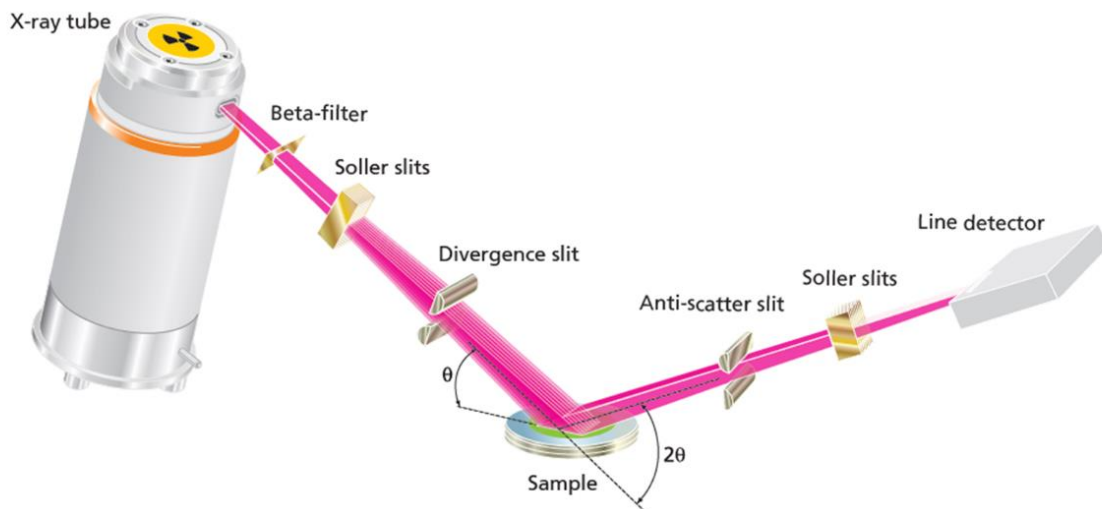


Figure II-7. Schematic representation of the Bragg-Brentano symmetry (θ - 2θ), taken from the PANalytical X'Pert brochure.

Two diffractometers were employed for the work in this thesis. The first was a PANalytical X'Pert MRD X-Ray diffractometer with Bragg-Brentano symmetry (θ - 2θ), whose geometry is shown in schematic representation in Figure II-7, in collaboration with the C.E.I.T. (Centro de Estudios e Investigaciones Técnicas de Gipuzkoa) laboratory in Spain. It was a fixed Cu-anode diffractometer using both Cu $K_{\alpha 1}$ and Cu $K_{\alpha 2}$ radiation ($\lambda_1 = 1.5406 \text{ \AA}$, and $\lambda_2 = 1.5444 \text{ \AA}$, respectively), using a 2θ angle range between 20° to 90° at ambient temperature. The second diffractometer was a Siemens D5000R with a Co anode source ($\lambda = 1.791 \text{ \AA}$) and a graphite (0 0 2) monochromator with the same geometry at Néel Institute.

2.1.3. Powder neutron diffraction

The unique properties of neutron are adapted to probe condensed matter in various domains. The wavelength of neutron (1.8 \AA at 300 K) is at the same order of magnitude as the interatomic distances in solids. With a neutral electric charge, neutrons can penetrate the material without being stopped by the Coulomb force, which allows the extraction of information not only on the surface but also at the interior of the material.

In X-ray diffraction, the scattering amplitude by an element is proportional to its atomic number, which sets a limitation on the amount of information obtained in substances containing hydrogen or in oxides and carbides of heavy elements. In practice, it is highly difficult to distinguish the small contribution made by the light elements such as hydrogen, oxygen, or carbon, in face of the overwhelming amplitude from the heavy constituents. Neutron powder diffraction allows for the determination of the atomic position of the light elements, since the scattering amplitude is less dependent on the atomic number. This is particularly beneficial for the detection of light interstitial elements such as hydrogen and carbon in $\text{La}(\text{Fe}_{1-x}\text{Si}_x)_{13}$ compounds.

Moreover, it is difficult to distinguish between neighboring elements such as Fe and Mn in the same compounds based on XRD data alone. With neutron, the scattering amplitude of such elements may be quite different, as shown in Table II-2.

Table II-2. Neutron scattering lengths for different elements concerned in this work. Except for the first two isotopes, the other values are provided for the elements in their naturally occurring state. All data taken from Neutron News, Vol. 3, No. 3, 1992, pp. 29-37, <https://www.ncnr.nist.gov/resources/n-lengths/list.html> accessed online March 31st, 2016.

Element	Coherent scattering length (fm=1E-15m)	Incoherent scattering length (fm=1E-15m)
¹ H hydrogen	-3.7406	25.274
² H deuterium	6.671	4.04
C	6.6460	--
Si	4.1491	--
Mn	-3.73	1.79
Fe	9.45	--
La	8.24	--
Ce	4.84	--

In these cases, a distinction can be made between neighboring elements from the neutron intensity data. There are two terms associated with the neutron scattering lengths: the coherent scattering length and the incoherent scattering length. Similar to X-ray diffraction, the first term corresponds to the average response of all the atoms and contributes to the intensity of Bragg peaks in ordered structures. The incoherent part comes from individual

response of each atom and is due to the difference from the average scattering length of all the atoms in the material. The incoherent term contributes to the continuous background in a neutron diffraction experiment. For instance, the incoherent scattering length of hydrogen is very high compared with that of deuterium, which gives off an important background contrast in materials containing hydrogen.

The spin $\frac{1}{2}$ present in neutrons is associated with a magnetic moment of about $1.91 \mu_{\text{BN}}$ (the nuclear Bohr magneton, which is three orders of magnitude smaller than the electronic Bohr magneton). This moment interacts with the magnetic moments from unfilled electronic orbitals, allowing the examination of magnetic materials.

Therefore, in neutron powder diffraction, the structure factor has a nuclear $F_{(hkl)N}$ and a magnetic $F_{(hkl)M}$ component:

$$F_{hkl}^2 = |F_{(hkl)N}|^2 + |F_{(hkl)M}|^2 \quad (\text{II-5})$$

$$F_{(hkl)N} = \sum_j b_j e^{2\pi i(hx_j + ky_j + lz_j)} e^{-\frac{B_j \sin \theta}{\lambda^2}} \quad (\text{II-6})$$

$$F_{(hkl)M} = \sum_j (C_{hkl})_j e^{2\pi i(hx_j + ky_j + lz_j)} e^{-\frac{B_j \sin \theta}{\lambda^2}} \quad (\text{II-7})$$

$$\text{and } (C_{hkl})_j = \eta \vec{M}_{j\perp} A(\vec{Q}) \quad (\text{II-8})$$

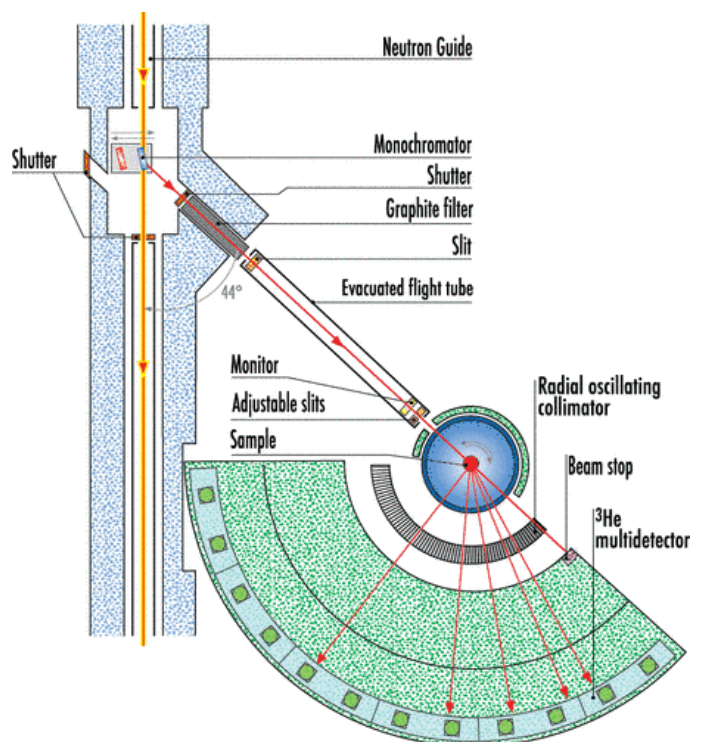
Here b_j is the Fermi level of atom j , $(C_{hkl})_j$ denotes the magnetic scattering length, $\vec{M}_{j\perp}$ represents the projection of the magnetic moment on the perpendicular plan to scattering vector \vec{Q} , η is the scattering amplitude when $Q=0$, and $A(\vec{Q})$ is the Fourier transformation of the spatial distribution of the magnetization density.

Both X-ray and neutron diffraction can be used to determine the lattice expansion during hydrogen loading. Neutron scattering can be used to determine the presence and position of hydrogen within the crystal structure. Powder neutron diffraction has been widely used before and after interstitial charging as well as with *in-situ* solid-gas reactions. This technique is a particularly powerful tool to locate the light elements and to measure accurately the changes in intermetallic distances.

Powder neutron diffraction is able to obtain an average over a significantly larger number of crystalline grains as compared with X-ray diffraction due to the high penetrating power of the neutron. In order to resolve the various Bragg peaks, neutron diffractometer must have high angular resolution by using a high monochromator take-off angle. This high resolution is achieved by having a stack of thin neutron absorbing blades, also called fine Söller collimators, to carefully define the neutron direction to within a few minutes of arc. The monochromating crystal then selects a particular wavelength λ of the neutron beam to be scattered by the powdered sample. A second Söller collimator is placed in front of a detector through all scattering angles in order to measure the scattering intensity. In practice, a multi-detector with a bank of collimators is used to speed up data collection.

In this work, two neutron diffractometers were employed for different purposes. The D1B spectrometer at the ILL (Institut Laue Langevin) was used to obtain *in-situ* neutron diffraction data as the compound was absorbing and releasing deuterium interstitial atoms.

D1B is a two-axis spectrometer dedicated to diffraction experiments with a high neutron flux. The layout of the instrument is shown in Figure II-8 (a).



High Resolution Powder Diffractometer

3T2

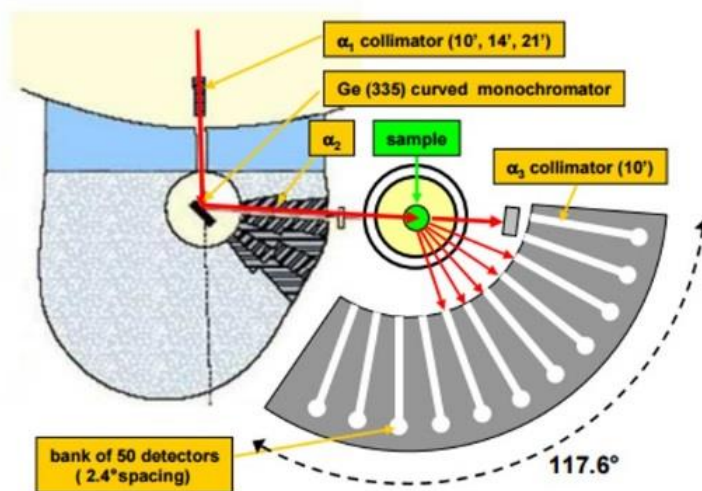


Figure II-8. Schematic layout of two neutron diffractometers used in this work, D1B two-axis diffractometer (top) at ILL [5] and 3T2 high-resolution two-axis diffractometer (bottom) at LLB [6].

In our experiments, a 1.28 Å wavelength was used and deuterium absorption and desorption experiments were performed at 540 K inside an orange cryostat to obtain a sufficiently observable kinetics. Sample was first placed inside the neutron diffraction cell and was heated from room temperature to 540 K in vacuum. As temperature stabilized, ultra-pure deuterium gas was introduced to the cell. Deuterium gas flow was controlled at 20 ml/min

at a constant pressure of 1200 mbar to mimic an industrial process of hydrogenation (constant free flow of hydrogen). Desorption was carried out by switching the gas flow from deuterium to helium at 540 K to trigger mobility of interstitial atoms. After the kinetics reached equilibrium, the sample was cooled down to room temperature and taken out of the cryostat.

The *in-situ* experiments were performed in collaboration with Claire Colin (MRS/CRG-Néel) and Vivian Nassif (CRG-Néel). The diffraction patterns collected at D1B had a 2θ range from 0 to 128° with a step increment of 0.1° . Diffraction patterns were collected every 5 minutes. These raw files can then be summed to obtain files with good statistics.

In order to have precise knowledge of the effect of the interstitial atoms, high-resolution diffraction patterns were recorded at the 3T2 instrument (shown in Figure II-8 (b)) at the LLB (Laboratoire Léon Brillouin) in collaboration with Florence Porcher (LLB). 3T2 provided an incident wavelength of about 1.225 \AA , corresponding to the Ge (335) plane. The diffractograms were collected at room temperature from 4.5° to 115.35° at 0.05° interval.

High resolution and high flux are two conflicting requirements of powder neutron diffraction. In order to resolve the Bragg peaks and obtain information on the crystal structure, using a peak stripping computer program to extract individual peaks is not sufficient. Moreover, there are correlations between peak heights and positions in such a procedure. Rietveld analysis proposes a nice solution to use individual peaks to obtain the crystal structure. Since for a periodic structure, the peak positions (d-spacings) are all determined by the dimensions and angles of the unit cell and the peak intensities are all determined by the positions of the individual atoms in the unit cell, it is possible to refine physically real parameters that describe the structure to fit the observed diffraction profile directly. Therefore, a Rietveld analysis offers much deeper insight into specific details of the structure.

2.1.4. Rietveld analysis

Rietveld full profile refinement [9, 10, 11] is an iterative procedure to refine powder diffraction patterns by the least squares method. A number of parameters are used to describe both sample and instrument. An approximated diffraction pattern that corresponds to a set of given parameters is calculated, after which all or some of the parameters are then refined and a new pattern is calculated. This step is repeated until the difference between the measured and the calculated pattern reaches a minimum. Good initial knowledge of the parameter values are needed since the parameters are approximated by Taylor expansions in the refinement. The program converges by minimizing the following equation:

$$\chi^2 = \sum_i \omega_i (y_{obs,i} - y_{calc,i})^2 \quad (\text{II-9})$$

where $y_{obs,i}$ is the observed intensity and $y_{calc,i}$ the calculated one at point i . ω_i is the weight assigned to each intensity, which is the inverse of the variation of $y_{obs,i}$.

Two groups of parameters are taken into account in the Rietveld method. The first group consists of parameters that describe the instrumental characteristics of the diffractometer, such as the neutron wavelength λ , the zero position of the counter, and three parameters U ,

V, W, which describe the variation with 2θ of the angular width H of the Gaussian curve. The second group involves crystal structure parameters, such as the symmetry, unit cell parameter, and the coordinates and thermal parameters of the individual atoms. For a magnetic phase, both its nuclear and the magnetic contributions are considered and described in distinctive phases.

Rietveld method is a process of refinement in terms of a postulated model. Clearly only those parameters and features that are described in the model can appear in the result. Care should be taken when refining several parameters simultaneously. The program itself works by the least square method and can give non-physical minimum.

All Rietveld refinements in this work were performed with the FullProf Suite program [7] with the assumption of a peak-line profile of Thompson-Cox-Hasting [8] including anisotropic broadening. The background is described by linear interpolation of selected points in the pattern. Low angle peak asymmetry (usually below $2\theta=40^\circ$) was taken into account using the Berar-Baldinozzi model [12].

2.2. Magnetic measurements

2.2.1. Extraction vector magnetometer

Indirect measurements of the MCE via temperature- and field-dependent magnetization curves are the most common measuring technique.

Typically, two procedures were used to probe the magnetic properties of the samples:

- Isofield measurements determined the critical temperature, thermal hysteresis and the width of the transition
- Isothermal measurements were used to calculate the isothermal magnetic entropy change using the Maxwell relation

The magnetization curves obtained in this work were performed with extraction vector magnetometers developed at Néel Institute, in collaboration with Didier Dufeu (Experimental Engineering-Néel) and Yves Deschanel (Experimental Engineering-Néel). Two magnetometers of similar configurations were constructed to measure magnetization in low temperature range (from 1.5 K to 330 K) and high temperature range (200 K – 850 K). The schematic representation and photo of the low-temperature extraction vector magnetometer are shown in Figure II-9.

The two instruments were employed with respect to the Curie temperature range of each sample. Sample holders for the low temperature magnetometer were made of Pyrex and those for the high temperature magnetometer were made of copper.

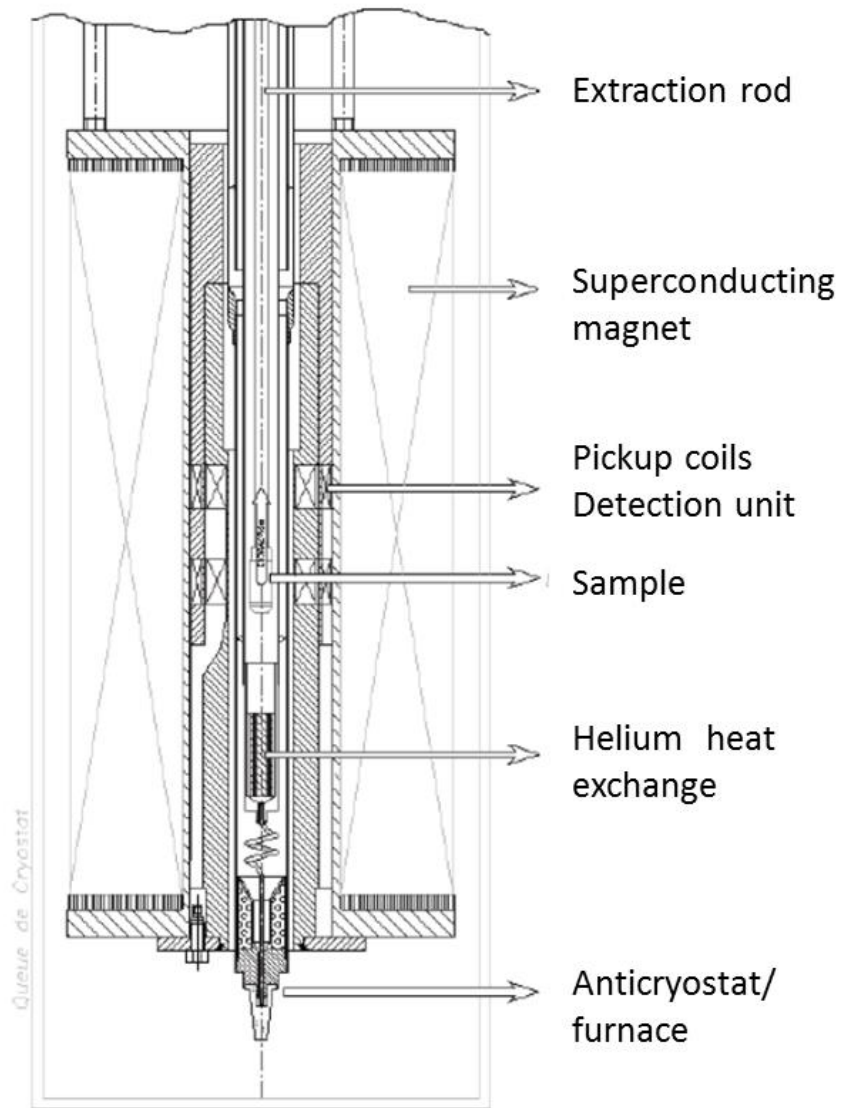


Figure II-9. Schematic representation (top) and photo (bottom) of the extraction vector magnetometer for low-temperature range at the Néel Institute.

The working principal is as follows: the sample is placed in the field of the superconductor coil that can obtain maximum field of 10.5 Tesla. Two pickup coils of reverse directions constitute a detection unit where the sample can be displaced. When the sample of volume V_0 and magnetization $\sigma = J V_0 / \mu_0$ (J is the magnetization per unit volume) is moved from the center of one coil to the other, the induced flux variation is given by the reciprocity theorem

$$\delta\phi = \iiint (\mathbf{B}/I) \mathbf{J} dv / \mu_0 \quad (\text{II-10})$$

where \mathbf{B} is the fictitious magnetic field, which would be produced by a current I circulating in a pickup coil, the integral being extended over the sample volume V_0 . Generally, this equation is reduced, in the case of z-axis pickup coils, to

$$\delta\phi = J_z \iiint (\mathbf{B}/I) \mathbf{J} dv / \mu_0 = \frac{K J_z V_0}{\mu_0} = K \sigma_z \quad (\text{II-11})$$

with

$$K = \frac{1}{V_0} \iiint (\mathbf{B}_z/I) dv \quad (\text{II-12})$$

The flux extraction method gives good precision and sensitivity up to $10^{-7} \text{ A}\cdot\text{m}^2$.

2.2.2. Thermomagnetic analysis

Thermomagnetic Faraday's Balance is principally used to determine the transition temperature and detect existence of additional phases within the prepared alloy. The principle of the thermomagnetic analysis is based on Faraday's theory and the schematic representation is shown in Figure II-10.

The sample is placed in a non-homogeneous magnetic field \vec{H} produced by a permanent magnet, it experiences a force \vec{F} :

$$\vec{F} = \overrightarrow{\text{grad}}(\vec{M} \cdot \vec{H}) = m\chi H \frac{\partial H}{\partial x} \vec{x} \quad (\text{II-13})$$

$$\vec{M} = m\chi \vec{H} \quad (\text{II-14})$$

where m is the mass of the sample, \vec{M} is the magnetization and χ refers to the magnetic susceptibility per unit mass. The force is proportional to the magnetization of the sample and allows us to determine the variation of magnetization with temperature.

The measurements were done with the help of Frédéric Gay (Automatization and Characterization-Néel). The sample was sealed in an evacuated quartz tube and measured inside a temperature-regulated furnace. The Faraday's Balance instrument in Néel Institute can scan temperature range from room temperature up to 1473 K. The sweeping rate used was 6.7 K/min.

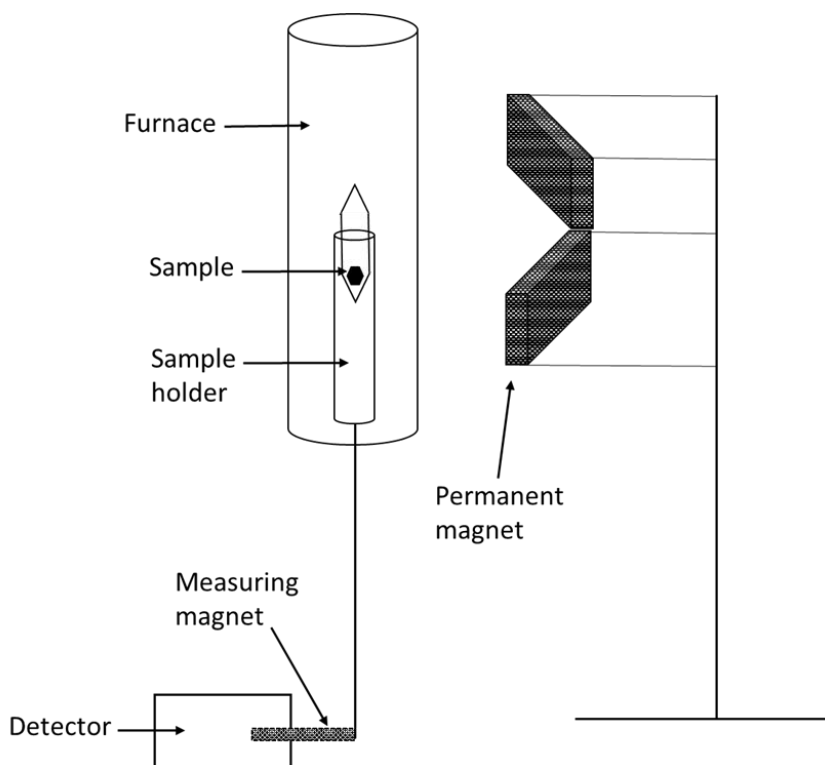


Figure II-10. Schematic representation of the thermomagnetic Faraday's Balance.

2.3. Thermal measurements

The differential scanning calorimetry (DSC) is a common thermos-analytical technique that studies the thermal transition of a material. As the sample passes through a phase transition, the amount of heat required depends on the endothermic or exothermic nature of the transition. This technique measures then the amount of heat required to increase the temperature of the sample and the reference. Differential thermal analysis (DTA) is also used to determine characteristics temperatures of samples. In absence of any reaction or transformation, the temperature difference is weak and regular, indicated by the baseline. As a phase transformation takes place in the sample, it induces energy difference between the sample and reference. The differential temperature (DT) is recorded as a peak or succession of several peaks as a function of time. The sample temperature is tracked simultaneously.

Additionally, DSC allows for the determination of caloric values such as the heat of fusion or heat of crystallization. Both DTA and heat-flux DSC measure the temperature difference between a sample and the reference in μV (thermal voltage). In DSC, the value can also be converted into a heat-flux difference in mW by means of an appropriate calibration.

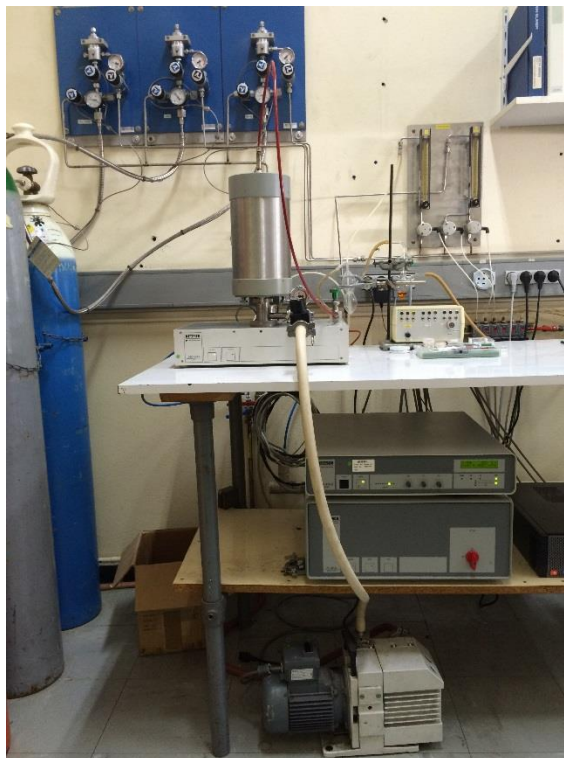


Figure II-11. Netzsch-DSC-404-S instrument at the Néel Institute.

The thermal measurements were carried out using a Netzsch-DSC-404-S instrument in collaboration with Philippe Plaindoux (Automatization and Characterization-Néel). The instrument setup for both DSC and DTA is shown in Figure II-11. Both the sample and the reference were maintained at the same temperature throughout the experiment. The measuring chamber was rinsed with pure argon gas several times before each measurement. The heat flux was measured as a function of temperature, which can vary from room temperature to 1473 K with variable temperature sweep rates. The sweep rate selected for the hydride desorption measurement in this thesis was 5 K/min. To determine the phase transition of Fe-based alloys (Chapter VI), the sweep rate was between 2-10 K/min. For the DTA measurements, the maximum temperature was 177 K with a sweeping rate up to 30 K/min. The experiments were performed under Ar flux of 140 ml/min.

2.4. Hydrogen dynamics

The hydrogen dynamics measurements were performed in collaboration with Patricia de Rango (MRS-Néel) and Emmanuel Verloop (TEMA-Néel).

2.4.1. Kinetics

Generally speaking, the hydrogen sorption measurement can be operated based on both gravimetric and volumetric method. The gravimetric method is relatively simple in principle: the mass loss or gain is recorded as the sample experiences temperature change in equilibrium state. In order to obtain accurate sorption data, however, it is necessary to have a rather sensitive testing system to simulate equilibrium state as much as possible. In the volumetric method, a Sievert's type instrument is employed to precisely determine the volume of sorption and heat equilibrium can be quickly obtained in the testing system.

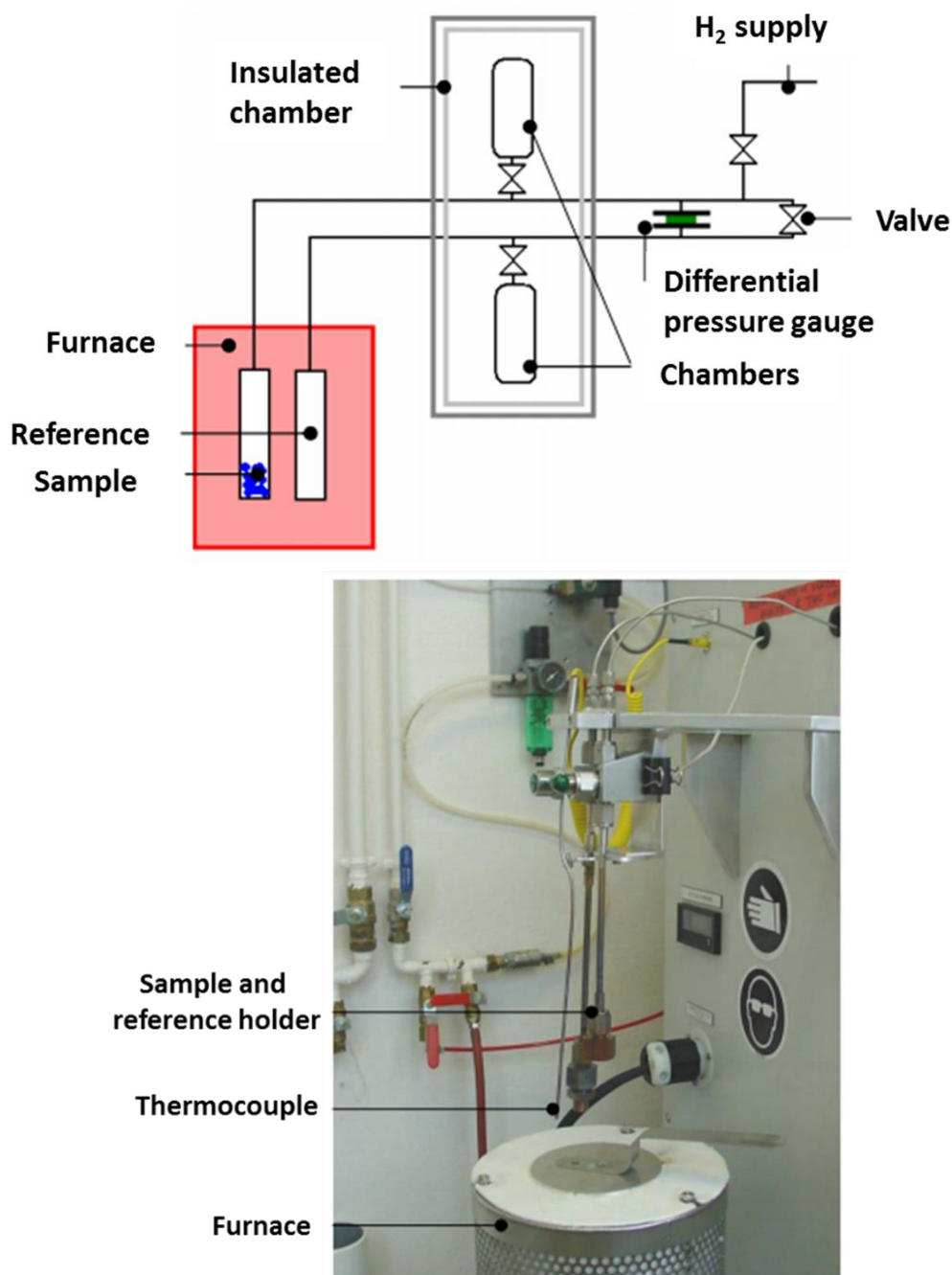


Figure II-12. Simplified schematic representation (top) and photo (bottom) of the hydrogen kinetics-measuring device based on Sievert volumetric method.

In this work, measuring system model HERA C2-3000 designed by HERA Hydrogen System is used to evaluate the hydrogen sorption properties of the investigated materials. The simplified schematic representation and photo are shown in Figure II-12. The amount of material utilized for each measurement is about 500 mg for the HERA volumetric apparatus.

The device calculates the quantity of hydrogen absorbed and desorbed by measuring the variation of the hydrogen partial pressure in a sample holder with a known volume. At a given temperature and pressure, the device allows measuring the absorption and desorption

kinetics as a function of time. In order to obtain a good precision, the partial pressure is measured differentially: two sample chambers of known volume are used, both of which are connected with a sample holder and only one of which contains the sample to be measured while the other chamber is an empty reference.

Therefore, by measuring the pressure difference between the two chambers, one can measure directly the quantity of hydrogen absorbed or desorbed, under given absolute pressure. The two chambers are placed in an isolated furnace regulated in temperature. An additional thermocouple is placed inside the furnace close to the sample holder position in order to give precise temperature reading at the sample holder position. The gas flow in this device is automated with pneumatic valves.

The acquisition procedure is as follows: sample is placed in an initial thermodynamically-stable state under given temperature and pressure. The pressure becomes rapidly superior or inferior than equilibrium pressure and the device records the evolution of hydrogen concentration every 0.5 second until the sample is totally saturated with hydrogen or dehydrogenated.

A very high precision can be achieved by comparing the pressure difference from the sample chamber and a reference chamber. Both chambers are situated in an isolated furnace with temperature regulation. The measuring process is automated with a sophisticated system of gas flux control using pneumatic valves. The sensitivity of the differential gauge is about 0.1 kPa and that of the absolute gauge is 10 kPa. For a classical measurement, the obtained precision of each point on the sorption curve is about 0.01 wt% of hydrogen. The reservoir tank and the cell with total inner volume of approximately 50cc are used for the measurements. The apparatus has a working pressure range from 0.01 to 10 MPa with a precision of 0.005 MPa.

The hydrogen absorption measurements were carried out in a range of applied pressures between 0.1 to 2 MPa, by heating up the sample from room temperature to the desired final temperatures and then keeping it under isothermal and isobaric conditions until the end of the experiment. The hydrogen desorption measurements were performed at the lowest hydrogen pressure possible (typically 0.1 MPa) at the same temperature as absorption. Between each absorption measurement, remaining hydrogen was then released by heating up the sample to 623 K for a few hours under static vacuum conditions.

2.4.2. Pressure-Composition-Isotherm

The Pressure-Composition-Isotherm (PCI) measurement was carried out in a volumetric sorption analyzer of model Hiden Isochema (Figure II-13). The system is combined with a thermal desorption analyzer specifically designed for the measurement of hydrogen storage in milligram quantities. The apparatus can load or activate the material with pure hydrogen pressure for up to 10 MPa and temperature up to 773 K. The sample can be thermally desorbed in helium by linear ramp heating. The hydrogen desorption is measured by a dynamic sampling mass spectrometer (DSMS) with high sensitivity. The hydrogen uptake is measured with a debit analyzer before and after the sample chamber. Typical P-C-I measurements is conducted at constant temperature and by gradually increasing or

decreasing the hydrogen pressure, the hydrogen uptake and release is recorded as a function of pressure.



Figure II-13. HIDEN Isochema IMI series, taken from website http://www.hidenisochema.com/our_products/imi_series/ (accessed on 31/08/2016).

References

- [1] M. Rosca, Ph.D. thesis manuscript "*Matériaux de type LaFe_{13-x}Si_x à fort pouvoir magnéto-calorique - Synthèse et optimisation de composés massifs et hypertexturés – Caractérisations fondamentales*", Grenoble: l'Université Joseph Fourier, 2012. French. <tel-00663184>
- [2] ASM Handbook Volume 4: Heat Treating, vol. 4, ASM International, 1991, p. 398.
- [3] A. Sommerfeld, *Electrodynamics: lectures on theoretical physics*, New York: Academic Press, 1966, p. 372.
- [4] A. Dubrez, P. Vikner, C. Mayer and M. Pierronnet., Patent WO 2013/135908 A1, 19 September 2013.
- [5] Institut Laue-Langevin, "D1B - High resolution neutron two-axis powder diffractometer," Grenoble.
- [6] Laboratoire Léon Brillouin, "3T2 High Resolution Powder Diffractometer," Gif sur Yvette, 2009.
- [7] J. Rodriguez-Carvajal, *Physica B*, vol. 192, p. 55, 1992.
- [8] L. Finger, D. Cox and A. Jephcoat, *J. Appl. Cryst.*, vol. 27, p. 892, 1994.
- [9] H. Rietveld, *Acta Cryst.*, vol. 22, p. 151, 1967.
- [10] H. Rietveld, *J. Appl. Cryst.*, vol. 2, p. 65, 1969.
- [11] R. Young, *The Rietveld Method*, Oxford University Press, 1995.
- [12] J. Bérar and G. Baldinozzi, *J. Appl. Cryst.*, vol. 26, p. 128, 1993.

Chapter III. Studies on the composition optimization

Table of Contents

Chapter III. Studies on the composition optimization.....	71
1. Structural and metallographic study.....	71
1.1. Phase identification.....	71
1.2. Magnetic properties	74
1.3. Evaluation of the magnetocaloric effect	76
2. Effect of substitution	76
2.1. Substitution on the La site by Ce	76
2.2. Substitution on the Fe site.....	86
3. Process optimization	90
3.1. Microstructure.....	91
3.2. Structural properties.....	95
3.3. Magnetic and magnetocaloric properties	96
4. Conclusion.....	98
References	99

Chapter III. Studies on the composition optimization

1. Structural and metallographic study

The $\text{La}(\text{Fe}_{1-x}\text{Si}_x)_{13}$ phases are typically prepared via conventional laboratory melting techniques such as arc melting and induction melting. These techniques generally require very long (one week or longer) annealing time for homogenization. Rapid solidification techniques can effectively reduce the elaboration time (in the order of minutes to hours) while maintaining the phase homogenization quality, hence, suitable for industrial upscaling. Rapid solidification also leads to an increased MCE, which Gutfleisch *et al.* attributed to a more homogeneous element distribution [1]. Combining high energy ball milling and spark plasma sintering can shorten significantly the synthesis time needed for $\text{La}(\text{Fe}_{1-x}\text{Si}_x)_{13}$ phases and shape the material at the same time [2]. At an industrial scale, Erasteel [3] and Vacuumschmelze [4] use powder metallurgy processes to produce $\text{La}(\text{Fe}_{1-x}\text{Si}_x)_{13}$ materials. Hitachi Metals has also explored the strip casting methods [5] in Japan. In the first part of this Chapter, we focus on the structural, magnetic, and magnetocaloric properties of $(\text{La,Ce})(\text{Fe,Mn,Si})_{13}\text{C}_x\text{H}_y$ samples specific to our laboratory elaboration process, which typically consists of high frequency induction melting, homogenization annealing, and hydrogenation. Secondly, the effect of substitutional changes on the La and Fe sites are investigated by means of neutron diffraction and magnetization measurements. Lastly, in order to optimize the laboratory process, we present a study on the influence of the amount of excess rare earth elements on the property of the material.

1.1. Phase identification

The structural properties of the samples were characterized with XRD and SEM. Figure III-1 shows the diffraction pattern for the as-cast sample $\text{LaFe}_{11.7}\text{Si}_{1.3}$ synthesized by high frequency induction melting. The experimental diffractogram is represented in red dots, the black line is the calculated pattern with Rietveld refinement, the blue line on the bottom shows the difference between the observed and calculated pattern, and the vertical lines indicate the Bragg position of the crystallized phase. From the refinement results, the as-cast sample shows a majority of $\alpha\text{-Fe}(\text{Si})$ phase (84%) and LaFeSi phase (15%), with negligible $\text{La}(\text{Fe}_{1-x}\text{Si}_x)_{13}$ phase.

During solidification, $\alpha\text{-Fe}(\text{Si})$ dendrites precipitate and grow in the first place from the liquid. Figure III-2 shows the uniform distribution of $\alpha\text{-Fe}(\text{Si})$ dendrites (in grey), which corresponds to a solid solution of Fe and Si in the cubic structure with more than 90 % in atomic percent of Fe. The dendrites then react peritectically with the surrounding liquid to form a La-rich phase in the interdendritic region [6]. The La-rich phase (in white in Figure III-2) corresponds to the tetragonal LaFeSi phase. The formation of the LaFeSi phase is thermodynamically more favorable than that of the $\text{La}(\text{Fe}_{1-x}\text{Si}_x)_{13}$ phase [7]. The tetragonal LaFeSi phase crystallizes rapidly during cooling, whereas for the formation of the $\text{LaFe}_{13-x}\text{Si}_x$ phase, it is necessary to allow sufficient amount of time in the existence domain of the phase for the atomic diffusion to take place.

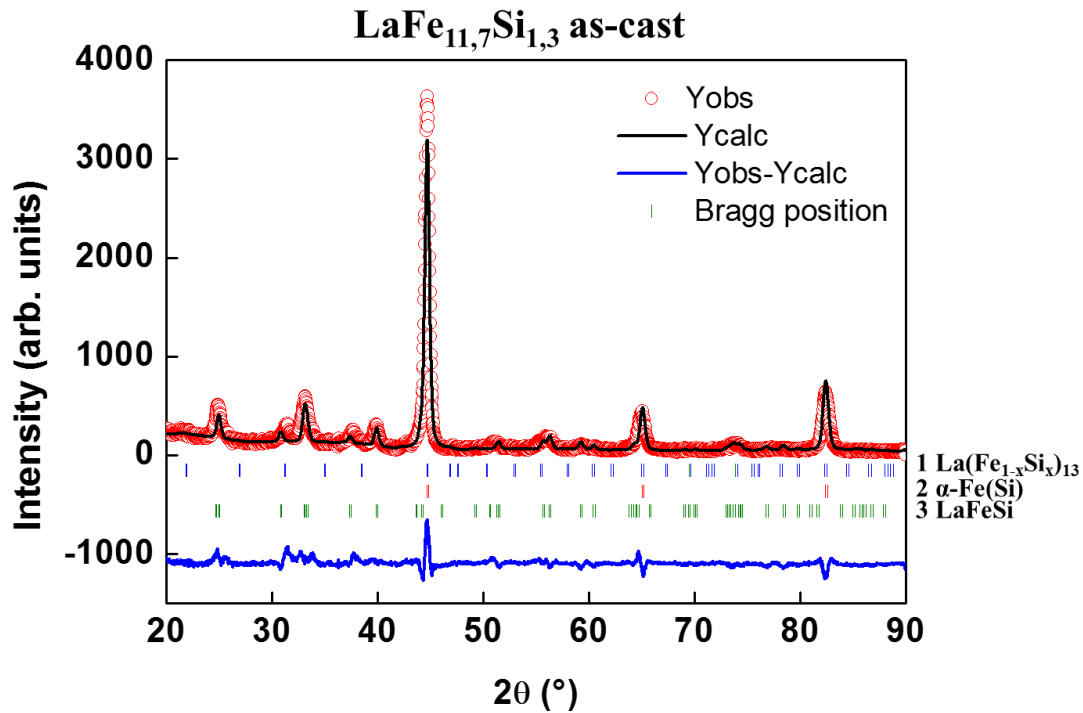


Figure III-1. XRD pattern with Rietveld refinement of as-cast $\text{LaFe}_{11.7}\text{Si}_{1.3}$ sample prepared by high frequency induction melting.

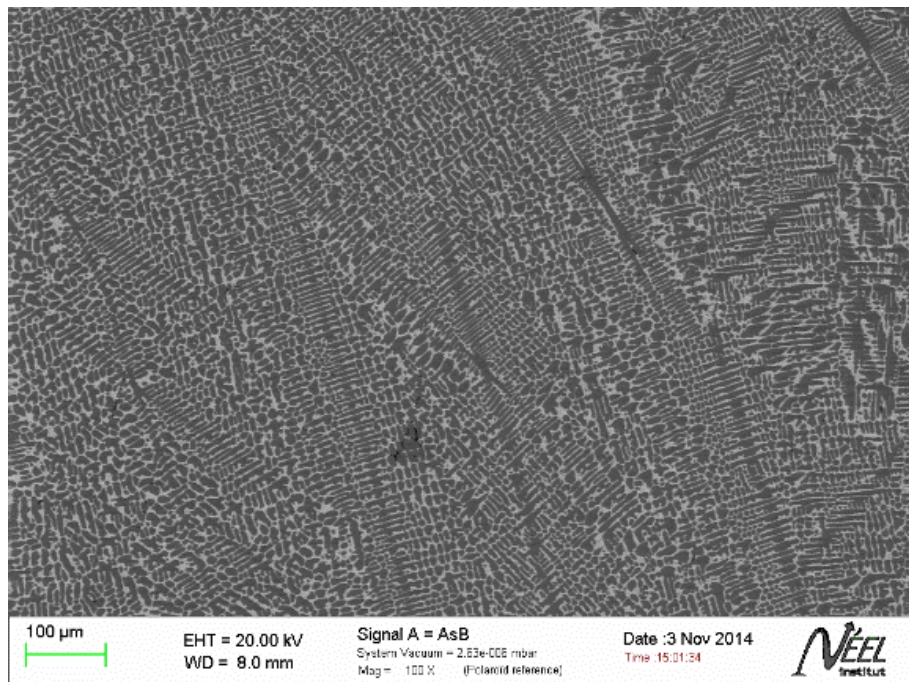


Figure III-2. Backscattered electron image of the as-cast compound $\text{LaFe}_{11.7}\text{Si}_{1.3}$.

After annealing in quartz tube at 1373 K for about two weeks, the same analysis was performed to identify the phases and the microstructure of the annealed sample. As seen from Figure III-3, the peaks from the tetragonal LaFeSi phase have all disappeared and those from the $\alpha\text{-Fe}(\text{Si})$ phase have greatly reduced their intensity, showing only 2% remaining in phase percentage. The annealed sample is almost single-phase $\text{LaFe}_{13-x}\text{Si}_x$.

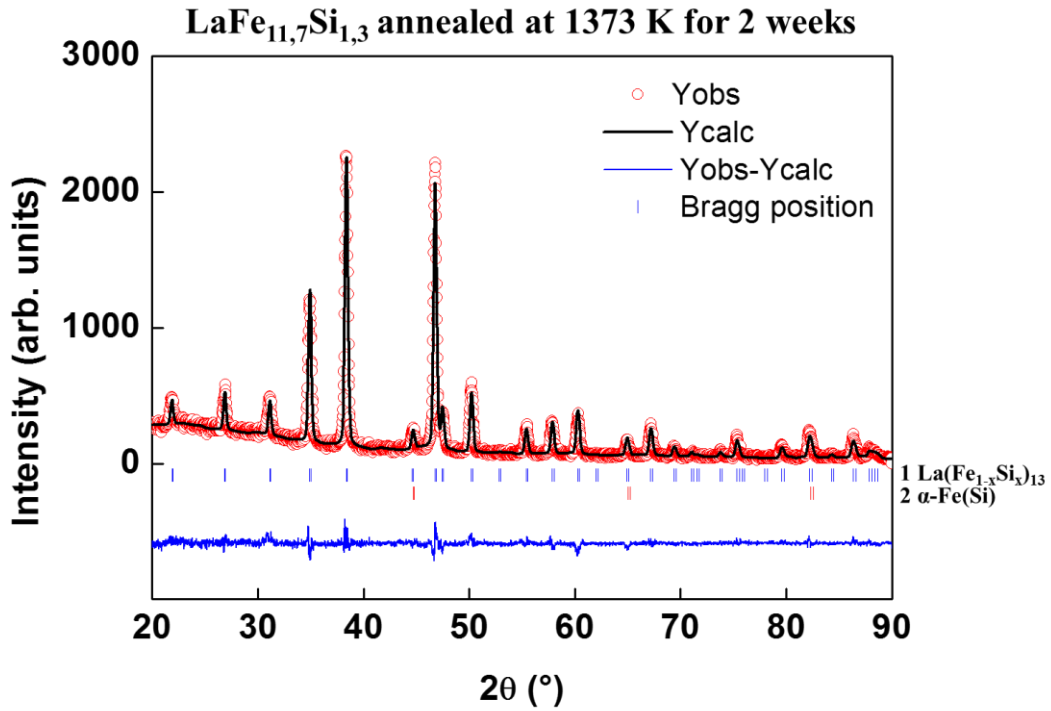


Figure III-3. XRD pattern with Rietveld refinement of annealed $\text{LaFe}_{11.7}\text{Si}_{1.3}$ compound.

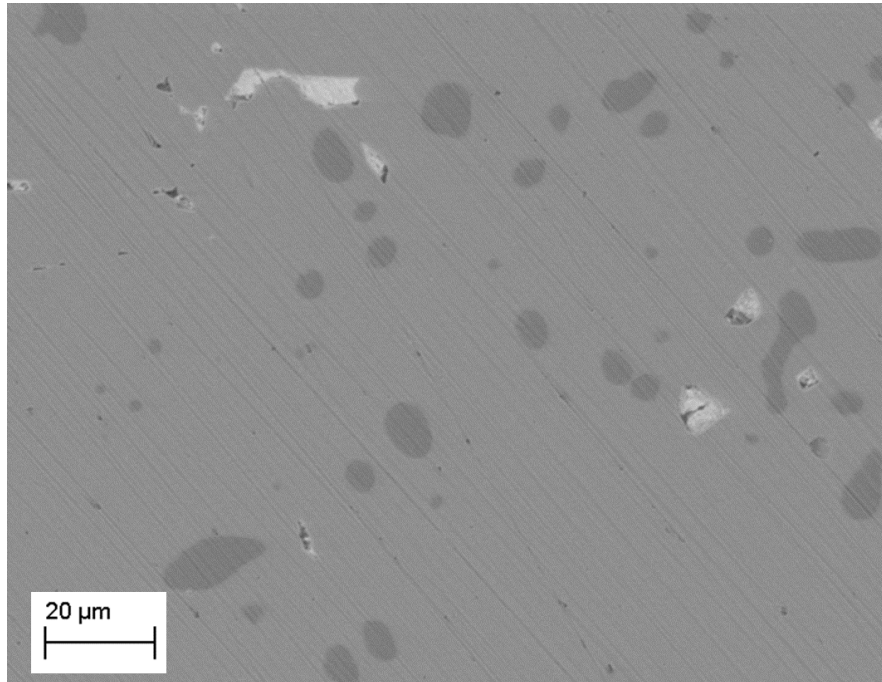
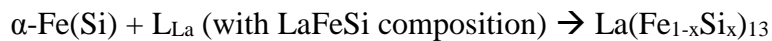


Figure III-4. Microstructure of the annealed $\text{LaFe}_{11.7}\text{Si}_{1.3}$ sample in backscattered electrons.

Niitsu and Kainuma proposed the following peritectic reaction for the formation of single-phase $\text{La}(\text{Fe}_{1-x}\text{Si}_x)_{13}$ with a low Si concentration [8]:



The LaFeSi phase is formed from the liquid (L_{La}) phase during cooling. The vertical section phase diagram is presented in Appendix C. The $\text{La}(\text{Fe}_{1-x}\text{Si}_x)_{13}$ phase has low phase stability

at elevated temperatures and low atomic diffusivity below 1173 K [8, 9], making long-term annealing necessary. Therefore, obtaining a fine α -Fe(Si) and LaFeSi solidification microstructure can facilitate the formation of single-phase $\text{La}(\text{Fe}_{1-x}\text{Si}_x)_{13}$ without long-term annealing [10].

In a non-equilibrium solidification process, the intrinsic incompleteness of a peritectic reaction often results in the preservation of α -Fe(Si) impurity phase at room temperature. The light grey phase on the background corresponds to the $\text{La}(\text{Fe}_{1-x}\text{Si}_x)_{13}$ phase with nominal composition close to desired stoichiometric proportion. The dark grey phases represent the remaining α -Fe(Si) phase. The phase formation correlates strongly with the annealing temperature and duration. It is, however, very difficult to eliminate the α -Fe(Si) phase completely. The annealing at 1373 K for two weeks has been proven as rather optimal to obtain quasi-monophase samples.

1.2. Magnetic properties

The magnetic measurements presented in this part were realized with an extraction magnetometer, whose working principle and characteristics are presented in Chapter II. The magnetization curves as a function of temperature and field were systematically measured for each composition. Figure III-5 (a) shows a typical magnetization curve as a function of temperature under a weak field of 0.05 T for the $\text{La}(\text{Fe}_{1-x}\text{Si}_x)_{13}$ phase exhibiting a first-order magnetic transition (sample of composition $\text{LaFe}_{11.7}\text{Si}_{1.3}$). The ferromagnetic phase at low temperature transforms to the paramagnetic state at high temperature. The ordering temperature is then determined with the differential of the magnetization with respect to the temperature, as indicated by the inset of Figure III-5 (a). For sample of composition $\text{LaFe}_{11.7}\text{Si}_{1.3}$, T_C evaluated from the minimum of dM/dT is around 190 K. The magnetic phase transition is a reversible process. Sample of composition $\text{LaFe}_{11.7}\text{Si}_{1.3}$ shows first-order transition characteristics with a thermal hysteresis of 6 K between the magnetization curves upon heating and cooling, as shown in Figure III-5 (b).

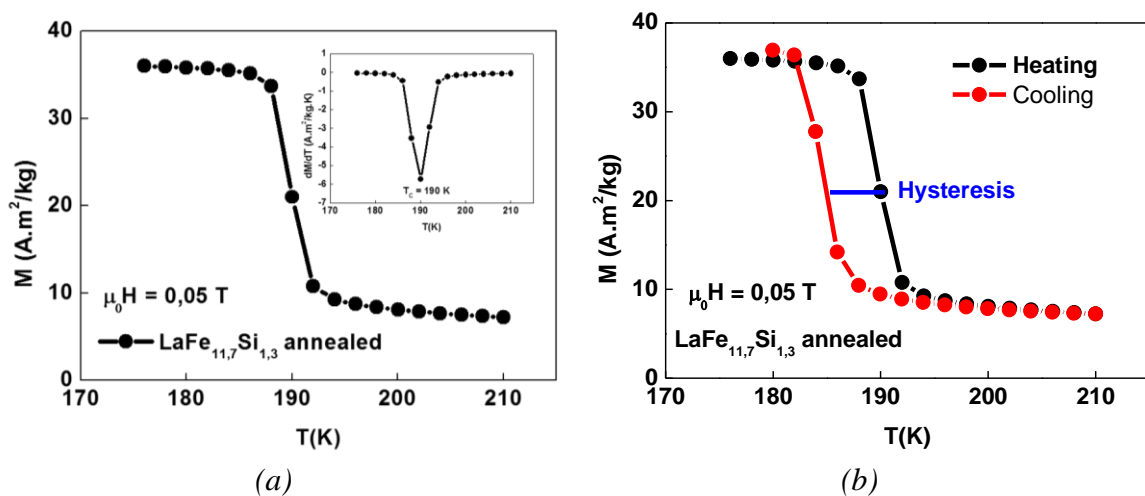


Figure III-5. (a) Magnetization curve as a function of temperature for an external field of 0.05 T for sample of composition $\text{LaFe}_{11.7}\text{Si}_{1.3}$. The inset shows the derivative used to determine the Curie temperature. (b) The heating and cooling curves together to show the thermal hysteresis.

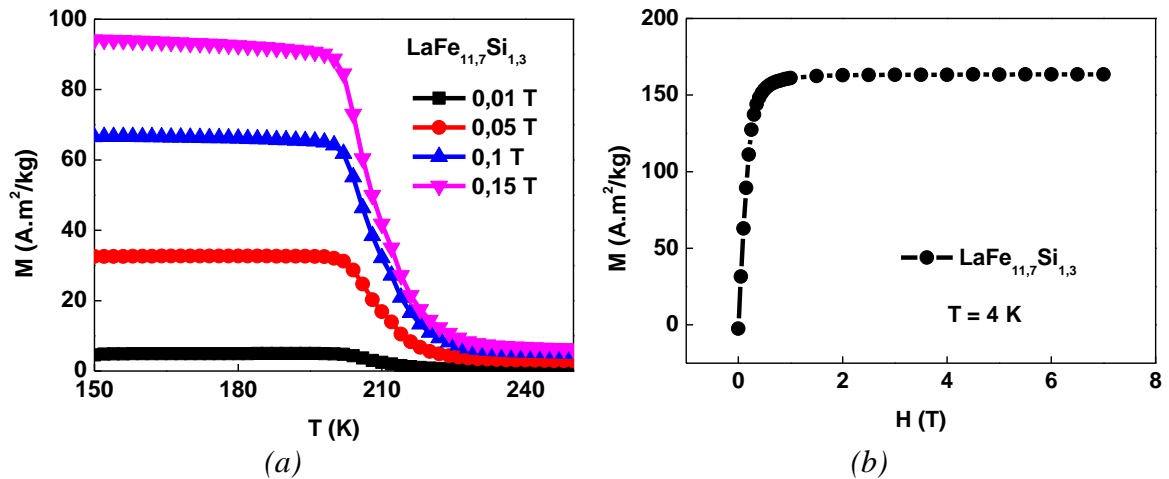


Figure III-6. Example of (a) isofield measurements showing the magnetic transition and (b) isothermal measurement from 0 to 7 T at 4 K for sample of composition $\text{LaFe}_{11.7}\text{Si}_{1.3}$.

By increasing the applied field, the material passes from a weakly magnetized state to a strongly magnetized one, as demonstrated by Figure III-6 (a). This effect is more prominent below the ordering temperature as the sample is in the ferromagnetic state. An isothermal magnetization curve at 4 K in the ferromagnetic domain in Figure III-6 (b) shows that the magnetization increases linearly with increasing external field applied until it saturates at 2 T.

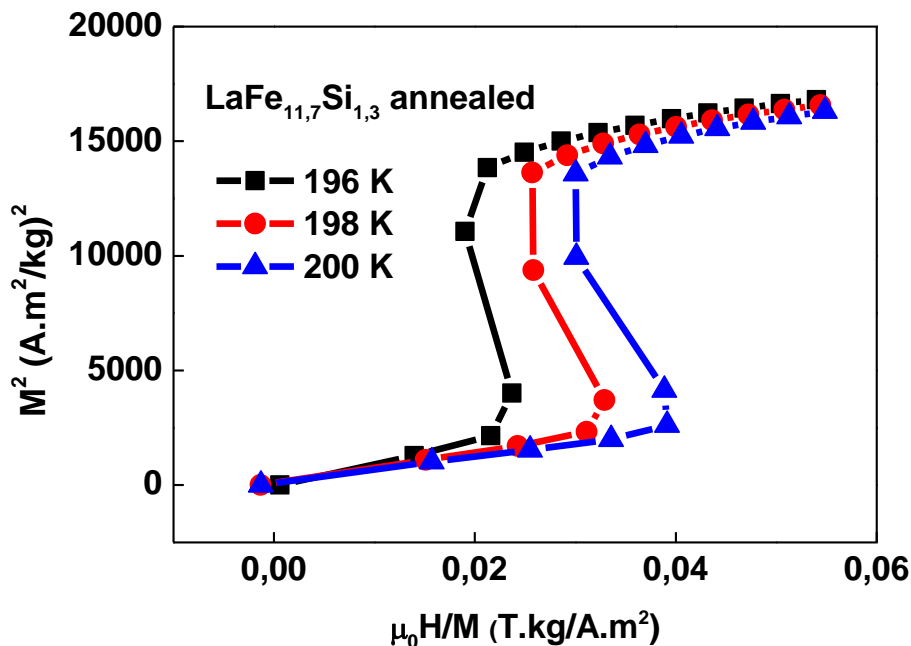


Figure III-7. Example of an Arrott-Belov plot from isothermal magnetization measurement taken above 190 K of sample $\text{LaFe}_{11.7}\text{Si}_{1.3}$.

Figure III-7 shows the Arrott-Belov plot of M^2 as a function of H/M , taken from an isothermal magnetization curve right above the Curie temperature (190 K). A typical S-shape can be observed, corresponding to a field-induced itinerant electron metamagnetism. The inflection of the curve is also an indication of the first-order characteristics of the transition.

1.3. Evaluation of the magnetocaloric effect

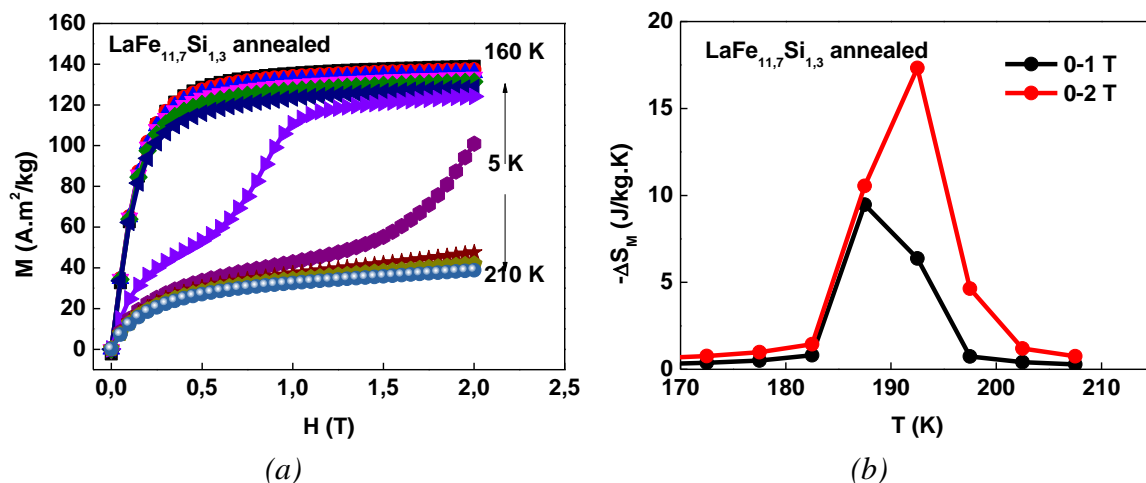


Figure III-8. (a) Isotherm magnetization curves and (b) the deduced isothermal magnetic entropy change from magnetization measurements for sample $\text{LaFe}_{11.7}\text{Si}_{1.3}$.

By scanning the isothermal magnetization curves from about $T_C - 30$ K to $T_C + 30$ K with a field variation from 0 to 2 T, the isothermal magnetic entropy change can be deduced. Figure III-8 (a) presents the magnetization isotherms for sample $\text{LaFe}_{11.7}\text{Si}_{1.3}$ obtained from 160 to 210 K with step of 5 K. The isothermal magnetic entropy change calculated from the magnetization isotherms based on Maxwell relation are presented in Figure III-8 (b). The maximum ΔS_M is shown as the peak value of the curve. With increasing field change, the peak value increases and the peak width also widens in temperature range.

2. Effect of substitution

Practically, it is necessary to adjust the T_C to room temperature range to maximize the magnetocaloric effect near this temperature range. The material properties of the $(\text{LaFe}_{1-x}\text{Si}_x)_{13}$ phase is highly dependent on the composition. One way to tune the T_C is via substitutional changes on the composition. Substitutional composition changes can take place on the three atomic sites ($8a$, $8b$, and $96i$) of the $(\text{LaFe}_{1-x}\text{Si}_x)_{13}$ phase, as mentioned in Chapter I.

2.1. Substitution on the La site by Ce

From an industrial point of view, Ce is the removed in the last step of purification process of Lanthanum salts. Therefore, it is a strategic choice to partially substitute La by Ce. While the effect of Ce on the magnetic and magnetocaloric properties of $(\text{LaFe}_{1-x}\text{Si}_x)_{13}$ phase has been studied before, it is important to further explore the problem by considering the structural changes and the consequences on hydrogenated compositions in details.

Fujieda *et al.* [11] found that substitution of La by Ce atoms reduced the lattice volume, which in turn, shortened the Fe-Fe distances. Since the lattice volume and interatomic bonds are important parameters that play a role in the hydrogenation behaviors of the 1:13 phases, we have elaborated samples with Ce partial substitution to La in the compositions

$\text{La}_{0.7}\text{Ce}_{0.3}\text{Fe}_{11.3}\text{Si}_{1.3}$ and $\text{La}_{0.7}\text{Ce}_{0.3}\text{Fe}_{11.44}\text{Si}_{1.56}$. The amount of Ce substitution was fixed at 30% as no single phase can be obtained above this level [12]. The structures of the reference and Ce-substituted samples were characterized by powder neutron diffraction. Furthermore, the consequences of Ce substitution on the hydrogen sorption dynamics were investigated by means of neutron diffraction and volumetric method.

2.1.1. Structural characterization

Here we make the comparison between the sample pair characterized by the same diffractometer at the same neutron source. As can be seen in Figure III-9, the sample with 0.3 Ce/f.u. shows the same cubic $(\text{LaFe}_{1-x}\text{Si}_x)_{13}$ phase at room temperature as the sample without Ce partial substitution. At this temperature, both samples are in the paramagnetic state and no magnetic contribution is expected. A high-angle shift can be seen for Ce-substituted sample due to the reduced lattice volume.

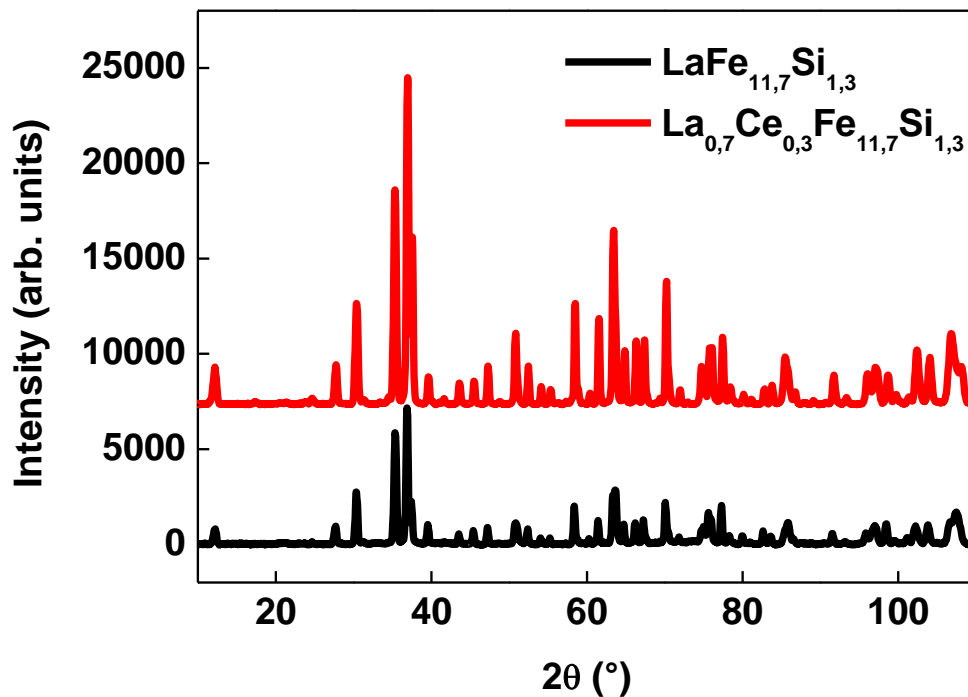


Figure III-9. Powder neutron diffraction pattern of for sample of composition $\text{LaFe}_{11.7}\text{Si}_{1.3}$ and $\text{La}_{0.7}\text{Ce}_{0.3}\text{Fe}_{11.7}\text{Si}_{1.3}$, data acquired at the 3T2 diffractometer at LLB at 300 K.

Rietveld refinement was performed with a default Thompson-Cow-Hastings pseudo-Voigt convoluted with axial divergence asymmetry function [13] for sample of composition $\text{La}_{0.7}\text{Ce}_{0.3}\text{Fe}_{11.7}\text{Si}_{1.3}$. Three impurity phases were added in pattern matching mode: $\alpha\text{-Fe}(\text{Si})$, LaFeSi , and $\text{Ce}_2\text{Fe}_{17}$, as shown in Figure III-10.

The refined unit cell parameter of the 1:13 phase of nominal composition $\text{La}_{0.7}\text{Ce}_{0.3}\text{Fe}_{11.7}\text{Si}_{1.3}$ is 11.46 Å, smaller than that of Ce-free sample (11.48 Å). The refined composition is $\text{La}_{0.67}\text{Ce}_{0.33}\text{Fe}_{11.88}\text{Si}_{1.2}$. A structural representation of the 1:13 phase is shown in Figure III-11 to illustrate the location of the constituent elements and the important Fe-Fe distances in the lattice. Detailed structure representations can be found in Appendix B.

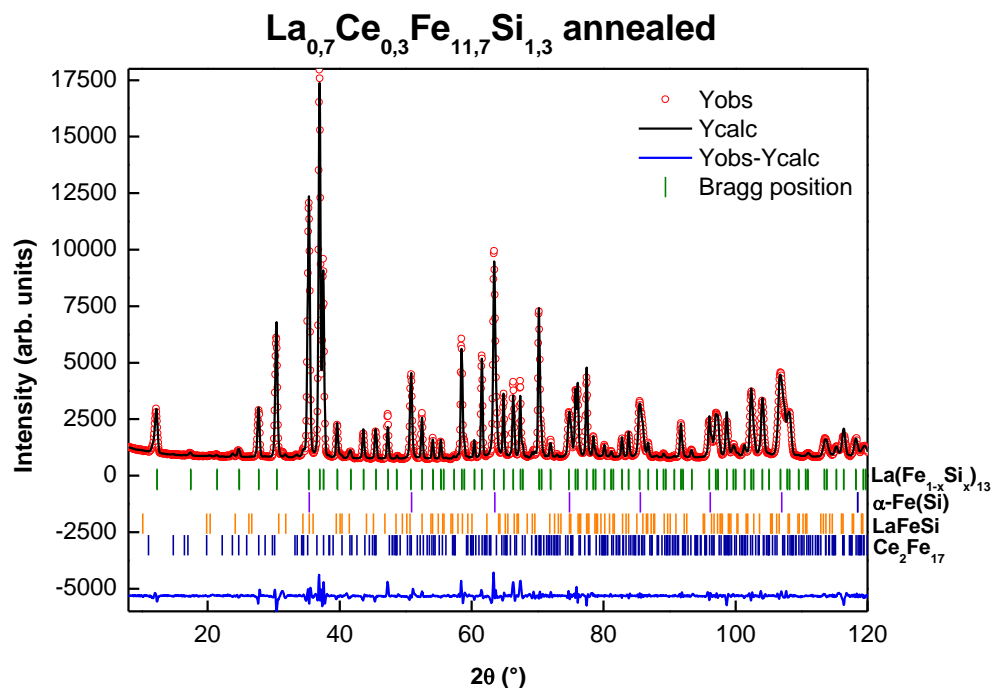


Figure III-10. Powder neutron diffraction pattern with Rietveld refinement analysis of for sample of composition $La_{0.7}Ce_{0.3}Fe_{11.7}Si_{1.3}$, data acquired at the 3T2 diffractometer at LLB at 300 K.

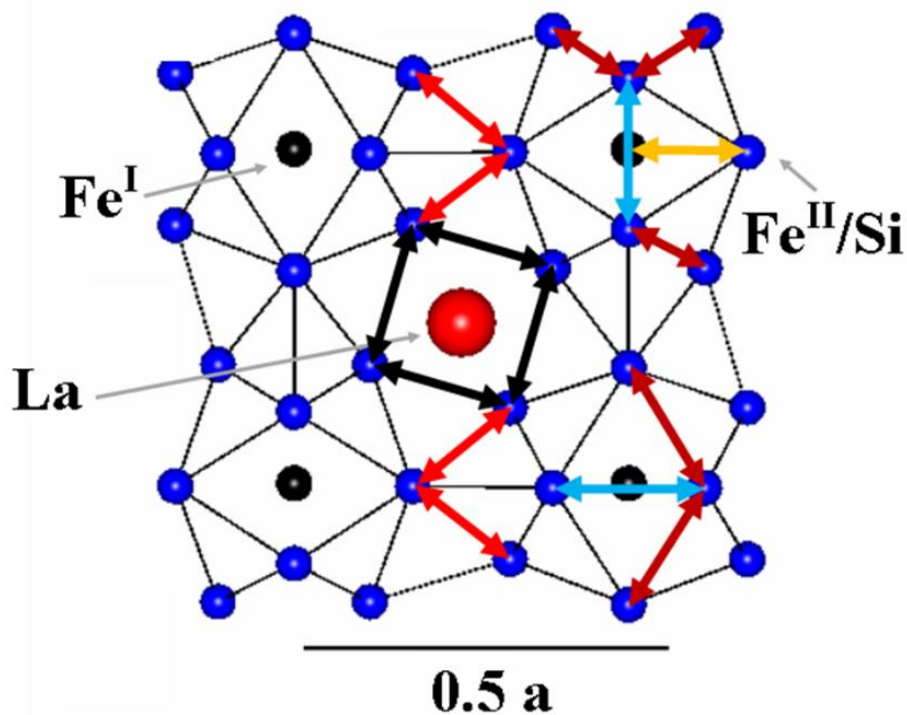


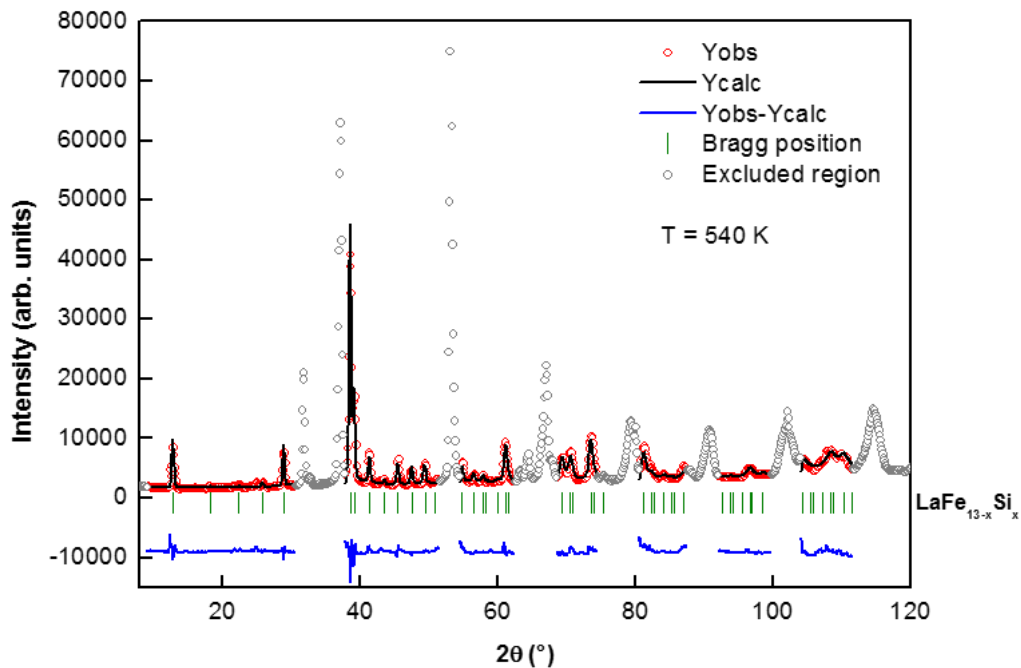
Figure III-11. A projection along the c -axis of four icosahedra plus the central atoms of $La(Fe_{1-x}Si_x)_{13}$ showing Fe-Fe bonds and the constituent elements.

The refined structural parameters and interatomic distances are listed in Table III-1. The effect of Ce substitution on the structure can be illustrated by the changes of the interatomic Fe-Fe distances.

Table III-1. Refined structural parameters for sample of composition $\text{LaFe}_{11.7}\text{Si}_{1.3}$ and $\text{La}_{0.7}\text{Ce}_{0.3}\text{Fe}_{11.7}\text{Si}_{1.3}$, data acquired at the 3T2 diffractometer at LLB at 300 K.

Sample	$\text{LaFe}_{11.7}\text{Si}_{1.3}$	$\text{La}_{0.7}\text{Ce}_{0.3}\text{Fe}_{11.7}\text{Si}_{1.3}$
T_c (K)	190	170
$a=b=c$ (Å)	11.4772 (2)	11.4605 (1)
site 96i (0, y, z) y	0.1798 (1)	0.1791 (1)
site 96i (0, y, z) z	0.1169 (1)	0.1166 (1)
B1 (Fe^{8b} - Fe^{96i}) (Å)	2.461 (1)	2.449 (1)
B2 (Å)	2.684 (1)	2.673 (1)
B3 (Å)	2.565 (1)	2.552 (1)
B4 (Å)	2.443 (1)	2.449 (1)
B5 (Å)	2.490 (1)	2.493 (1)
χ^2	7.7	17.7
R_{Bragg} (%)	8.2	4.3
R_f (%)	5.0	2.3

Neutron diffraction at room temperature shows that Ce partial substitution reduces the lattice volume by 20 \AA^3 for each Ce atom. The volume reduction is achieved by the contraction of intra-icosahedral bonds and the elongation of inter-icosahedral distances. The bond population of B1:B2:B3:B4:B5 is 2:1:4:2:2. The weighted average intra-icosahedral Fe-Fe distances is reduced from 2.55 Å to 2.54 Å after Ce partial substitution.

Figure III-12. Neutron powder diffraction pattern with Rietveld refinement for sample $\text{La}_{0.7}\text{Ce}_{0.3}\text{Fe}_{11.44}\text{Si}_{1.56}$ at 540 K at the D1B diffractometer.

The same volume reduction is seen for sample of nominal composition $\text{LaFe}_{11.44}\text{Si}_{1.56}$ and $\text{La}_{0.7}\text{Ce}_{0.3}\text{Fe}_{11.44}\text{Si}_{1.56}$. The powder neutron diffraction was performed at the D1B diffractometer at Institut Laue Langevin. The sample holder used in this experiment, for the purpose of the solid-gas reaction that follows, was of stainless steel, which produced textured iron peaks. These regions of iron peaks superposed certain reflections of the 1:13 phase and

they were subsequently excluded in the refinement for clarity, as shown in Figure III-12. This leads to reduced statistics for peak identification. Table III-2 shows the refined structural parameters for sample of composition $\text{LaFe}_{11.44}\text{Si}_{1.56}$ and $\text{La}_{0.7}\text{Ce}_{0.3}\text{Fe}_{11.44}\text{Si}_{1.56}$.

Table III-2. Refined structural parameters for sample of composition $\text{LaFe}_{11.44}\text{Si}_{1.56}$ and $\text{La}_{0.7}\text{Ce}_{0.3}\text{Fe}_{11.44}\text{Si}_{1.56}$, data acquired at the DIB diffractometer at ILL at 300 K.

Sample	$\text{LaFe}_{11.44}\text{Si}_{1.56}$	$\text{La}_{0.7}\text{Ce}_{0.3}\text{Fe}_{11.44}\text{Si}_{1.56}$
T_C (K)	206	188
$a=b=c$ (Å)	11.4751 (3)	11.4688 (3)
site 96i (0, y, z) y	0.1805 (3)	0.1794 (3)
site 96i (0, y, z) z	0.1176 (3)	0.1177 (3)
B1 ($\text{Fe}^{8b}\text{-Fe}^{96i}$) (Å)	2.472 (3)	2.461 (3)
B2 (Å)	2.699 (5)	2.700 (5)
B3 (Å)	2.575 (3)	2.561 (4)
B4 (Å)	2.427 (5)	2.432 (5)
B5 (Å)	2.487 (4)	2.503 (4)
χ^2	16.0	23.7
R_{Bragg} (%)	12.4	9.7
R_f (%)	9.5	8.0

The contraction of B1 and B3 and the elongation of B5 is confirmed as the mechanism of reducing unit cell volume with 0.3 Ce atom substituted to La. The weighted average intra-icosahedral Fe-Fe distances is reduced from 2.56 Å to 2.55 Å after Ce partial substitution. Although in this case, the volume reduction is about 1 Å³ per Ce atom in the formula unit. The difference in the order of magnitude can be attributed to the Si substitution on the Fe site, which induced a unit cell contraction with increasing Si content.

The same pair of samples is heated up to 540 K to observe *in-situ* their hydrogenation behavior. The structural parameters at this temperature are shown in Table III-3. The lattice volume for sample of composition $\text{LaFe}_{11.44}\text{Si}_{1.56}$ is increased by 1% due to thermal dilation. B3 remains stable when all the other Fe-Fe distances increase. The weighted average intra-icosahedral distance is slightly larger for Ce-substituted sample at this temperature. From 300 to 540 K, the lattice dilatation upon heating is about 1.2% in volume for sample of nominal composition $\text{La}_{0.7}\text{Ce}_{0.3}\text{Fe}_{11.44}\text{Si}_{1.56}$.

Table III-3. Refined structural parameters for sample of composition $\text{LaFe}_{11.44}\text{Si}_{1.56}$ and $\text{La}_{0.7}\text{Ce}_{0.3}\text{Fe}_{11.44}\text{Si}_{1.56}$, data acquired at the DIB diffractometer at ILL at 540 K.

Samples at 540 K	$\text{LaFe}_{11.44}\text{Si}_{1.56}$	$\text{La}_{0.7}\text{Ce}_{0.3}\text{Fe}_{11.44}\text{Si}_{1.56}$
$a=b=c$ (Å)	11.5112 (2)	11.5138 (4)
site 96i (0, y, z) y	0.1796 (2)	0.1794 (3)
site 96i (0, y, z) z	0.1175 (2)	0.1188 (3)
B1 ($\text{Fe}^{8b}\text{-Fe}^{96i}$) (Å)	2.473 (2)	2.477 (3)
B2 (Å)	2.712 (3)	2.736 (5)
B3 (Å)	2.573 (2)	2.574 (3)
B4 (Å)	2.438 (3)	2.426 (5)
B5 (Å)	2.510 (2)	2.527 (4)
χ^2	1030	13.2
R_{Bragg} (%)	9.6	16.5
R_f (%)	9.6	12.7

In order to characterize the ferromagnetic state of $\text{La}_{0.7}\text{Ce}_{0.3}\text{Fe}_{11.44}\text{Si}_{1.56}$, the sample was cooled to 150 K in neutron beam, well below the Curie temperature of the $(\text{LaFe}_{1-x}\text{Si}_x)_{13}$ phase. The refined parameters at different temperatures are shown in Table III-4.

At 300 K, the unit cell parameter is about 11.4688 (3) Å for sample of nominal composition $\text{La}_{0.7}\text{Ce}_{0.3}\text{Fe}_{11.44}\text{Si}_{1.56}$. The lattice constant at 150 K is 11.5189 (3) Å. Logically, the ferromagnetic state has a larger volume than the paramagnetic phase, which corresponds to a volume increase of 1.3%. The lattice volume at ferromagnetic state at 150 K is slightly larger than that of the paramagnetic state at 540 K. By comparing the interatomic distances at 300 K (PM) and 150 K (FM), it can be seen that the magnetovolume effect leads to a strong elongation (from 2.55 to 2.59 Å) of the weighted average intra-icosahedral distance (namely, B1, B2, and B3) upon cooling. A small reduction of the weighted average inter-icosahedral distance can be seen (from 2.47 to 2.46 Å), suggesting a preference of short inter-cluster bond of the FM state. In particular, the shortest bond B4 is contracted, indicating a reduced interstitial site volume for $24d$ in the FM state. The $\text{Fe}^{\text{I}}\text{-Fe}^{\text{II}}$ distance (B1) is found to be very close to the Fe-Fe distance in $\alpha\text{-Fe}(\text{Si})$ phase, which is around 2.48 Å according to the measurements by Néel [14].

Table III-4. Refined structural parameters for sample of composition $\text{LaFe}_{11.44}\text{Si}_{1.56}$ and $\text{La}_{0.7}\text{Ce}_{0.3}\text{Fe}_{11.44}\text{Si}_{1.56}$, data acquired at the D1B diffractometer at ILL at 150K, 300 K, and 540 K.

$\text{La}_{0.7}\text{Ce}_{0.3}\text{Fe}_{11.44}\text{Si}_{1.56}$	150 K	300 K	540 K
$a=b=c$ (Å)	11.5189 (3)	11.4688 (3)	11.5138 (4)
Cell volume V (Å ³)	1528.38 (6)	1508.53 (6)	1526.34 (8)
site $96i$ (0, y, z) y	0.1810 (3)	0.1794 (3)	0.1794 (3)
site $96i$ (0, y, z) z	0.1194 (3)	0.1177 (3)	0.1188 (3)
B1 ($\text{Fe}^{8b}\text{-Fe}^{96i}$) (Å)	2.498 (3)	2.461 (3)	2.477 (3)
B2 (Å)	2.751 (5)	2.700 (5)	2.736 (5)
B3 (Å)	2.597 (3)	2.561 (4)	2.574 (3)
B4 (Å)	2.406 (5)	2.432 (5)	2.426 (5)
B5 (Å)	2.512 (4)	2.503 (4)	2.527 (4)
χ^2	1E5	23.7	13.2
R_{Bragg} (%)	19.0	9.72	16.5
R_{f} (%)	13.6	8	12.7
R_{Magnetic} (%)	11.2	-	-

The majority of interatomic distances approach the critical distance of the competition between the ferromagnetic and antiferromagnetic interactions. Within the icosahedron, B2 and B3 are superior to the distance in $\alpha\text{-Fe}(\text{Si})$ phase. According to the Néel-Slater rule, the interactions between Fe^{II} atoms within the same icosahedron are ferromagnetic [15]. B4, which connects the neighboring icosahedra, is inferior to the distance in $\alpha\text{-Fe}(\text{Si})$ phase. By considering the bond population mentioned previously (B1:B2:B3:B4:B5 = 2:1:4:2:2), the global exchange interaction remains ferromagnetic.

2.1.2. Magnetic and magnetocaloric properties

The thermal magnetization curves were measured for the two pairs of samples elaborated for the powder neutron diffraction experiments under 0.05 T (Figure III-13). The Curie temperature is defined as the minimum of dM/dT in the temperature-dependent magnetization measurement in heating process. The measuring protocol was the same for all samples.

The partial substitution of Ce to La induces a decrease of T_C . As demonstrated with neutron diffraction analysis, Ce atoms have smaller atomic radii, which brings the Fe atoms closer and reduces their positive contribution to the global exchange energy. As seen in Figure III-13, Ce substitution allows a lowering of T_C without affecting the transition order, which remains first-order. A larger thermal hysteresis accompanies the magnetic transition for Ce-substituted samples.

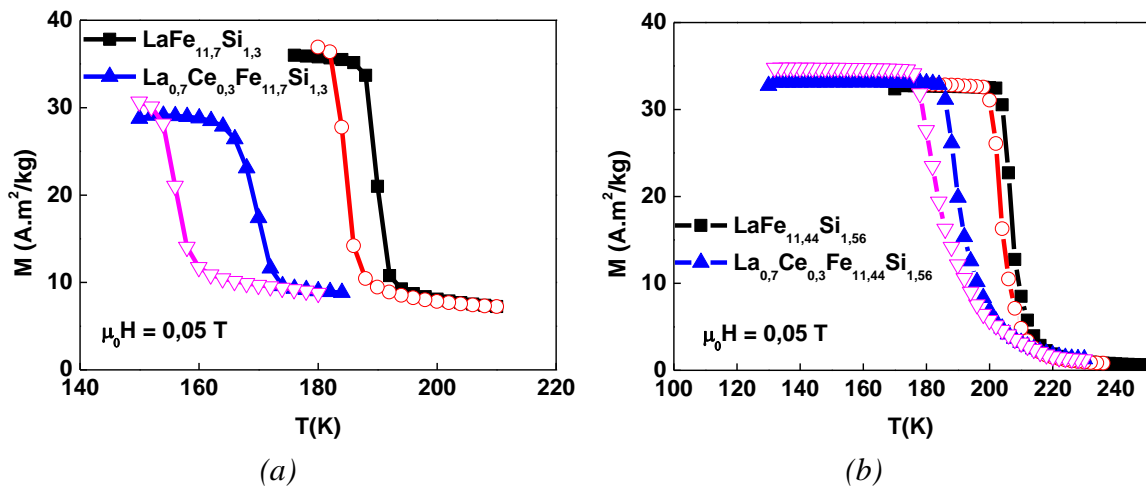


Figure III-13. Thermal magnetization curves for samples of composition (a) $\text{LaFe}_{11.7}\text{Si}_{1.3}$ and $\text{La}_{0.7}\text{Ce}_{0.3}\text{Fe}_{11.7}\text{Si}_{1.3}$ and (b) $\text{LaFe}_{11.44}\text{Si}_{1.56}$ and $\text{La}_{0.7}\text{Ce}_{0.3}\text{Fe}_{11.44}\text{Si}_{1.56}$.

Their magnetocaloric effect was evaluated by comparing the isothermal magnetic entropy change calculated from isothermal magnetization measurements for a field change of 0 to 1 T and 0 to 2 T (Figure III-14).

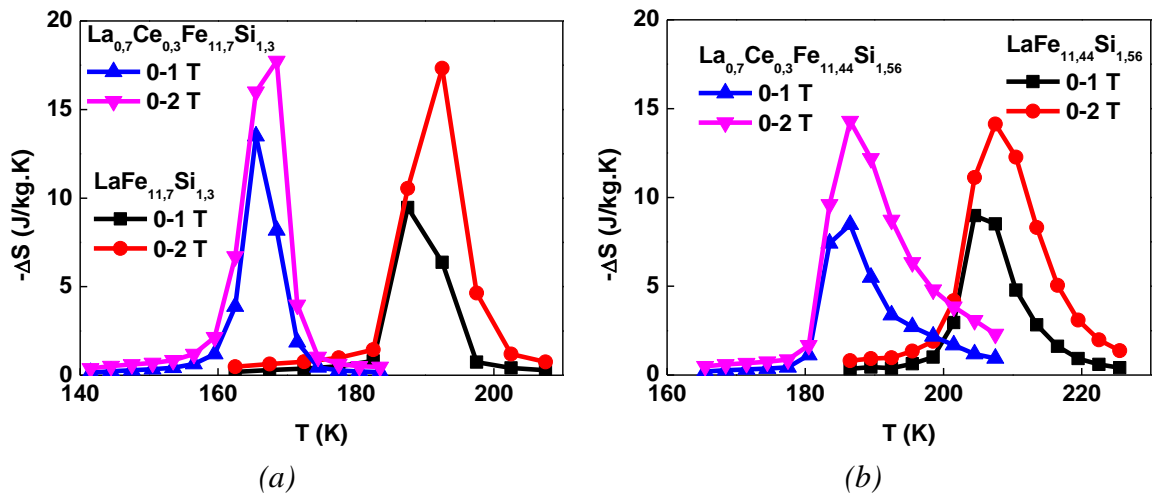


Figure III-14. Isothermal magnetic entropy change evaluation for sample of composition (a) $\text{LaFe}_{11.7}\text{Si}_{1.3}$ and $\text{La}_{0.7}\text{Ce}_{0.3}\text{Fe}_{11.7}\text{Si}_{1.3}$ and (b) $\text{LaFe}_{11.44}\text{Si}_{1.56}$ and $\text{La}_{0.7}\text{Ce}_{0.3}\text{Fe}_{11.44}\text{Si}_{1.56}$.

Care should be taken in estimating the isothermal entropy change using Maxwell equation. Due to the reinforcement of the first-order transition nature, an over-estimation of the peak value of ΔS_M can take place. This observation strongly depends on the measuring procedure and the steps used in the isothermal magnetization measurements. A study on one sample showing strongly first-order characteristics is presented in Appendix A to illustrate this effect. The validity of applying Maxwell equation is examined for the present samples and the resulting estimation of ΔS_M is found reasonable. Ce substitution allows extending the working temperature range towards lower temperature and leads to an enhanced isothermal magnetic entropy change.

In addition, the large thermal hysteresis results a wide window of coexistence of the paramagnetic and ferromagnetic phases around T_C , and the large volume difference of the two magnetic states triggers the instability of hydrogen around its ordering temperature.

2.1.3. Multi-tuning scenario

It is interesting to verify the effect of Ce substitution on compositions close to those commercially developed by Erasteel. For this purpose, we elaborated a series of samples based on nominal composition $\text{La}_{1-x}\text{Ce}_x\text{Fe}_{11,52}\text{Mn}_{0,18}\text{Si}_{1,3}\text{H}_{\text{max}}$. When $x=0.3$, the fully hydrogenated 1:13 phase has a Curie temperature of 292 K. By varying the Ce substitution content systematically, we can study the structural and magnetic properties of these samples. The samples in this series had the exact same processing route. After annealing at 1373 K for 15 days, the samples were fully hydrogenated by heating in H_2 flux at 573 K for 3 hours in an industrial furnace.

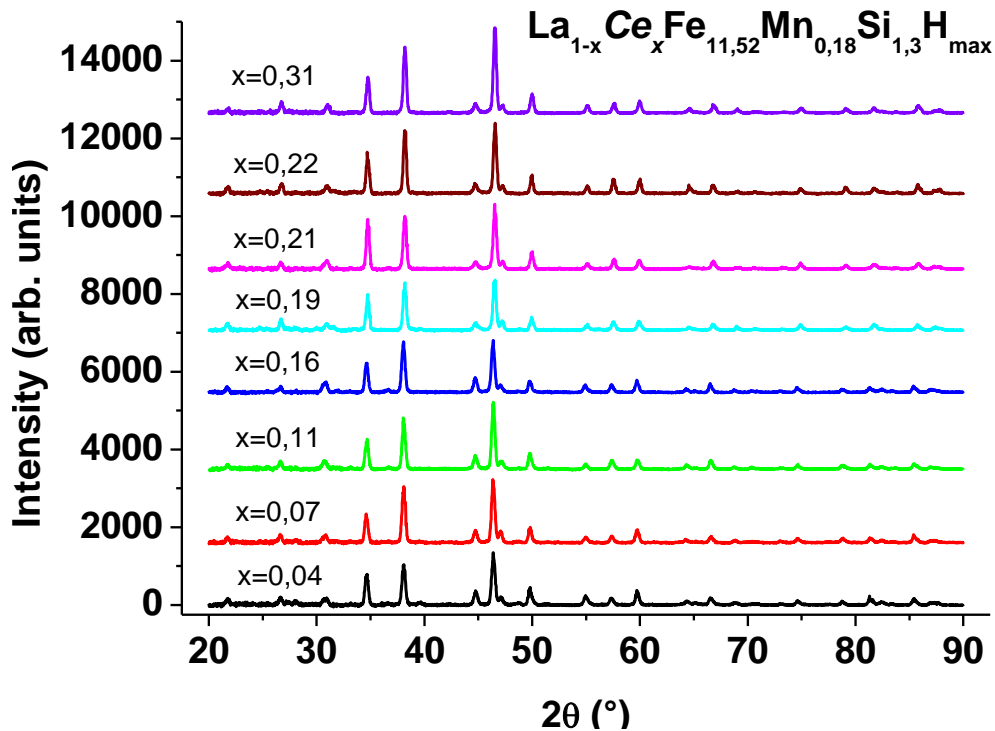


Figure III-15. XRD patterns for samples of composition $\text{La}_{1-x}\text{Ce}_x\text{Fe}_{11,52}\text{Mn}_{0,18}\text{Si}_{1,3}\text{H}_{\text{max}}$ ($x=0.04-0.31$) measured at 300 K.

The diffraction patterns at 300 K of the fully hydrogenated samples are shown in Figure III-15. The phase fractions are determined from Rietveld refinement and are plotted in Figure III-16. The fully hydrogenated samples have all shown more than 90% of the 1:13 phase, small proportion of the α -Fe(Mn,Si) phase, and negligible LaFeSi phase. The Ce content does not have a significant contribution to the phase formation of the 1:13 phase.

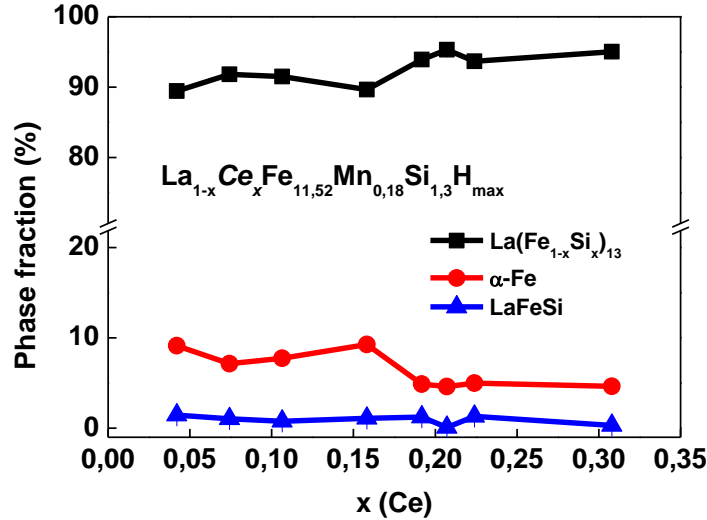


Figure III-16. Phase fraction from Rietveld refinement samples of composition $La_{1-x}Ce_xFe_{11.52}Mn_{0.18}Si_{1.3}H_{max}$ ($x=0.04-0.31$).

By analyzing the T_C change and the lattice constant evolution with Ce concentration (Figure III-17), it can be seen that from $x_{Ce}=0$ to $x_{Ce}=0.3$, T_C of the fully hydrogenated samples is gradually decreasing and crossing the room temperature line. Samples with $x_{Ce}<0.16$ are ferromagnetic at room temperature while for higher Ce concentration, the ferromagnetic state is stabilized at lower temperature range, so the paramagnetic state is being measured at 300 K. Therefore, the lattice constant in Figure III-17 (b) is measured for the ferromagnetic phase for $x_{Ce}<0.16$ and for $x_{Ce}>0.16$, the refined unit cell parameter is for the paramagnetic state. This is consistent with the sharp unit cell parameter drop between $x_{Ce}=0.16$ ($T_C=301$ K) and $x_{Ce}=0.2$ ($T_C=298$ K). The low-temperature ferromagnetic phase has a larger volume than the high-temperature paramagnetic phase. Compared with literature data, the slope of the linear fit of the T_C evolution is within the same order of magnitude.

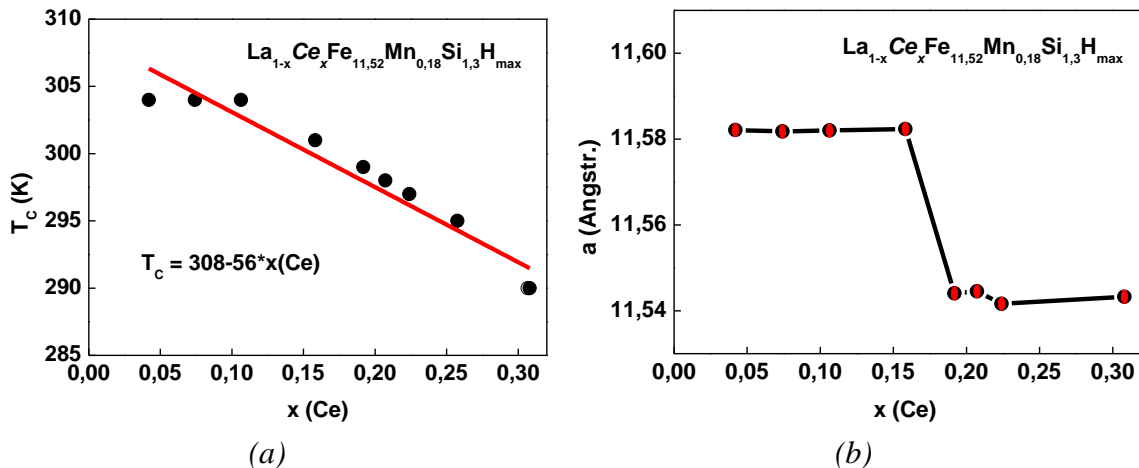


Figure III-17. (a) The Curie temperature and (b) unit cell parameter as a function of Ce concentration for fully hydrogenated samples of composition $La_{1-x}Ce_xFe_{11.52}Mn_{0.18}Si_{1.3}H_{max}$ ($x=0.04-0.31$).

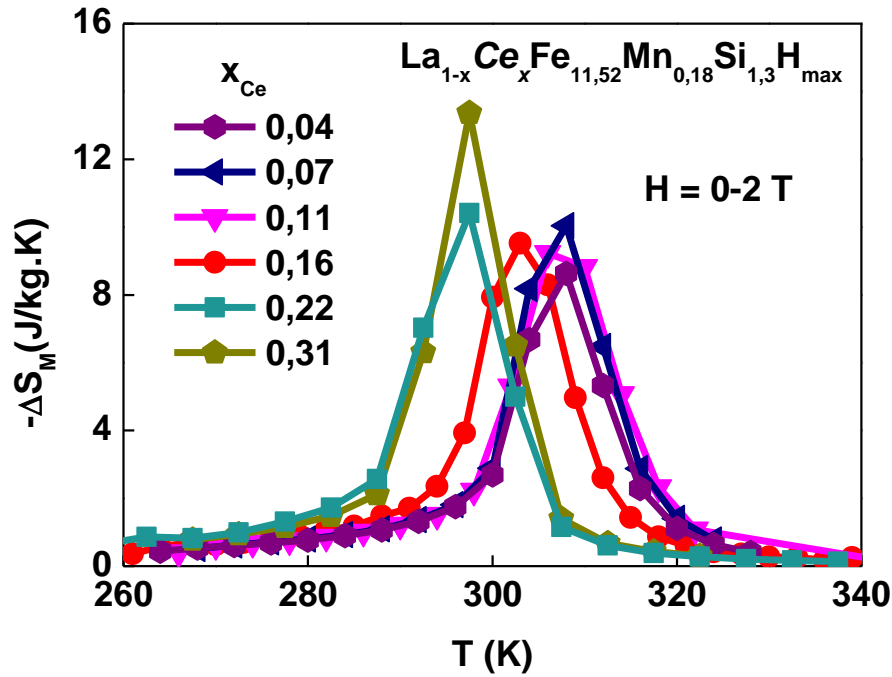


Figure III-18. Isothermal magnetic entropy change for samples of composition $La_{1-x}Ce_xFe_{11,52}Mn_{0,18}Si_{1,3}H_{max}$ ($x=0.04-0.31$).

The field-induced magnetocaloric effect represented by the isothermal entropy change is shown for selected Ce contents in Figure III-18. A gradual increase of ΔS_M can be seen with Ce increase, which is consistent with the trend observed by Fujita *et al.* [16]. The value T_{peak} is defined as the temperature at which the isothermal magnetic entropy change upon increasing the external field is at the maximum. Table III-5 shows the small discrepancy between the two values, as both are highly dependent on the measuring step.

Table III-5. T_C and T_{peak} values for samples of composition $La_{1-x}Ce_xFe_{11,52}Mn_{0,18}Si_{1,3}H_{max}$ ($x=0.04-0.31$).

x_{Ce}	T_C (K)	T_{peak} (K)	ΔT (K) step size for M(H)
0.04	304	308	4
0.07	304	308	4
0.11	304	306	4
0.16	301	303	3
0.22	297	298	5
0.31	290	298	5

Arrott plots right above the ordering temperature can also indicate the nature of the magnetic transition, as shown in Figure III-19. An increase of the first-order character is seen with increasing Ce concentration. In particular, the typical “S-shape” attributed to the itinerant electron metamagnetism can be seen for samples with $x_{Ce}=0.22$ and 0.31 .

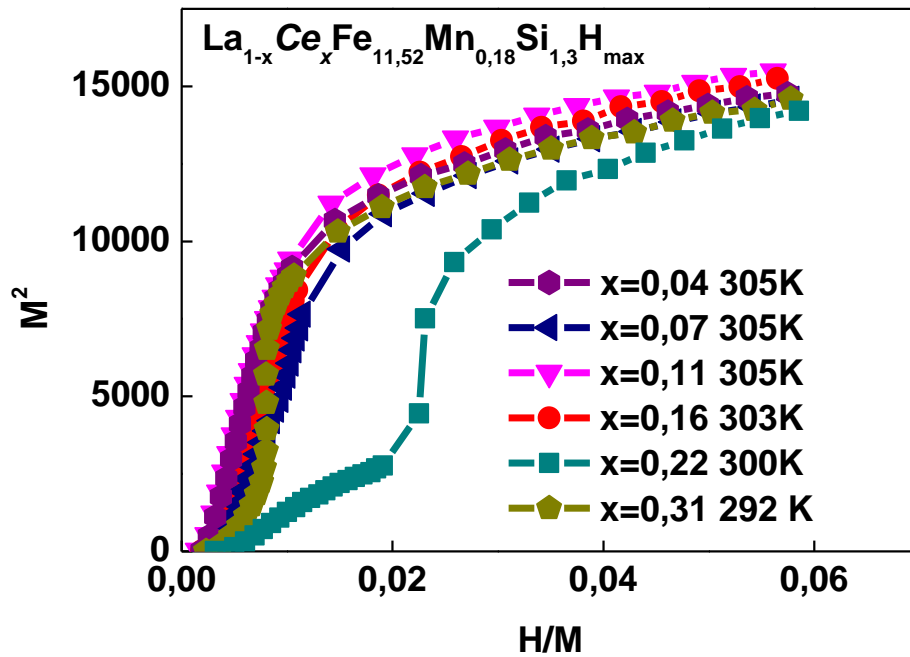


Figure III-19. Arrott plot taken right above the Curie temperature of samples of composition $\text{La}_{1-x}\text{Ce}_x\text{Fe}_{11.52}\text{Mn}_{0.18}\text{Si}_{1.3}\text{H}_{\text{max}}$ ($x=0.04-0.31$).

In summary, the partial substitution of Ce on the La site results in a lowering of T_C with decreasing lattice constant. The change in T_C is mainly attributed to the magnetovolume effect caused by the small radius of Ce atoms. Moreover, Ce substitution for La leads to a reduced volume of the octahedral interstitial site ($24d$) due to steric effect. From the neutron diffraction data, the lattice reduction from Ce substitution is achieved notably by the contraction the intra-icosahedral Fe-Fe distances. In a series of samples with varying Ce concentration, we have shown that Ce substitution gradually shifts the magnetic transition towards more first-order-like. The composition modulation by Ce substitution can effectively adjust the Curie temperature of the 1:13 phase. The enhanced first-order characteristics seems to have a positive effect on the magnetocaloric effects of these samples.

2.2. Substitution on the Fe site

Secondly, T_C of the $(\text{LaFe}_{1-x}\text{Si}_x)_{13}$ phase can be effectively modulated by substituting Fe by Mn and Si atoms. Since the effect of Si on the structure is rather well studied, a series of samples with nominal composition $\text{La}_{0.7}\text{Ce}_{0.3}\text{Fe}_{11.4-x}\text{Mn}_x\text{Si}_{1.56}\text{H}_{\text{max}}$ with varying Mn concentration were elaborated in order to study the effect of Mn on the structural and magnetic properties of the $(\text{LaFe}_{1-x}\text{Si}_x)_{13}$ phase. The annealed samples were bathed in pure hydrogen flow at 573 K for 3 h to fully saturate the lattice with hydrogen interstitials.

2.2.1. Structural properties

The structural property of fully hydrogenated samples were examined by XRD. The samples all show the cubic NaZn_{13} -type phase. The phase fraction from Rietveld analysis indicates impurity phases (α -Fe(Si) and LaFeSi) of less than 10%. There is a preferred solubility of Mn in the α -Fe phase compared with that in the $\text{LaFe}_{13-x}\text{Si}_x$ phase since the heat of formation for La-Mn is negative. M. Krautz *et al.* [17] postulated that Mn was likely to inhibit the homogenization process to form the $\text{LaFe}_{13-x}\text{Si}_x$ phase. However, in the tested range, Mn substitution does not seem to lead to the formation of new parasitic phases and the residual impurity phases are well controlled, as seen in Figure III-20 and Figure III-21. On the contrary, increasing Mn partial substitution seems to slightly increase the amount of $\text{LaFe}_{13-x}\text{Si}_x$ phase in the sample.

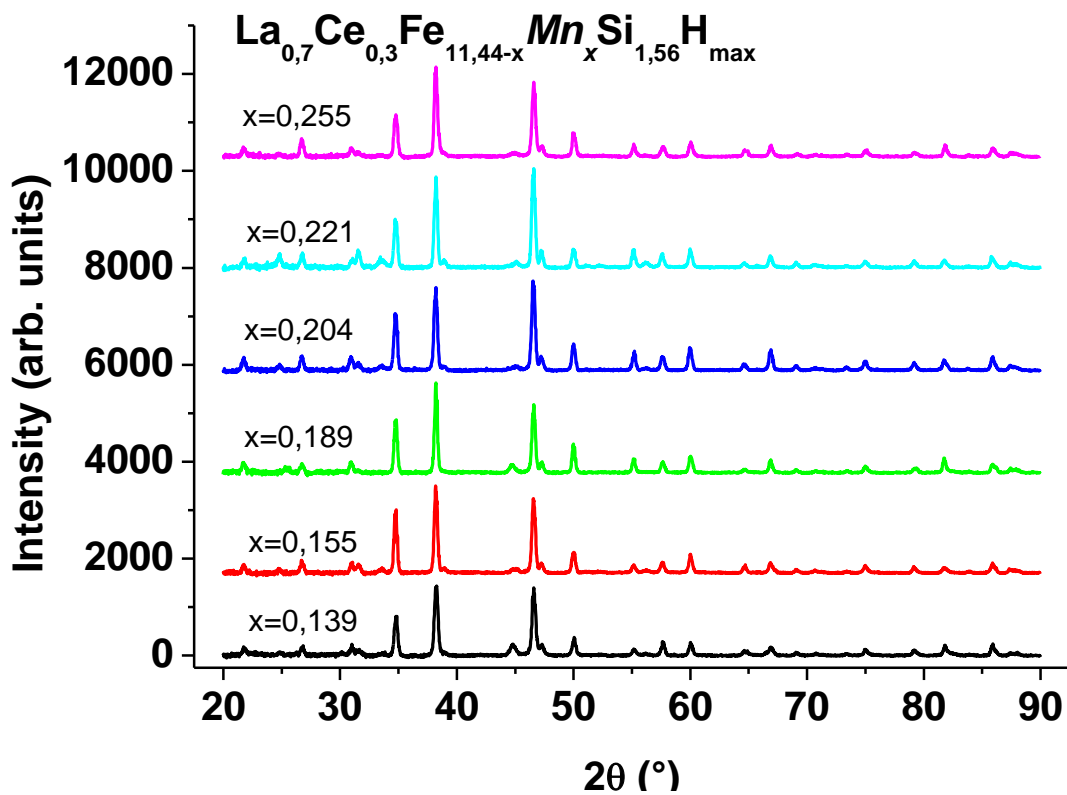


Figure III-20. XRD patterns for samples of composition $\text{La}_{0.7}\text{Ce}_{0.3}\text{Fe}_{11.44-x}\text{Mn}_x\text{Si}_{1.56}\text{H}_{\text{max}}$ ($x=0.14-0.26$).

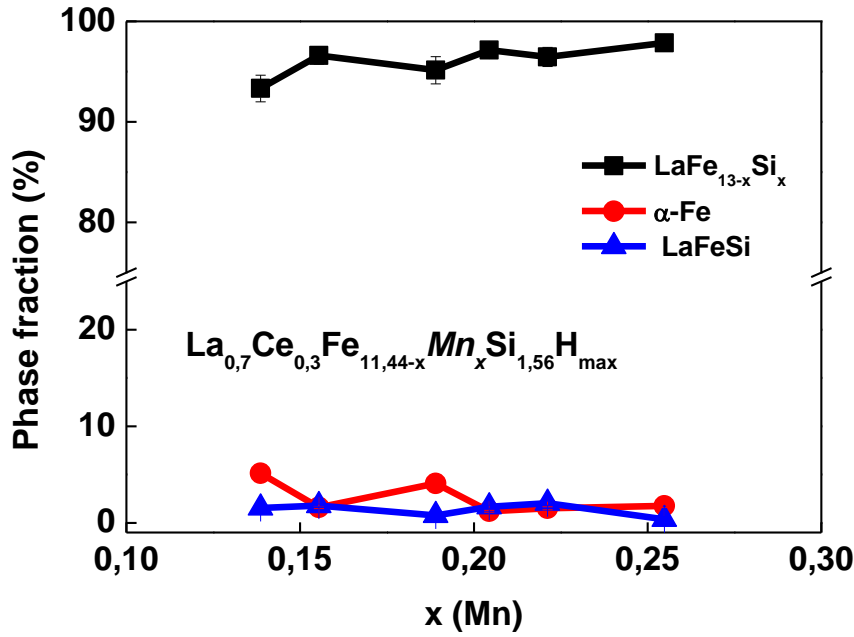


Figure III-21. Phase fraction from Rietveld refinement samples of composition $\text{La}_{0.7}\text{Ce}_{0.3}\text{Fe}_{11.44-x}\text{Mn}_x\text{Si}_{1.56}\text{H}_{\max}$ ($x=0.14-0.26$).

2.2.2. Magnetic properties

On the other hand, Mn substitution has significant influence on the magnetic properties of the 1:13. The effect of Mn on non-hydrogenated 1:13 phases from literature is shown in Figure III-22. Similar to Co, the replacement of Fe by Mn also progressively shifts the transition order from first-order to second-order, which reduces greatly the thermal hysteresis. The magnetic ordering temperature decreases almost linearly with Mn content. The increasing substitution of Mn to Fe induces an reduction of the first-order characteristics of the transition with broadened magnetization change around T_C . As remarked by Fujieda *et al.*, the IEM transition above T_C disappears for $x_{\text{Mn}} > 0.39$.

After hydrogenation, T_C of hydrogenated samples also decreases with increasing Mn concentration. Figure III-23 presents T_C as a function of Mn content for several series of samples. In our study, T_C is defined as the temperature where dM/dT is the minimum from the thermal magnetization curve of heating process in a magnetic field of 0.05 T. For samples from Krautz *et al.* [17], transition temperature is defined as the temperature at which ΔS_M or ΔT_{ad} is at its maximum for a field change from 0 to 2 T.

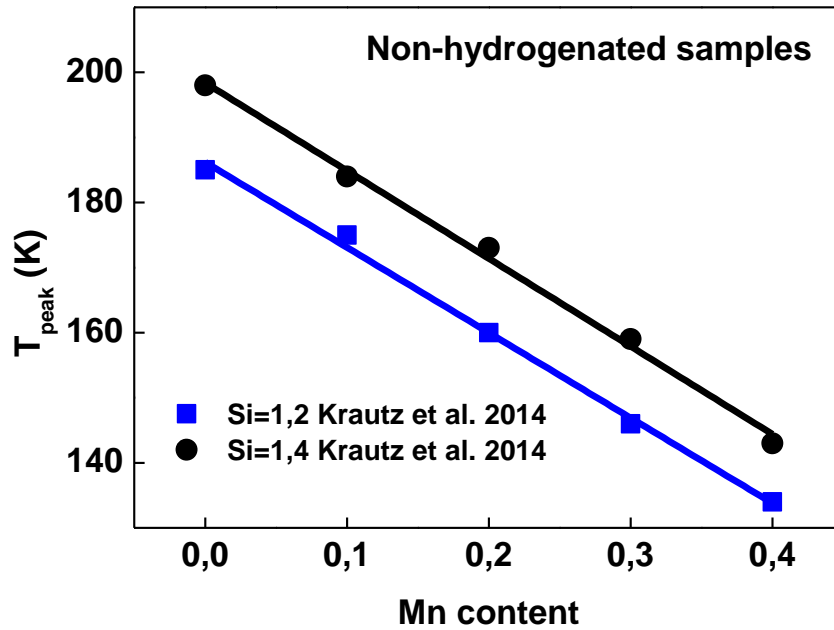


Figure III-22. Influence of Mn content on the Curie temperature for non-hydrogenated samples reported in the literature. Data extracted from reference [17].

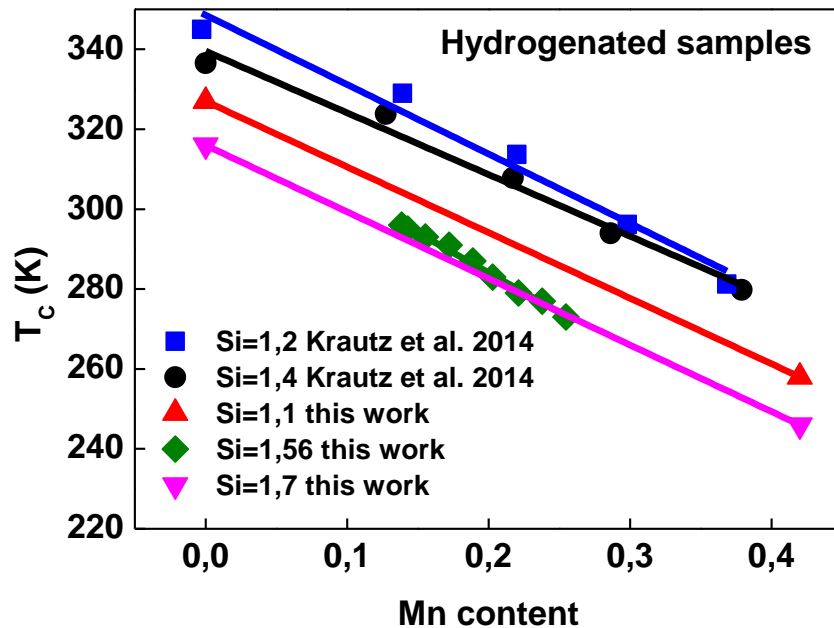


Figure III-23. Influence of Mn content on the Curie temperature for hydrogenated samples with various Si concentration, data extracted from reference [17] and this work.

However, by considering the samples reported by the same author, an interesting phenomenon can be observed by comparing Figure III-22 and Figure III-23. Before hydrogenation, samples with higher content in Si show higher T_C . For fully hydrogenated samples $\text{La}_{0,7}\text{Ce}_{0,3}\text{Fe}_{13-y}\text{Mn}_y\text{Si}_x\text{H}_{\text{max}}$, however, those with higher Si content show lower T_C , which suggests that increasing Si concentration has an impeding effect on the maximum capacity of hydrogenation. The extent of the effect of Si on adjusting T_C is limited by the hydrogenation step. This can be attributed, on one hand, to the reduction of the interstitial

space available for hydrogen atoms in the lattice with increasing Si content. On the other hand, it is important to consider the structural modification occurring upon Si substitution. Further investigation on the effect of Si via high-resolution neutron diffraction techniques can help provide more sights in the explanation of this effect.

3. Process optimization

With limited knowledge available on the pseudo-binary phase diagram of the $\text{La}(\text{Fe}_{1-x}\text{Si}_x)_{13}$ phase, it is necessary to systematically study the influence of elaboration conditions on the microstructure and magnetic properties of bulk samples to optimize specific laboratory process. In the Ph.D. work of M. Rosca [18], a study on controlling the stoichiometry of La is realized on atomized powder samples of $\text{La}(\text{Fe}_{1-x}\text{Si}_x)_{13}$. Different amount of La (2-10 wt.%) is added during the annealing process and she found that from 5 wt.% in excess La, the amount of secondary phases is greatly reduced. The additional La also seems to help adjusting the sample composition to the targeted stoichiometry. Therefore, it is suggested to add excess La even at the initial stage of melting to reduce the formation of secondary phases for atomized powder.

Would it be necessary to compensate for La loss in the laboratory elaboration process? In the literature, an excess of 5-15 at.% La is systematically added to anticipate the evaporation of La during arc melting [19, 20, 21, 22]. Bao *et al.* [23] have proposed that an 18 at.% excess of La, a 1:11 ratio with $\text{La}(\text{Fe}_{1-x}\text{Si}_x)_{11}$ as the starting composition, can directly form NaZn_{13} -type single-phase material without annealing treatment. They reported starting materials $\text{La}(\text{Fe}_{0.8}\text{Si}_{0.2})_{11}$ and $\text{La}(\text{Fe}_{0.78}\text{Si}_{0.22})_{11}$ can be used to obtain $\text{La}(\text{Fe}_{1-x}\text{Si}_x)_{13}$ phase with similar content in Si without impurity phases. It is proposed that the abundant La fully reacts with α -(Fe,Si) to form the NaZn_{13} -type phase. However, the homogeneity from HF induction melting is rather impressive and the small quantity of sample is contained in the quartz tube. In order to validate and optimize the elaboration process with the high frequency induction melting technique, samples $\text{La}_{0.7}\text{Ce}_{0.3}(\text{Fe}_{0.88}\text{Mn}_{0.02}\text{Si}_{0.1})_n$, ($n=13, 12, 11, 10$) were elaborated, corresponding to different amount of excess rare earth contents. The weight proportion of each element before melting is listed in Table III-6.

Table III-6. Proportion of each element in weight percent (wt%) in the elaborated samples.

Rare earth excess in at.%	La	Ce	Fe	Mn	Si
none (1:13)	11.73	5.07	77.07	1.72	4.40
10% (1:12)	12.69	5.49	75.80	1.69	4.33
18% (1:11)	13.44	5.81	74.81	1.67	4.28
30% (1:10)	14.52	6.82	73.37	1.64	4.19

All samples followed the same induction melting procedure and subsequent annealing at 1373 K for 15 days in evacuated sealed quartz tube with Mo foil protection. The as-cast and annealed microstructures were observed in backscattered electron (BSE) mode by scanning electron microscopy (SEM). The phase composition was detected by energy dispersive spectrometry (EDS). After full hydrogenation, the crystal structure was studied using X-ray diffraction (XRD) with Cu irradiation. Quantitative phase analysis was performed with Rietveld refinement in Fullprof Suite. Thermally and magnetically induced transitions were measured with an extraction vector magnetometer.

3.1. Microstructure

3.1.1. As-cast samples

Table III-7 shows the mass loss during induction melting in levitation from a simple weight comparison.

Table III-7. Mass comparison for samples elaborated with different amount of excess in rare earth elements, the last digit is significant.

Rare earth excess in at%	Mass before melting (g)	Mass after melting (g)	Mass loss (%)
none (1:13)	4.999	4.994	0.11
10% (1:12)	4.999	4.992	0.15
18% (1:11)	4.998	4.993	0.10
30% (1:10)	4.993	4.987	0.12

The mass loss for each sample is less than 0.2%. The mass loss, which is primarily due to the evaporation of La, Ce, and Mn, is not strongly affected by the amount of excess rare earth elements. Moreover, the negligible mass loss does not justify a 10 at.% excess of rare earth (more than 1% in weight percentage) to ensure stoichiometry. From the BSE images in Figure III-24, the as-cast samples all contain dendritic microstructures.

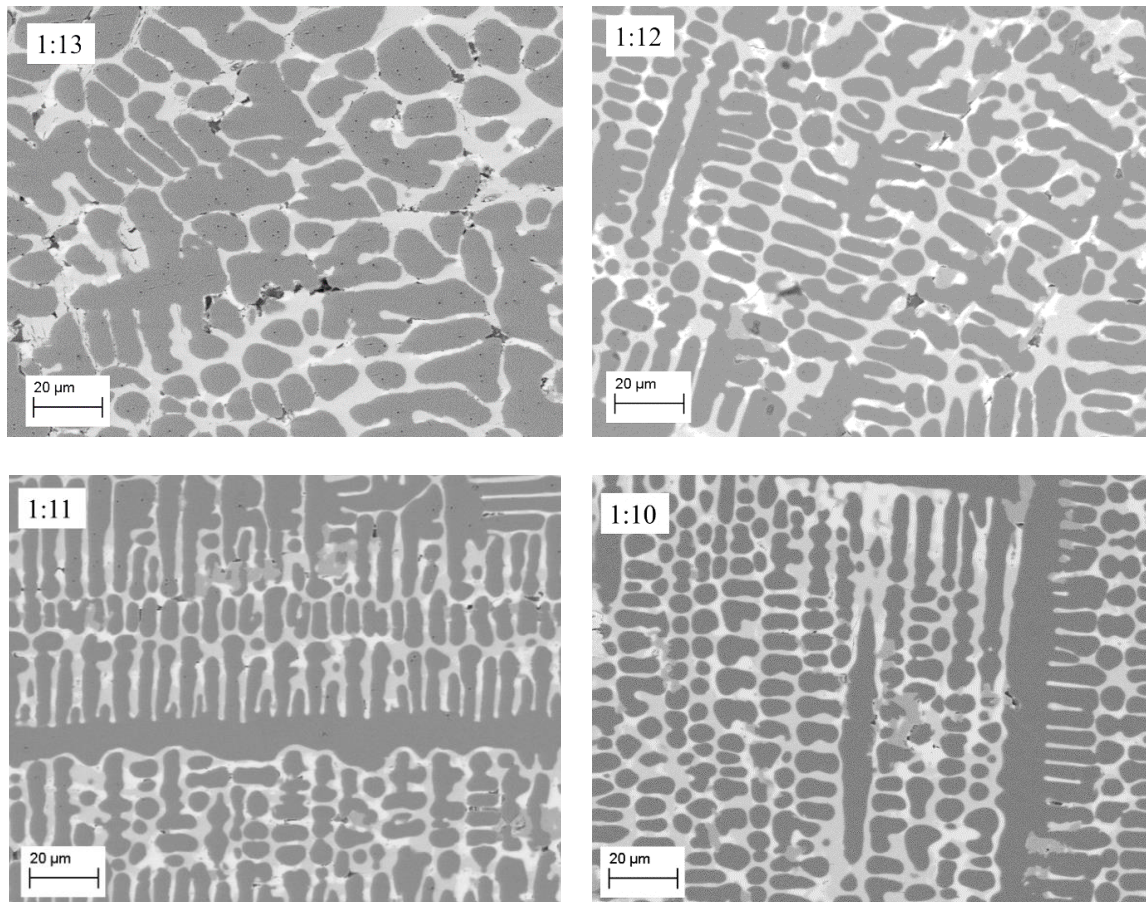


Figure III-24. Backscattered electron images of as-cast samples of composition $La_{0.7}Ce_{0.3}(Fe_{0.88}Mn_{0.02}Si_{0.1})_n$, ($n=13, 12, 11, 10$), corresponding to different at.% excess in rare earth elements.

With no extra rare earth content, the as-cast sample (1:13 initial ratio) contains essentially large dark grey dendrites that are α -Fe(Si) solid solutions with more than 92 at.% in Fe and a lighter phase corresponding to the LaFeSi phase in composition. Small white spots can be seen between the two previous phases, which are rich in La and Ce.

Table III-8. Atomic percent of each element for the main phases in as-cast sample of composition $La_{0.7}Ce_{0.3}(Fe_{0.88}Mn_{0.02}Si_{0.1})_{13}$.

at% ($\pm 3\%$)	La	Ce	Fe	Mn	Si
α-Fe(Si)	0.16	0.07	92.5	1.18	5.46
LaFeSi	22.86	7.83	35.95	1.01	32.35

The excitation spectra of the two main phases are shown in Figure III-25 and the composition of each phase is shown in atomic percent in Table III-8.

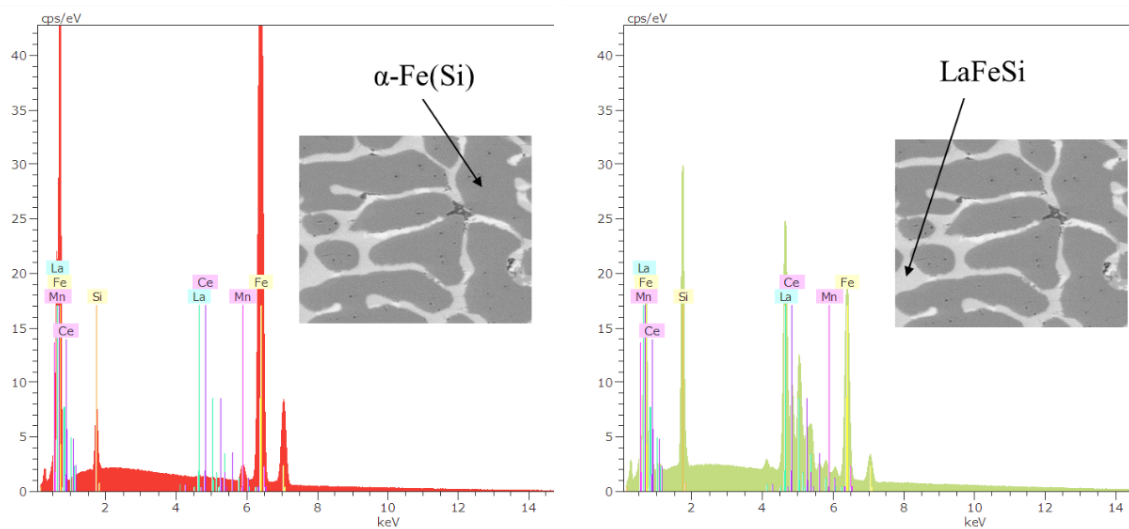


Figure III-25. Energy-dispersive X-ray spectrum for the main phases in as-cast sample of composition $La_{0.7}Ce_{0.3}(Fe_{0.88}Mn_{0.02}Si_{0.1})_{13}$.

By having 10 at.% of extra La and Ce before melting, the sample (1:12 initial ratio) shows a majority of α -Fe(Si) and LaFeSi phases. However, there are also two distinguishable minority phases rich in Fe (with 10 at.% of La and Ce) and in rare earth elements (in bright white).

Table III-9. Atomic percent of each element for the main phases in as-cast sample of composition $La_{0.7}Ce_{0.3}(Fe_{0.88}Mn_{0.02}Si_{0.1})_{12}$.

at% ($\pm 3\%$)	La	Ce	Fe	Mn	Si
Intermediate Fe-rich phase with 10% La	2.70	9.08	80.50	2.14	5.59
La,Ce-rich phase	35.73	16.51	11.27	0.68	35.81

The EDX spectra for the minority phases in sample of composition $La_{0.7}Ce_{0.3}(Fe_{0.88}Mn_{0.02}Si_{0.1})_{12}$ are shown in Figure III-26 and the composition of each phase is shown in atomic percent in Table III-9.

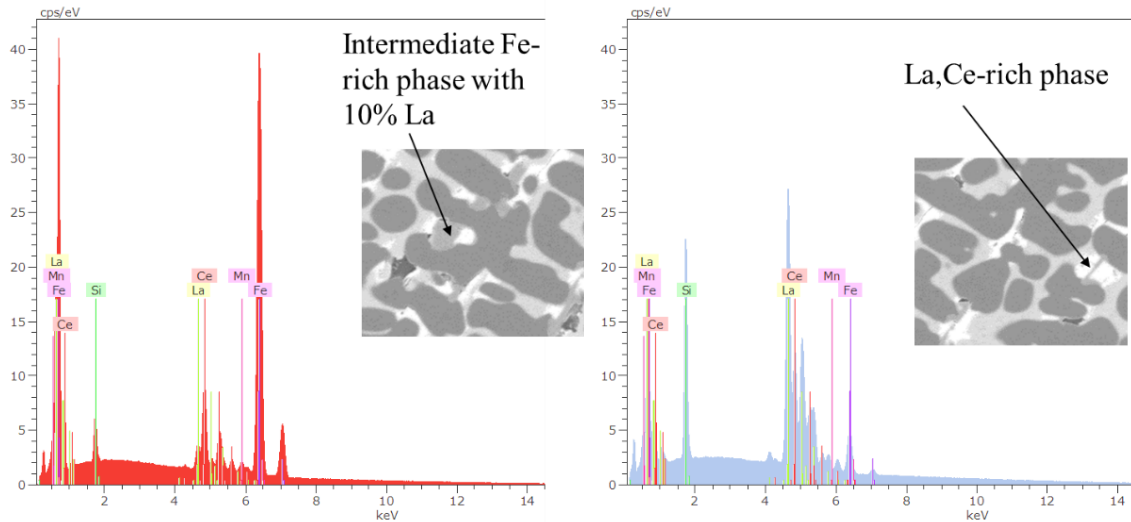


Figure III-26. Energy-dispersive X-ray spectrum for the minority phases in sample of composition $La_{0.7}Ce_{0.3}(Fe_{0.88}Mn_{0.02}Si_{0.1})_{12}$.

For 18 at.% and 30 at.% of additional rare earth elements, the α -Fe(Si) dendrites remain as the major phase, the chemical composition of which is very close to that of pure iron. However, there is no phase corresponding to a stoichiometry close to the LaFeSi phase. Instead, EDX analysis shows three intermediate phases containing rare earth elements from 10%, 30%, and more than 50%. Table III-10 lists the phase identifications from different chemical contrasts.

Table III-10. EDX analysis of phases for as-cast samples, calibration with standards.

Rare earth excess in at%	Main phase	Additional phases
none (1:13)	α -Fe(Si) ; LaFeSi	La,Ce-rich phase
10% (1:12)	α -Fe(Si) ; LaFeSi	La,Ce-rich phase ; iron-rich phase with 10% rare earth
18% (1:11)	α -Fe(Si)	3 distinguishable phases containing Fe and rare earth elements
30% (1:10)	α -Fe(Si)	3 distinguishable phases containing Fe and rare earth elements

To summarize, with increasing rare earth content, the α -Fe(Si) dendrites show less grain growth, whereas the sample without any rare earth excess shows larger grain size. The microstructure evolutions are consistent with the EDX analysis. In presence of extra rare earth elements, the α -Fe(Si) dendrites have more difficulty to grow and mix with other elements, which explains that the dendrites for 1:11 and 1:10 samples contain almost exclusively iron element. The excess rare earth concentrations impede the formation of the LaFeSi phases, instead the melt solidifies into several intermediate phases with different mixtures of Fe and La/Ce.

3.1.2. Annealed samples

After annealing at 1373 K for 15 days, the samples were observed with SEM in order to determine the microstructure evolution. Figure III-27 shows the backscattered electron images of all four samples. With no extra rare earth content, the annealed sample with initial 1:13 ratio shows a typical microstructure for annealed laboratory samples. The majority phase is the $\text{La}(\text{Fe}_{1-x}\text{Si}_x)_{13}$ phase and small darker spots of remaining $\alpha\text{-Fe}(\text{Si})$ phase are included in the matrix. Very few small white spots of La-rich phase are visible.

In samples with initial stoichiometry ratio of 1:12, 1:11, and 1:10, the $\text{La}(\text{Fe}_{1-x}\text{Si}_x)_{13}$ phase remains as the majority one in the microstructure. However, large areas of inhomogeneous microstructure can be found. We observe La/Ce-rich phases that enclose the $\alpha\text{-Fe}(\text{Si})$ phases. Very fine lamellae in bright white color can be seen. This is attributed to the disrupted element diffusion due to the additional rare earth elements. Moreover, the low atomic diffusivity of the $\text{La}(\text{Fe}_{1-x}\text{Si}_x)_{13}$ phase at 1373 K and the multiple substitutions in these samples lead to increased difficulty in the formation of single-phase microstructure.

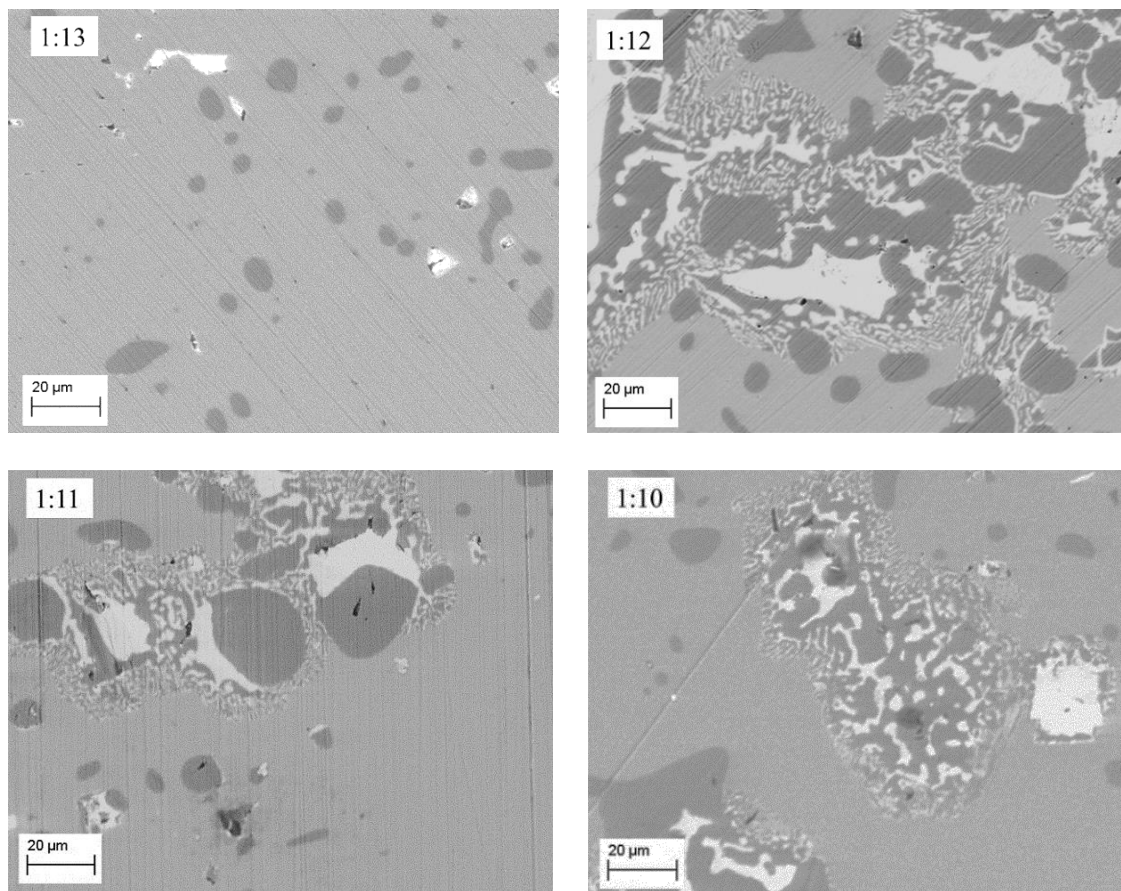


Figure III-27. Microstructure images for annealed samples of composition $\text{La}_{0.7}\text{Ce}_{0.3}(\text{Fe}_{0.88}\text{Mn}_{0.02}\text{Si}_{0.1})_n$, ($n=13, 12, 11, 10$), corresponding to different at.% excess in rare earth elements.

EDX analysis is employed to verify the chemical composition after annealing. For all four samples, the bright white phase corresponds to a phase of composition close to $(\text{La,Ce})\text{FeSi}$ and the dark grey spots are rich in Fe, which correspond to remaining $\alpha\text{-Fe}(\text{Si})$ at the end of the annealing step. The compositions of the main light grey phase are shown in Table III-11.

Table III-11. EDX analysis of the main phase showing normalized atomic percent of each elements

Rare earth excess in at% ($\pm 3\%$)	La	Ce	Fe	Mn	Si
target	5.00	2.14	81.71	1.86	9.29
none (1:13)	5.20	2.28	80.84	1.53	10.05
10% (1:12)	5.28	2.24	76.95	1.46	14.07
18% (1:11)	5.07	2.19	82.34	1.56	8.84
30% (1:10)	5.25	2.16	81.21	1.06	10.31

Initial ratios of 1:12 and 1:11 lead to deviated Si content. Since the material properties are highly sensitive to the Fe/Mn/Si ratio in the composition, this deviation can be problematic to the quality control of these samples. The sample with initial ratio of 1:10 (30% excess rare earth elements) shows similar stoichiometry with the target composition. However, as can be seen from the microstructure analysis, the phase homogeneity is degraded and there are higher proportions of impurity phases in the sample.

3.2. Structural properties

After annealing and hydrogenation steps, the crystal structure was verified with XRD patterns and Rietveld refinement. All four samples show the cubic NaZn₁₃-type structure with a unit-cell parameter of 11.54 Å. Figure III-28 shows the refined phase fractions for all four samples. The results show increasing impurity phases with high content of excess rare earth elements. The presence of impurity phases will have a direct consequence on the magnetic properties of these samples for given mass or volume of material.

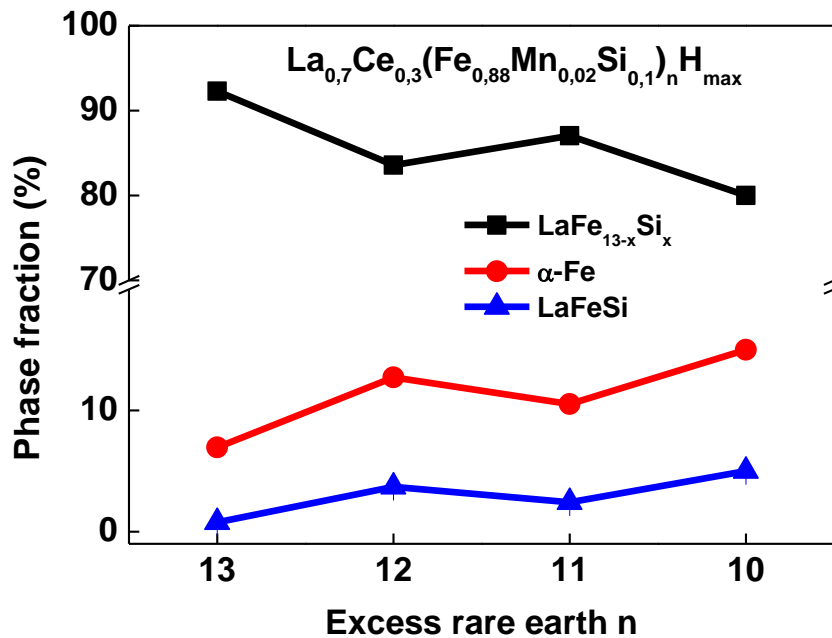


Figure III-28. The phase fractions of samples of composition $La_{0.7}Ce_{0.3}(Fe_{0.88}Mn_{0.02}Si_{0.1})_n$, ($n=13, 12, 11, 10$), with different amount of excess in rare earth contents.

3.3. Magnetic and magnetocaloric properties

3.3.1. Annealed samples

The magnetic properties of annealed samples are summarized in Table III-12. The Curie temperature is defined as the minimum of dM/dT in the temperature-dependent magnetization measurement in heating process. This can deviate from the temperature at which the isothermal entropy change is the maximum, T_{peak} , which is highly dependent on the measuring temperature step.

Table III-12. T_C and T_{peak} values for annealed samples of composition $La_{0.7}Ce_{0.3}(Fe_{0.88}Mn_{0.02}Si_{0.1})_n$ ($n=13, 12, 11, 10$).

Rare earth excess in at%	T_C (K)	Hysteresis (K) ($T_{C\text{ heating}} - T_{C\text{ cooling}}$)	T_{peak} (K)	$-\Delta S_M$ (J/kg·K) (0-2 T)
none (1:13)	116	16	112.5	13.29
10% (1:12)	118	16	117.5	9.44
18% (1:11)	118	18	112.5	12.6
30% (1:10)	120	16	117.5	10.67

It can be seen that T_C shifts towards higher temperature with increasing excess rare earth content. The deviation in T_C can be attributed to the stoichiometry deviation of the 1:13 phase in terms of La/Ce ratio and Fe/Mn/Si ratio, as observed in Table III-11. On the other hand, an increase in the α -Fe(Mn,Si) impurity phase can also lead to a high-temperature shift in T_C measured in the whole sample, which takes into account the magnetization of the α -Fe(Mn,Si) phase.

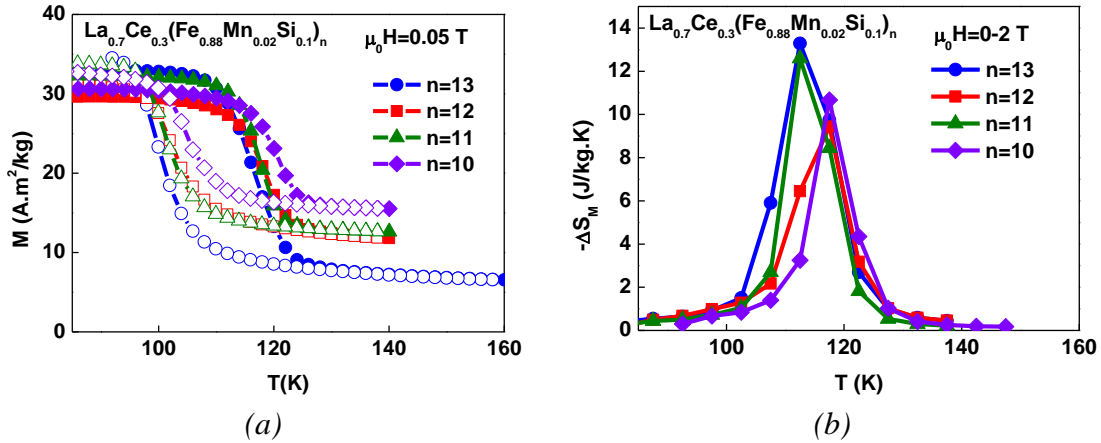


Figure III-29. (a) Magnetization under 0.05 T and (b) isothermal entropy change as a function of temperature for compound $La_{0.7}Ce_{0.3}Fe_{11.44}Mn_{0.26}Si_{1.3}$ with different excess rare earth elements.

The influence of adding rare earth elements before melting on the magnetic transition is presented in Figure III-29 (a). The solid symbols represent the heating curves and the empty symbols show the cooling ones. With increasing rare earth element content, there is an increase of the magnetization level above the T_C of the 1:13 phase. This indicates that the sample contains more proportion of α -Fe(Mn,Si) impurity phase, which is consistent with the microstructure observations and structural analysis from XRD patterns. The isothermal entropy change as a function of temperature is shown in Figure III-29 (b). For $n=12$ and $n=10$, there is a clear decrease of the peak height of ΔS_M . The sample with 1:11 initial ratio shows a narrowed peak width of ΔS_M . The impact on ΔS_M is less significant due to the measuring step.

3.3.2. Hydrogenated samples

After hydrogenation, the magnetic properties are summarized in Table III-13.

Table III-13. T_C and T_{peak} values for hydrogenated samples of composition of composition $La_{0.7}Ce_{0.3}(Fe_{0.88}Mn_{0.02}Si_{0.1})_n$ ($n=13, 12, 11, 10$).

Rare earth excess in at%	T_C (K)	Hysteresis (K) (T_C heating - T_C cooling)	T_{peak} (K)	$-\Delta S_M$ (J/kg·K) (0-2 T)
none (1:13)	282	0	287.5	11.93
10% (1:12)	284	0	287.5	10.23
18% (1:11)	286	0	287.5	9.67
30% (1:10)	286	0	287.5	9.9

The thermal hysteresis has disappeared for all samples after full hydrogenation, which is a typical consequence of hydrogen insertion. The Curie temperature value shows similar tendency with that of the annealed samples. The T_{peak} value does not present the same trend because the measuring step for M(H) curves is not as precise as the M(T) measurements. The ΔS_M estimation is similar for all four samples with the 5 K measuring step, as shown in Figure III-30.

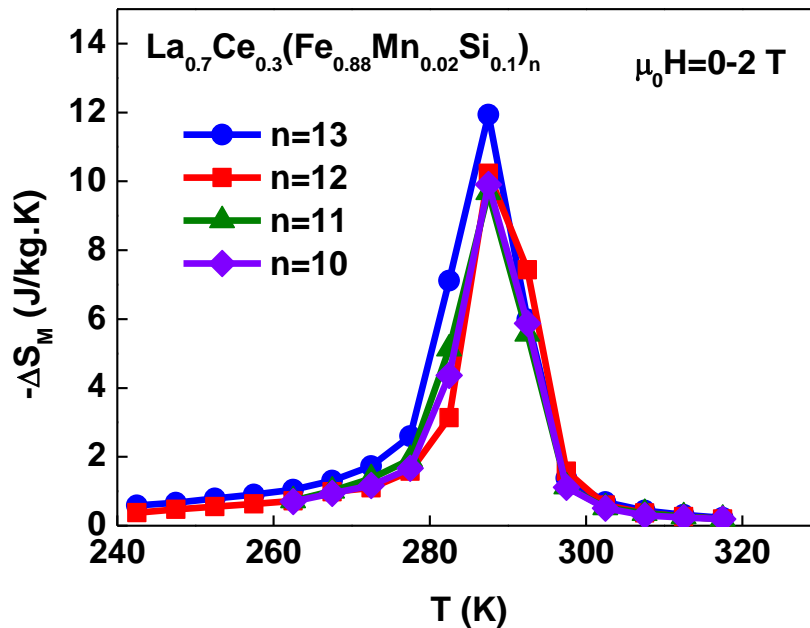


Figure III-30. Isothermal entropy change for hydrogenated samples of composition $La_{0.7}Ce_{0.3}(Fe_{0.88}Mn_{0.02}Si_{0.1})_n$ ($n=13, 12, 11, 10$) with different excess rare earth content.

Therefore, it can be concluded that for the laboratory process specific to the instruments used in this work, having excess rare earth elements before melting is not necessary for the compensation of evaporation loss. The high vacuum level and induction melting can ensure good quality of homogeneity and avoid material loss during melting. The extra rare earth content leads to impeded grain growth in the as-cast samples. Consequently, under the same annealing conditions, the microstructure is less homogeneous due to the difficulty in element mixing. The annealed samples contain higher concentration of impurity phases. The additional rare earth content also influences the magnetic properties of the annealed and hydrogenated samples. There is a high-temperature shift of the Curie temperature and the

magnetization level above T_C is much higher due to increased α -Fe(Mn, Si) phase. In order to have precise control of the material quality, no additional rare earth elements were added for samples elaborated in our laboratory process.

4. Conclusion

In this Chapter, we have systematically studied the effect of substitution of Ce to La and of Mn to Fe atoms on the structural and magnetic properties of the $\text{La}(\text{Fe}_{1-x}\text{Si}_x)_{13}$ phase. In particular, the effect of Ce substitution on the structure is investigated with neutron diffraction and magnetization measurements. Cerium substitution leads to a reduction of the Curie temperature and the first-order characteristics of the transition is more pronounced. Moreover, this partial substitution leads to a reduction of the unit cell parameter, which results in a reduced interstitial volume at the octahedral site $24d$. Ce substitution induces contraction of the intra-icosahedral bonds and a slight expansion of the inter-icosahedral Fe-Fe distances. From the study on the effect of Mn substitution to Fe, we have observed that the extent of Si to shift T_C is impeded by hydrogenation.

The laboratory elaboration process is optimized in terms of having additional rare earth content during melting. For better quality control of the samples, raw elements of 1:13 ration are used.

In the next Chapter, we present studies on the effect of interstitial insertions on the structural and magnetic properties of the 1:13 phase. We are interested to explore how these composition changes lead to various consequences on the hydrogenation behavior of the $\text{La}(\text{Fe}_{1-x}\text{Si}_x)_{13}$ phase.

References

- [1] O. Gutfleisch, A. Yan and K. Muller, *J. Appl. Phys.*, vol. 97, p. 10M305, 2005.
- [2] A. Patissier and V. Paul-Boncour, *J. Alloy Compd.*, vol. 645, p. 143, 2015.
- [3] C. Mayer, A. Dubrez, M. Pierronnet and P. Vikner, *Phys. Status Solidi C*, vol. 11, p. 5, 2014.
- [4] A. Barcza, M. Katter, V. Zellmann, S. Russek, S. Jacobs and C. Zimm, *IEEE Trans. on Mag.*, vol. 47, p. 3391, 2011.
- [5] S. Hirozawa, H. Tomizawa and K. Bekki, *IEEE Trans. on Mag.*, vol. 42, p. 3608, 2006.
- [6] H. Zhang, B. Bao, P. Shi, B. Fu, Y. Long and Y. Chang, *J Rare Earths*, vol. 26, p. 727, 2008.
- [7] T. Liu, Y. Chen, Y. Tang, S. Xiao, E. Zhang and J. Wang, *J. Alloys Compd.*, vol. 475, p. 672, 2009.
- [8] K. Niitsu and R. Kainuma, *Intermetallics*, vol. 20, p. 160, 2012.
- [9] J. Liu, M. Krautz, K. Skokov, T. G. Woodcock and O. Gutfleisch, *Acta. Mater.*, vol. 59, p. 3602, 2011.
- [10] K. Niitsu and R. Kainuma, *Key Eng. Mater.*, vol. 508, p. 172, 2012.
- [11] S. Fujieda, A. Fujita and K. Fukamichi, *IEEE Trans. on Mag.*, vol. 41, p. 2787, 2005.
- [12] A. Fujita, S. Fujieda and K. Fukamichi, *IEEE Trans. Magn.*, vol. 45, p. 2620, 2009.
- [13] L. Finger, D. Cox and A. Jephcoat, *J. Appl. Cryst.*, vol. 27, p. 892, 1994.
- [14] L. Néel, *Oeuvres Scientifiques*, Paris, 1978.
- [15] R. Helmholdt, T. Pastra, G. Nieuwenhuys, J. Mydosh, A. van der Kraan and K. Buschow, *Phys. Rev. B*, vol. 34, p. 169, 1986.
- [16] A. Fujita, S. Fujieda and K. Fukamichi, *J. Magn. Magn. Mater.*, vol. 321, pp. 3553-3558, 2009.
- [17] M. Krautz, K. Skokov, T. Gottschall, C. Teixeira, A. Waske, J. Liu, L. Schultz and O. Gutfleisch, *J. Alloys Compd.*, vol. 598, p. 27, 2014.
- [18] M. Rosca, Ph.D. thesis manuscript "*Matériaux de type LaFe_{13-x}Si_x à fort pouvoir magnéto-calorique - Synthèse et optimisation de composés massifs et hypereffortés - Caractérisations fondamentales*", Grenoble: l'Université Joseph Fourier, 2012. French. <tel-00663184>
- [19] L. Jia, J. Sun, H. Zhang, F. Hu, C. Dong and B. Shen, *J. Phys: Cond. Matter*, vol. 18, p. 9999, 2006.
- [20] L. Jia, J. Sun, B. Shen, D. Li and S. Nimori, *J. Appl. Phys.*, vol. 101, p. 106108, 2007.
- [21] J. Zou, B. Shen and J. Sun, *J. Phys.: Cond. Matter*, vol. 19, p. 196220, 2007.

Chapter III. Studies on the composition optimization

[22] G. Wang, L. Song, F. Li, Z. Ou, O. Tegus, E. Brück and K. Buschow, *J Magn. Magn. Mater.*, vol. 321, p. 3548, 2009.

[23] L. Bao, W. Wei, W. Fan and O. Tegus, *J. Alloy Compd*, vol. 589, p. 416, 2014.

Chapter IV. Influence of interstitial elements

Table of Contents

Chapter IV. Influence of interstitial elements	103
1. Overview of interstitial element insertion	103
2. Influence of hydrogen/deuterium	105
2.1. Neutron diffraction.....	106
2.2. Magnetic properties	112
2.3. Hydrogen instability.....	114
3. Influence of carbon interstitial	118
3.1. Synthesis conditions.....	118
3.2. Influence of carbon concentration	124
3.3. Effect of carbon interstitials in La-Fe-Si and La-Ce-Fe-Si.....	128
4. Conclusion.....	136
Reference	136

Chapter IV. Influence of interstitial elements

1. Overview of interstitial element insertion

When describing a solid system capable of accommodating atoms of smaller sizes to fill its “interstices”, the term “interstitial alloy” is often used. First used by Hägg [1] for pure metal host lattice, the definition has been extended to more than primary solid solution to include many other systems. The addition of interstitial atoms in rare-earth transition-metal intermetallic phases such as R_2Fe_{17} , $R(FeM)_{12}$, $Nd_2Fe_{14}B$, and $ThFe_{11}$, has been shown to effectively increase the Curie temperature [2]. Structural studies have demonstrated that this effect is often associated with the increase of anomalously short interatomic Fe-Fe distances induced by the insertion of light atoms [2]. This steric consequence of light interstitial elements is particularly strong for carbon and nitrogen, as compared with hydrogen.

Due to the large difference in electronegativity between the rare earth elements and the interstitial atoms (H, C, N, B), a strong affinity between these two types of elements should be expected. Typical values of the volume increase induced by different interstitial elements in the 1:13 phase is summarized in Figure IV-1. The effect of C and N is much more important than that of H.

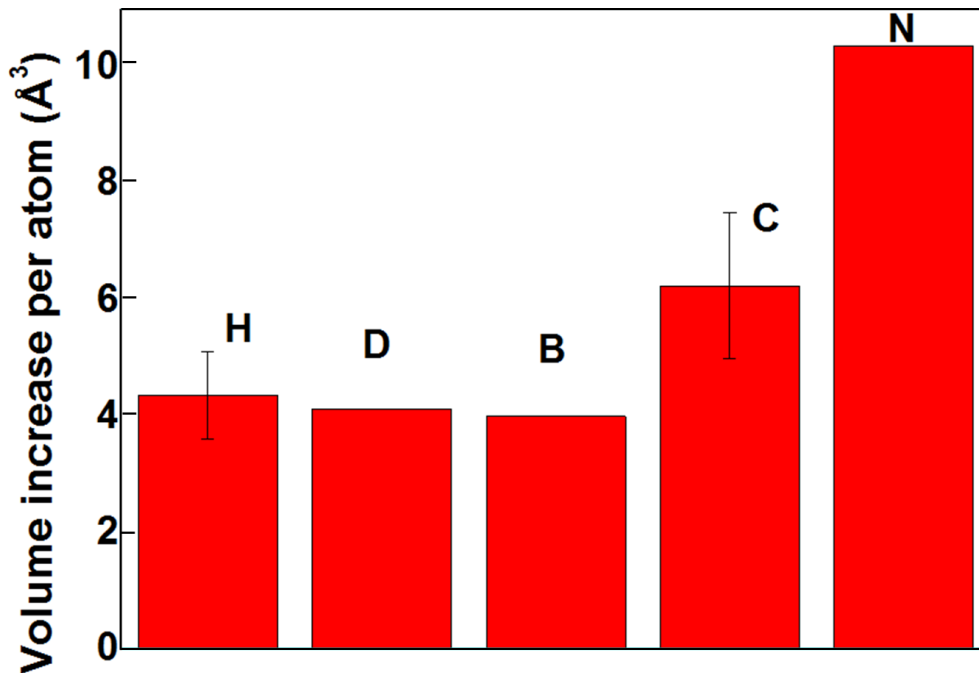


Figure IV-1. Volume increase per atom for light atoms as interstitials H, D, B, C, N in the $La(Fe_{1-x}Si_x)_{13}$ phase, data taken from reference [3, 4, 5, 6, 7] and data from this work.

Accordinging the work of Rao *et al.* [8, 9], the average magnetic moment per atom, $\langle\mu\rangle$, could be well predicted by a parameter-free formula that is valid for both $NaZn_{13}$ -type and its derivative structure: $\langle\mu\rangle = \langle Z_m \rangle + 2N_{sp}\uparrow$ based on the magnetic valence model [10, 11]. In this formula, $2N_{sp}\uparrow$ is taken as 0.8, $\langle Z_m \rangle$ is the magnetic valence averaged over all constituents and $N_{sp}\uparrow$ is the number of spin-up electrons in the unpolarized s-p conduction band. The magnetic valence of an atom, Z_m , is defined as $2N_d\uparrow - Z$. $N_d\uparrow$ is taken as 5 for the

late 3d elements (Fe, Co, Ni, Cu, and Zn), and zero for the early transition elements, the rare earths, and metalloid. Z is the chemical valence of the atom. We have calculated the average magnetic moment per atom for individual interstitial element and the result is presented in Figure IV-2. Hydrogen has the least significant influence on the average magnetic moment per atom in the $\text{La}(\text{Fe}_{1-x}\text{Si}_x)_{13}$ phase while N interstitial strongly decreases the magnetization. The influence of interstitial H on the magnetic properties of the $\text{La}(\text{Fe}_{1-x}\text{Si}_x)_{13}$ phase is discussed in Section 2.2.

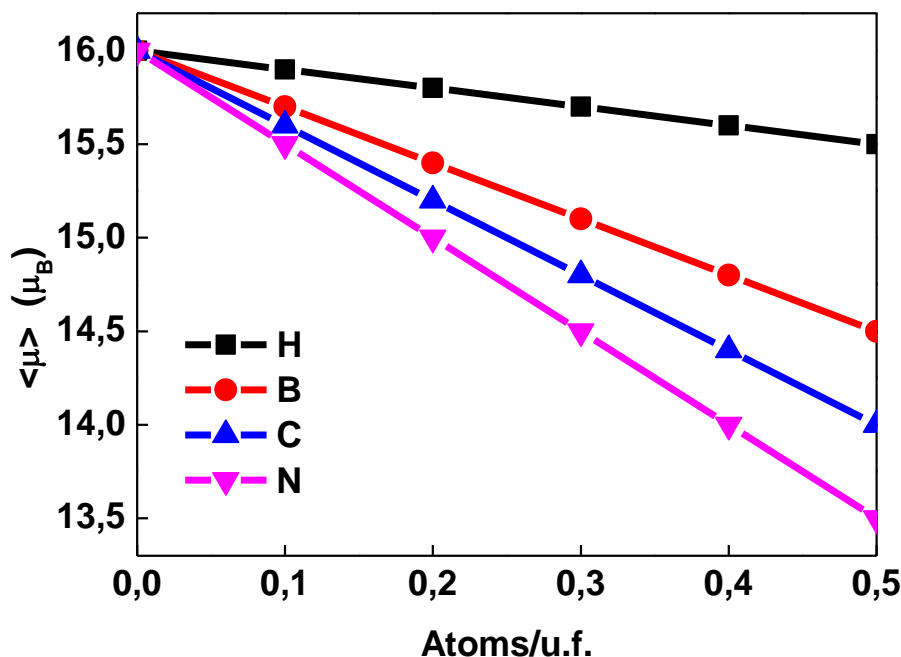


Figure IV-2. Average magnetic moment per atom $\langle \mu \rangle$ in μ_B as a function of interstitial element concentration based on the magnetic valence model, described in [10, 11].

In the $\text{La}(\text{Fe}_{1-x}\text{Si}_x)_{13}$ phase, twelve Fe^{II} atoms form an icosahedral cluster and the Fe^{I} atom is located at the center of the cluster. Interstitial H atoms expand the lattice in a symmetrical manner, resulting in a macroscopically isotropic volume expansion. Hydrogen insertion in the crystalline lattice of the $\text{La}(\text{Fe}_{1-x}\text{Si}_x)_{13}$ phase induces a significant volume increase, in the order of 4.5 \AA^3 per H atom. In R_2Fe_{14} phases, the volume increase by H interstitial atoms is in the order of $2 \text{ \AA}^3/\text{H}$. Neighboring H atoms have a distance of about 4.1 \AA between each other. For reference, the empirical value reported by Switendick [12] for the volume increase induced by H interstitials is around 2.9 \AA^3 per H atom. The itinerant electron metamagnetism in $\text{La}(\text{Fe}_{1-x}\text{Si}_x)_{13}$ phase is conserved in the hydrogenated material, which is the reason that the high isothermal magnetic entropy change is maintained after hydrogenation.

In this chapter, we analyze the consequences of H insertion with detailed structural characterization. Carbon insertion is introduced by describing the synthesis condition and metallurgical characterizations. The basis of structural consideration upon H and C insertion is laid here and the consequences of various composition changes are further developed in Chapter V.

2. Influence of hydrogen/deuterium

After standard hydrogenation procedure described in Chapter II, the H content in sample of composition $\text{LaFe}_{11.7}\text{Si}_{1.3}$ is determined by the mass gain, which is about 1.6 H/f.u. From the XRD patterns, a peak shift towards lower-angle is observed due to the expansion of lattice with hydrogenation. X-ray diffraction peak intensity is associated with the element number Z . Therefore, it is difficult to distinguish light elements with other heavy atoms in XRD.

Contrastingly, powder neutron diffraction is much more sensitive to the presence of light elements, as shown in Figure IV-3 (b). Particularly, hydrogen atoms have significant incoherent scattering cross section with neutron. The neutron diffraction is performed at 300 K, lower than T_C of sample of composition $\text{LaFe}_{11.7}\text{Si}_{1.3}\text{H}_{1.6}$ (342 K). Therefore, magnetic contributions should be expected in the measured diffraction pattern, which is also one significant advantage of neutron diffraction. M. Rosca [6] has demonstrated with neutron diffraction data that the magnetic contribution is visible principally at the (2 2 0) peak. More details on the magnetic structure of the hydrogenated La-Fe-Si samples are discussed in Section 2.2.

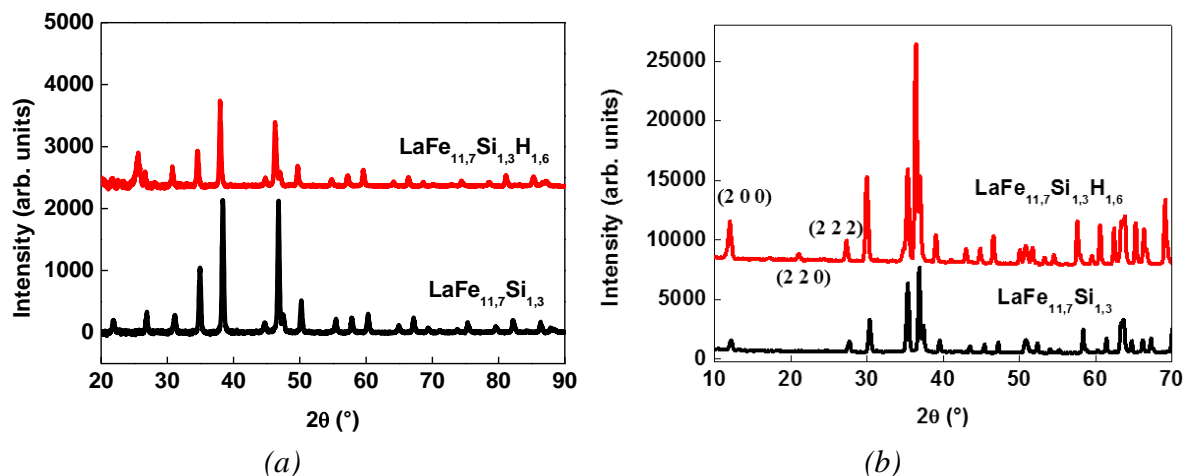


Figure IV-3. (a) X-ray diffraction patterns showing low angle shift of hydrogenated sample, (b) neutron diffraction pattern performed at 300 K for sample $\text{LaFe}_{11.7}\text{Si}_{1.3}$ and $\text{LaFe}_{11.7}\text{Si}_{1.3}\text{H}_{1.6}$ showing not only angle shifts but also magnetic structure peaks.

Chen *et al.* [4] reported that with 1.8 H per formula unit, T_C of $\text{LaFe}_{11.5}\text{Si}_{1.5}$ can be brought from 195 K up to 340 K. The Curie temperature increases in a linear fashion with increasing H content. The isothermal magnetic entropy change, ΔS_M , only slightly decreases after hydrogenation while ΔT_{ad} exhibits an increase as compared with non-hydrogenated samples [13].

Hydrogen insertion can be obtained via gas absorption process between 473 K and 673 K for a few hours under 0.1 MPa (ambient pressure) [14, 15]. Temperature and pressure can be used to control the hydrogenation kinetics, which, generally speaking, accelerates with increasing pressure and increasing temperature. For example, Chen *et al.* [4] have reported that bulk $\text{LaFe}_{11.5}\text{Si}_{1.5}$ is saturated in high purity H_2 at 5 MPa and 423 K for about 5h to obtain $\text{LaFe}_{11.5}\text{Si}_{1.5}\text{H}_{1.8}$ and later performed H absorption at 3 MPa pressure at 523 K for 5h to reach the same H level.

Particle size and surface area also play an important role in H sorption kinetics. For example, reactive milling can effectively produce samples with small particle size. Mandal *et al.* [16] have reported that their reactive milled samples can achieve H saturation in only 1 h at 0.5 MPa H₂ pressure at 473 K. Precise tuning of T_C can be obtained by saturation and subsequent annealing under vacuum or inert gas atmosphere to desorb some of the inserted H [17]. Alternatively, a room-temperature electrolytic process is proposed by Lyubina *et al.* [18].

2.1. Neutron diffraction

Generally the factors affecting interstitial diffusion are intrinsic (size of the diffusing species, bonding, host lattice) and extrinsic (temperature, microstructure, *etc.*). It is our contention that the interstitial insertion scheme particular to the NaZn₁₃-type structure, may be in some way correlated with the interstitial diffusion. Therefore, we have undertaken a careful structural investigation by means of neutron power diffraction (NPD). Steady-state NPD (this Chapter) on selected compositions of the La-Fe-Si system has been used to locate the sites accommodated by the interstitial species and to reveal the structural modifications (breathing) that occur upon metal substitution and/or interstitial insertion.

In addition, *in-situ* NPD is used to investigate the hydrogenation of the pair LaFe_{11.44}Si_{1.56} and LaFe_{11.44}Si_{1.56}C_{0.2} and the pair La_{0.7}Ce_{0.3}Fe_{11.44}Si_{1.56} and La_{0.7}Ce_{0.3}Fe_{11.44}Si_{1.56}C_{0.2}. In this type of time-resolved experiment, the sequential filling of the interstitial sites by hydrogen is followed. This type of measurement allows to extract some useful hydrogenation kinetics data. This structural investigation shows that the kinetics variation (depression or enhancement of the hydrogen absorption rate) may be correlated with the structural results (local lattice distortions) and a mechanism for the diffusion path is suggested in Chapter V.

2.1.1. Hydrogen location

The La-centered snub cubes share faces with Fe^I atom-centered icosahedra of Fe^{II} atoms. The snub cubes and the icosahedra are not perfect but slightly distorted, as shown in Figure IV-4 and in Appendix B. The Fe-Fe interatomic bonds are consisted of three bonds (B1-3) that are formed by the Fe atoms in the same cluster and two inter-icosahedra bonds (B4-5). These interatomic bonds play an important role in the structural evolution in the course of interstitial atom insertion and desorption.

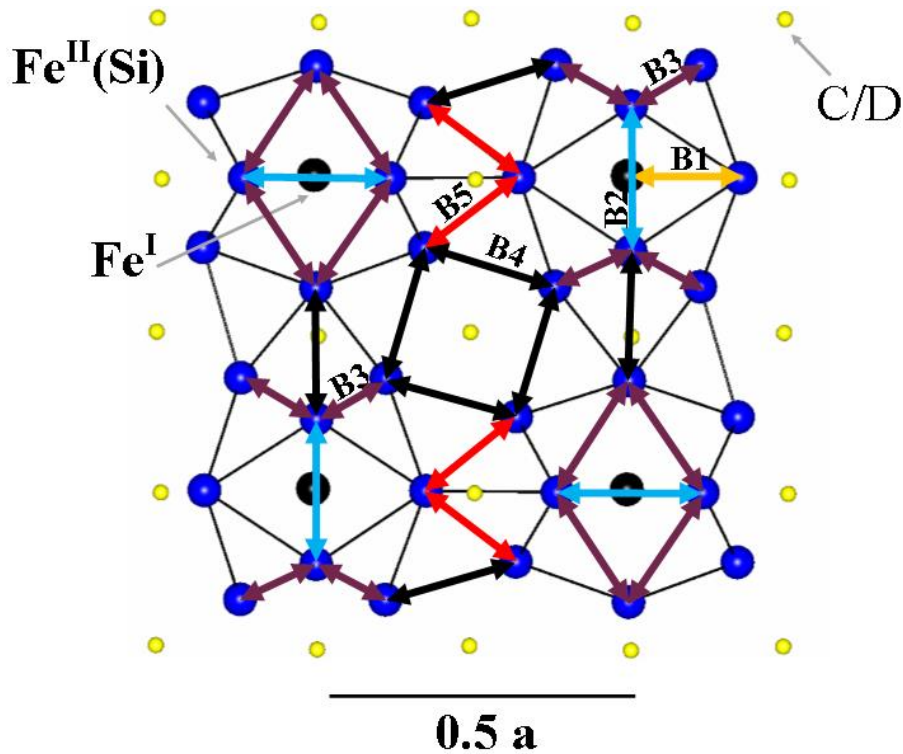


Figure IV-4. Projection along the $(0\ 0\ 1)$ plane of the NaZn_{13} cubic structure showing Fe-Fe distances and H atoms in the $24d$ interstitial site.

B4 and B5 are part of the important building blocks of the NaZn_{13} cubic structure, the *stella quadrangula* (tetrahedral star), which occupies the empty space between the snub cubes and the icosahedra. H. Nyman [19] describes the structure in terms of a framework of slightly distorted corner-connected tetrahedral stars, graphically represented in Figure IV-5. The size of the unit cell and of the snub cube is not determined by the centered atom (La in this case) but only by the structure building unit, i.e., the tetrahedral stars. As discussed in Chapter III, the substitution of La by Ce modifies principally B4 and B5, which confirms that the structural modulation at the La site modifies the structure by adjusting the size of the tetrahedral stars.

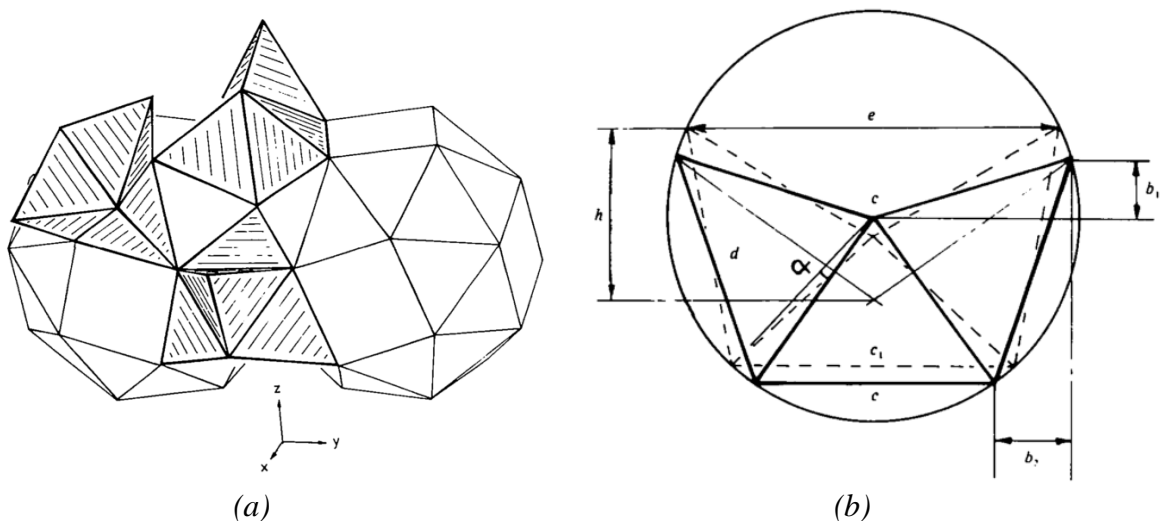


Figure IV-5. (a) A part of the NaZn_{13} structure, showing two face-sharing snub cubes sharing faces with three corner-connected tetrahedral stars. (b) The distortion of a regular tetrahedral star to make it usable as a building block in the NaZn_{13} structure, taken from reference [19].

The difference nuclear scattering density Fourier map shows the spatial distribution of the difference between the measured nuclear scattering density of the crystal and the nuclear scattering density explained by the current model. The negative density suggests parts of the model are not backed up by nuclear scattering density, indicating an atom is absent or not correctly described in the model. By defining the model without H atoms, the difference map can show the location of H atoms, indicated by the negative nuclear scattering density in Figure IV-6.

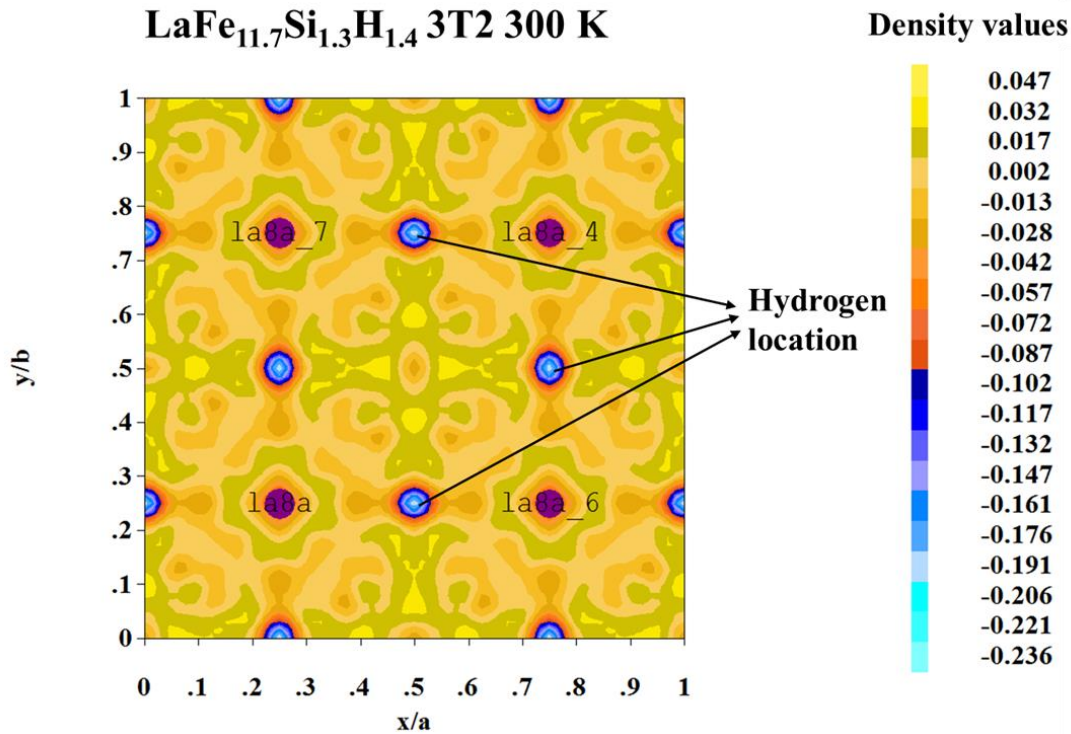


Figure IV-6. Difference nuclear scattering density Fourier map for sample of composition $\text{LaFe}_{11.7}\text{Si}_{1.3}\text{H}_{1.4}$, H is not included in the model to show negative peaks of density.

In the Fourier map calculation, three negative peaks are found at sites $24d$ (0.25, 0.25, 0), $8a$ (0.25, 0.25, 0.25), and $8b$ (0, 0, 0), as shown in Table IV-1. The negative peak at site $24d$ is the most significant. The Fourier map indicates atoms missing at the $24d$ octahedral site, and the lack of nuclear density of H also influences the position and nuclear scattering density around La and Fe atoms.

Table IV-1. Nuclear scattering density peaks calculated from Fourier difference map for sample of composition $\text{LaFe}_{11.7}\text{Si}_{1.3}\text{H}_{1.4}$.

Peak	x/a	y/b	z/c	Occ	Density
1	0.25	0.25	0	0.125	-0.251
2	0.25	0.25	0.25	0.042	-0.103
3	0.20	0.05	0	0.5	0.062
4	0	0	0	0.042	-0.056
5	0.21	0.09	0.09	1	0.048

In the $\text{RFe}_{12-x}\text{M}_x$ (M=Ti, V, Mo, Si) systems, hydrogen was found to fill only the $2b$ octahedral site with R_2Fe_4 environment [20, 21, 22]. From the neutron diffraction data on our samples, H and D atoms are accommodated in the $24d$ (0, 0.25, 0.25) octahedral interstitial site, which has an environment of 4 nearest Fe^{II} atoms (Fe-Fe distance around

2.44 Å) and 2 nearest La atoms with distance 5.73 Å. This is in agreement with the findings of A. Fujita *et al.* [23] and K. Irisawa *et al.* [24], who have demonstrated that the atomic positions occupied by H correspond to that of the *24d* site and that the first-neighbor distances the most affected after H insertion are the Fe^{II}-Fe^{II} distances close to the *24d* site. The volume of the interstitial site plays a major role in the stability of interstitial compounds [25].

Based on the thermal agitation of the H atoms, M. Rosca [6] showed that H atoms are positioned not in the exact center of the plane formed by the 4 Fe^{II} atoms. She demonstrated that the *48f* (*x*, 0.25, 0.25) site is a more appropriate description for the H atomic position. The two sites, *24d* and *48f*, are practically identical, with the exception that H atoms are given an extra degree of freedom around its equilibrium position in the *48f* description. This allows an artificial improvement of the refinement result. For the consideration in this work, we accept the conclusion of the *24d* site as the accommodating site for H and D atoms.

A full occupancy of the *24d* site would correspond to the formula La(Fe_{1-x}Si_x)₁₃H₃, which is not attainable practically because of H-H repulsive interactions. Switendick [12] verified the existence of a minimum distance H-H between two neighboring H atoms by band calculation. Westlake [25, 26] generalized the minimum distance criteria between H atoms to about $d_{\text{H-H}}=2.1$ Å. In the following analysis, H and D saturation refers to the maximum amount of H or D interstitial atoms at given temperature and pressure conditions.

2.1.2. Hypotheses on additional sites

Based on the Wigner-Seitz cell volume (WSV) and void calculation method given by Koch [27], there exists 4 different sites (*24d*, *48f*, *192j*, and *64g*) with volumes susceptible to accommodate interstitial atoms smaller or similar to 2.0 Å³ [28]. As demonstrated in Section 2.1.1, site *48f* offers one extra degree of freedom around the center position. Two additional tetrahedral sites with 3 Fe^{II} and 1 La nearest neighbors are evaluated for H accommodation with neutron diffraction data for compounds saturated with H. The results are shown in Table IV-2.

The refined atomic position for the *192j* site is (0.252, 0.095, 0.147). The hypothesis of H located in both octahedral *24d* and tetrahedral *192j* results in quite small H-H distances for H in the two sites, unacceptable considering the H-H repulsion. Moreover, the refined occupancy on the *192j* site leads to a total H content of 2.76 H/f.u., which deviates from the concentration calculated from the mass gain after hydrogenation (1.6 H/f.u.). It is possible to constrain the total H occupancy so that it is physically reasonable. But this approach does not improve the neighboring H-H distances.

The refined atomic position for the *64g* site is (0.24, 0.24, 0.24), very close to the *48f* position (*x*, 0.25, 0.25). That is to say, H atom has a preference in the octahedral site, which has a much bigger volume. By considering H occupying both octahedral *24d* and tetrahedral *64g* sites, the total H content (1.66 H/f.u.) seems plausible. However, the occupation in the *64g* site results in unacceptable small H-H distances, particularly for those occupying the tetrahedral sites.

Table IV-2. The refined structural parameters and interatomic distances for three hypothesis in H location for sample of composition $\text{LaFe}_{11.7}\text{Si}_{1.3}\text{H}_{1.6}$, based on neutron diffraction data at room temperature. The interatomic distances do not take into account the partial occupancy of sites.

Parameters	Hypothesis	Hypothesis	Hypothesis
	(1)	(2)	(3)
	24d only	24d + 192 j	24d + 64g
site 192j or 64g (x, y, z) x	-	0.252	0.241
site 192j or 64g (x, y, z) y	-	0.095	0.241
site 192j or 64g (x, y, z) z	-	0.147	0.241
B_{24d} (\AA^2)	1,68	1,78	2,12
Occupancy 24d	0,472 (1)	0,472 (1)	0,472 (1)
192j/64g occupancy without constraint	-	0,056 (1)	0,030 (1)
192j/64g occupancy with constraint	-	0,006 (1)	0,021 (1)
$H_{24d}-H_{192j/64g}$ (\AA)	-	1,63 (1)	2.81 (1)
$H_{192j/64g}-H_{192j/64g}$ (\AA)	-	0,86 (1)	0.21 (1)
H/f.u. without constraint	1.42	2.76	1.66
χ^2	12.7	11.6	11.8
R_{Bragg} (%)	6,5	5,8	6,2
R_t (%)	3,9	3,7	3,9

Therefore, the addition of secondary tetrahedral site does not further improve (or only artificially improves) the refinement result and it is quite difficult to distinguish between the results from various hypotheses. The hypotheses of secondary tetrahedral sites for H accommodation lead to either unreasonable total H concentration or unacceptable first-neighbor distances between H atoms. The small quantity of H atoms and their dispersive nature in the NaZn_{13} -type cubic structure make it quite difficult to distinguish secondary interstitial sites that might provide available volume. Even with high-resolution powder neutron diffraction, one cannot conclude with certainty on the existences of secondary interstitial sites.

2.1.3. Influence of hydrogen at room temperature

By comparing the Fe-Fe distances from Rietveld refinement (Table IV-3), we observe that hydrogenation results in an expansion of all distances except for B2. The most affected Fe-Fe distance by H presence is B4, the shortest Fe-Fe distance. B4 is increased from 2.44 \AA to 2.52 \AA . The refined hydrogen content in the 24d site is 1.4 H/f.u., comparable to the value obtained by mass gain after hydrogenation (1.6 H/f.u.).

In the $\text{R}_2\text{Fe}_{17}\text{H}_x$ compounds, the most affected Fe-Fe distance by H interstitial is also the shortest one in the so-called dumbbell lattice. Therefore, even though the H interstitials are not in direct contact with the neighboring Fe atoms, the latter are quite sensitive to the presence of hydrogen. The center of the Fe-Fe exchange interaction is relaxed, which helps stabilizing the ferromagnetic phase at high temperature after H insertion.

Table IV-3. Refined structural parameters and interatomic distances for sample of composition $\text{LaFe}_{11.7}\text{Si}_{1.3}$ and $\text{LaFe}_{11.7}\text{Si}_{1.3}\text{H}_{1.6}$, data taken at room temperature at the 3T2 diffractometer at LLB.

Sample	$\text{LaFe}_{11.7}\text{Si}_{1.3}$	$\text{LaFe}_{11.7}\text{Si}_{1.3}\text{H}_{1.6}$
T_C (K)	190	342
$a=b=c$ (Å)	11,4772 (2)	11,6220 (1)
site $96i$ (0, y, z) y	0,1798 (1)	0,1785 (1)
site $96i$ (0, y, z) z	0,1169 (1)	0,1147 (1)
Occupancy $24d$	-	0,472 (1)
Temperature factor B_{24d} (Å ²)	-	1.68 (1)
$B1$ (Fe^{8b} - Fe^{96i}) (Å)	2,461 (1)	2,466 (1)
$B2$ (Å)	2,684 (1)	2,667 (1)
$B3$ (Å)	2,565 (1)	2,575 (1)
$B4$ (Å)	2,443 (1)	2,515 (1)
$B5$ (Å)	2,490 (1)	2,514 (1)
Fe^{96i} -H (Å)	-	1.779 (1)
χ^2	7.7	12.7
R_{Bragg} (%)	8,2	6,5
R_f (%)	5,0	3,9

The La-H distance is around 2.90 Å for sample of composition $\text{LaFe}_{11.7}\text{Si}_{1.3}\text{H}_{1.6}$, which is considerably larger than the distance R-H (R=rare earth element) in the hydrides of rare earth elements (typically 2.5 Å). This shows that the chemical connection between La and H is not as strong. On the other hand, the bond Fe-H is quite short around 1.8 Å. Since Fe does not have a strong affinity with H atoms, the short distance is therefore unfavorable for interstitial occupation on site $24d$. The short Fe-H bond leads to a repulsion between H atoms occupying the octahedral sites. Both of the above reasons lead to an unstable environment for H interstitials in the 1:13 structure.

The selective occupation of the octahedral sites is probably not ordered since this does not result in lowering of the symmetry. There is thus static disorder present in the lattice. Moreover, H has a high capacity to jump from site to site, which gives rise to a dynamic disorder. It is possible that H jumps from one octahedral site to another. The high thermal agitation coefficient (B_{24d} (Å²) in Table IV-3) of this interstitial site is a supporting element for this hypothesis. Further quasi-elastic neutron scattering experiment can provide insight on the jumping energy of H within the interstitial sites.

2.2. Magnetic properties

To illustrate the effect of H insertion on the magnetic properties of the $\text{La}(\text{Fe}_{1-x}\text{Si}_x)_{13}$ phase, T_C and ΔS_M of a few selected samples are listed in Table IV-4. For sample of composition $\text{LaFe}_{11.7}\text{Si}_{1.3}$, T_C is increased from 190 K to 342 K with 1.6 H/f.u. The isothermal magnetic entropy change is not significantly compromised after hydrogenation.

Table IV-4. T_C and $-\Delta S_M$ values for selected samples before and after hydrogenation.

Composition	Annealed	$-\Delta S_M^{\max}$	Hydrogenated	$-\Delta S_M^{\max}$
	T_C	(0-2 T)	T_C	(0-2 T)
LaFe_{11.7}Si_{1.3}	190	17.33	342	10.66
La_{0.7}Ce_{0.3}Fe_{11.7}Si_{1.3}	170	20.31	328	16.69
La_{0.7}Ce_{0.3}Fe_{11.44}Mn_{0.26}Si_{1.3}	116	13.29	282	11.93

Hydrogen insertion exerts a negative pressure on the $\text{La}(\text{Fe}_{1-x}\text{Si}_x)_{13}$ lattice. Since the lattice volume is sensitive to hydrogenation, it should have rather sensitive response with external pressure as well. Fujita *et al.* [29] have analyzed the response of the ordering temperature of $\text{LaFe}_{11.44}\text{Si}_{1.56}$ with hydrostatic pressure. They found that the value of T_C decreased with increasing pressure and dT_C/dP is about -89 K/GPa. The magnitude of dT_C/dP also depends on the H content in the material. For reference, in the R_2Fe_{17} system, the response of T_C against hydrostatic pressure obtained by Nitikin *et al.* is in the order of -47 K/GPa [30]. It is clear that H induces a strong lattice constraint in the intermetallic system involving rare earth elements and transition metals.

The volume variation around the transition temperature is attributed to an itinerant electron model of Stoner-Wolfarth. It seems that the T_C increase after H insertion is essentially due to the volume increase in the lattice. This confirms the previous analysis underlining the negative pressure exerted by H atoms on the lattice.

In most of the R-Fe (R=rare earth element) intermetallics, H insertion leads to an increase of the magnetization level of the iron sublattice. In the case of YFe_2H_5 , however, large H concentration has negative effects on the iron sublattice magnetization [31]. The effects of H on the magnetic phase diagrams are dependent on the location of H atoms around the R element. The magneto-crystalline anisotropy in R-Fe systems has two distinct and competing contributions, namely, the transition metal (M) anisotropy and the rare-earth element (R) anisotropy [32].

The magnetic behavior of the R_2Fe_{17} systems is very sensitive to local characteristics. In the R_2Fe_{17} systems, the hydrogenated compounds show larger magnetization than the R_2Fe_{17} alloys, particularly at room temperature. Magnetization level increases with H content. Rupp and Wiesinger [33] have observed an increase in the hyperfine field on the ^{57}Fe nucleus with increasing H content.

Neutron diffraction patterns measured at 300 K ($T_C=342$ K) also contain information from the magnetic phase. Previous neutron diffraction experiments have been performed as a function of temperature to probe the magnetic transitions of $\text{La}(\text{Fe}_{1-x}\text{Si}_x)_{13}$ lattice upon hydrogenation [34, 35, 6]. From their results, the authors demonstrated that the Fe atoms at the $96i$ site present a magnetic moment higher than those at the $8b$ site at temperature range below T_C . The magnetic moments of Fe atoms are the maximum at temperature far below

T_C and drops abruptly at T_C . For our purposes, it is helpful to verify the refined average magnetic moments in the samples with the ones measured from thermal magnetization experiments in order to identify the level of correlation between the refined parameters.

The experimental temperature for the recording of neutron diffraction patterns was close to T_C of the hydrogenated samples. The refined magnetic moments are correlated with several other parameters, including the presence of impurity phases and magnetic moment of α -Fe(Si). In order to determine the saturation magnetization at this temperature, isothermal magnetization curves were measured at 300 K for hydrogenated samples by extraction vector magnetometer (Figure IV-7).

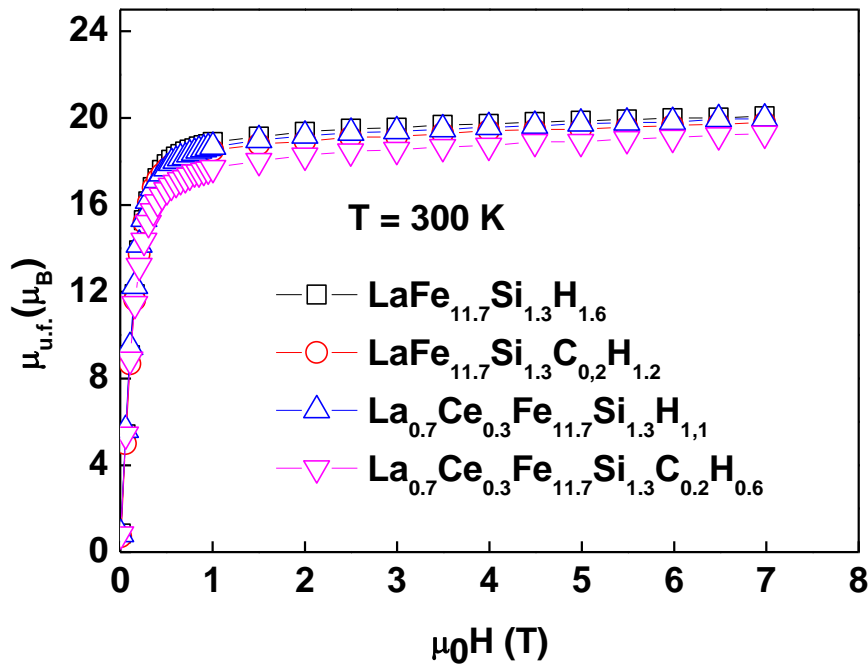


Figure IV-7. Isothermal magnetization curves at 300 K for hydrogenated samples for neutron diffraction (the hydrogen concentration here is determined from mass gain after hydrogenation).

At this temperature, the four samples all exhibit a total magnetic moment around 20 μ_B per formula unit. At low temperature (4 K), the obtained total magnetic moment is roughly 22-23 μ_B /f.u. for all samples. This is consistent with the results reported by Rosca *et al.* [6]. The refined total magnetic moments are compared with those obtained from magnetization measurement at the same temperature (Table IV-5).

Table IV-5. The total magnetic moments obtained from isothermal magnetization measurements and the refined total magnetic moments from Rietveld method for four hydrogenated samples for steady-state neutron diffraction at 300 K.

Total $\mu_{f.u.}$ (μ_B) at 300 K	Magnetometer	T_C (K)	Rietveld
$\text{LaFe}_{11.7}\text{Si}_{1.3}\text{H}_{1.6}$	20.1	342	17
$\text{LaFe}_{11.7}\text{Si}_{1.3}\text{C}_{0.2}\text{H}_{1.2}$	19.8	346	15
$\text{La}_{0.7}\text{Ce}_{0.3}\text{Fe}_{11.7}\text{Si}_{1.3}\text{H}_{1.1}$	20.0	328	10
$\text{La}_{0.7}\text{Ce}_{0.3}\text{Fe}_{11.7}\text{Si}_{1.3}\text{C}_{0.2}\text{H}_{0.6}$	19.3	330	22

As can be seen in Table IV-5, the bulk total magnetic moments obtained show a small deviation from the magnetic moment deduced from saturation magnetization measurement

at the same temperature (300 K). These values are in good agreement considering that in neutron diffraction, the magnetic polarization of the conduction band is not visible whereas the magnetization measurement provides the total magnetization. For the Ce-substituted samples, the presence of an additional impurity phase $\text{Ce}_2\text{Fe}_{17}$ (space group R-3M) increases the correlation among different parameters, leading to a significant difference between the refined and the obtained total magnetic moment. Therefore, for the determination of structural parameters for the hydrogenated samples, the magnetic moment is fixed to the value from the magnetization measurement shown in Figure IV-7.

2.3. Hydrogen instability

Hydrogen insertion was introduced from as early as 2003 [36], yet low stability of fully hydrogenated materials at elevated temperature is still an issue. Two types of phenomena appear for hydrogenated $\text{La}(\text{Fe}_{1-x}\text{Si}_x)_{13}$ phases. For compositions that are saturated with H interstitials, they are generally quite stable when stored around their T_C . However, it is observed that the aged samples show a T_C shift towards lower temperature, indicating a loss in H concentration. This event is particularly visible at elevated temperature and for $\text{La}(\text{Fe}_{1-x}\text{Si}_x)_{13}$ phases showing a rather first-order transition. As for partially hydrogenated (partial removal of H in the fully hydrogenated parent compound) samples aged around their initial Curie temperature, they gradually show a peak splitting of the initial T_C , suggesting a redistribution of H in the structure. Hydrogen atoms diffuse from the small volume paramagnetic phase towards the large volume ferromagnetic state. The two phases can coexist near the transition temperature region, which can be particularly problematic for materials showing first-order transition.

2.3.1. Hydrogen loss at high temperature for fully hydrogenated samples

The concentration of absorbed H is difficult to control. For atomized powder below saturation, there is a distribution of inhomogeneous absorption in each grain. Therefore, fine T_C tuning involving hydrogenation is done first by fully saturating the sample with H then partially releasing the H by annealing in Ar between 373 and 573 K under 0.1 MPa [15].

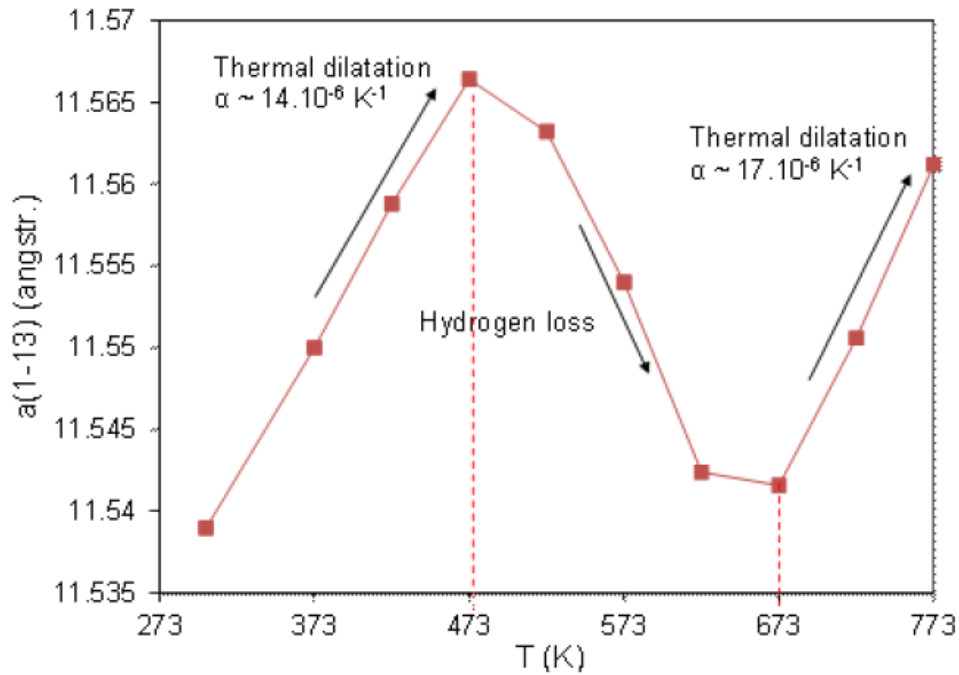


Figure IV-8. Evolution of the lattice parameter of the magnetocaloric phase versus temperature in fully hydrogenated $\text{La}_{0.7}\text{Ce}_{0.3}\text{Fe}_{11.44}\text{Mn}_{0.26}\text{Si}_{1.3}\text{H}_{1.8}$.

From evolution of the lattice parameter in Figure IV-8, H loss takes place between 473 K and 673 K as the lattice parameter ceases to dilate with increasing temperature. The behavior of the NaZn_{13} -type phase during dehydrogenation is studied by analyzing the H content with temperature. Gas atomized samples of different compositions show similar thermal desorption behaviors (Figure IV-9). H content decreases continuously with increasing temperature. At macroscopic scale, partial substitution by Ce and Mn does not seem to have a dramatic effect on the H stability.

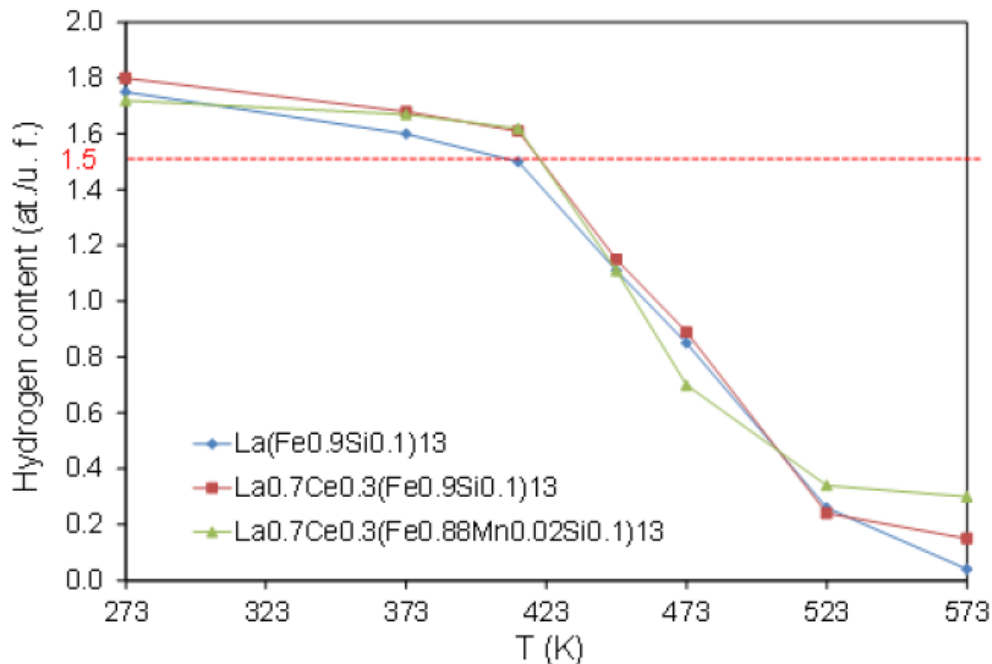


Figure IV-9. Evolution of the H content versus temperature during 4h of heat treatment for three fully hydrogenated powders of compositions $\text{LaFe}_{11.7}\text{Si}_{1.3}\text{H}_{1.75}$, $\text{La}_{0.7}\text{Ce}_{0.3}\text{Fe}_{11.7}\text{Si}_{1.3}\text{H}_{1.8}$, and $\text{La}_{0.7}\text{Ce}_{0.3}\text{Fe}_{11.44}\text{Mn}_{0.26}\text{Si}_{1.3}\text{H}_{1.8}$.

2.3.2. Age splitting for partially hydrogenated samples

First communicated at the conference Thermag V at Grenoble [37], the instability of partially hydrogenated $\text{La}(\text{Fe}_{1-x}\text{Si}_x)_{13}$ samples has been extensively studied. It has been observed that partially hydrogenated samples produce two separate magnetic transitions with time, the T_C peak splits into two different ones, a so-called “age splitting” phenomenon. Several authors [14, 38, 39] have reported peak splitting from DSC or ΔT_{ad} curves after storing the material around its T_C , indicating two phases with different ordering temperatures.

Krautz *et al.* [38] have proposed that H atoms diffuse from the paramagnetic phase to the ferromagnetic one in the region near T_C of the original magnetocaloric phase where the two phases coexist. The migration of H atoms results in the coexistence of two phases with different H concentrations and different T_C .

As the sample is aged further around its original T_C , the two phases with two T_C both show a shift in T_C towards lower temperatures. This means that after the splitting has reached its maximum, the material starts to lose some H. Mayer *et al.* [15] have shown that this age splitting phenomenon is closely linked with the transition order, therefore, composition of the material.

Figure IV-10 and Figure IV-11 show examples of age splitting associated with transition order. The samples were measured in DSC right after hydrogenation. After aging around their T_C for some time, the DSC measurements were repeated and the curves were compared to verify any peak shifts or splits.

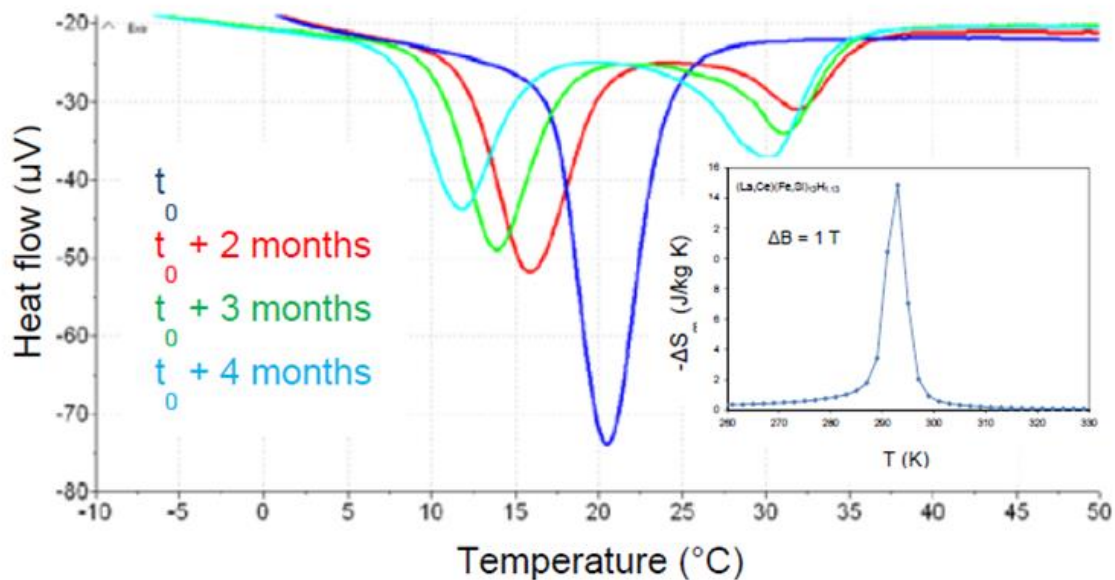


Figure IV-10. DSC measurements of a partially hydrogenated sample $\text{La}_{0.7}\text{Ce}_{0.3}\text{Fe}_{11.7}\text{Si}_{1.3}\text{H}_{1.13}$, the inset shows the variation of isothermal entropy change versus temperature of this sample for a magnetic field change from 0 to 1 T.

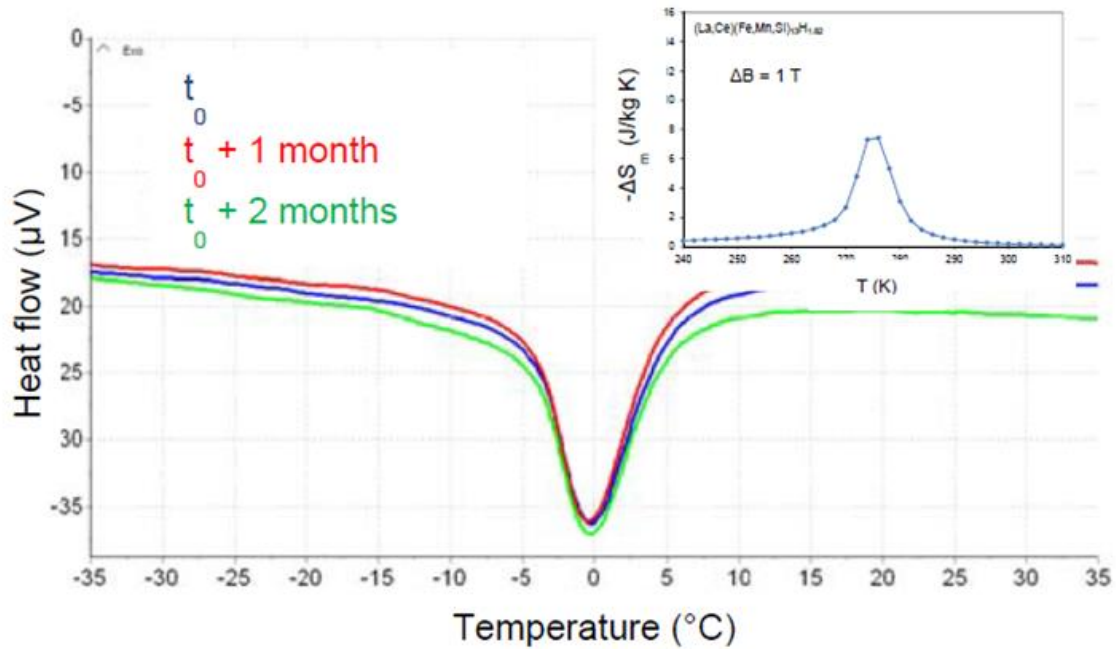


Figure IV-11. DSC measurements of a partially hydrogenated powder $\text{La}_{0.7}\text{Ce}_{0.3}\text{Fe}_{11.44}\text{Mn}_{0.26}\text{Si}_{1.3}\text{H}_{1.62}$, the inset shows the isothermal magnetic entropy change versus temperature of this sample for a magnetic field change from 0 to 1 T.

For a typical material exhibiting first-order transition characteristics (with Ce partial substitution for La, low Si content, and no substitution for Fe), the peak splitting is very obvious after a few months of storage near T_C , as shown in Figure IV-10. The partial substitution of La by Ce tends to induce a very strong first-order behavior, which contributes to the H instability in the material due to the occurrence of a wide thermal hysteresis and a large temperature domain of coexistence of paramagnetic and ferromagnetic phases in the material.

As for a rather second-order material (with higher Si content and partial substitution of Mn for Fe), the ordering temperature is stable with no splitting after 2 months, as shown in Figure IV-11. For instance, Co substitution to La leads to an enhancement of the second-order characteristics of the magnetic transition. Consequently, the thermal hysteresis is rather small and age splitting is slow or not observed. However, as can be seen from the insets in Figure IV-10 and Figure IV-11, materials exhibiting second-order transitions show reduced isothermal entropy change, therefore, the magnetocaloric effect is compromised as compared with materials with first-order transition characteristics.

The risk of age splitting depends on the magnetic transition characteristics of the $\text{La}(\text{Fe}_{1-x}\text{Si}_x)_{13}$ phase. The occurrence of large thermal hysteresis gives rise to a large temperature span for the PM and FM phases to coexist. This coexistence domain is the key to the splitting of peaks.

3. Influence of carbon interstitial

Zhao *et al.* [40] have shown that C introduction can improve the thermal stability of the hydrogenated $\text{La}(\text{Fe}_{1-x}\text{Si}_x)_{13}$ phases. This can be a possibility to have a better control of the H content. It appears to be very practical to involve only a small amount of C (≤ 0.2 C/f.u.) in order to avoid a drastic reduction of the MCE [41]. It is possible to insert C in the matrix either through a solid-gas reaction with hydrocarbides or by adding C directly during melting. Solid-gas reaction is not very practical for precise concentration control and it has not been demonstrated that this can be achieved homogeneously in large batches.

The synthesis of carbides by arc melting for R_2Fe_{17} and $\text{RFe}_{12-x}\text{M}_x$ (R=rare earth metal and M=Ti, Mo) has been reported since the 1980s [42], which has proven to be relatively easy to handle. The insertion of C during melting is selected for the $\text{La}(\text{Fe}_{1-x}\text{Si}_x)_{13}$ phases. Yet the details of the melting procedure need to be clarified to have good control and reproducibility. Therefore, a part of the compound synthesis is dedicated to optimize the melting procedure.

3.1. Synthesis conditions

Three sequences of melting are tested in order to optimize the melting procedures. Sequence 1 consists of melting all elements of nominal compositions together in a one-step procedure. In Sequence 2, an intermediate ingot without rare earth elements of type Fe-Si-C is first melted and then La is added and the mixture is melted a few times together to have a homogenous ingot. Sequence 3 consists of making a La-Fe-Si intermediate ingot first and then C in the form of graphite is added and the mixture is melted again. The amount of C dopants is verified by LECO combustion analysis, as shown in Table IV-6. Combustion testing is a technique often used in industrial and manufacturing applications to accurately detect low levels of carbon, sulfur, nitrogen, oxygen, and hydrogen by heating and combusting the sample to release these specific elements. Carbon level is measured by combustion in the presence of pure oxygen to oxidize C to form CO_2 . The LECO trademark is an acronym of the original name of the company, Laboratory Equipment Corporation.

Table IV-6. C concentration verified by LECO combustion analysis for as-cast $\text{LaFe}_{11.7}\text{Si}_{1.3}\text{C}_{0.2}$ samples in each melting sequence.

Sequence	wt% C before melting	combustion analysis after melting
1	0.296	0.324+/- 0.007
2	0.262	0.288+/- 0.004
3	0.278	0.300 +/- 0.011

The C content measured by combustion analysis shows superior values than the weight percent of graphite measured before melting. This is because the combustion method analyzes the C content present in the entire testing material, regardless of different phases present within the material. Since C has much higher affinity with Fe and La, it is reasonable to suspect that part of the C content inserted before melting goes into the impurity phases such as α -Fe and leads to the formation of carbides phases with Fe and La elements. The presence of such carbide phases can be determined by X-ray diffraction,

shown in the following section. Therefore, the C content from combustion analysis is higher than expected because not all of the C is able to enter the $\text{La}(\text{Fe}_{1-x}\text{Si}_x)_{13}$ phase.

Sample elaborated by Sequence 3 has the smallest deviation of C content compared with the desired nominal composition before melting. The small deviation between analysis before and after melting confirms a positive impact of this Sequence in reducing the amount of C content in the impurity phases.

3.1.1. X-ray diffraction

Figure IV-12 shows the XRD patterns of the as-cast samples from three sequences and the C-free reference. The refined structural parameters are listed in Table IV-7. The as-cast samples show a majority of $\alpha\text{-Fe}(\text{Si})$ and LaFeSi phases, regardless of the melting sequences.

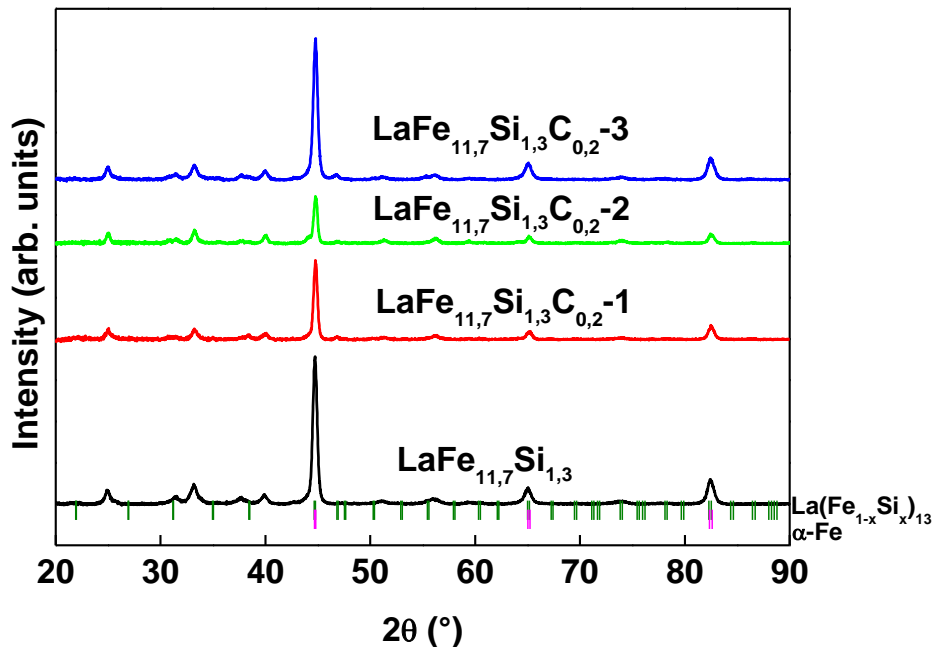


Figure IV-12. XRD patterns of as-cast samples of composition $\text{LaFe}_{11.7}\text{Si}_{1.3}$ and C-doped ones by three different sequences.

The sample of nominal composition $\text{LaFe}_{11.7}\text{Si}_{1.3}$ has negligible 1:13 phase, whereas the C-doped samples all show approximately 5 vol.% of 1:13 phase. No carbide phases are detected. Therefore, the higher value of C content measured by LECO combustion analysis is due to the presence of C in impurity phases. The C-doped samples from Sequence 1 and 2 have a slightly smaller volume of $\alpha\text{-Fe}(\text{Si})$ phase. The peak intensities of $\alpha\text{-Fe}(\text{Si})$ are also reduced for these two samples, which is confirmed by a lowered phase fraction from Rietveld refinement.

Table IV-7. Rietveld analysis results for as-cast sample $\text{LaFe}_{11.7}\text{Si}_{1.3}$ and C-doped ones by three different melting sequences.

Sample	Cell parameter $a=b=c$ (Å) α -Fe phase	Phase fraction 1:13 (%)	Phase fraction α -Fe (%)	Phase fraction LaFeSi (%)
$\text{LaFe}_{11.7}\text{Si}_{1.3}$	2.8656 (1)	0.6 (2)	83.2 (7)	16.2 (2)
$\text{LaFe}_{11.7}\text{Si}_{1.3}\text{C}_{0.2}$ -1	2.8639 (1)	6.7 (3)	78.8 (7)	14.5 (2)
$\text{LaFe}_{11.7}\text{Si}_{1.3}\text{C}_{0.2}$ -2	2.8637 (1)	5.0 (4)	66.9 (7)	28.1 (4)
$\text{LaFe}_{11.7}\text{Si}_{1.3}\text{C}_{0.2}$ -3	2.8659 (1)	6.0 (2)	80.5 (6)	13.5 (2)

After annealing at 1373 K for 2 weeks and full hydrogenation, the structural information is examined once again by XRD for the same samples. The XRD patterns are shown in Figure IV-12.

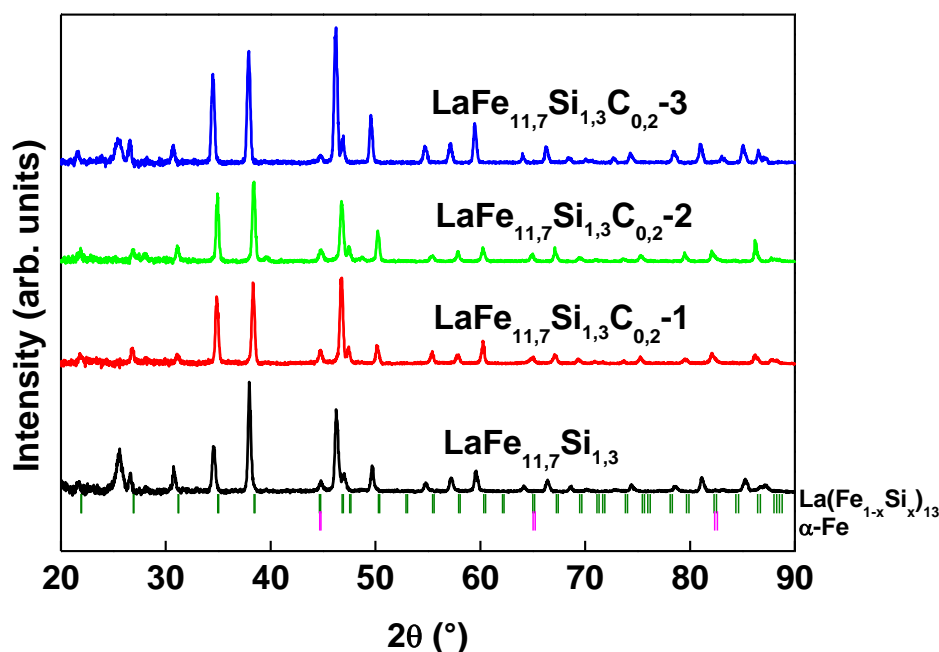
Figure IV-13. XRD patterns of hydrogenated compounds $\text{LaFe}_{11.7}\text{Si}_{1.3}$ and C-doped ones by three different sequences.

Table IV-7 shows the lattice constant and phase fractions from refinement. Hydrogen content is estimated by the mass gain after hydrogenation. $\text{LaFe}_{11.7}\text{Si}_{1.3}\text{C}_{0.2}$ samples from Sequence 1 and 2 do not have any measurable uptake in mass. Indeed, the unit cell parameters from Rietveld refinement for these two samples are significantly lower than for sample $\text{LaFe}_{11.7}\text{Si}_{1.3}\text{H}_{1.4}$, which correspond to the non-hydrogenated lattice constant range. Via Sequence 3, sample $\text{LaFe}_{11.7}\text{Si}_{1.3}\text{C}_{0.2}$ -3 has successfully taken up H interstitials, as seen from lattice constant increase.

Table IV-8. Rietveld analysis results for annealed and hydrogenated sample $\text{LaFe}_{11.7}\text{Si}_{1.3}\text{C}_x\text{H}_y$ by three different melting sequences.

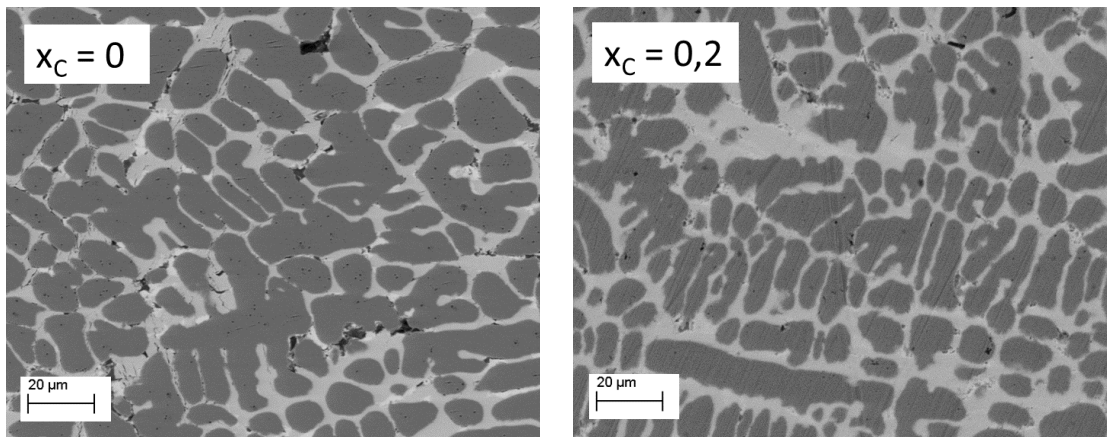
First hydrogenation	Mass gain (%)	Cell parameter 1:13 phase (Å)	Phase fraction 1:13	Cell parameter α -Fe phase	Phase fraction α -Fe
$\text{LaFe}_{11.7}\text{Si}_{1.3}\text{H}_{1.4}$	0.201	11.611 (2)	96.5 (8)	2.8632 (5)	3.5 (2)
$\text{LaFe}_{11.7}\text{Si}_{1.3}\text{C}_{0.2}\text{H}_0$ -1	0.000	11.492 (1)	89.0 (1)	2.8616 (5)	11.0 (4)
$\text{LaFe}_{11.7}\text{Si}_{1.3}\text{C}_{0.2}\text{H}_0$ -2	0.000	11.496 (1)	88.6 (11)	2.8623 (6)	11.4 (5)
$\text{LaFe}_{11.7}\text{Si}_{1.3}\text{C}_{0.2}\text{H}_{1.2}$ -3	0.136	11.627 (1)	98.1 (17)	2.8640 (6)	1.9 (2)

Sequence 1 and 2 lead to excess amount of the α -Fe(Si) phase after long-term annealing and hydrogenation procedure, and they do not lead to H uptake in the lattice. XRD pattern of sample from Sequence 3 shows a clear reduction of the peak intensity of the α -Fe(Si) phase.

By melting all elements at once, as in the method of Sequence 1, the thermodynamics favors low-energy phases and the element distribution is guided by the affinity among atoms. Although C content is confirmed by combustion analysis in the as-cast samples, it does not confirm the homogenous distribution of C atoms. La and Fe both have very strong affinity with C atoms. It is possible that C atoms have been accommodated in the α -Fe(Si) structures and are no longer able to diffuse into the 1:13 phase formed during annealing. Sequence 2 presents similar risks of favoring an inhomogeneous distribution of C atoms.

3.1.2. Microstructure

The microstructure of as-cast samples was examined and BSE images are shown in Figure IV-14 for the C-free sample and C-doped sample from Sequence 3. Both elaborated by induction melting, the as-cast samples show similar microstructures with dendritic α -Fe(Si) phase in dark grey, surrounded by LaFeSi phase.

Figure IV-14. BSE images of $\text{LaFe}_{11.7}\text{Si}_{1.3}$ and $\text{LaFe}_{11.7}\text{Si}_{1.3}\text{C}_{0.2}$ (Sequence 3) as-cast ingots.

There are some white areas at the boundary of LaFeSi phases, which is La-rich phase based on EDX analysis. The first phase to crystallize during solidification is the α -Fe(Si) phase, followed by LaFeSi phase. The remaining rare earth elements solidify in the end to form the La-rich phases. Due to the small Z number of C, it is difficult to quantitatively determine the fraction of C in the 1:13 phase using X-ray microanalysis. Moreover, the

resin for SEM preparation contains C element, making it difficult to distinguish the contribution from the sample.

By examining the microstructure evolution and phase transition dependence, Fu *et al.* [43] suggested that C insertion had a positive influence on the formation of the 1-13 phase. According to these authors, samples with 0.2 C/f.u. are able to obtain 90 vol.% of the 1:13 phase after only 3 days of annealing at 1353 K. Indeed, the process of C insertion can be further optimized by conducting systematic study on the microstructural evolution during different annealing temperature and duration. This is out of the scope of this study, however, since the purpose here is mainly to compare physical properties of samples with and without C insertion under the same experimental conditions. Carbon-free and C-doped samples were annealed at 1373 K for 2 weeks and no distinctive difference was observed in the microstructure.

3.1.3. Magnetic properties

Thermal magnetic measurements were performed for samples after annealing at 1373 K for 15 days. Carbon interstitials shift T_C towards higher temperature, as can be seen in Figure IV-15. As expected, the melting sequence has an impact on the magnetic transitions of the C-doped samples. Sequence 1 results a magnetic transition with strong second-order characteristics and T_C is shifted from 190 K to 228 K. After annealing, the residual α -Fe(Si) phase is quite important in sample from Sequence 1, as manifested by the high magnetization level at temperature higher than T_C . Sequence 2 and 3 have shown good incorporation of C in the 1:13 phase, as represented by the diminution of thermal hysteresis and high-temperature shift of the Curie temperature. The thermal hysteresis is effectively reduced after C insertion for all three cases.

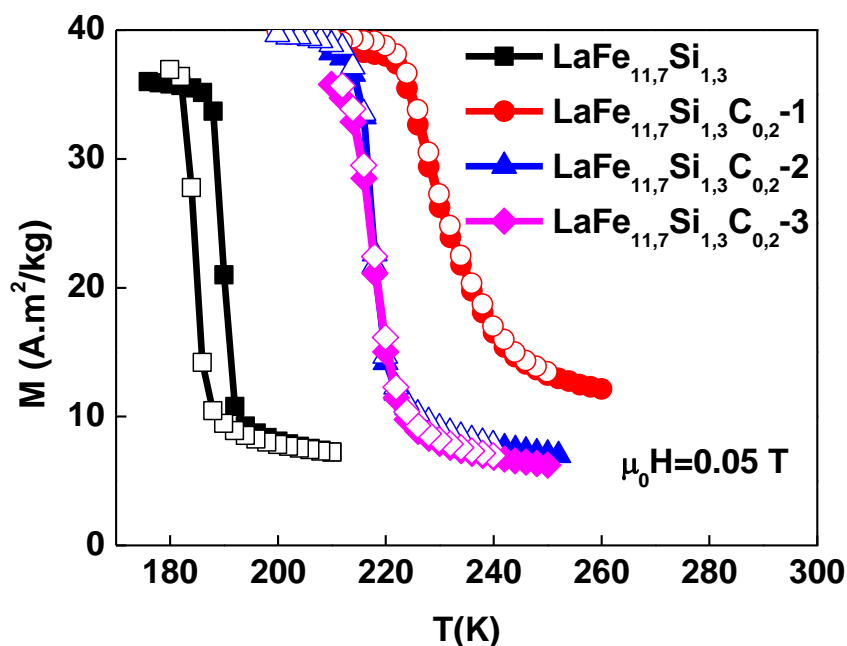


Figure IV-15. Thermal magnetic measurement for sample of composition $\text{LaFe}_{11.7}\text{Si}_{1.3}$ and the C-doped samples from different melting sequences.

In order to verify the H absorption capacity of the two samples with unsuccessful hydrogenation ($\text{LaFe}_{11.7}\text{Si}_{1.3}\text{C}_{0.2}$ -1 and $\text{LaFe}_{11.7}\text{Si}_{1.3}\text{C}_{0.2}$ -2), the samples were further annealed in H_2 flow at higher temperature (623 K) for longer duration (5 h) to increase the chances for H insertion. Figure IV-16 shows the magnetization curves as a function of temperature for the hydrogenated samples.

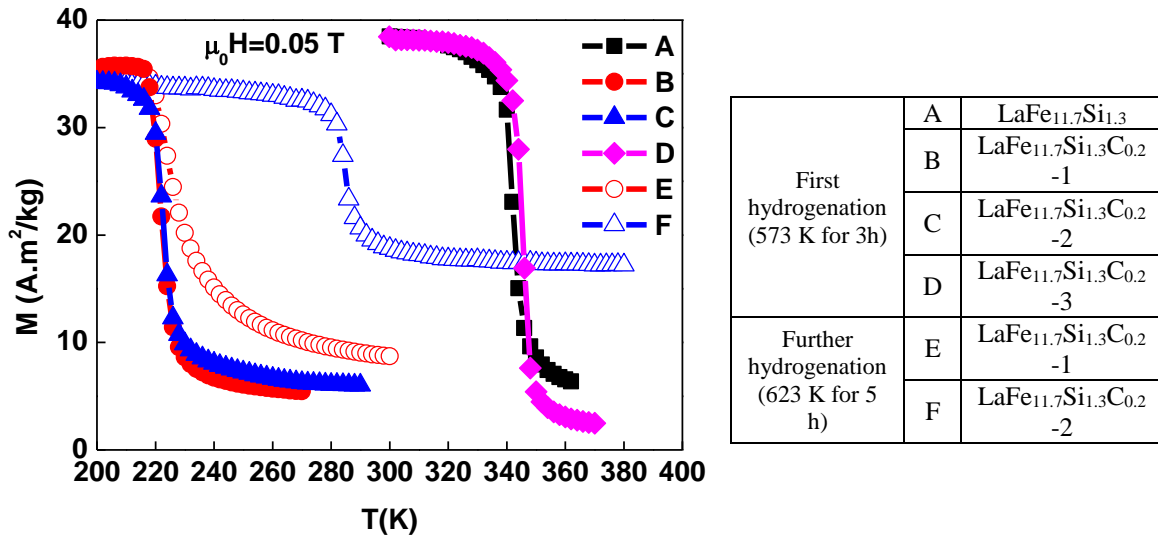


Figure IV-16. Thermal magnetization measurements of annealed and hydrogenated compounds $\text{LaFe}_{11.7}\text{Si}_{1.3}$ (curve A) and C-doped ones by three different sequences (curve B, C, D), a second hydrogenation trial is performed for C-doped samples $\text{LaFe}_{11.7}\text{Si}_{1.3}\text{C}_{0.2}$ -1 and -2 (curve E and F).

It is clear from the T_C shift that $\text{LaFe}_{11.7}\text{Si}_{1.3}\text{C}_{0.2}$ samples from Sequence 1 (B) and Sequence 2 (C) show great difficulty in H activation and barely take up any H after 3 hours in pure H_2 flow at 573 K. On the contrary, sample from Sequence 3 (curve D) has successfully absorbed H interstitials. From the mass gain estimation, sample of composition $\text{LaFe}_{11.7}\text{Si}_{1.3}$ has absorbed 1.6 H/f.u. while sample of composition $\text{LaFe}_{11.7}\text{Si}_{1.3}\text{C}_{0.2}$ -3 takes up less H (1.1 H/f.u.) under the same conditions. The Curie temperature for the hydrogenated sample of composition $\text{LaFe}_{11.7}\text{Si}_{1.3}$ is around 342 K and that of composition $\text{LaFe}_{11.7}\text{Si}_{1.3}\text{C}_{0.2}$ -3, 346 K. This is consistent with the lattice constant shown in Table IV-8.

Even after further hydrogenation treatment, $\text{LaFe}_{11.7}\text{Si}_{1.3}\text{C}_{0.2}$ -1 remains incapable of H accommodation and $\text{LaFe}_{11.7}\text{Si}_{1.3}\text{C}_{0.2}$ -2 absorbs some H interstitials as T_C increased from 222 to 284 K. Therefore, Sequence 3 has proven to be the most optimized melting procedure in order to provide high-purity phase formation and high capacity for subsequent H incorporation.

3.2. Influence of carbon concentration

In order to optimize the C content, samples of composition $\text{La}_{0.7}\text{Ce}_{0.3}\text{Fe}_{11.44}\text{Mn}_{0.26}\text{Si}_{1.3}\text{C}_x$ were elaborated to examine the effect of different C concentration. The amount of C content in the as-cast samples is evaluated with LECO combustion analysis (Table IV-9).

Table IV-9. LECO combustion analysis for the C level in as-cast samples of composition $\text{La}_{0.7}\text{Ce}_{0.3}\text{Fe}_{11.44}\text{Mn}_{0.26}\text{Si}_{1.3}\text{C}_x$.

$\text{La}_{0.7}\text{Ce}_{0.3}\text{Fe}_{11.44}\text{Mn}_{0.26}\text{Si}_{1.3}\text{C}_x$	wt% C before melting	LECO analysis after melting
x=0	-	-
x=0.2	0.290	0.322 +/- 0.012
x=0.4	0.580	0.622 +/- 0.003
x=0.6	0.860	0.905 +/- 0.010

After melting, it can be confirmed that appropriate amounts of C content are incorporated. LECO analysis shows higher value of C content since it takes into account the entire material and not the C content specifically in the $\text{La}(\text{Fe}_{1-x}\text{Si}_x)_{13}$ phase.

3.2.1. Phase determination

The samples were annealed at 1373 K for 15 days. The phase information was obtained via XRD for the annealed samples. As can be seen from Figure IV-17, all samples contain a major phase crystallized in the cubic NaZn_{13} -type structure.

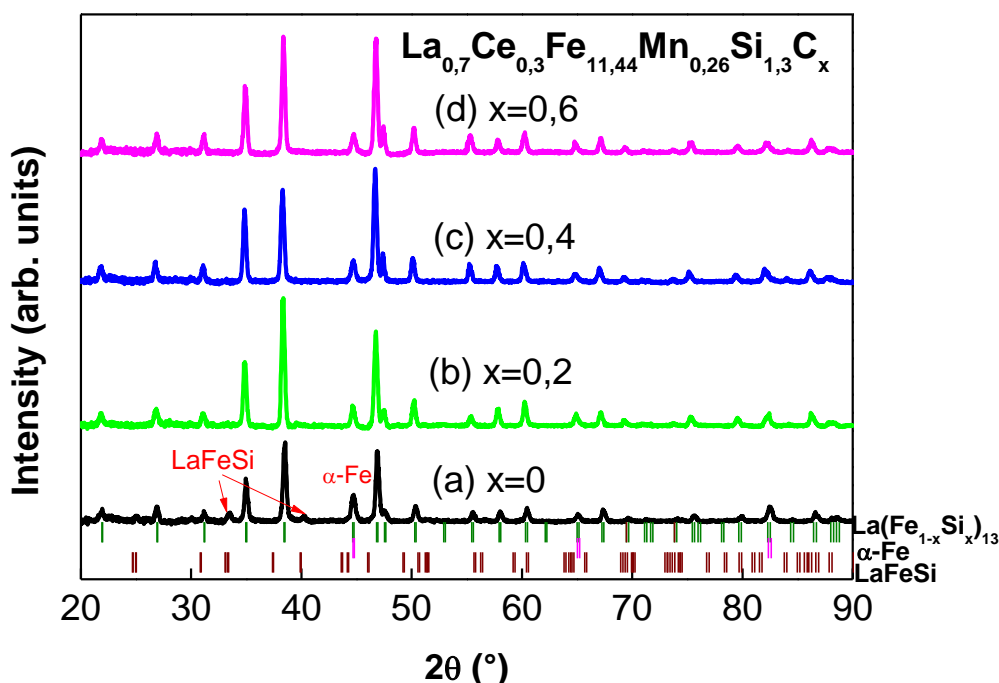


Figure IV-17. XRD patterns of annealed samples of composition $\text{La}_{0.7}\text{Ce}_{0.3}\text{Fe}_{11.44}\text{Mn}_{0.26}\text{Si}_{1.3}\text{C}_x$ for $x=0$ to 0.6.

Figure IV-18 (a) shows the phase fractions of annealed $\text{La}_{0.7}\text{Ce}_{0.3}\text{Fe}_{11.44}\text{Mn}_{0.26}\text{Si}_{1.3}\text{C}_x$ samples as determined by XRD and Rietveld refinement. The lattice constant of the 1:13

phase versus C concentration x is shown in Figure IV-18 (b). Liu *et al.* [28] reported the appearance of a small amount of α -Fe(Si) for $x > 0.5$ in $\text{La}(\text{Fe}_{0.88}\text{Al}_{0.12})_{13}\text{C}_x$ compounds. For the $\text{La}_{0.7}\text{Ce}_{0.3}\text{Fe}_{11.44}\text{Mn}_{0.26}\text{Si}_{1.3}\text{C}_x$ samples, there are about 10% of α -Fe(Si) for $x=0-0.6$. However, there does not seem to have a linear correlation between the C content and the amount of α -Fe(Si) impurity phase. Apart from visible impurities peaks of α -Fe and LaFeSi phases, no additional peaks of foreign phases have been observed in the XRD patterns. The lattice constant of the 1:13 phase increases accordingly with C concentration, which, as shown later, is correlated with an increase in T_C .

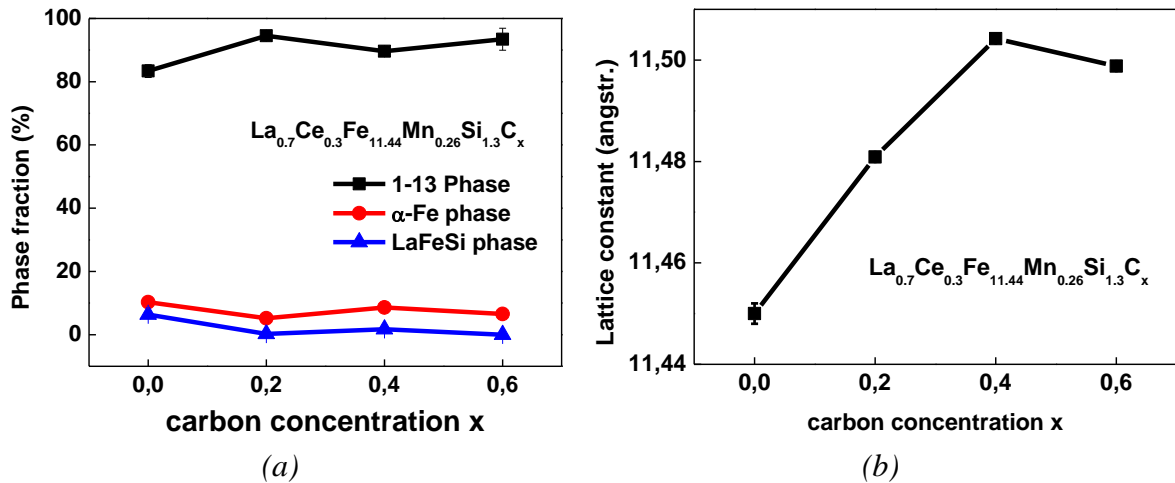


Figure IV-18. (a) Evolution of phases with increasing C concentration, (b) evolution of lattice constant of the 1:13 phase with increasing C concentration for samples of composition $\text{La}_{0.7}\text{Ce}_{0.3}\text{Fe}_{11.44}\text{Mn}_{0.26}\text{Si}_{1.3}\text{C}_x$.

Table IV-10 lists the lattice expansion induced by C insertion. Sample of nominal composition $\text{La}_{0.7}\text{Ce}_{0.3}\text{Fe}_{11.44}\text{Si}_{0.26}\text{Si}_{1.3}\text{C}_{0.6}$ is a peculiar case. The lattice expansion after 0.6 C/f.u. has caused a volume increase quite similar to the sample with only 0.4 C/f.u. before induction melting. The content of C in the as-cast samples has been verified by LECO combustion technique in the as-cast sample and the targeted composition is kept in the material. This suggests that the formation of $\text{La}(\text{Fe}_{1-x}\text{Si}_x)_{13}\text{C}_x$ becomes difficult for higher carbon content. Due to the high affinity of C with La and Fe, some of the C atoms may form La-C and Fe-C phases, limiting the complete dissolution of C into the NaZn_{13} structure.

Table IV-10. The lattice expansion induced by C insertion for samples of composition $\text{La}_{0.7}\text{Ce}_{0.3}\text{Fe}_{11.44}\text{Mn}_{0.26}\text{Si}_{1.3}\text{C}_x$.

Composition	$a=b=c$ (Å)	$\Delta a/a$ (%)	$V(\text{Å}^3)$	$\Delta V/V$ (%)	$\Delta V/C$ (Å^3)	y (C/f.u.)
$\text{La}_{0.7}\text{Ce}_{0.3}\text{Fe}_{11.44}\text{Mn}_{0.26}\text{Si}_{1.3}$	11,4450 (1)	-	1501,1 (2)	-	-	-
$\text{La}_{0.7}\text{Ce}_{0.3}\text{Fe}_{11.44}\text{Mn}_{0.26}\text{Si}_{1.3}\text{C}_{0.2}$	11,4812 (1)	0,32	1513,4 (1)	0,82	7.69	0,2
$\text{La}_{0.7}\text{Ce}_{0.3}\text{Fe}_{11.44}\text{Mn}_{0.26}\text{Si}_{1.3}\text{C}_{0.4}$	11,5043 (2)	0,52	1522,6 (1)	1,43	6.72	0,4
$\text{La}_{0.7}\text{Ce}_{0.3}\text{Fe}_{11.44}\text{Mn}_{0.26}\text{Si}_{1.3}\text{C}_{0.6}$	11,4988 (2)	0,47	1520,4 (1)	1,29	6.03	0,4

The effective electron concentration is an indirect indication that the interstitial atoms are diffused into the structure. It is calculated by the following equation:

$$\frac{e}{A} = \frac{e_1 \times x_1 + e_2 \times x_2 \cdots + e_n \times x_n}{x_1 + x_2 + \cdots x_n} \quad \text{VI-1}$$

where e_i ($i=1, 2, \dots, n$) is the i^{th} constituent element in the composition, x_i ($i=1, 2, \dots, n$) is the corresponding molar fraction of the element. It is evident from Figure IV-19 that $x=0-0.4$, there is a linear relationship between the lattice constant and the effective electron concentration. From the discussion above, it is more reasonable to take the carbon content in sample $\text{La}_{0.7}\text{Ce}_{0.3}\text{Fe}_{11.44}\text{Si}_{0.26}\text{Si}_{1.3}\text{C}_{0.6}$ as 0.4 C/f.u.

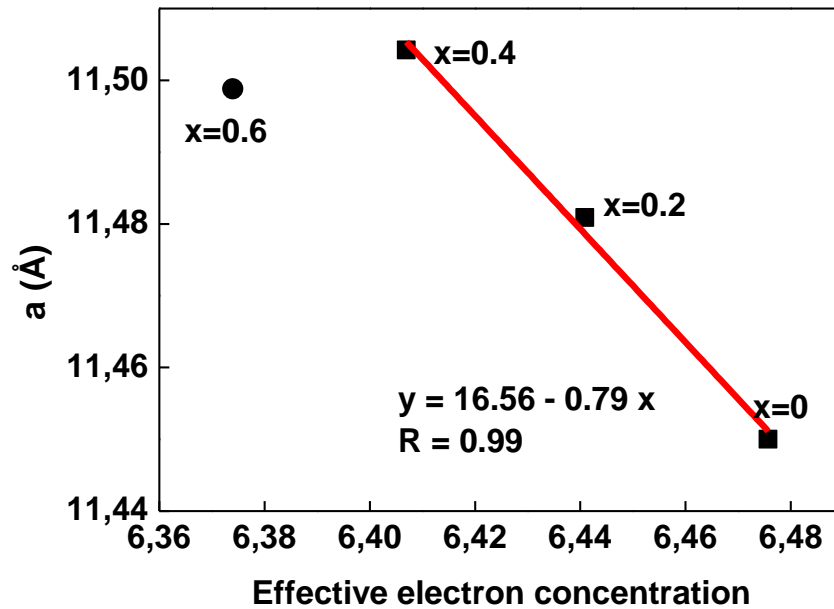


Figure IV-19. Effective electron concentration plotted against the lattice constant for samples of composition $\text{La}_{0.7}\text{Ce}_{0.3}\text{Fe}_{11.44}\text{Mn}_{0.26}\text{Si}_{1.3}\text{C}_x$.

Liu *et al.* [28] have reported similar observation in their investigation of $\text{La}(\text{Fe}_{0.88}\text{Al}_{0.12})_{13}\text{C}_x$ interstitial compounds. The dependence of lattice constant and Curie temperature increases almost linearly with carbon content for $x \leq 0.4$ but for $x=0.6$ and 0.8 , they are smaller than the extrapolated value. The authors have suggested that the carbon content is lower than the nominal one for $x=0.6$ and 0.8 . By assuming a linear correlation between the lattice constant and carbon content, they suggested that the actual carbon content in 1:13 compounds for $x=0.6$ and 0.8 should be about $x=0.53$ and 0.62 , respectively.

Contrary to carbides synthesized via solid-gas reaction between the intermetallic and anthracene, solid melting does not allow C insertion in the $\text{LaFe}_{13-x}\text{Si}_x$ phase above $x=0.6$. The high affinity of C to the α -Fe(Si) phase is in competition with C diffusion in the $\text{LaFe}_{13-x}\text{Si}_x$ phase. Indeed, in the literature, apart from the work of S. Fu *et al.* in 2013 [44] in synthesizing $\text{LaFe}_{11.5}\text{Si}_{1.5}\text{C}_1$, the majority of the authors have not reported carbides with C content above $x>0.6$ from solid melting technique.

3.2.2. Microstructure

Previously we have discussed the microstructure evolution for C-doped compound $\text{LaFe}_{11.7}\text{Si}_{1.3}\text{C}_{0.2}$. With increasing amount of C dopant, the microstructure of annealed samples shows large areas of La-rich phase and the homogeneity is reduced, as shown in

Figure IV-20. The difficulty to insert C above $x_C=0.6$ can also be attributed to the inhomogeneous distribution of elements.

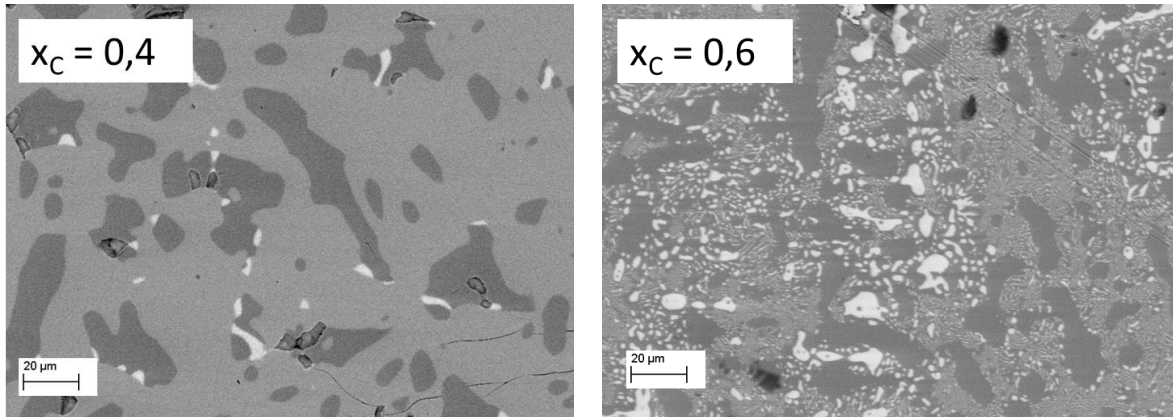


Figure IV-20. Evolution of microstructure for high level of C doping for annealed samples of composition $La_{0.7}Ce_{0.3}Fe_{11.44}Mn_{0.26}Si_{1.3}C_x$.

This result is in good agreement with the phase evolution of $LaFe_{11.6}Si_{1.4}C_x$ with C content ($x_C=0; 0.1; 0.2; 0.3; 0.4$), reported by Teixeira *et al.* [41] in 2012. At modest concentration of C doping, C is well incorporated in the 1:13 lattice. In our case of 1:13 phase with Ce and Mn substitutions, it seems rather difficult to include C interstitials in the lattice above $x_C=0.4$.

3.2.3. Magnetic properties

The temperature dependence of the magnetization for $La_{0.7}Ce_{0.3}Fe_{11.44}Mn_{0.26}Si_{1.3}C_x$ ($x=0; 0.2; 0.4; 0.6$) is shown in Figure IV-21 (a). The ΔS_M curves appearing in Figure IV-21 (b) for a field change of 2 T show that x should not exceed 0.2, as this results in a significant drop in magnetic entropy change near T_C . The magnetic properties of the 1-13 phase are strongly dependent on the concentration of C. For samples with Ce and Mn substitution, modest C insertion can be used to raise T_C and not degrade the MCE, as seen in Figure IV-21 (b).

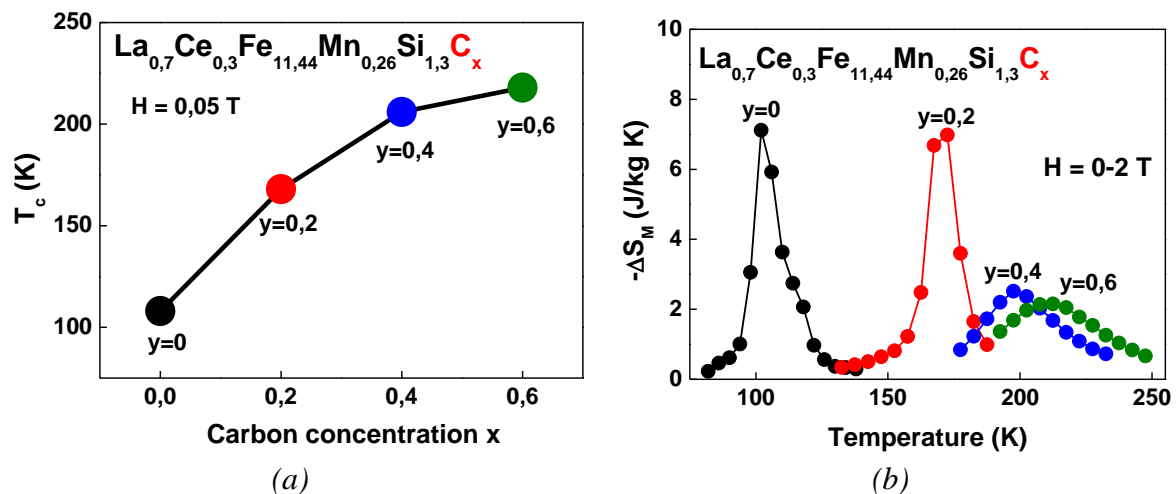


Figure IV-21. (a) The temperature dependence of the magnetization for samples of composition $La_{0.7}Ce_{0.3}Fe_{11.44}Mn_{0.26}Si_{1.3}C_x$ ($x=0; 0.2; 0.4; 0.6$) (b) the isothermal magnetic entropy change estimation for different C concentration.

Figure IV-22 compares T_C for annealed and hydrogenated samples. At small concentration of C, there is an additive rule that limits the interstitial accommodation capacity, as illustrated in Figure IV-22, samples $x=0$ and $x=0.2$ lead to very similar final ordering temperature after full hydrogenation. At higher content of C ($x=0.4$ and $x=0.6$), however, the lattice has already been expanded by the C atoms that there seems not to have any space for H interstitials left. Under the same hydrogenation conditions, the lattice has reached its limits in terms of interstitial absorption.

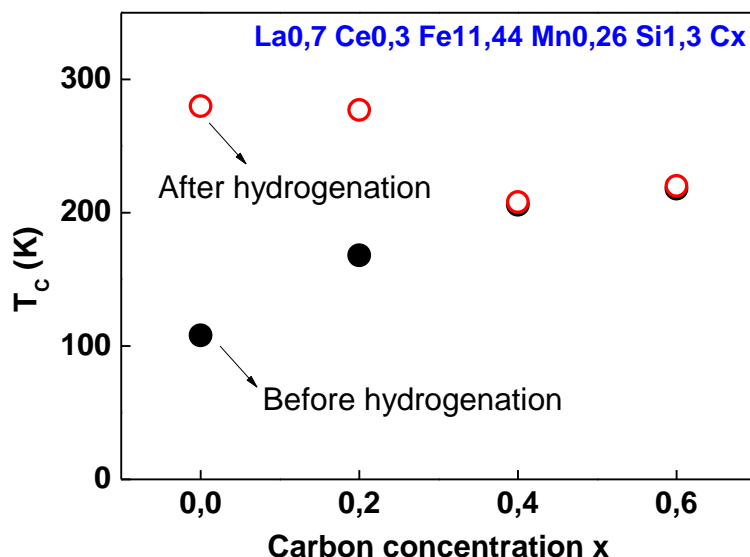


Figure IV-22. Curie temperature before and after hydrogenation process for samples of composition $La_{0.7}Ce_{0.3}Fe_{11.44}Mn_{0.26}Si_{1.3}C_x$ ($x=0; 0.2; 0.4; 0.6$). The solid dots represent annealed samples and the empty dots show those after full hydrogenation

As a figure of reference, C insertion leads to an increase in the measured saturation magnetization in R_2Fe_{17} compounds [45, 2]. The itinerant electron model can predict the magnetization increase following the volume variation [46]. The magnetization variation becomes evident at high C content. For example, the saturation magnetization at 4 K for $Ho_2Fe_{17}C_x$ ($x=0.7, 1.2, \text{ and } 1.4$) is 17, 17.4, and 17.4 μ_B , respectively [2]. In the $La(Fe_{1-x}Si_x)_{13}C_x$ samples measured in this work, we did not observe significant change in the saturation magnetization measured from 0 to 7 T at 4 K, which may be associated with the small quantity of C content.

3.3. Effect of carbon interstitials in La-Fe-Si and La-Ce-Fe-Si

Once the C insertion method is validated and the C concentration is optimized, the effect of C interstitials is systematically studied in $La(Fe,Si)_{13}C_x$, $(La,Ce)(Fe,Si)_{13}C_x$, and $(La,Ce)(Fe,Mn,Si)_{13}C_x$ phases.

3.3.1. Neutron diffraction at 300 K

In order to localize C in the crystalline lattice, sample of nominal composition $\text{LaFe}_{11.7}\text{Si}_{1.3}\text{C}_{0.2}$ was studied with neutron powder diffraction after annealing and the refined diffractogram is shown in Figure IV-23. After long-term annealing, the indexed peaks correspond to the NaZn_{13} -type structure of the $\text{LaFe}_{13-x}\text{Si}_x$ phase and the solid solution of Fe and Si in the $\alpha\text{-Fe}(\text{Si})$ phase.

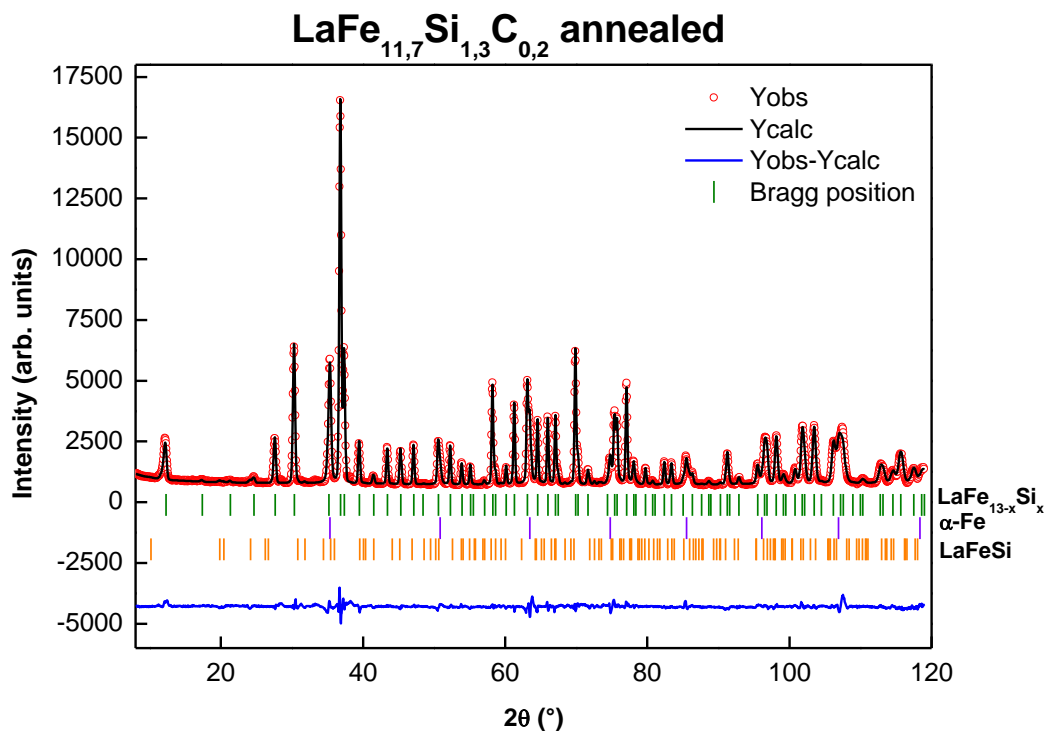


Figure IV-23. Neutron powder diffraction pattern with Rietveld refinement for sample $\text{LaFe}_{11.7}\text{Si}_{1.3}\text{C}_{0.2}$ at 300 K at the 3T2 diffractometer.

A covalent C atom occupies a volume of about 2 \AA^3 and for a neutral C atom, it is about 3.2 \AA^3 . Both the $24d$ and $48f$ sites have sufficient volume to accommodate C atoms. In order to have reasonable La-Ce and Fe-C interatomic distances, C atoms should occupy the $24d$ octahedral site. This way, the La-C and Fe-C interatomic distances are similar to that of the La-C and Fe-C bond lengths in LaC_2 and Fe_3C compounds, respectively [47].

If C atoms occupy the $48f$ site, it is not possible for C atoms to occupy the two closest equivalent voids, since the distance between the latter is of similar length to the radius of the carbon atom [28]. The Fe-C distance for C atoms at $48f$ is longer than at the $24d$ site. Carbon atoms have a more stable environment at the $24d$ site compared to the $48f$ site. Therefore, for the Rietveld refinement, C atoms are located in the $24d$ site.

The refined C concentration ($\approx 0.15 \text{ C/f.u.}$) is consistent with the initially targeted value (0.2 C/f.u.). A small concentration of C can be expected in the $\alpha\text{-Fe}(\text{Si})$ phase. This modest doping of C extends the unit cell parameter by 0.3%, which corresponds to a volume increase of 1%. The volume inflation is about 60 \AA^3 per C atom.

Table IV-11 compared the refined structural parameters between the C-free and carbonated samples. The lattice expansion caused by C insertion is highly anisotropic in terms of Fe-

Fe distances. The intra-icosahedral bonds (B1, B2, B3) are contracted while the inter-icosahedral ones (B4, B5) are elongated. Occupying the same interstitial site, the effect of C is quite similar to that of H or D. The most affected distance is the shortest Fe-Fe distance, B4, which directly associates with the interstitial site 24d. The capacity of influence of C is more significant than H due to the large atomic radius.

Table IV-11. Refined structural parameters from neutron diffraction for $\text{LaFe}_{11.7}\text{Si}_{1.3}$ and $\text{LaFe}_{11.7}\text{Si}_{1.3}\text{C}_{0.2}$ obtained at 300 K at 3T2 diffractometer.

Sample	$\text{LaFe}_{11.7}\text{Si}_{1.3}$	$\text{LaFe}_{11.7}\text{Si}_{1.3}\text{C}_{0.2}$
T_C (K)	190	228
$a=b=c$ (Å)	11,4772 (2)	11,5058 (1)
site 96i (0, y, z) y	0,1798 (1)	0,1788 (1)
site 96i (0, y, z) z	0,1169 (1)	0,1162 (1)
Occupancy 24d	-	0,048 (1)
Temperature factor B_{24d} (Å ²)	-	0,624 (1)
B1 (Fe ^{8b} -Fe ⁹⁶ⁱ) (Å)	2,461 (1)	2,454 (1)
B2 (Å)	2,684 (1)	2,674 (1)
B3 (Å)	2,565 (1)	2,557 (1)
B4 (Å)	2,443 (1)	2,466 (1)
B5 (Å)	2,490 (1)	2,502 (1)
Fe ⁹⁶ⁱ -C (Å)	-	1,744 (1)
χ^2	7,7	9,8
R_{Bragg} (%)	8,2	4,5
R_t (%)	5,0	3,2

The influences of Ce partial substitution on the $\text{La}(\text{Fe}_{1-x}\text{Si}_x)_{13}$ structure has been discussed in Chapter III. Carbon atoms were introduced in Ce-substituted samples to study the effect of C on the strained lattice. The refined parameters from steady-state neutron diffraction are shown in Table IV-12.

Table IV-12. Results of the structural characterization from neutron diffraction for $\text{La}_{0.7}\text{Ce}_{0.3}\text{Fe}_{11.7}\text{Si}_{1.3}$ and $\text{La}_{0.7}\text{Ce}_{0.3}\text{Fe}_{11.7}\text{Si}_{1.3}\text{C}_{0.2}$ obtained at 300 K at 3T2 diffractometer.

Sample	$\text{La}_{0.7}\text{Ce}_{0.3}\text{Fe}_{11.7}\text{Si}_{1.3}$	$\text{La}_{0.7}\text{Ce}_{0.3}\text{Fe}_{11.7}\text{Si}_{1.3}\text{C}_{0.2}$
T_C (K)	170	194
$a=b=c$ (Å)	11,4605 (1)	11,4773 (1)
site 96i (0, y, z) y	0,1791 (1)	0,1792 (1)
site 96i (0, y, z) z	0,1166 (1)	0,1165 (1)
Occupancy 24d	-	0,04 (1)
Temperature factor B_{24d} (Å ²)	-	1,14 (1)
B1 (Fe ^{8b} -Fe ⁹⁶ⁱ) (Å)	2,450 (1)	2,453 (1)
B2 (Å)	2,674 (1)	2,674 (1)
B3 (Å)	2,552 (1)	2,557 (1)
B4 (Å)	2,448 (1)	2,453 (1)
B5 (Å)	2,493 (1)	2,494 (1)
Fe ⁹⁶ⁱ -C (Å)	-	1,734 (1)
χ^2	17,7	4,7
R_{Bragg} (%)	4,3	3,5
R_t (%)	2,3	1,9

Carbon insertion inflates the La-Ce-Fe-Si lattice volume by 0.1%, much smaller than in the non-substituted La-Fe-Si case. The volume inflation per C atom is also reduced to 4 Å³. B4 remains as the most affected Fe-Fe distance after C tuning for sample $\text{La}_{0.7}\text{Ce}_{0.3}\text{Fe}_{11.7}\text{Si}_{1.3}$.

From the above neutron diffraction data, it can be concluded that lattice breathing with C interstitial is similar to that after H insertion: reduction of intra-icosahedral distances and expansion of inter-icosahedral distances.

3.3.2. Magnetic properties

Carbon interstitial absorption produces two effects: lattice expansion, which results a visible augmentation of the Curie temperature, and hybridization between the electronic orbitals of interstitial and magnetic atoms. The isotropic volume expansion results in a decrease in overlap of the Fe-3d wavefunctions, therefore, a 3d band narrowing, which leads to an increase of T_C and the saturated magnetic moment μ_S .

The effect of C on the magnetic transitions of the $\text{LaFe}_{13-x}\text{Si}_x$ phase is illustrated in Figure IV-24. For the annealed samples, C effectively increases T_C and reduces hysteresis, indicating a softening of the first-order transition nature. For sample $\text{LaFe}_{11.7}\text{Si}_{1.3}$, T_C is shifted up 20 K with 0.2 C/f.u. and the thermal hysteresis (6 K) has been completely eliminated. With Ce partial substitution, C decreases the thermal hysteresis of sample $\text{La}_{0.7}\text{Ce}_{0.3}\text{Fe}_{11.7}\text{Si}_{1.3}$ to almost half of that of the C-free sample.

By comparing Figure IV-24 (a) and (b), the magnetic transition of sample $\text{La}_{0.7}\text{Ce}_{0.3}\text{Fe}_{11.7}\text{Si}_{1.3}$ seems not as sharp as that of sample $\text{LaFe}_{11.7}\text{Si}_{1.3}$, even though the effect of Ce on the thermomagnetic curve is demonstrated by the T_C shift and the increase of thermal hysteresis. Generally, Ce partial substitution leads to a reinforcement of the first-order characteristic of the magnetic transition. The small difference shown here can be explained by the slight deviation in impurity phase concentration and Fe/Si ratio between samples.

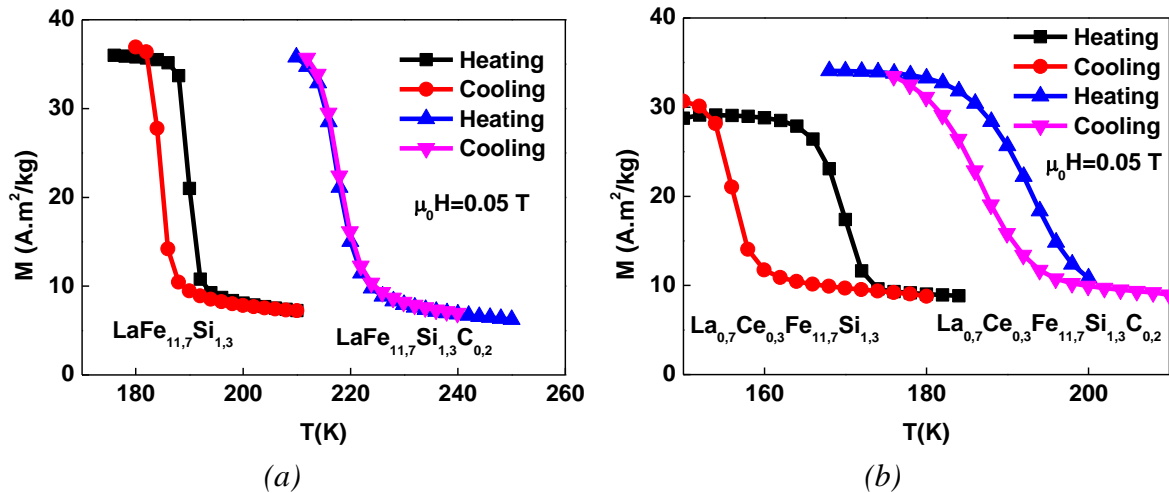


Figure IV-24. Effect of C on the magnetic transition on (a) $\text{LaFe}_{11.7}\text{Si}_{1.3}\text{C}_x$ ($x=0$ and 0.2) and (b) $\text{La}_{0.7}\text{Ce}_{0.3}\text{Fe}_{11.7}\text{Si}_{1.3}\text{C}_x$ ($x=0$ and 0.2) samples.

The priority of this series of samples is to verify the effect of C interstitial in $\text{La}(\text{Fe},\text{Si})_{13}\text{C}_x$, $(\text{La},\text{Ce})(\text{Fe},\text{Si})_{13}\text{C}_x$, and $(\text{La},\text{Ce})(\text{Fe},\text{Mn},\text{Si})_{13}\text{C}_x$ ($x=0$ and 0.2) phases. The impacts of various internal and external parameters are reduced to the minimum between samples with and without C interstitials. Specifically, the Fe/Si ratio is kept the same by first elaborating a parent sample and dividing this parent sample to form two identical samples, one of which is then remelted with graphite to insert C content.

Therefore, it is possible to have small deviations of impurity phase concentration and Si content between samples not elaborated from the same parent sample, such as the case for sample $\text{LaFe}_{11.7}\text{Si}_{1.3}$ and $\text{La}_{0.7}\text{Ce}_{0.3}\text{Fe}_{11.7}\text{Si}_{1.3}$. However, this does not change the conclusions in this section regarding the effect of C interstitials.

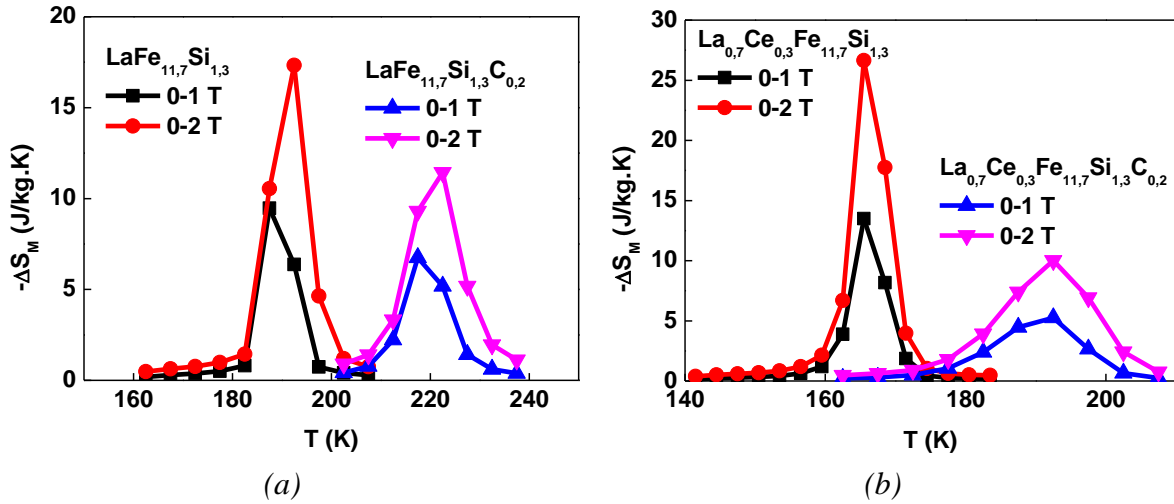


Figure IV-25. Effect of C on the isothermal entropy change on (a) $\text{LaFe}_{11.7}\text{Si}_{1.3}\text{C}_x$ ($x=0$ and 0.2) samples (b) $\text{La}_{0.7}\text{Ce}_{0.3}\text{Fe}_{11.7}\text{Si}_{1.3}\text{C}_x$ ($x=0$ and 0.2) samples for a field change of 0-1 and 0-2 T.

Figure IV-25 shows ΔS_M for a field change of 0-1 and 0-2 T for $\text{LaFe}_{11.7}\text{Si}_{1.3}\text{C}_x$ ($x=0$ and 0.2) and $\text{La}_{0.7}\text{Ce}_{0.3}\text{Fe}_{11.7}\text{Si}_{1.3}\text{C}_x$ ($x=0$ and 0.2). A reduction of the peak value of ΔS_M can be seen, confirming that the insertion of C results in diminished metamagnetic characteristics for the itinerant electrons around T_C . The modest change of ΔS_M is an acceptable compromise with the prospect of improved stability for hydrogenated samples.

3.3.3. Hydrogenation behavior

The interstitial elements have different effects on the physical property of the host phase according to their nature. In order to investigate the combined effects of C and H, the carbonated samples are hydrogenated to synthesize mixed compounds containing two interstitial elements.

3.3.3.1. Structural properties

With the appropriate elaboration sequence, carbonated samples can successfully take up further H interstitials. All four samples maintains the NaZn_{13} -type cubic structure after C and H absorption, as shown in the XRD patterns in Figure IV-26.

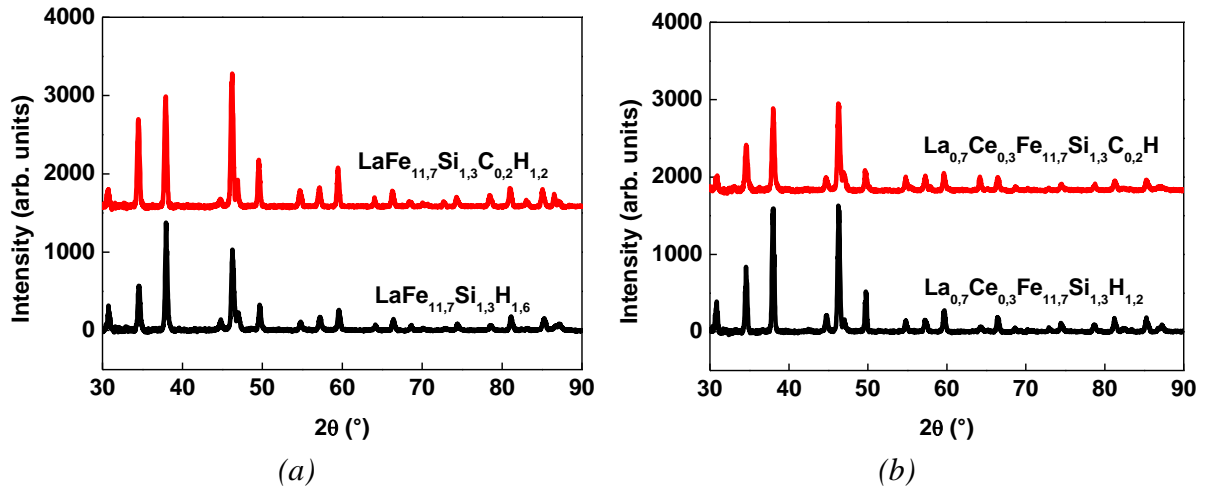


Figure IV-26. XRD patterns of fully hydrogenated (a) $\text{LaFe}_{11.7}\text{Si}_{1.3}\text{C}_x$ ($x=0$ and 0.2) samples; (b) $\text{La}_{0.7}\text{Ce}_{0.3}\text{Fe}_{11.7}\text{Si}_{1.3}\text{C}_x$ ($x=0$ and 0.2) samples.

The lattice parameters and interatomic distances were refined from neutron diffraction data. Two impurity phases ($\alpha\text{-Fe}(\text{Si})$ and LaFeSi) were added in the refinement. The results for $\text{LaFe}_{11.7}\text{Si}_{1.3}\text{C}_x$ ($x=0$ and 0.2) samples are shown in Table IV-13.

Table IV-13. Results of the structural characterization of annealed and hydrogenated $\text{LaFe}_{11.7}\text{Si}_{1.3}\text{C}_x$ ($x=0$ and 0.2) samples from neutron diffraction obtained at 300 K at 3T2 diffractometer.

Sample	$\text{LaFe}_{11.7}\text{Si}_{1.3}$	$\text{LaFe}_{11.7}\text{Si}_{1.3}\text{H}_{1.6}$	$\text{LaFe}_{11.7}\text{Si}_{1.3}\text{C}_{0.2}$	$\text{LaFe}_{11.7}\text{Si}_{1.3}\text{C}_{0.2}\text{H}_{1.2}$
T_c (K)	190	342	228	346
$a=b=c$ (Å)	11,4772 (2)	11,6220 (1)	11,5058 (1)	11.6345 (1)
site $96i$ (0, y, z) y	0,1798 (1)	0,1785 (1)	0,1788 (1)	0,1782 (1)
site $96i$ (0, y, z) z	0,1169 (1)	0,1147 (1)	0,1162 (1)	0,1143 (1)
Occupancy $24d$	-	0,472 (1)	0,048 (1)	0,048 (1) + 0,408 (1)
Temperature factor B_{24d} (Å ²)	-	1.68 (1)	0.62 (1)	1.94 (1)
$B1$ ($\text{Fe}^{8b}\text{-Fe}^{96i}$) (Å)	2,461 (1)	2,466 (1)	2,454 (1)	2,463 (1)
$B2$ (Å)	2,684 (1)	2,667 (1)	2,674 (1)	2,659 (1)
$B3$ (Å)	2,565 (1)	2,575 (1)	2,557 (1)	2,573 (1)
Weighted average ($2B1+B2+4B3$)/7 (Å)	2.552	2.557	2.544	2.554
$B4$ (Å)	2,443 (1)	2,515 (1)	2,466 (1)	2,526 (1)
$B5$ (Å)	2,490 (1)	2,514 (1)	2,502 (1)	2,515 (1)
$\text{Fe}^{96i}\text{-H}$ (Å)	-	1.779 (1)	1.744 (1)	1.786 (1)
χ^2	7.7	20.4	9.8	24.8
R_{Bragg} (%)	8,2	6,5	4,5	4,7
R_f (%)	5,0	3,9	3,3	3,0

Carbon addition does not change the general mechanism of hydrogenation. Hydrogenation in $\text{LaFe}_{11.7}\text{Si}_{1.3}\text{C}_{0.2}$ results in a supplementary increase in $B4$ and a reduction of $B2$. $B4$ is shorter than $B5$ before hydrogenation and it is extended and larger than $B5$ after H interstitial insertion.

The double-interstitial inserted $\text{LaFe}_{11.7}\text{Si}_{1.3}\text{C}_{0.2}\text{H}_{1.2}$ has a superior lattice constant compared with the hydrogenated $\text{LaFe}_{11.7}\text{Si}_{1.3}\text{H}_{1.6}$. Similar phenomenon has been observed in the R_2Fe_{17} compounds containing C and H interstitials. It is the H-H interactions that limit the quantity of H interstitials in the lattice. Carbon provokes a lattice expansion, in

the case of a few R_2Fe_{17} compounds, a structural transition from hexagonal to rhombohedral lattice. The presence of C opens up the distances between H atoms and stabilize a secondary tetrahedral site for H atoms in $Ho_2Fe_{17}C_xH_{5-x}$ [2].

The neutron diffraction data is also exploited in our case to examine secondary tetrahedral site in presence of C interstitials. The refined parameters can be found in Appendix D. Compared with the results in Table IV-2 in Section 2.1.1 on H location, the presence of C atom does extend the lattice and leads to increased H-H distances. However, the negative site occupancy and increased thermal parameter lead to the conclusion that in the La-Fe-Si lattice, 0.2 C/f.u. is not sufficient to stabilize the tetrahedral site for H interstitials.

For Ce-substituted samples, three impurity phases were added in the refinement for Ce-substituted samples: α -Fe(Si), LaFeSi, and Ce_2Fe_{17} . The refined parameters for $La_{0.7}Ce_{0.3}Fe_{11.7}Si_{1.3}C_x$ ($x=0$ and 0.2) samples are shown in Table IV-14. Hydrogenation for $La_{0.7}Ce_{0.3}Fe_{11.7}Si_{1.3}$ results in an increase of the weighted average intra-icosahedral. On the contrary, H absorption in $La_{0.7}Ce_{0.3}Fe_{11.7}Si_{1.3}C_{0.2}$ leads to a reduced weighted average of the intra-icosahedral distances. B4 is the most affected distance for both cases, the extent of the increase is more significant in $La_{0.7}Ce_{0.3}Fe_{11.7}Si_{1.3}C_{0.2}$ (4 %) than in $La_{0.7}Ce_{0.3}Fe_{11.7}Si_{1.3}$ (3 %). The maximum capacity of hydrogenation is reduced in the carbonated sample. The effect of C on the hydrogenation dynamics is further studied in details in the next Chapter.

Table IV-14. Refined structural parameters of annealed and hydrogenated of $La_{0.7}Ce_{0.3}Fe_{11.7}Si_{1.3}C_x$ ($x=0$ and 0.2) samples from neutron diffraction obtained at 300 K at 3T2 diffractometer.

Sample	$La_{0.7}Ce_{0.3}Fe_{11.7}Si_{1.3}$	$La_{0.7}Ce_{0.3}Fe_{11.7}Si_{1.3}H_{1.6}$	$La_{0.7}Ce_{0.3}Fe_{11.7}Si_{1.3}C_{0.2}$	$La_{0.7}Ce_{0.3}Fe_{11.7}Si_{1.3}C_{0.2}H_{1.6}$
T_C (K)	170	328	194	330
$a=b=c$ (Å)	11,4605 (1)	11,6091 (1)	11,4773 (1)	11,6112 (1)
site $96i$ (0, y, z) y	0,1791 (1)	0,1780 (1)	0,1792 (1)	0,1765 (1)
site $96i$ (0, y, z) z	0,1166 (1)	0,1144 (1)	0,1165 (1)	0,1137 (1)
Occupancy $24d$	-	0.57 (1)	0,04 (1)	0,04 (1) + 0,54 (1)
Temperature factor B_{24d} (Å ²)	-	1.61 (1)	1.14 (1)	0.94 (1)
B1 (Fe^{96i} - Fe^{96i}) (Å)	2,450 (1)	2,456 (1)	2,453 (1)	2,438 (1)
B2 (Å)	2,674 (1)	2,656 (1)	2,674 (1)	2,640 (1)
B3 (Å)	2,552 (1)	2,564 (1)	2,557 (1)	2,545 (1)
Weighted average $(2B1+B2+4B3)/7$ (Å)	2.540	2.546	2.544	2.528
B4 (Å)	2,448 (1)	2,521 (1)	2,453 (1)	2,543 (1)
B5 (Å)	2,493 (1)	2,515 (1)	2,494 (1)	2,529 (1)
Fe^{96i} -H (Å)	-	1,783 (1)	1,734 (1)	1,798 (1)
χ^2	17.7	35.5	4.68	54.9
R_{Bragg} (%)	4,3	4,3	3,5	5,8
R_t (%)	2,3	3,0	1,9	3,0

Overall, the variations of the interatomic distances are consistent with the fact that the atomic radius of C is almost twice as large as that of H. Moreover, they are additional indications of the double interstitial occupancy of the $24d$ site by H and C atoms [28, 34]. The (Fe/Si)₁₃ icosahedra undergo a noticeable reshaping upon interstitial accommodation or substitution at the rare earth site. It is interesting to note that different light elements do

no contribute to the breathing of the polyanionic network in the same manner. In this respect, some counterintuitive results are worthy to be noticed. While H insertion in $\text{LaFe}_{11.7}\text{Si}_{1.3}$ and $\text{La}_{0.7}\text{Ce}_{0.3}\text{Fe}_{11.7}\text{Si}_{1.3}$ leads to slight but significant increase of the intracenter Fe-Fe distances (weighted average calculated), C insertion leads to a decrease in $\text{LaFe}_{11.7}\text{Si}_{1.3}$ and a slight increase in $\text{La}_{0.7}\text{Ce}_{0.3}\text{Fe}_{11.7}\text{Si}_{1.3}$.

3.3.3.2. Magnetic properties

In the H-saturated samples (Figure IV-27), T_C is brought up to the same level with either H-only insertion or C+H double interstitial insertion. Samples with double interstitial insertion show a slightly higher T_C . After hydrogenation, we do not observe any detrimental effect on the performance by a modest amount of C insertion. The final isothermal entropy change of samples with both C and H interstitial insertion is quite comparable to the conventional hydrogenated samples.

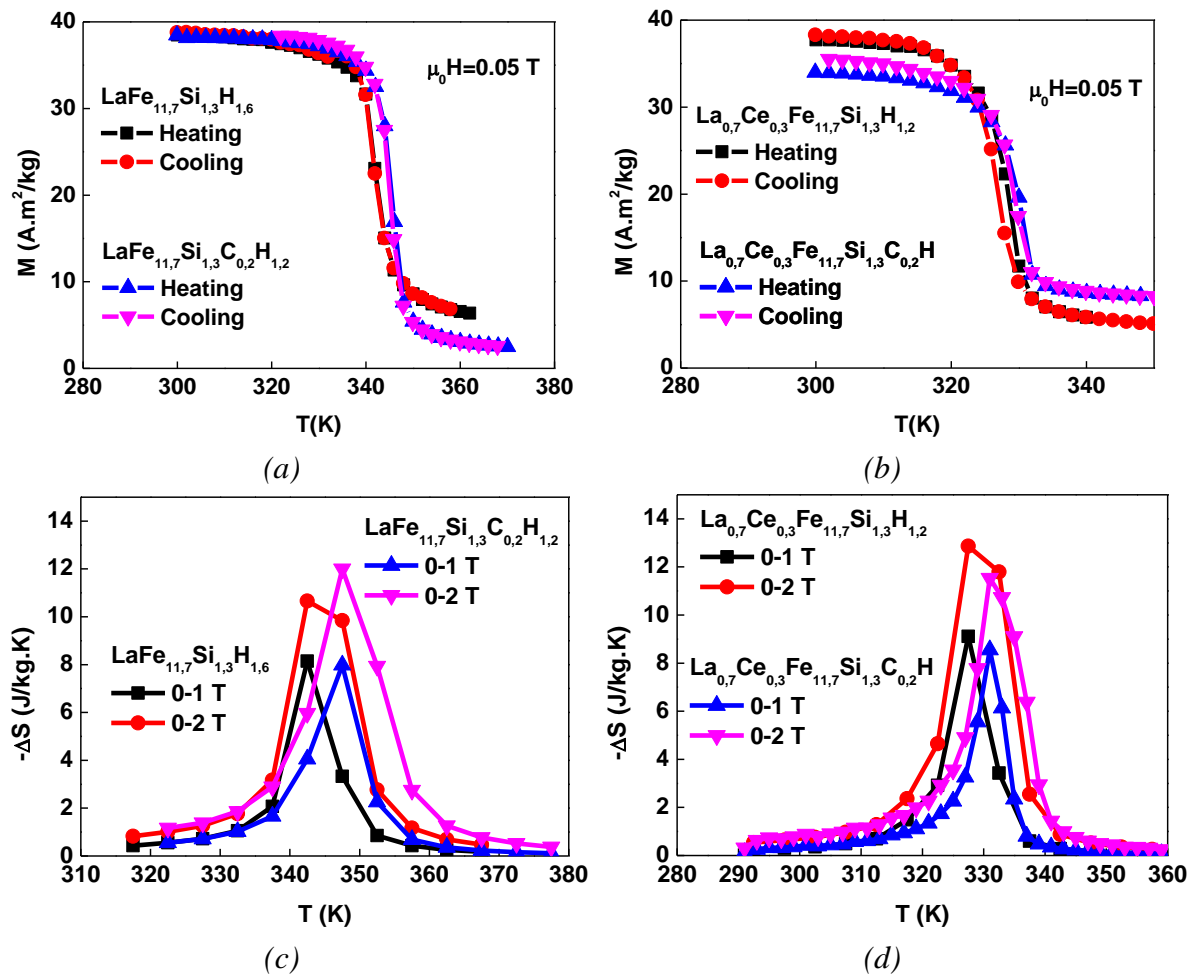


Figure IV-27. Thermal magnetization curves for fully hydrogenated (a) $\text{LaFe}_{11.7}\text{Si}_{1.3}\text{C}_x$ ($x=0$ and 0.2) (b) $\text{La}_{0.7}\text{Ce}_{0.3}\text{Fe}_{11.7}\text{Si}_{1.3}\text{C}_x$ ($x=0$ and 0.2) samples and isothermal magnetic entropy change for fully hydrogenated (c) $\text{LaFe}_{11.7}\text{Si}_{1.3}\text{C}_x$ ($x=0$ and 0.2) and (d) $\text{La}_{0.7}\text{Ce}_{0.3}\text{Fe}_{11.7}\text{Si}_{1.3}\text{C}_x$ ($x=0$ and 0.2) samples.

For compositions viable of commercial application, the ordering temperature is tuned by Ce and Mn substitutions. Cerium and Manganese substitution decrease T_C by modifying the Fe-Fe distances. Carbon insertion applied in samples containing both Ce and Mn substitutions is an effective method to increase T_C . The variation of T_C and the thermal

hysteresis after 0.2 C/f.u. is the most remarkable for sample $\text{La}_{0.7}\text{Ce}_{0.3}\text{Fe}_{11.44}\text{Mn}_{0.26}\text{Si}_{1.3}$, as shown in Figure IV-28. The green bar represents the compound with H interstitials, and the blue bar represents those having double interstitial occupancy.

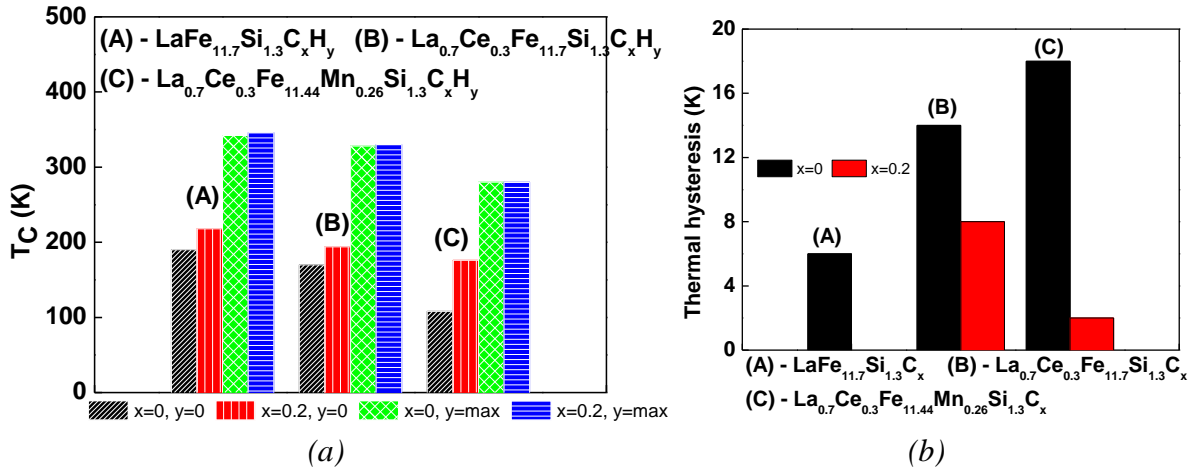


Figure IV-28. (a) Effect of C and H on (a) T_C and (b) the thermal hysteresis under a field of 0.05 T for $\text{LaFe}_{11.7}\text{Si}_{1.3}\text{C}_x\text{H}_y$ ($x=0$ and 0.2, $y=0$ and max), $\text{La}_{0.7}\text{Ce}_{0.3}\text{Fe}_{11.7}\text{Si}_{1.3}\text{C}_x\text{H}_y$ ($x=0$ and 0.2, $y=0$ and max), and $\text{La}_{0.7}\text{Ce}_{0.3}\text{Fe}_{11.44}\text{Mn}_{0.26}\text{Si}_{1.3}\text{C}_x\text{H}_y$ ($x=0$ and 0.2, $y=0$ and max) samples.

4. Conclusion

In this Chapter, we have examined the effects of H and C interstitial insertion on the structural and magnetic properties of the 1:13 phase. Small interstitial elements can enter in the voids in the 1:13 lattice and expand the unit cell. The changes in the Fe-Fe distances, consequently, lead to an increase in T_C . Carbon can be employed like hydrogen atoms to raise the working temperature close to room temperature. We have optimized the C insertion method to control the C content and to facilitate further H insertion. A modest amount of C interstitials can increase the Curie temperature without compromising the magnetocaloric performance. With increasing C content, the transition shows more second-order characteristics and ΔS_M decreases consequently.

The neutron powder diffraction patterns of various samples with nominal compositions in Table IV-13 and Table IV-14 have been recorded at room temperature. The aim was to locate the light interstitial species (H or C), and measure the structural modifications of the host lattice induced by interstitial insertion and/or rare earth substitution at the cation site of the NaZn_{13} structure. The structural investigation has allowed specifying the deformations undergone by the complex La-Fe-Si metallic alloys when subjected to light interstitial insertion. The Fe-Fe interatomic distance analysis suggests that H and C do not contribute to the structural breathing in the same manner. Now the important question is whether these modifications can lead to improved H stability in the lattice. Chapter V will be dedicated to investigate and evaluate the effect of composition modulation on the thermodynamic properties of H sorption.

References

- [1] G. Hägg, *Phys. Chem. B*, vol. 6, p. 221, 1930.
- [2] O. Isnard, Ph.D. thesis manuscript, "*Rôle des éléments interstitiels sur les alliages pour aimants permanents à base d'éléments de terre rare et de fer*", Grenoble: l'Université Joseph Fourier - Grenoble 1, 1993. French.
- [3] Z. Wang, L. He, F. Cuevas, M. Latroche, J. Shen et F. Wang, *Chinese Phys. B*, vol. 20, p. 067502, 2011.
- [4] Y. Chen, F. Wang, B. Shen, F. Hu, J. Sun, G. Wang et Z. Cheng, *J. Phys.: Condens. Matter*, vol. 15, p. L161, 2003.
- [5] X. Chen, Y. Chen et Y. Tang, *J. Alloy Compd.*, vol. 509, p. 2864, 2011.
- [6] M. Rosca, Ph.D. thesis manuscript "*Matériaux de type LaFe₁₃-xSix à fort pouvoir magnéto-calorique - Synthèse et optimisation de composés massifs et hypereutectiques – Caractérisations fondamentales*", Grenoble: l'Université Joseph Fourier, 2012. French. <tel-00663184>
- [7] M. Balli, M. Rosca, D. Fruchart et D. Gignoux, *J Magn. Magn. Mater.*, vol. 321, p. 123, 2009.
- [8] G. Rao, *J. Magn. Magn. Mater.*, vol. 139, p. 204, 1995.
- [9] G. Rao, J. Liang, Y. Zhang, W. Tang et X. Cheng, *J. Appl. Phys.*, vol. 80, p. 1, 1996.
- [10] A. Williams, V. Moruzzi, A. Malozemoff et K. Tarakura, *IEEE Trans. Magn.*, vol. 19, p. 1983, 1983.
- [11] A. Malozemoff, A. Williams et V. Moruzzi, *Phys. Rev. B*, vol. 29, p. 1620, 1984.
- [12] A. Switendick, chez *Hydrogen in metals I*, G. Alefeld, Éd., Berlin, Springer, 1978.
- [13] K. Gschneider Jr., V. Pecharsky et A. Tsokol, *Rep. Prog. Phys.*, vol. 68, p. 1479, 2005.
- [14] A. Barcza, M. Katter, V. Zellmann, S. Russek, S. Jacobs et C. Zimm, *IEEE Trans. on Mag.*, vol. 47, p. 3391, 2011.
- [15] C. Mayer, A. Dubrez, M. Pierronnet et P. Vikner, *Phys. Status Solidi C*, vol. 11, p. 5, 2014.
- [16] K. Mandal, O. Gutfleisch, A. Yan, A. Handstein et K. Müller, *J Magn. Magn. Mater.*, vol. 290, p. 673, 2004.
- [17] K. Mandal, D. Pal, O. Gutfleisch, P. Kersch et K. Müller, *J. Appl. Phys.*, vol. 102, p. 053906, 2007.
- [18] J. Lyubina, U. Hannemann, M. Ryan et L. Cohen, *Adv. Mater.*, vol. 24, p. 2042, 2012.
- [19] H. Nyman et S. Andersson, *Acta Cryst.*, vol. A35, p. 937, 1979.
- [20] K. Buschow, *J. Appl. Phys.*, vol. 63, p. 3130, 1988.

- [21] K. Ohashi, Y. Tawara, R. Osugi, J. Sakurai et Y. Komura, *J. Less-Common Met.*, vol. 139, p. L1, 1988.
- [22] J. Brabers, G. Zhou, F. de Boer et K. Buschow, *J. Magn. Magn. Mater.*, vol. 118, p. 340, 1993.
- [23] A. Fujita, S. Fujieda et K. Fukamichi, *J. Magn. Magn. Mater.*, vol. 321, pp. 3553-3558, 2009.
- [24] K. Irisawa, A. Fujita, K. Fukamichi, Y. Yamazaki, Y. Iijima et E. Matsubara, *J. Alloys Compd.*, vol. 316, p. 70, 2001.
- [25] D. Westlake, *J. Less Comm. Met.*, vol. 90, p. 251, 1983.
- [26] D. Westlake, *J. Less Comm. Met.*, vol. 91, p. 275, 1983.
- [27] E. Koch et W. Fischer, *Z. Kristallogr.*, vol. 211, p. 251, 1996.
- [28] X. Liu, Z. Altounian et A. Beath, *Journal of Applied Physics*, vol. 95, p. 7067, 2004.
- [29] A. Fujita, S. Fujieda, K. Fukamichi et M. Ohta, *J. Phys. D: Appl. Phys.*, vol. 43, p. 295003, 2010.
- [30] S. Nikitin, A. Tishin, M. Kuz'min et Y. Spichkin, *Phys. Lett. A*, vol. 153, p. 155, 1991.
- [31] O. Isnard et V. Pop, *J. Alloy Compd.*, vol. 509, p. S549, 2011.
- [32] D. Fruchart, S. Miraglia, P. De Rango et P. Wolfers, *J. Alloy Compd.*, vol. 383, p. 17, 2004.
- [33] B. Rupp et G. Wiesinger, *J. Magn. Magn. Mater.*, vol. 71, p. 269, 1988.
- [34] S. Fujieda, A. Fujita, K. Fukamichi, Y. Yamaguchi et K. Ohoyama, *J. Phys. Soc. Jpn.*, vol. 77, pp. 1-8, 2008.
- [35] M. Phejar, Ph.D. thesis manuscript "*Etude de nouveaux matériaux de type La(Fe_{1-x}Si_x)₁₃ pour la réfrigération magnétique à température ambiante*", Engineering Sciences, Université Paris-Est, 2010. French. <NNT : 2010PEST1085>. <tel-00575658v2>
- [36] A. Fujita, S. Fujieda, Y. Hasegawa et K. Fukamichi, *Phys. Rev. B*, vol. 67, p. 104416, 2003.
- [37] M. Krautz et al., chez *Book of Abstracts, Thermag V*, Grenoble, 2012.
- [38] M. Krautz, J. Moore, K. Skokov, J. Liu, C. Teixeira, R. Schafer, L. Schultz et O. Gutfleisch, *J. Appl. Phys.*, vol. 112, p. 083918, 2012.
- [39] C. B. Zimm et S. A. Jacobs, *J. Appl. Phys.*, vol. 113, p. 17A908, 2013.
- [40] J. Zhao, J. Shen, H. Zhang, Z. Xu, J. Wu, F. Hu, J. Sun et B. Shen, *J. Alloy Compd.*, vol. 520, pp. 227-280, 2012.
- [41] C. S. Teixeira, M. Krautz, J. D. Moore, K. Skokov, J. Liu, P. A. Wendhausen et O. Gutfleisch, *J. Appl. Phys.*, vol. 111, p. 07A927, 2012.
- [42] D. de Mooij et K. Buschow, *J. Less-Common Metals*, vol. 142, p. 349, 1988.

- [43] S. Fu, Y. Long, J. Hu et Y. Sun, *Mater. Lett.*, vol. 112, p. 149, 2013.
- [44] S. Fu, Y. Long, Y. Sun et J. Hu, *Intermetallics*, vol. 39, p. 79, 2013.
- [45] X. Zhong, R. Radwanski, F. de Boer, T. Jacobs et K. Buschow, *Physica B*, vol. 168, p. 181, 1991.
- [46] H. Sun, Ph.D. thesis, Dublin: Trinity College Dublin, 1992.
- [47] P. Villars et L. Calvert, *Pearson's Handbook of Crystallographic Data for Intermetallic Phase*, Metal Park: American Society of Metals, 1986, pp. 1520, 1542.

Chapter V. Hydrogen dynamics

Table of Contents

Chapter V. Hydrogen dynamics	143
1. Hydrogen sorption kinetics	143
1.1. Pressure-composition isotherms	143
1.2. Hydrogen kinetics	146
1.3. Effect of Si concentration	152
1.4. <i>In-situ</i> neutron diffraction	153
1.5. Evaluation of the stability	158
1.6. Discussion	159
2. Hydrogenation behavior with Ce substitution.....	160
2.1. <i>In-situ</i> Neutron diffraction	160
3. Hydrogenation behavior with C insertion	163
3.1. Effect of carbon insertion on La-Fe-Si	163
3.2. Effect of C insertion in Ce-substituted samples.....	174
4. Conclusion.....	181
References	184

Chapter V. Hydrogen dynamics

In the previous Chapter, we have discussed the importance to have a better control of the hydrogen stability in the structure. This Chapter is dedicated to the investigation of hydrogen mobility and kinetics in the La-Fe-Si structure.

1. Hydrogen sorption kinetics

1.1. Pressure-composition isotherms

In this work, the hydrogen dynamics were investigated by the macroscopic constant volume measurements to relate the H_2 pressure with the H concentration in the composition. Sample particle size was sieved to 40-200 μm range in powder form. The pressure-composition isotherms (P-C-I) were performed at 523 K to simulate realistic hydrogenation conditions. The H_2 pressure was gradually increased until 1 MPa.

At each pressure gain, the hydrogen uptake was measured until equilibrium is reached. An equilibrium state is considered reached when the pressure change is minimized based on the internal calculation of the program. The time needed to reach equilibrium state in each measured point was in the order of a few hours for absorption and desorption. Afterwards, partial H_2 pressure is decreased to measure the desorption dynamics. The resulting P-C-I demonstrates the hydrogenation behavior of the sample during absorption and desorption, as shown in Figure V-1 and Figure V-2. In the corresponding H concentration range (< 2 H/f.u.), the pressure isotherms fairly resemble those of LaNi_5 [1] and R_2Fe_{17} [2] systems in the alpha phase (solid solution state), where the H concentration increases rapidly with pressure before saturation is reached.

At very low pressure (< 0.1 MPa), the curves start directly with a plateau region. The hydrogen sorption kinetics can be traced simultaneously at each pressure change. Figure V-2 shows the absorption kinetics during each step of the pressure increase. The absorption kinetics at this pressure range is extremely slow, and first sign of absorption starts only after 1000 min.

The width of the plateau shown in Figure V-1 is about 0.5 H/f.u. M. Phejar has reported in his Ph.D. work [3] a plateau at the first instance of the absorption stage as large as 1.5 H/f.u. at 298 K. The width of the plateau reduces with increasing temperature. Indeed, the small width of the plateau observed in our work is consistent with the elevated temperature, which facilitates H mobility in the structure. At the experimental temperature and pressure, the P-C-I relations in the equilibrium state show no sign of a distinct hydride phase with H concentration $x < 1.6$ in $\text{LaFe}_{11.7}\text{Si}_{1.3}\text{H}_x$. Previous XRD patterns have shown a large volume increase due to H uptake with no hydride phase formed. The hysteresis between the absorption and desorption stage indicates the presence of elastic strain in the material. The positive volume changes of hydrogenated La-Fe-Si phase can cause cracks, a so-called hydrogen decrepitation (HD) phenomenon, which is frequently encountered in the processing of Nd-Fe-B permanent magnet materials. This indicates a “nucleation and

growth” mechanism for hydrogenation by favoring the nucleation on the newly created surfaces.

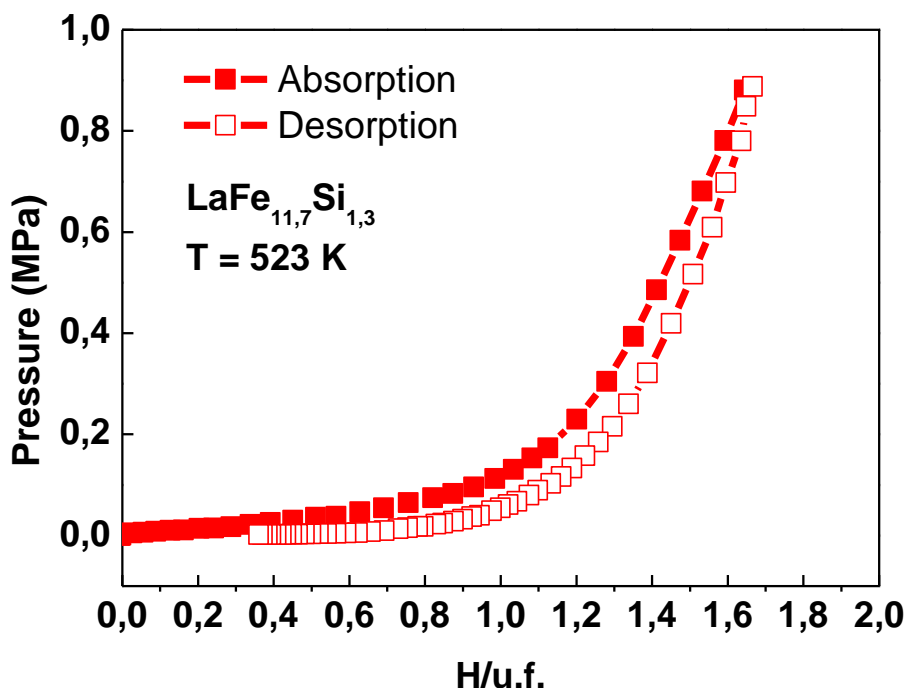


Figure V-1. Variation of H content with pressure for sample $\text{LaFe}_{11.7}\text{Si}_{1.3}$ measured at 520 K in absorbing and releasing processes.

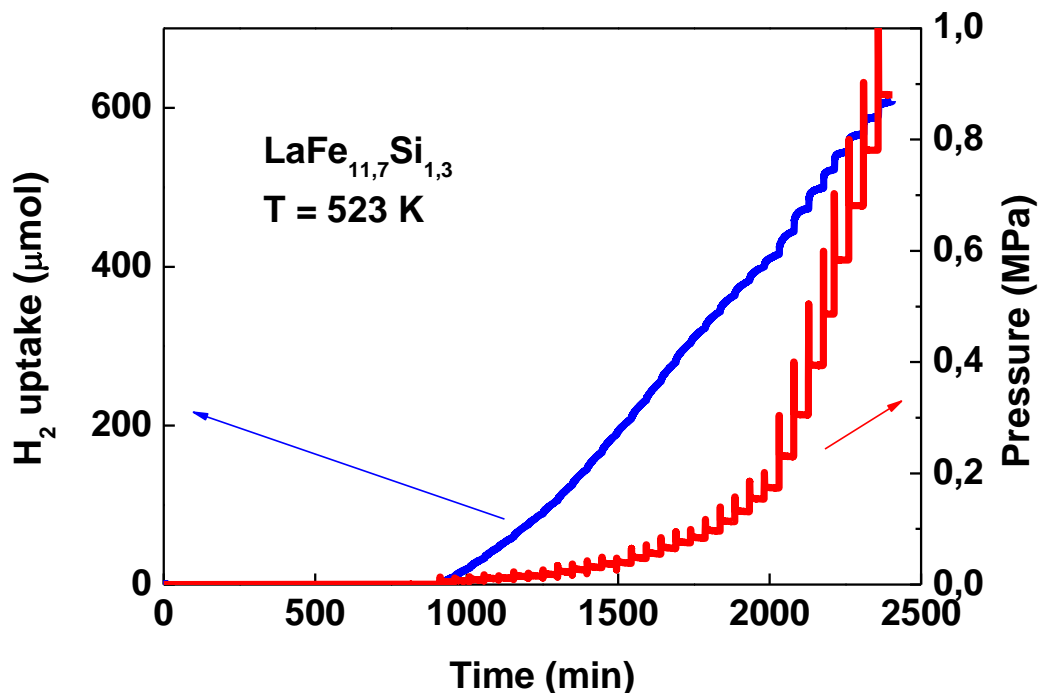


Figure V-2. Hydrogen uptake at each pressure step during pressure increase as a function of time at 523 K in order to demonstrate the hydrogen sorption kinetics measured in the pressure-composition isotherms.

Desorption is obtained by gradually decreasing the H_2 pressure until the lowest detectable range of the apparatus. The desorption curve confirms the instability of H at high temperature range. Nonetheless, desorption is not complete at given experimental

conditions. Wang *et al.* [4] showed in their P-C-I curves that the H desorption plateau does not appear, which is an indication the system stays in the interstitial solid solution regime.

At 523 K, the material continues to desorb and the lowest H content detected is about 0.3 H/f.u. (Figure V-1). In fact, desorption capacity is directly related to the partial pressure of H₂. It seems like the material does not reach desorption equilibrium within the detection limit. Full desorption is obtained via dynamic pumping at elevated temperature.

In Figure V-3, the square root of P is plotted as a function of the H concentration. It is seen that the solution of H in the La(Fe_{1-x}Si_x)₁₃ phase follows the Sieverts' law:

$$P^{1/2} = k \cdot c \quad (\text{V-1})$$

where P denotes the pressure and c is the H concentration in the metal. The linear relation in Figure V-3 shows that this is a chemisorption regime instead of a physisorption one. The system stays within a solid solution insertion regime. The P-C-I does not show any sign of phase separation due to formation of a distinct stoichiometric hydride phase at 523 K under the pressure range between 0.005 and 0.9 MPa.

A kink is observed around 1 H/f.u. and this change of slope suggests a change of Sieverts' constant, k . Usually a decrease of the slope is observed when approaching the solubility limit as the formation of the hydride phase begins. In our case, the slope increases at higher H concentration, which may be associated with the formation of defects in the H solid solution region.

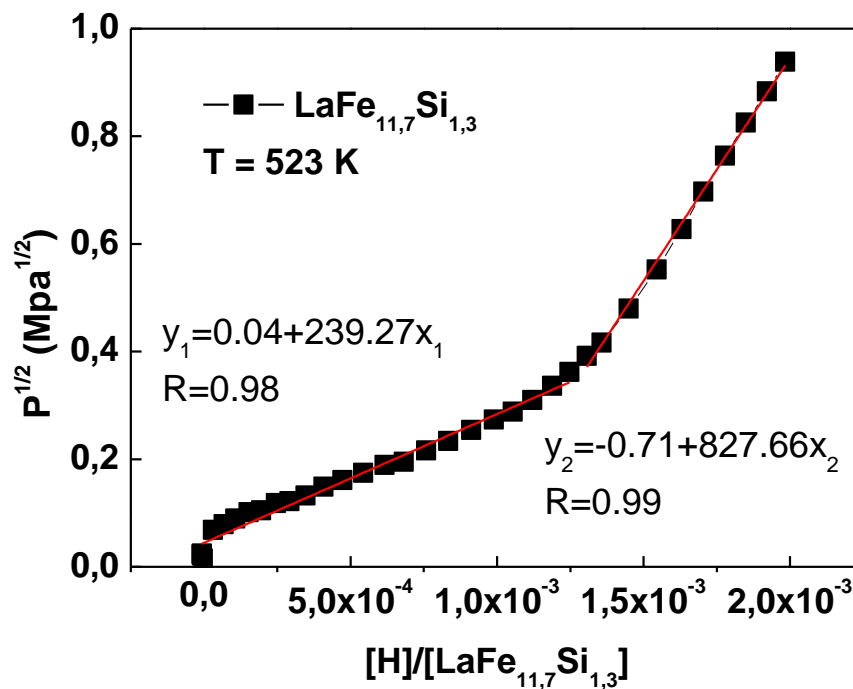


Figure V-3. The H absorption isotherms at 523 K of the LaFe_{11.7}Si_{1.3}-H system showing H solid solution regions.

Both the intrinsic and extrinsic parameters influence the hydrogenation dynamics. In R(rare earth)-M(transition metal) hydrides such as the LaNi₅ system, H solubility and relevant thermodynamic properties are found to depend on the sample size within certain ranges [5] [1] in the solid solution region. This effect can be quite dominant in such

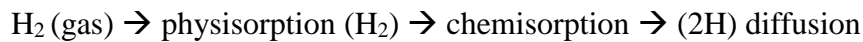
systems with a volume expansion of over 20%. In the $\text{La}(\text{Fe}_{1-x}\text{Si}_x)_{13}$ system, the hydrogen uptake is extremely small compared with in the LaNi_5 system that we did not observe remarkable dependence of the H solubility and absorption kinetics upon sample particle size.

Moreover, at the experimental temperature range, hydrogenation readily takes place and the effect of particle size is rather secondary. The particle size before hydrogenation is often absent in publications involving the $\text{La}(\text{Fe}_{1-x}\text{Si}_x)_{13}$ system, whereas it is one important detail for the LaNi_5 material.

Nonetheless, the stress sensitive characteristics of the $\text{La}(\text{Fe}_{1-x}\text{Si}_x)_{13}$ phase (as mentioned in Chapter VI) should be taken into account when analyzing the thermodynamics properties. Uchida *et al.* [1] highlighted the importance of density of defects in H sorption isotherm measurements. Hydrogen uptake or release can result in the generation, accumulation, or annihilation of dislocations. This induces the redistribution of stress and H atoms in the sample and result in a change in the H chemical potential. Such changes in the chemical potential of H atoms can be associated with the H stability in the material.

1.2. Hydrogen kinetics

Cyclic absorption and desorption experiments were performed using a Sieverts' type instrument with constant volume and a differential pressure gauge (HERA C2-3000). A number of phenomena come in play in the physical and reactional behavior of interstitial H introduction. For the objective of having a better control of H stability, it is important to determine the mechanisms of these phenomena and their relationships with temperature, pressure, and H concentration. Other factors also affect the reaction kinetics, such as aging, oxidation, annealing conditions, and reaction cycles. According to the work of Koeninger *et al.* [6], the H absorption reaction of R_2Fe_{17} alloys can be decomposed into the following steps:



Their study has shown that the transition between the physisorbed state to the chemisorbed state of H is the most rate-limiting step of the absorption reaction. Similar mechanism can be applied in the $\text{LaFe}_{13-x}\text{Si}_x\text{H}_y$ system.

In order to analyze the hydrogenation kinetics, the early work of Snidjer [7] has shown that a fit to the absorption isotherms can be realized by using a generalized equation, based on the Kolmogorov-Johnson-Mehl-Avrami (KJMA) relation for the description of the solid phase reaction. Although this model dates back to the end of the 1930s, it has been extensively used based on its extreme simplicity. The essence of the model can be summed up in Eq.(V-2):

$$F(\alpha) = 1 - e^{(-k \cdot t^n)} \quad (\text{V-2})$$

where α is the volume fraction of the product, t is the reaction time, and k the reaction rate constant. The constant n , called the Avrami exponent, indicates the constancy of the nucleation rate, the dimension of nuclei growth and rate-controlling step. Eq.(V-3) can be rewritten as:

$$F(\alpha) = (-\ln(1 - \alpha)) = kt^n \quad (\text{V-3})$$

In general, k contains all the temperature-dependent terms because thermal activation strongly affects the growth through interface mobility. In addition, the nucleation density depends on the driving force. The Avrami exponent can be determined from the slope of the line described by plotting the quantity $-\ln(1 - \alpha)$ versus *time* on a double-logarithmic plot. The slope of the line is then the exponent, n .

$$\ln(-\ln(1 - \alpha)) = \ln(k) + n \cdot \ln(t) \quad (\text{V-4})$$

Due to the interactions of various steps, it is impossible to linearize the absorption/desorption kinetics by a function $F(\alpha) = kt$ over the whole time range. Several phenomena that are very slow often systematically interact at the end of the reaction. In this work, the first part (90% of the total absorption) of the reaction is modelled to represent a valid reaction constant to compare with.

Temperature and pressure are the two most important extrinsic parameters to control the H sorption kinetics. Increasing the H pressure can lead to increased H saturation capacity and shortens the time necessary for saturation. In the following section, the effect of temperature on the sorption kinetics is discussed.

1.2.1. Temperature effect on absorption

The effect of temperature on the hydrogenation behavior of the 1:13 phase was investigated by measuring the hydrogen uptake at temperatures ranges between 433 and 573 K under the same pressure. In order to perform cyclic experiments, the sample was desorbed under vacuum pumping condition at 573 K between each measurement. The material shows reversible absorption and desorption behavior at temperature range between 433 K and 573 K. The H absorption kinetics with initial H₂ pressure of 1 MPa was measured at different temperatures for sample LaFe_{11.7}Si_{1.3}. The evolution of H per formula unit with time is shown in Figure V-4.

The H uptake kinetics begins with a constant rate, then gradually decreases and saturates with time. At 433 K, the amount of time needed to reach 90% of the total H fraction is around 90 min and the maximum capacity at absorption is 1.53 H/f.u. The absorption kinetics accelerates with increasing temperature as the latter favors the H atomic diffusion. At 623 K, the absorption saturation is reached within a few minutes. The saturation hydrogen contents in the LaFe_{11.7}Si_{1.3} under 1 MPa are 1.53, 1.42, 1.53, 1.58, and 1.11 at 433, 483, 523, 573, and 623 K, respectively.

At constant pressure, the maximum H sorption capacity is stable except at 623 K, where it considerably reduces due to the high mobility of H at elevated temperatures. Wang *et al.* [4] also observed a decrease of the hydrogen absorption capacity as temperature increases from 273 to 353 K under 6.5 MPa for their LaFe_{11.44}Si_{1.56} samples. The small variations of maximum H content below 623 K can be attributed to the cycling effect, which leads to small yet unavoidable deviations between each cycle. This effect is reduced by the dynamic pumping dehydrogenation between each cycle.

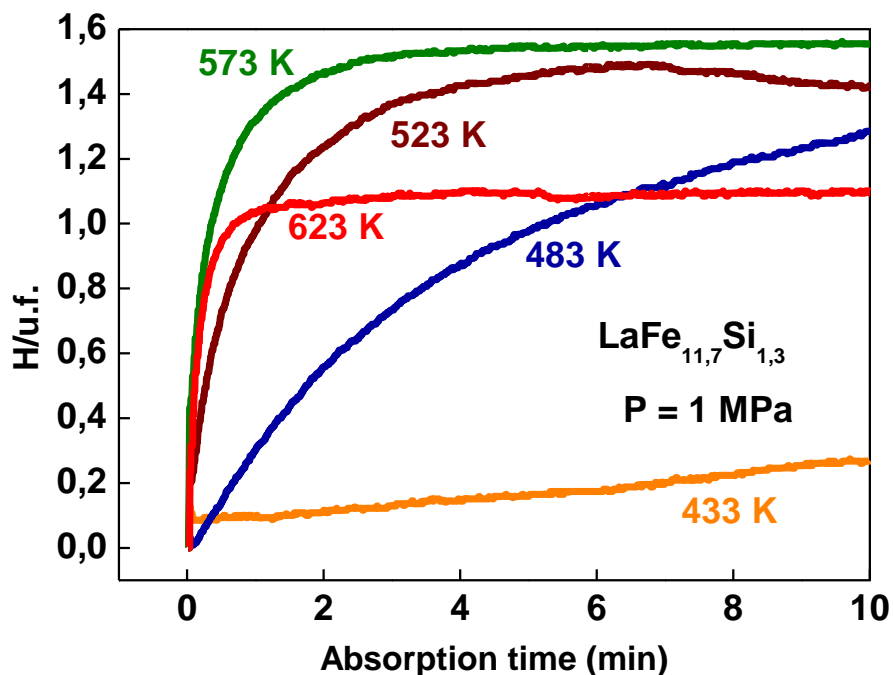


Figure V-4. Hydrogen absorption kinetics at 1 MPa at different temperatures for compound $\text{LaFe}_{11.7}\text{Si}_{1.3}$.

The linearization of Eq. (V-4) results in a range of Avrami exponent from 1.0 to 0.6 in the temperature range measured. Several arbitrary values of the coefficient n have been tested and n equals to 1 can fit all the curves with good agreement for up to 90% of the reaction. The reaction constant k is then extracted as the slope of each line in Figure V-5.

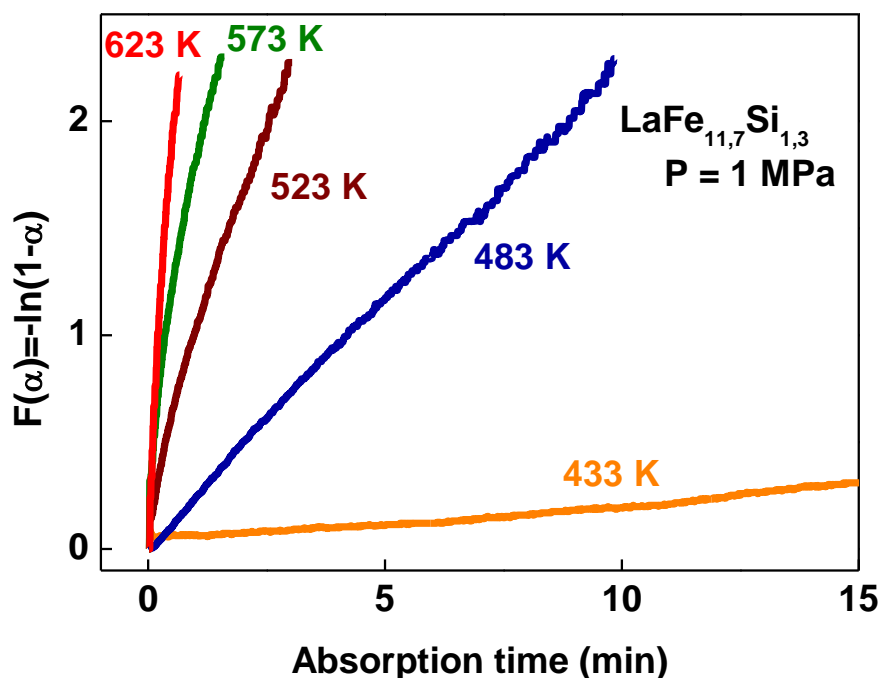


Figure V-5. Linearization of absorption kinetics at 1 MPa with a mechanism of nucleation and growth, exponent $n = 1$ for compound $\text{LaFe}_{11.7}\text{Si}_{1.3}$.

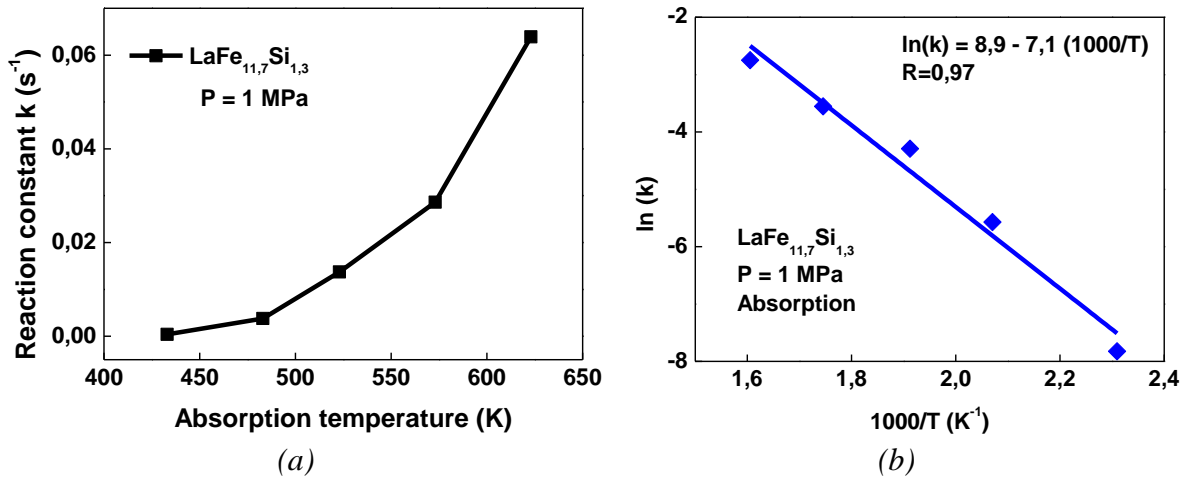


Figure V-6. (a) The calculated reaction constant from the slope of the linearization from Figure V-5 for sample LaFe_{11.7}Si_{1.3} and (b) determination of k_0 and E_a from linearization of the measured kinetics of absorptions at different temperatures at 1 MPa for compound LaFe_{11.7}Si_{1.3}.

The temperature influence on the absorption kinetics is presented in Figure V-6 (a). The temperature dependence of a chemical reaction is classically represented by the Arrhenius law:

$$k(T) = k_0 \cdot e^{\frac{-E_a}{RT}} \quad (\text{V-1})$$

where k_0 is a constant and the term E_a represents the activation energy of the reaction, which describes, in particular, the limiting step of the reaction. The value k is determined for different temperatures at the same pressure previously mentioned. Therefore, $\ln(k)$ can be plotted as a function of $1/T$, as shown in Figure V-6 (b). With the following equation, the activation energy can be deduced:

$$\ln(k) = \ln(k_0) - \frac{E_a}{1000R} \cdot \frac{1000}{T} \quad (\text{V-2})$$

Therefore, for 1 MPa pressure applied at absorption, the activation energy E_a for sample LaFe_{11.7}Si_{1.3} to absorb H interstitials is about 59 kJ/mol of H₂ and the constant k_0 is in the order of $7.51\text{E}^3 \text{ s}^{-1}$.

1.2.2. Temperature effect on desorption

In order to create a concentration gradient for the specimen to release H, the H₂ partial pressure was reduced to the minimum detectable range and was stabilized at 0.01 MPa. The advantage of setting a desorption pressure is to precisely track desorption behavior, whereas in a dynamic pumping scenario, the data recording would be difficult. The H desorption curves obtained are hyperbolic (Figure V-7), similar to the absorption curves. Desorption begins instantaneously for all the temperatures. No incubation period is needed for desorption to start, indicating that H atoms are highly mobile at these temperature ranges in the intermetallic solid solution phase.

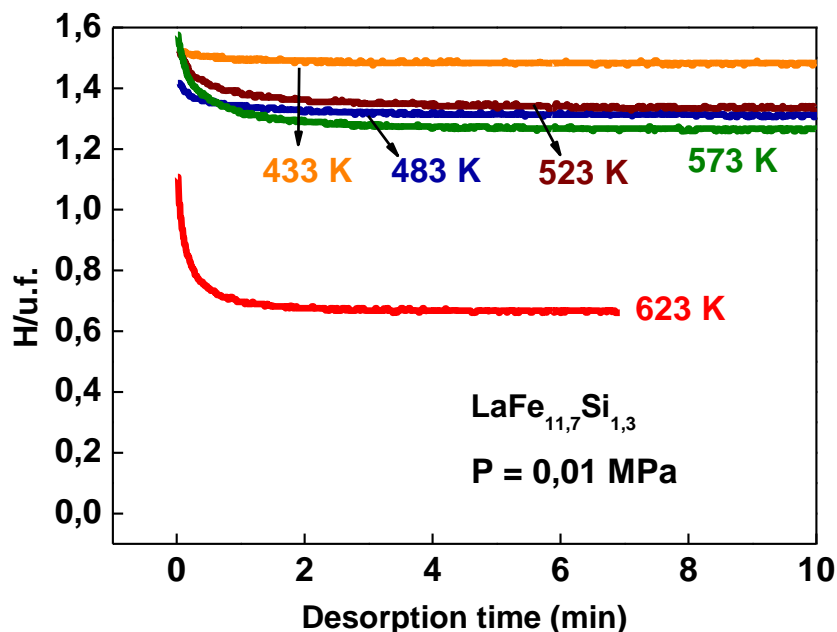


Figure V-7. Hydrogen desorption kinetics at 0.01 MPa at different temperatures for compound $\text{LaFe}_{11.7}\text{Si}_{1.3}$

Temperature was kept constant during desorption for both the cyclic experiments using Sieverts' apparatus and during *in-situ* neutron powder diffraction (NPD). Under isothermal conditions, the KJMA equation remains valid. The isothermal desorption experiments allow us to investigate the H desorption dynamics at one temperature and pressure at a time. In order to track the H desorption phase transformation under constant heating rate, the readers are referred to the work of Leblond *et al.* [7] on the YFe_2 laves phases, where they studied thermal desorption in DSC in-beam while performing NPD.

The Avrami exponent n values are around 0.1 – 0.6 for the different temperatures and the linear fitting from the KJMA relation is not always satisfactory. An exponent below 1 suggests that the rate-limiting step is the diffusion of H atoms.

A useful way to express the reaction kinetics is by defining an apparent rate of reaction. In this case, we take the time needed to achieve 90% of the desorption reaction, t_{90} , and the apparent rate of reaction is defined as $w_{90} = \frac{1}{t_{90}}$ for the time needed up to 90% of the phase transformation, w_{90} . Similarly, the apparent rate constant can be defined based on the time needed to complete half of the H release, t_{50} and w_{50} .

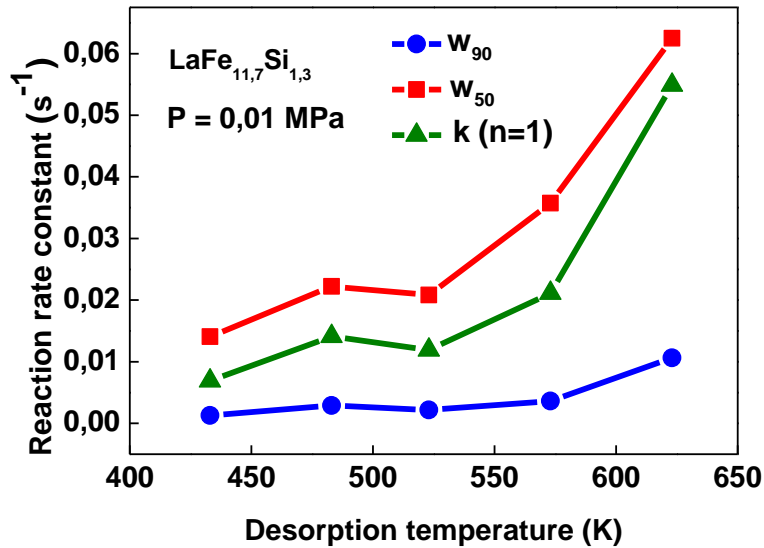


Figure V-8. Reaction rate constant calculated from $n=1$ and defined apparent rate constant w_{90} and w_{50} .

Figure V-8 demonstrates the evolution of desorption reaction rate with temperature, calculated from KJMA relation with $n=1$ and the defined reaction rate w_{90} and w_{50} , expressed in s^{-1} .

Hydrogen desorption rate is low below 523 K and shows obvious increase for 573 and 623 K. The amount of H desorbed is directly related to the desorbing temperature, as shown in Figure V-9. At 423 K (150 °C), the H content under 0.01 MPa corresponds to 1.45 H/f.u., whereas the maximum H content at absorption under 1 MPa is around 1.53 H/f.u., showing a first sign of H instability at this temperature. This is consistent with the issues reported by Mayer *et al.* [8] discussed in Chapter VI, Section 2.3.1. The amount of H desorbed increases with increasing temperature, as indicated by the difference between the two curves in Figure V-9. At 623 K, the sample desorbs 60% of the previously absorbed H atoms.

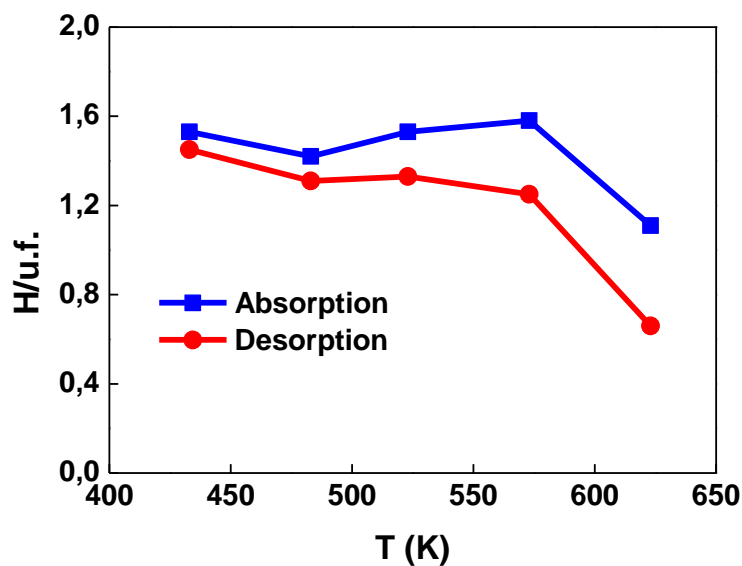


Figure V-9. The maximum H absorption capacity and the H capacity at desorption with different temperatures for sample $LaFe_{11.7}Si_{1.3}$.

To summarize, the absorption kinetics increases while the hydrogen sorption capacity decreases upon temperature augmentation. During desorption, the hydrogen content at the end of the desorption decreases with increasing temperature. This is consistent with the observation by Wang *et al.* [4], who suggested that the hydrogen storage capacity or the numbers of hydrogen atoms per formula unit in La-Fe-Si alloy can be adjusted by changing temperature.

1.3. Effect of Si concentration

The impact of Si on the H sorption dynamics has already been observed on the reduced maximum H sorption capacity in high-Si samples. As shown in Chapter III, samples with higher Si content show lower T_C after hydrogenation. It is a nice example of how interstitial insertion is directly associated with the structure and the composition. To illustrate the effect of Si concentration on the sorption kinetics, H sorption dynamics for two samples with different Si content ($\text{LaFe}_{11.7}\text{Si}_{1.3}$ and $\text{LaFe}_{11.44}\text{Si}_{1.56}$) are compared in Figure V-10. Samples underwent the same experimental conditions: 523 K with initial H_2 pressure of 1 MPa at absorption stage and 0.1 MPa at desorption.

At the end of absorption, specimen with $x_{\text{Si}}=1.3$ saturates at about 1.5 H/f.u., which corresponds to about 50% of the full site occupancy for 24d. For $x_{\text{Si}}=1.56$, the maximum H absorption capacity is reduced to 1 H/f.u., that is, 30% of the 24d occupancy. The absorption kinetics is twice as slow for $\text{LaFe}_{11.44}\text{Si}_{1.56}$, while its desorption reaction rate is much faster.

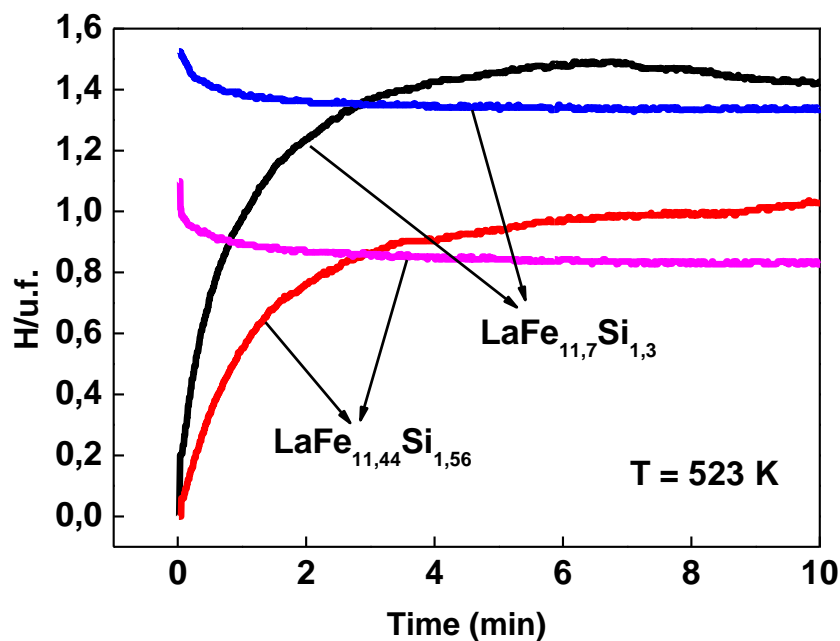


Figure V-10. The H absorption and desorption kinetics obtained at 523 K with an initial H_2 pressure of 1 and 0.01 MPa, respectively for specimen $\text{LaFe}_{11.7}\text{Si}_{1.3}$ and $\text{LaFe}_{11.44}\text{Si}_{1.56}$.

Two factors from room-temperature observations might be associated with the effect of Si observed here:

- 1) **Volume effect:** Silicon substitution induces a volume contraction, which impedes the H absorption due to reduced space. Hydrogen diffusion induces lattice decrepitation by creating mechanical strain. Therefore, after H absorption, the desorption reaction takes place rapidly because the effective size of particles is smaller.
- 2) **Repulsive force:** S. Rundqvist *et al.* [9] have demonstrated that there are repulsive interactions between the *p* elements (B, Si, Al) and the H (D) atoms. The *s*-like character atoms do not bond directly with the *p*-electron elements. This claim is supported by the H location in $R_2Fe_{14}B$ systems and in Si to Fe substituted compounds [10]. Absorption of H is more difficult due to the repulsion with high concentration of Si atoms. At desorption stage, the repulsive force facilitates the departure of H atoms from the lattice, resulting in a faster kinetics.

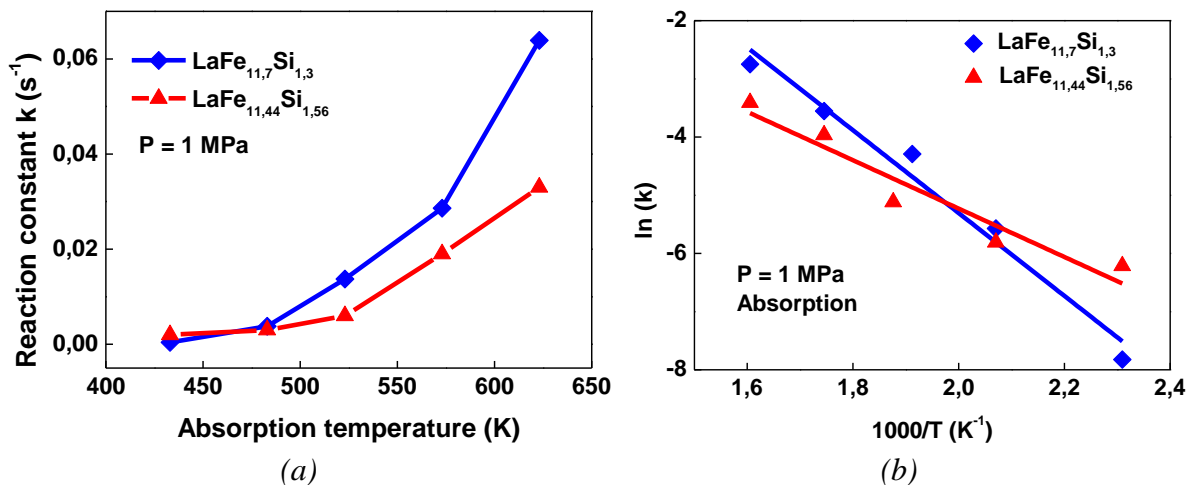


Figure V-11. The temperature effect on the absorption reaction rate constant k for sample $LaFe_{11.7}Si_{1.3}$ and $LaFe_{11.44}Si_{1.56}$.

The temperature effects on the absorption and desorption kinetics remain similar for samples with both high and low Si concentrations (Figure V-11). Absorption reaction accelerates with increasing temperature while desorption trend is not linear. The activation energy for $LaFe_{11.44}Si_{1.56}$ to absorb H interstitials is much smaller than that for $LaFe_{11.7}Si_{1.3}$, as shown in the slope in Figure V-11 (b). The more contracted lattice in Si-rich sample is at a higher-energy state, which might contribute to the onset of hydrogenation reaction. This shows that the hydrogen dynamics is associated with several parameters. The increased lattice strain and modified diffusion path can lead to counterintuitive reaction mechanism. In order to have better insight on the role of Si substitution to Fe on the hydrogen sorption dynamics, further experiments at different temperatures should be carried out with a series of Si concentrations.

1.4. *In-situ* neutron diffraction

The *in-situ* NPD experiment is performed with D instead of H to have a smaller incoherent background and therefore a better signal/noise ratio. The sequential refinement of this series consists of refining several parameters such as the lattice constant and scale factor, the atomic position of Fe^{II}, the site occupancy of D interstitial site, and the Debye-Waller thermal coefficient.

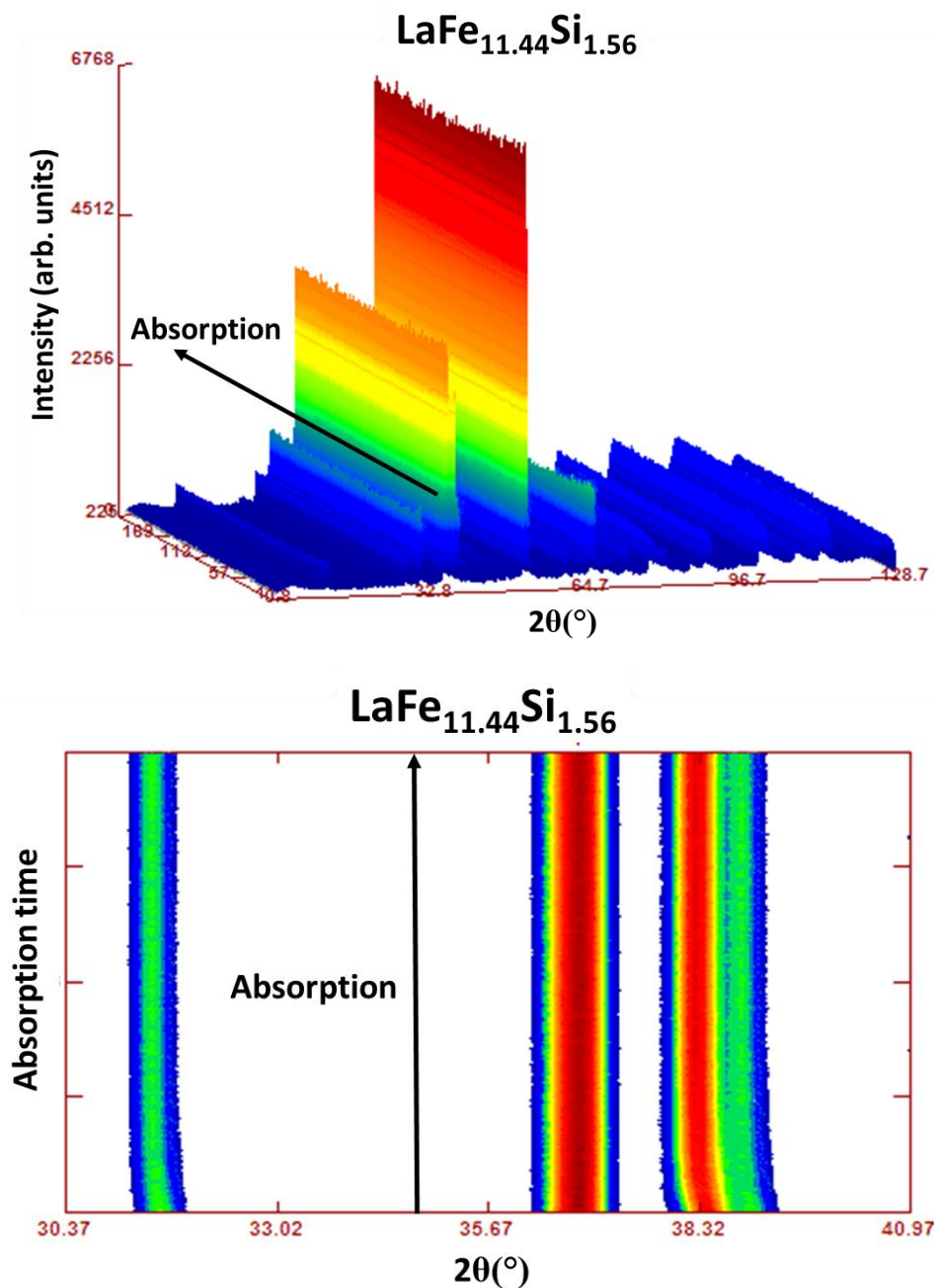


Figure V-12. 3D (top) and 2D (bottom) projection of the neutron diffractograms of sample of composition $\text{LaFe}_{11.44}\text{Si}_{1.56}$ in the course of deuterium absorption at 540 K.

The interstitial occupancy and interatomic distance variations from the insertion and emptying of D atoms can be studied in details (Figure V-12). The relative kinetics can be obtained from the evolution of a few parameters. On one hand, the expansion and contraction of the refined lattice parameter is directly related to D uptake and discharge. In this case, chemical pressure is indirectly measured through the variation of lattice volume. On the other hand, the refined occupancy of the interstitial site indicates explicitly the amount of D inserted.

A pair of samples of nominal composition $\text{LaFe}_{11.44}\text{Si}_{1.56}$ and $\text{LaFe}_{11.44}\text{Si}_{1.56}\text{C}_{0.2}$ were measured under the same conditions in order to investigate the effect of C on the hydrogenation behavior of $\text{La}(\text{Fe}_{1-x}\text{Si}_x)_{13}$ phases. Let's first take a look at the C-free sample. The experimental conditions (temperature, pressure) were selected to establish an appropriate reaction rate for observation with good statistics and within the given beam time. The composition free of Ce or Mn substitution allows us to address the effect of D sorption only. A constant flux of D_2 gas was introduced at 540 K and neutron diffraction patterns were recorded *in-situ* in the course of D absorption and desorption. At this temperature range, the ferromagnetic contribution was quite weak from magnetization measurements. The low-angle shifts can be seen at the beginning of D absorption and certain reflections show increased intensities.

Figure V-13 shows the evolutions of both the unit cell parameter and the D content per formula unit calculated from the refined interstitial site occupancy. The two parameters are in accordance with the filling and emptying of the $24d$ site for sample $\text{LaFe}_{11.44}\text{Si}_{1.56}$. This is a good indication that D atoms are accommodated only in the $24d$ site.

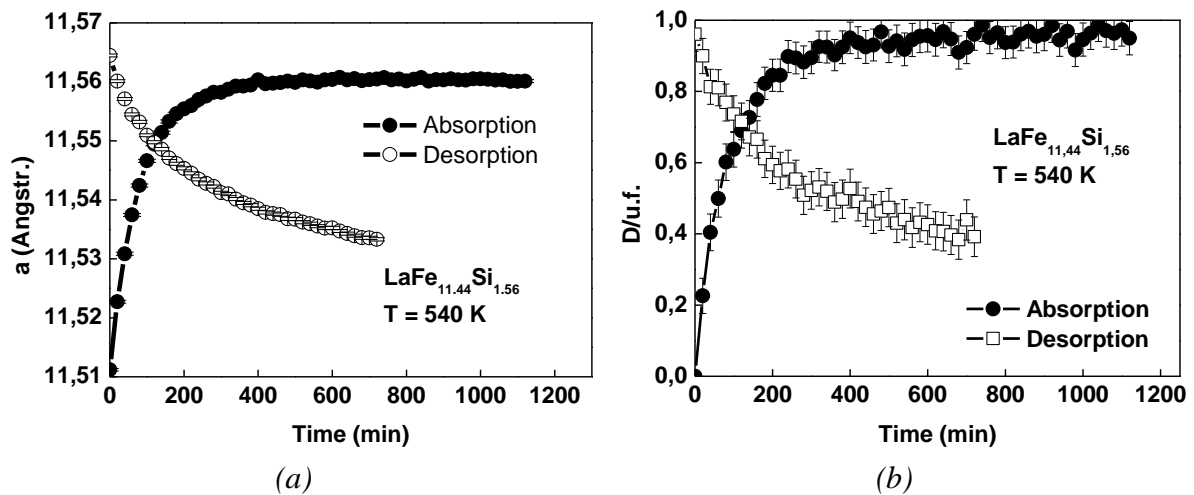


Figure V-13. Deuterium absorption-desorption kinetics for sample $\text{LaFe}_{11.44}\text{Si}_{1.56}$ observed from neutron diffraction, indicated by (a) lattice constant evolution and (b) the D content per formula unit from refined site occupancy of the $24d$ interstitial site.

The amount of D absorbed increases with time and saturates at 1 D/f.u. in $\text{LaFe}_{11.44}\text{Si}_{1.56}$. Fujieda *et al.* [11] reported a maximum D sorption capacity at 1.5 D/f.u., in a neutron diffraction experiment on a sample of the same nominal composition. This discrepancy is reasonable by considering the experimental conditions. In the work of Fujieda *et al.*, the D_2 gas pressure applied is 2 MPa, much higher than in this experiment (0.12 MPa with constant flow).

An analysis based on the KJMA model can be applied to the evolution of the lattice constant a and the $24d$ site occupancy during absorption. The Avrami exponent n is around 0.8 for good simulation with both parameters. For coherence, we take integer value $n=1$ in order to compare the reaction rate constant k . For sample $\text{LaFe}_{11.44}\text{Si}_{1.56}$, k is the same ($2 \text{ E}^{-4} \text{ s}^{-1}$) for both parameters. Indeed, the lattice expansion is directly linked to the number of D atoms in the interstitial site. This one-to-one relationship confirms the existence of one interstitial site of accommodation.

Desorption was proceeded by switching D₂ flow with He. There is a continuous decrease of the lattice constant and the interstitial site occupancy (Figure V-13). Therefore, within the 800 min of desorption, no contribution from additional interstitial site is visible. Analysis of the desorption scheme is rather difficult with the KJMA model because the kinetics constant is dependent of the assumed end-point of the desorption stage. Information at the first instances of desorption is obscure since it took a few minutes for the gas flow to stabilize and establish a constant flux. The available beam time did not allow sufficient time to achieve equilibrium for desorption. Moreover, the temperature used was very close to the onset of hydrogen desorption [12], thus rendering the desorption kinetics data unreliable and hard to exploit in order to accurately describe the desorption scheme. At the end of the desorption stage (720 min), the remaining D content is 0.34 D/f.u., which is 35% of the maximum D content at absorption. Table V-1 summarizes the refined parameters for compound LaFe_{11.44}Si_{1.56} before absorption, at the end of absorption, and at the end of desorption.

Table V-1. Refined parameters and interatomic distances for sample of composition LaFe_{11.44}Si_{1.56} before deuterium absorption, after 1120 min of absorption and after 720 min of desorption, taken from neutron diffraction data obtained at the D1B diffractometer at 540 K.

Sample	LaFe _{11.44} Si _{1.56}	LaFe _{11.44} Si _{1.56} D _{0.96} (end of absorption 1120 min)	LaFe _{11.44} Si _{1.56} D _{0.34} (end of desorption 720 min)
<i>T_c</i> (K)	206	(estimated 340 K from lattice constant comparison)	254
a=b=c (Å)	11.5112 (2)	11.5604 (2)	11.5333 (3)
site 96i (0, y, z) y	0.1796 (2)	0.1793 (2)	0.1800 (2)
site 96i (0, y, z) z	0.1175 (2)	0.1162 (2)	0.1171 (2)
Occupancy 24d	0	0.320 (1)	0.128 (2)
B1 (Å)	2.473 (2)	2.470 (2)	2.477 (2)
B2 (Å)	2.712 (3)	2.688 (3)	2.701 (3)
B3 (Å)	2.573 (2)	2.575 (2)	2.581 (3)
Weighted average (2B1+B2+4B3)/7 (Å)	2.564 (2)	2.561 (2)	2.568 (3)
B4 (Å)	2.438 (3)	2.474 (3)	2.450 (3)
B5 (Å)	2.510 (2)	2.507 (3)	2.501 (3)
Weighted average (2B4 + 2B5)/4 (Å)	2.474 (3)	2.491 (3)	2.476 (3)
χ^2	1030 (high-statistics)	7.2	8.1
R_{Bragg} (%)	9.6	8.8	11.7
R_f (%)	9.6	7.9	9.4

The *in-situ* neutron diffraction experiment allows us to follow the evolution of important Fe-Fe distances in the course of absorption and desorption, as presented in Figure V-14. Fe-D distance is based on the shortest distance between one Fe^{II}/Si atom and a theoretical atom at the center of the octahedral void in the 24d site. Based on the experimental data, the following mechanism for interstitial H/D insertion and desorption is proposed:

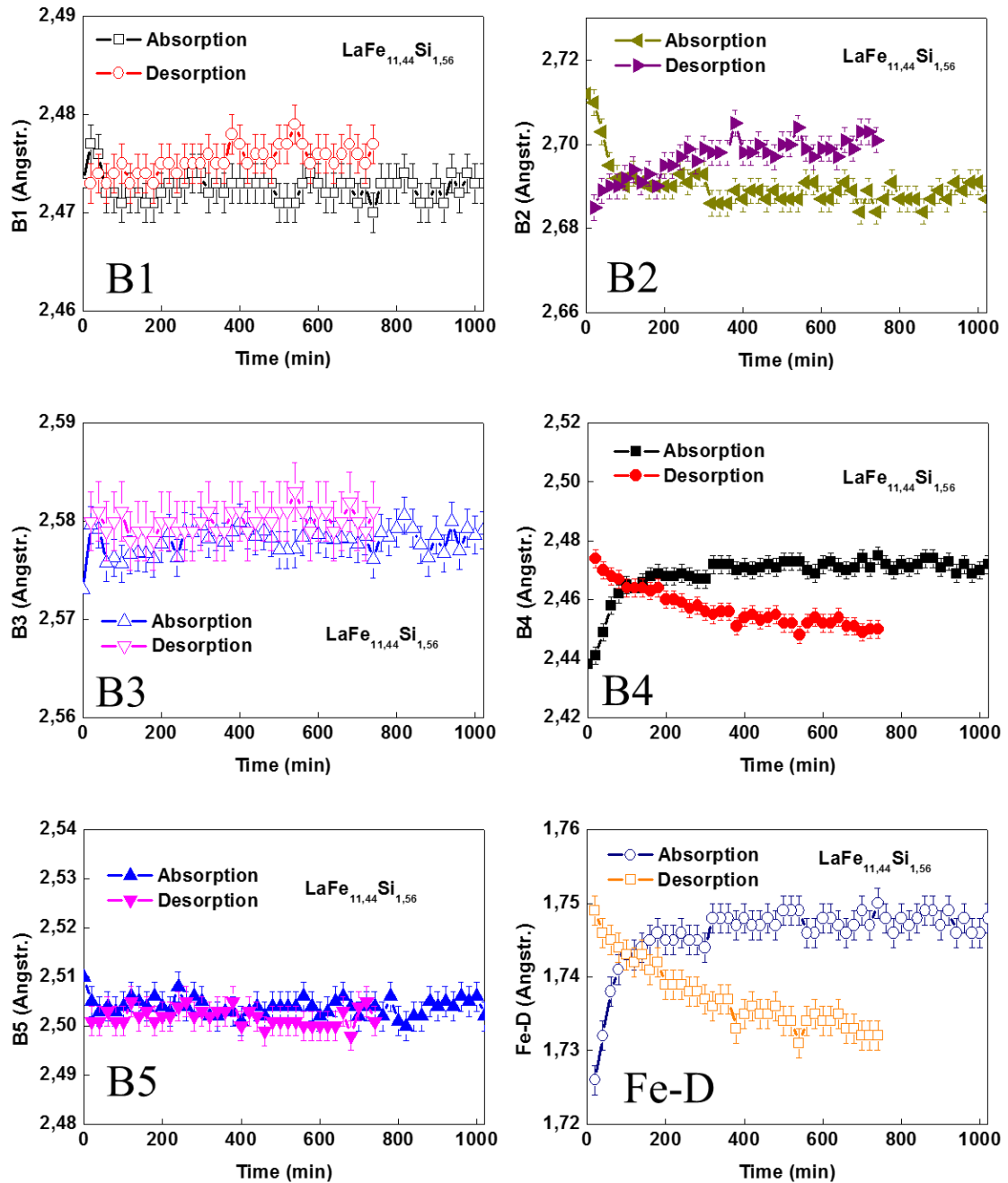


Figure V-14. Progression of selected interatomic bonds in the course of D absorption and desorption dynamics.

First of all, the $\text{La}(\text{Fe}_{1-x}\text{Si}_x)_{13}$ phase is not able to take in small atoms at the interstitial sites at room temperature and atmospheric pressure. Either elevated temperature or negative pressure (i.e. lattice expansion) is required to activate the absorption process.

As discussed in Chapter IV, H insertion induces particular intensity changes in the following reflections (2 0 0), (2 2 0), and (2 2 2). It seems like the H atoms preferentially diffuse along planes that are rich in metallic atoms rather than between these plans. This explains that the D diffusion involves principally the intra-icosahedron Fe-Fe bonds (B1, B2, B3). For an H/D interstitial atom to move to the next empty $24d$ site, it must pass through the bottleneck defined by the icosahedral network. The accommodation of light

atoms in the octahedral site is then achieved by a small reduction of the icosahedral volume.

The extension of the B4 Fe^{II}-Fe^{II} bond indicates the sequential filling of the interstitial site. In order to maintain the cubic NaZn₁₃-type structure, the structure imposes a limit in the capacity of extension. Therefore, the degree of modification of B4 is related to the maximum amount of light atoms (H_{\max} or D_{\max} , in this case) that the structure can take in before significant modification of the lattice (i.e., cubic to tetragonal). The most significant evolution of the interatomic bonds during absorption is shown as the reduction of the B2 bond and the extension of the B4.

As we switched the D₂ flux to He, the material experiences a drop in D₂ pressure and the pressure gradient drives the D atoms out of the structure. The desorption process is achieved by kicking H or D out of the interstitial site and then releasing from the 1:13 phase. This not only leads to a decrease in the interstitial site volume, indicated here by the contraction of B4, but also shows that it is necessary to open up the diffusion path in the opposite direction of the absorption process. We observe, therefore, an extension of the intra-icosahedron distances (B1, B2, and B3).

In the previous Chapter, we have observed the interatomic bond variation for sample of nominal composition LaFe_{11.7}Si_{1.3} and LaFe_{11.7}Si_{1.3}H_{1.3}. Hydrogenation results in a significant reduction of B2 and an extension of B4. This is consistent with interatomic distances analysis taken at room temperature for the 1:13 phase in the literature [13] [14] [15]. The refined interatomic distances show larger average intra-icosahedral bonds after hydrogenation. The two pairs of samples were measured in two neutron sources with different diffractometers and at different temperatures. Moreover, the nominal compositions are not identical. Further confirmation is necessary with *in-situ* neutron diffraction data for samples with different compositions at appropriate temperature and pressure conditions in order to propose a generalized mechanism. Nonetheless, the association of the reshaping of the (Fe,Si) icosahedra with interstitial insertion is confirmed.

1.5. Evaluation of the stability

The kinetics study is a very important approach to have better stability control. Certainly, there are direct ways of evaluating the H stability by addressing the two symptoms of instability mentioned in Chapter VI. The onset of the thermal desorption temperature indicates when the material starts to lose H atoms. Since desorption is an endothermic process, we are able to identify a variation in the heat flow by heating up the sample in Differential Scanning Calorimetry (DSC), as demonstrated in Figure V-15 (a). The heating rate was 5 K/min.

The onset is taken at where the two tangent lines meet at the change of baseline. In this example, two desorption peaks are visible, which is also observed in the work of Teixeira *et al.* [13]. In YFe₂-H Laves phases, the multi-plateau behavior in thermal desorption is considered from (1) different deuteride phases and (2) different interstitial sites. The work of Leblond *et al.* showed that this phenomenon is related to the phase diagram of the laves phase compound [8]. In Chapter IV, we have tried to identify different interstitial sites for H atoms but no evidence of a clear secondary tetrahedral site is seen. Hydrogen interstitials

do not form a hydride phase but rather stay within solid solution regime. In pure iron, the different hydrogen release peaks are attributed to trapped hydrogen being released from grain boundaries, dislocations, and microvoids [17]. Therefore, the multippeak desorption behavior in the $\text{La}(\text{Fe}_{1-x}\text{Si}_x)_{13}$ system is more likely to be related to the experimental sweeping rates or defects in the material acting as trapping sites.

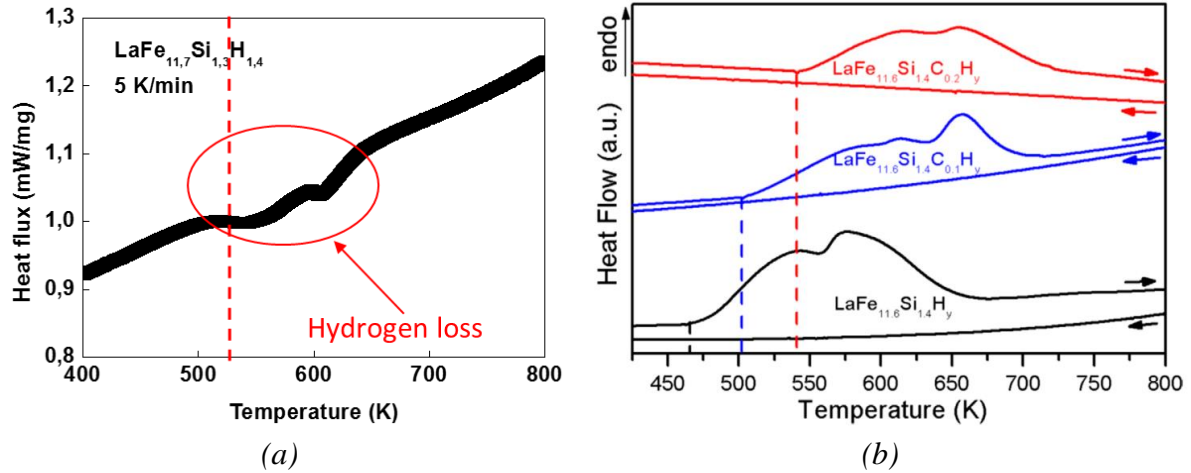


Figure V-15. Heat flux as a function of temperature showing H desorption peak measured in DSC for (a) sample $\text{LaFe}_{11.7}\text{Si}_{1.3}\text{H}_{1.4}$ and (b) figure taken from reference [13].

The Curie temperature of the specimen is controlled before and after thermal desorption to confirm the loss of H, which corresponds to a decrease in T_C . Age splitting can be directly observed by maintaining the material close to its T_C for various amounts of duration and measuring the T_C systematically after ageing. In this work, we focus on fully hydrogenated material and the stability improvement is, therefore, manifested by an increase in the onset of the desorption temperature.

1.6. Discussion

While the maximum absorption capacity is strongly dependent on the H_2 pressure, the kinetics is rather sensitive to the temperature. Moreover, the material composition plays an important role in the H absorption dynamics (Table V-2).

Table V-2. Maximum capacity of H absorption for intermetallic compound $\text{LaFe}_{13-x}\text{Si}_x$ at 523 K under an initial H_2 pressure of 1 MPa (last digit is significant).

Nominal composition	Maximum capacity at absorption H/f.u.
$\text{LaFe}_{11.44}\text{Si}_{1.56}$	1.1
$\text{LaFe}_{11.44}\text{Si}_{1.56}\text{C}_{0.2}$	0.8
$\text{LaFe}_{11.7}\text{Si}_{1.3}$	1.6
$\text{LaFe}_{11.7}\text{Si}_{1.3}\text{C}_{0.2}$	1.0
$\text{La}_{0.7}\text{Ce}_{0.3}\text{Fe}_{11.7}\text{Si}_{1.3}$	1.5
$\text{La}_{0.7}\text{Ce}_{0.3}\text{Fe}_{11.7}\text{Si}_{1.3}\text{C}_{0.2}$	1.0
$\text{La}_{0.7}\text{Ce}_{0.3}\text{Fe}_{11.44}\text{Mn}_{0.26}\text{Si}_{1.3}$	1.3
$\text{La}_{0.7}\text{Ce}_{0.3}\text{Fe}_{11.44}\text{Mn}_{0.26}\text{Si}_{1.3}\text{C}_{0.2}$	0.9

By engineering the chemical packing of the material, it is possible to modulate the hydrogenation behavior. The P-C-I curves show no sign of phase segregation due to the

formation of a hydride phase. The H sorption is under a solid solution regime with H diffusion as the dominating rate-controlling step. The $\text{LaFe}_{13-x}\text{Si}_x$ phase is not able to accommodate interstitial atoms at ambient temperature and pressure. We observe very fast kinetics above 523 K under H_2 pressure of 1 MPa. The absorption capacity of the intermetallic compound remains quite weak (< 1.6 H/f.u.) compared with other intermetallic compounds in the rare earth and transition metal family.

Composition substitution and interstitial insertion have direct consequences on the maximum absorption capacity. Other extrinsic parameters such as the presence of impurity phases might also influence the hydrogenation dynamics. From the mechanism deduced from *in-situ* neutron diffraction experiment at 540 K, H/D sorption involves a reduction of the intra-icosahedra bonds and an extension of the inter-icosahedral Fe-Fe distances. The maximum absorption capacity seems to be associated with the space available in the interstitial voids, whereas the kinetics of the reaction seems more related to the H diffusion path. In the following sections, we investigate the hydrogenation behavior of the 1:13 phase of compositions involving Ce-substitution and C-interstitials. Their impacts on the H sorption thermodynamics are discussed in terms of the icosahedra deformation.

2. Hydrogenation behavior with Ce substitution

2.1. *In-situ* Neutron diffraction

The experimental conditions for sample of composition $\text{La}_{0.7}\text{Ce}_{0.3}\text{Fe}_{11.44}\text{Si}_{1.56}$ were identical to those described in the previous section. The beam time available for absorption and desorption was slightly longer. The refined structural parameters and interatomic distances before absorption, at the end of absorption, and at the end of desorption are presented in Table V-3.

Table V-3. Refined structural parameters for sample $\text{La}_{0.7}\text{Ce}_{0.3}\text{Fe}_{11.44}\text{Si}_{1.56}$ before absorption, after 1020 min of absorption, and after 1320 min of desorption.

540 K	$\text{La}_{0.7}\text{Ce}_{0.3}\text{Fe}_{11.44}\text{Si}_{1.56}$	$\text{La}_{0.7}\text{Ce}_{0.3}\text{Fe}_{11.44}\text{Si}_{1.56}\text{D}_{0.8}$ 1020 min absorption	$\text{La}_{0.7}\text{Ce}_{0.3}\text{Fe}_{11.44}\text{Si}_{1.56}$ 1320 min desorption
$a=b=c$ (Å)	11.5138 (4)	11.5643 (3)	11.5196 (4)
site 96i (0, y, z) y	0.1794 (3)	0.1798 (3)	0.1821 (3)
site 96i (0, y, z) z	0.1188 (3)	0.1179 (3)	0.1218 (3)
Occupancy 24d	-	0.256 (2)	0.000 (3)
La/Ce-D (Å)	-	2.8911 (1)	-
Fe ⁹⁶ⁱ -D (Å)	-	1.723 (6)	-
B1 (Å)	2.477 (3)	2.492 (3)	2.524 (3)
B2 (Å)	2.736 (5)	2.741 (5)	2.806 (5)
B3 (Å)	2.574 (3)	2.591 (3)	2.618 (3)
B4 (Å)	2.426 (5)	2.437 (5)	2.363 (5)
B5 (Å)	2.527 (4)	2.526 (4)	2.527 (4)
χ^2	13.2	2.5	2.7
R_{Bragg} (%)	16.5	13.6	24.6
R_{f} (%)	12.7	12.1	36.1

Hydrogen absorption expands the Ce-substituted lattice. The reduction of B2 is not seen due to previous contraction of the lattice with Ce. After 1320 min of desorption, the intricosahedral distances are greatly extended. The opening of the H diffusion path facilitates in the emptying of the $24d$ site, as seen by the significant reduction of B4.

2.1.1. Kinetics

The progression of unit cell parameter and the $24d$ site occupancy is traced in the course of D insertion and release at 540 K (Figure V-16 and Figure V-17). At the end of the available absorption time, the specimen has taken in about 0.8 D/f.u. with Ce presence, slightly less than the Ce-free sample (1 D/f.u.). Considering the kinetics, there is a clear delay of the absorption dynamic due to Ce substitution. It takes sample $\text{La}_{0.7}\text{Ce}_{0.3}\text{Fe}_{11.44}\text{Si}_{1.56}$ twice as long to finish the first ramp of the unit cell expansion. We observe several changes of the slope for the progression of the lattice constant for $\text{La}_{0.7}\text{Ce}_{0.3}\text{Fe}_{11.44}\text{Si}_{1.56}$.

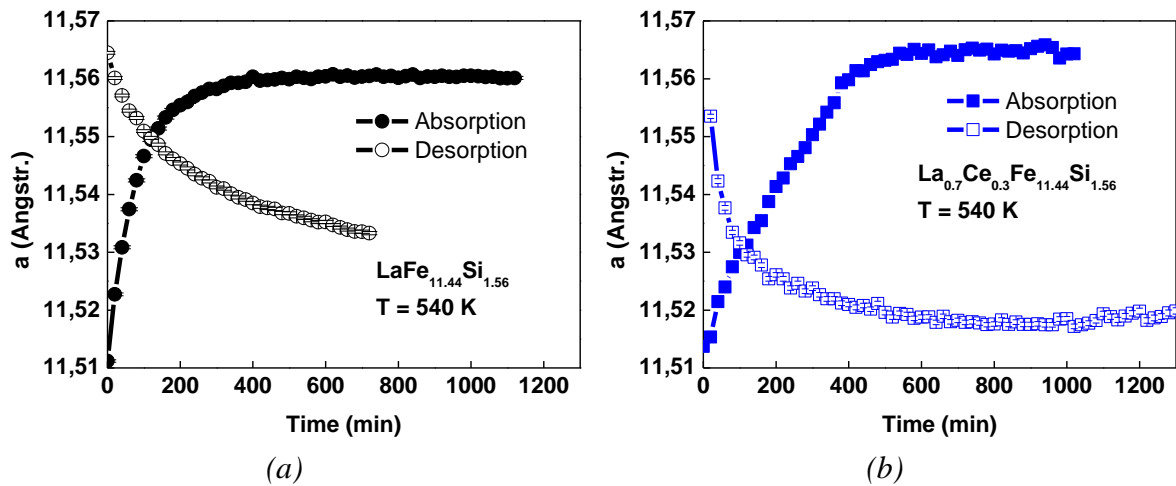


Figure V-16. Evolution of unit cell parameter for sample of composition $\text{LaFe}_{11.44}\text{Si}_{1.56}$ and $\text{La}_{0.7}\text{Ce}_{0.3}\text{Fe}_{11.44}\text{Si}_{1.56}$ versus time, results obtained from Rietveld refinement of neutron diffraction patterns.

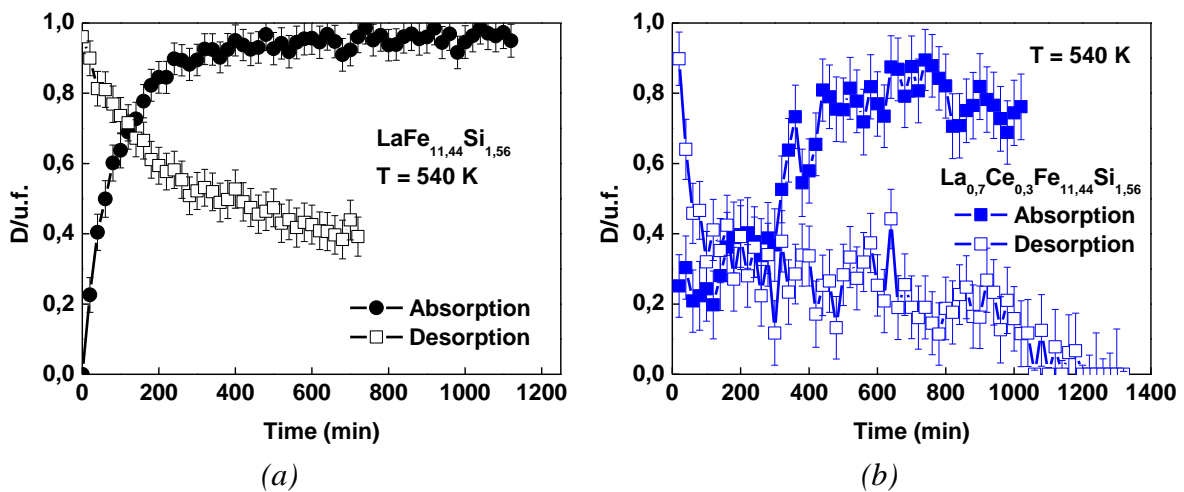


Figure V-17. Concentration of D interstitials during absorption and desorption for compound $\text{LaFe}_{11.44}\text{Si}_{1.56}$ and $\text{La}_{0.7}\text{Ce}_{0.3}\text{Fe}_{11.44}\text{Si}_{1.56}$ versus time.

The effect is even more evident by examining the D content per formula unit deduced from the $24d$ occupancy (Figure V-17). While the lattice constant increases continuously to make room for interstitial atoms, the sequential filling of the octahedral site is not continuous, rather step-like for $\text{La}_{0.7}\text{Ce}_{0.3}\text{Fe}_{11.44}\text{Si}_{1.56}$. The evolution of the two parameters is not as correlated as one would expect from a simple model.

This disparity between the unit cell parameter and the site occupancy is confirmed by modeling with KJMA relation. Unlike sample $\text{LaFe}_{11.44}\text{Si}_{1.56}$ and $\text{LaFe}_{11.44}\text{Si}_{1.56}\text{C}_{0.2}$, the calculated Avrami exponent n is 1.2 for the kinetics of unit cell expansion and 0.5 for that of interstitial filling. This underlines very different mechanisms for the evolution of these two parameters in reaction. Upon desorption, the releasing of D atoms is almost instantaneous for Ce-substituted specimen, showing a much faster desorption kinetics than that for compound $\text{LaFe}_{11.44}\text{Si}_{1.56}$. The mechanical strain from D absorption can partially contribute to the accelerated desorption kinetics in Ce-substituted sample as the lattice has a smaller volume due to Ce substitution. But as seen in Table V-3, the lattice at 540 K is thermally expanded for both the Ce-free and Ce-substituted samples. The strain accumulation and release during absorption and desorption is a secondary factor. It is more important to consider that Ce substitution modifies the D diffusion path by a selective contraction of certain interatomic distances (Section 2.1.2). Desorption is nearly complete for sample $\text{La}_{0.7}\text{Ce}_{0.3}\text{Fe}_{11.44}\text{Si}_{1.56}$, as shown in Figure V-17 (b). This suggests the important role of diffusion path on the facility to release interstitial atoms.

2.1.2. Interatomic distances

Figure V-18 shows the evolution of the intra-icosahedral bonds and B4 during absorption and desorption. In the first 200 min, the structure stretches the (Fe/Si) icosahedral cluster while reducing B4, which corresponds to an initial lattice rearrangement and the opening of the D diffusion path. We refer to this period as an incubation stage for absorption. From 200 to 600 min, there is an accelerated absorption stage where D concentration jumps from 0.4 to 0.8 D/f.u. The mechanism at this stage is similar the classical D absorption mechanism observed for samples of composition $\text{LaFe}_{11.44}\text{Si}_{1.56}$ [15] under the same experimental conditions: a reduction of the intra-icosahedral bonds and an increase of the inter-icosahedral bonds.

Desorption is proceeded with the increase of the intra-icosahedral bonds and a decrease of the inter-icosahedral bonds, notably B4. After 1000 min of desorption, we suspect an emptying of the interstitial site due to the large deviation of interatomic distances. However, by measuring the Curie temperature of the sample after neutron diffraction, it is confirmed that there are still remaining D atoms in the lattice as T_C is higher than that of the annealed sample. The remaining D content at desorption stage is quite small and the dispersive nature of D atoms can be challenging for the refinements.

It is possible that there are critical distances beyond which the repulsion force within the interstitial site is too strong to hold interstitial atoms. In this case further investigations are necessary in order to focus more on the end of the desorption scheme for Ce-substituted sample. In order to study the thermal desorption of residual D atoms, samples after in-beam desorption were heated up in DSC and details are presented in Section 3.2.3.1.

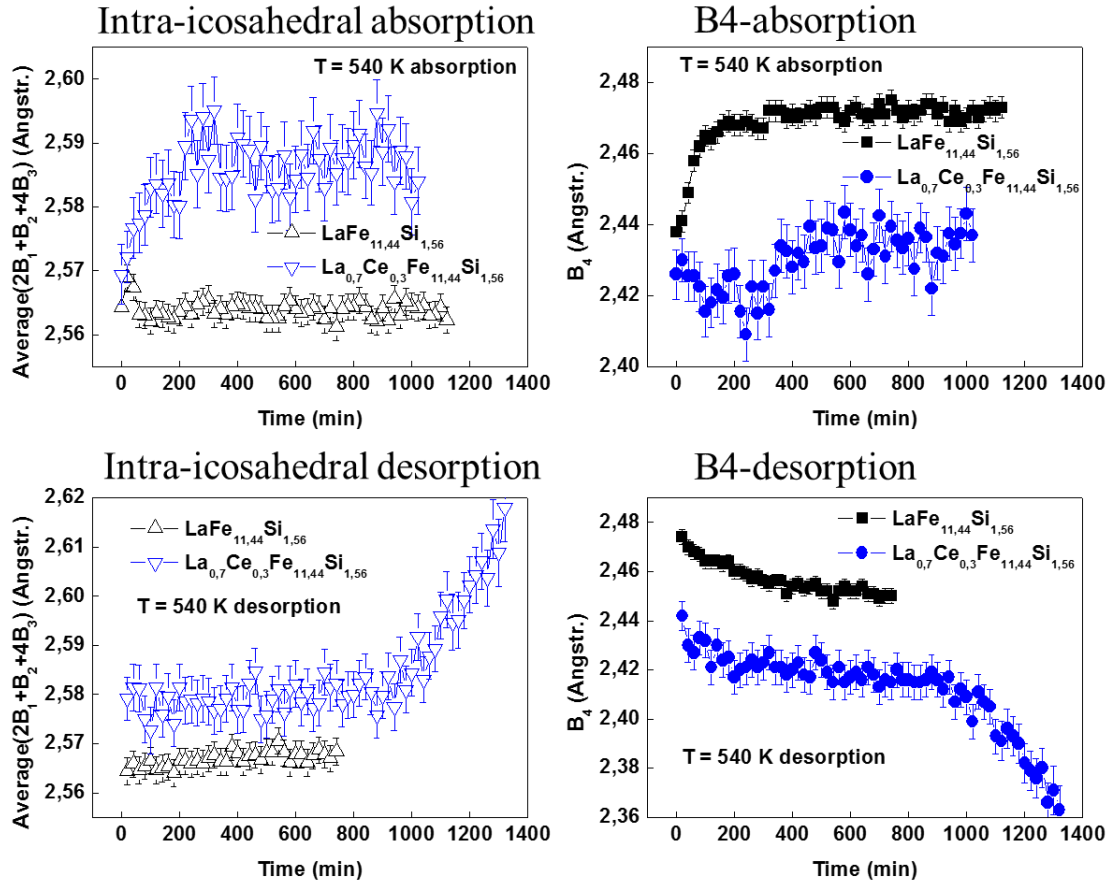


Figure V-18. Evolution of Fe-Fe distances in the course of absorption and desorption.

3. Hydrogenation behavior with C insertion

3.1. Effect of carbon insertion on La-Fe-Si

3.1.1. Pressure-composition isotherms

In Chapter IV, we have shown the double interstitial occupancy of C and H at $24d$. Carbon insertion offers a prospect to stabilize H in the $\text{LaFe}_{13-x}\text{Si}_x$ phase. In order to follow the effect of C on the H sorption mechanism, we have measured the P-C-I for sample $\text{LaFe}_{11.7}\text{Si}_{1.3}\text{C}_{0.2}$ and the result is presented in Figure V-19.

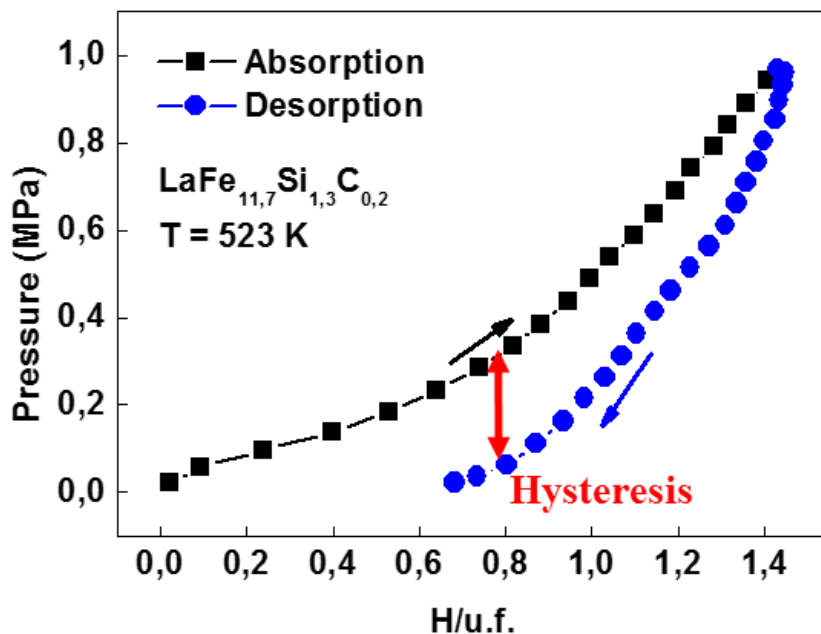


Figure V-19. Variation of H content with pressure for sample $\text{LaFe}_{11.7}\text{Si}_{1.3}\text{C}_{0.2}$ measured at 520 K in absorbing and releasing processes.

A few characteristics are similar to those of sample $\text{LaFe}_{11.7}\text{Si}_{1.3}$:

- The absorption begins directly with a narrow plateau.
- After the plateau, H content increases significantly with the pressure. The maximum absorption capacity is around 1.4 H/f.u. at 523 K.
- The desorption curve lags behind the absorption one, which indicates mechanical strain in the lattice.
- Desorption is not complete within the detectable pressure range.

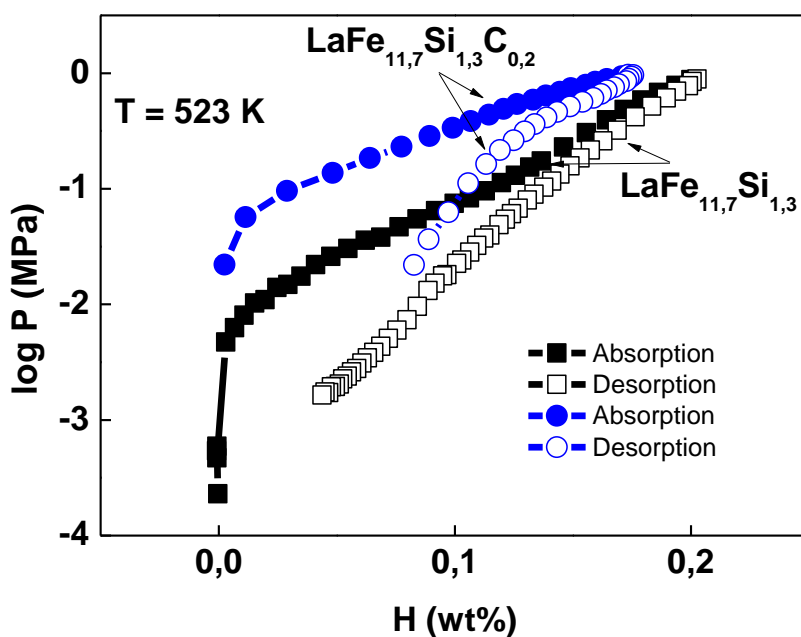


Figure V-20. Variation of H partial pressure as a function of H concentration for sample $\text{LaFe}_{11.7}\text{Si}_{1.3}$ and $\text{LaFe}_{11.7}\text{Si}_{1.3}\text{C}_{0.2}$ measured at 523 K in absorbing and releasing processes.

The influence of C on the H sorption thermodynamics is shown by comparing the H content variation with pressure (Figure V-20). At 523 K under 1 MPa H₂ pressure, the maximum absorption capacity for sample LaFe_{11.7}Si_{1.3}C_{0.2} is around 1.4 H/f.u., slightly inferior to the C-free sample. This can be partially explained by the amount of available space in the octahedral site occupancy. Under given pressure, sample LaFe_{11.7}Si_{1.3}C_{0.2} shows larger hysteresis between the absorption and desorption processes. Zhao *et al.* [16] have reported the variation of H content with pressure for La_{0.7}Pr_{0.3}Fe_{11.5}Si_{1.5} and La_{0.7}Pr_{0.3}Fe_{11.5}Si_{1.5}C_{0.2} samples at 623 K. They have observed a lagging H releasing process in La_{0.7}Pr_{0.3}Fe_{11.5}Si_{1.5}C_{0.2} behind the absorption process, which is in good agreement with our results. The remaining H content after desorption is about 1.5 times more than that in C-free compound [16].

3.1.2. Sieverts' method

As mentioned in Section 1.3, Si concentration has a noticeable influence on the hydrogenation process. Therefore, in order to understand the changes on the H sorption dynamics with C doping, we consider two separate cases with different Si concentrations ($x_{Si}=1.3$ and 1.56) to illustrate the effect. In order to verify the evolution of reaction kinetics in response to varying pressure at constant temperature. A study on the influence of pressure was carried out for sample LaFe_{11.7}Si_{1.3}C_{0.2} as well, the details are presented in Appendix E. The influence of temperature on the H sorption dynamics is shown in this section for the two samples with different Si concentrations.

3.1.2.1. Low-Si case ($x_{Si}=1.3$): influence of temperature

Temperature influences primarily the reaction kinetics. At constant pressure, the absorption capacity for LaFe_{11.7}Si_{1.3}C_{0.2} remains rather stable, as shown in the maximum H absorption capacity and remaining H content after desorption in Table V-4.

Table V-4. The maximum H absorption capacity and the retaining H capacity at desorption with different temperature for sample LaFe_{11.7}Si_{1.3}C_{0.2} (last digit is significant).

Temperature (K)	Maximum capacity at absorption H/f.u.	Remaining H at desorption H/f.u.
433	1.1	1.0
483	1.1	1.0
523	1.0	0.9
573	0.9	0.7
623	0.9	0.4

At elevated temperature, the high mobility of H leads to reduced maximum absorption capacity. The increased diffusion rate at high temperature facilitates the releasing of H atoms, as can be seen from Figure V-21 (b), the H release is more exhaustive with increasing temperature.

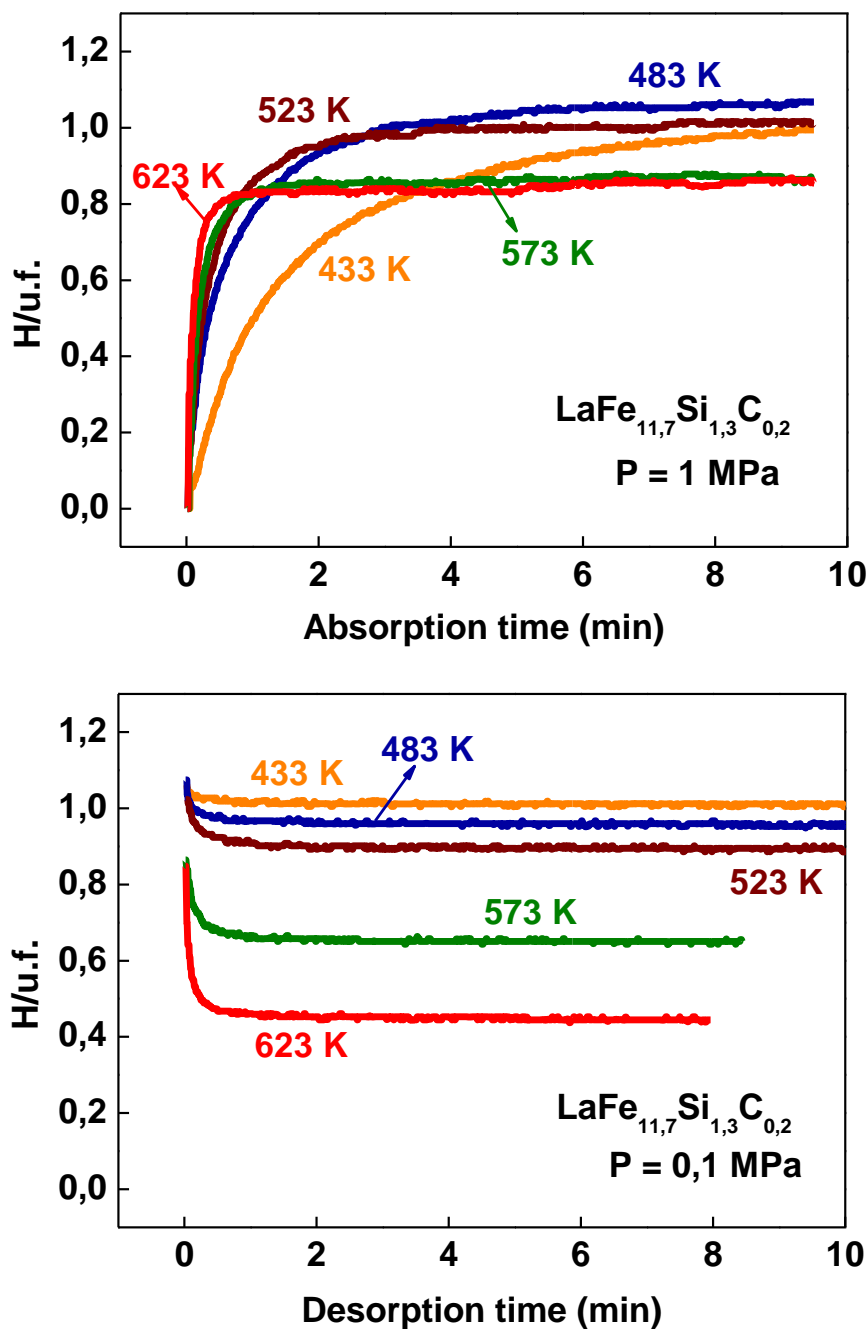


Figure V-21. Hydrogen (top) absorption and (bottom) desorption measurement of $\text{LaFe}_{11.7}\text{Si}_{1.3}\text{C}_{0.2}$ at different temperatures.

The Avrami exponent varies from 1 to 0.65 for absorption and from 0.4 to 0.7 for desorption. The value $n=1$ is chosen to compare k . Based on the slope of the Arrhenius plots (Figure V-22 (b)), the activation energy of $\text{LaFe}_{11.7}\text{Si}_{1.3}\text{C}_{0.2}$ for H absorption at 1 MPa is 39 kJ/mol H_2 . This value is smaller than the E_a for the C-free sample (59 kJ/mol H_2) for the same conditions. This can be related to the lattice expansion after C insertion, which might facilitate hydrogenation. The constant k_0 of $\text{LaFe}_{11.7}\text{Si}_{1.3}\text{C}_{0.2}$ is one order of magnitude smaller than sample $\text{LaFe}_{11.7}\text{Si}_{1.3}$. In the low-Si case, C-free sample shows slower absorption kinetics.

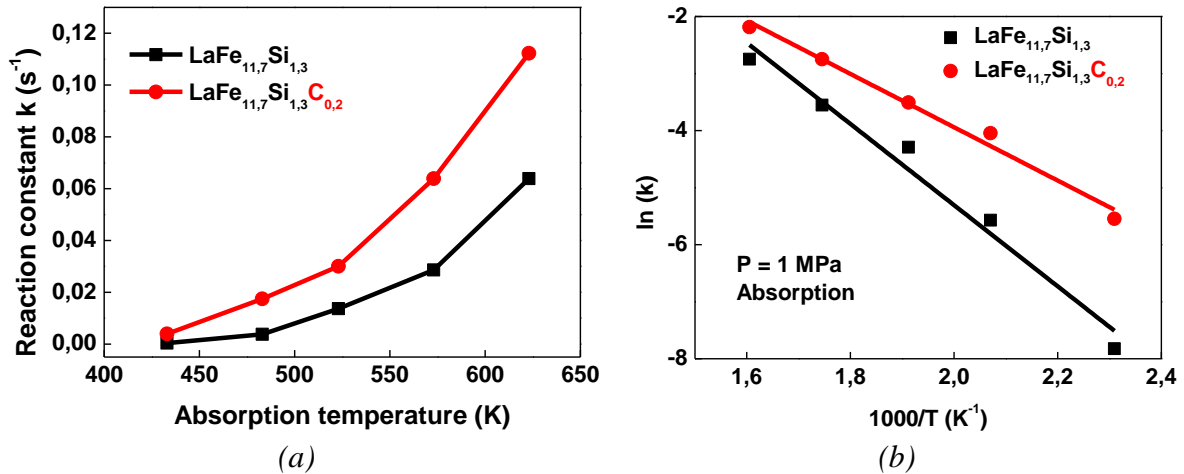


Figure V-22. Determination of k_0 and E_a from linearization of the measured kinetics of absorptions at different temperatures at 1 MPa for compound $\text{LaFe}_{11.7}\text{Si}_{1.3}\text{C}_{0.2}$.

3.1.2.2. High-Si case ($x_{\text{Si}}=1.56$): influence of temperature

For sample $\text{LaFe}_{11.44}\text{Si}_{1.56}\text{C}_{0.2}$, the H absorption kinetics is shown in Figure V-23 (a). The reaction kinetics increases with increasing temperature. The maximum H concentration at absorption is around 0.8-0.9 H/f.u. at all the measuring temperatures. Figure V-23 (b) compares the reaction constant of sample $\text{LaFe}_{11.44}\text{Si}_{1.56}$ and $\text{LaFe}_{11.44}\text{Si}_{1.56}\text{C}_{0.2}$. The absorption kinetics is clearly delayed in carbonated sample. At 433 K, it takes the sample $\text{LaFe}_{11.44}\text{Si}_{1.56}\text{C}_{0.2}$ twice as long (about 4 hours) to reach its full H absorption capacity. Moreover, the last 10% of the reaction (not shown here) is not as smooth as for the C-free sample. The H content varies $\pm 1\%$ continuously.

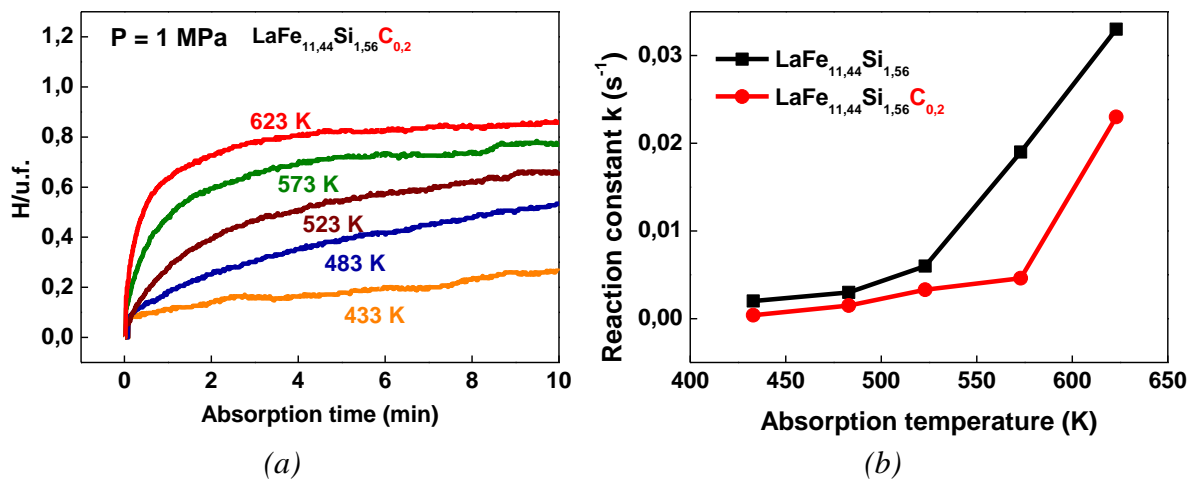


Figure V-23. H absorption kinetics at 1 MPa at different temperatures for compound $\text{LaFe}_{11.44}\text{Si}_{1.56}\text{C}_{0.2}$.

The activation energy of sample $\text{LaFe}_{11.44}\text{Si}_{1.56}\text{C}_{0.2}$ is 44 kJ/mol H_2 for 1 MPa applied H_2 pressure (slope in Figure V-24), which is higher than that of sample $\text{LaFe}_{11.44}\text{Si}_{1.56}$. The constant k_0 is twice as large as that of the C-free sample $\text{LaFe}_{11.44}\text{Si}_{1.56}$. This can be associated with the lattice contraction with Si partial substitution and the lattice expansion with C interstitials. The two competing forces result in modified energy state before hydrogenation.

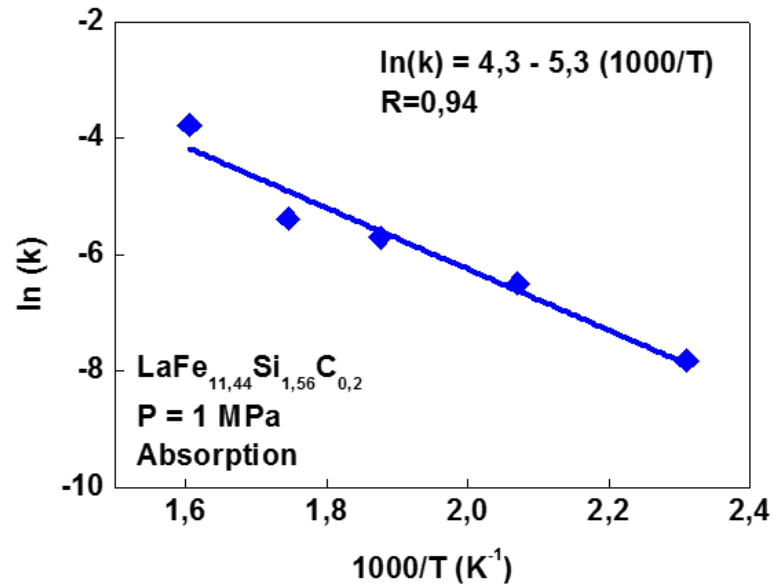


Figure V-24. Determination of k_0 and E_a from linearization of the measured kinetics of absorptions at different temperatures at 1 MPa for compound $\text{LaFe}_{11.44}\text{Si}_{1.56}\text{C}_{0.2}$.

The desorption kinetics at various temperatures is shown in Figure V-25. Hydrogen release takes place as soon as the partial H pressure drops. Elevated temperature contributes to the acceleration of desorption kinetics and the amount of released H.

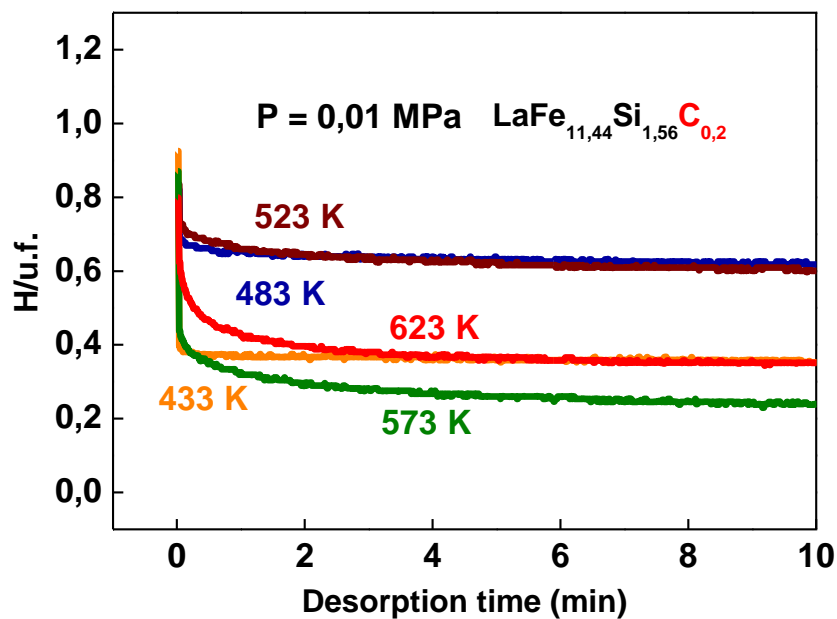


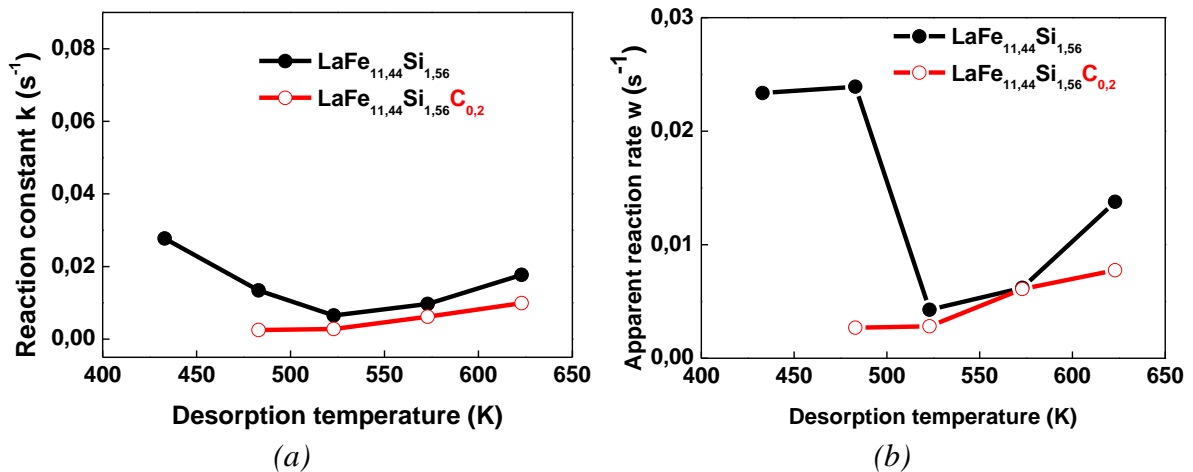
Figure V-25. H desorption kinetics at 0.01 MPa at different temperatures for compound $\text{LaFe}_{11.44}\text{Si}_{1.56}\text{C}_{0.2}$.

The maximum H absorption capacity and the remaining H after desorption are listed in Table V-5. The maximum H loss occurs at 573 K for sample $\text{LaFe}_{11.44}\text{Si}_{1.56}\text{C}_{0.2}$ (-75%). Temperature has significant effects on the thermal stability of hydrogenated samples, while its influence on the maximum amount of H at absorption is less dramatic.

Table V-5. The maximum H absorption capacity and the retaining H capacity at desorption at different temperatures for sample $\text{LaFe}_{11.44}\text{Si}_{1.56}\text{C}_{0.2}$.

Temperature (K)	Maximum capacity at absorption H/f.u.	Retaining capacity at desorption H/f.u.
433	0.9	0.4
483	0.8	0.6
523	0.8	0.6
573	0.9	0.2
623	0.80	0.3

The desorption kinetics is too fast to be modelled with the KJMA relation. Figure V-26 compares the reaction rate constant k from KJMA relation ($n=1$) and the defined apparent rate of reaction, w_{90} for sample $\text{LaFe}_{11.44}\text{Si}_{1.56}$ and $\text{LaFe}_{11.44}\text{Si}_{1.56}\text{C}_{0.2}$. In this sample, the thermal stability of hydrogenated $\text{LaFe}_{11.44}\text{Si}_{1.56}\text{C}_{0.2}$ is particularly low. At 433 K, H releasing is extremely fast that it is difficult to correctly measure the first minutes of desorption. The reaction constant k at this temperature was carefully removed from analysis in Figure V-26 in order to avoid unrealistic conclusion. The effect of C insertion on the desorption kinetics is difficult to conclude from Figure V-26. In Section 3.1.3, in-situ neutron diffraction data is analyzed to give more insight in this aspect.

Figure V-26. Rate of desorption reaction calculated in two different manners for sample $\text{LaFe}_{11.44}\text{Si}_{1.56}$ and $\text{LaFe}_{11.44}\text{Si}_{1.56}\text{C}_{0.2}$.

3.1.2.3. Discussion

From the previous discussions, we have seen that C insertion influences the hydrogenation dynamics of La-Fe-Si compounds in different manners in the two examples containing different Si contents ($x_{\text{Si}}=1.3$ and $x_{\text{Si}}=1.56$). Both Si and C are p -electron elements, but they do not affect the absorption and desorption of H interstitials in the lattice in the same way. This indicates that the H sorption dynamics is very sensitive to the local environment. The mobility and diffusivity of H atoms are associated with the nature of the neighboring elements, their atomic positions, the structure building units they are associated with, and how these neighbors are reshaping the structural environment.

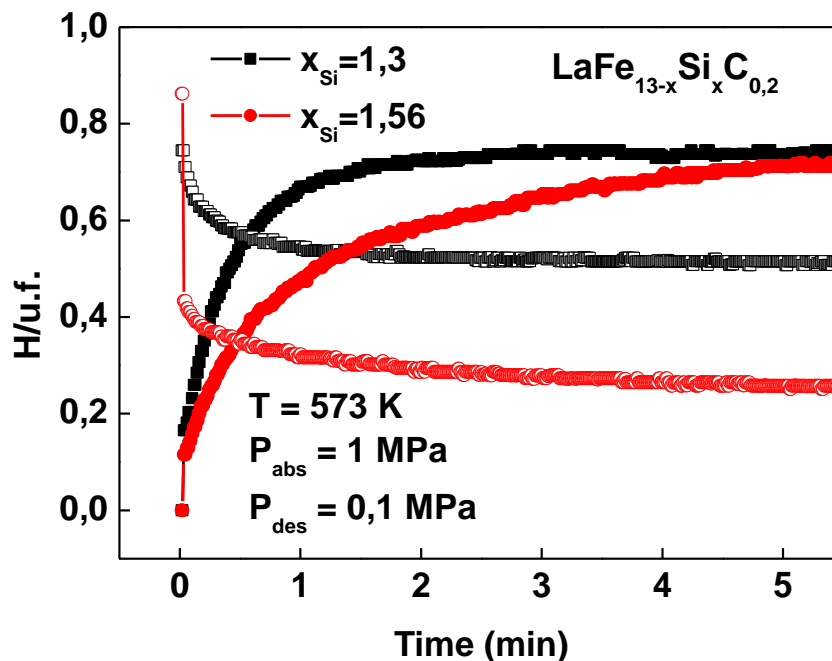


Figure V-27. Absorption-desorption kinetics for specimen $\text{LaFe}_{11,7}\text{Si}_{1,3}\text{C}_{0,2}$ and $\text{LaFe}_{11,44}\text{Si}_{1,56}\text{C}_{0,2}$ at 573 K with the same H_2 pressure.

Figure V-27 compares the two carbonated samples with different Si contents at 573 K. Si-rich sample shows considerably delayed absorption kinetics and sharp H loss at the desorption stage. This is associated with how Si element modulates the structure and the interatomic distances. Nonetheless, in order to confirm the effect of Si on the hydrogenation behavior of the La-Fe-Si phase, *in-situ* neutron diffraction on samples with different Si concentrations should be performed. Within the frame of this work, the effect of Si is only discussed based on measurements from the Sieverts' apparatus.

3.1.3. Neutron diffraction

From the Sieverts-type measurements, C insertion in sample $\text{LaFe}_{11,44}\text{Si}_{1,56}$ leads to delayed absorption kinetics. Due to the complexity of the H sorption in the La-Fe-Si phase, *in-situ* neutron diffraction is employed to provide more insights on the local characteristics in the lattice.

Table V-6 shows the refined structural parameters and interatomic distances for samples $\text{LaFe}_{11,44}\text{Si}_{1,56}$ and $\text{LaFe}_{11,44}\text{Si}_{1,56}\text{C}_{0,2}$ at 540 K. At this temperature, the lattice is already well extended by thermal expansion, yet a remarkable volume expansion (+1.1%) can still be seen for sample of composition $\text{LaFe}_{11,44}\text{Si}_{1,56}\text{C}_{0,2}$ compared to $\text{LaFe}_{11,44}\text{Si}_{1,56}$. In terms of interatomic distances, the carbonated sample has shorter intra-icosahedral bonds and longer connections between neighboring icosahedra. Carbon insertion leads to a reduction of B2 and an elongation of B4, similar to the effect of H insertion.

Table V-6. Refined cell parameters and interatomic distances for $\text{LaFe}_{11.44}\text{Si}_{1.56}$ and $\text{LaFe}_{11.44}\text{Si}_{1.56}\text{C}_{0.2}$ from neutron powder diffraction at the D1B diffractometer in ILL at 540 K.

540 K	$\text{LaFe}_{11.44}\text{Si}_{1.56}$	$\text{LaFe}_{11.44}\text{Si}_{1.56}\text{C}_{0.2}$
$a=b=c$ (Å)	11.5112 (2)	11.5489 (3)
site $96i$ (0, y, z) y	0.1796 (2)	0.1782 (2)
site $96i$ (0, y, z) z	0.1175 (2)	0.1166 (3)
Occupancy $24d$	-	0.056 (2)
B1 (Å)	2.473 (2)	2.459 (3)
B2 (Å)	2.712 (3)	2.693 (5)
B3 (Å)	2.573 (2)	2.560 (3)
B4 (Å)	2.438 (3)	2.474 (5)
B5 (Å)	2.510 (2)	2.525 (4)
$\text{Fe}^{96i}\text{-C}$ (Å)	-	1.750 (3)
χ^2	1030	354
R_{Bragg} (%)	9.6	9.9
R_{F} (%)	9.6	9.0

3.1.4. Kinetics

Figure V-28 shows the evolution of the lattice constant and D concentration deduced from the $24d$ site occupancy for sample $\text{LaFe}_{11.44}\text{Si}_{1.56}\text{C}_{0.2}$. The absorption Avrami exponent n is 1.2 for describing the unit cell expansion and 1.5 for interstitial occupancy. These values confirm the one-to-one relationship between the lattice breathing and the uptake in D atoms. Carbon tuning does not change this mechanism. Interestingly, the unit cell parameter continues to expand towards the end of the absorption timeline, though D content remains steady.

The absorption and desorption reactions are followed by the inflation and deflation of the lattice. For the desorption scheme, it can be seen that equilibrium is not achieved after 400 min. The partial pressure drop pushes out about half of the D atoms and 0.4 D/f.u. remains. The contraction of the unit cell is gradual yet uninterrupted, while the movement of D atoms in the interstitial site is abrupt at first and stabilizes within the last 200 min.

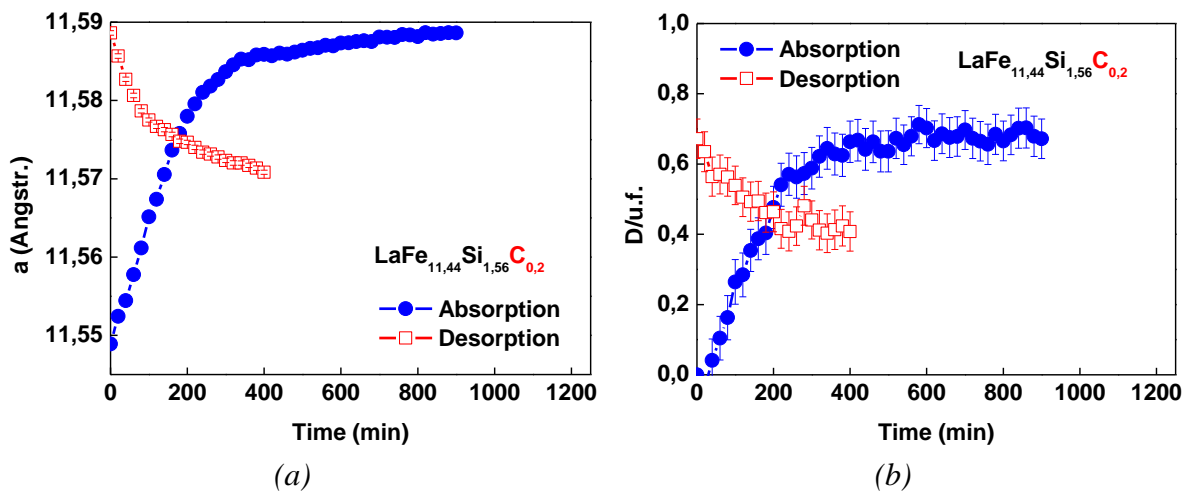


Figure V-28. Evolution of unit cell parameter and $24d$ site occupancy (occupancy due to C is already taken into account) for sample $\text{LaFe}_{11.44}\text{Si}_{1.56}\text{C}_{0.2}$, results obtained from Rietveld refinement of neutron diffraction patterns.

A comparison between sample $\text{LaFe}_{11,44}\text{Si}_{1,56}$ and $\text{LaFe}_{11,44}\text{Si}_{1,56}\text{C}_{0,2}$ in the course of absorption is presented in Figure V-29. The maximum D concentration at absorption is 0.7 D/f.u., smaller than that for $\text{LaFe}_{11,44}\text{Si}_{1,56}$ (1 D/f.u.). Neutron diffraction confirms the slowed absorption kinetics after C insertion.

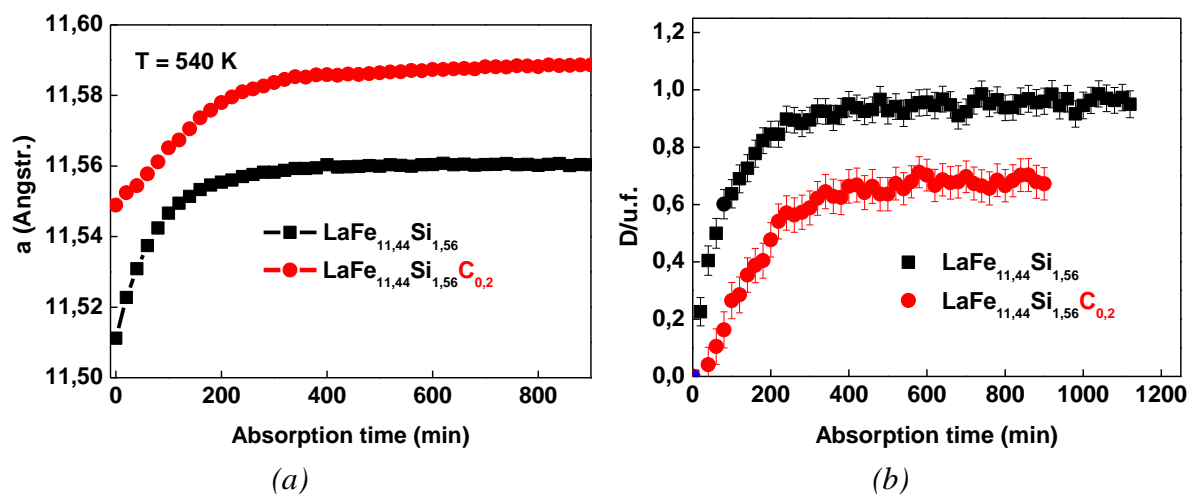


Figure V-29. Kinetics comparison for sample $\text{LaFe}_{11,44}\text{Si}_{1,56}$ and $\text{LaFe}_{11,44}\text{Si}_{1,56}\text{C}_{0,2}$, indicated by (a) the unit cell expansion, (b) increase in deuterium atoms in the octahedral sites (occupancy due to C is already taken into account), both from Rietveld refinement of neutron data.

3.1.5. Interatomic distances

Table V-7. Refined structural parameters and interatomic distances for $\text{LaFe}_{11,44}\text{Si}_{1,56}$, at the end of absorption, and at the end of desorption reaction at 540 K.

540 K	$\text{LaFe}_{11,44}\text{Si}_{1,56}\text{C}_{0,2}$	$\text{LaFe}_{11,44}\text{Si}_{1,56}\text{C}_{0,2}\text{D}_{0,7}$	$\text{LaFe}_{11,44}\text{Si}_{1,56}\text{C}_{0,2}\text{D}_{0,4}$
$\alpha=b=c$ (Å)	11.5489 (3)	11.5886 (3)	11.5708 (3)
site $96i$ (0, y, z) y	0.1782 (2)	0.1793 (2)	0.1793 (2)
site $96i$ (0, y, z) z	0.1166 (3)	0.1148 (3)	0.1160 (2)
Occupancy $24d$	0.056 (1) C	0.056 C + 0.224 (3) D	0.056 C + 0.136 (2) D
B1 (Å)	2.459 (3)	2.467 (3)	2.471 (2)
B2 (Å)	2.693 (5)	2.661 (5)	2.684 (3)
B3 (Å)	2.560 (3)	2.578 (3)	2.577 (3)
B4 (Å)	2.474 (5)	2.500 (5)	2.479 (3)
B5 (Å)	2.525 (4)	2.495 (3)	2.506 (3)
La-C/D (Å)	2.887 (1)	2.897 (1)	2.893 (1)
Fe-C/D (Å)	1.750 (1)	1.768 (1)	1.753 (1)
χ^2	354	12.1	10.6
R_{Bragg} (%)	9.9	10.7	9.3
R_{F} (%)	9.0	8.6	8.4

Detailed structural parameters after refinement can be found Table V-7. Absorption is driven by the contraction of B2 and expansion of B4 whereas desorption is achieved by the reversal process, as shown in Figure V-30. Carbon addition prior to D insertion does not modify the sorption mechanism.

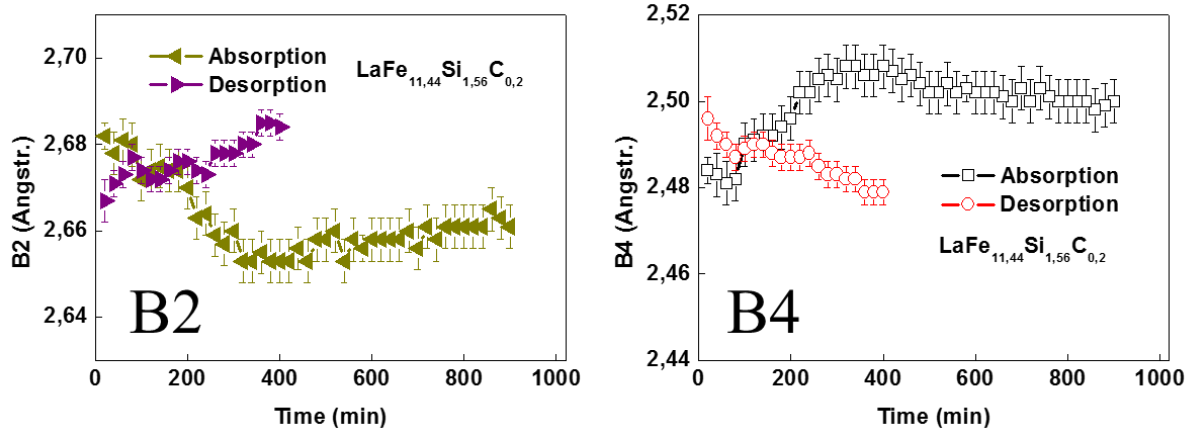


Figure V-30. Evolution of B2 and B4 Fe^{II}-Fe^{II} distances during absorption and desorption for sample LaFe_{11.44}Si_{1.56}C_{0.2}.

The preserved structural breathing mechanism can be further illustrated by comparing interatomic distances for LaFe_{11.44}Si_{1.56} and LaFe_{11.44}Si_{1.56}C_{0.2} at the end of the absorption reactions (Table V-8). Deuterium insertion for sample of composition LaFe_{11.44}Si_{1.56}C_{0.2} follows the same progression of all interatomic distances with further stretched lattice.

Table V-8. Refined structural parameters and interatomic distances for LaFe_{11.44}Si_{1.56} and LaFe_{11.44}Si_{1.56}C_{0.2} at the end of the absorption reaction.

540 K	LaFe _{11.44} Si _{1.56}	LaFe _{11.44} Si _{1.56} D _{0.96}	LaFe _{11.44} Si _{1.56} C _{0.2} D _{0.72}
$a=b=c$ (Å)	11.5112 (2)	11.5604 (2)	11.5886 (3)
site $96i$ (0, y, z) y	0.1796 (2)	0.1793 (2)	0.1793 (2)
site $96i$ (0, y, z) z	0.1175 (2)	0.1162 (2)	0.1148 (3)
Occupancy $24d$	0	0.320 (1) D	0.056 C + 0.224 (3) D
B1 (Å)	2.473 (2)	2.470 (2)	2.467 (3)
B2 (Å)	2.712 (3)	2.688 (3)	2.661 (5)
B3 (Å)	2.573 (2)	2.575 (2)	2.578 (3)
B4 (Å)	2.438 (3)	2.474 (3)	2.500 (5)
B5 (Å)	2.510 (2)	2.507 (3)	2.495 (3)
La-C/D (Å)	-	2.890 (1)	2.897 (1)
Fe-C/D (Å)	-	1.749 (1)	1.768 (1)
χ^2	1030	7.2	12.1
R _{Bragg} (%)	9.6	8.8	10.7
R _F (%)	9.6	7.9	8.6

Although C insertion does not modify the general mechanism for the structural breathing during absorption, it does modulate significantly the absorption kinetics. For the C-doped sample, the changes in interatomic distances are accentuated and the stabilization arrives much later than for the C-free sample (Figure V-31). For desorption, C doping preserves the classical mechanism, too. The structure releases D atoms by contracting the basal plane of the octahedral site and extending isotropically the Fe^{II} icosahedron volume.

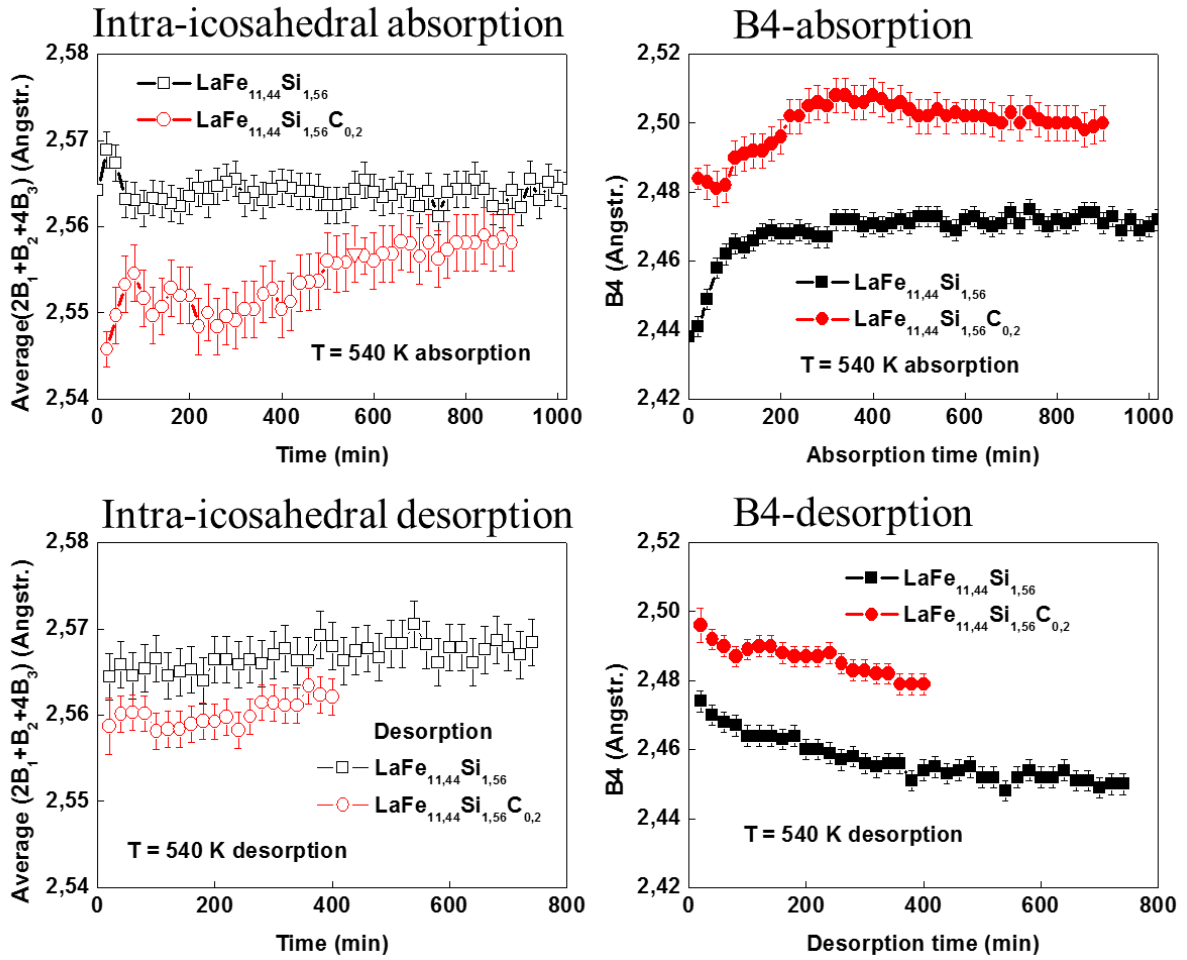


Figure V-31. Evolution of intra-icosahedral bonds and B4 distance in the course of absorption for sample $\text{LaFe}_{11.44}\text{Si}_{1.56}$ and $\text{LaFe}_{11.44}\text{Si}_{1.56}\text{C}_{0.2}$ at 540 K.

3.2. Effect of C insertion in Ce-substituted samples

Ce substitution modifies the interstitial site volume and leads to particular hydrogenation behavior. However, C insertion does not modify the D insertion mechanism and the structural modulation upon D introduction remains the same. Therefore, it is interesting to investigate the impact of C on the D sorption dynamics of Ce-substituted sample.

3.2.1. Neutron diffraction

For Ce-substituted sample of composition $\text{La}_{0.7}\text{Ce}_{0.3}\text{Fe}_{11.44}\text{Si}_{1.56}\text{C}_{0.2}$, small C doping increases the lattice volume at 540 K by 0.5%, as shown in Table V-9. This indicates that although the Ce-substituted sample has increased difficulty in D absorption, the incorporation of 0.2 C/f.u. interstitials has succeeded through induction melting for sample $\text{La}_{0.7}\text{Ce}_{0.3}\text{Fe}_{11.44}\text{Si}_{1.56}\text{C}_{0.2}$.

Table V-9. Refined cell parameters and interatomic distances for $\text{La}_{0.7}\text{Ce}_{0.3}\text{Fe}_{11.44}\text{Si}_{1.56}$ and $\text{La}_{0.7}\text{Ce}_{0.3}\text{Fe}_{11.44}\text{Si}_{1.56}\text{C}_{0.2}$ from neutron powder diffraction at the D1B diffractometer in ILL at 540 K.

540 K	$\text{La}_{0.7}\text{Ce}_{0.3}\text{Fe}_{11.44}\text{Si}_{1.56}$	$\text{La}_{0.7}\text{Ce}_{0.3}\text{Fe}_{11.44}\text{Si}_{1.56}\text{C}_{0.2}$
$\alpha=b=c$ (Å)	11.5138 (4)	11.5339 (3)
site 96i (0, y, z) y	0.1794 (3)	0.1809 (3)
site 96i (0, y, z) z	0.1188 (3)	0.1182 (3)
Occupancy 24d	-	0.088 (3)
B1 (Å)	2.477 (3)	2.492 (3)
B2 (Å)	2.736 (5)	2.727 (5)
B3 (Å)	2.574 (2)	2.595 (3)
B4 (Å)	2.426 (5)	2.427 (5)
B5 (Å)	2.527 (4)	2.502 (4)
$\text{Fe}^{96i}\text{-H}$ (Å)	-	1.718 (3)
χ^2	13.2	19.2
R_{Bragg} (%)	16.5	14.8
R_{F} (%)	12.7	11.6

Figure V-32 demonstrates the influence of C insertion on the lattice constant of Ce-substituted sample in the course of absorption and desorption. The absorption kinetics is similar for both samples, with C-doped one showing slightly faster kinetics between 200 and 400 min of absorption. This observation suggests that the modulation on the absorption kinetics here is dominated by the substitution of Ce and C doping seems to assist the D insertion. At the desorption stage, C doping clearly has a softening effect on the fast unit cell contraction in Ce-substituted sample.

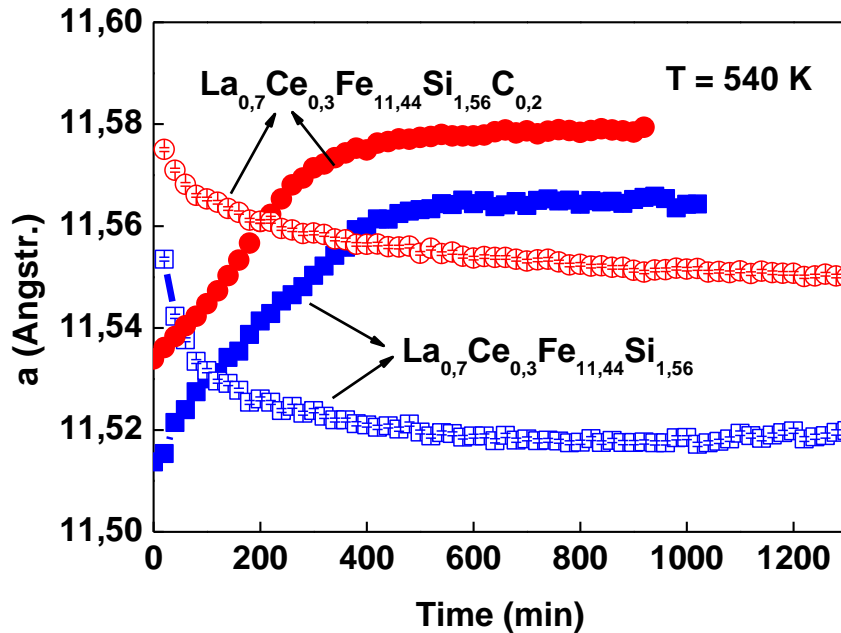


Figure V-32. Unit cell parameter in the course of absorption and desorption for sample of composition $\text{La}_{0.7}\text{Ce}_{0.3}\text{Fe}_{11.44}\text{Si}_{1.56}$ and $\text{La}_{0.7}\text{Ce}_{0.3}\text{Fe}_{11.44}\text{Si}_{1.56}\text{C}_{0.2}$ at 540 K. Solid symbols represent absorption and empty symbols show desorption.

Figure V-33 highlights the different evolutions of the site occupancy. Carbon insertion smooths the D insertion reaction since the step-like D content evolution has disappeared

for sample $\text{La}_{0.7}\text{Ce}_{0.3}\text{Fe}_{11.44}\text{Si}_{1.56}\text{C}_{0.2}$. Deuterium concentration stabilizes after 500 min. At desorption, however, sample $\text{La}_{0.7}\text{Ce}_{0.3}\text{Fe}_{11.44}\text{Si}_{1.56}$ has emptied nearly all the interstitial D from the $24d$ site, while $\text{La}_{0.7}\text{Ce}_{0.3}\text{Fe}_{11.44}\text{Si}_{1.56}\text{C}_{0.2}$ has retained about half of its D atoms.

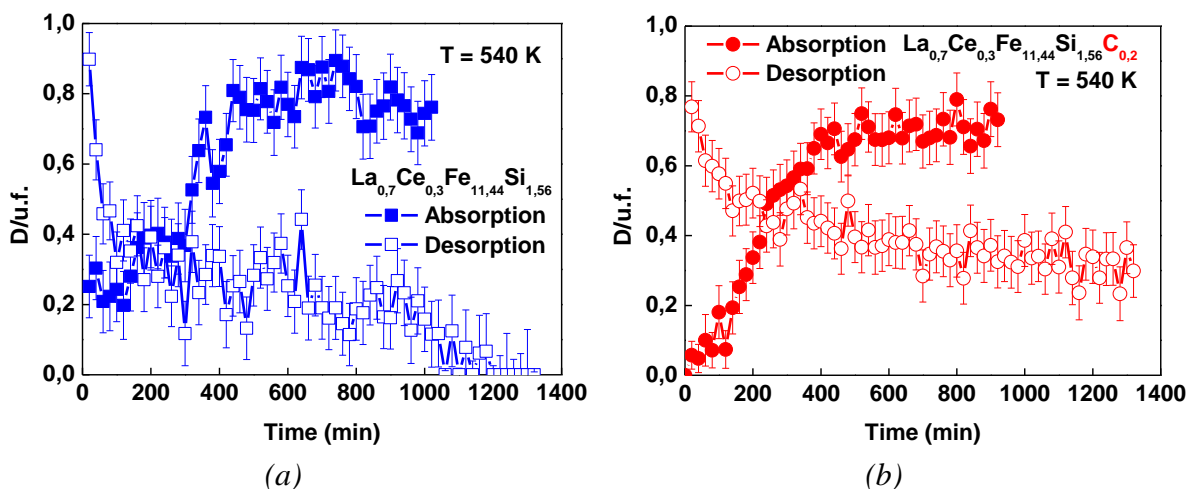


Figure V-33. D content per formula unit in the course of absorption and desorption for sample of composition $\text{La}_{0.7}\text{Ce}_{0.3}\text{Fe}_{11.44}\text{Si}_{1.56}$ and $\text{La}_{0.7}\text{Ce}_{0.3}\text{Fe}_{11.44}\text{Si}_{1.56}\text{C}_{0.2}$ at 540 K. Solid symbols represent absorption and empty symbols show desorption.

Similar to sample of composition $\text{La}_{0.7}\text{Ce}_{0.3}\text{Fe}_{11.44}\text{Si}_{1.56}$, its C-doped counterpart is also measured at ambient temperature and temperature at which the material is ferromagnetic (170 K). The refined structural parameters and interatomic distances are listed in Table V-10. The refined C concentration is close to the target stoichiometry. The ferromagnetic phase has a much larger volume than that of the paramagnetic phase. The magnetovolume effect principally results in the expansion of B4 and contraction of the B2 distance. The La/Ce-C distance is shorter than 2.9 Å due to the higher affinity of C with the rare-earth elements as compared with D.

Table V-10. Refined parameters and interatomic distances for sample of composition $\text{La}_{0.7}\text{Ce}_{0.3}\text{Fe}_{11.44}\text{Si}_{1.56}\text{C}_{0.2}$ from neutron powder diffraction at the D1B diffractometer in ILL at 170 K, 300 K, and 540 K.

$\text{La}_{0.7}\text{Ce}_{0.3}\text{Fe}_{11.44}\text{Si}_{1.56}\text{C}_{0.2}$	170 K	300 K	540 K
$a=b=c$ (Å)	11.5305 (3)	11.4925 (3)	11.5339 (3)
site $96i$ (0, y, z) y	0.1800 (2)	0.1804 (3)	0.1809 (3)
site $96i$ (0, y, z) z	0.1164 (2)	0.1174 (3)	0.1182 (3)
Occupancy $24d$	0.096 (2)	0.088 (2)	0.088 (3)
La(Ce) – C (Å)	2.8826 (1)	2.8731 (1)	2.8835 (1)
B1 (Å)	2.472 (3)	2.474 (3)	2.492 (3)
B2 (Å)	2.684 (5)	2.699 (5)	2.727 (5)
B3 (Å)	2.578 (3)	2.577 (3)	2.595 (3)
B4 (Å)	2.459 (5)	2.434 (5)	2.427 (5)
B5 (Å)	2.492 (4)	2.490 (4)	2.502 (4)
χ^2	30.0	25.2	19.2
R_{Bragg} (%)	10.1	9.41	14.8
R_{F} (%)	7.96	7.64	11.6
R_{Magnetic} (%)	14.8	-	-

The structural parameters are compared before absorption, at the end of absorption (920 min), and at the end of desorption (1320 min) in Table V-11. Deuterium absorption for

sample of composition $\text{La}_{0.7}\text{Ce}_{0.3}\text{Fe}_{11.44}\text{Si}_{1.56}\text{C}_{0.2}$ leads to a volume increase of 1% at 540 K. With C insertion, D introduction induces the expansion of B4 and contraction of B2. Desorption is guided by the reversal process.

Table V-11. Refined parameters and interatomic distances for sample of composition $\text{La}_{0.7}\text{Ce}_{0.3}\text{Fe}_{11.44}\text{Si}_{1.56}\text{C}_{0.2}$ before absorption, after 920 min of absorption, and after 1320 min of desorption at 540 K.

540 K	$\text{La}_{0.7}\text{Ce}_{0.3}\text{Fe}_{11.44}\text{Si}_{1.56}\text{C}_{0.2}$	$\text{La}_{0.7}\text{Ce}_{0.3}\text{Fe}_{11.44}\text{Si}_{1.56}\text{C}_{0.2}\text{D}_{0.7}$ 920 min absorption	$\text{La}_{0.8}\text{Ce}_{0.2}\text{Fe}_{11.3}\text{Si}_{1.7}\text{C}_{0.2}\text{D}_{0.3}$ 1320 min desorption
$\alpha=b=c$ (Å)	11.5340 (3)	11.5793 (4)	11.5495 (4)
site $96i$ (0, y, z) y	0.1808 (3)	0.1801 (3)	0.1808 (3)
site $96i$ (0, y, z) z	0.1181 (3)	0.1168 (3)	0.1179 (3)
Occupancy $24d$	0.08 C	0.08 C + 0.24 D	0.08 C + 0.08 D
La(Ce)- C(D) (Å)	2.8835 (1)	2.8948 (1)	2.8874 (1)
B1 (Å)	2.491 (3)	2.488 (3)	2.492 (3)
B2 (Å)	2.724 (5)	2.710 (5)	2.722 (5)
B3 (Å)	2.594 (3)	2.593 (3)	2.597 (3)
B4 (Å)	2.430 (5)	2.460 (5)	2.437 (5)
B5 (Å)	2.502 (4)	2.506 (4)	2.503 (4)
χ^2	19.3	5.0	5.0
R_{Bragg} (%)	14.6	14.3	15.7
R_{F} (%)	11.6	11.1	11.8

3.2.2. Discussion

The evolution of the relevant Fe-Fe interatomic distances (intra-cluster and inter-cluster) in the course of the hydrogenation process of these samples is shown in Figure V-34. Results from the cyclic refinement for Ce-substituted sample after 1000 min show large deviations and are not shown here to avoid unreasonable conclusions.

Carbon insertion in $\text{LaFe}_{11.44}\text{Si}_{1.56}$ shrinks the average intra-cluster Fe-Fe distances, which then remain stable throughout the hydrogenation process. In the case of $\text{La}_{0.7}\text{Ce}_{0.3}\text{Fe}_{11.44}\text{Si}_{1.56}$, the situation is a little different since C insertion slightly elongates the intra-cluster Fe-Fe distances at the beginning of the absorption process, then these bonds remain almost unchanged with respect to the C-free sample (Figure V-34). Regarding the inter-cluster distances, C insertion in $\text{LaFe}_{11.44}\text{Si}_{1.56}$ results in increased inter-cluster Fe-Fe distances (and La-La distances as well), this increase is softened in the case of $\text{La}_{0.7}\text{Ce}_{0.3}\text{Fe}_{11.44}\text{Si}_{1.56}$.

The above results show that C insertion or substitution at the rare earth site Ce-substitution induces a reshaping of the (Fe,Si) icosahedra. The icosahedra deformation witnessed by the (B1-3) bond length variation correlates with the hydrogenation kinetics. In the NaZn_{13} structure type, for an H interstitial atom to move to the next empty $24d$ site, it must pass through the bottleneck defined by the icosahedral network. A more open bottleneck is generally associated with higher interstitial diffusion, whereas a more shrunk icosahedral network will hinder H diffusion. The associated variations of the hydrogenation kinetics can be, therefore, correlated with not only the available space of accommodation but also

the modifications of the diffusion path in the lattice through a selective contraction of certain interatomic distances that is the “breathing” of the icosahedral network.

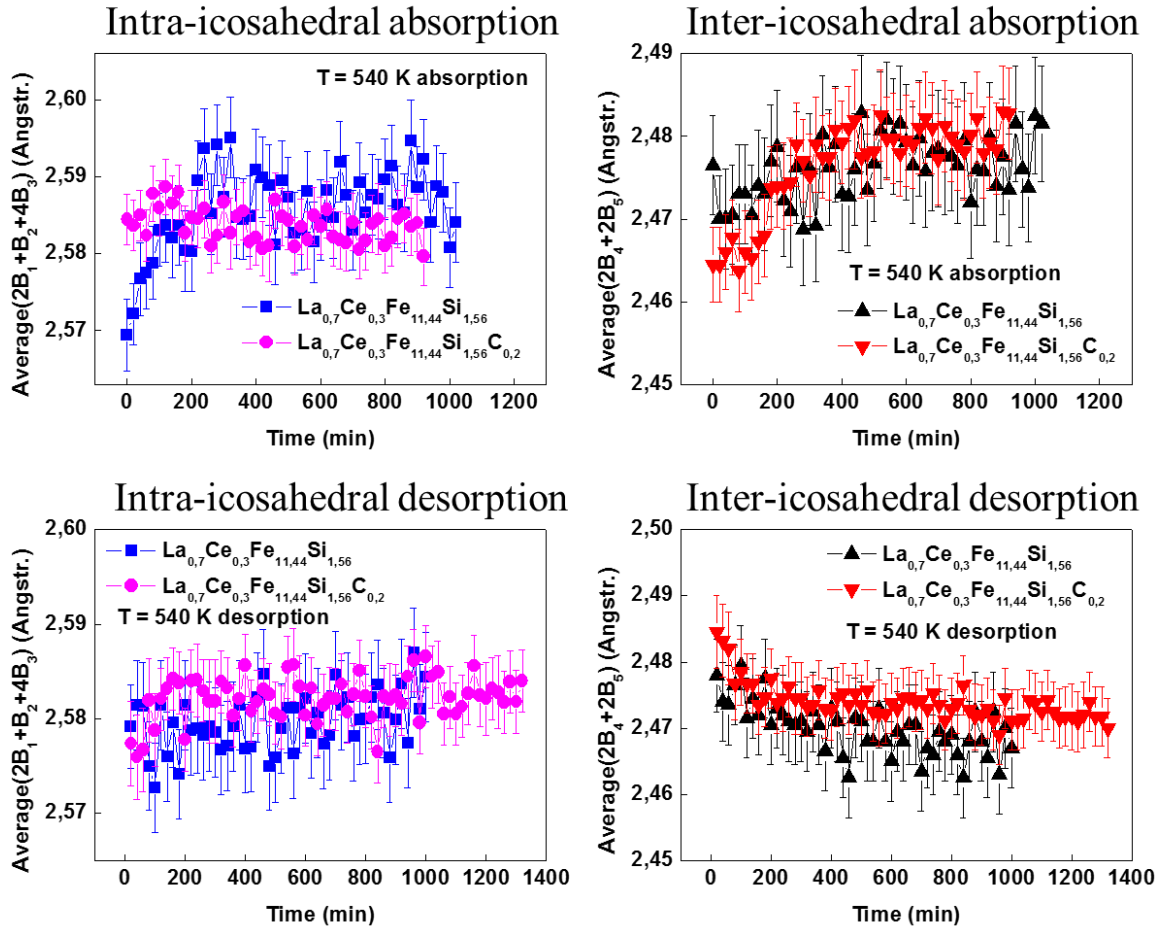


Figure V-34. Evolution of B2 and B4 distance during D absorption for sample of composition $\text{La}_{0.7}\text{Ce}_{0.3}\text{Fe}_{11.44}\text{Si}_{1.56}$ and $\text{La}_{0.7}\text{Ce}_{0.3}\text{Fe}_{11.44}\text{Si}_{1.56}\text{C}_{0.2}$ at 540 K.

The relation between diffusion kinetics, activation energy (E_a) and the temperature usually follows an Arrhenius-type equation. Generally, without considering the structural variations and resultant changes in the activation energy, the diffusion rate of H atoms will increase as a function of temperature. But it is also obvious from our results that the impact of structural changes on the activation energy is a driver for the hydrogen migration rate.

The rigorous structural investigations have allowed to specify the deformations undergone by the complex metallic alloys of $\text{La}(\text{Fe}_{1-x}\text{Si}_x)_{13}$ when subjected to light interstitial insertion or rare earth substitution at the cation site of the NaZn_{13} -structure type. We have shown that hydrogenation kinetics may be closely related to the particular inhomogeneous cell variation (breathing) and bonding. In a more general way, we suggest that the hydrogenation kinetics may be related with the icosahedron deformation induced either by interstitial insertion or by substitutions at the rare earth site or the Fe site (including Si-doping). This study shows that the packing of metal atom clusters that forms this family of complex metallic alloys is structurally intricate. Their degree of deformation and/or disorder has an effect on the hydrogenation kinetics of the LaFeSi-H interstitial solid solution system.

3.2.3. Differential Scanning Calorimetry

It is important to keep in mind that the thermal desorption of H occurs rapidly at temperatures not far above room temperature. From an application point of view, the most important aspect of C insertion is the improved thermal stability during H desorption.

3.2.3.1. Residual deuterium desorption

Neutron diffraction has confirmed the potential of C insertion to 1) slow down the absorption kinetics for sample pair $\text{LaFe}_{11.44}\text{Si}_{1.56}\text{D}_x$ and $\text{LaFe}_{11.44}\text{Si}_{1.56}\text{C}_{0.2}\text{D}_x$ and 2) retain H during desorption for the sample pair $\text{La}_{0.7}\text{Ce}_{0.3}\text{Fe}_{11.44}\text{Si}_{1.56}\text{D}_x$ and $\text{La}_{0.7}\text{Ce}_{0.3}\text{Fe}_{11.44}\text{Si}_{1.56}\text{C}_{0.2}\text{D}_x$. After the desorption experiments in-beam, the Curie temperature of the four samples were controlled and the presence of residual D interstitials was confirmed since T_C was higher than that of the annealed samples (Table V-12).

Table V-12. Curie temperature of the four samples after the in-situ neutron diffraction experiments and the original T_C after annealing without any hydrogenation process.

Sample composition	T_C after neutron diffraction (K)	T_C in annealed samples (K)
$\text{LaFe}_{11.44}\text{Si}_{1.56}$	254	206
$\text{LaFe}_{11.44}\text{Si}_{1.56}\text{C}_{0.2}$	298	258
$\text{La}_{0.7}\text{Ce}_{0.3}\text{Fe}_{11.44}\text{Si}_{1.56}$	196	188
$\text{La}_{0.7}\text{Ce}_{0.3}\text{Fe}_{11.44}\text{Si}_{1.56}\text{C}_{0.2}$	256	218

The four samples were heated up in DSC at 5 K/min in order to observe the thermal desorption of residual D. The D desorption reaction corresponds to an endothermic peak in the heat flow. Figure V-35 shows the heat flux measured in DSC during temperature scan from room temperature to 800 K. For the pair $\text{LaFe}_{11.44}\text{Si}_{1.56}\text{D}_x$ and $\text{LaFe}_{11.44}\text{Si}_{1.56}\text{C}_{0.2}\text{D}_x$, change of baseline is visible for both samples. The carbonated sample shows a smaller area of D desorption and the onset of the thermal desorption appears at higher temperature.

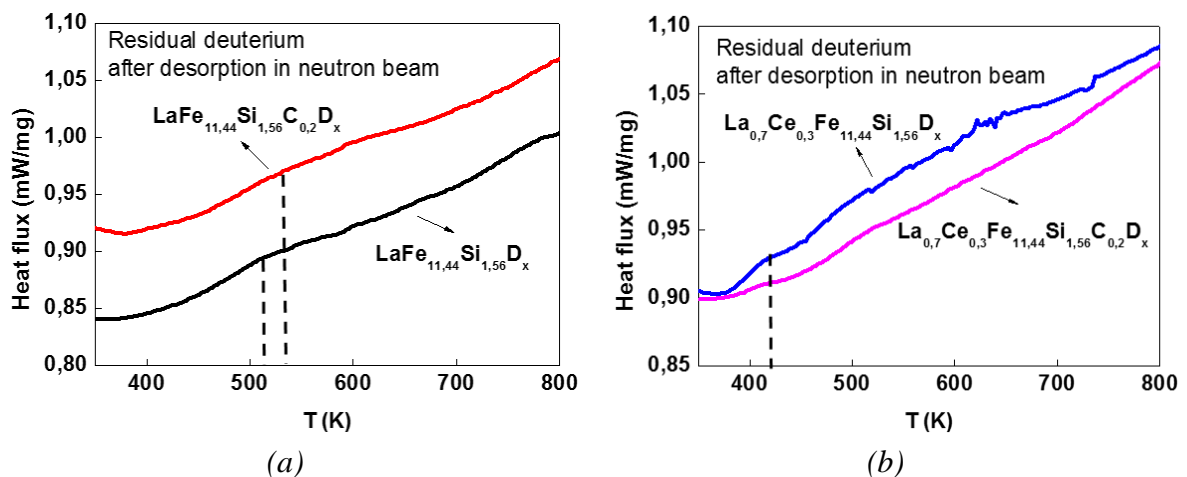


Figure V-35. DSC curves for samples after neutron diffraction experiments (a) $\text{LaFe}_{11.44}\text{Si}_{1.56}\text{D}_x$ and $\text{LaFe}_{11.44}\text{Si}_{1.56}\text{C}_{0.2}\text{D}_x$ and (b) $\text{La}_{0.7}\text{Ce}_{0.3}\text{Fe}_{11.44}\text{Si}_{1.56}\text{D}_x$ and $\text{La}_{0.7}\text{Ce}_{0.3}\text{Fe}_{11.44}\text{Si}_{1.56}\text{C}_{0.2}\text{D}_x$.

As for the pair of Ce-substituted samples in Figure V-35 (b), the change of baseline for $\text{La}_{0.7}\text{Ce}_{0.3}\text{Fe}_{11.44}\text{Si}_{1.56}\text{D}_x$ is peculiar, which might be related to the particular structure

reshaping seen from neutron diffraction. The difference of the onset desorption temperature for residual D is very small (a few K) between $\text{La}_{0.7}\text{Ce}_{0.3}\text{Fe}_{11.44}\text{Si}_{1.56}\text{D}_x$ and $\text{La}_{0.7}\text{Ce}_{0.3}\text{Fe}_{11.44}\text{Si}_{1.56}\text{C}_{0.2}\text{D}_x$. The Ce-substituted sample can be an interesting study subject for inelastic neutron scattering or nuclear magnetic resonance experiments to further probe the local characteristics of D atoms in such systems.

3.2.3.2. Thermal desorption of hydrogen

In order to properly probe the thermal desorption of hydrogen in the La-Fe-Si structure, thermal desorption in DSC was performed on fully hydrogenated samples. The improved thermal stability of $\text{LaFe}_{11.6}\text{Si}_{1.4}\text{C}_{0.2}\text{H}_y$ compared to $\text{LaFe}_{11.6}\text{Si}_{1.4}\text{H}_y$ has been demonstrated by Teixeira *et al.* [13]. Here we show thermal desorption behavior of Ce-substituted samples.

After annealing (no hydrogenation), sample $\text{La}_{0.7}\text{Ce}_{0.3}\text{Fe}_{11.7}\text{Si}_{1.3}$ has a lower T_C (188 K) than $\text{La}_{0.7}\text{Ce}_{0.3}\text{Fe}_{11.7}\text{Si}_{1.3}\text{C}_{0.2}$ (212 K). The difference in T_C due to 0.2 C/f.u. inserted is about 24 K. Fully hydrogenated samples show much smaller difference (12 K) in T_C : 328 K for $\text{La}_{0.7}\text{Ce}_{0.3}\text{Fe}_{11.7}\text{Si}_{1.3}\text{H}_x$ and 316 K for $\text{La}_{0.7}\text{Ce}_{0.3}\text{Fe}_{11.7}\text{Si}_{1.3}\text{C}_{0.2}\text{H}_x$.

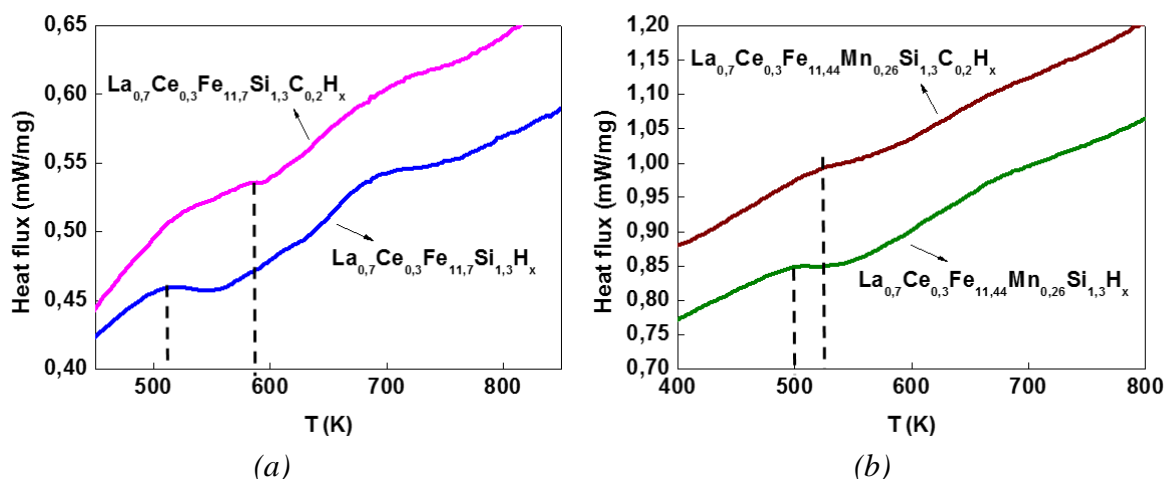


Figure V-36. DSC measurement showing the onset of H desorption temperature for (a) compound $\text{La}_{0.7}\text{Ce}_{0.3}\text{Fe}_{11.7}\text{Si}_{1.3}\text{H}_x$ and $\text{La}_{0.7}\text{Ce}_{0.3}\text{Fe}_{11.7}\text{Si}_{1.3}\text{C}_{0.2}\text{H}_x$ and (b) for compound $\text{La}_{0.7}\text{Ce}_{0.3}\text{Fe}_{11.44}\text{Mn}_{0.26}\text{Si}_{1.3}\text{H}_x$ and $\text{La}_{0.7}\text{Ce}_{0.3}\text{Fe}_{11.44}\text{Mn}_{0.26}\text{Si}_{1.3}\text{C}_{0.2}\text{H}_x$.

Interstitial modulations by H only and by C and H combined lead to similar levels of T_C after maximum H absorption. This suggests a similar manner in how the Fe-Fe distances are modified for these two modulations, which is then confirmed from the neutron diffraction data (3T2). The dehydrogenated T_C corresponds to the T_C of annealed samples and confirms the total desorption of H atoms in the material. As shown in Figure V-36 (a), the onset of H desorption is shifted from 521 K to 582 K for sample $\text{La}_{0.7}\text{Ce}_{0.3}\text{Fe}_{11.7}\text{Si}_{1.3}$ and $\text{La}_{0.7}\text{Ce}_{0.3}\text{Fe}_{11.7}\text{Si}_{1.3}\text{C}_{0.2}$, respectively. The stability of H atoms at high temperature is improved for fully hydrogenated $\text{La}_{0.7}\text{Ce}_{0.3}\text{Fe}_{11.7}\text{Si}_{1.3}\text{C}_{0.2}$.

Additionally, complex systems with both Mn and Ce substitution are employed to precisely adjust the T_C of the La-Fe-Si magnetocaloric phase. The effect of C on the thermal stability of fully hydrogenated samples is studied for such systems. After annealing, sample of composition $\text{La}_{0.7}\text{Ce}_{0.3}\text{Fe}_{11.44}\text{Mn}_{0.26}\text{Si}_{1.3}$ has a lower T_C (136 K) than

the C-doped sample of composition $\text{La}_{0.7}\text{Ce}_{0.3}\text{Fe}_{11.44}\text{Mn}_{0.26}\text{Si}_{1.3}\text{C}_{0.2}$ (190 K). Carbon insertion effectively expands the lattice and increases the shortest Fe-Fe distance, B4. The thermal hysteresis between heating and cooling curves at 0.05 T field is reduced from 12 K to 2 K with C insertion. After hydrogenation step, sample of composition $\text{La}_{0.7}\text{Ce}_{0.3}\text{Fe}_{11.44}\text{Mn}_{0.26}\text{Si}_{1.3}\text{H}_x$ has a slightly higher T_C (288 K) than the C-doped sample of composition $\text{La}_{0.7}\text{Ce}_{0.3}\text{Fe}_{11.44}\text{Mn}_{0.26}\text{Si}_{1.3}\text{C}_{0.2}\text{H}_x$ (282 K). Carbon insertion takes up the interstitial space and limits the maximum H absorption capacity. The thermal stability of fully hydrogenated samples is measured with DSC at 5 K/min heating rate. As shown in Figure V-36 (b), the onset of the H desorption temperature is shifted 40 K higher for the C-doped sample.

4. Conclusion

In this Chapter, we surveyed the hydrogenation behavior for the $\text{La}(\text{Fe}_{1-x}\text{Si}_x)_{13}$ phase by means of Sieverts' constant volume method and neutron diffraction. In particular, we evaluated the effect of composition modification such as Ce partial substitution and C doping on the hydrogenation dynamics.

Pressure-composition-isotherms demonstrate that the H sorption reaction in the $\text{La}(\text{Fe}_{1-x}\text{Si}_x)_{13}$ phase stays within a solid solution regime and no sign of hydride formation of specific stoichiometry is seen at given experimental conditions.

From the kinetics measurements in the Sieverts' apparatus, we have seen that C has a significant effect in modulating the H sorption kinetics. For sample of composition $\text{LaFe}_{11.44}\text{Si}_{1.56}$, modest amount of C doping leads to delayed H absorption kinetics. The ability of C to slow down the hydrogenation kinetics is further confirmed by *in-situ* neutron diffraction data [15].

By analyzing the neutron powder diffraction data, we have suggested a mechanism to associate hydrogenation behavior with the evolution of interatomic Fe-Fe distances. Hydrogenation is driven by the elongation of inter-icosahedral bond B4 and the contraction of inter-icosahedral Fe-Fe distance B2. Desorption is achieved by the reversal process.

The effect of Ce substitution and C interstitials can be summarized with the two pairs of samples measured: $\text{LaFe}_{11.44}\text{Si}_{1.56}$ and $\text{LaFe}_{11.44}\text{Si}_{1.56}\text{C}_{0.2}$; $\text{La}_{0.7}\text{Ce}_{0.3}\text{Fe}_{11.44}\text{Si}_{1.56}$ and $\text{La}_{0.7}\text{Ce}_{0.3}\text{Fe}_{11.44}\text{Si}_{1.56}\text{C}_{0.2}$, shown in Figure V-37. The introduction of C atoms into the interstitial sites modifies the D absorption kinetics of La-Fe-Si and La-Ce-Fe-Si in different manners.

Whereas C insertion significantly lowers D absorption kinetics for La-Fe-Si and corroborates the visual inspection of Figure V-37; the effect of C insertion on the hydrogenation kinetics of La-Ce-Fe-Si is less distinct. In the C-doped sample $\text{La}_{0.7}\text{Ce}_{0.3}\text{Fe}_{11.44}\text{Si}_{1.56}\text{C}_{0.2}$, the D insertion reaction is softened. Actually the slopes for samples $\text{La}_{0.7}\text{Ce}_{0.3}\text{Fe}_{11.44}\text{Si}_{1.56}$ and $\text{La}_{0.7}\text{Ce}_{0.3}\text{Fe}_{11.44}\text{Si}_{1.56}\text{C}_{0.2}$ are almost equal, a slight enhancement of the hydrogenation kinetics in $\text{La}_{0.7}\text{Ce}_{0.3}\text{Fe}_{11.44}\text{Si}_{1.56}\text{C}_{0.2}$ can be revealed.

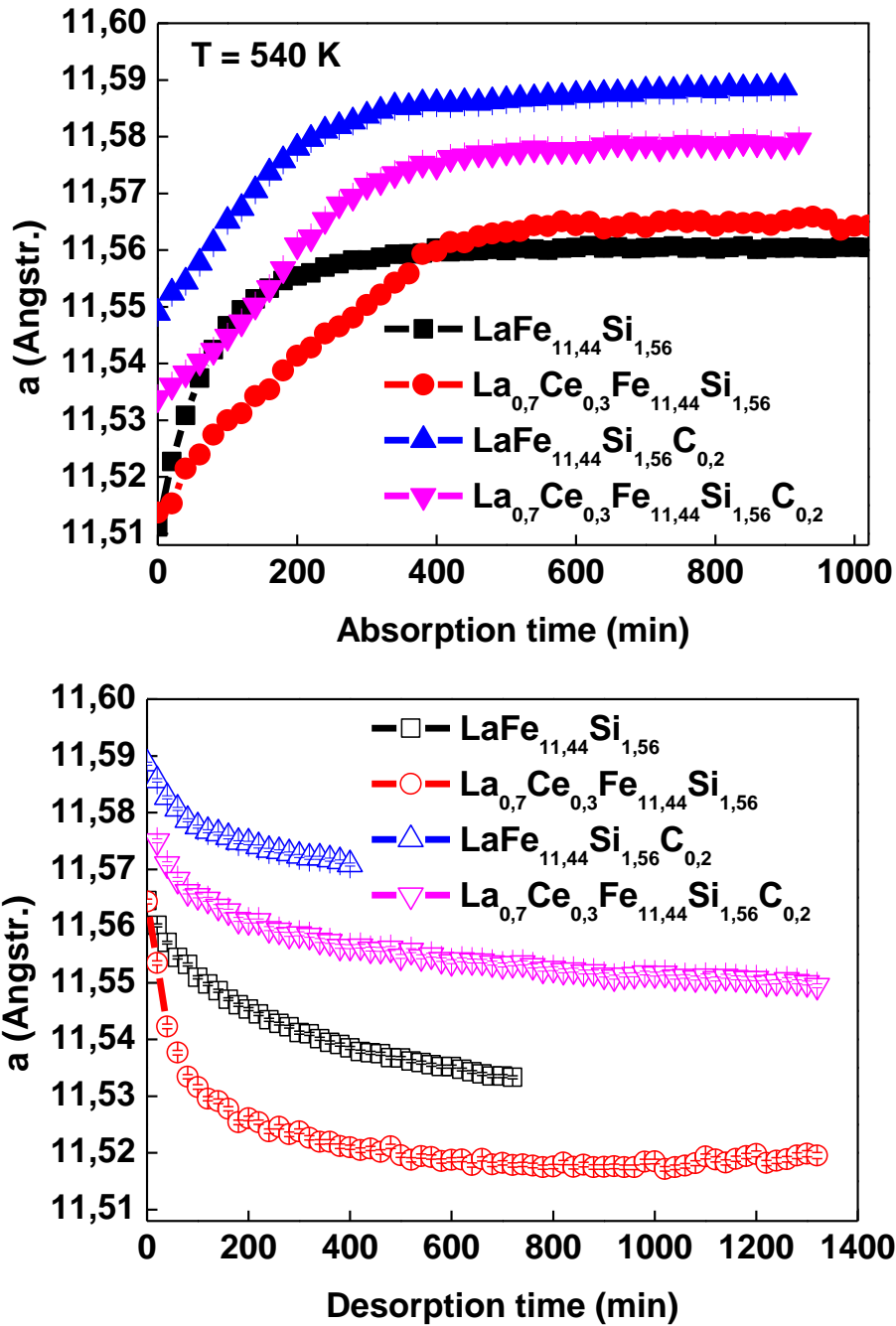


Figure V-37. Unit cell parameter in the course of (top) absorption and (bottom) desorption for all four samples at 540 K.

The mechanism of light atom insertion into the interstitial site is associated with not only the available space of accommodation, but also the facilitation of the diffusion path in the lattice. The delayed kinetics seen in $\text{LaFe}_{11,44}\text{Si}_{1,56}\text{C}_{0,2}$ can be considered as a shortage of available space compared to $\text{LaFe}_{11,44}\text{Si}_{1,56}$. If the available space is the rate-limiting step, this phenomenon should be highlighted in Ce-substituted sample since interstitial volume is reduced.

However, the slightly accelerated absorption kinetics in $\text{La}_{0,7}\text{Ce}_{0,3}\text{Fe}_{11,44}\text{Si}_{1,56}\text{C}_{0,2}$ than in $\text{La}_{0,7}\text{Ce}_{0,3}\text{Fe}_{11,44}\text{Si}_{1,56}$ suggests that it might be more of a changed insertion mechanism through modified interatomic distances. The arrival of D atoms into the interstitial site could be assisted by C insertion as it stretches the lattice volume. At the same time, the

diffusion of interstitial atoms in the lattice is governed by the interatomic distances, which needs to be considered as well. At the desorption stage, C insertion clearly has a softening effect on the fast lattice contraction in Ce-substituted sample.

The above experimental observations are favorable for an accurate control of H content in industrial processes. Carbon insertion can be used in combination with H insertion to improve the thermal stability in La-Fe-Si-based materials, including the partially substituted compositions.

References

- [1] H. Uchida, M. Sato and O. Moriwaki, *J. Alloy Compd.*, Vols. 253-254, p. 235, 1997.
- [2] O. Isnard, S. Miraglia, D. Fruchart, E. Akiba and K. Nomura, *J. Alloy Compd.*, vol. 257, p. 150, 1997.
- [3] M. Phejar, Ph.D. thesis manuscript "*Etude de nouveaux matériaux de type La(Fe_{1-x}Si_x)₁₃ pour la refrigeration magnétique à température ambiante*", Engineering Sciences, Université Paris-Est, 2010. French. <NNT : 2010PEST1085>. <tel-00575658v2>
- [4] J. Wang, Y. Chen, Y. Tang, S. Xiao, T. Liu and E. Zhang, *J. Alloy Compd.*, vol. 485, p. 313, 2009.
- [5] S. Seta and H. Uchida, *J. Alloy Compd.*, vol. 231, p. 448, 1995.
- [6] V. Koeninger, U. Koike, K. Kamata, Y. Matsumura, T. Noguchi, T. Kurino, H. Kaneko, T. Yanagisawa, H. Uchida and H. Uchida, *Zeitschrift für Physikalische Chemie*, vol. 181, p. 299, 1993.
- [7] E. Snidjer, G. Versteeg and G. van Swaaij, *AIChE Journal*, vol. 39, p. 1444, 1993.
- [8] T. Leblond, V. Paul-Boncour, F. Cuevas, O. Isnard and J. Fernandez, *Inter. J. H. Energy*, vol. 34, p. 2278, 2009.
- [9] C. Mayer, A. Dubrez, M. Pierronnet and P. Vikner, *Phys. Status Solidi C*, vol. 11, p. 5, 2014.
- [10] S. Rundqvist, R. Tellgren and Y. Andersson, *J. Less-Common Metals*, vol. 101, p. 145, 1984.
- [11] D. Fruchart, S. Miraglia, P. De Rango and P. Wolfers, *J. Alloy Compd.*, vol. 383, p. 17, 2004.
- [12] S. Fujieda, A. Fujita, K. Fukamichi, Y. Yamaguchi and K. Ohoyama, *J. Phys. Soc. Jpn.*, vol. 77, pp. 1-8, 2008.
- [13] C. S. Teixeira, M. Krautz, J. D. Moore, K. Skokov, J. Liu, P. A. Wendhausen and O. Gutfleisch, *J. Appl. Phys.*, vol. 111, p. 07A927, 2012.
- [14] J. Lyubina, *J. Appl. Phys.*, vol. 109, p. 07A902, 2011.
- [15] L. Jia, J. Sun, J. Shen, B. Gao, T. Zhao, H. Zhang, F. Hu and B. Shen, *J. Alloys Compd.*, vol. 509, p. 5804, 2011.
- [16] F. Wang, G. Wang, F. Hu, A. Kurbakov, B. Shen and Z. Cheng, *J Phys.: Condens. Matter*, vol. 15, p. 5269, 2003.
- [17] W. Choo and J. Lee, *Metallurg. Trans. A*, vol. 13, p. 135, 1982.
- [18] X. Hai, C. Mayer, C. V. Colin and S. Miraglia, *J. Magn. Magn. Mater.*, vol. 400, p. 344, 2016.
- [19] J. Zhao, J. Shen, H. Zhang, Z. Xu, J. Wu, F. Hu, J. Sun and B. Shen, *J. Alloy Compd.*, vol. 520, pp. 227-280, 2012.

Chapter VI. Phase transformation in Fe-based alloys
for magnetocaloric applications

Table of Contents

Chapter VI. Phase transformation in Fe-based alloys for magnetocaloric applications ...	187
1. Motivation	187
2. General notions	190
2.1. Alloying elements and microstructure	190
2.2. Experimental details.....	192
3. Fe-Cr-Ni system	193
3.1. Series Fe-Cr-Ni with 15 wt%Cr.....	195
3.2. Effect of Ni with 5% Cr	205
3.3. Effect of Cr with 10% Ni	211
4. Fe-Cr-Mn system.....	215
4.1. Series Fe-Cr-Mn with 15% Cr	216
4.2. Addition of carbon in 15/25 Fe-Cr-Mn.....	223
4.3. Series Fe-Cr-Mn with 5% Cr	228
5. Conclusion.....	231
References	232

Chapter VI. Phase transformation in Fe-based alloys for magnetocaloric applications

1. Motivation

Metallurgy has always been an important research topic in material science because the practical use of metals has shed light on many aspects of human interactions with the environment. Decades of research and development have made major innovations increasingly difficult to find. As a result, one of the major routes of progress remains the discovery of new purposes and applications of existing products.

In the search for new materials systems for magnetic refrigeration, scientists are turning to rare-earth-free materials due to the abundance of the raw material. In this Chapter, we investigate the potential of Fe-based alloys for magnetocaloric application. It is interesting to explore the possibility of such phase transition in astonishingly simple materials for their magnetocaloric properties. Furthermore, it is of great importance for raw material producers such as Erasteel to develop new functionalities for these Fe-based alloys.

Among the Fe-containing alloys, $\text{Fe}_x\text{Pt}_{100-x}$ alloys exhibit a temperature and magnetic field induced phase transition from disordered γ phase to ordered α phase. This gives rise to a magnetic entropy change up to 39.8 J/kg. K for alloy $\text{Fe}_{79}\text{Pt}_{21}$ under a field change of 0 to 7 T [1]. Their magnetocaloric effect near room temperature makes $\text{Fe}_x\text{Pt}_{100-x}$ alloys interesting candidates for magnetic refrigeration applications. Nonetheless, the price of Pt remains a challenge for the upscaling of these alloys.

In 2012, P. Souvatzis and colleagues [2] reported a theoretical prediction to achieve a structural and magnetic phase transition in alloy systems $\text{Fe}_{1-y-x}\text{Cr}_y\text{Ni}_x$ and $\text{Fe}_{1-y-x}\text{Cr}_y\text{Mn}_x$ where $0.1 < y < 0.3$ and $0.1 < x < 0.3$.

When considering any new material system with magnetocaloric potential, an important parameter is the large change in the magnetization at the ordering temperature. Precisely, it is interesting to have a material with a large dM/dT at constant applied field.

By alloying with Ni or Mn, the ferromagnetic bcc-phase of $\text{Fe}_{1-y}\text{Cr}_y$ ($y < 20$) can degenerate with the paramagnetic fcc-phase [3, 4]. As the ferrite bcc-phase is being heated, it becomes destabilized and results in transforming into the paramagnetic fcc-phase at the transition temperature [4]. This structural and magnetic transition is expected to be accompanied by a large entropy change. Therefore, it should be possible to tailor the bcc to fcc transformation with the composition and microstructure engineering.

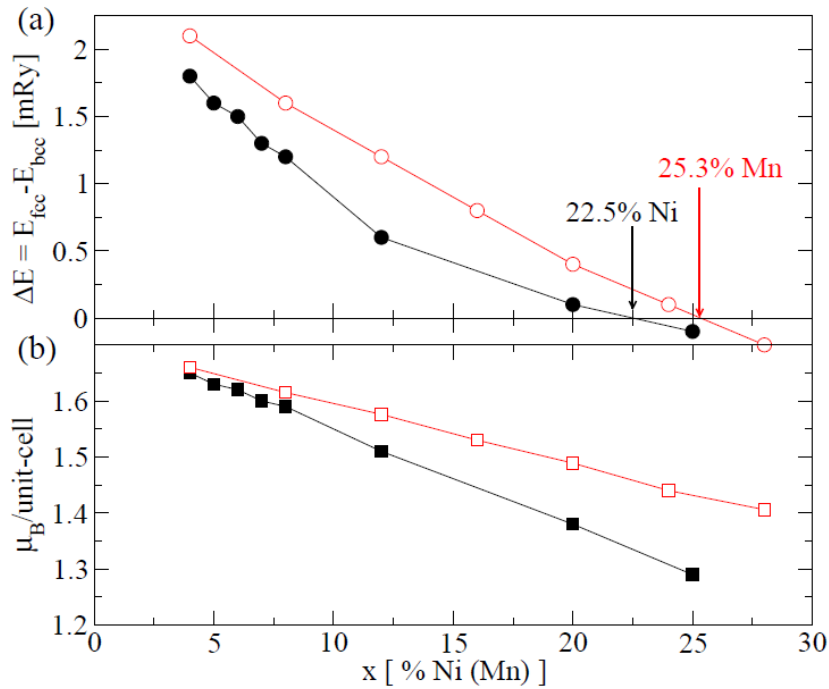


Figure VI-1. Calculated (a) total energy differences and (b) magnetic moments obtained within the local density approximation (LDA) as a function of Ni(Mn) concentration, the filled black symbols are for Fe-Cr-Ni systems and the open red symbols are for the Fe-Cr-Mn systems, taken from reference [2].

They performed qualitative calculations based on density function theory at $T=0$ K neglecting thermal effects. In Figure VI-1, the ferromagnetic α and the paramagnetic γ phases become degenerate at Ni content of 22.5% and Mn content of 25%. At the same composition range, α -bcc phase has a large magnetic moment and the local magnetic moment of γ -fcc phase is much smaller compared with α -bcc phase. Accordingly, a substantial magnetic entropy change can be expected during the bcc to fcc phase transition.

They predicted that it was possible to tune the composition so that the bcc to fcc phase transition took place in a temperature range close to room temperature, accompanied with a large change in entropy of the spin-system. At small Ni content, the hcp phase becomes more stable than fcc. Since the hcp phase has zero local magnetic moments, the magnetic entropy drop from bcc to hcp is expected to be even larger. Their work had definitely inspired us to investigate such systems experimentally from a magnetocaloric perspective.

Some authors have used ball milling to synthesize nanocrystalline powder of Fe-Ni alloys. Ipus, Ucar, and McHenry have shown that γ -FeNi nanoparticles have modest near room-temperature second-order magnetocaloric response [3]. The peak entropy change is in the order of 2.8 J/kg·K for a maximum applied field of 5 T.

Later in 2013, Ucar and colleagues studied mechanically alloyed $\text{Fe}_{70}\text{Ni}_{30}$ and $\text{Fe}_{72}\text{Ni}_{28}$ and characterized them in terms of their structural and magnetic properties [4]. The maximum magnetic entropy change observed for $\text{Fe}_{70}\text{Ni}_{30}$ and $\text{Fe}_{72}\text{Ni}_{28}$ are 0.65 and 0.5 J/kg·K, respectively, at a field of 5 T. The peak temperatures are around 90 and 60 °C, respectively. The Curie temperature of these nanoparticles were tuned by controlling the oxidation kinetics of Fe during ball milling.

The Fe-Ni phase diagram shows that the magnetic properties and Curie temperature of these alloys strongly depend on the composition. Chaudhary *et al.* reported the magnetocaloric effect and magnetic properties of $(\text{Fe}_{70}\text{Ni}_{30})_{95}\text{Mn}_5$ nanoparticles prepared by ball milling [5]. The quenched sample shows a Curie temperature at 65 °C. They show that the maximum entropy change is 1.45 J/kg·K for a field change of 5T.

A multiphase Fe-Ni-B bulk alloy is investigated as a solution for inadequate temperature span in developing a magnetic cooling system [6]. The bcc phase forms during slow cooling from the fcc phase region to room temperature in the furnace. The coexistence of bcc, fcc, and spinel phases results in large working temperature spans of 439 °C for magnetic field change of 5 T. The mass fraction of the phases can be tuned by controlling the synthesis parameters.

Likewise, MCE in cementite (Fe_3C) has been explored in a very recent publication by B. Kaeswurm *et al.* [7]. While the transition temperature (202 °C) is still high for room-temperature magnetic refrigeration, the material has a measured magnetocaloric effect of $\Delta T_{ad} = 1.76$ K and $\Delta S = 3$ J/kg·K for a field change from 0 to 2 T. The Curie temperature of cementite can be adjusted by substitution of various elements. For instant, small concentration of Molybdenum can reduce T_C from 202 °C to 147 °C [8]. Other variations have been examined, including $(\text{Fe}_{0.9}\text{Mn}_{0.1})_3\text{C}$ [9], with a reported ΔS of 3.4 J/kg·K at 32 °C for a field change of 5 T, and $\text{Fe}_{2.85}\text{Cr}_{0.05}\text{C}$ [10], which crystallizes in the cementite type structure and shows a temperature-induced second-order magnetic phase transition at 87 °C.

In this Chapter, we focus on Fe-Cr-Ni or Fe-Cr-Mn alloy systems and investigate their bulk structural and magnetic properties for magnetocaloric applications. The composition ranges are chosen to cover a wide range of transition types. Since the Curie temperature of these systems are generally in the temperature range higher than room temperature, °C is used instead of K as the temperature unit in this Chapter.

2. General notions

To begin with, some general notions appropriate to the steel industry are introduced and one section is dedicated to the experimental techniques specific to this Chapter.

2.1. Alloying elements and microstructure

With at least 11 wt% Cr level, Fe-Cr systems can be classified as stainless steel since Cr oxide forms on the steel surface as protection layer. There are three main types of microstructure in Fe-based alloys similar to stainless steels: ferritic (α -bcc), austenitic (γ -fcc), and martensitic (α' -bcc), which can be obtained by adjusting the composition and heat treatment. Most structure-sensitive properties depend on the microstructure.

The austenitic grades are the largest group of stainless steels, including both Cr-Mn and Cr-Ni grades. They are paramagnetic in the temperature range of use due to their microstructure. They may be ferromagnetic due to the presence of some martensite, or at very low temperature.

The standard ferritic grades contain Cr and Ni are ferromagnetic due to the ferritic microstructure and Fe-Fe distances in the bcc lattice. The ferrite forming below the temperature range of austenite is often referred to as alpha ferrite and that forming above as delta ferrite, though both are structurally similar. Similarly, martensitic stainless steel contains small amount of Ni. They are ferromagnetic and tend to increase the hardness of ferrites. The properties of stainless steels have been extensively studied with well-documented sources in the literature [13]. Upon high-temperature exposure, a variety of phases may precipitate, resulting in different properties.

Interstitial and substitutional alloying of Fe induce subtle variations of phases and morphology. To an extent, the variety of microstructures leads to the versatility of steels. Interstitially dissolved elements such as C are located in the octahedral vacancy sites of the Fe lattice, whereas substitutional elements like Mn, Cr, and Ni are located at the same lattice sites as the Fe atoms. Alloying not only shifts the transformation temperature but also changes the temperature span of the transition. Apart from their locations in the lattice, the alloying elements can also be classified according to their ability to stabilize certain phases [11].

Chromium is the most important alloying element in stainless steels because it gives the basic corrosion resistance [12]. It stabilizes ferrite domain since it has the same body-centered cubic structure.

Nickel, having a face-centered cubic structure itself, favors the formation of an austenitic solid solution. Nickel generally increases ductility and toughness.

Manganese is generally used in stainless steels to improve hot ductility. Its effect on the ferrite-austenite balance varies with temperature and concentration. It stabilizes austenite at low temperature and low concentration, and at high concentration, it will stabilize ferrite.

Carbon favors the formation of austenite, which has a much larger solubility of C compared to that in the ferrite phase. Due to the carbide formation, C also reduces the corrosion resistance of the stainless steel. In ternary alloy systems, the addition of C to Fe-Cr alloy expands the existence domain of the austenite phase in temperature. Nickel has similar effect but C affects the phase formation much more significantly.

To summarize, α -promoting elements include Cr, Mo, Nb, V, Ta, Si, and Al and γ -promoting elements include Ni, Mn, C, N, and Co.

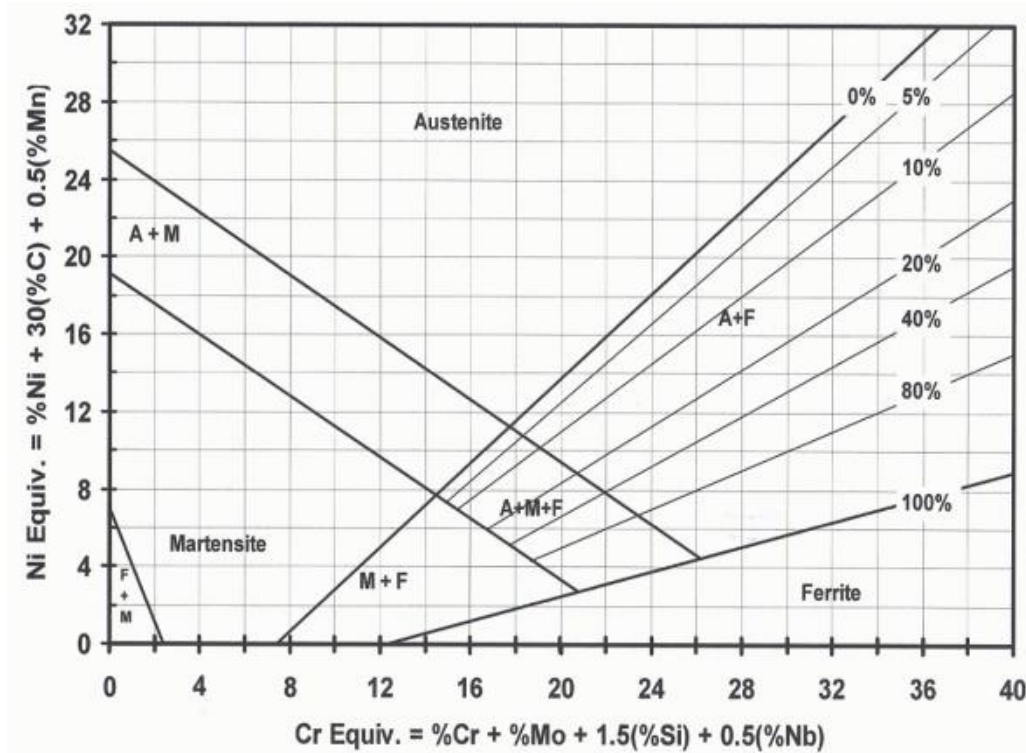


Figure VI-2. The Schaeffler diagram taken from reference [15].

The Schaeffler diagram (Figure VI-2) was originally developed to describe the structure after melting and rapid cooling for weld metals. By taking into account the austenite stabilizer ability of Ni and the ferrite stabilizer ability of Cr, it is possible to anticipate the total ferrite and austenite stabilizing effect of the alloying elements in the steel.

This gives the so-called chromium equivalent Cr_{eq} and nickel equivalent Ni_{eq} , defined as below [14]:

$$Cr_{eq} = \%Cr + \%Mo + 1.5\%Si + 0.5\%Nb$$

$$Ni_{eq} = \%Ni + 30\%C + 0.5\%Mn$$

Nowadays based on the experimental data collected over decades, the ever-evolving thermodynamic database such as ThermoCalc[®] becomes the primary alloy development tool. In temperature regions lower than equilibrium range, *ab-initio* or first principle calculations are being used to predict the phase formation and atomic arrangements of alloys.

2.2. Experimental details

The magnetic response and transition temperatures of alloys in this Chapter were determined by the Faraday's Balance apparatus and the extraction vector magnetometer, described in Chapter II. Only α -ferrite and α' -martensite phases are known to possess ferromagnetic properties at and above room temperature. The respective transition temperatures depend on the composition of the phases.

In the Faraday's Balance, the sample can be heated and cooled in a temperature-controlled furnace and a magnetic signal in arbitrary units shows the magnetic signal of the sample under the field of a permanent magnet. Sample is sealed in evacuated quartz tube before being placed in the furnace.

A signal in the magnetic response comes from the ferromagnetic phase within the sample. A decrease in magnetic response can take place for two reasons:

- (1) The sample temperature exceeds the Curie temperature of a given ferromagnetic constituent of the sample. If no structural or compositional alternation takes place, the ferromagnetic response will reappear upon cooling. A reversible effect is observed.
- (2) A structural phase transition occurs by which a ferromagnetic phase (α' -martensite or α -ferrite) transforms into a paramagnetic phase (γ -austenite). Such a phase transformation can only be followed if it occurs between the low temperature FM structure 1 to the high temperature PM structure 2 ($2 \neq 1$), i.e., below or very close to the Curie temperature of the ferromagnetic phase. Such a transition may or may not be detected on cooling depending on whether the transformation is reversible or if it occurs at the same temperature.

Calorimetric measurements were carried out using Differential Scanning Calorimeter (DSC) in the range from room temperature to 800 °C and Differential Thermal Analysis (DTA) from RT to 1300 °C. The sample mass for the measurement is about 100 mg and pure Al_2O_3 is used as a reference material.

According to the thermodynamic principles of phase transformation from a low temperature to a high temperature phase, the transition is associated with a discontinuity of the enthalpy function of the system. The endothermic transformation corresponds to a discrete increase in heat absorption during heating. The reversible transformation gives rise to a detectable exothermic peak in DSC during cooling. Any transition from a retained or formed metastable phase to a stable phase can also be detected as an exothermic peak during heating in the calorimeter, which corresponds to a release of stored energy.

Qualitative information on the phase presence were determined by XRD measurements. The presence of different phases can be distinguished by distinctive lattice parameters and space groups. Phase microstructure were examined by optical and electronic microscopes with appropriate attack on the surface. Since the alloying elements are all neighboring elements with very similar atomic number, the accurate composition of the different phases was difficult to obtain in EDX analysis.

3. Fe-Cr-Ni system

The compositions for samples elaborated in this system are listed in the table below. The shorthand notation is used in the text for clarity.

Table VI-1. The samples elaborated in different series in the Fe-Cr-Ni systems with the shorthand with the weight percentage of each element, the last column shows the martensite start temperature (M_s) estimated from Andrews empirical formula [19].

Shorthand wt% Cr/Ni	Fe wt%	Cr wt%	Ni wt%	Calculated M_s (°C)
15/10	75	15	10	181
15/25	60	15	25	-85
5/15	80	5	15	213
5/20	75	5	20	125
5/25	70	5	25	36
5/35	60	5	35	-141
25/10	65	25	10	60
35/10	55	35	10	-62

The phase formation is first simulated with Thermocalc[®] software with TCFE6 database. The calculation does not provide information on the kinetics of precipitation, only that it is the thermodynamically stable solution at equilibrium. Kinetics is usually described in experimentally determined TTT (time-temperature-transformation) diagrams.

Austenite phase is stabilized at high temperatures. However, if the total alloy content is low enough, a spontaneous transformation from austenite to martensite may occur upon cooling. The temperature at which this transformation starts is called the M_s temperature. Generally it is considerably below the temperature at which austenite and ferrite are at equilibrium [19].

Andrews empirical formula below [18] gives an estimation of the martensite start temperature M_s at which the austenite transforms into martensite (also given in Table VI-2 for all samples):

$$M_s(^{\circ}\text{C}) = 539 - 423\%C - 30.4\%Mn - 12.1\%Cr - 17.7\%Ni - 7.5\%Mo$$

Ternary diagrams of Fe-Cr-Ni system [20] with very small amount of carbon (< 0.1%) are presented here in addition to the Schaeffler diagram in order to have good estimation of the phase formation at given composition.

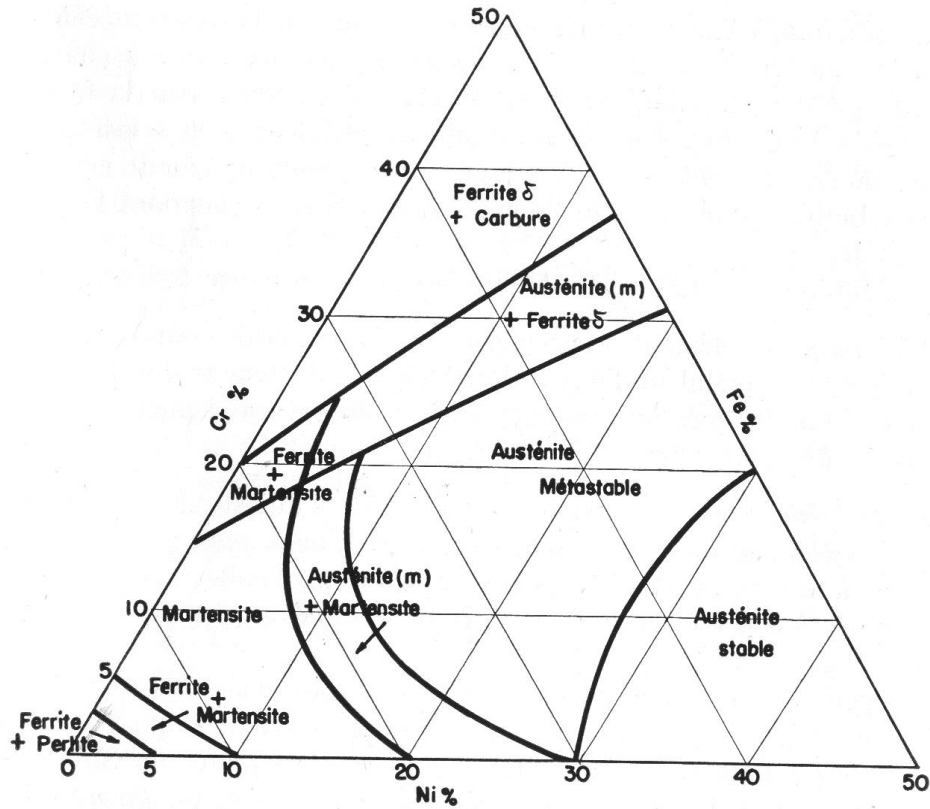


Figure VI-3. Room temperature ternary diagram of Fe-Cr-Ni system ($C < 0.10$ wt%), taken from reference [19].

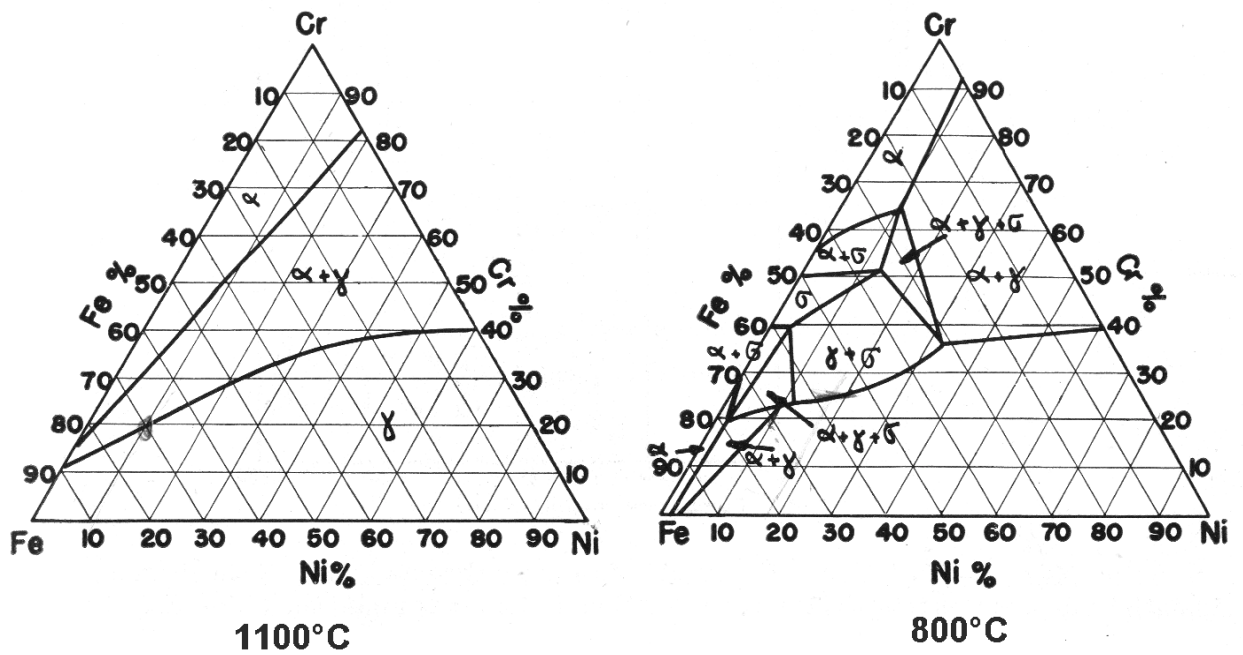


Figure VI-4. Ternary diagram of Fe-Cr-Ni systems at 800 and 1100°C , taken from reference [19].

3.1. Series Fe-Cr-Ni with 15 wt%Cr

The alloys 15/10 and 15/25 (inspired by reference [2]) were elaborated by induction melting appropriate amount of starting elements Fe, Cr, and Ni. The melted buttons were homogenized in sealed quartz tube at 1000 °C for 15 days and cooled in the furnace (slow cooling).

3.1.1. Alloy 15/10

For alloy 15/10, thermodynamic calculation is presented in Figure VI-5. Austenite is the primary solidification phase, stable at high temperature. Two bcc phases appears at 620 °C and 420 °C. After slow-cooling from the fcc phase region to room temperature, these bcc phases should be expected in the annealed alloy 15/10.

The Andrews formula calculation with composition 15/10 gives a Ms temperature of 181°C, much lower than the appearance of the α' -martensite (BCC_A2#2) phase given by ThermoCalc. The thermodynamic calculation gives a plausible result for $\gamma \rightarrow \alpha$ transformation but give no reliable information on the formation of martensite.

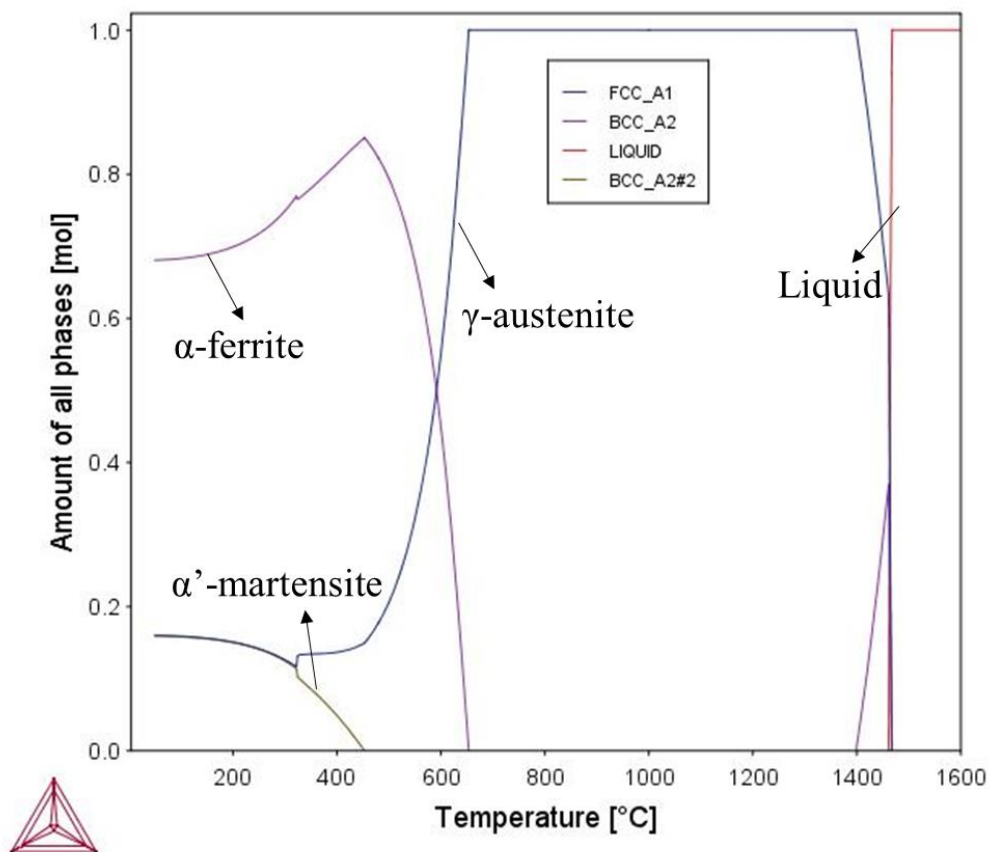


Figure VI-5. Phase fraction as a function of temperature for alloy 15/10 calculated using ThermoCalc®.

X-ray diffraction was performed on 15/10 bulk ingot with polished surface after annealing at 800, 900, and 1000 °C and furnace cooled, and the diffraction patterns of as-cast and annealed 15/10 samples are shown in Figure VI-6.

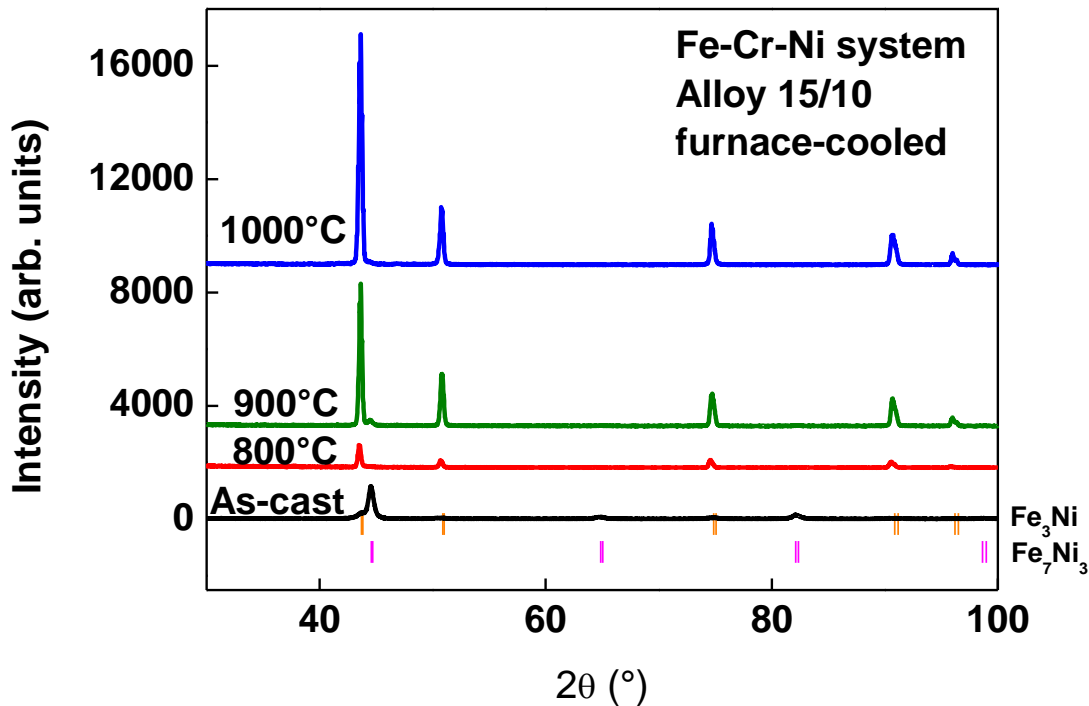


Figure VI-6. XRD patterns of as-cast and annealed sample 15/10 in the Fe-Cr-Ni system.

The as-cast 15/10 sample shows a body-centered cubic Fe_7Ni_3 -type structure in the space group $Im-3m$. Alloys 15/10 annealed at 800 °C and 1000 °C show a face-centered cubic Fe_3Ni -type structure in the space group $Fm-3m$ with a lattice parameter of 3.59 Å. No additional impurity phase is detected at given orientation. However, sample 15/10 annealed at 900 °C shows a small peak around 44.4°, indicating the presence of a bcc-type phase in addition to the fcc-phase.

According to the phase diagrams, this composition lies in the zone of mixed of Austenite (γ -fcc) and Martensite (α' -bcc) at room temperature. The absence of the bcc phase in XRD patterns for samples annealed at 800 °C and 1000 °C might be attributed to the degree of texturing as the measurement was performed on polished surface with possible grain orientation.

The sample annealed at 1000 °C was observed in optical microscope after Kalling $n^{\circ}2$ etching. The image in Figure VI-7 shows austenite grains with martensite developed inside and strongly attacked ferrite in the inter-granular area. This confirms the presence of bcc phases in the annealed alloy.

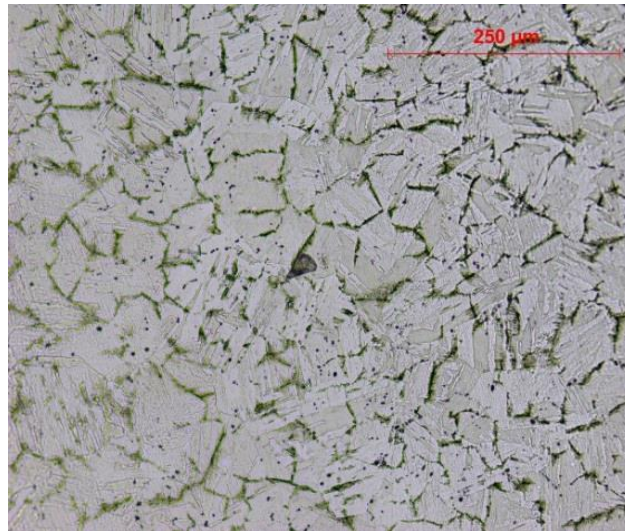


Figure VI-7. Microstructure observed with optical microscope after Kalling n^2 etching for Fe-Cr-Ni alloy 15/10 annealed at 1000 °C and slow-cooled.

The magnetization level under a field of 0.05 T was measured at the temperature range of the high-temperature extraction vector magnetometer (-73 °C to 577 °C). Samples 15/10 annealed at different temperatures all show magnetization in the order of $24 \text{ A} \cdot \text{m}^2/\text{kg}$, shown in Figure VI-8. Alloy 15/10 annealed at 1000 °C has the lowest magnetization level. This is in accordance with the further stabilization of austenite with increasing annealing temperature.

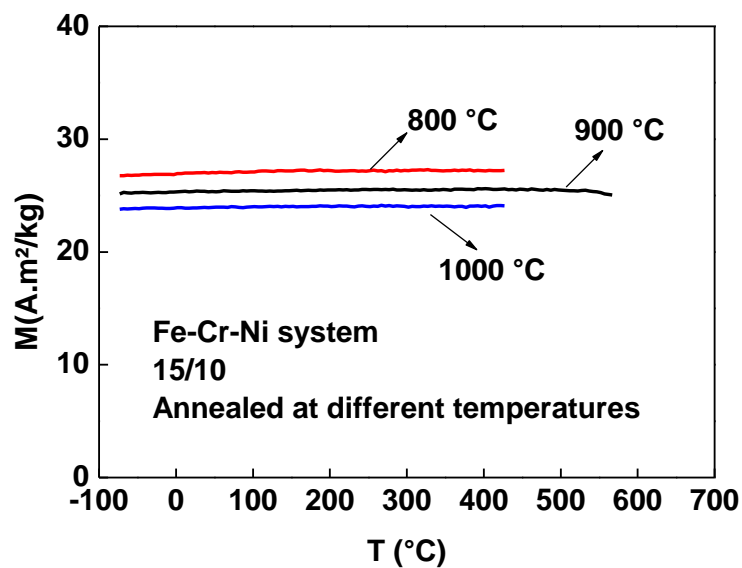


Figure VI-8. Magnetization as a function of temperature measured by extraction vector magnetometer for alloy 15/10.

The magnetic and structural response as a function of temperature of sample 15/10 annealed at 1000 °C was measured in Faraday's Balance and DTA. The results are shown in Figure VI-9. The sample was heated from room temperature to high temperature and cooled down at 10 K/min rate. The Faraday's Balance instrument does not distinguish between ferrite and martensite. If both of these ferromagnetic phases are present, one must resort to microscopic examination to determine their relative proportions.

Sample 15/10 exhibits a sharp drop in magnetic signal at 600 °C upon heating, which corresponds to an endothermic peak in the DTA curve at the same temperature. Upon cooling, the sample stays paramagnetic until a transition at 150 °C, after which the sample becomes ferromagnetic again. This structural transformation is confirmed in the DTA cooling curve around the same temperature.

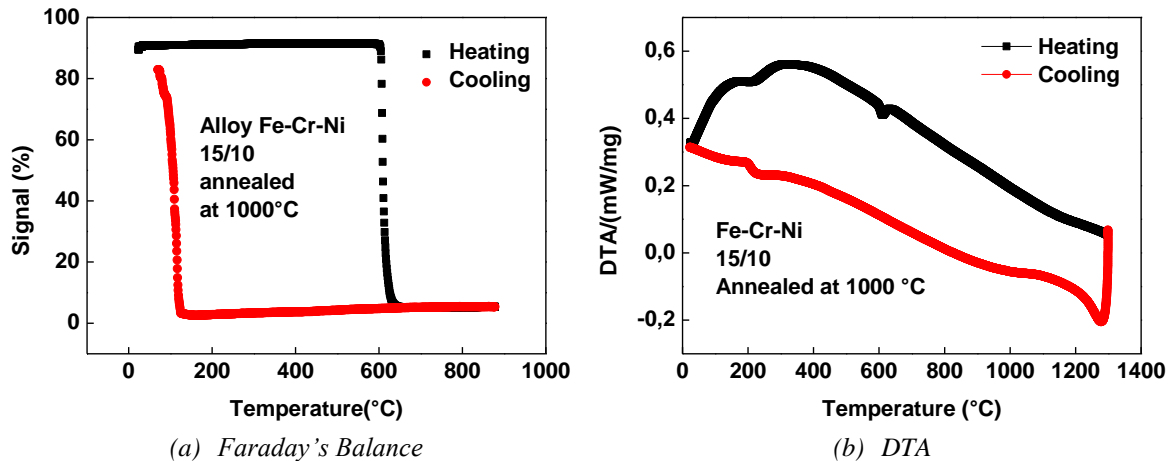


Figure VI-9. (a) The magnetic response in arbitrary units of annealed sample 15/10 is plotted as a function of increasing and decreasing temperatures. (b) the heat flux variation as a function of temperature in differential thermal analysis (DTA) for the same sample. The heating rate is 10 K/min for both experiments.

The difference between the magnetic change of state during heating and during cooling (the “thermal hysteresis”) can be explained by the nature of the two phase transitions. Upon heating from room temperature, we see the transformation from α ferrite to γ austenite starting at 600 °C. Upon cooling from 800°C, this transformation is not occurring due to the stabilization of austenite. The magnetic response increases at the spontaneous transformation from γ austenite to α' martensite around 150-200°C, which is coherent with the estimation of M_s temperature by Andrews empirical formula (181 °C).

Therefore, the first structural transition in DTA heating curve at 200 °C should correspond to the reversed martensite to austenite transformation or the transformation into more stable ferrite at low temperature, possibly with some austenite traces. There is a small kink in the thermomagnetic curve around the same temperature, by taking a closer look. The magnetic signal shows no significant change, indicating a major phase being ferrite until the second transition observed at 600°C.

This suggests that both changes in magnetic response are not the magnetic transition of a given ferromagnetic constituent of the sample but it is due to structural transformations between ferromagnetic and paramagnetic phases during heating and cooling.

The sample 15/10 annealed at 900 °C was measured and cycled in Faraday's Balance. The magnetic response shows the same behavior as the sample annealed at 1000 °C. Cycling gives the same transition behavior. During heating, the sample stays in the ferromagnetic (ferrite and martensite) phase up until 600 °C. As it is cooled down, the sample maintains the paramagnetic phase (austenite) from temperature higher than 600 °C until cooling below 200 °C, where it transforms into ferromagnetic martensite. The phase transition is highly temperature-dependent and this "thermal hysteresis" will remain in all cycles, as shown in Figure VI-10. During the cycles without cooling to room temperature Figure VI-10 (a), only the first heating curve results in the phase transition from the ferromagnetic (ferrite and martensite) to the paramagnetic (austenite) phase. The material stays in the austenite phase during the rest of the cycles between 270 °C and 780 °C, and 480 °C and 780 °C. Similarly, during the cycles cooling to room temperature at each cycle, if the material is not heated beyond the transition temperature at 600 °C, it remains in the ferrite and martensite phase, which is ferromagnetic, shown in the superposed curves in Figure VI-10 (b).

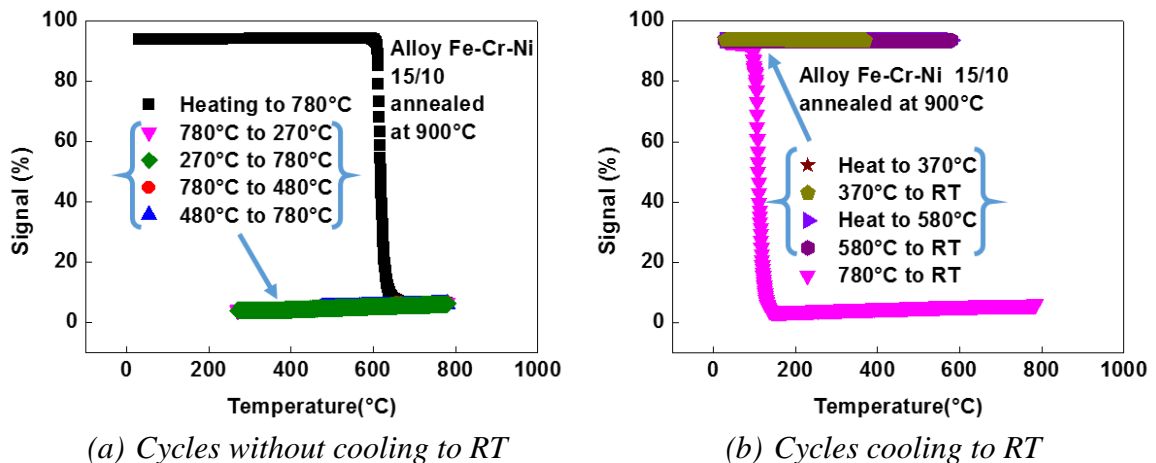


Figure VI-10. The magnetic response in arbitrary units of annealed sample 15/10 is plotted as a function temperature during (a) thermal cycles without going back to room temperature at each cycle and (b) thermal cycles cooling down to RT at each cycle. The curves in different colors superpose.

By combining the thermodynamic calculation and the phase transitions measured with thermomagnetic Faraday's Balance and DTA, it can be concluded that the alloy 15/10 contains mixed phases of martensite, ferrite, and austenite at room temperature. The transformation into martensite begins at the martensitic start temperature (M_s), regardless of the kinetics.

There seems to be a reversible transition between martensite and ferrite (possibly with some austenite) upon heating to 200 °C, which does not alter the magnetic response since both phases are ferromagnetic. Upon heating up further, the transition between ferrite and austenite phases results in a large decrease in magnetic response in the Faraday's Balance measurement and an endothermic peak in DTA. The high temperature austenite phase becomes the majority phase above 600 °C and persists during cooling until reaching the M_s temperature to form martensite from austenite.

A sample of similar composition was examined in the Ph.D. work of M. Hudl [17] in 2012. Sample of composition Fe10%Cr10%Ni lies much closer to the martensitic area on the Schaeffler diagram. The magnetization is measured under a field of 1 T. Upon heating, the system goes through a structural phase transition from bcc (martensite and ferrite) (FM) to fcc (austenite) (PM) at about 697 °C. Upon cooling, the reverse transition PM to FM occurs at much lower temperature, as seen from Figure VI-11. The huge “thermal hysteresis” is very similar to the behavior of alloy 15/10 mentioned above and is also coherent with the transformation of austenite into martensite below ~270°C (calculated Ms for this composition of 241°C)

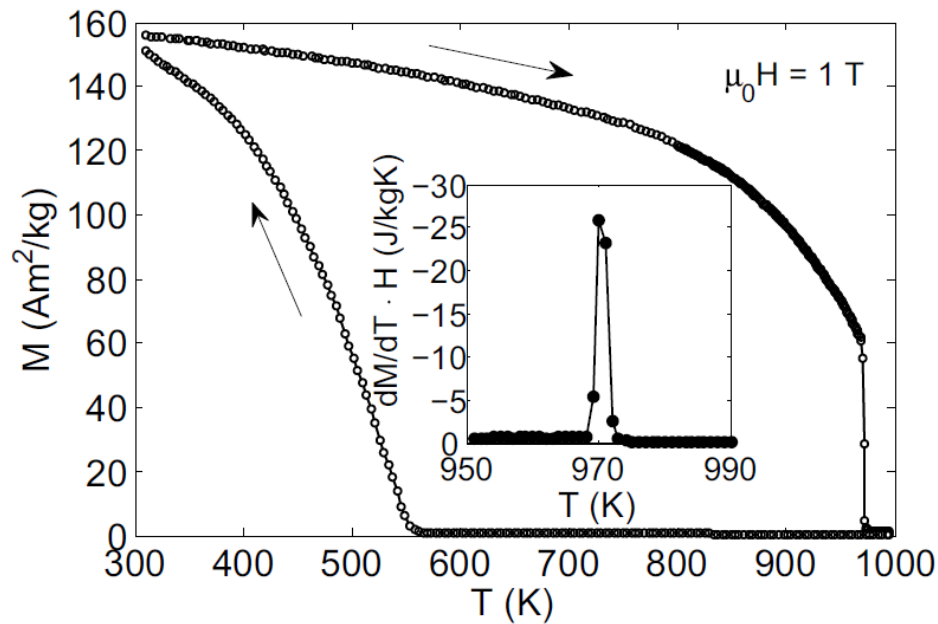


Figure VI-11. Magnetic properties of bcc Fe10%Cr10%Ni. Magnetization as a function of temperature in 1 T magnetic field. The inset shows $\frac{dM}{dT} \cdot H$ as a function of temperature, which corresponds to the magnitude of the magnetic entropy change, taken from reference [17].

3.1.2. Alloy 15/25

Increasing the Ni content should stabilize further the austenite phase at lower temperatures. The equilibrium phase fraction as a function of temperature is calculated by Thermocalc[®] for sample 15/25, as shown in Figure VI-12. Cooling from liquid melt, the austenite (γ -fcc) phase is the primary solidification phase and the ferrite (α -bcc) phase appears below 516 °C to reach a mixed ferrite/austenite structure.

Thermodynamic calculations predict a small equilibrium region for an intermetallic σ phase. Generally, this Fe-Cr phase features a high Cr content and brittleness. The sigma phase precipitation is promoted by alloying with Si, Mo, and W and is found in highly-alloyed ferrite. The austenite phase here has a moderate Cr content and does not contain Molybdenum, which requires a long time at very narrow temperature window to form the intermetallic σ phase. It is, therefore, less sensitive to the precipitation of σ phase.

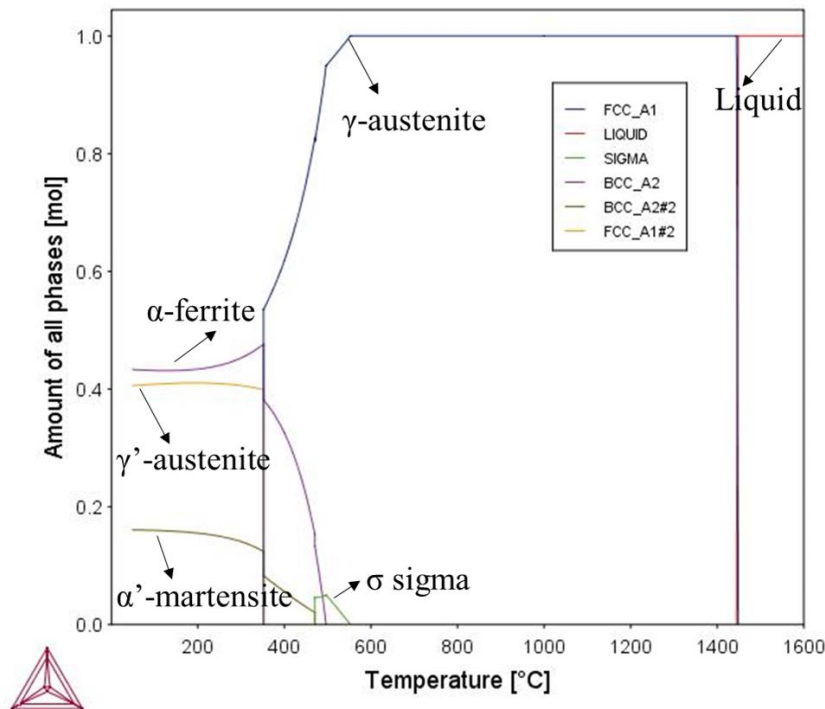


Figure VI-12. Phase fraction as a function of temperature for alloy 15/25 calculated using Thermocalc[®].

Figure VI-13 shows the XRD pattern of the as-cast alloy 15/25, showing the fcc phase structure. After annealing at 800, 900, and 1000 °C for 15 days (slowly furnace-cooled), XRD measurement shows that the majority phase is the fcc Fe₃Ni-type structure. Samples annealed at 800 °C and 900 °C seem to be particularly not well-crystallized. Therefore, the diffraction pattern of the alloys annealed at 1000 °C is shown in Figure VI-13 to compare with the as-cast sample. The refined lattice parameter is 3.58 Å, slightly smaller compared with sample 15/10. This is coherent with the high alloying content of Ni, which has a smaller atomic radius of Ni compared with Fe. Both the Schaeffler diagram and thermodynamic simulation confirm the presence of the fcc austenite phase.

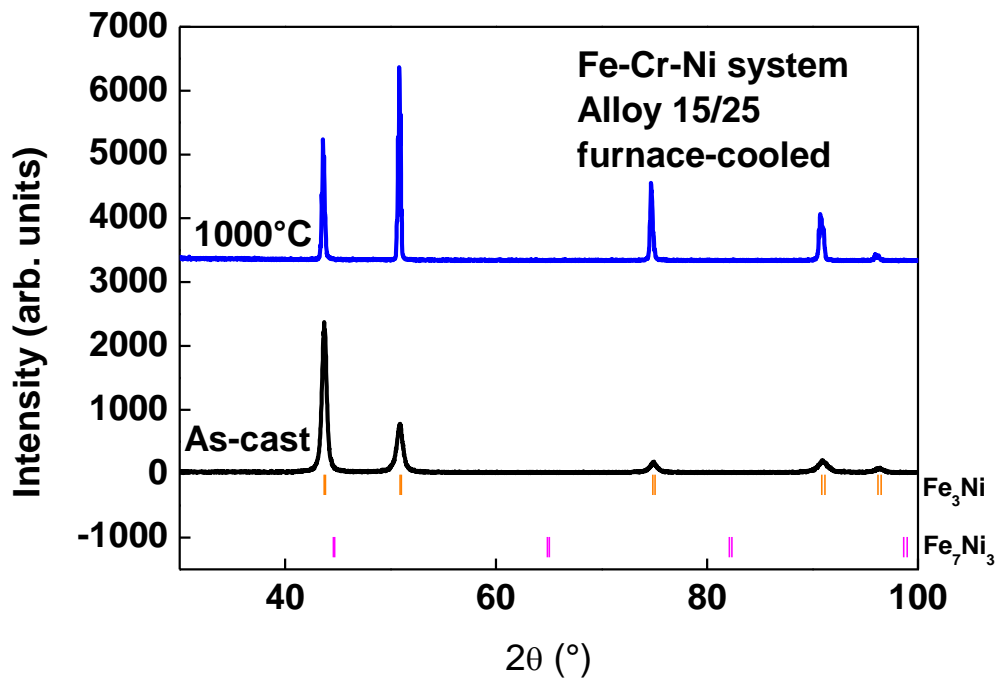


Figure VI-13. XRD patterns of as-cast and annealed sample 15/25 in the Fe-Cr-Ni system.

The microstructure confirms the existence of the austenite phase with rather large grains, as shown in Figure VI-14 for alloy 15/25 annealed at 1000 °C and slow-cooled. The furnace cooling might have contributed in the grain growth.

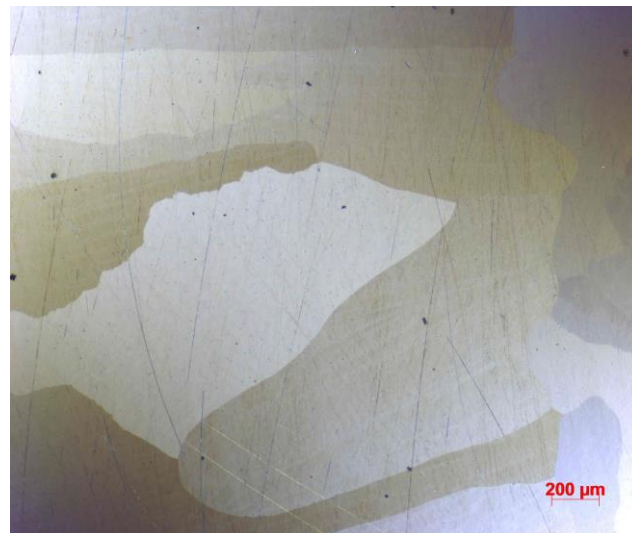


Figure VI-14. Microstructure observed with optical microscope after Kalling n^o2 etching for Fe-Cr-Ni alloy 15/25 annealed at 1000 °C and slow-cooled.

The magnetization level for alloy 15/25 annealed at 1000 °C is shown in Figure VI-15 for both the high temperature and low temperature range. The measuring procedure begins with a zero field cooling and heating after the application of field. The sample shows paramagnetic behavior at room temperature but there is a weak ferromagnetic to paramagnetic transition at low temperature (34 K). This corresponds to the Curie temperature of the austenite fcc phase corresponding to a fully magnetic transition.

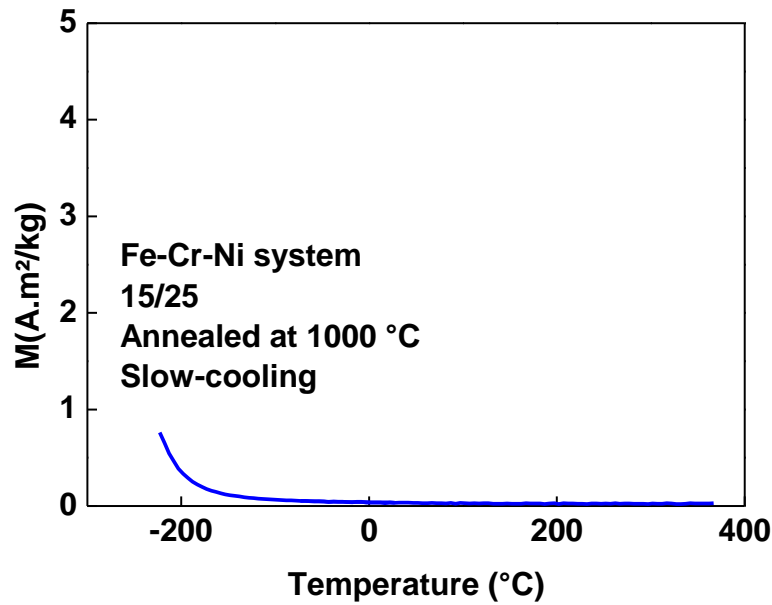


Figure VI-15. Magnetization level as a function of temperature under a field of 0.05 T measured by extraction vector magnetometer of alloy 15/25 annealed at different temperatures and furnace cooled.

The magnetic response of alloy 15/25 was also measured in thermomagnetic Faraday's Balance. The sample annealed at 1000 °C shows paramagnetic response in the measured temperature range. The magnetic response agrees with both the thermodynamic calculations and the XRD measurement. However, the heating and cooling curves measured in DSC (Figure VI-16(b)) show a reversible structural transition at 500 °C and 570 °C, respectively. One possible explanation is that this is due to a structural transition between two paramagnetic austenite phases (γ -austenite fcc_A1 and γ' -austenite fcc_A1#2 in thermodynamic calculations), considering that it is not observed in the magnetic response.

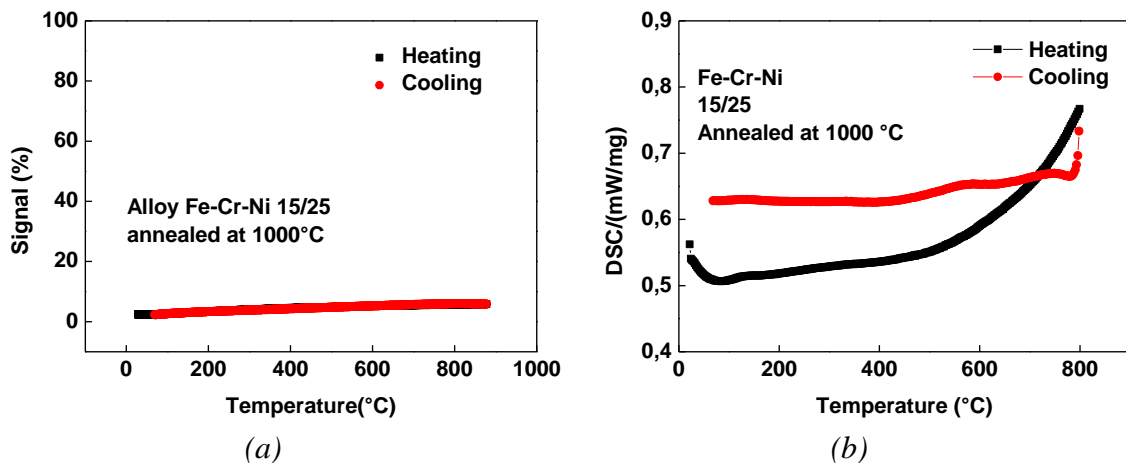


Figure VI-16. (a) Magnetic response in arbitrary units and (b) DSC measurement for alloy 15/25 annealed at 1000 °C.

3.1.3. Discussion

Alloys 15/10 and 15/25 exhibit different phase transformations under heat treatments. Alloy 15/10 show bcc to fcc transformation upon heating. The fcc-austenite phase is stabilized at high temperature and persists until the martensite starting temperature. The austenite to martensite transformation occurs spontaneously once the M_s temperature is reached. The two phase transformations (ferrite+martensite to austenite on heating and austenite to martensite on cooling) cannot be isolated due to the phase formations in the sample. Therefore, the structural transformations are not completely reversible and the two transformations take place at very different temperatures, making this material difficult to cycle in a narrow temperature range.

With higher Ni alloy content, alloy 15/25 shows principally austenitic phase, confirmed in both XRD and magnetic response in Faraday's Balance. The paramagnetic behavior is stable near room temperature. The austenite to ferrite transformation predicted from equilibrium thermodynamic calculation is absent under experimental conditions.

3.2. Effect of Ni with 5% Cr

In order to examine the transition with the ferrite phase, a series of samples were elaborated with 5 wt% Cr content and varying Ni contents. Samples with shorthand notation Cr/Ni contents of 5/15, 5/20, 5/25, and 5/35 were homogenized in sealed quartz tube at 1100 °C for 24 h before quenching in iced water (fast-cooling).

The thermodynamic calculations are similar for all four compositions. With increasing Ni concentration, the γ -austenite phase is stabilized at lower temperature range and less α -bcc phase is able to form in the mixed domain of $\alpha+\gamma$, which is coherent with both the thermodynamic calculations and the phase diagrams.

Shown in Figure VI-17, annealed sample 5/15 shows a typical martensitic microstructure with very small amounts of ferrite (darker phase after Kalling $n^{\circ}2$ etching) and maybe some remaining austenite. As Ni concentration increases, the alloy moves from martensite-rich microstructure to a ferrite-rich one in 5/20. With further Ni alloying, the microstructure shows even richer in austenite with some ferrite for 5/25. At 35 wt% Ni, the alloy shows typical austenitic large grains microstructure after Kalling $n^{\circ}2$ etching. There is a possible presence of ferrite (dark dots on the microstructure). This is coherent with the Schaeffler diagram, which shows the alloy 5/35 in an austenitic zone.

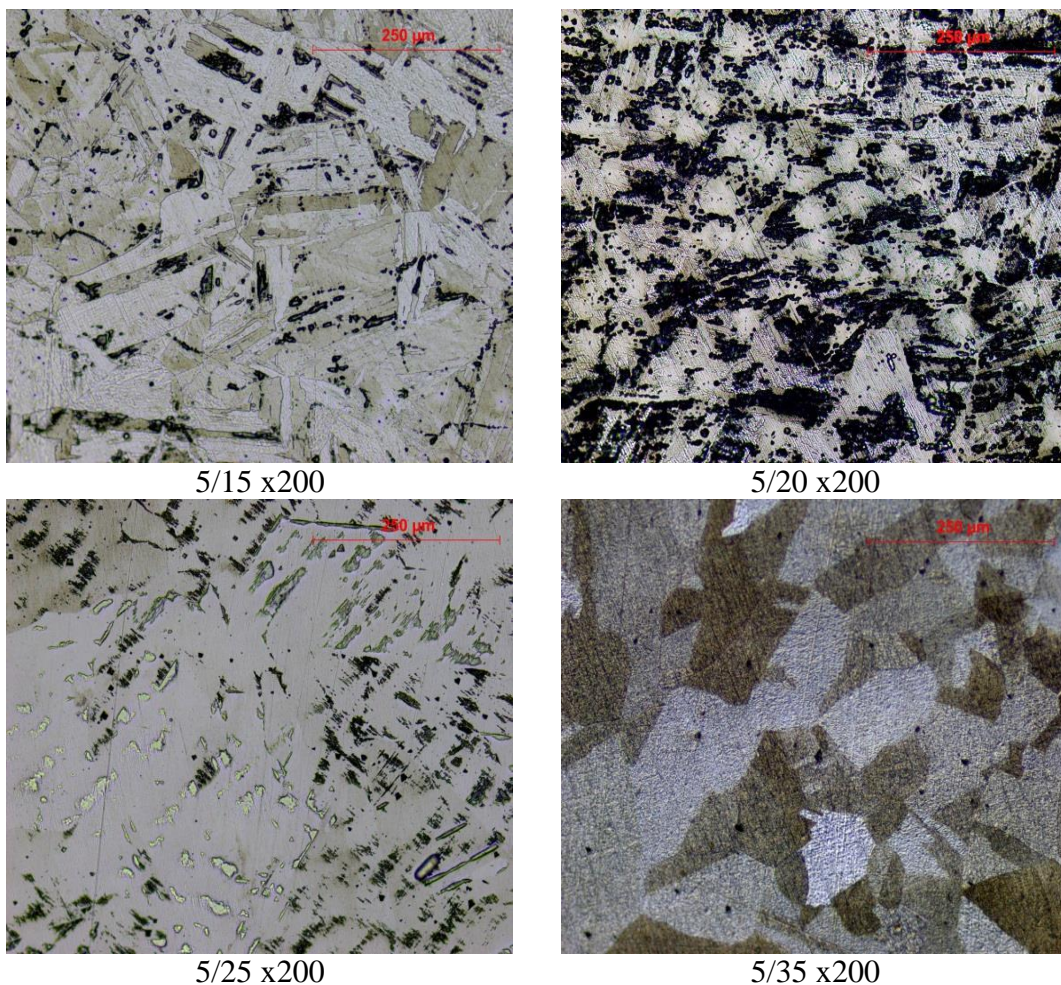


Figure VI-17. Microstructure observed with an optical microscope after Kalling's $n^{\circ}2$ etching for alloys 5/15, 5/20, 5/25, and 5/35.

The magnetic responses are consistent with the observations and some data from the thermodynamic calculations, as demonstrated in Figure VI-18. The magnetic signal in Faraday's Balance is in arbitrary units and the signal is consequently normalized with the magnetization measurement at 300 K under 1 T field with extraction vector magnetometer to properly compare the magnetic response.

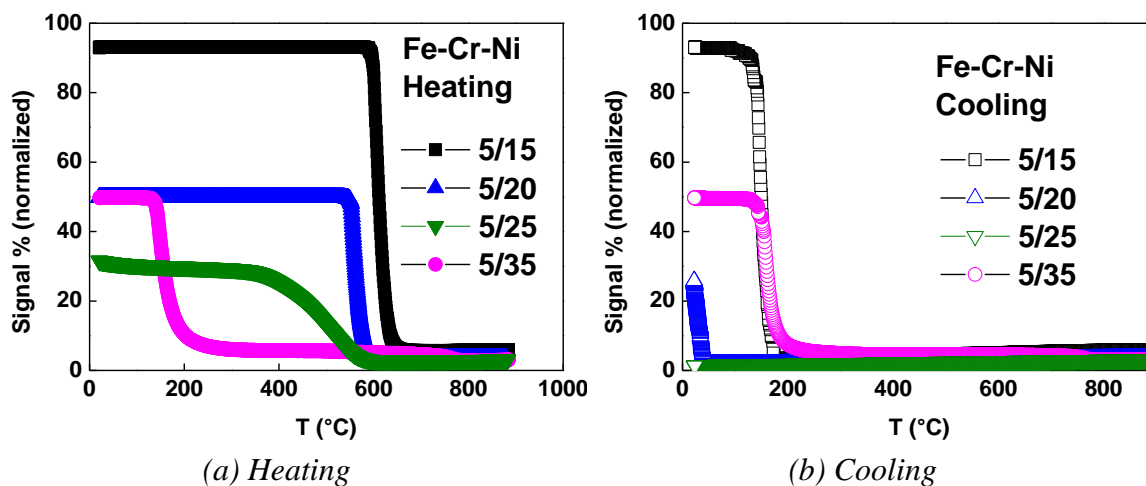


Figure VI-18. Magnetic response for alloys with fixed Cr content (5 wt%) and varying Ni concentration (15-35 wt%) measured (a) from room temperature to 900 °C and (b) subsequent cooling. Signal is normalized by magnetization measurement in extraction vector magnetometer.

As Ni content increases, austenite is stabilized at lower temperature. The magnetization level measured under 1 T field at 300 K for 5/25 is considerably lower. The magnetic transition from ferrite to austenite upon heating in the Faraday's Balance shows much softer behavior.

Alloys 5/15 and 5/20 show similar transition behavior as sample 15/10 from the previous section. The sample transforms from α ferrite+ α' martensite ferromagnetic phases at room temperature to the paramagnetic γ austenite phase above 650 and 600 °C, respectively. The recovery of the ferromagnetic martensite phase is not realized until 190°C (for a calculated value of 213°C) for 5/15 and ~50°C (for a calculated value of 125°C) for 5/20. By increasing Ni content from 15% to 20%, both the transition temperature from ferrite to austenite phase and the martensite start temperature shift towards lower temperature range.

Alloy 5/25 shows a transition from ferrite+martensite to austenite phases from 400 to 600 °C. No magnetic signal is recovered upon cooling, indicating that austenite is stable at this composition.

In the Faraday's Balance measurement for alloy 5/35, we observe a reversible transition from ferromagnetic to paramagnetic state near 200 °C during heating and cooling with no thermal hysteresis.

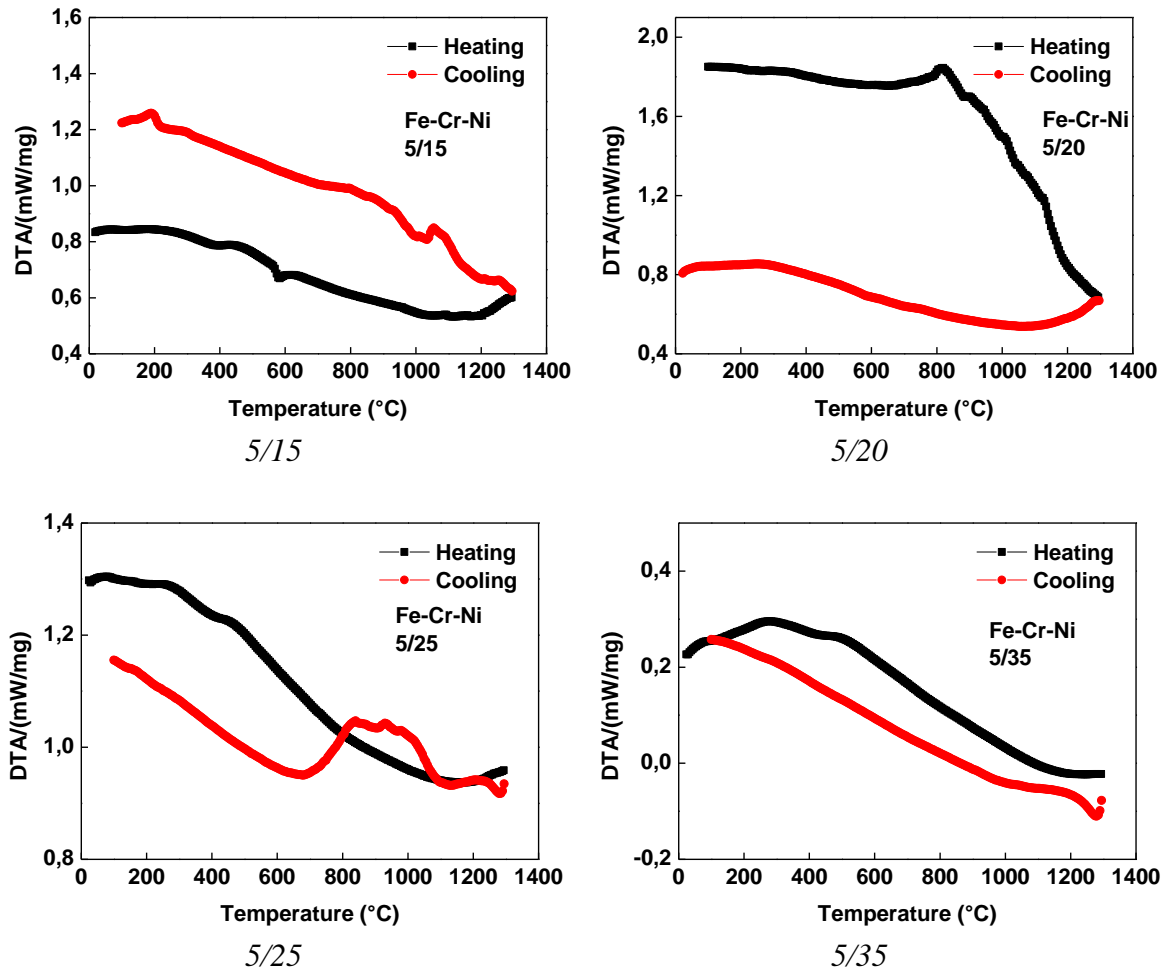


Figure VI-19. DTA curves for Fe-Cr-Ni alloys with 5 wt% Cr.

The DTA measurement for alloy 5/15 shows the ferrite to austenite transition at 620 °C upon heating. Upon cooling, the austenite to ferrite reversible transition occurs at 700 °C and the recovery of the martensite phase takes place at 190 °C. The phase transitions in alloy 5/20 are characterized by soft, large changes of the baseline, which is attributed to the smaller amount of ferrite and martensite phase to begin with.

The DTA measurements for alloy 15/25 show changes of baseline at 270 °C and 400 °C upon heating, which can be 1) the transitions between two austenite phases calculated from thermodynamic calculations or 2) the transitions between ferrite and austenite phases. Upon cooling, the transformation at 730 °C might correspond to a phase transition of two austenite phases. This can be explained by the austenite-rich microstructure of alloy 5/25 (shown in Figure VI-17). The amount of ferrite and martensite phases being able to transform into austenite is considerably less in alloy 5/25. The estimated M_s for this composition is 36 °C, which probably explains that no magnetic transition is recovered at low temperature.

From the DTA measurement, small transitions at 270 °C and 400 °C are similar to what is observed for alloy 15/25, although the corresponding magnetic responses between 15/25 and 15/35 are quite different. The transition below 200°C seems to be the ferromagnetic transition of γ austenite phase, with a Curie point near 200°C. The theoretical M_s temperature after Andrew's formula for such a composition is around -141°C, therefore, no martensite phase is able to form in this sample upon cooling to room temperature.

3.2.1. Alloy 5/20

With a lowered martensite starting temperature, alloy 5/20 does not recover the maximum amount of martensite phase when cooled to room temperature. The sample was measured in extraction vector magnetometer in order to examine the magnetization level at lower temperature ($-73\text{ }^{\circ}\text{C}$). Sample was zero field cooled and a field of 0.05 T was applied at low temperature before the thermal cycles. Each temperature was stabilized before the moment measure.

Due to the temperature limit of the instrument, the heating curve was performed from -73 to $560\text{ }^{\circ}\text{C}$. The transition between ferrite to austenite is probably not complete. Indeed, as less austenite is able to nucleate at this temperature, in the subsequent cooling and heating curves, the martensite recovered at low temperature was also much less, as seen by the difference in magnetization level in Figure VI-20 (b). This confirms that these phase transitions are highly temperature-dependent.

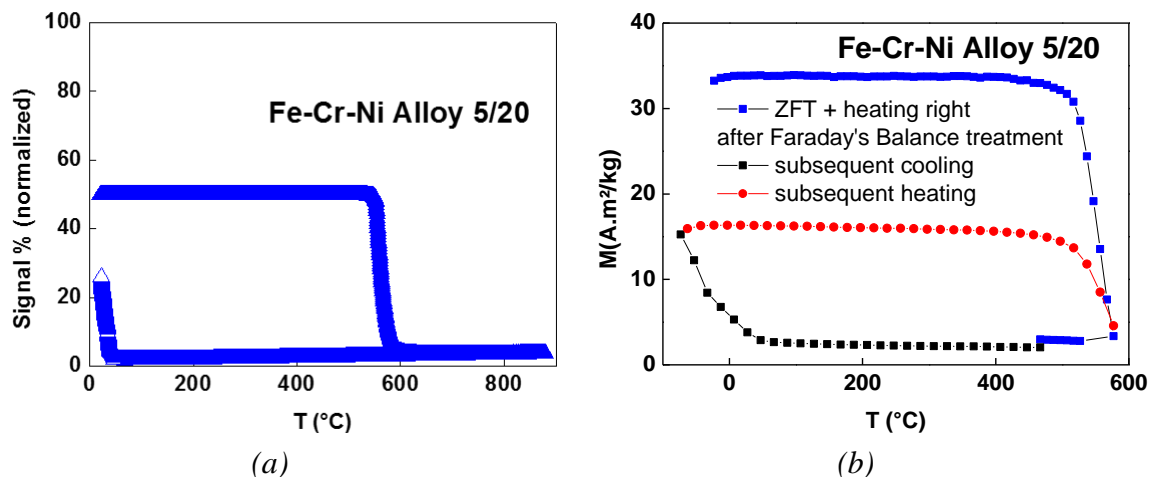


Figure VI-20. (a) Magnetic response in Faraday's Balance and (b) thermal magnetic curves measured for sample 5/20 after treatment in Faraday's Balance in extraction vector magnetometer.

In order to examine the effect of cooling rates, the as-cast sample 5/20 (no previous annealing treatment) was melt-spun from $1600\text{ }^{\circ}\text{C}$ at 12 m/s quenching rate. The ribbons were measured by grazing incident X-ray diffractometer and the measurement was performed on a sample with alternating faces of the melt-spun ribbons. The resulting XRD pattern, shown in Figure VI-21 (a), shows a majority of bcc phase, with weak intensities of fcc reflections hidden in the background.

The melt-spun ribbons were also characterized by Faraday's Balance in different heating and cooling cycles. The magnetic signal, shown in Figure VI-21 (b), shows very similar behavior with the sample annealed at $1100\text{ }^{\circ}\text{C}$ for 24h and quenched in iced water.

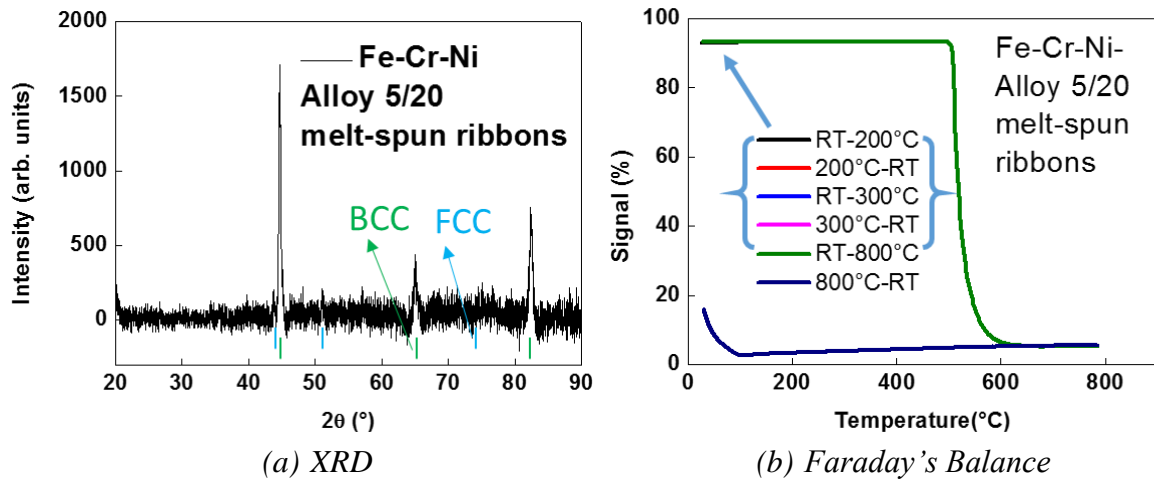


Figure VI-21. (a) XRD and (b) Faraday's Balance cyclic measurements on Fe-Cr-Ni alloy 5/20 melt-spun ribbons.

By comparing the magnetic signals for alloy 15/20 undergone different heat treatments, the melt-spun ribbons show slightly lower transition temperatures for the two structural transformations, as shown in Figure VI-22.

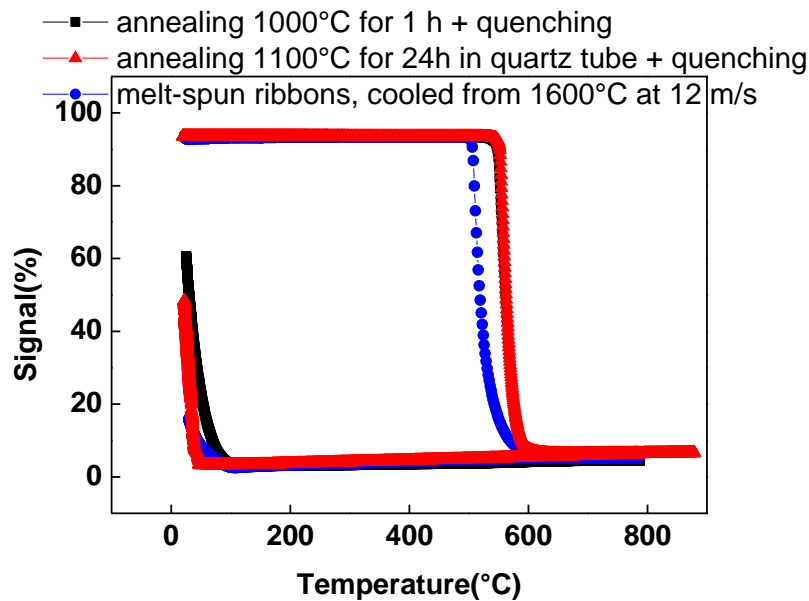
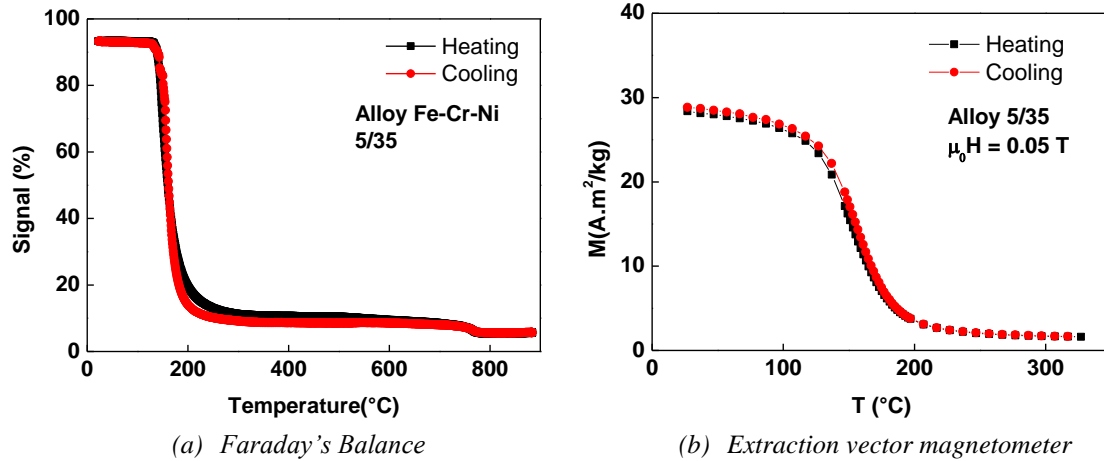


Figure VI-22. Magnetic signals in arbitrary units measured for alloy 5/20 undergone different thermal treatments.

3.2.2. Alloy 5/35

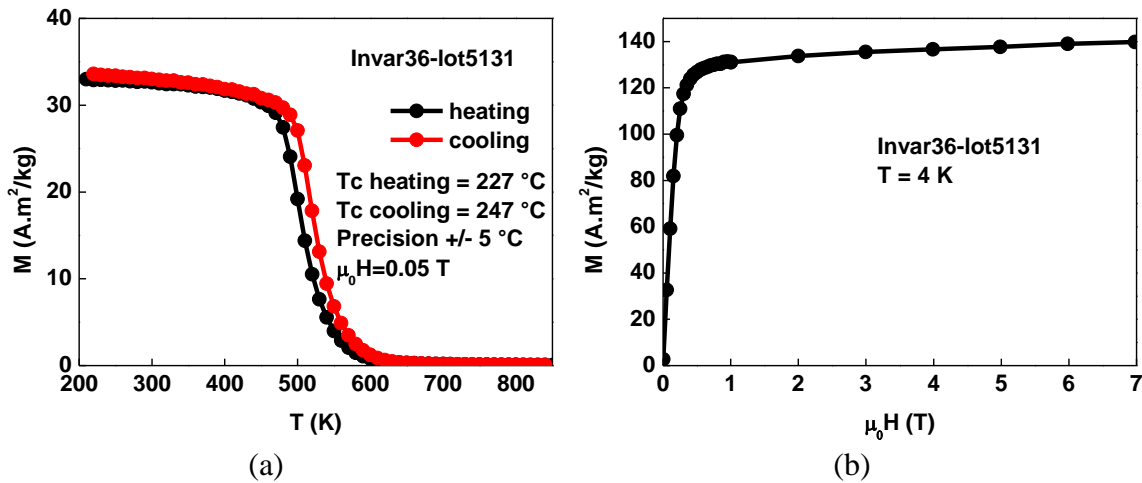
The magnetic transition of alloy 5/35 was measured in extraction vector magnetometer in order to verify precisely the order of magnetization and the transition behavior. The $M(T)$ curve under a field of 0.05 T shows a typical second-order magnetic transition without abrupt discontinuation at the transition temperature (Figure VI-23).



(a) Faraday's Balance (b) Extraction vector magnetometer
 Figure VI-23. Comparison between (a) the magnetic response in arbitrary units measured in Faraday's Balance and (b) the thermal magnetization measured in an extraction vector magnetometer under a field of 0.05 T.

The difference in transition shape from the two measuring techniques is due to the temperature-screening rate. The Faraday's Balance apparatus has a very small furnace with fast heating rate whereas for the extraction vector magnetometer, the temperature has to be stabilized for each point, which has a much slower heating rate. The alloy 5/35 has a T_C of 153 °C and a reversible ferromagnetic transition in a range of temperature close to the application but it is not the expression of a structural transition inducing a magnetic transition.

With only small amount of Cr, alloy 5/35 has a very similar composition to commercial Invar36 alloy (Fe36%Ni). We have measured the magnetic transition of a commercial Invar36 powder sample from Erasteel for comparison, as shown in Figure VI-24.



(a) (b)
 Figure VI-24. Magnetization measurements (a) as a function of temperature under a field of 0.05 T and (b) at low temperature with increasing field for Invar36-lot5131 sample from Erasteel.

The $M(T)$ is measured under an external field of 0.05 T with a step of 10 °C. As can be seen in Figure VI-24, the magnetic transition shows a soft, second-order transition around 227 °C. The magnetization at low temperature (4 K) increases with increasing field and the sample is not saturated at 7 T. The difference in transition temperature and low-temperature magnetization is attributed to the 5 wt% of Cr added in sample 5/35.

The isothermal magnetic entropy change is estimated from magnetization measurements. Commercial powder Invar36-lot5131 shows very modest ΔS_M in the order of 1.3 J/kg·K

under a field change from 0 to 2 T (Figure VI-25). Therefore, we estimate a similar MCE for sample 5/35.

Iorga *et al.* [21] have studied the effect of Cr and Mn on decreasing the T_C of Fe-Cr-Ni-Mn alloys in the composition range close to Invar and have reported samples with transition temperature around room temperature. Similar to what we report in this work, the near room temperature transition is purely magnetic, without structural changes.

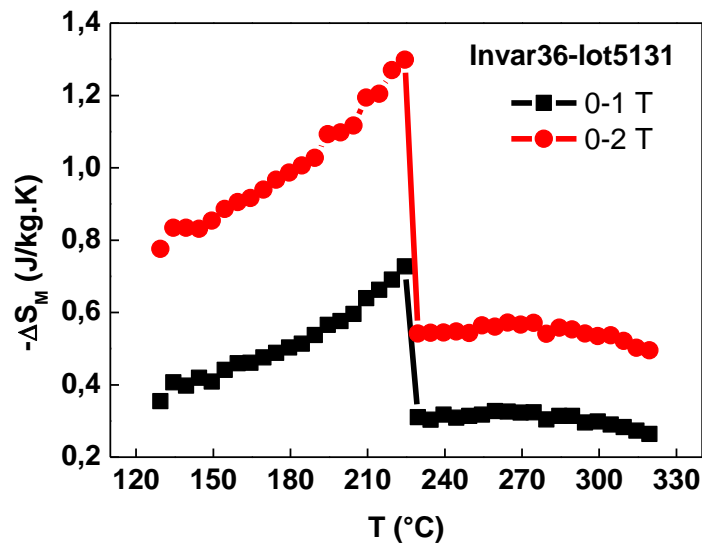


Figure VI-25. Isothermal magnetic entropy estimated from the thermal magnetization measurements for powder sample Invar36-lot5131.

3.2.3. Discussion

With 5 wt% Cr, the Fe-Cr-Ni alloys with Ni content ranging from 15 to 35 wt% exhibit diverse transition nature. Nickel content stabilizes the austenite phase and decreases the transition temperature from bcc (ferrite and martensite) to fcc austenite phase upon heating. With Ni alloying content ≤ 20 wt%, the martensitic transition temperature is above room temperature, therefore, a spontaneous transition from austenite to martensite is observed upon cooling for alloy 5/15 and 5/20. Alloy 5/35 shows similar second-order magnetic transition behavior of commercial Invar alloy. Microstructure confirms its austenitic phase, which has a reversible magnetic transition at 153 °C.

3.3. Effect of Cr with 10% Ni

A series of samples with 10 wt% Ni (25/10 and 35/10) were elaborated in order to cover the δ -ferrite phase (which forms above the temperature range of austenite) regions. The as-cast samples were annealed at 1100 °C for 4 h before quenching in iced water in order to retain the δ -ferrite phase during rapid cooling. According to the phase diagrams, sample 15/10 lies in a triple-phase austenite, ferrite, and martensite or a mixed austenite/ferrite zone (40%

ferrite) depending on the reference taken into account. Alloy 35/10 lies in an austenite and ferrite phase zone with 90% ferrite, according to the Schaeffler diagram.

The thermodynamic calculations (Figure VI-26) predict the presence of δ -ferrite (BCC_A2 above the temperature range of austenite) and σ phases in both alloys. The austenite equilibrium domain of existence is much larger in alloy 25/10 than in 35/10. The presence of σ phase is expected considering the Cr content.

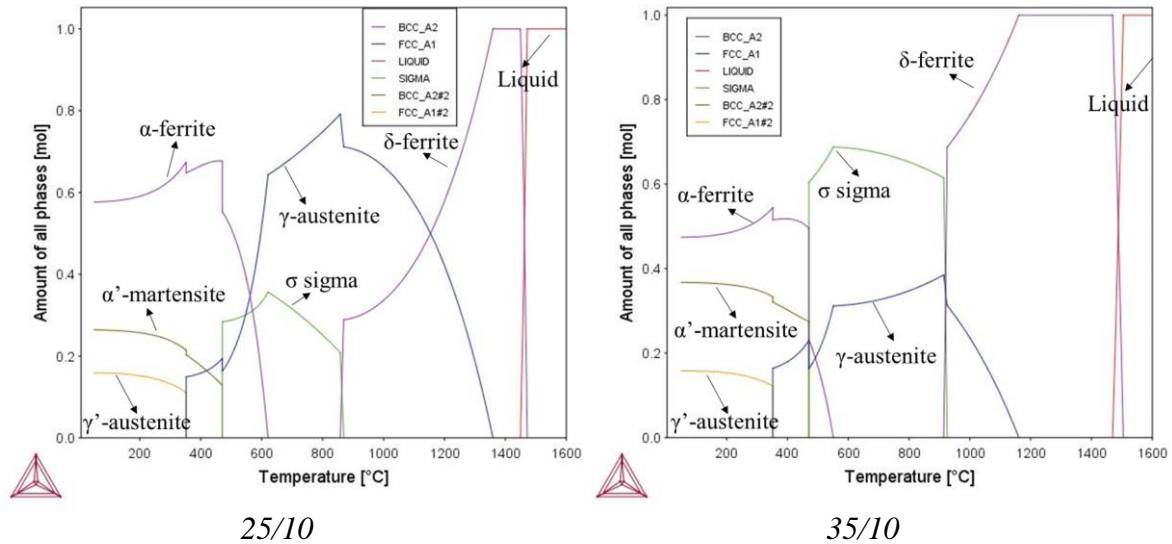


Figure VI-26. Thermodynamic calculations for Fe-Cr-Ni alloys 25/10 and 35/10.

The microstructure of annealed samples is shown in Figure VI-27. Sample 25/10 exhibits a mixture of typical microstructures of white rounded shape δ -ferrite grains and austenite in the intergranular area after Kalling n^o2 etching.

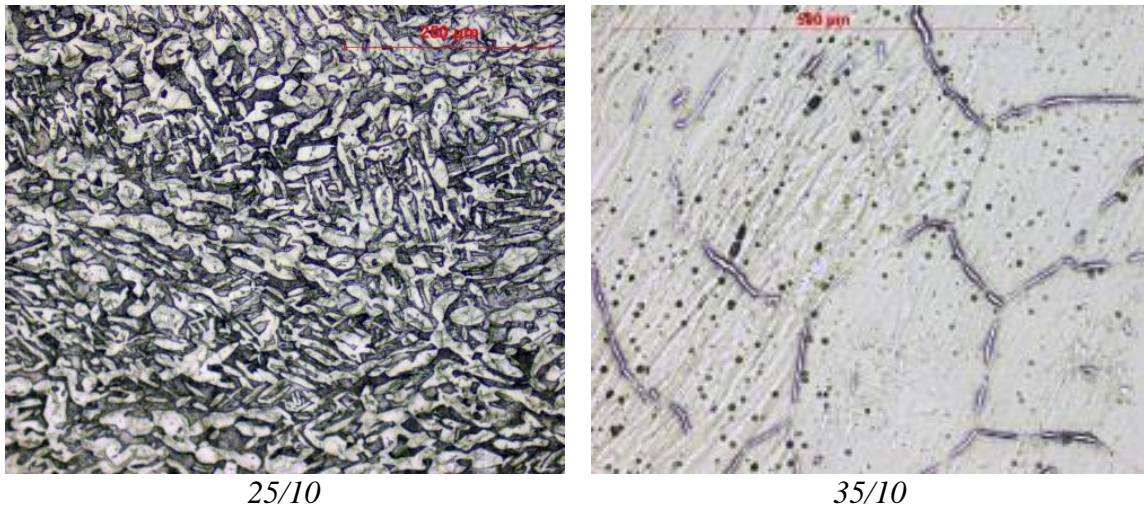


Figure VI-27. Microstructure of alloys 25/10 and 35/10 observed with an optical microscope after HNO_3 etching.

Sample 35/10 probably consists of large δ -ferrite grains with some thin austenite phase in the inter-granular area, according to the microstructure image after electrolytic etching in HNO_3 . The black dotted phase was not identified but could be σ phase considering the amount of Cr contents.

The magnetization level measured under 1 T field at 300 K for alloy 25/10 and 35/10 is 48 and 85 $A \cdot m^2/kg$, respectively, which is consistent with the large δ -ferrite grains observed for alloy 35/10 and large δ -ferrite proportion predicted by the Schaeffler diagram.

The magnetic responses and thermal analysis of alloy 25/10 and 35/10 are shown in Figure VI-28. In alloy 25/10, the magnetic transition observed around 550°C could be the transition from δ -ferrite to austenite, which corresponds to the baseline change in the DTA measurement on the right. Small changes can be seen on the heating curves at temperatures lower than 200 °C, which might be due to the presence of small amount of martensite phase. Upon cooling, the δ -ferrite is not retained due to the slow cooling. Therefore, we observe transformations from δ -ferrite to austenite around 900 °C and the transition from austenite to α -ferrite upon further cooling. The transition between ferrite and austenite is possibly facilitated due to the presence of sigma phase in the sample. The formation of α -ferrite can also explain the different magnetic response at the end of the cycle. Moreover, the lowered magnetic signal at the end of the cooling curve could be due to both precipitations of some paramagnetic austenite (between 800 and 900°C) and sigma phase (between 400 and 600°C).

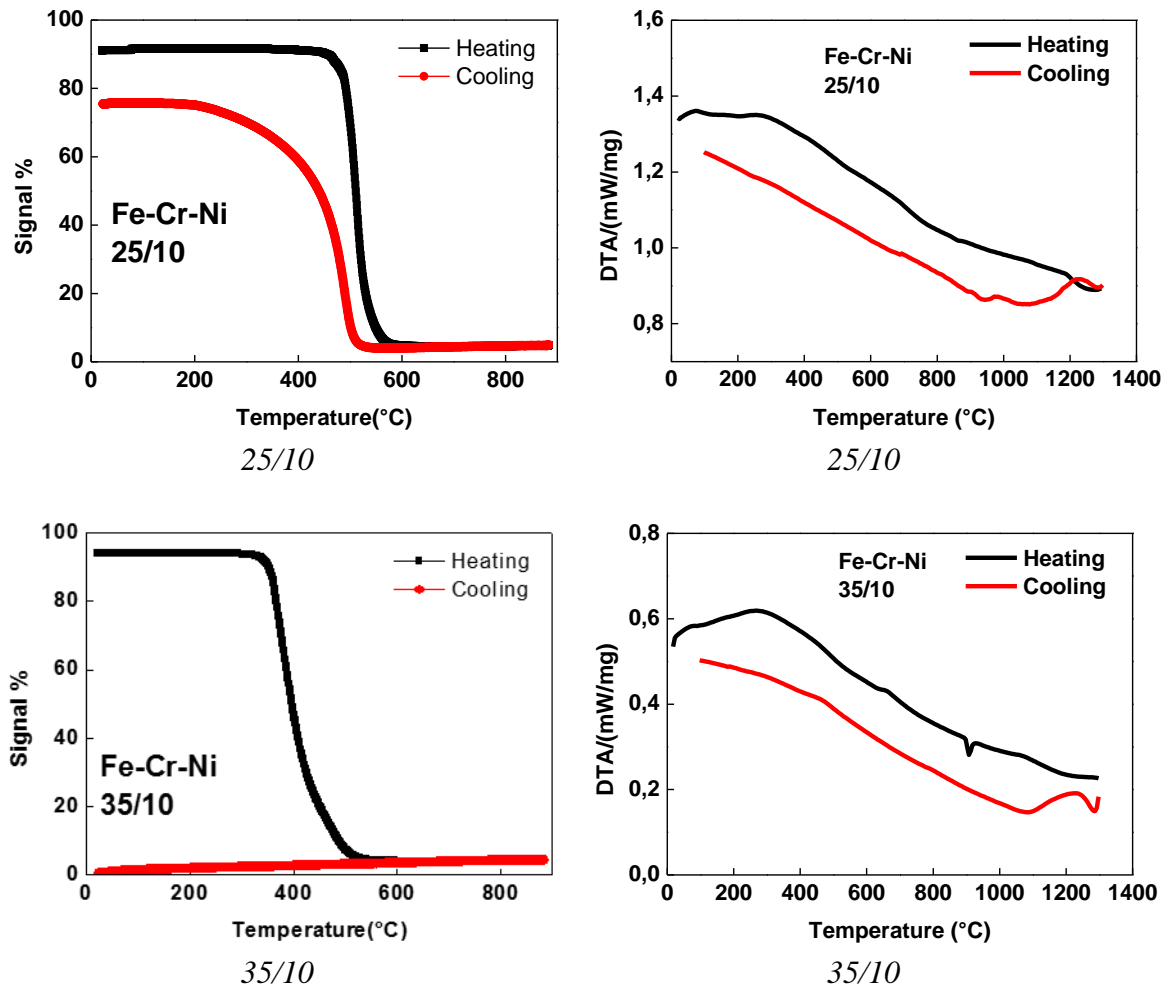


Figure VI-28. Magnetic response in arbitrary units and corresponding DTA measurements in heating and cooling for alloys with fixed Ni content (10%) and varying Cr concentration (25-35%).

For the magnetic response of alloy 35/10, during heating we observe a transition from ferromagnetic to paramagnetic phase similar to 25/10 but at lower temperature, around 400°C. The DTA measurement for alloy 35/10 supports the observations in the magnetic

response. Shown in Figure VI-28, the transition from δ -ferrite to austenite is seen around 400 °C upon heating. Above 800 °C, we observe the precipitation of δ -ferrite from austenite in the normal existence domain for δ -ferrite phase. The cooling curves in both magnetic signal and DTA measurement are not fast enough to ensure the retention of δ -ferrite. Therefore, we observe the stabilization of austenite phase upon cooling. No austenite to martensite transition occurs during cooling, considering the M_s temperature calculated for this composition is -62 °C.

These two alloys (25/10 and 35/10) help to identify the effect of σ phase in the phase transformation between ferrite and austenite. In alloy 25/10, the reversible transformation between two types of ferrite phases and austenite is probably facilitated by an intermediate transformation through the precipitation of σ phase. In the case of alloy 35/10, the transition from ferrite to austenite coincides with the transition from ferrite to sigma (according to the thermodynamic calculation). The presence of sigma phase seems to facilitate the stabilization of austenite phase during cooling.

In the Fe-Cr-Ni systems, we have seen the phase transformation between ferromagnetic (ferrite and martensite) and paramagnetic (austenite) phases. The magnetic response changes with the structural transformation, which is highly dependent on the temperature and the alloy composition. In the next section, the Fe-Cr-Mn system is examined.

4. Fe-Cr-Mn system

High-manganese austenitic steels have a reduced level of long-time radioactivation and are therefore, suitable as a replacement for the widely used Fe-Cr-Ni stainless steels in fusion reactors [18]. In 1990, Y. Murata and colleagues have studied the phase stability of the austenite phase in Fe-Cr-Mn ternary system at 650 °C (923 K) [19], which is referred to in our choice of compositions. The Fe-Cr σ phase, with soft ferromagnetic transition near 300 K, was detected even in low-Cr alloys, indicating a $\gamma/\gamma+\sigma$ phase boundary at the low-Cr content region of the Fe-Cr-Mn ternary diagram (Figure VI-29). They showed that the γ single-phase region was quite narrow from the experimental data.

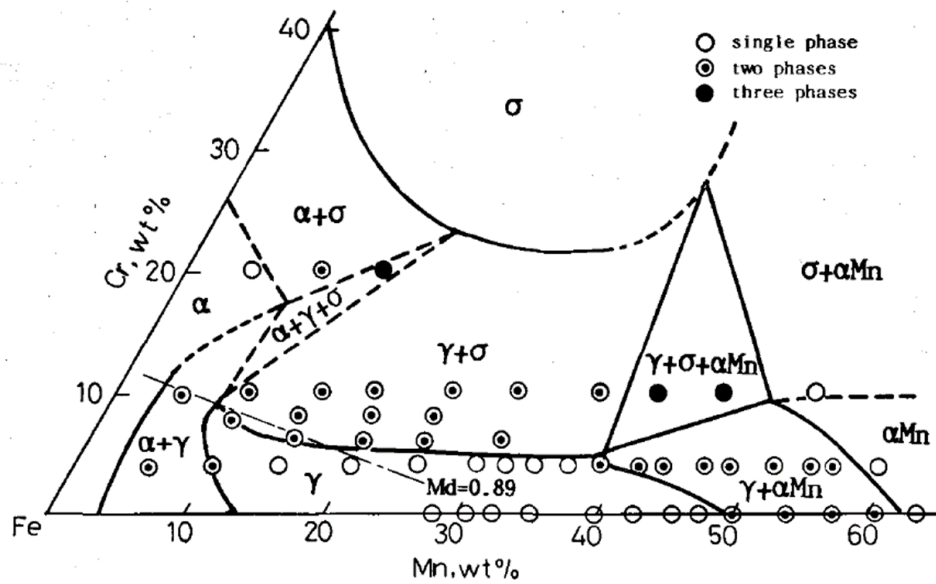


Figure VI-29. Isothermal section of Fe-Cr-Mn at 650 °C, taken from reference [19]

The atomic concentrations of the samples in this section are shown in Table VI-3. A first series of materials comprises two experimental ternary Fe-Cr-Mn alloys with constant Cr content (15%) and varying Mn levels (10% and 25%), guided by reference [2]. The alloys of a second series have carbon added to the 15/25 alloy in different concentrations (0.05%, 0.1%, 0.2%) to investigate the effect of C on stabilizing the γ phase and thus to reduce the transformation temperature from γ to α during cooling. A third series has alloys with smaller Cr content (5%) and varying Mn levels (20% and 25%). From M_s calculation, it can be seen that only alloy 15/10 shows possibility to form martensite phase upon cooling.

Table VI-3. The Fe-Cr-Mn samples in this section with their stoichiometric compositions in weight percent and the estimated martensite starting temperature from Andrews empirical formula [18].

Alloy Shorthand	Fe wt%	Cr wt%	Mn wt%	C wt%	Calculated M_s ($^{\circ}\text{C}$)
15/10	75	15	10	0	53.5
15/25	60	15	25	0	-402.5
15/25/0.05	60	15	25	0.05	-423.65
15/25/0.1	60	15	25	0.1	-444.8
15/25/0.2	60	15	25	0.2	-487.1
5/20	75	5	20	0	-129.5
5/25	70	5	25	0	-281.5

4.1. Series Fe-Cr-Mn with 15% Cr

The samples of composition 15/10 and 15/25 were elaborated by induction melting appropriate amount of starting elements Fe, Cr, and Mn. The melted buttons were homogenized in sealed quartz tube at 800 $^{\circ}\text{C}$, 900 $^{\circ}\text{C}$, and 1000 $^{\circ}\text{C}$ for 15 days and furnace-cooled (slow-cooling).

4.1.1. Alloy 15/10

From Figure VI-30, the austenite (γ -fcc) phase is the primary solidification phase. After the thermodynamic calculation for this composition, the intermetallic σ phase appears below 750 $^{\circ}\text{C}$ and the ferrite phase starts to form below 605 $^{\circ}\text{C}$. The sample might be sensitive to the precipitation of σ phase.

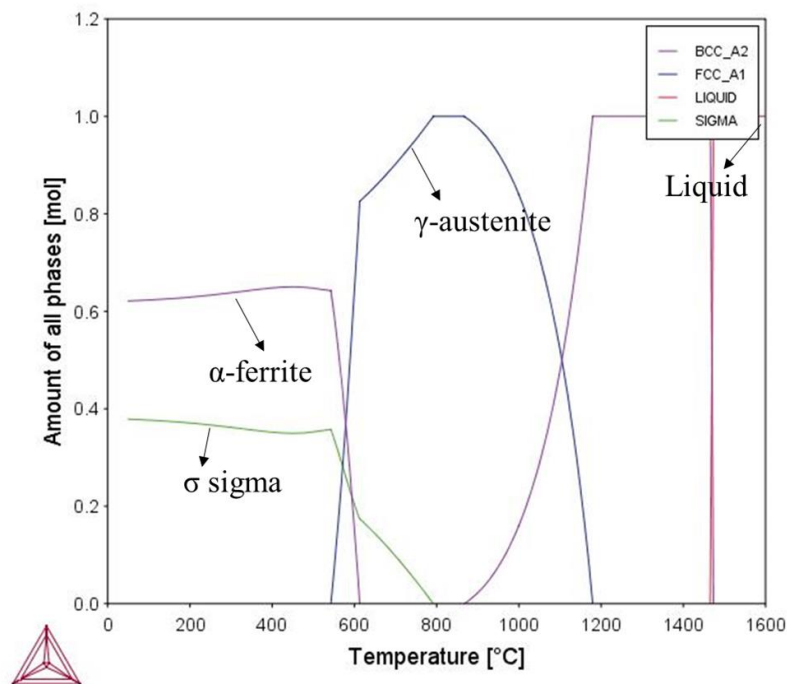


Figure VI-30. Phase fraction as a function of temperature for alloy 15/10 calculated using Thermocalc[®] with database TCFE6.

As seen from the XRD patterns in Figure VI-31, the majority phase in sample 15/10 (annealed at 3 different temperatures) is a body-centered cubic structure in the space group $Im-3m$. The lattice parameter is 2.87 \AA . This is in accordance with the Schaeffler's diagram for this composition which gives a mixture of ferrite and martensite at room temperature. The magnetization measurements confirm the presence of ferrite and martensite phases (shown in Figure VI-32).

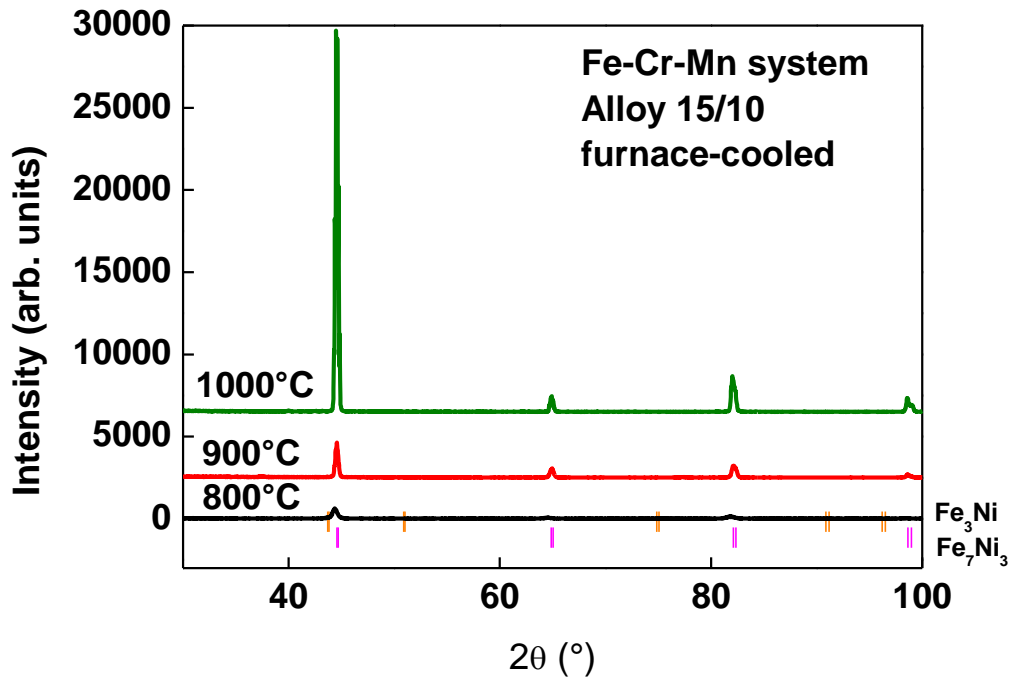


Figure VI-31. XRD pattern for alloy 15/10 annealed at different temperatures for 15 days.

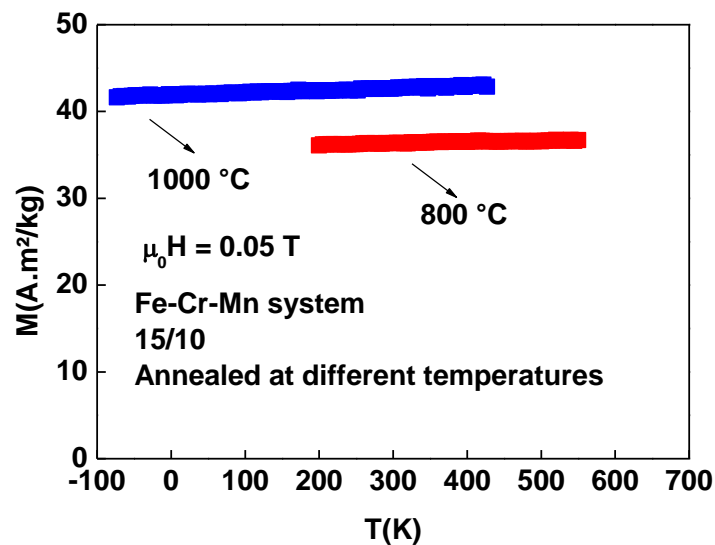


Figure VI-32. Magnetization as a function of temperature for Fe-Cr-Mn alloy 15/10 annealed at 800 °C and 1000 °C under 0.05 T field.

The microstructure in Figure VI-33 show white ferrite grains with a typical plate-like structure of martensite. The small dots in Figure VI-33 (b) are probably sigma phase.

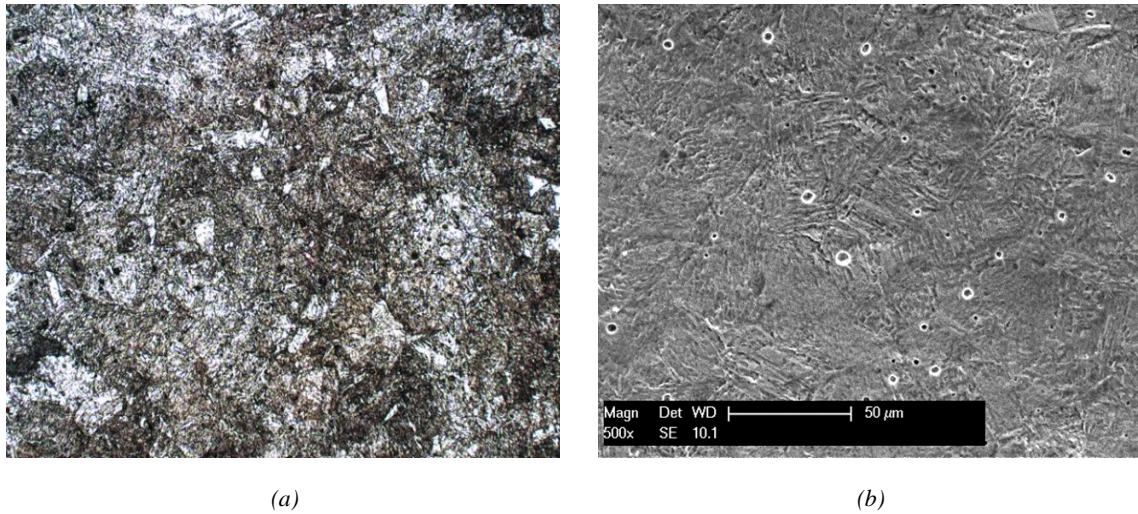


Figure VI-33. (a) Optical and (b) electronic microstructures after aqua regia etching for Fe-Cr-Mn alloy 15/10 annealed at 1000 °C for 15 days.

Under an external field of 1 T at 300 T, alloy 15/10 shows a magnetization level of 153.49 A·m²/kg, confirming the presence of ferromagnetic phases (ferrite and martensite). The magnetic response in arbitrary units shows that at room temperature, alloy 15/10 exhibits ferromagnetic response, confirming the presence of the bcc (ferrite and martensite) phase, as shown in Figure VI-34. At 550 °C during heating from this mixed phase, a transition from bcc ferrite to fcc austenite is observed, as indicated by the drop in magnetic response. This is coherent with the thermodynamic calculation in Figure VI-30. In the course of cooling, part of the austenite phase starts to transform into the ferrite phase around 600 °C in a reversible structural transition, as seen by an increase of magnetic signal. But this transformation does not reach 100% of the sample.

Between 400 °C and 150 °C, the potential formation of sigma phase might explain why the magnetic signal increase has a limited rate. Then, below 50 °C, the change of slope for the magnetic signal could be in line with the formation of martensite phase from remaining austenite, which is also visible on the DSC curve at low temperature. This is in accordance with the Ms temperature calculated with the Andrews formula (54 °C). Below 200 °C, sigma phase stops to precipitate.

The difference in transitions between heating and cooling is due to the large difference of sigma phase concentration accompanying the austenitic and ferritic phases (0-38% at equilibrium according to the thermodynamic calculation). The formation of σ phase during cooling adds another step for the transformation between the γ and α phases.

The transformation at 100 °C (austenite to martensite) can be observed in DSC as an exothermic peak during cooling, shown in Figure VI-34 (b) and (d). At fast cooling rate of 10 K/min, we only observe the beginning of such a transition but the full transformation is clearly seen when heating/cooling rate is reduced to 2 K/min.

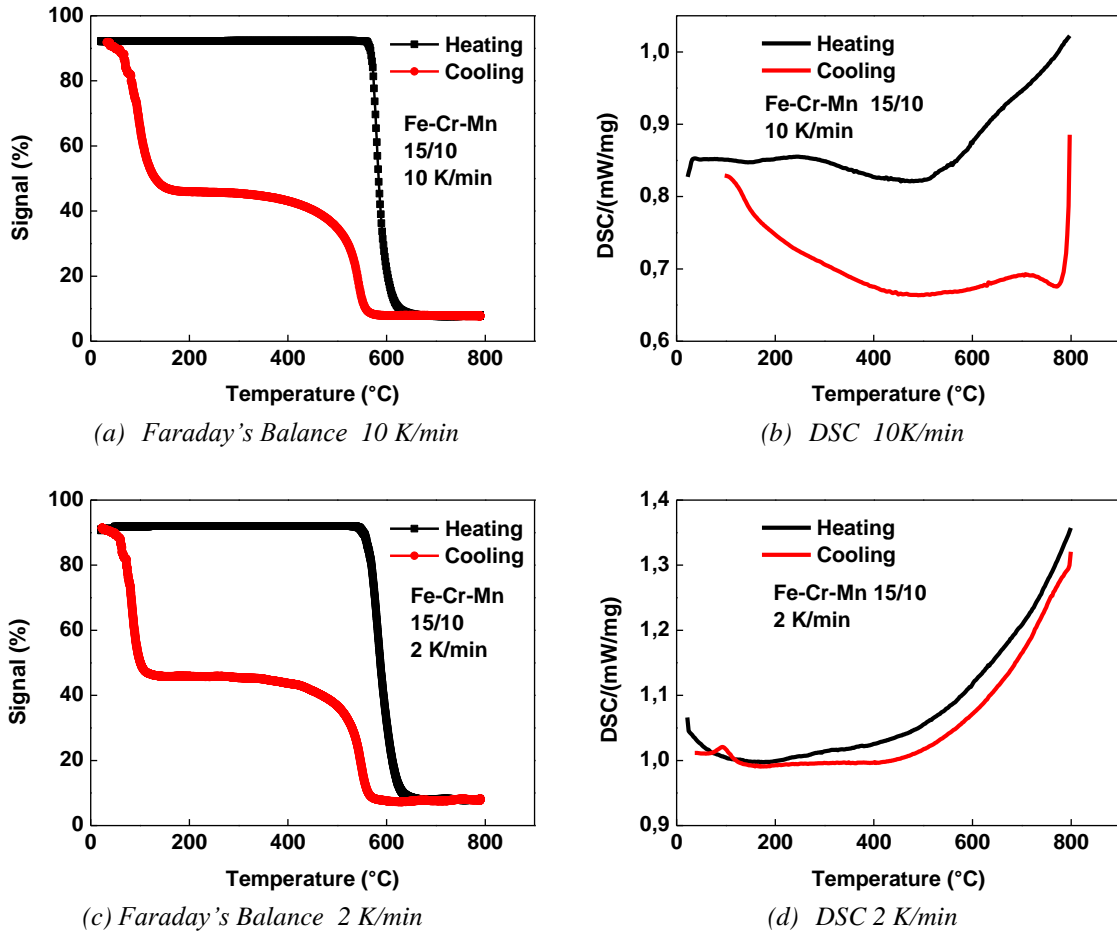
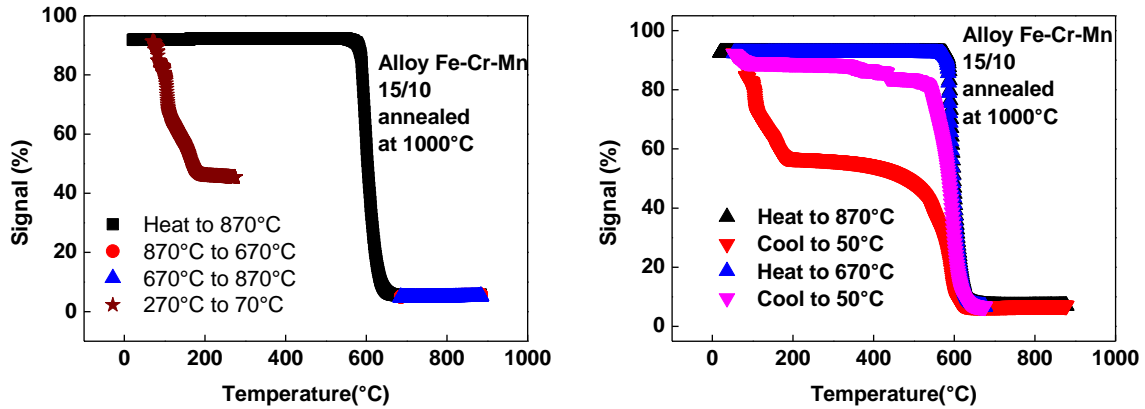


Figure VI-34. On the left side, magnetic response in arbitrary units measured in Faraday's Balance apparatus and on the right, the corresponding DSC measurements with the same heating rate for Fe-Cr-Mn alloy 15/10.

The cycling behavior of sample 15/10 is shown in Figure VI-35. After heating beyond 600 °C, if the material is cycled in high temperature without going back to room temperature (red dots and blue triangles superposing in Figure VI-35 (a)), the ferromagnetic phase is not recovered. By heating the material at low temperature range (room temperature to 270 °C), the transition between ferrite and austenite phases is not achieved but the transition involving sigma phase is visible, as shown by the brown stars in the same figure.

By cycling the material in cooling to room temperature at each cycle, the ferrite phase is restored at each cycle, which can be seen by the two heating curves to 670 °C and 870 °C superposing. In the cycle from room temperature to 670 °C in Figure VI-35 (b), the ferrite phase has sufficient energy to transform into austenite but the sigma phase has not yet transformed. Therefore, upon cooling from 670 °C, there is no recovering of σ phase taking place since the phase fraction of σ phase did not change upon heating. In this case, we did not observe the two-step transition as shown before.



(a) Cycles without backing to RT
 (b) Cycles going back to RT
 Figure VI-35. The magnetic response in arbitrary units of annealed Fe-Cr-Mn sample 15/10 is plotted as a function temperature during (a) thermal cycles without going back to room temperature at each cycle and (b) thermal cycles cooling down to RT at each cycle. Certain curves superpose.

4.1.2. Alloy 15/25

Based on the thermodynamic calculation (Figure VI-36) for alloy 15/25, austenite (γ -fcc) phase is the primary solidification phase, together with a small percentage of σ phase (20%). The ferrite phase starts to form below 500 °C. The σ phase is present both before and after the transformation between bcc and fcc phases.

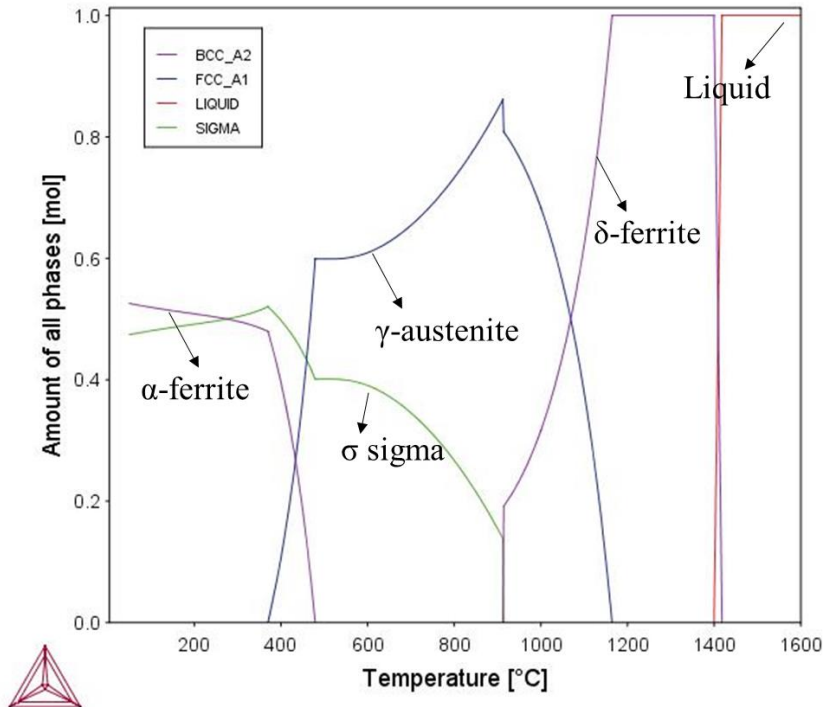


Figure VI-36. Phase fraction as a function of temperature for alloy 15/25 calculated using Thermocalc®.

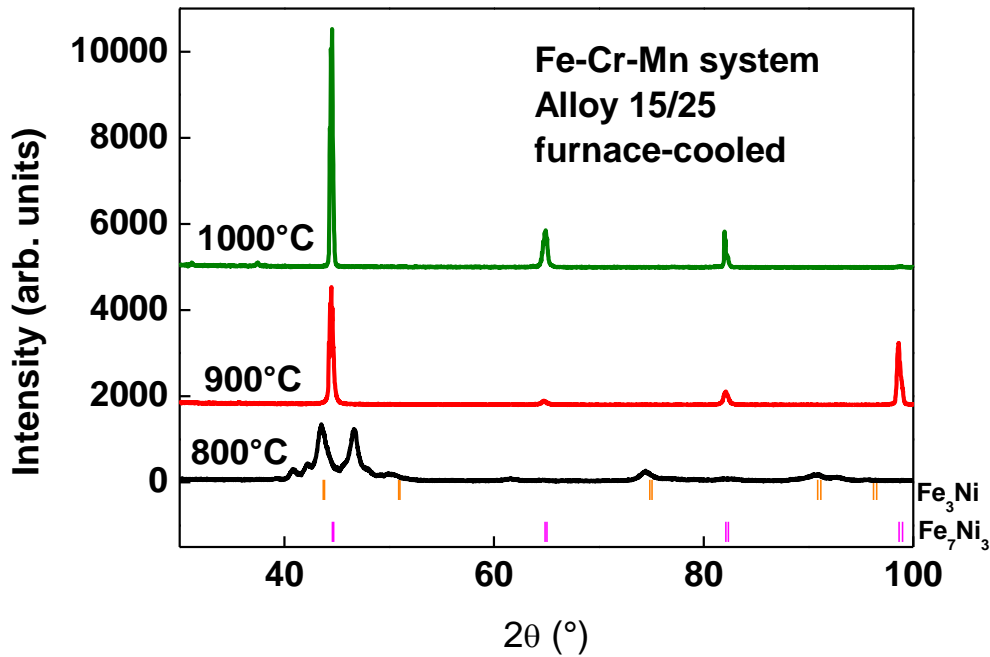


Figure VI-37. XRD patterns for Fe-Cr-Mn alloy 15/25 annealed at 800 °C, 900 °C, and 1000 °C and furnace-cooled.

Similar to the lower-Mn alloy 15/10, the XRD pattern (Figure VI-37) shows that alloy 15/25 contains a majority phase in a bcc structure with a lattice parameter of 2.86 Å. Sample 15/25 annealed at 800 °C and furnace-cooled shows reflections from an impurity phase, which is probably the sigma phase formed during slow cooling. The magnetization measurement in Figure VI-38 confirms the lack of crystallization of the bcc phase in the sample annealed at 800 °C.

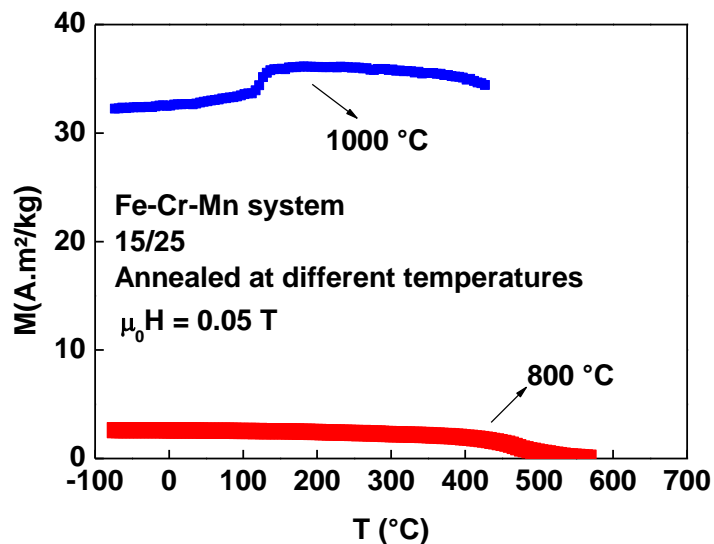


Figure VI-38. Magnetization as a function of temperature under a field of 0.05 T measured for Fe-Cr-Mn alloy 15/25 annealed at different temperatures.

Alloy 15/25 annealed at 1000 °C is observed in optical microscope after HNO₃ electrolytic etching on the surface. The microstructure shown in Figure VI-39 shows austenite phase with ferrite grains and small dark dots of sigma phase.

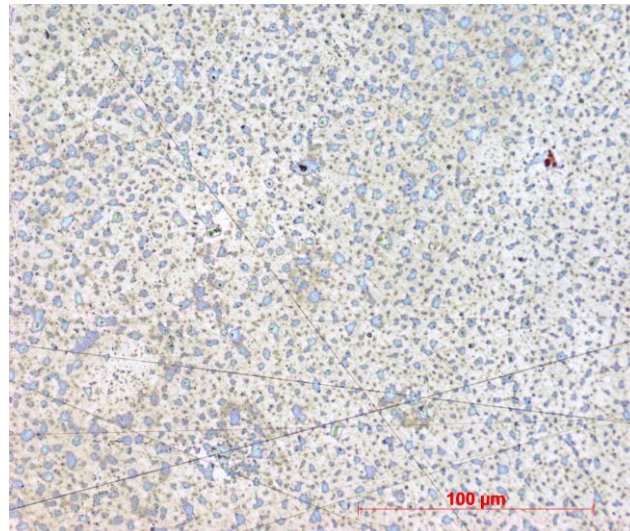


Figure VI-39. Microstructure after HNO_3 electrolytic etching for alloy 15/25 annealed at 1000°C for 15 days.

Figure VI-40 (a) shows a transition from a ferromagnetic ferrite phase to a paramagnetic austenite phase during heating for sample 15/25. The transition temperature is slightly lower than alloy 15/10. The reversed process is observed upon cooling. The reduced thermal hysteresis in the case of 15/25 compared with alloy 15/10 is attributed to the reduced concentration difference of σ phase below and above the transition $\alpha \leftrightarrow \gamma$ (20-45% according to thermodynamic calculations). The DSC measurements in Figure VI-40 (b) confirm that the changes in magnetic signal are attributed to the structural change between ferrite and austenite.

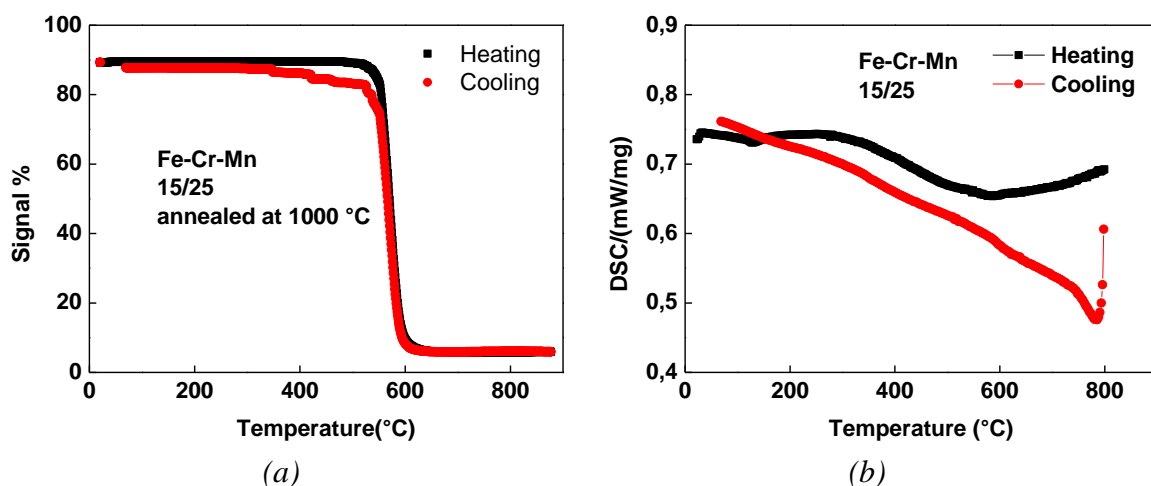


Figure VI-40. (a) Magnetic response in arbitrary units for samples 15/25 and (b) DSC measurement for alloy 15/25.

In this α/γ material, we manage to find the reversible structural transformation inducing a magnetic transition, even though the transformation temperature is too high for room-temperature application. Alloy 15/25 was treated in thermal cycles to observe its cyclic behavior. The transition is quite stable from both (a) cycling without cooling to RT at each cycle and (b) cycling with going to RT at each cycle, as shown in Figure VI-41.

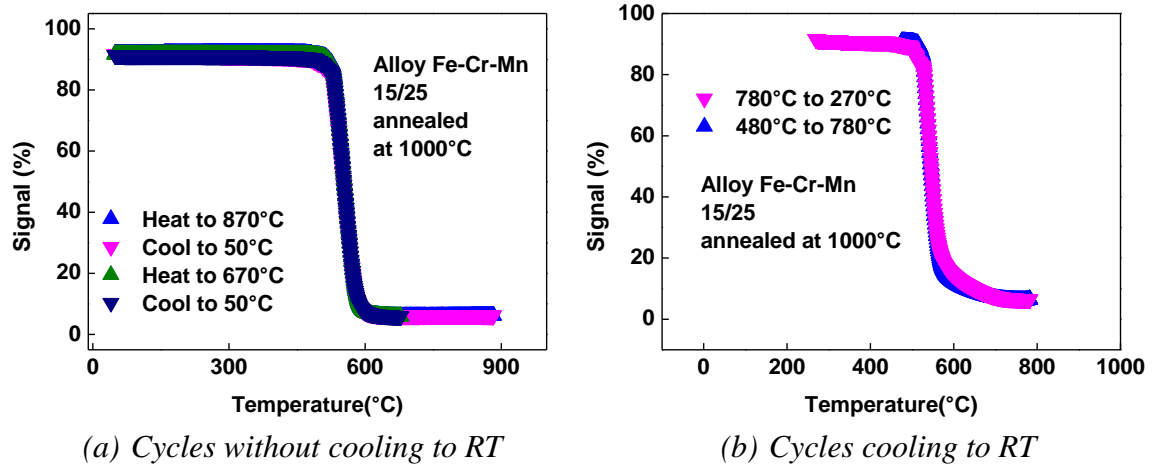


Figure VI-41. The magnetic response in arbitrary units of annealed sample 15/10 is plotted as a function temperature during (a) thermal cycles without going back to room temperature at each cycle and (b) thermal cycles cooling down to RT at each cycle.

4.1.3. Discussion

In the Fe-Cr-Mn systems with 15 wt% Cr, two alloys (15/10 and 15/25) are studied for their magnetic and structural transitions. Alloy 15/10 shows a bcc to fcc transition upon heating. The precipitation of sigma phase upon cooling leads to a two-step transition in order to restore the bcc phase. Alloy 15/25 has a smaller difference of sigma phase below and above the transition temperature between bcc and fcc phases, which then has less impact on the reversibility of the phase transformation from austenite to ferrite upon cooling. Alloy 15/25 is an interesting candidate with reversible structural transition accompanied by a change in magnetic signal. In order to bring down the transition temperature, carbon is added to the 15/25 base alloy in the next section.

4.2. Addition of carbon in Fe-Cr-Mn alloy 15/25

Carbon is one of the γ -promoting alloying elements, which means that the addition of carbon stabilizes the high temperature austenite phase, lowering the ferrite to austenite transition temperature. Seen from the previous section, sample 15/25 shows very little thermal hysteresis, which is an advantage to study the influence of carbon on the transition temperature. Different concentrations of carbon were added by induction melting graphite with the other starting elements in order to elaborate samples 15/25 with 0.05, 0.1, and 0.2 wt% of C. The alloys were annealed in air at 1100 °C for 1 h before quenching in iced water in order to facilitate quenching. The surface oxides were subsequently removed before further measurements.

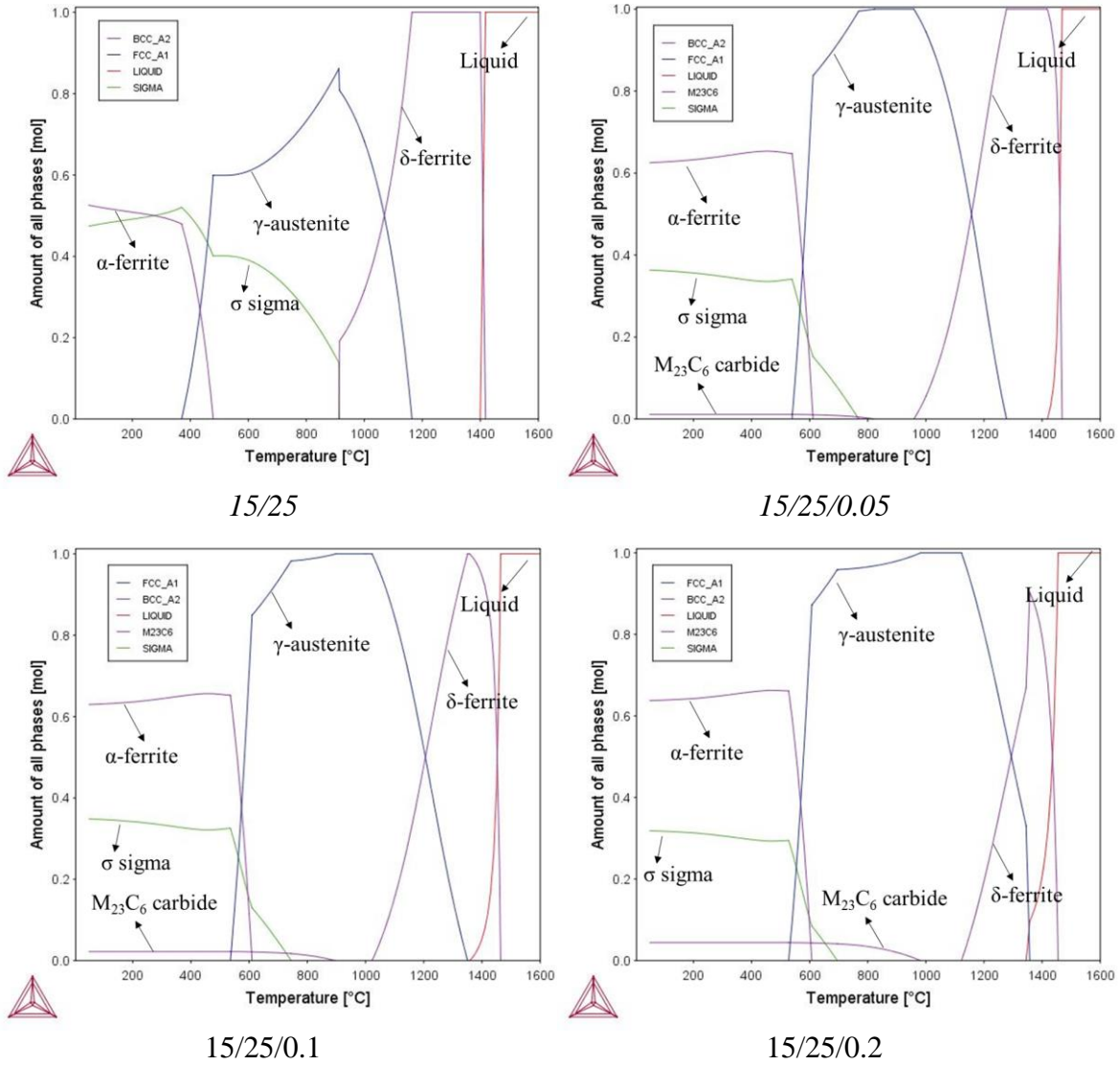


Figure VI-42. Thermodynamic calculations for alloy 15/25 and the carbonated samples.

As shown in the thermodynamic calculation (Figure VI-42), the sigma phase is stabilized at lower temperature with increasing carbon content. The phase fraction of sigma phase at low temperature decreases for carbonated samples and a carbide phase appears at 800-900 °C with different carbon concentration. Therefore, these carbon-containing alloys might be more sensitive to the precipitation of σ phase.

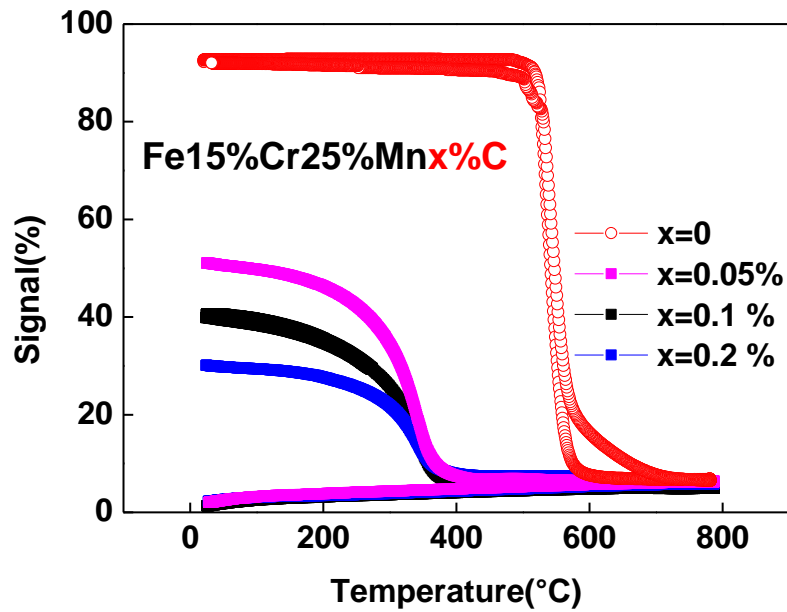


Figure VI-43. Magnetic response in arbitrary units for samples $Fe_{60}Cr_{15}Mn_{25}$ and the carbon-doped counterparts.

As seen in Figure VI-43, the addition of carbon stabilizes the austenite phase to lower temperature, from 600 to 350 °C. The magnetic signals from the Faraday's balance are shown in arbitrary units, thus only indicative. The magnetization level of the carbon-containing alloys is verified by measuring the magnetization level in extraction vector magnetometer. The magnetization level decreases with increasing carbon content. Alloy 15/25/0.05 has a magnetization value of $31.36 \text{ A}\cdot\text{m}^2/\text{kg}$ and for alloy 15/25/0.1, this value is dropped to $20.35 \text{ A}\cdot\text{m}^2/\text{kg}$.

The paramagnetic behavior upon cooling in carbonated samples also suggests the presence of sigma or carbide phases. The martensite starting temperatures calculated for these samples are all below 0 °C, which explains the absence of the recovering of martensite phase upon cooling. In the following sections, we present specific studies on alloys 15/25/0.05 and 15/25/0.1.

4.2.1. Alloy 15/25/0.05

After HNO_3 electrolytic etching on the surface, sample 15/25/0.05 was observed in optical and electron microscopes. The microstructure images (shown in Figure VI-44) exhibit layers of ferrite lamellae. This microstructure is very similar to the typical colonies of pearlite in Fe-C steel system, which is a two-phased structure composed of alternating layers of ferrite and cementite (Fe_3C). Pearlite forms by the cooperative growth of both of these phases at a single front with the parent austenite. Although considering the carbon concentration in this sample (0.05%), it is unlikely that there are large proportion of pearlite formation taking place during cooling. Typical eutectoid composition of the parent austenite contains much higher carbon content (0.76%). Therefore, the lamellae in the microstructure are probably pure ferrite.

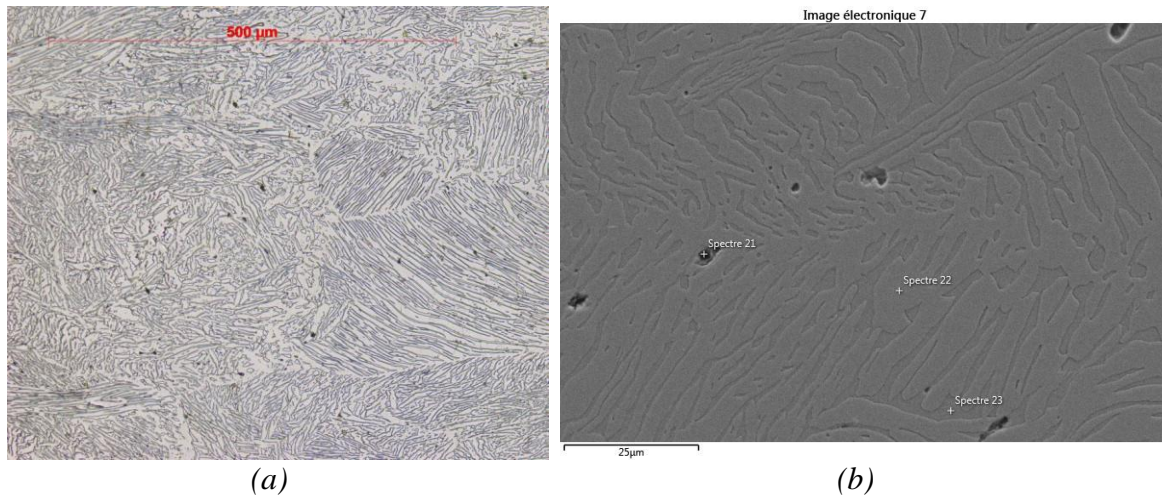


Figure VI-44. (a) Optical and (b) electronic microscopy images on Fe-Cr-Mn-C alloy 15/25/0.05 after HNO_3 electrolytic etching.

The EDX analysis was performed on the three phases in the microstructure (lamellae, inter-lamellae, and black dots) and the spectra are shown in Table VI-4. The point measured on the black dot phase is more Cr-rich than the other phases, which suggests a likelihood of sigma phase. For further confirmation, it is necessary to perform transmission electron microscopy with the electron diaphragm focused on the specific phase regions. The resulting electron diffraction patterns can help deduce the phase structure and the space group, therefore, helping determining the actual phases observed on the microstructure.

Table VI-4. EDX analysis showing atomic percent of each elements for the spots shown in Figure VI-44 (b) for Fe-Cr-Mn-C alloy 15/25/0.05.

at %	Fe	Cr	Mn
21 – black dot	57.17	19.33	23.50
22 – lamellae	58.19	15.25	26.57
23 – inter-lamellae	60.05	14.20	25.75

4.2.2. Alloy 15/25/0.1

The thermal-magnetization curve measured for sample 15/25/0.1 under 0.05 T field shows a weak magnetization at room temperature and a very soft and lagging transition upon heating, shown in Figure VI-45. The transition temperature is 362 °C. In the temperature range measured (100 – 500 °C), the alloy shows a reversible magnetic transition with hysteresis and the same magnetization level is not recovered upon cooling. The magnetization as a function of field in Figure VI-45 (b) illustrates the soft magnetic transition with no saturation magnetization seen at the measured fields.

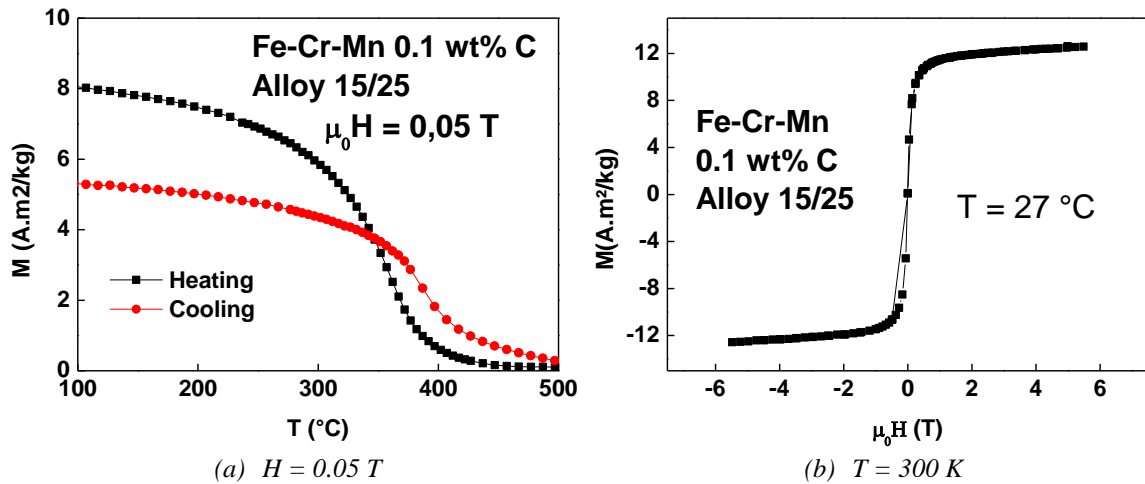


Figure VI-45. (a) Magnetization as a function of temperature under constant field of 0.05 T for sample 15/25/0.1 and (b) magnetization as a function of field at 300 K.

Figure VI-46 shows the magnetic response measured in Faraday's Balance and the heat flow measured in DSC in the same temperature range (room temperature to 800 °C). From the DSC curve, two endothermic reactions at 110 °C and 460 °C upon heating are observed. The magnetic signal drop at 362 °C upon heating corresponds to the endothermic transformation at 460 °C shown in DSC. However, upon cooling no magnetic signal is restored, whereas the DSC curve upon cooling does show a change of baseline at 430 °C. Therefore, we postulate that the reversible phase transformation is probably between austenite and sigma phases. Austenite had sufficient thermal stability due to the Mn and carbon concentrations, that no ferrite phase is formed during cooling.

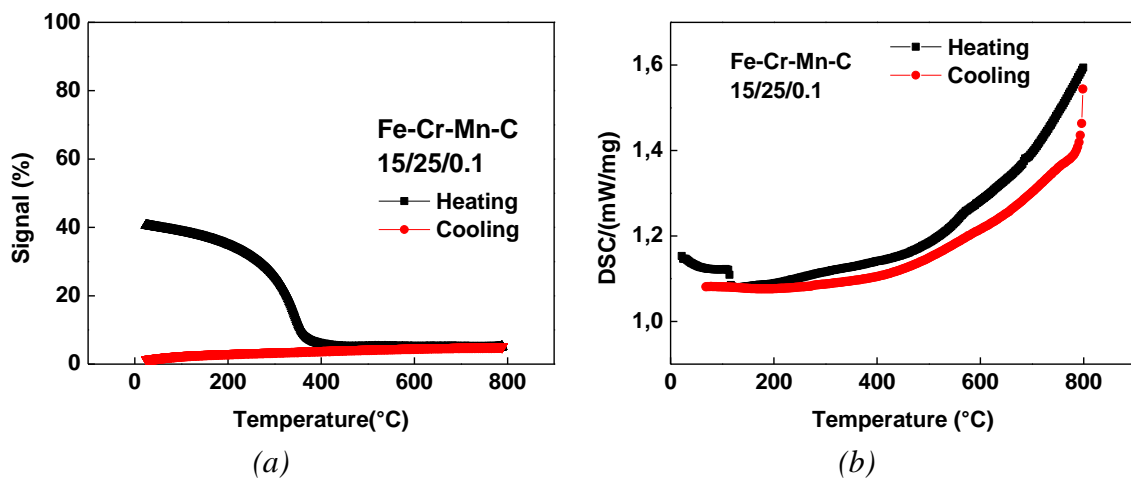


Figure VI-46. (a) Thermomagnetic response and (b) DSC curve for Fe-Cr-Mn alloy 15/25/0.1.

4.2.3. Discussion

The carbon addition to Fe-Cr-Mn alloy 15/25 can effectively decrease the transition temperature from ferrite to austenite during heating. However, this is accompanied by a change of structural transitions in the sample. The carbon-containing alloys show bcc to fcc transition upon heating. However, the Mn and C concentrations further stabilize austenite

phase, which is not transformed into ferrite upon cooling. Therefore, carbon alloying has compromised the reversibility of the magneto-structural transition observed in 15/25 alloy.

4.3. Series Fe-Cr-Mn with 5% Cr

The samples of composition 5/20 and 5/25 were elaborated by induction melting appropriate amount of starting elements Fe, Cr, and Mn. The melted buttons were homogenized in sealed quartz tube at 1100 °C for 24 h before quenching in iced water.

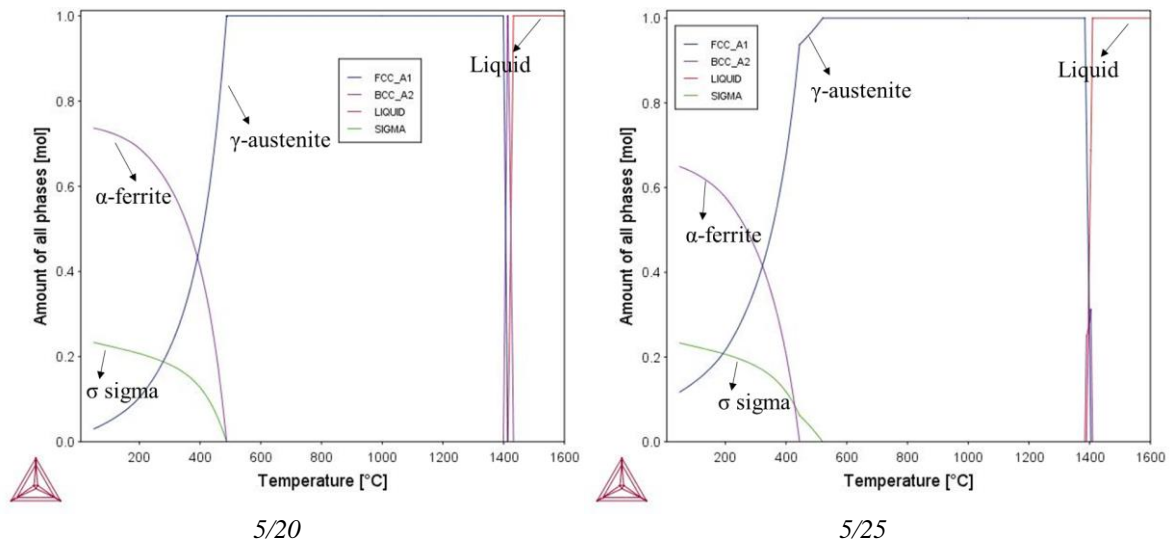


Figure VI-47. Phase fraction as a function of temperature for alloys 5/20 and 5/25 calculated using ThermoCalc®.

According to the thermodynamic calculations (Figure VI-47), in both samples 5/20 and 5/25, the austenite phase is the primary solidification phase from the liquid melt. For sample 5/20, α and σ begin to precipitate around 500 °C and at low temperature the bcc phase is the predominant one. With slightly more Mn content, sample 5/25 has very similar low-temperature phase fractions. The sigma phase starts to form around 500 °C and at lower temperature, α phase precipitates and becomes the majority phase.

Typical microstructures of the series of 5Cr alloys aged at 1000 °C for 24 h are shown in Figure VI-48. Alloy 5/20 (left) show a major martensite phase with dots of sigma phase and possibly some remaining austenite or ferrite, whereas alloy 5/25 (right) contains austenite-rich microstructure with martensite and sigma phases.

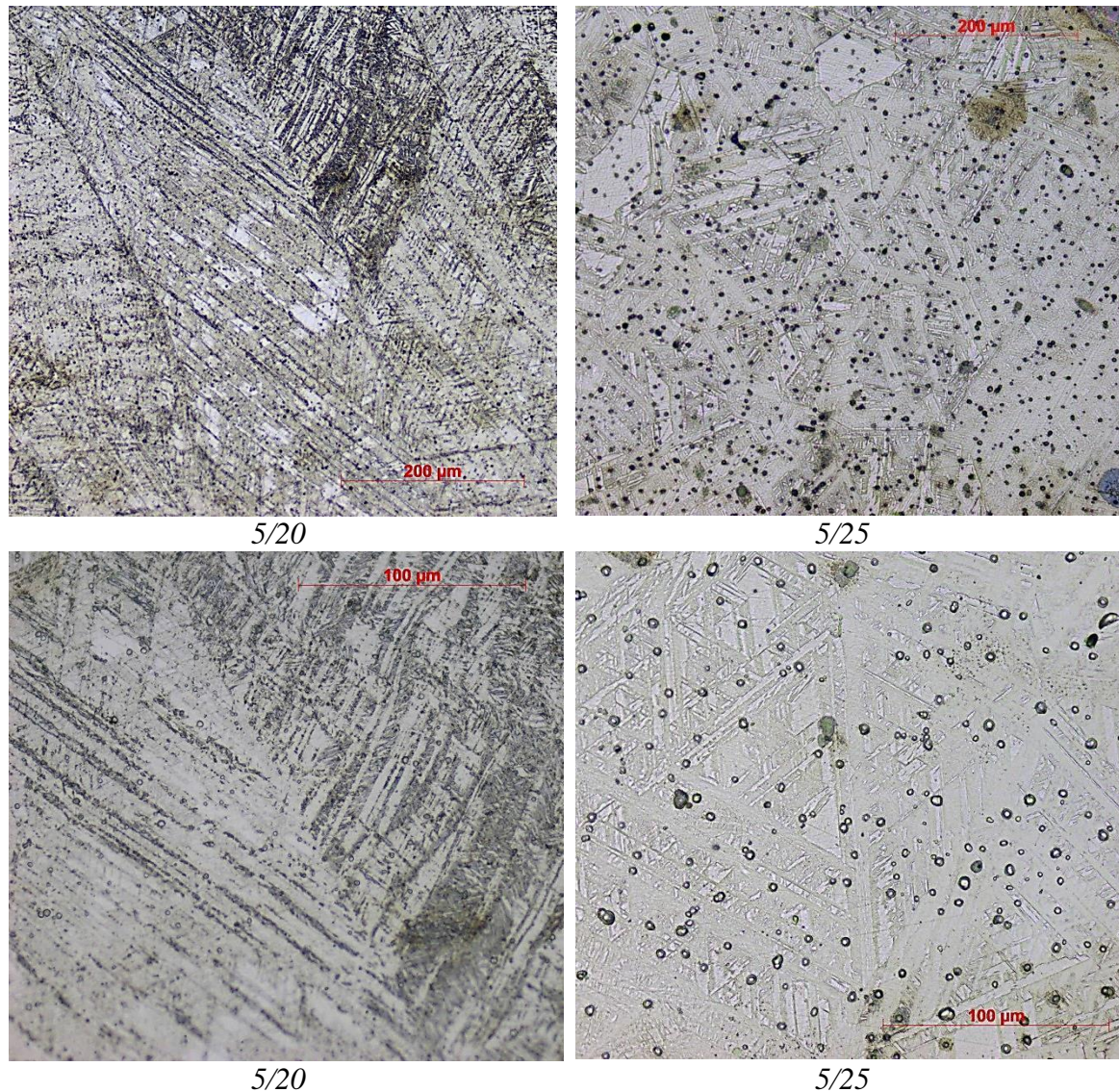


Figure VI-48. Microstructure of alloy 5/20 (left) and 5/25 (right) after HNO_3 electrolytic etching.

The magnetization level at 300 K under a field of 1 T is 45.77 and 1.35 $\text{A}\cdot\text{m}^2/\text{kg}$ for alloy 5/20 and 5/25, respectively. This confirms the presence of ferromagnetic phase (martensite) for alloy 5/20. The low magnetization for alloy 5/25 is consistent with the austenite-rich microstructure.

Interpreted from the Faraday's Balance measurements in Figure VI-49 (a), sample 5/20 is martensitic and ferromagnetic at room temperature after annealing. During heating from room temperature, martensite transforms paramagnetic austenite at 500 °C. This transition coincides with the transition from sigma to austenite at the same temperature, from the thermodynamic calculation. This structural transition is confirmed on the DTA heating curve in Figure VI-49 (c). The involvement of sigma phase can explain the large window of the magnetic signal drop between 450 and 600 °C. Austenite phase is stable upon cooling and the martensitic starting temperature is too low to recover martensite.

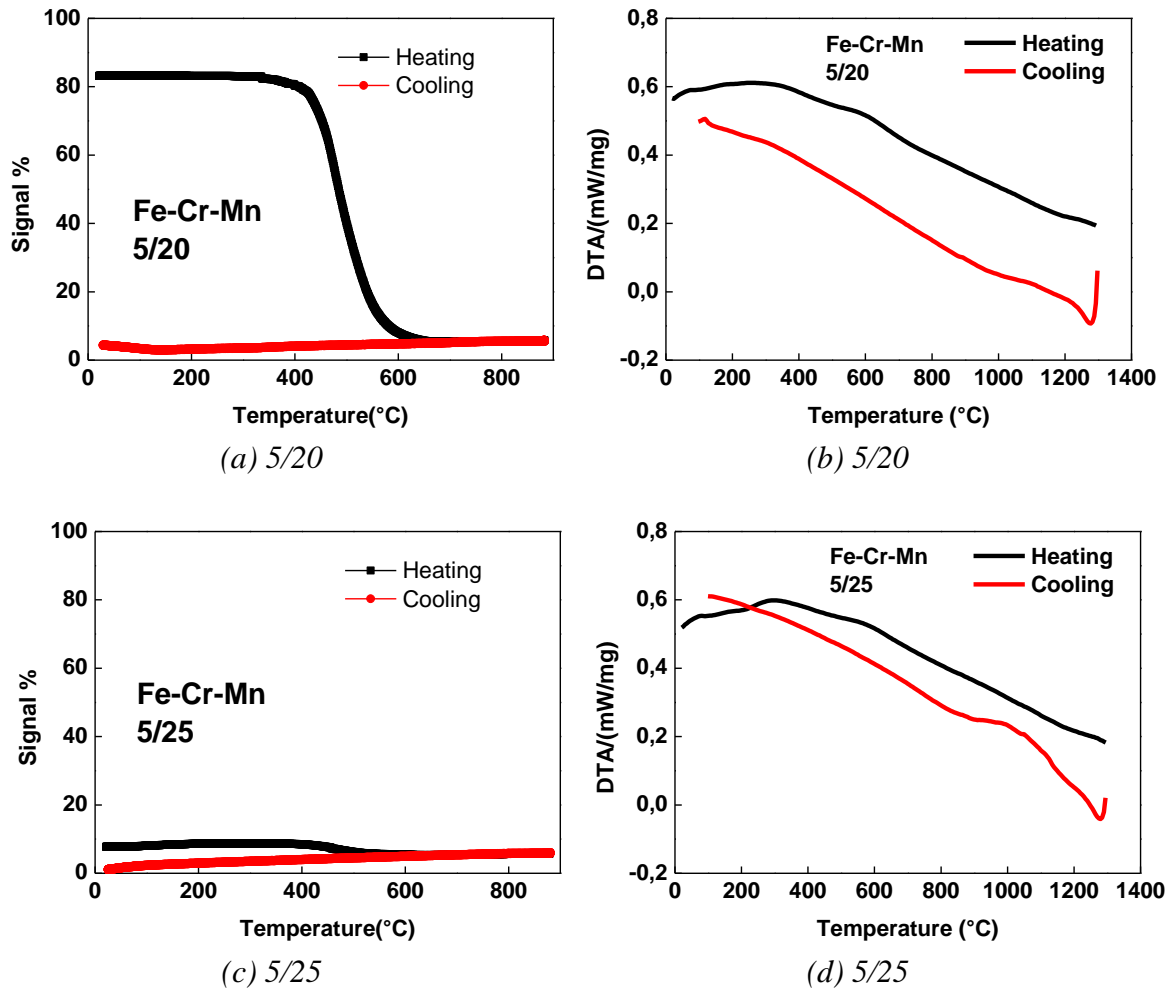


Figure VI-49. Magnetic response in arbitrary units (a) and (c) and corresponding DTA measurements in heating and cooling (b) and (d) for alloys 5/20 and 5/25.

On the other hand, sample 5/25 shows a majority of austenite paramagnetic phase (which is coherent with the Schaeffler diagram) with smaller content of martensite. After martensite turning into austenite during heating, the system austenite + sigma is stable and no formation of martensite at low temperature upon cooling. The high Mn alloying content facilitates the stabilization of austenite. The martensite to austenite transition is confirmed in DTA measurement. A transformation at 900 °C is seen on the cooling curve, which can be attributed to the transformation of the austenite phase at high temperature.

With 5% Cr and high Mn alloying concentration, alloy 5/20 and 5/25 show very different microstructures and magnetic responses in Faraday's Balance. As a γ -promoting element, Mn further stabilizes austenite phase, leading to steady non-magnetic response upon cooling for both samples.

5. Conclusion

For the Fe-Cr-Ni alloys, two types of phase transitions are investigated. In the composition range allowing the formation of martensite phase, the alloys show a structural transition from martensite/ferrite to austenite between 575 and 650 °C depending on the composition at heating and from austenite to martensite between 50 to 200 °C at cooling. This results in a magnetic cycle with two structural transitions taking place at very different temperatures the heating and cooling curves. This is a disadvantage for magnetic cooling application as the material is subjected to magnetization-demagnetization cycles in a much narrower temperature span.

In all Fe-Cr-Ni samples tested, it has never been possible to isolate only the ferrite/austenite transformation without the formation of martensite at cooling neither to isolate the martensite transformation into a reversible magnetic cycle. The only reversible magnetic cycle observed was for a purely magnetic transformation, which was not the targeted behavior.

Fe-Cr-Mn alloys show mixed transitions involving ferrite, austenite, sigma and martensite phases. Carbon addition decreases the ferrite/austenite transition temperature while forming more sigma phase (and possibly some carbides) in the low temperature region thus decreasing the intensity of the magnetic transition upon heating.

Only one alloy tested did not lie in the issues of mixed ferrite to austenite and austenite to martensite transformations respectively at heating and cooling; and in the issues due to sigma phase precipitation during cooling. The Fe-Cr-Mn alloy 15/25 shows the targeted reversible structural transformation between ferrite and austenite, but this transformation occurs around 550-600°C and the trials with C doping did not allow to decrease this transition temperature while maintaining a large magnetic change and a reversible transformation.

From the above discussions, it is obvious that an important issue is to undertake a variable temperature X-ray diffraction analysis for all the investigated samples. It would be interesting to perform in-situ X-ray diffraction measurements to monitor in real time the formation of austenite, ferrite, and martensite phases, using laboratory X-ray instrument or even high-energy synchrotron radiation. The variable temperature X-ray diffraction facility was not functional at Néel Institute at the time of writing and future collaborations with other laboratories are planned for such purposes.

References

- [1] C. Rong and J. Liu, *Appl. Phys. Lett.*, vol. 90, p. 222504, 2007.
- [2] P. Souvatzis, L. Vitos and O. Eriksson, *Cond. Mat. Mtrl. Sci.*, p. 15, 2012.
- [3] A. Majumdar and P. Blanckenhagen, *Phys. Rev. B*, vol. 29, p. 4079, 1984.
- [4] M. Acet, T. Schneider and E. Wassermann, *J. Phys. IV C2-105, supp. J. Phys. III*, vol. 5, 1995.
- [5] J. J. Ipus, H. Ucar and M. E. McHenry, *IEEE Trans. Magn.*, vol. 47, no. 10, p. 2494, 2011.
- [6] H. Ucar, J. J. Ipus, D. E. Laughlin and M. E. McHenry, *J. Appl. Phys.*, vol. 113, p. 17A918, 2013.
- [7] V. Chaudhary, A. Chaturvedi, I. Sridhar and R. V. Ramanujan, *IEEE Magn. Lett.*, vol. 5, p. 6800104, 2014.
- [8] V. Chaudhary and R. V. Ramanujan, *IEEE Magn. Lett.*, vol. 6, p. 6700104, 2015.
- [9] B. Kaeswurm, K. Friemert, M. Gürsoy, K. Skokov and O. Gutfleisch, *J. Magn. Magn. Mater.*, vol. 410, p. 105, 2016.
- [10] T. Sato, T. Nishizawa and K. Tamaki, *Trans. JIM*, vol. 3, p. 196, 1962.
- [11] E. Brück, O. Tegus, D. Thanh, N. Trung and K. Buschow, *Int. J. Refrig.*, vol. 31, p. 763, 2008.
- [12] F. Zhao, O. Tegus, B. Fuquan and E. Brück, *Int. J. Miner. Metall. Mater.*, vol. 16, p. 314, 2009.
- [13] D. Peckner and I. Bernstein, Eds., *Handbook of stainless steels*, McGraw-Hill Inc., 1977.
- [14] E. Bain, *Function of the alloying elements in steel*, Pittsburgh, 1939.
- [15] K. Lo, C. Shek and J. Lai, *Mat. Sci. Eng. R*, vol. 65, p. 39, 2009.
- [16] A. Schaeffler, *Metal Progress*, vol. 56, p. 680, 1949.
- [17] M. McGuire, *Stainless steel for design engineers*, Ohio: ASM International, 2008.
- [18] K. Andrews, *J. Iron Steel Inst.*, vol. 203, p. 721, 1965.
- [19] F. Hull, *Supplement to the Welding Journal*, vol. May, p. 193, 1973.
- [20] J. Ruste. [Online]. Available: micro.icaunais.free.fr/04_acier.pdf. [Accessed 23 09 2016].
- [21] M. Hudl, Ph.D. thesis manuscript, "*Magnetic materials with tunable thermal, electrical, and dynamic properties*", Uppsala: Uppsala University, 2012. ISBN 978-91-554-8287-9
- [22] A. Iorga, M. Codescu, R. Saban and E. Patroi, *U.P.B. Sci. Bull. Series B*, vol. 73, p. 195, 2011.
- [23] H. Brager, F. Garner, D. Gelles and M. Hamilton, *J. Nucl. Mater.*, vol. 133, p. 907, 1985.

- [24] Y. Murata, K. Koyama, Y. Matsumoto, M. Morinaga and N. Yukawa, *ISIJ Inter.*, vol. 30, p. 927, 1990.

Conclusions and outlook

In this thesis, the structural and magnetic properties of La-Fe-Si-based magnetocaloric materials have been systematically explored and optimized by substituting both the rare earth and transition metals with other elements. The effects of the inclusion of light interstitials are studied and a major part of this thesis focuses on identifying these interstitial stability conditions in the material.

The aim of this doctoral work was to contribute towards a better understanding of the fundamental material characteristics, with an emphasis on the relationship between the composition modification and the alternation in the structural properties.

This work has contributions towards an understanding of the role of substitutional and interstitial structural modulation in tuning the hydrogen sorption dynamics. The main results of the thesis are summarized as follows:

The hydrogenation process is an important step in the application of La-Fe-Si-based material in room-temperature magnetic refrigeration. The hydrogen stability is closely related to the structural reshaping in the course of interstitial absorption and desorption. Substitutional modifications of the structure not only affect the volume of the structure, but also lead to modified diffusion path for hydrogen interstitials via the bottleneck of Fe/Si icosahedra. The structural breathing in the course of interstitial sorption have been studied in detail with neutron diffraction and laboratory-scale techniques.

The insertion of light interstitials is implemented by both solid-gas reaction and melting techniques. The insertion of carbon interstitials is optimized for the laboratory conditions.

Carbon insertion can influence the hydrogen sorption kinetics and the hydrogen sorption capacity. As demonstrated by both kinetics studies in Sieverts' apparatus and via *in-situ* deuterium absorption/desorption experiments, the effect of carbon on hindering hydrogen absorption rate is confirmed for the sample studied. We have demonstrated that particularly in Ce-substituted compositions, carbon introduction can help retain hydrogen during desorption and enhance the thermal stability of hydrogenated materials.

The rigorous structural investigations in this work have allowed to specify the deformations undergone by the complex metallic alloys La-Fe-Si when subjected to light interstitial insertion or rare earth substitution at the cation site of the NaZn₁₃-type structure. It is my hope that this work may act as a foundation for further research in the development of a roadmap connecting structural modification with hydrogen stability in the La-Fe-Si material. Ideally, this work can be completed by series of similar analysis with different substitutional and interstitial modulations in order to provide a composition engineering guidebook for material producers. This way, not only we will know the effects of each composition modulation on the magnetic and magnetocaloric properties, but also we can understand the consequences on the hydrogen sorption dynamics and eventually the hydrogen stability in the material.

An exploratory Chapter is also provided in this thesis, in which the potential of Fe-Cr-Ni and Fe-Cr-Mn alloys as possible magnetocaloric materials is examined. The objective was

to search for compositions that have a structural transformation that coincide with a magnetic transition at temperature range not too far from room temperature. Only one alloy composition tested, Fe-Cr-Mn alloy shorthanded 15/25 shows the targeted reversible structural transformation between ferrite and austenite around 550 – 600 °C. While this temperature range is not compatible with room-temperature magnetic refrigeration application, this family of alloys has potential in high-temperature magnetocaloric applications. Moreover, the purely magnetic transitions in these alloys can be exploited in thermomagnetic power generation.

Different methods of synthesis of the compounds as well as rapid cooling techniques (melt-spinning) have been addressed to identify the best formation conditions of appropriate phases.

This work can be followed by details investigations suggested here:

In order to further investigate the hydrogen mobility, it is possible to conduct quasi-elastic neutron scattering or nuclear magnetic resonance experiments.

With the difficulties we have encountered in analyzing and interpreting the desorption mechanisms, it is important to design specific experimental conditions and environment in order to properly probe the diffusion and changes in the structure during desorption.

Moreover, it can be interesting to study the correlation between grain boundary density/grain size/microstructure and the hydrogen stability. The results from such studies can be a guide to further optimize the heat treatment processes in order to engineer the microstructure adapting to the desired hydrogen stability property.

The presence and quantitative determination of the carbon content in the 1-13 phase and the impurity phases can be further investigated by an electron probe microanalyzer (EPMA) in order to further optimize the carbon insertion route.

Previously the strain effect on the X-ray diffraction patterns was analyzed by Williamson-Hall method. Due to the cubic nature of the lattice, there were only a few peaks from the same family, making the strain analysis difficult. No visible difference was observed in the carbon-free and carbonated samples with our data resolution. The neutron diffraction experiments were performed with wavelengths of 1.22 and 1.28 Å, which are not suitable to determine the strain and crystallite size, either.

Therefore, in order to investigate the effect of microstructural crystallite size on the hydrogenation dynamics, it would be very interesting to measure the diffraction pattern with a synchrotron source with very short wavelength to collect maximum amount of peaks. In particular, it would be extremely helpful to observe the evolution of internal strain in real time in the course of hydrogenation and desorption.

The insertion of hydrogen in Fe-rich intermetallics is a rich field for experimentalists and theoreticians. Pressure-assisted investigations can be very helpful in understanding and tailoring of the magnetic and magnetocaloric properties of La-Fe-Si system.

Conclusions et Perspective

Dans cette thèse, les propriétés structurales et magnétiques des matériaux magnétocaloriques dans la famille $\text{La}(\text{Fe},\text{Si})_{13}$ ont été systématiquement explorées et optimisées en remplaçant aussi bien la terre rare que le métal de transition par d'autres éléments. L'effet de l'insertion d'éléments interstitiels légers est également étudié et une grande partie du travail a porté sur la détermination des conditions de stabilité de ces interstitiels dans les matériaux.

Le but de ce travail de doctorat était de contribuer à une meilleure compréhension des caractéristiques fondamentales des matériaux, en mettant l'accent sur la relation entre la modification de la composition et l'alternance dans les propriétés structurales.

Ce travail apporte des contributions vers une compréhension du rôle de la modulation structurale substitutive et interstitielle dans le réglage de la dynamique de sorption d'hydrogène. Les principaux résultats de la thèse sont résumés comme ci-dessous :

Le procédé d'hydrogénation est une étape importante pour l'application de matériau à base de La-Fe-Si pour la réfrigération magnétique à température ambiante. La stabilité de l'hydrogène est étroitement liée à la déformation structurale au cours de l'absorption et de la désorption de cet élément interstitiel. Les modifications structurales induites par la substitution métallique affectent non seulement le volume de la maille, mais aussi conduisent également à un chemin de diffusion modifié pour les interstitiels d'hydrogène via l'étranglement des icosaèdres $(\text{Fe}/\text{Si})_{13}$. La respiration structurale associée à l'insertion ou la désorption de l'élément interstitiel a été étudiée en détail par diffraction des neutrons et par d'autres techniques de laboratoire.

L'insertion d'interstitiels légers est mise en œuvre par la réaction solide-gaz et la technique de fusion-solidification. L'insertion de carbone est optimisée à l'échelle du laboratoire. L'insertion du carbone peut influencer la cinétique et la capacité de sorption d'hydrogène. Comme cela est démontré par des études de cinétique dans le dispositif de Sievert et par l'intermédiaire d'expériences *in situ* d'absorption / désorption de deutérium, l'effet entravant du carbone sur le taux d'absorption d'hydrogène est confirmé pour l'échantillon étudié. Nous avons démontré que, en particulier dans des compositions substituées au Ce, l'introduction de carbone peut aider à retenir l'hydrogène lors de la désorption et à améliorer la stabilité thermique des matériaux hydrogénés.

Les investigations structurales rigoureuses dans ce travail ont permis de préciser les déformations subies par les alliages métalliques complexes La-Fe-Si lorsqu'ils sont soumis à l'insertion d'éléments interstitiels ou à la substitution des terres rares sur le site cationique de la structure de type NaZn_{13} . J'ai espoir que ce travail puisse servir de base pour poursuivre la recherche dans le développement d'une feuille de route reliant la modification structurale et stabilité de l'hydrogène dans le matériau La-Fe-Si. Idéalement, ce travail peut être complété par une série d'analyses similaires avec différentes modulations de substitution et interstitiels afin de fournir un guide d'ingénierie de composition pour les producteurs de matériaux. De cette façon, non seulement nous pourrions appréhender les effets de chaque modulation de composition sur les propriétés magnétiques et magnétocaloriques, mais également comprendre les conséquences sur la dynamique de sorption d'hydrogène et, éventuellement, la stabilité de l'hydrogène dans le matériau.

Un volet exploratoire est également abordé dans cette thèse. Il est consacré aux alliages Fe-Cr-Ni et Fe-Cr-Mn qui pourraient potentiellement avoir un effet magnétocalorique exploitable. L'objectif était de rechercher des compositions qui présentent une transformation structurale entre deux phases d'états d'aimantation différents dans une plage de température pas trop éloignée de la température ambiante. Seule une composition d'alliage testée, Fe-Cr-Mn 15/25 montre la transformation structurale réversible ciblée entre ferrite et austénite autour de 550-600 °C. Bien que cette gamme de température ne soit pas compatible avec domaine d'application de réfrigération magnétique à la température ambiante, cette famille d'alliages a un potentiel dans les applications magnétocaloriques à haute température. De plus, les transitions purement magnétiques dans certains alliages observés dans la thèse peuvent être exploitées dans la production d'énergie thermomagnétique.

Différentes méthodes de synthèse des composés, ainsi que des techniques de refroidissement rapide (hypertrempe) ont été traitées pour identifier les meilleures conditions de formation de phases appropriées.

Ce travail peut être poursuivi par investigations suggérées ci-dessous :

Afin d'étudier davantage la mobilité de l'hydrogène, il est possible d'effectuer de la diffraction neutronique quasi-élastique ou des expériences de résonance magnétique nucléaire. Avec les difficultés que nous avons rencontrées dans l'analyse et l'interprétation des données dans la désorption, il est important de designer des conditions expérimentales spécifiques afin de sonder correctement la diffusion et les changements dans la structure lors de la désorption.

De plus, il peut être intéressant d'étudier la corrélation entre la densité des joints de grains / taille de grain / microstructure et la stabilité de l'hydrogène. Les résultats de ces études peuvent constituer un guide pour optimiser les procédés de traitement thermique afin de concevoir la microstructure adaptée à la propriété de stabilité d'hydrogène souhaitée.

La présence et la détermination quantitative de la teneur en carbone dans la phase de 1-13, et les phases d'impuretés peuvent encore être examinées par un microanalyseur à sonde électronique afin d'optimiser encore le mode d'insertion du carbone.

Auparavant, l'effet de contrainte sur les motifs de diffraction de rayons X a été analysé par la méthode Williamson-Hall. En raison de la nature cubique du réseau, il y a seulement quelques pics de la même famille, ce qui rend l'analyse de déformation difficile. Aucune différence visible est observée dans les échantillons et avec et sans carbone avec notre résolution de données. Les expériences de diffraction de neutrons ont été réalisées avec des longueurs d'onde 1,22 et 1,28 Å, qui ne permettent pas l'exploration d'un grand domaine en $\sin \theta / \lambda$. A cet effet et afin d'étudier l'effet de la taille de cristallite microstructure sur la dynamique d'hydrogénation, il serait très intéressant de recueillir les diagrammes de diffraction des très courtes longueurs d'onde (synchrotron) pour recueillir quantité maximale de pics. En particulier, il serait extrêmement utile d'observer l'évolution de la contrainte interne en temps réel au cours de l'hydrogénation et la désorption.

L'insertion de l'hydrogène dans des intermétalliques riches en Fe est un champ riche pour les expérimentateurs et théoriciens. Des études sous la pression peuvent être très utiles dans la compréhension et l'adaptation des propriétés magnétiques et magnétocaloriques du système La-Fe-Si.

Appendix

Appendix A

The loop process proposed in the work of L. Caron *et al.* in isothermal magnetization measurements is verified for sample of composition $\text{La}_{0.7}\text{Ce}_{0.3}\text{Fe}_{11.7}\text{Si}_{1.3}$, which shows strong first-order characteristics in the magnetic transition. After each temperature step, the sample is cooled from its paramagnetic state before starting a new isothermal measurement. This process seems to be particularly effective when the hysteresis far exceeds the temperature step size.

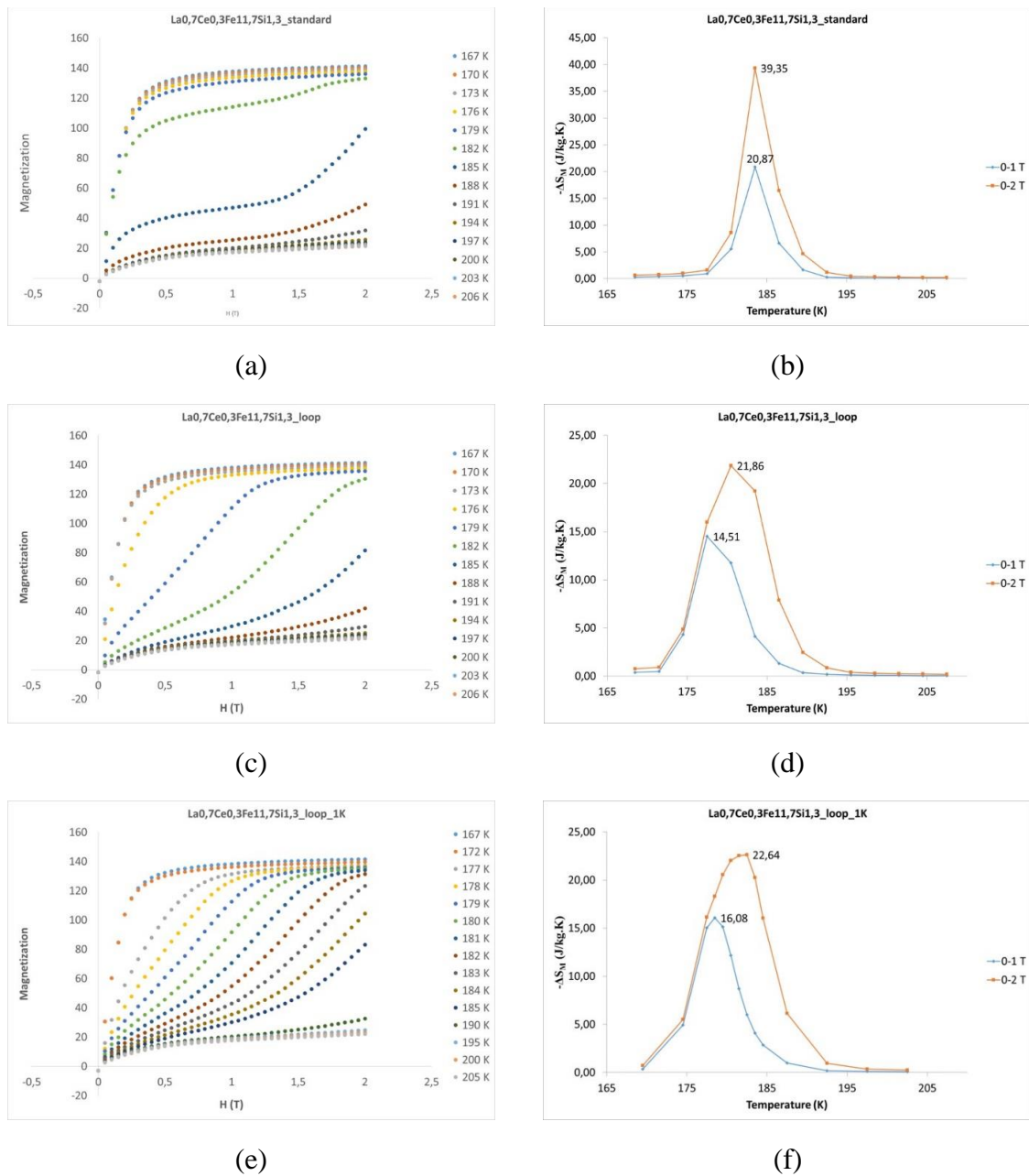


Figure A-1. An example exhibiting FOMT characterized with different measuring procedures

Figure A-1 shows how the resulting peak and shape of the isothermal entropy change can be influenced by the measuring procedure. The sample in question shows a very sharp transition

with a thermal hysteresis of about 12 K. With the standard procedure in (a) and (b), the material is brought to the ferromagnetic state and isotherm magnetization curves are recorded from typically $T_C-20\text{K}$ to $T_C+20\text{K}$. The coexistence region of ferromagnetic and paramagnetic phases close to the Curie temperature makes it troublesome to estimate the entropy change. By using a loop procedure, shown in (c) and (d), in which the sample is brought to its paramagnetic phase before each isotherm, a clear improvement can be seen in the isotherm shape and estimated peak values. Smaller temperature step size, 1 K instead of 3 K step, figure (e) and (f), can slightly improve the precision of the approximation, although it is not absolutely necessary considering the prolonged measuring time.

Appendix B

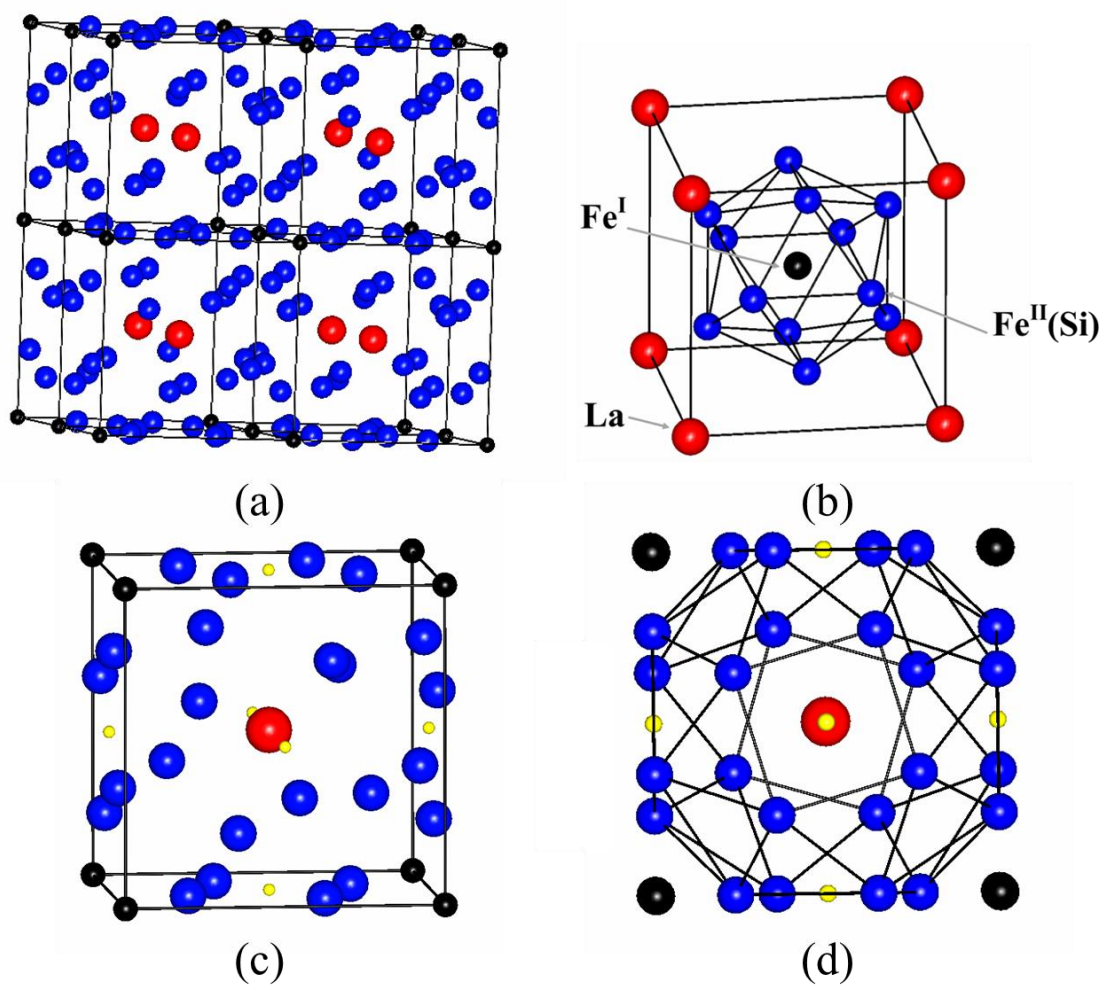


Figure B-1. (a) Unit cell representation of the $\text{La}(\text{Fe}_{1-x}\text{Si}_x)_{13}$ NaZn_{13} -type structure. (b) The structure representation showing La atoms on the corner positions and one icosahedral cluster composed of 1 Fe^{I} atom in the center, surrounded by 12 $\text{Fe}^{\text{II}}(\text{Si})$ atoms. (c) 1/8 of the unit cell showing interstitial elements in the 24d octahedral site with Fe^{I} atoms connected. (d) 1/8 of the unit cell showing interstitial elements in the 24d octahedral site with $\text{Fe}^{\text{II}}(\text{Si})$ atoms connected.

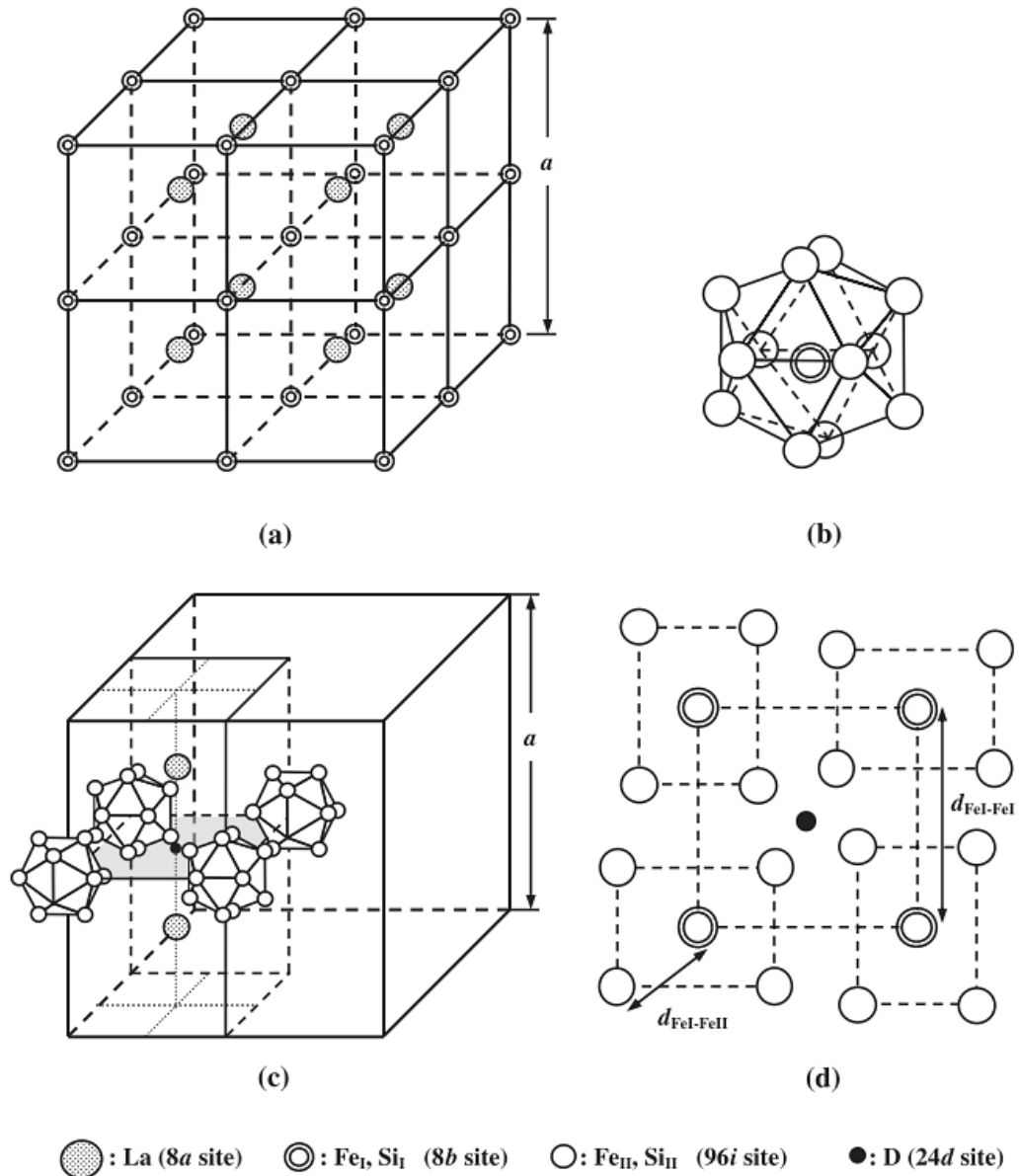


Figure B-2. (a) Schematic view of the 8a and 8b site in the crystal structure of $\text{La}(\text{Fe}_{1-x}\text{Si}_x)_{13}$. (b) Icosahedral cluster illustrated by the 8b and 96i sites. (c) Schematic view of a part of the crystal structure of $\text{La}(\text{Fe}_{1-x}\text{Si}_x)_{13}\text{D}_x$ formed by two La atoms, four icosahedral clusters, and one deuterium atom. The thick line represents the unit cell given by the lattice constant a . (d) Atomic arrangement on the shadow (002) plane indicated in (c). The atomic distances between Fe^{I} and Fe^{II} , and between Fe^{I} and Fe^{I} are represented by $d_{\text{Fe}^{\text{I}}-\text{Fe}^{\text{II}}}$ and $d_{\text{Fe}^{\text{I}}-\text{Fe}^{\text{I}}}$, respectively. Figure taken from S. Fujieda et al., *J. Phys. Soc. Jpn.*, 77 (2008)

Appendix C

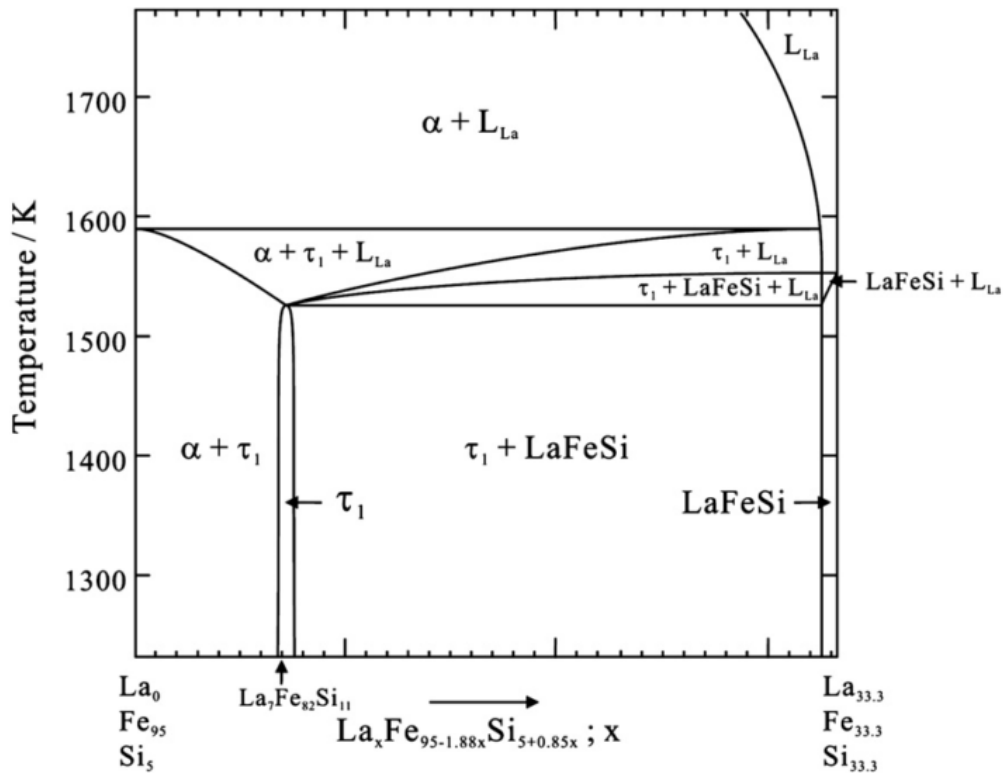


Figure C-1. Vertical section phase diagram in the section from $\text{Fe}_{95}\text{Si}_5$ to $\text{La}_{33.3}\text{Fe}_{33.3}\text{Si}_{33.3}$ (at.%), taken from reference Niitsu et Kainuma, *Intermetallics*, 20 (2012).

Appendix D

Table D-1. The refined structural parameters and interatomic distances for 4 hypotheses in H location for sample of composition $\text{LaFe}_{11.7}\text{Si}_{1.3}\text{C}_{0.2}\text{H}_{1.2}$, based on neutron diffraction data at room temperature.

Parameters	<i>Hypothesis (1)</i>	<i>Hypothesis (2)</i>	<i>Hypothesis (3)</i>	<i>Hypothesis (4)</i>
	<i>24d only</i>	<i>24d + 192 j</i>	<i>24d + 64g</i>	<i>24d + 64g</i>
site <i>192j</i> or <i>64g</i> (x, y, z) x	-	0.216	0.144	0.075
site <i>192j</i> or <i>64g</i> (x, y, z) y	-	0.099	0.144	0.075
site <i>192j</i> or <i>64g</i> (x, y, z) z	-	0.140	0.144	0.075
B_{24d} (\AA^2)	1.94	3.18	3.19	4.20
Occupancy <i>24d</i>	0.051 (1)	0.053 (1)	0.056 (1)	0.055
<i>192j/64g</i> occupancy without constraint	-	0.019 (1)	-0.007 (1)	-0.014
<i>192j/64g</i> occupancy with constraint	-	-0.003 (1)	-0.003 (1)	-0.011 (1)
$H_{24d}-H_{192j/64g}$ (\AA)	-	1.89 (1)	2.42 (1)	3.01 (1)
$H_{192j/64g}-H_{192j/64g}$ (\AA)	-	1.21 (1)	2.47 (1)	1.75 (1)
H/f.u. without constraint	1.22	1.73	1.18	0.98
R_{Bragg} (%)	6.5	6.4	6.5	6.4
R_f (%)	4.7	4.6	4.6	4.6

Appendix E

Low-Si case ($x_{Si}=1.3$): influence of pressure

In order to have a complete picture of the hydrogenation behavior with presence of C, a series of measurements is performed using the Sieverts' apparatus to highlight the evolution of reaction kinetics and H sorption capacity in response to varying pressure at constant temperature (573 K). The H content as a function of time during absorption and desorption is shown in Figure E-1 for various pressures.

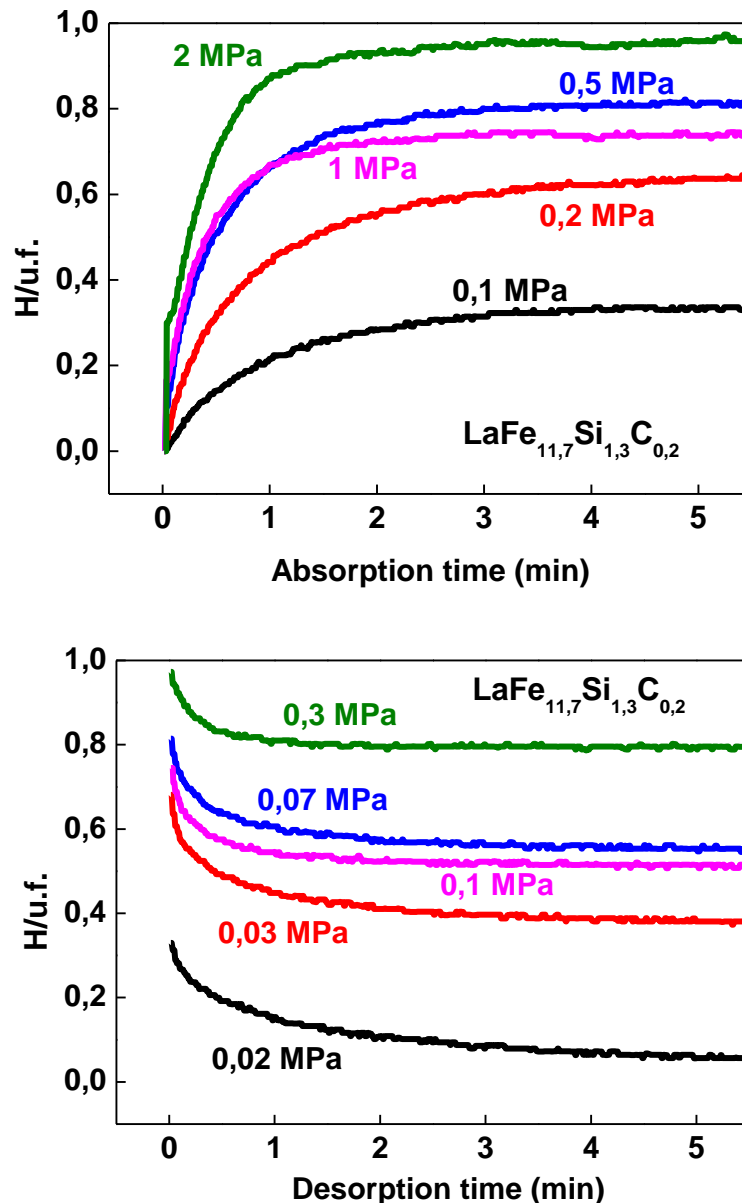


Figure E-1. H sorption measurement of $\text{LaFe}_{11.7}\text{Si}_{1.3}\text{C}_{0.2}$ at different H_2 initial pressures ($T=573\text{ K}$)

It should be emphasized that H absorption and desorption capacity is mainly driven by pressure. The H sorption capacities under different pressure are shown in Table E-1. The

maximum capacity at absorption increases quasi-linearly with increasing initial H₂ pressure. The lower the pressure at desorption, the more complete H release.

Table E-1. The maximum H absorption capacity and the retaining H capacity at desorption under different initial H₂ pressure for sample LaFe_{11.7}Si_{1.3}C_{0.2}.

Absorption pressure (MPa)	Maximum capacity at absorption H/f.u.	Desorption pressure (MPa)	Retaining capacity at desorption H/f.u.
0.1	0.3	0.02	0.0
0.2	0.7	0.03	0.4
0.5	0.8	0.07	0.6
1	0.7	0.1	0.5
2	1.0	0.3	0.8

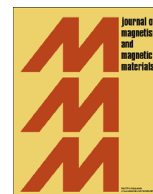
Journal articles



ELSEVIER

Contents lists available at ScienceDirect

Journal of Magnetism and Magnetic Materials

journal homepage: www.elsevier.com/locate/jmmm

In-situ neutron investigation of hydrogen absorption kinetics in $\text{La}(\text{Fe}_x\text{Si}_{1-x})_{13}$ magnetocaloric alloys for room-temperature refrigeration application



Xueying Hai^{a,b}, Charlotte Mayer^b, Claire V. Colin^a, Salvatore Miraglia^{a,*}

^a Univ. Grenoble Alpes, Institut Néel CNRS, 38042 Grenoble, France

^b Erasteel SAS, Tour Maine Montparnasse, 33 Avenue du Maine, 75 755, Paris Cedex 15, France

ARTICLE INFO

Article history:

Received 29 May 2015

Received in revised form

9 July 2015

Accepted 10 July 2015

Available online 17 July 2015

Keywords:

Magnetocaloric effect

Hydrogen kinetics

Interstitial atoms

$\text{La}(\text{Fe},\text{Si})_{13}$ intermetallic alloy

ABSTRACT

Promising magnetocaloric material $\text{La}(\text{Fe},\text{Si})_{13}$ with a first-order magnetic transition has been widely investigated. The observed instability of hydrogen in the material is detrimental for its industrial upscale and a better control of the hydrogen absorption/desorption is necessary to optimize its application potential. In this article, the hydrogen absorption kinetics is studied through an in-situ neutron diffraction experiment. The results allow us to have an inside look at the structure “breathing” to accommodate the interstitial atoms and compare the effect of hydrides with carbonydrides.

© 2015 Elsevier B.V. All rights reserved.

1. Introduction

The exploration of new types of refrigeration technologies that are environmentally-friendly and energy-efficient has pointed magnetic refrigeration as an emerging technology with important application prospect. It is based on the magnetocaloric effect (MCE) of magnetic material, that is, the thermal response of a material subjected to a change in applied magnetic field. Today, a large set of magnetic materials show ‘large’ or ‘giant’ magnetocaloric effects [1]. Among the materials which display a large MCE, $\text{La}(\text{Fe}_{1-x}\text{Si}_x)_{13}$ -based compounds have a very promising practicability [2–5]. $\text{La}(\text{Fe}_{1-x}\text{Si}_x)_{13}$ in the concentration range $0.1 \leq x \leq 0.14$ shows a thermally induced first-order magnetic phase transition from the ferromagnetic (F) to the paramagnetic (P) phase at the Curie temperature T_C , while being accompanied by an obvious lattice contraction. At the same time, it exhibits a magnetic field induced first-order transition from the P to the F phase just above the Curie temperature, which is known as the itinerant-electron metamagnetic (IEM) transition [6–8].

For practical applications T_C needs to be raised up to room temperature. This can be achieved by partly substituting Co for Fe [9], or by inserting light elements such as H [10] or C [11]. Partial

substitution of Fe by Co leads to a weakened first-order magnetic transition [9], whereas the MCE is still maintained at a high value for interstitial insertion with hydrogen and small concentration of carbon [11–13].

However, it is important to keep in mind that the thermal desorption of H in La–Fe–Si alloys occurs rapidly at temperatures not far above room temperature e.g. 175 °C [14], which is an underlying problem for practical application. Therefore, the thermal stability of $\text{LaFe}_{13-x}\text{Si}_x\text{H}_y$ against H desorption has to be improved. A fundamental understanding of the underlying rate-controlling steps in hydrogen sorption and desorption is necessary to effectively support application.

In order to overcome this drawback, carbon insertion has been used in combination with H insertion to improve the thermal stability of $\text{LaFe}_{13-x}\text{Si}_x\text{H}_y$. A significant enhancement in desorption temperature of H was observed in the hydrided $\text{LaFe}_{11.6}\text{Si}_{1.4}\text{C}_x$ samples with $x=0.1$ and 0.2 [15]. The investigation of hydrogen sorption properties in $\text{La}_{0.7}\text{Pr}_{0.3}\text{Fe}_{11.5}\text{Si}_{1.5}\text{C}_{0.2}$ showed that the addition of interstitial carbon atom, not only slows down hydrogen absorption, but also prevents hydrogen from being released [16,17]. In this respect, a knowledge of the interstitial insertion scheme is profitable and has prompted the current investigation. In order to get a precise knowledge of the hydrogen location and sequential filling of the interstitial sites, an in situ neutron powder diffraction investigation of the hydrogenation of $\text{La}(\text{Fe},\text{Si})_{13}$ and

* Corresponding author.

E-mail address: salvatore.miraglia@neel.cnrs.fr (S. Miraglia).

La(FeSi)₁₃C_x has been performed at Institut Laue Langevin (ILL). Moreover, carbon addition as an interstitial element, allows the investigation of the interstitial site accommodation.

2. Experimental details

The La(Fe_xSi_{1-x})₁₃ alloys are prepared by high-frequency induction melting ultra-pure elemental compounds in appropriate nominal compositions. Carbon insertion is performed via a solid-solid reaction with an intermediate alloy type Fe–Si–C. The as-cast alloys are then wrapped in Mo foil, sealed in quartz ampoule, and filled with partial pressure of argon. Annealing was performed for 15 days at 1373 K for all samples. The sample structures and phases were checked by a PANalytical X'Pert MRD X-ray diffractometer operated at the Cu wavelength, using a 2θ angle between 20° and 90°.

In order to get a precise knowledge of the hydrogen location and sequential filling of the interstitial sites, an in-situ high-energy neutron diffraction experiment has been performed at Institut Laue–Langevin (ILL) at the D1B beamline with an incident neutron wavelength of 1.28 Å. Deuterium absorption and desorption experiments are performed at 540 K inside a cryostat to obtain a sufficiently observable kinetics. The sample is first placed inside the neutron diffraction cell and is heated from room temperature to 540 K in vacuum. As the temperature stabilizes, ultra-pure deuterium gas is introduced to the cell. Deuterium gas flow is controlled at 20 ml/min at a constant pressure of 1200 mbar to mimic an industrial process of free flow of hydrogen. Desorption is carried out by switching the gas flow from deuterium to helium at 540 K, to allow mobility of interstitial atoms. After the kinetics has reached equilibrium, the sample is cooled down to room temperature and taken out of the cryostat.

The neutron diffraction patterns collected over the range 2θ=0–128° with a step increment of 0.1° have been refined with using the Fullprof code with the assumption of a peak-line profile of Thompson–Cox–Hasting [18]. Diffraction patterns are collected every 5 min. These raw files can then be summed to obtain files with good statistics.

3. Result and discussion

3.1. Structure analysis

The neutron diffraction results confirm the cubic unit cell and the occupancy of sites, and that the 8a site is fully occupied by La, the 8b site is fully occupied by Fe, and Si preferentially substitutes Fe in the 96i site. This is in agreement with a recent study by Lyubina [19], which used the same neutron source at the D1B diffractometer and earlier neutron studies by Rosca [20] and Fujieda [21]. Powder diffraction patterns confirm that the annealed sample retains the cubic NaZn₁₃-type structure (space group Fm-3c) over the whole process of absorption and desorption of deuterium interstitials at 540 K, with approximately 6–7% of α-Fe as a secondary phase. There is an obvious increase and decrease of lattice parameter upon hydrogenation and desorption, respectively.

Good refinements of our neutron diffraction data have shown that carbon interstitials enter the 24d site, an octahedral site with 4Fe^{II}/Si and 2La nearest neighbors, the same site is found to be accommodated by hydrogen atoms. Although the 48f site (a Fe^{II}-based asymmetric pyramid with one La vertex) has also been suggested [20], in this work we accept the conclusions of Fujieda [21] and Liu [22] in favor of the 24d site. As explained by Liu et al. through the Wigner–Seitz cell volume calculations for the La(Fe,

Al)₁₃C_x structure, there are seven different interstitial sites likely to accommodate a covalent C atom (volume ~2.0 Å³), amongst with one with volume larger than that of a neutral carbon atom (~6.0 Å³). The difference between the 24d and 48f sites lies in the fact that occupancy of the 48f site leads to a small and artificial improvement of the structural refinement because the 24d (0 ¼ ¼) position coordinates split into (x ¼ ¼) coordinates allowing an additional degree of freedom for the Rietveld refinement. Accommodating carbon in the 48f site also leads to much shorter La–C distances as compared with typical La–C bond length such as in LaC₂ compounds, whereas carbon occupying 24d sites allows much reasonable La–C and Fe–C interatomic distances. Deuterium interstitial atoms are accommodated in the 24d site and the refined compositions after absorption are LaFe_{11.44}Si_{1.56}D_{0.97} and LaFe_{11.44}Si_{1.56}C_{0.2}D_{0.71}. These compositions correspond to an occupancy fraction of the 24d sites by hydrogen of 33% and 24% respectively; the fraction of 24d sites occupied by carbon atoms being 7%. Our results agree with the 50% maximum occupancy fraction reported in the works of Lyubina [19] and Fujieda [21] within the reasonable range of experimental conditions. The absorption pressure applied in this work is about 0.12 MPa as compared with 2 MPa in the work by Fujieda.

3.2. Absorption kinetics

In order to analyze the kinetics law, a fit to the absorption isotherms was realized by using a generalized equation, based on the Kolmogorov–Johnson–Mehl–Avrami (KJMA) model for the description of the solid phase reaction. The KJMA equation was developed for process nucleation/growth during interactions gas/metal. It is very suitable for the modeling of solid hydrides formation phenomena in the presence of hydrogen. It is based on the following modified equation

$$F = 1 - e^{-(k \cdot t^n)}$$

where F is the fraction of hydrogen absorbed, t is the reaction time, k the reaction constant at the temperature and n a constant related to the reaction mechanism and is dependent on the shape of the new phase particles.

The degree of perturbation from equilibrium drives the absorption/desorption of hydrogen in the compound. The kinetics of hydrogen uptake and release may involve many complex steps including adsorption, dissociation, surface diffusion, bulk hydrogen diffusion, hydride formation, reactant diffusion, phase separation, catalysis, etc. The in-situ absorption experiment yields the following kinetics law for the two samples.

The reaction constant k shows that C insertion significantly lowers hydrogen sorption kinetics and corroborates the visual inspection (slope of the occupancy factor increase in the course of the absorption experiments). (Fig. 1).

3.3. Insertion scheme, structure and bonding

Fig. 2 shows the observed and calculated neutron diffraction patterns for selected sample LaFe_{11.44}Si_{1.56} (regions containing contributions from Aluminum sample holders are excluded for clarity). A satisfactory agreement is obtained in the whole 2θ range investigated. The deduced atomic positions, cell parameter, Fe–Fe bonds, and weighted profile R factors are given in Table 1 in Annex.

The cubic NaZn₁₃-type structure can be described as a CsCl-type packing of La and Fe^I-centered icosahedra. The La atoms are surrounded by 24 Fe^{II}/Si atoms in an almost spherical polyhedron arrangement (actually a “snub cube”). Two Fe^I-centered icosahedra are interconnected by *stella quadrangula* [23] such that they are

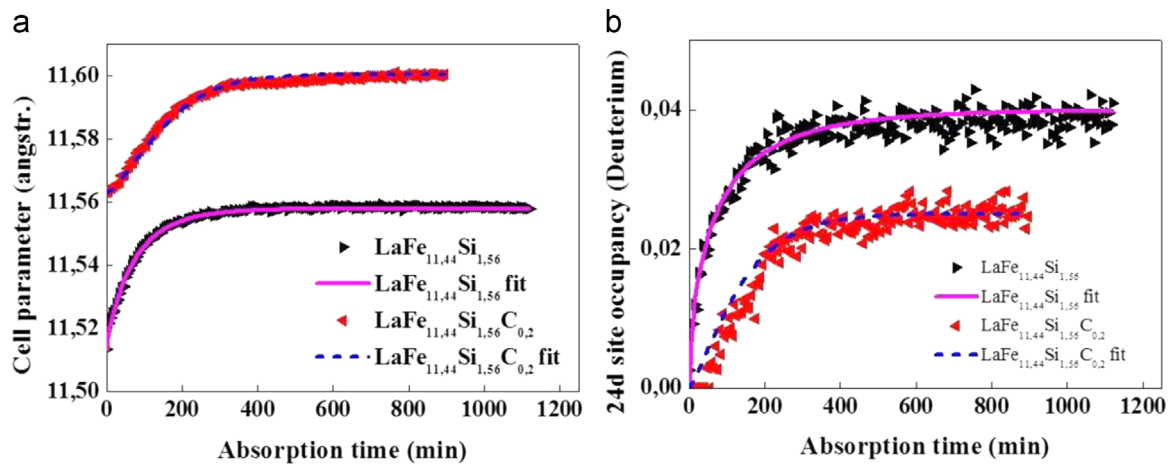


Fig. 1. Evolution of cell parameter and deuterium 24d site occupancy recorded during the in-situ absorption experiment.

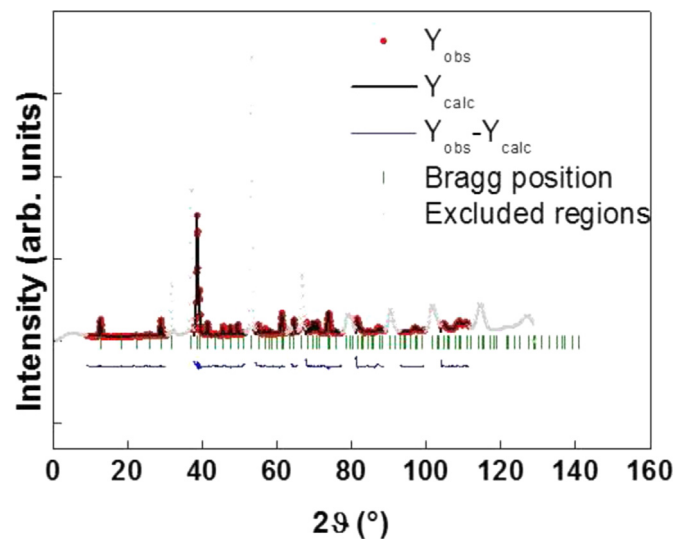


Fig. 2. The observed and calculated neutron diffraction patterns for $\text{LaFe}_{11.44}\text{Si}_{1.56}$ (the Aluminum sample holder contributions are excluded, shown in gray, for clarity).

Table 1

Modeling of the absorption kinetics during the in-situ absorption experiment (n is chosen arbitrarily as 1 for a good precision in linearization and for a valid comparison of k , the last digit is significant).

Sample		Reaction constant k	
		Cell parameter	24d site occupancy
A	$\text{LaFe}_{11.44}\text{Si}_{1.56}$	0.012	0.009
B	$\text{LaFe}_{11.44}\text{Si}_{1.56}\text{C}_{0.2}$	0.008	0.007

arranged in an alternate pattern with adjacent icosahedra rotated 90° with respect to each other.

There are in total five kinds of Fe–Fe bonds (B1–B5) within the distance of 2.7 Å for the $\text{LaFe}_{11.44}\text{Si}_{1.56}$ sample, as can be seen in Fig. 3. The first three bonds are formed by the Fe atoms in the same cluster: the intra-icosahedron ones (B2, B3) and the $\text{Fe}^{\text{I}}\text{–Fe}^{\text{II}}$ distance is the radius of the icosahedron (B1). The last two $\text{Fe}^{\text{I}}\text{–Fe}^{\text{II}}$ bond lengths, referred to as inter-icosahedron bond lengths (B4, B5), are significantly smaller than the intra-icosahedron ones. The shortest Fe–Fe bond is an inter-cluster bond (B4) in this work. Finally, note that the *stella quadrangula* also contain two different distances, 4 longer distances (B5) and 4 shorter distances (B4). These results are consistent with those previously reported

[19,24,25].

Fig. 4 shows the variation of Fe–Fe bonds before and after deuterium insertion for both $\text{LaFe}_{11.44}\text{Si}_{1.56}$ and $\text{LaFe}_{11.44}\text{Si}_{1.56}\text{C}_{0.2}$ compounds. For $\text{LaFe}_{11.44}\text{Si}_{1.56}$ sample, four of the five Fe–Fe bonds show a tendency to expand after introduction of deuterium. The largest elongation occurs for the shortest inter-cluster bond B4, and the relative change is about 1.3% as deuterium concentration increases from 0 to 0.97. In contrast, the longest bond B2, one of the intra-cluster bonds, shows a small shrinkage (–0.8%). The tendency of Fe–Fe bond variation is agreeable with the result obtained between $\text{LaFe}_{11.5}\text{Si}_{1.5}$ and $\text{LaFe}_{11.5}\text{Si}_{1.5}\text{H}_2$ compounds in [24].

Taking a closer look at Fig. 4, the addition of carbon changes the bond variations between iron atoms in a different manner. The inter-icosahedron bond lengths (B4, B5) are more sensitive to interstitial insertion than the intra-icosahedron ones (B2, B3). The largest elongation for carbon-containing sample occurs at B5 instead of B4, with the relative increase of 5.4% and 0.85% for B5 and B4, respectively, for an introduction of 0.71 deuterium per unit formula. B2 shrinks considerably more for the $\text{LaFe}_{11.44}\text{Si}_{1.56}\text{C}_{0.2}\text{D}_z$ compound (–0.97%). 0.2 atoms of carbon per unit formula seems to produce almost identical variations of the Fe–Fe bonds as 0.97 deuterium atoms per unit formula, which is reasonable since the cell parameter of $\text{LaFe}_{11.44}\text{Si}_{1.56}\text{D}_{0.97}$ and $\text{LaFe}_{11.44}\text{Si}_{1.56}\text{C}_{0.2}$ are nearly identical.

The $(\text{Fe}/\text{Si})_{13}$ icosahedra undergo considerable reshaping in

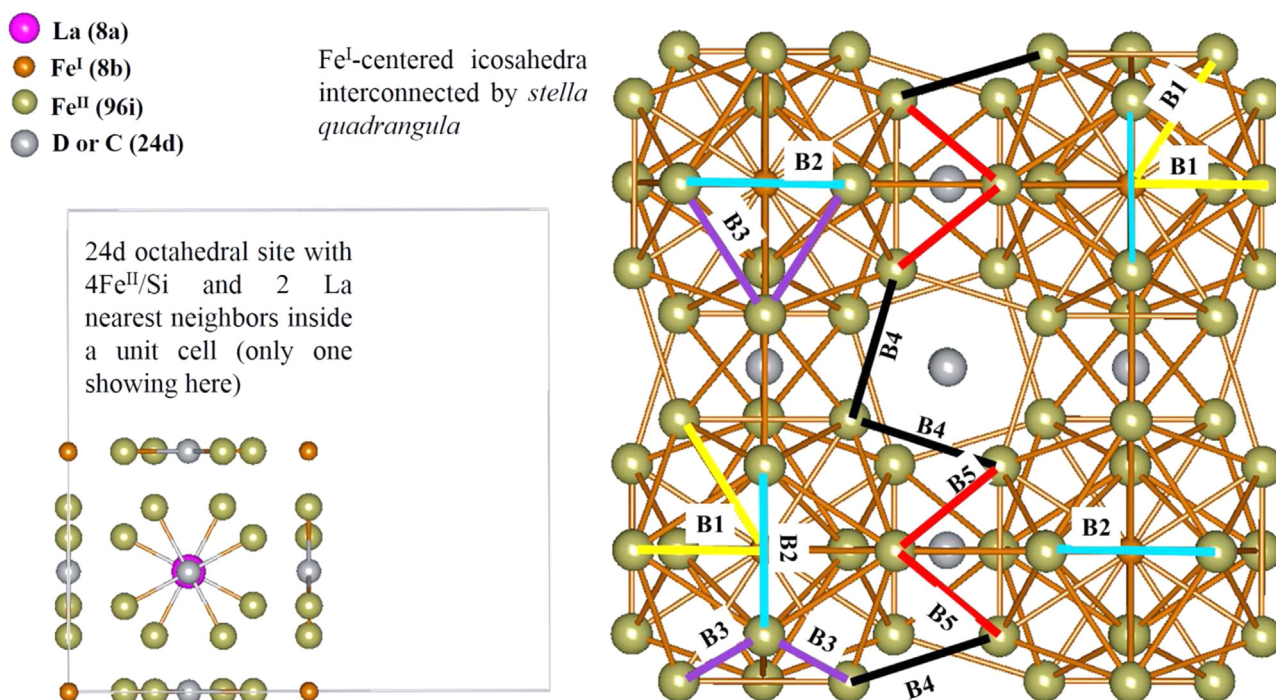


Fig. 3. A schematic representation of the atomic structure of the NaZn13-type cubic structure, highlighting the octahedral interstitial site 24d and the inter- and intra-icosahedral Fe–Fe bond.

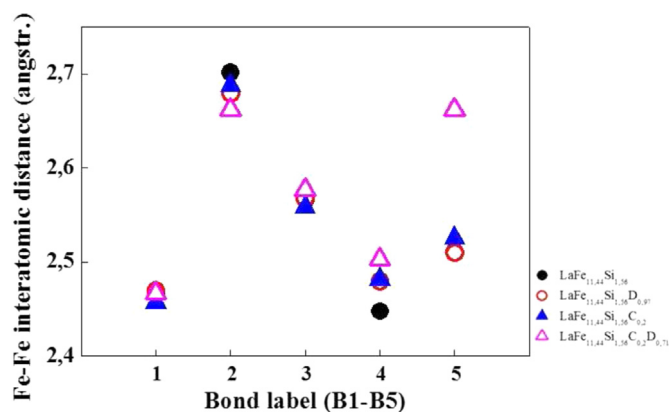


Fig. 4. Change of Fe–Fe bond length before (solid dots) and after (empty dots) deuterium absorption for the selected compounds.

order to accommodate interstitial insertion. B4 is the bond directly connected with interstitial element introduction. In the case with the presence of carbon, B4 has reached its limit in expansion and B5, the next direct neighboring bond, is incorporated into the expansion in order to stabilize the cubic structure. This selective variation can be understood within the framework of the crystal chemistry of NaZn₁₃-type structure. The corner-connected *stella quadrangula* which occupy the empty space between the snub cubes and the icosahedra are the basic structural unit of cubic structure. Moreover, the size of the unit cell and the snub cube is not determined by the large atom centering the snub cube (La). Instead, it is determined only by the structure building unit, that is the *stella quadrangula*. Within this framework, the preferential variation of interatomic distances that is observed upon interstitial insertion, in turn, is understandable since the inter-icosahedra distances (B4 and B5) belong to the *stella quadrangula*.

4. Conclusion and prospects

In conclusion, the in-situ deuterium absorption/desorption

experiments with high-flux neutron diffractometer D1B at ILL allow us to study in depth the interstitial effect of hydrides and carbonydrides on the crystal structure of La(Fe_{1-x}Si_x)₁₃ magneto-caloric material. The effect of carbon on hindering hydrogen absorption rate is confirmed by this “in-situ” observation. Desorption studies are ongoing to confirm the effect of carbon on the hydrogen desorption kinetics. Further investigation on different concentration of carbon as well as substitution of La by other rare-earth effect, will also be explored in future, in order to illustrate a generalized relation between the evolution of magnetic properties, and the changes in crystal structure for La(Fe_{1-x}Si_x)₁₃ alloys.

Acknowledgment

This work is supported by the CIFRE Project no. 2013/0827. The beam time granted at the Institut Laue Langevin at Grenoble, France and the support from the CRG project of the CNRS are greatly appreciated.

Appendix

See appendix [table A1](#) here

Table A1

The deduced atomic coordinates of the 96i site, cell parameter, Fe–Fe bonds, and weighted profile *R* factors for LaFe_{11.44}Si_{1.56} and LaFe_{11.44}Si_{1.56}C_{0.2} and their hydrides at saturation (refined from summed data of good statistical quality).

Composition		LaFe _{11.44} Si _{1.56}	LaFe _{11.44} Si _{1.56} D _{0.97}	LaFe _{11.44} Si _{1.56} C _{0.2}	LaFe _{11.44} Si _{1.56} C _{0.2} D _{0.71}
96i site atomic coordinates	x	0	0	0	0
	y	0.1792 (4)	0.1788 (8)	0.1780 (5)	0.1791 (6)
	z	0.1173 (4)	0.1161 (8)	0.1163 (6)	0.1148 (6)
Cell parameter of the cubic phase	a	11.511 (2)	11.559 (1)	11.556 (3)	11.595 (1)
Fe–Fe bond lengths	B1	2.466 (4)	2.47 (1)	2.457 (5)	2.467 (6)
	B2	2.702 (7)	2.68 (1)	2.688 (8)	2.662 (9)
	B3	2.566 (4)	2.568 (8)	2.559 (8)	2.577 (9)
	B4	2.448 (7)	2.480 (1)	2.482 (8)	2.503 (9)
	B5	2.511 (6)	2.510 (1)	2.526 (8)	2.662 (9)
Weighted profile R factor	R_{wp}	11.1	13.8	19.5	20.1

References

- [1] K. Sandeman, *Scr. Mater.* 67 (2012) 566.
- [2] A. Saito, T. Kobayashi, H. Tsuji, *J. Magn. Magn. Mater.* 30 (2007) 2808.
- [3] S.L. Russek, C.B. Zimm, *Int. J. Refrig.* 29 (2006) 1366.
- [4] C.B. Zimm, A. Boeder, J. Chell, A. Sternberg, A. Fujita, S. Fujieda, K. Fukamichi, *Int. J. Refrig.* 29 (2006) 1302.
- [5] A. Fujita, S. Koiwai, S. Fujieda, K. Fukamichi, T. Kobayashi, H. Tsuji, S. Kaji, A. Saito, *Jpn. J. Appl. Phys.* 46 (2007) L154.
- [6] A. Fujita, S. Fujieda, K. Fukamichi, H. Mitamura, T. Goto, *Phys. Rev. B* 65 (2001) 014410.
- [7] A. Fujita, K. Fukamichi, J.-T. Wang, Y. Kawazoe, *Phys. Rev. B* 68 (2003) 104431.
- [8] A. Fujita, K. Fukamichi, K. Koyama, K. Watanabe, *J. Appl. Phys.* 95 (2004) 6687.
- [9] X. Liu, Z. Altounian, *J. Magn. Magn. Mater.* 264 (2003) 209.
- [10] S. Fujieda, A. Fujita, K. Fukamichi, Y. Yamazaki, Y. Lijima, *Appl. Phys. Lett.* 79 (2001) 653.
- [11] Y. Chen, F. Wang, B. Shen, G. Wang, J. Sun, *J. Appl. Phys.* 93 (2003) 1323.
- [12] Y. Chen, F. Wang, B. Shen, F. Hu, J. Sun, G. Wang, *Z. Cheng, J. Phys.: Condens. Matter* 15 (2003) L161.
- [13] A. Fujita, S. Fujieda, K. Fukamichi, *J. Magn. Magn. Mater.* 321 (2009).
- [14] J. Wang, Y. Chen, Y. Tang, S. Xiao, T. Liu, E. Zhang, *J. Alloy Compd.* 485 (2009) 313.
- [15] C.S. Teixeira, M. Krautz, J.D. Moore, K. Skokov, J. Liu, P.A. Wendhausen, O. Gutfleisch, *J. Appl. Phys.* 111 (2012) 07A927.
- [16] J. Zhao, J. Shen, H. Zhang, Z. Xu, J. Wu, F. Hu, J. Sun, B. Shen, *J. Alloy Compd.* 520 (2012) 277.
- [17] H. Zhang, B. Shen, Z. Xu, X. Zheng, J. Shen, F. Hu, J. Sun, Y. Long, *J. Appl. Phys.* 111 (2012) 07A909.
- [18] L. Finger, D. Cox, A. Jephcoat, *J. Appl. Crystallogr.* 27 (1994) 892.
- [19] J. Lyubina, *J. Appl. Phys.* 109 (2011) 07A902.
- [20] M. Rosca, M. Balli, D. Fruchart, D. Gignoux, E. Hlil, S. Miraglia, B. Ouladdiaf, P. Wolfers, *J. Alloy Compd.* 490 (2010) 50.
- [21] S. Fujieda, A. Fujita, K. Fukamichi, Y. Yamaguchi, K. Ohoyama, *J. Phys. Soc. Jpn.* 77 (2008) 1.
- [22] X. Liu, Z. Altounian, A. Beath, *J. Appl. Phys.* 95 (2004) 7067.
- [23] H. Nyman, S. Andersson, *Acta Crystallogr.* A35 (1979) 937.
- [24] L. Jia, J. Sun, J. Shen, B. Gao, T. Zhao, H. Zhang, F. Hu, B. Shen, *J. Appl. Compd.* 509 (2011) 5804.
- [25] F. Wang, G. Wang, F. Hu, A. Kurbakov, B. Shen, Z. Cheng, *J. Phys.: Condens. Matter* 15 (2003) 5269.

SUBSTITUTIONAL AND INTERSTITIAL MODULATION OF LA-FE-SI STRUCTURE DISCUSSED WITH HYDROGEN SORPTION KINETICS

X. Hai^{(a)(b)*}, C. Mayer^(b), V. Nassif^(a), F. Porcher^(c), S. Miraglia^(a)

^(a) Institut Néel, Univ. Grenoble Alpes, 25 Avenue des Martyrs, 38042, Grenoble, France

^(b) Erasteel SAS, Tour Montparnasse, 33 Avenue du Maine, 75755, Paris, France

^(c) Laboratoire Léon Brillouin, UMR12 CEA-CNRS, Bât. 563 CEA Saclay, 91191, Gif sur Yvette, France

*Corresponding author. E-mail: xueying.hai@neel.cnrs.fr

ABSTRACT

Magnetocaloric materials $(\text{La,Ce})(\text{Fe,Mn,Si})_{13}\text{H}_x$ have great potential as commercializable candidate for room-temperature magnetic refrigeration technology. It is important to have a better understanding of their hydrogen stability for the industrial upscaling. The hydrogenation reaction is investigated by powder neutron diffraction in order to have insights on the interaction between hydrogen and the host lattice. The reaction kinetics of absorption and desorption of interstitial elements can be influenced by presence of other interstitial and substitutional atoms. We demonstrate with neutron diffraction data the effects of C and Ce atoms on the deuterium absorption and desorption kinetics. The influence of substitutions and interstitial modification to the crystal structure are discussed at the level of interatomic Fe-Fe bond variations.

Keywords: magnetocaloric materials, hydrogen sorption kinetics, neutron diffraction

DOI: 10.18462/iir.thermag.2016.0043

1. INTRODUCTION

Magnetocaloric materials in the family of $\text{La}(\text{Fe}_{1-x}\text{Si}_x)_{13}$ exhibit tunable ordering temperature and magnetocaloric performance from composition modification [1-5]. Currently the most effective method of tuning T_C to room temperature is the insertion of interstitial hydrogen (H) because of the preservation of favorable magnetocaloric effect [6]. However, interstitial H shows unstable characteristics that manifest in two ways. Fully hydrogenated compounds desorb H with time from even below 150°C [7], which can be problematic for shaping processes. Partially hydrogenated material that exhibits strong first-order magnetic transition characteristics shows age splitting of T_C peak [8, 9], which is associated with the phase segregation and coexistence of the paramagnetic and ferromagnetic phases [10]. Therefore, it is important to investigate the H interstitial behavior inside the host lattice. Recently, we have demonstrated that a modest addition of carbon (C) interstitial atoms in the $\text{La}(\text{Fe}_{1-x}\text{Si}_x)_{13}$ prior to hydrogenation can slow down the H insertion kinetics and therefore, offers a prospect to have improved stability of hydrogenated materials in long-term application [11]. In this paper, we present recent developments in H sorption kinetics, which will be discussed with influences from both C interstitial insertion and Cerium (Ce) substitution.

2. MAIN SECTION

2.1 Experimental Conditions

The samples are elaborated by high-frequency induction melting appropriate amounts of starting materials. The ingots are homogenized in a sealed quartz tube with partial pressure of Ar and Mo-foil as protection at 1373 K for 15 days. The ingots are mechanically grinded and sieved to irregularly-shaped powder between 40 and 200 μm in size for the neutron diffraction experiments. Deuterium (D) gas is used instead of H for better signal-to-noise ratio in neutron. Details of the *in-situ* neutron diffraction experimental conditions are described elsewhere [11]. High-resolution neutron diffraction patterns are recorded at the 3T2 diffractometer at Laboratoire Léon Brillouin for annealed and hydrogenated samples. The incident neutron wavelength is 1.225 Å. The diffractograms are collected at room temperature from 4.50° to 115.35° at 0.05° step.

2.2 Effect of Partial Substitution of Ce to La

The partial substitution of Ce to La results in a lowering of the Curie temperature T_C with decreasing lattice constant. The change in T_C is mainly attributed to the magnetovolume effect caused by the small radius of Ce atoms [4]. With 0.3 Ce substitution, T_C shifts from 206 K to 188 K under a magnetic field of 0.05 T. The thermal hysteresis increases from 2 to 8 K [12]. Samples of nominal composition $\text{La}_{0.7}\text{Ce}_{0.3}\text{Fe}_{11.44}\text{Si}_{1.56}$ and $\text{La}_{0.7}\text{Ce}_{0.3}\text{Fe}_{11.44}\text{Si}_{1.56}\text{C}_{0.2}$ are studied at the D1B diffractometer. Neutron diffraction gives us access to information at various scales. On the mesoscopic scale, the unit cell expansion and contraction is recorded *in-situ*. At the atomic level, we are able to observe significant changes in the Fe-Fe distances (Section 2.3). A full occupancy of the $24d$ site would correspond to the formula $\text{LaFe}_{13-x}\text{Si}_x\text{H}_3$, which is not attainable practically because of H-H repulsive interactions. In the following analysis, H and D saturation refers to the maximum amount of H or D interstitial atoms absorbed at given temperature and pressure conditions.

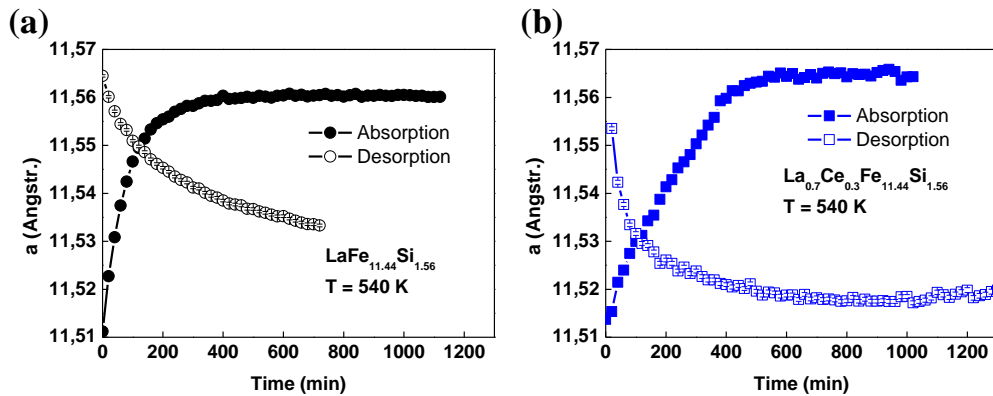


Figure 1. Refined unit cell parameter a during absorption and desorption for samples of composition $\text{LaFe}_{11.44}\text{Si}_{1.56}$ and $\text{La}_{0.7}\text{Ce}_{0.3}\text{Fe}_{11.44}\text{Si}_{1.56}$ vs. time at 540 K.

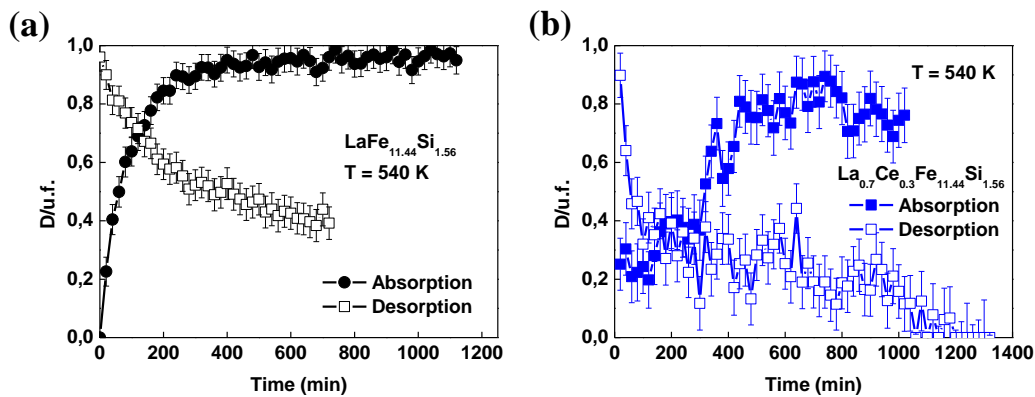


Figure 2. Refined concentration of D interstitials during absorption and desorption for samples of composition $\text{LaFe}_{11.44}\text{Si}_{1.56}$ and $\text{La}_{0.7}\text{Ce}_{0.3}\text{Fe}_{11.44}\text{Si}_{1.56}$ vs. time at 540 K.

Ce substitution for La results in a reduced volume of the octahedral interstitial site ($24d$) due to steric effect. The progressions of unit cell parameter and the $24d$ site occupancy are tracked in the course of D insertion and release at 540 K (Fig. 1 and Fig. 2). At the end of the available absorption time, the specimen has taken in about 0.8 D/u.f. in Ce-substituted sample, slightly less than the Ce-free reference (1 D/u.f.). Considering the kinetics, there is a clear delay for D absorption at 540 K in the case of Ce-substituted sample. It takes specimen $\text{La}_{0.7}\text{Ce}_{0.3}\text{Fe}_{11.44}\text{Si}_{1.56}$ twice as long to finish the initial climb of the unit cell expansion. The effect is even more evident by examining the D content per unit formula deduced from the $24d$ site occupancy. While the unit cell parameter increases continuously to make room for interstitial atoms, the sequential filling of the $24d$ site is not continuous, rather step-like for $\text{La}_{0.7}\text{Ce}_{0.3}\text{Fe}_{11.44}\text{Si}_{1.56}$, as illustrated in Fig. 2. The evolution of the two parameters is not as correlated as one could expect from a simple model. We observe several changes of the slope for the progression of the unit cell parameter for $\text{La}_{0.7}\text{Ce}_{0.3}\text{Fe}_{11.44}\text{Si}_{1.56}$, shown in Fig. 1 (b).

Based on the Kolmogorov-Johnson-Mehl-Avrami (KJMA) relation (Eq.1) for solid phase reaction, the amount of absorption reaction occurred, F , is related to the reaction time, t , and the deuterium sorption kinetics can be evaluated in terms of the reaction constant k .

$$F = 1 - e^{(-k \cdot t^n)} \quad (1)$$

This disparity between the unit cell parameter and the $24d$ site occupancy is confirmed by modeling with KJMA relation. Unlike samples $\text{LaFe}_{11.44}\text{Si}_{1.56}$ and $\text{LaFe}_{11.44}\text{Si}_{1.56}\text{C}_{0.2}$, the Avrami exponent n calculated from the linearization of $\ln(-\ln(1 - F)) = \ln(k) + n \cdot \ln(t)$ is 1.2 for the kinetics of unit cell expansion and 0.5 for that of interstitial filling. This underlines very different mechanisms for the evolution of these two parameters in reaction. Upon desorption, the releasing of the deuterium atoms is almost instantaneous for Ce-substituted specimen, showing a much faster desorption kinetics than that for compound $\text{LaFe}_{11.44}\text{Si}_{1.56}$. For all the samples measured, desorption reaction is much faster than absorption. This can be considered as a consequence of decrepitation of the material due to D massive absorption during heat treatments, as we observe that the effective size of the samples is smaller during desorption due to crack formation. The mechanical strain from D absorption can partially contribute to the accelerated desorption kinetics in Ce-substituted sample as the lattice has a smaller volume due to Ce substitution. But more importantly, Ce-substitution modifies the D diffusion path by a selective contraction of certain interatomic distances (Section 2.3). Desorption is nearly complete for sample $\text{La}_{0.7}\text{Ce}_{0.3}\text{Fe}_{11.44}\text{Si}_{1.56}$, as shown by the emptying of the interstitial site in Fig. 4. This suggests the important role of diffusion path on the facility to release interstitial atoms.

2.3 Effect of C Interstitial Insertion

C interstitial insertion increases T_C and reduces the thermal hysteresis in the magnetic transitions. In the measurements under 0.05 T external field, the T_C increase with 0.2 C inserted is 30 K for samples of composition $\text{LaFe}_{11.44}\text{Si}_{1.56}$ and $\text{La}_{0.7}\text{Ce}_{0.3}\text{Fe}_{11.44}\text{Si}_{1.56}$ [12]. Previously, a noticeable obstructing effect of C on the D absorption reaction was observed for sample of composition $\text{LaFe}_{11.44}\text{Si}_{1.56}\text{C}_{0.2}$ compared with its C-free counterpart [11]. However, C insertion does not modify the D insertion mechanism and the structural modulation upon D introduction remains the same [11]. As mentioned above, Ce-substituted sample $\text{La}_{0.7}\text{Ce}_{0.3}\text{Fe}_{11.44}\text{Si}_{1.56}$ shows a step-like evolution of D concentration during absorption. Therefore, it is interesting to investigate the impact of C on the D sorption dynamics of Ce-substituted sample. Although the Ce-substituted sample has increased difficulty in D absorption, the incorporation of 0.2 C/u.f. interstitials is well succeeded through induction melting for sample $\text{La}_{0.7}\text{Ce}_{0.3}\text{Fe}_{11.44}\text{Si}_{1.56}\text{C}_{0.2}$. C-doped sample $\text{La}_{0.7}\text{Ce}_{0.3}\text{Fe}_{11.44}\text{Si}_{1.56}\text{C}_{0.2}$ smooths the D insertion reaction, as seen in Fig. 3. D concentration stabilizes after 500 min, with C-doped sample showing slightly faster kinetics between 200 and 400 min of absorption. At desorption, however, sample $\text{La}_{0.7}\text{Ce}_{0.3}\text{Fe}_{11.44}\text{Si}_{1.56}$ has emptied nearly all the interstitial D from the $24d$ site while $\text{La}_{0.7}\text{Ce}_{0.3}\text{Fe}_{11.44}\text{Si}_{1.56}\text{C}_{0.2}$ has retained about half of its D atoms.

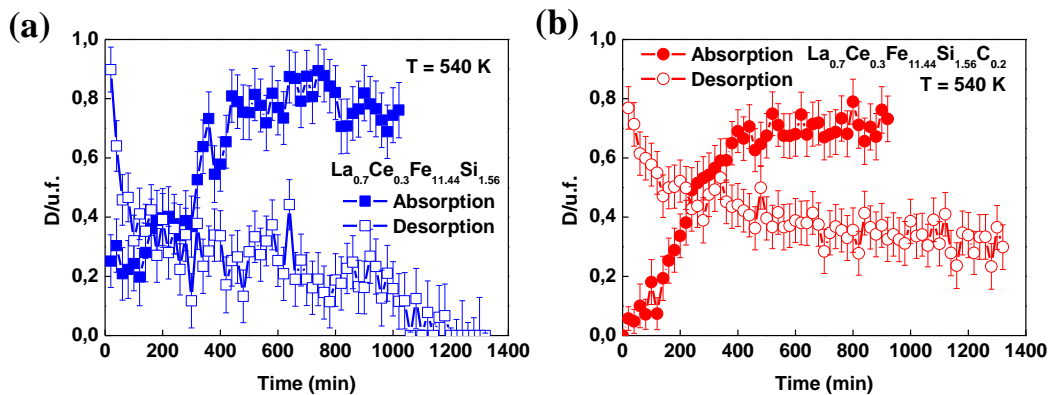


Figure 3. Effect of C on the D absorption and desorption kinetics demonstrated by the D concentration per unit formula for sample of composition $\text{La}_{0.7}\text{Ce}_{0.3}\text{Fe}_{11.44}\text{Si}_{1.56}$ and $\text{La}_{0.7}\text{Ce}_{0.3}\text{Fe}_{11.44}\text{Si}_{1.56}\text{C}_{0.2}$ at 540 K.

The mechanism of light atom insertion into the interstitial site is associated with not only the available space of accommodation, but also the facilitation of the diffusion path in the lattice. Fig. 4 summarizes variations of the unit cell parameter due to C insertion and Ce substitution. The delayed kinetics seen in $\text{LaFe}_{11.44}\text{Si}_{1.56}\text{C}_{0.2}$ can be considered as a shortage of available space compared to $\text{LaFe}_{11.44}\text{Si}_{1.56}$. If the available space is the rate-limiting step, this phenomenon should be highlighted in Ce-substituted sample since interstitial volume is reduced. However, the slightly accelerated absorption kinetics in $\text{La}_{0.7}\text{Ce}_{0.3}\text{Fe}_{11.44}\text{Si}_{1.56}\text{C}_{0.2}$ than in $\text{La}_{0.7}\text{Ce}_{0.3}\text{Fe}_{11.44}\text{Si}_{1.56}$ suggests that it might be more of a changed insertion mechanism through modified interatomic distances. The arrival of D atoms into the interstitial sites could be assisted by C insertion as it stretches the lattice volume. At the same time, the diffusion of interstitial atoms in the lattice is governed by the interatomic distances, which needs to be considered as well. At the desorption stage, C insertion clearly has a softening effect on the fast unit cell contraction in Ce-substituted sample.

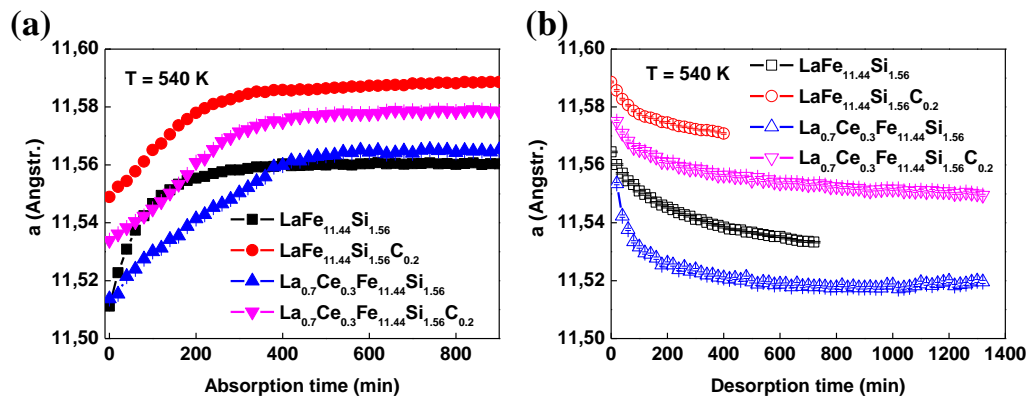


Figure 4. Evolution of unit cell parameter from “in-situ” neutron diffraction for D absorption at 540 K.

2.4 Discussion

Neutron powder diffraction allows us to look inside the structural breathing as the compound accommodates interstitial atoms while maintaining the cubic structure. In $\text{La}(\text{Fe}_{1-x}\text{Si}_x)_{13}$ materials, the magnetocaloric effect relies on the magnetic interaction between Fe sites. The Fe-Fe interatomic bonds are consisted of three bonds that are formed by the Fe atoms in the same cluster and two inter-icosahedra bonds (Fig. 5). Based on the refined results from hydrogenated samples measured at 3T2, H insertion results in the extension of the basal plane of the $24d$ site (B4) and the contraction of the Fe^{I} -centered icosahedron (B2). By tracking the interatomic distances at 540K in the course of absorption and desorption, we are able to confirm this mechanism for D absorption and the D desorption reaction proceeds with the reversal process.

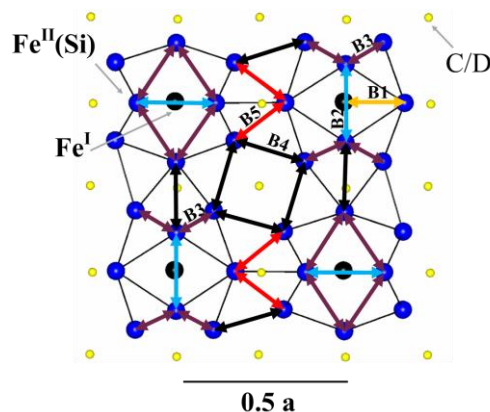


Figure 5. Structural representation of $\text{La}(\text{Fe}_{1-x}\text{Si}_x)_{13}$ phase showing Fe-Fe bonds and interstitial atoms (yellow dots) on the $24d$ site.

Ce substitution reduces the lattice volume by reducing notably the B4 and B5 distances, directly affecting the interstitial $24d$ site volume. Fig. 6 shows the evolution of B4, and B2 in the course of D absorption for sample of composition $\text{La}_{0.7}\text{Ce}_{0.3}\text{Fe}_{11.44}\text{Si}_{1.56}$ and $\text{La}_{0.7}\text{Ce}_{0.3}\text{Fe}_{11.44}\text{Si}_{1.56}\text{C}_{0.2}$. D absorption in sample

$\text{La}_{0.7}\text{Ce}_{0.3}\text{Fe}_{11.44}\text{Si}_{1.56}$ shows deviated interatomic bond evolution compared to the Ce-free sample. The first 200 min, the structure stretches B2 while reducing B4, which corresponds to an initial lattice rearrangement. Only very small amount of D atoms are able to enter and the unit cell slowly expands. We refer to this period as an incubation stage for absorption. Afterwards, the period from 200 to 600 minutes corresponds to an accelerated absorption stage where D content jumps from 0.4 to 0.8 D/u.f. The mechanism in this stage is similar to the classical D absorption mechanism observed for samples of composition $\text{LaFe}_{11.44}\text{Si}_{1.56}$ and $\text{LaFe}_{11.44}\text{Si}_{1.56}\text{C}_{0.2}$ under the same experimental conditions [11].

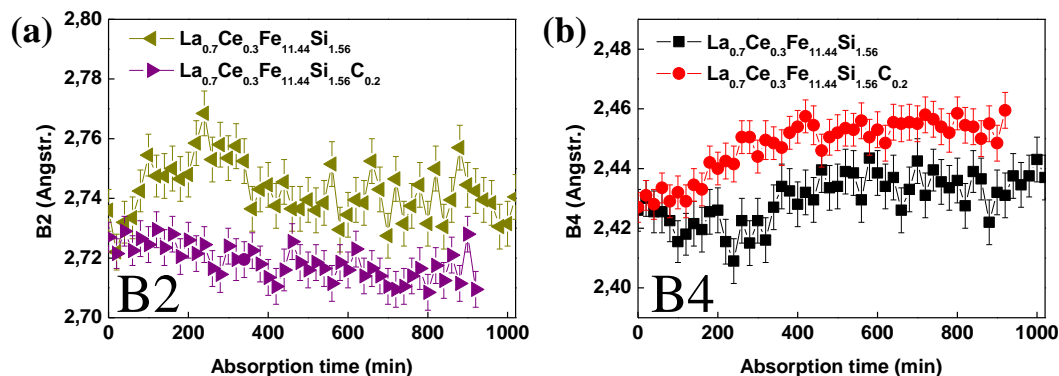


Figure 6. Effect of C insertion on the D absorption kinetics demonstrated by variation of Fe-Fe distances B2 and B4 for samples of composition $\text{La}_{0.7}\text{Ce}_{0.3}\text{Fe}_{11.44}\text{Si}_{1.56}$ and $\text{La}_{0.7}\text{Ce}_{0.3}\text{Fe}_{11.44}\text{Si}_{1.56}\text{C}_{0.2}$.

C insertion results in increased B4 and La-La distances, which constitute the volume of the $24d$ site. The C-doped sample demonstrates typical D absorption mechanism by elongating B4 and reducing B2. The rate-limiting step is the D atomic diffusion within the lattice and C insertion modifies the space within the diffusion path by modifying the interatomic distances. C addition in Ce-substituted sample, therefore, works as a springboard, which smoothes the lattice breathing that is restrained by Ce, as illustrated in the Fe-Fe distance variation for sample $\text{La}_{0.7}\text{Ce}_{0.3}\text{Fe}_{11.44}\text{Si}_{1.56}\text{C}_{0.2}$ in Fig. 6. The interstitial and substitutional modulations on the structure provoke very interesting dynamics at the level of interstitial diffusion path, which leads to further modification of the mechanism of D sorption.

Besides the octahedral $24d$ site, there exists two smaller tetrahedral sites that are likely to accommodate H or D interstitials, $192j$ (0.216, 0.099, 0.14) and $64g$ (0.14, 0.14, 0.14). With the high-resolution neutron data obtained at for $\text{La}(\text{Fe}_{1-x}\text{Si}_x)_{13}$ and $\text{La}(\text{Fe}_{1-x}\text{Si}_x)_{13}\text{H}_{\text{max}}$ samples, these secondary interstitial sites have been tested for compounds saturated with hydrogen. However, adding secondary tetrahedral sites for H accommodation leads to either unreasonable total H concentration or unacceptable distances between H atoms. The small quantity of H atoms and their dispersive nature in the NaZn_{13} -type cubic structure make it quite difficult to distinguish secondary interstitial sites that might provide available volume. Even with high-resolution powder neutron diffraction, one cannot conclude with certainty on the existences of secondary interstitial sites.

Differential Scanning Calorimetry (DSC) can be used to measure the onset of H desorption, which corresponds to an endothermic peak in the heat flow, as shown in Fig. 7. Fully hydrogenated pairs of samples of composition $\text{La}_{0.7}\text{Ce}_{0.3}\text{Fe}_{11.7}\text{Si}_{1.3}$ and $\text{La}_{0.7}\text{Ce}_{0.3}\text{Fe}_{11.7}\text{Si}_{1.3}\text{C}_{0.2}$ are measured in order to confirm the effect of C on H desorption of Ce-substituted La-Fe-Si phase. The T_C of the samples is controlled before and after thermal desorption. Before hydrogenation, annealed sample of composition $\text{La}_{0.7}\text{Ce}_{0.3}\text{Fe}_{11.7}\text{Si}_{1.3}$ has a lower T_C (188 K) than $\text{La}_{0.7}\text{Ce}_{0.3}\text{Fe}_{11.7}\text{Si}_{1.3}\text{C}_{0.2}$ (212 K). The difference in T_C due to 0.2 C/u.f. inserted is about 24 K. Fully hydrogenated samples of composition $\text{La}_{0.7}\text{Ce}_{0.3}\text{Fe}_{11.7}\text{Si}_{1.3}$ has a higher T_C (328 K) than $\text{La}_{0.7}\text{Ce}_{0.3}\text{Fe}_{11.7}\text{Si}_{1.3}\text{C}_{0.2}$ (316 K). The insertion of carbon lowers slightly the maximum hydrogen absorption capacity. Moreover, the difference in T_C after H saturation is reduced to only 12 K. Interstitial modulations by H only and by C and H combined lead to similar levels of T_C after maximum H absorption. This suggests a similar manner in how the Fe-Fe distances are modified for these two modulations, which is then confirmed from the neutron diffraction data (3T2). The dehydrogenated T_C corresponds to the T_C of annealed samples and confirms the total desorption of H atoms in the material. The onset of H desorption is shifted from 521 K (248 °C) to 582 K (309 °C) for sample $\text{La}_{0.7}\text{Ce}_{0.3}\text{Fe}_{11.7}\text{Si}_{1.3}$ and $\text{La}_{0.7}\text{Ce}_{0.3}\text{Fe}_{11.7}\text{Si}_{1.3}\text{C}_{0.2}$,

respectively. The stability of H atoms at high temperature is improved for fully hydrogenated $\text{La}_{0.7}\text{Ce}_{0.3}\text{Fe}_{11.7}\text{Si}_{1.3}\text{C}_{0.2}$.

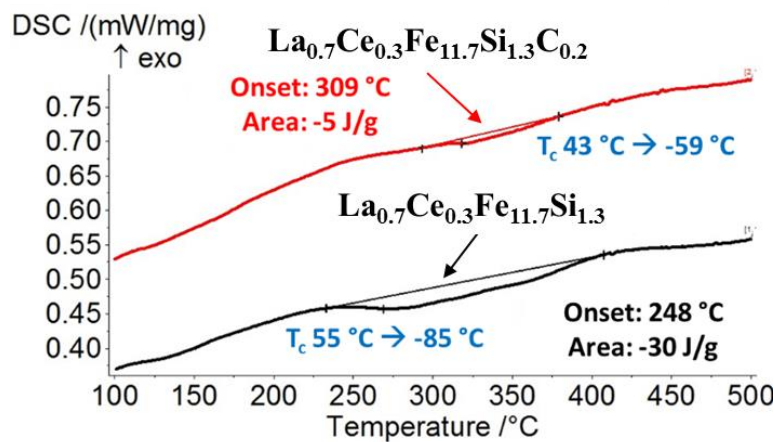


Figure 7. DSC measurement showing the onset of H desorption temperature for sample of composition

3. CONCLUSIONS

We demonstrate with neutron diffraction data that the interstitial insertion is impeded by Ce partial substitution. The analysis of the interatomic distances confirms that Ce substitution has significant modification on the D absorption mechanism. Ce has two noticeable effects on the D sorption kinetics. Smaller interstitial volume makes it difficult for the lattice to expand, therefore leading to a very slow absorption reaction. However, the desorption reaction occurs almost instantaneously and Ce seems to prohibit the retaining of deuterium atoms. A modest introduction of C atoms to the interstitial sites, on the other hand, does not change the sorption mechanism but modifies the kinetics. By introducing C dopants in Ce-substituted sample, the agitated lattice modulation is softened and the classical hydrogenation mechanism is restored. Moreover, C addition in Ce-substituted sample can help retain 50% of the absorbed D during desorption at given experimental conditions.

ACKNOWLEDGMENTS

This work is supported by project CIFRE n°2013/0827. The authors appreciate the French CRG project for assistance in the neutron diffraction facility and experiment.

REFERENCES

- [1] F. Wang *et al.*, *J. Phys. D.: Appl. Phys.*, **36**, 1 (2003).
- [2] X. Liu *et al.*, *J. Magn. Magn. Mater.*, **270**, 305 (2004).
- [3] M. Balli *et al.*, *J. Phys.: Cond. Matter*, **19**, 236230 (2007).
- [4] S. Fujieda *et al.*, *J. Magn. Magn. Mater.*, **321**, 3567 (2009).
- [5] M. Krautz *et al.*, *J. Alloys Compd.*, **598**, 27 (2014).
- [6] Y. Chen *et al.*, *J. Phys.: Condens. Matter*, **15**, L161 (2003).
- [7] C. Mayer *et al.*, *Phys. Status Solidi C*, **11**, 5 (2014).
- [8] A. Barcza *et al.*, *IEEE Trans. on Magn.*, **47**, 3391 (2011).
- [9] C. B. Zimm and S. A. Jacobs, *J. Appl. Phys.*, **113**, 17A908 (2013).
- [10] M. Krautz *et al.*, *J. Appl. Phys.*, **112**, 083918 (2012).
- [11] X. Hai *et al.*, *J. Magn. Magn. Mater.*, **400**, 344 (2016).
- [12] X. Hai *et al.*, to be published

Paper in preparation

Structural effects in the interstitial solid solution system (La,Ce)(Fe,Si)₁₃C_x-H : correlation with hydrogenation kinetics

X. Hai, F. Porcher, C. Colin, C. Mayer, S. Miraglia

Submitted to Journal of Alloys and Compounds

Light interstitial solid solution (La,Ce)(Fe,Si)₁₃C_x-H

X. Hai, C. Mayer, S. Miraglia in preparation

Conferences

1. **X. Hai**, C. Mayer, V. Nassif, F. Porcher, S. Miraglia, “Exploring the hydrogen sorption kinetics in magnetocaloric La-Fe-Si structure via in-situ neutron diffraction”, *61st Annual Conference on Magnetism and Magnetic Materials (MMM)* (Oct. 31 – Nov. 4, 2016), New Orleans, Louisiana, USA, (*Oral presentation*).
2. **X. Hai**, C. Mayer, V. Nassif, F. Porcher, S. Miraglia, “ Substitutional and interstitial modulation of La-Fe-Si structure discussed with hydrogen sorption kinetics”, *7th International Conference on Magnetic Refrigeration at Room Temperature (THERMAG-VII)* (September 11-14, 2016), Turin, Italy, (*Oral presentation, Session highlight talk*).
3. **X. Hai**, C. Mayer, C.V. Colin, V. Nassif, S. Miraglia, “Hydrogen sorption kinetics investigation with in-situ neutron powder diffraction for magnetocaloric alloy (La,Ce)(Fe,Si)₁₃H_x”, *First workshop in Sustainable Energies and Neutron Scattering (SENS)* (May 30th – June 1st, 2016), Bordeaux, France, (*Oral presentation*).
4. **X. Hai**, C. Mayer, C.V. Colin, S. Miraglia, “Effect of Carbon Interstitials on the Hydrogen Stability in La(Fe_xSi_{1-x})₁₃C_yH_z Magnetocaloric Materials”, *Delft Days on Magnetocalorics (DDMC)* (November 2-3, 2015), Delft, Netherlands (*Oral presentation*).
5. **X. Hai**, C. Mayer, C.V. Colin, S. Miraglia, “In-situ neutron investigation of hydrogen absorption kinetics in La(Fe_xSi_{1-x})₁₃ magnetocaloric alloys for room-temperature refrigeration application”, *20th International Conference on Magnetism (ICM)* (July 5-10, 2015), Barcelona, Spain, (*Oral presentation*).
6. **X. Hai**, C. Mayer, S. Miraglia, “Magnetocaloric material for room-temperature refrigeration application”, *Matériaux2014* (November 24-28, 2014), Montpellier, France (*Poster presentation*).

Curriculum Vitae

Xueying Hai was born in Xi'an, Shaanxi province in China. After high school, she went abroad to obtain her Bachelor of Chemistry degree in Emory & Henry College, a private liberal arts university in Emory, Virginia, USA. With an interest to focus on materials science, she joined the Erasmus Mundus Master program in functional materials and engineering (FAME). The program curriculum was divided between Grenoble Institute of Technology – PHELMA at Grenoble, France and Technische Universität Darmstadt at Darmstadt, Germany. She graduated with a master thesis project at Schneider Electric SAS on an R&D project to search for innovative thermal materials for heat dissipation in electro-technical appliances. Drawn by the applied sciences, she later pursued an industrial Ph.D. project between the Néel Institute and Erasteel SAS, in which this thesis work has been developed.

Abstract

With the increasing efficiency issues and environmental problems caused by traditional gas-compression refrigeration, magnetic refrigeration based on the magnetocaloric effect (MCE) is an emerging technology responding to this need of innovation in the cooling industry. MCE is reflected by an entropy variation or a temperature variation of the material under a magnetic field. Magnetocaloric material system La-Fe-Si has great potential as commercializable candidate for magnetic refrigeration technology. It is important to have a better understanding of its hydrogen stability to optimize its application potential. In this thesis, the structural and magnetic properties of La-Fe-Si and common steel alloys are investigated. In particular, we focus on the investigation of the hydrogen sorption properties in La-Fe-Si materials with the help of large instruments. The thermal stability of hydrogenated materials is improved with the help of composition engineering.

Résumé

La réfrigération magnétique est une alternative intéressante aux méthodes de réfrigération traditionnelles, basées sur des cycles de compression et de détente de gaz, car elle présente des rendements énergétiques nettement plus élevés et permet d'éviter l'utilisation de gaz nocifs contribuant à l'effet de serre et problématique pour l'environnement. Cette technologie s'appuie sur l'effet magnétocalorique (EMC) géant de certains matériaux magnétiques autour de la température ambiante. Cet effet permet d'augmenter ou de diminuer la température du matériau lors de son aimantation ou désaimantation adiabatique autour de sa température de transition magnétique. Dans cette thèse, les propriétés structurales et magnétiques des matériaux magnétocaloriques La-Fe-Si et des alliages d'acier sont étudiés. En particulier, nous nous concentrons sur l'étude des propriétés de sorption d'hydrogène dans des matériaux La-Fe-Si, avec l'aide de grands instruments.

Abstract

With the increasing efficiency issues and environmental problems caused by traditional gas-compression refrigeration, magnetic refrigeration based on the magnetocaloric effect (MCE) is an emerging technology responding to this need of innovation in the cooling industry. MCE is reflected by an entropy variation or a temperature variation of the material under a magnetic field. Magnetocaloric material system La-Fe-Si has great potential as commercializable candidate for magnetic refrigeration technology. It is important to have a better understanding of its hydrogen stability to optimize its application potential. In this thesis, the structural and magnetic properties of La-Fe-Si and common steel alloys are investigated. In particular, we focus on the investigation of the hydrogen sorption properties in La-Fe-Si materials with the help of large instruments. The thermal stability of hydrogenated materials is improved with the help of composition engineering.

Résumé

La réfrigération magnétique est une alternative intéressante aux méthodes de réfrigération traditionnelles, basées sur des cycles de compression et de détente de gaz, car elle présente des rendements énergétiques nettement plus élevés et permet d'éviter l'utilisation de gaz nocifs contribuant à l'effet de serre et problématique pour l'environnement. Cette technologie s'appuie sur l'effet magnétocalorique (EMC) géant de certains matériaux magnétiques autour de la température ambiante. Cet effet permet d'augmenter ou de diminuer la température du matériau lors de son aimantation ou désaimantation adiabatique autour de sa température de transition magnétique. Dans cette thèse, les propriétés structurales et magnétiques des matériaux magnétocaloriques La-Fe-Si et des alliages d'acier sont étudiés. En particulier, nous nous concentrons sur l'étude des propriétés de sorption d'hydrogène dans des matériaux La-Fe-Si, avec l'aide de grands instruments.